LEWIS-ACID BEHAVIOUR OF NEUTRAL AND CATIONIC FLUORIDOTUNGSTEN(V) AND (VI) COMPLEXES

DOUGLAS TURNBULL
Bachelor of Science, **University of Lethbridge, 2015**

A thesis submitted
in partial fulfilment of the requirements for the degree of

DOCTOR OF PHILOSOPHY

in

EARTH, SPACE, AND PHYSICAL SCIENCE

Department of Chemistry and Biochemistry
University of Lethbridge
LETHBRIDGE, ALBERTA, CANADA

LEWIS-ACID BEHAVIOUR OF NEUTRAL AND CATIONIC FLUORIDOTUNGSTEN(V) AND (VI) COMPLEXES

DOUGLAS TURNBULL

Date of defence: June 26, 2020

Dr. Michael Gerken Thesis Supervisor	Professor	Ph.D.
Dr. Stacey D. Wetmore Thesis Examination Committee Member	Professor	Ph.D.
Dr. René T. Boeré Thesis Examination Committee Member	Professor	Ph.D.
Dr. Locke Spencer Internal Examiner	Associate Professor	Ph.D.
Dr. Thomas Braun External Examiner Humboldt University of Berlin Berlin, Germany	Professor	Dr. rer. nat.
Dr. Paul G. Hayes Chair, Thesis Examination Committee	Professor	Ph.D.

Abstract

The Lewis-behaviour of WF_6 towards pyridine and derivatives thereof has been reinvestigated in detail. The stability of WF_6 towards main-group donor ligands has been exploited to develop synthetic routes to numerous complexes of $W(NC_6F_5)F_4$, $[WF_5]^+$, WF_5, and $[WF_4]^+$ with F^- and/or neutral N- and P-donor ligands. The isolation of such species has allowed for fundamental explorations of tungsten-based Lewis acids and weakly coordinating anions, the F^--donating and oxidising characteristics of the transition-metal hexafluorides, and the preparation of robust tungsten(V) complexes derived from thermodynamically unstable WF_5. The investigation of structure, bonding, and chemistry in these unique systems was undertaken using a combination of crystallographic, spectroscopic, and computational techniques, exemplifying the structural diversity found in hepta- and octacoordinate tungsten(V) and (VI) complexes.

Contributions of Authors

The following research chapters have been based on the following publications, the contents of which are reproduced with permission from the corresponding publishers:

Chapter 3 – Turnbull, D.; Kostiuk, N.; Wetmore, S. D.; Gerken, M. *J. Fluorine Chem.* **2018**, *215*, 1–9.

Chapter 4 – Turnbull, D.; Wetmore, S. D.; Gerken, M. *Inorg. Chem.* **2017**, *56* (20), 12581–12593.

Chapter 5 – Turnbull, D.; Wetmore, S. D.; Gerken, M. *Inorg. Chem.* **2019**, *58* (9), 6363–6375.

Chapter 6 – Turnbull, D.; Wetmore, S. D.; Gerken, M. *Angew. Chem. Int. Ed.* **2019**, *58* (37), 13035–13038.

Chapter 7 – Turnbull, D.; Hazendonk, P.; Wetmore, S. D.; Gerken, M. *Chem. Eur. J.* **2020,** *26* (30), 6879–6886.

In addition, sections of Chapters 1 and 2 are reproduced from the introductions and experimental sections, respectively, of the aforementioned publications as deemed necessary.

I am responsible for the entirety of the experimental and computational research reported herein. In Chapter 3, N.K. initially developed the synthesis of $WF_6(4\text{-}NC_5H_4N(CH_3)_2)$ and acquired a crystal structure and Raman spectrum of the compound, which I reproduced during the investigation. In Chapter 7, I performed preliminary simulations of the ^{19}F NMR spectrum of $[WF_5(NC_5H_5)_3]^+$ at –100 °C, and P.H. optimised the chemical shifts, coupling constants, and performed dynamic NMR simulations to generate rate constants.

Acknowledgements

First and foremost, I would like to thank my supervisor, Prof. Michael Gerken, for nearly a decade of mentorship during my time as an undergraduate and graduate student. He has been inspiring in his enthusiasm, kindness, and wisdom, all of which have helped me to mature as a chemist and, more generally, person. Words cannot adequately express my gratitude.

I extend my thanks to my committee members, Profs. René Boeré and Stacey Wetmore, for their advice and insight throughout my doctoral studies. I am especially grateful to Prof. Boeré for his knowledge in X-ray crystallography and electrochemistry, as well as Prof. Wetmore for her invaluable guidance and trust during our computational collaborations. I would also like to thank Profs. Locke Spencer and Thomas Braun for agreeing to participate in my defence and taking the time to read my thesis.

I would like to thank Tony Montina, Michael Opyr, and Prof. Paul Hazendonk for their expertise and assistance in NMR spectroscopy. More specifically, thanks go to Prof. Hazendonk for his aid with dynamic NMR simulations, and to Tony and Mike for helping solve the innumerable, seemingly unique, instrumental challenges I faced during my research. Similar thanks are extended to Kris and Heinz Fischer, to whom I, and our Raman spectrometer, are indebted.

During my time at the University of Lethbridge, I have had the honour and pleasure of working with several undergraduate and graduate students. Firstly, I would like to thank graduate students James Goettel and Praveen Chaudhary for their help during my initial undergraduate research, as well as Nathan Kostiuk, Daniel Stuart, Felix O'Donnell, and Nathan Hill for their camaraderie and patience during my extended rants about various

trivia. I would also like to thank undergraduate students Kyle Wynnyk for his friendship during our time together in the Gerken group, as well as Michael Harrison, Janelle Bykowski, and Dakota Leenstra, who I had the privilege of co-supervising.

I would like to thank the Natural Sciences and Engineering Research Council of Canada (NSERC), the Province of Alberta, and the University of Lethbridge for student scholarships. The computational resources provided by Prof. Wetmore, Westgrid and Compute Canada are also greatly appreciated.

Finally, my deepest thanks go to my parents, Renee McTighe and Jason Turnbull, and my brother, Stephen Turnbull, for their everlasting love, support, and confidence in me and my work. I would not be where I am without the three of you and, for that, I am eternally grateful.

Table of Contents

List of Tables

List of Figures

List of Abbreviations

General

aHF	anhydrous hydrogen fluoride
ax	axial
b.p.	boiling point
E_{ea}	electron affinity
$E_{½}$	half-wave potential
eq	equatorial
FEP	tetrafluoroethene-hexafluoropropene copolymer
FIA	fluoride-ion affinity
Kel-F	poly(chlorotrifluoroethene)
LMCT	ligand-to-metal charge transfer
m.p.	melting point
σ	standard deviation
θ	dihedral angle

Ligands

bipy	bipyridine
Cp	η^5-cyclopentadienyl
Cp*	η^5-pentamethylcyclopentadienyl
dmab	1,2-bis(dimethylarsino)benzene
dmpb	1,2-bis(dimethylphosphino)benzene
dmpe	1,2-bis(dimethylphosphino)ethane
dpb	1,2-diphosphinobenzene
dpe	1,2-diphosphinoethane
phen	phenanthroline

NMR Spectroscopy

d	doublet
dc	decet
J	scalar coupling constant
m	multiplet
NMR	nuclear magnetic resonance
q	quartet
qn	quintet
s	singlet
st	septet
t	triplet
δ	chemical shift

X-ray Crystallography

$a, b, c, \alpha, \beta, \gamma$	cell dimensions
F(000)	electrons per unit cell
GooF	goodness of fit
R_1	R-factor (agreement index)
T	temperature
V	cell volume
wR_2	weighted R-factor
Z	molecules per unit cell
λ	wavelength
μ	absorption coefficient
ρ_{calc}	calculated density

Chapter 1 - Introduction

1.1. Transition-Metal and Actinide Hexafluorides

The nine transition-metal hexafluorides, MF_6 (M = Mo, Tc, Ru, Rh, W, Re, Os, Ir, Pt), together with their actinide congeners, UF_6, NpF_6, and PuF_6, represent a class of compounds with fascinatingly diverse chemical properties despite their physical similarities.[1,2] The +6 oxidation state of the metal centres, which is unusually high in the cases of RhF_6, IrF_6, and PtF_6, and the electron deficiency caused by the electron-withdrawing fluorido ligands result in strong oxidising agents and Lewis-acids. As will be detailed in this chapter, the earlier transition-metal hexafluorides (WF_6 in particular) have been investigated heavily in terms of Lewis acid-base and ligand-substitution reactions with retention of the +6 oxidation state at the metal centre. However, the chemistry of those in groups 8–10 is dominated by their immensely oxidising behaviour. For the purposes of clarity, UF_6 will be considered together with the group-6 hexafluorides, as its chemical behaviours tend to be similar to those of MoF_6 and WF_6.

1.1.1. Syntheses and Physical Properties

The transition-metal and actinide hexafluorides are typically prepared via fluorination of the metal with F_2, either at high temperatures (≥ 300 °C) or, in the case of PtF_6, by passing electrical current through a platinum wire in the presence of F_2 at –196 °C.[2] The noteworthy exceptions are RuF_6 and RhF_6, which are best synthesised by oxidation of $[MF_6]^-$ (M = Ru, Rh) with AgF_3 in the presence of HF/BF_3 or HF/PnF_5 (Pn = As, Sb, Bi),[3,4] and ReF_6, which is prepared in high purity upon reduction of ReF_7 by rhenium metal at 250–400 °C.[5] Selected properties of the transition-metal and actinide hexafluorides are given in Table 1.1.

Table 1.1. Selected Physical and Chemical Properties of the Transition-Metal and Actinide Hexafluorides

	MoF_6	**TcF_6**	**RuF_6**	**RhF_6**
Configuration	[Kr]	[Kr]4*d*[1]	[Kr]4*d*[2]	[Kr]4*d*[3]
m.p. (°C)[a]	17.4	37.4	54.0	70.0
b.p. (°C)[a]	35.0	55.3	~70	~70
M–F (Å)[a]	1.813	1.812	1.816	1.821
E_{ea} (eV)[b]	4.23	5.89	7.01	6.80
$E_{½}$ ($[MF_6]^{0/-}$, V)[c]	1.70	3.0[e]	—	—
$E_{½}$ ($[MF_6]^{-/2-}$, V)[c]	–0.35	—	0.85	—
$E_{½}$ ($[MF_6]^{2-/3-}$, V)[c]	–2.25	—	–1.25	—
FIA (kJ mol^{-1})[b]	310 [82]	320 [232]	347 [366]	264 [316]

	WF_6	**ReF_6**	**OsF_6**	**IrF_6**	**PtF_6**
Configuration	[Xe]	[Xe]5*d*[1]	[Xe]5*d*[2]	[Xe]5*d*[3]	[Xe]5*d*[4]
m.p. (°C)[a]	1.9	18.5	33.2	44.4	61.3
b.p. (°C)[a]	17.5	33.7	45.9	53.0	69.1
M–F (Å)[a]	1.823	1.824	1.825	1.835	1.848
E_{ea} (eV)[d]	3.16	4.58	5.92	5.99	7.09
$E_{½}$ ($[MF_6]^{0/-}$, V)[c]	0.70	2.00	2.90	—	—
$E_{½}$ ($[MF_6]^{-/2-}$, V)[c]	–1.30	–0.20	0.25	1.25[f]	1.80[e,f]
$E_{½}$ ($[MF_6]^{2-/3-}$, V)[c]	—	—	–2.3	–1.0[f]	—
FIA (kJ mol^{-1})[d]	350 [–33]	338 [112]	345 [262]	293 [132]	331 [353]

	UF_6	**NpF_6**	**PuF_6**
Configuration	[Rn]	[Rn]5*f*[1]	[Rn]5*f*[2]
m.p. (°C)[a]	69.2	54.4	50.8
b.p. (°C)[a]	—	55.2	62.2
M–F (Å)[a]	1.996	1.981	1.971
E_{ea} (eV)	5.3[g]	—	—
$E_{½}$ ($[MF_6]^{0/-}$, V)	2.4[h]	—	—
FIA (kJ mol^{-1})	222[i]	—	—

[a]From reference 2. [b]From reference 11. Square brackets denote FIA under formation of "non-classical" $[MF_7]^-$. [c]From references 38 and 39, unless otherwise noted. [d]From reference 12. [e]Extrapolated potential. [f]From reference 40. [g]From reference 13. [h]From reference 30. [i]From reference 42.

The hexafluorides manifest as gases (M = W), liquids (M = Mo, Re), or highly volatile solids (M = Tc, Ru, Rh, Os, Ir, Pt, U) under standard conditions, with melting points ranging from 2 to 70 °C.[2] They, UF_6 notwithstanding, undergo solid-state phase transitions from a high-temperature disordered, liquid-crystalline cubic phase[6] to an ordered orthorhombic phase (*Pnma*) at *ca*. 0 °C.[2,7] Their low-temperature crystal structures reveal regular octahedral structures in which static Jahn-Teller effects are not unambiguously observed, regardless of the electron configuration of the metal centre.[7] The bond lengths are only slightly longer in the 5*d* species than their 4*d* counterparts and do not differ significantly across either period, with the exceptions of slight elongations in RhF_6 and IrF_6, and more prominent elongation in PtF_6. This slight increase in bond lengths is attributed to increased population of the t_{2g} orbital, which possesses $\pi^*(d(\mathrm{W})–p(\mathrm{F}))$ character. However, there is a simultaneous decrease in formula-unit volume across both periods, which would suggest greater intermolecular F···F interactions in the later transition-metal hexafluorides, consistent with their elevated melting points. Uranium hexafluoride prefers the ordered *Pnma* phase even at ambient temperature, as determined by neutron diffraction.[8]

Though static Jahn-Teller effects could not be observed crystallographically, dynamic Jahn-Teller effects have been observed in the vibrational spectra of MF_6 (M = Tc, Ru, Re, Os, Ir) as splitting of the e_g and/or t_{2g} vibrational modes.[1] This is noteworthy in the case of IrF_6, which is classically predicted to possess a non-degenerate t_{2g}^3 valence shell, as well as in the case of PtF_6, which does not undergo any observable Jahn-Teller distortion despite the expectation of a degenerate t_{2g}^4 valence shell. These anomalies are attributed to significant spin-orbit coupling, which can be observed in their absorption spectra in the

near-IR to UV regions;[9] such relativistic effects are not observed for the 4*d* hexafluorides. Spin-orbit coupling causes a splitting of the t_{2g} orbitals, resulting in degeneracy for IrF_6 and non-degeneracy for PtF_6. As such, PtF_6 exhibits temperature-independent paramagnetism, resulting in sharp resonances at highly unusual chemical shifts in its ^{19}F (3927.7 ppm) and ^{195}Pt (–4251.3 ppm) NMR spectra ($^1J(^{195}Pt–^{19}F)$ = 1086 Hz).[7] The remaining hexafluorides, with the obvious exceptions of MoF_6, WF_6, and UF_6, exhibit typical paramagnetic behaviour, though spin-orbit coupling serves to quench the magnetic moment of ReF_6 (0.25 μ_B) in comparison to TcF_6 (0.45 μ_B).[10]

1.1.2. Redox Chemistry

The transition-metal hexafluorides, as well as UF_6, are predicted to be immense oxidising agents,[11–13] with experimental and calculated E_{ea} values (3–7 eV) that rival, or even exceed, that of F_2 (3.40 eV).[14] This has allowed for the stabilisation of cations with elements in unusual oxidation states derived from oxidatively resistant substrates.

Platinum hexafluoride, one of the strongest oxidising agents of the series ($E_{ea} \simeq 7$ eV),[12] is famously capable of oxidising O_2 to $[O_2]^{+}$[15] and Xe to $[XeF]^+$,[16,17] the latter reaction being seminal in the field of noble-gas chemistry. The strongly oxidising $[O_2]^+$ cation is also stable as its $[RuF_6]^–$ and $[RhF_6]^–$ salts,[18] and the parent MF_6 (M = Ru, Rh) are expected to possess E_{ea} values close to that of PtF_6,[11] though their redox chemistry has not been explored in depth. Platinum hexafluoride has been observed directly to surpass the oxidising capabilities of F_2, as reactions with NOF and NO_2F have resulted in formation of F_2 along with $[NO]^+$ and $[NO_2]^+$ salts of $[PtF_6]^{n–}$ (n = 1, 2) anions,[19] though it seems to be stable in aHF.[20] Ab initio (CCSD(T)) studies of $[MF_7]^–$ (M = Ru, Rh, Pt) correspondingly reveal their thermodynamic instability towards formation of $[MF_6]^–$ and $F^{\cdot}$ via "non-

classical" anions.[11,12] In fact, only three oxidising agents are known to be stronger than PtF_6: superacidic HF/BF_3 or HF/PnF_5 (Pn = As, Sb, Bi) solutions of AgF_3 or NiF_4,[3,4] and $[KrF]^+$.[20]

Whereas IrF_6 ($E_{ea} \simeq 6$ eV) is not known to oxidise O_2, the reaction of Cl_2 (or CF_2Cl_2) with IrF_6 below –78 °C results in $[Cl_4][IrF_6]$, which is susceptible to decomposition to $[Cl_3][IrF_6]$ as well as oxidation to $[Cl_2O_2][HIr_2SbF_{12}]$ in aHF.[21] The reaction of Xe with IrF_6 to form $[XeF][IrF_6]$ only proceeds appreciably upon heating to 45 °C, though it is facilitated at –78 °C by HF/SbF_5, affording $[XeF][IrSbF_{11}]$.[22] Osmium hexafluoride ($E_{ea} \simeq 6$ eV) is incapable of oxidising Xe or Cl_2, though deeply coloured charge-transfer complexes occur in solution.[22,23] The $[Br_2][OsF_6]$ salt has, however, been isolated upon reaction of OsF_6 with Br_2.[23] Hexafluorobenzene was oxidised by OsF_6 in the presence of SbF_5, yielding $[C_6F_6][Os_2F_{11}]$; the reaction did not occur in the absence of SbF_5.[24] Reactions of PtF_6 with C_6F_6 resulted in ill-defined oxidative fluorination.[19]

The hexafluorides of molybdenum, rhenium, and uranium represent significantly weaker oxidising agents ($E_{ea} \simeq 4$–5 eV) than those of the later groups; the chemistry of TcF_6 has not explored in as much detail, likely due to its radioactivity. Rhenium hexafluoride is capable of reversibly oxidising I_2 to $[I_2]^+$ in IF_5, but not when WF_6 is used as solvent.[25] While MoF_6 and UF_6 are regarded as oxidising agents of similar strength, UF_6 oxidises Br_2 to $[Br(N_3C_6H_9)]^+$ and I_2 to $[I(NCCH_3)_2]^+$ in CH_3CN; MoF_6 oxidises I_2, but not Br_2, under similar conditions.[26,27] Uranium hexafluoride has been found to oxidise $C_2F_4Cl_2$, which typically resists oxidation, in the presence of SbF_5, resulting in the formation of $U^VF_5 \cdot 2SbF_5$.[28]

Tungsten hexafluoride is incapable of oxidising Br_2 or I_2 and is such a comparatively weak oxidising agent that it is, uniquely among the aforementioned hexafluorides, incapable of oxidising NO[19] or even Si.[29] Metallocenes, such as $FeCp_2$ (Cp = η^5-C_5H_5) and substituted derivatives thereof,[30,31] $CoCp_2$,[31] $NbCp_2Cl_2$,[32] and WCp_2Cl_2,[33] readily undergo one-electron oxidations upon reactions with the group-6 hexafluorides, yielding the corresponding "metallocenium" salts. Interestingly, the oxidation of WCp_2Cl_2 by WF_6 led to, alongside $[W^{VI}Cp_2Cl_2][W^{V}F_6]_2$, two-electron reduction of WF_6 to afford $[W^{V}Cp_2Cl_2]_2[W^{IV}{}_4F_{18}]$, the crystal structure of which reveals a distorted-tetrahedral cage anion.[34]

The group-6 hexafluorides have been subject to numerous cyclic-voltammetric studies, typically employing $[MF_6]^-$ (M = Mo, W, U) salts as the analytes in CH_3CN or CH_2Cl_2 solvent, though there have been direct voltammetric studies of MoF_6 and WF_6 in aHF.[35,36] In all cases, reversible $[MF_6]^{0/-}$ redox couples ($E_{½}$ vs. $[Ag]^+/Ag$; M = Mo: *ca*. +1.7 V, W: *ca*. +0.7 V, U: *ca*. +2.4 V) and $[MF_6]^{-/2-}$ (M = Mo: –0.4 V, W: –1.3 V, U: –2.8 V) could be established, as well as the $[MoF_6]^{2-/3-}$ couple (–2.25 V).[30,31,37–39] These studies corroborate UF_6 being the strongest, and WF_6 the weakest, oxidising agent of the group-6 series.

Heath and co-workers also conducted voltammetric and polarographic studies that elucidated reversible $[MF_6]^{0/-}$ redox couples for ReF_6 (+2.00 V) and OsF_6 (+2.90 V) in CH_3CN,[38,39] further establishing the proportional increase of E_{ea} with increasing *d*-electron count at the metal centre. Half-wave potentials for the remaining $[MF_6]^{0/-}$ couples have not been reported, though that of TcF_6 could be extrapolated (+3.0 V).[39]

The observed $E_{½}$ values and calculated E_{ea} values support the general trend that the oxidising capabilities of the transition-metal hexafluorides decrease within each group from the 4*d* to 5*d* periods, as well as increase across each period with increasing atomic number, in increments of *ca*. 1 V/1 eV. The exceptions to the cross-period trend occur between OsF_6 and IrF_6, as well as RuF_6 and RhF_6; IrF_6 is predicted to be 0.2 eV stronger than OsF_6,[12] whereas RhF_6 is predicted to be 0.1 eV weaker than RuF_6.[11] These phenomena have been attributed to an interelectronic repulsion energy in low-spin, d^4 $[MF_6]^-$ (M = Rh, Ir) resulting in a decreased E_{ea} for d^3 MF_6.[39] However, spin pairing alone would predict OsF_6 to be a stronger oxidising agent than IrF_6 in the absence of spin-orbit coupling.[40] Theoretical energy corrections for spin-orbit coupling in the 5*d* hexafluorides have been predicted to simultaneously decrease the E_{ea} of OsF_6 and increase the E_{ea} of IrF_6,[12] reflecting the experimentally observed trend in affinities.

1.1.3. Lewis-Acid Chemistry

1.1.3.1. Towards the Fluoride Ion

The transition-metal hexafluorides are invariably predicted to be moderate Lewis acids on the basis of their FIAs (264–345 kJ mol^{-1}),[11,12] which are comparable to that of BF_3 (344 kJ mol^{-1}),[41] while UF_6 is somewhat weaker (222 kJ mol^{-1}).[42] However, examples of $[MF_7]^-$ or $[MF_8]^{2-}$ anions are only known for the hexafluorides of groups 6 and 7. Molski and Seppelt have postulated that this is due to the lower charges on the metal centres of the hexafluorides of groups 8–10, or their partially filled *d* orbitals, either of which would serve to preclude bonding interactions between the metal centre and incoming fluorido ligand.[1] This is in addition to the aforementioned instability of $[PtF_7]^-$ towards oxidation of F^- to F_2.

Salts of $[MF_7]^-$ and $[MF_8]^{2-}$ (M = Mo, W, Re, U) are readily prepared upon the direct reaction of MF_6 with a F^- source, though [Cat][MF_7] ([Cat]$^+$ = Rb^+, Cs^+), save for $[UF_7]^-$, were initially prepared via reaction of MF_6 with [Cat]I in the presence of IF_5,[43–45] and $[MF_8]^{2-}$ salts have been prepared via pyrolysis of $[MF_7]^-$.[45,46] The stability of $[MF_7]^-$ salts towards such decomposition is dependent on the size of the cation, with larger cations (e.g., Cs^+) providing more stability than smaller ones (e.g., Rb^+, K^+).[45]

Crystallographic studies have determined that the anions of Cs[MoF_7] and Cs[WF_7] adopt ideal monocapped-octahedral geometries,[47] whereas the isoelectronic compound ReF_7 is a C_s-distorted pentagonal bipyramid.[48] Minimal differences in energy are known to exist between the three model polyhedra of heptacoordinate complexes (the pentagonal bipyramid, monocapped octahedron, and monocapped trigonal prism). For instance, multiple studies have concluded that the differences in energy between stereoisomers of $[WF_7]^-$ are within 5 kJ mol^{-1}.[12,49,50] This can be contrasted with the Bailar ($O_h \rightarrow D_{3h}$) twists of MoF_6 (28 kJ mol^{-1}) and WF_6 (46 kJ mol^{-1}),[51] illustrating a much greater disparity in the relative stabilities of the octahedron and trigonal prism. The stereochemical non-rigidity of $[MF_7]^-$ in solution is evidenced in their ^{19}F NMR spectra, which reveal broad singlets due to intramolecular exchange of the fluorido ligands.[47]

The $[WF_8]^{2-}$, $[ReF_8]^{2-}$, and $[UF_8]^{2-}$ anions adopt regular square-antiprismatic geometries irrespectively of the electron configuration of the metal centre,[52,53] which is also observed for d^0 $[ReF_8]^-$[53] and the main-group analogues $[IF_8]^-$[54] and $[XeF_8]^{2-}$.[52,55]

1.1.3.2. Towards Neutral Donor Ligands

Tungsten hexafluoride, as a relatively weak oxidising agent, is the only transition-metal hexafluoride that is known to be stable in the presence of organic donor ligands; the

reaction of UF_6 with 2,2′-bipyridine (2,2′-bipy) resulted in spontaneous reduction to uranium(V) and formation of UF_5(2,2′-bipy).[56] Tebbe and Muetterties originally reported reactions of WF_6 with $Pn(CH_3)_3$ (Pn = N, P) and C_5H_5N, isolating $WF_6\{Pn(CH_3)_3\}$ and $WF_6(NC_5H_5)_n$ (n = 1, 2) as thermally stable solids that were characterised by ^{19}F NMR spectroscopy.[57] Their ambient-temperature ^{19}F NMR spectra consisted of broad singlets (with the exception of a broad doublet produced by $WF_6\{P(CH_3)_3\}$ due to $^2J(^{19}F–^{31}P)$ coupling), attributed to the six fluorido ligands undergoing rapid exchange in solution. Low-temperature ^{19}F NMR spectroscopic studies of mixtures of WF_6 and $S(CH_3)_2$ revealed that $WF_6\{S(CH_3)_2\}$ still undergoes rapid intramolecular ligand exchange at –75 °C; further cooling results in precipitation from the vinyl chloride solvent. Meanwhile, $WF_6\{S(CH_3)_2\}_2$ adopts a rigid bicapped-trigonal-prismatic structure at –160 °C in which the sulfur atoms occupy the capping positions (though this was not deduced in the original article).[58] It was later determined by low-temperature ^{19}F NMR spectroscopy that the $WF_6(NC_5H_5)_n$ adducts adopt monocapped (n = 1) and bicapped (n = 2) trigonal-prismatic geometries in solution.[59] The similarities between the ^{19}F NMR spectra of $WF_6(NC_5H_5)_2$ and $WF_6\{S(CH_3)_2\}_2$ suggest that they share a common geometry.

Due to the fluxional nature of the adducts in solution on the NMR timescale, X-ray crystallography has been more commonly used to assess their geometries. The ambient-temperature crystal structures of WF_6(2-NC_5H_4F)[60] and $WF_6(NC_5H_5)_2$[59] revealed mono- and bicapped-trigonal-prismatic geometries for the adducts, respectively. Interestingly, it was determined that, although $WF_6\{P(CH_3)_3\}$ adopts the same geometry as the heptacoordinate N-donor adducts,[50] $WF_6\{P(C_6H_5)(CH_3)_2\}$ prefers a monocapped-octahedral ligand arrangement,[50] as observed for the $[WF_7]^–$ anion.[47] This further illustrates

the marginal differences in energy between heptacoordinate geometries, as well as the dependence of the resultant geometry on the chosen ligand.

The reaction of 2,2′-bipy with a molar equivalent of WF_6 was reported to result in WF_6(2,2′-bipy),[61] which was also claimed to arise upon dismutation of WOF_4(2,2′-bipy), the other product of which was WO_2F_2(2,2′-bipy).[62] However, if WF_6 is present in excess, ligand-induced autoionisation occurs and $[WF_4(2,2'\text{-bipy})_2]^{2+}$ salts are obtained.[61,63] Recently, reactions of WF_6 with 1,2-bis(dimethylphosphino)benzene (dmpb) and its arsenic-containing analogue (dmab) were reported to result in ligand-induced autoionisation and the formation of $[WF_4(L)_2][WF_7]_2$ (L = dmpb, dmab), whereas reactions of WF_6 with monodentate AsR_3 (R = CH_3, C_2H_5) yielded $WF_6(AsR_3)$.[64] Crystal structures of $[WF_4(2,2'\text{-bipy})_2]^{2+}$ and $[WF_4(L)_2]^{2+}$ salts revealed trigonal-dodecahedral geometries about the tungsten(VI) centres.

1.1.4. Ligand-Substitution Chemistry

1.1.4.1. Derivatives Containing M–C Bonds

The only isolated derivatives of MF_6 containing M–C σ bonds are $M(CH_3)_6$ (M = Mo, W), which have been prepared via reaction of MF_6 with $Zn(CH_3)_2$.[65,66] Hexamethyltungsten(VI) was initially prepared using WCl_6 and $LiCH_3$[67] or $Al(CH_3)_3$;[68] $Re(CH_3)_6$ is also known, though it was instead prepared using $ReOCl_4$[65] or $ReO(CH_3)_4$[68] as rhenium(VI) sources, rather than ReF_6. The group-6 complexes adopt C_{3v}-distorted trigonal-prismatic geometries,[65,66,69] whereas $Re(CH_3)_6$ prefers a trigonal prism of approximately D_{3h} symmetry.[65,69] Intermediate $WF_x(CH_3)_{6-x}$ species were observed in small quantities by ^{19}F NMR spectroscopy during the reaction of WF_6 with $Zn(CH_3)_2$, though only $WF_5(CH_3)$ could be assigned.[65]

A cyclopentadienyl derivative of WF_6, $W(Cp^*)F_5$ ($Cp^* = \eta^5\text{-}C_5(CH_3)_5$), was prepared upon oxidation of $W^V(Cp^*)F_4$ in air.[70] Its crystal structure reveals regular η^5-coordination of the $[Cp^*]^-$ ligand and an octahedral geometry with the centroid of the $[Cp^*]^-$ ligand representing one of the octahedral coordination sites. The ^{1}H NMR spectrum gives rise to a quintet as a result of through-space coupling to the fluorido ligands (J(H–F_{eq}) = 1.1 Hz, J(H–F_{ax}) = 0.7 Hz). The deviations of $M(CH_3)_6$ (M = Mo, W, Re) from regular octahedra can be attributed to second-order Jahn-Teller (SOJT) distortions (see section 8.2.5.2).

Such distortions from octahedra to trigonal prisms are predicted to be ubiquitous for exclusively σ-bonded, high-oxidation-state transition-metal complexes.[71] Systems with extensive π bonding, such as MoF_6 and WF_6, do not undergo such distortions. This has been attributed to increased steric repulsion between the charge-dense fluorido ligands, as well as π-donation that results in nominal 18-electron complexes,[72] though it could also be explained in terms of the increased HOMO-LUMO gap expected for d^0 complexes with π-donor (weak-field) ligands. The secondary SOJT distortion from D_{3h} to C_{3v} symmetry in $W(CH_3)_6$ (neglecting slight lowering of symmetry due to rotation of the methyl ligands) results in further mixing of metal- and ligand-based orbitals, resulting in increased $\sigma(CH)\rightarrow d_{z^2}(W)$ bonding (i.e., agostic interactions).[73] This secondary distortion does not occur in $Re(CH_3)_6$ as it would result in an unfavourable destabilisation of the SOMO; the hypothetical $[Re(CH_3)_6]^+$ cation is expected to undergo a more severe $D_{3h} \rightarrow C_{3v}$ distortion than $W(CH_3)_6$.[74]

1.1.4.2. Derivatives Containing M≡N or M=N Bonds

Reactions of WF_6 with primary amines, RNH_2, or their silazane derivatives, $RN\{Si(CH_3)_3\}_2$, result in the formation of imido complexes along with elimination of HF or $(CH_3)_3SiF$. It was first determined by ^{19}F NMR spectroscopy that the reaction of WF_6 with RNH_2 (R = H, C_4H_9) in CH_3CN affords $W(NR)F_4(NCCH_3)$ if the amine is carefully added in small amounts to the solution, whereas $[RNH_3][W(NR)F_5]$ were observed if additional amine was introduced to the reaction mixture.[75]

The formation of $[RNH_3][W(NR)F_5]$ (R = CH_3, C_2H_5, C_4H_9) salts upon the reaction of WF_6 with aliphatic primary amines was also noted by Winfield and co-workers,[76,77] whereas the reaction of WF_6 with $CH_3NHSi(CH_3)_3$ generated a mixture of $[CH_3NH_3][W(NCH_3)F_5]$ and $[CH_3NH_3][W_2(NCH_3)_2F_9]$.[76] Alkylammonium salts were observed even when an excess of WF_6 was employed, and it was hypothesised that an intermediate $WF_6(NH_2R)$ adduct is initially formed (Eq. 1.1), which eliminates HF to form $W(NHR)F_5$ as a second intermediate (Eq. 1.2) before the two intermediates react to form $[RNH_3][W(NR)F_5]$ and WF_6 (Eq. 1.3).[77] Meanwhile, neutral $W(NCH_3)F_4$ adducts with N- and O-donor ligands were accessed upon reaction of WF_6 with $CH_3N\{Si(CH_3)_3\}_2$ in the presence of excess ligand.[77,78] Multinuclear NMR spectroscopic studies of these complexes revealed $J(^{14}N–^{1}H)$ and $J(^{19}F–^{14}N)$ coupling, suggesting linear R–N–W–X (X = N, F) skeletons and thus significant W≡N character from the imido ligand.

$$WF_6 + RNH_2 \rightarrow WF_6(NH_2R) \quad (1.1)$$

$$WF_6(NH_2R) \rightarrow W(NHR)F_5 + HF \quad (1.2)$$

$$WF_6(NH_2R) + W(NHR)F_5 \rightarrow [RNH_3][W(NR)F_5] + WF_6 \quad (1.3)$$

In reactions of MF_6 (M = Mo, W) with $TeF_5NHSi(CH_3)_3$, equimolar amounts of neutral $M(NTeF_5)F_4$ and TeF_5NH_2 were obtained, rather than ionic products.[79] This, in addition to the extremely weak basicity of TeF_5NH_2,[80] corroborates the notion that iminolysis proceeds via formation of intermediate MF_6 adducts (Eq. 1.1).

The reaction of WF_6 with $C_6F_5NH_2$ in $CF_2ClCFCl_2$ was studied and several products, $[C_6F_5NH_3]^+$ salts of the $[W(NC_6F_5)F_5]^-$, $[W_2(NC_6F_5)_2F_9]^-$, and F^- anions, were observed in admixture.[81] This mixture was characterised by IR spectroscopy in the solid state and ^{19}F NMR spectroscopy in CH_3CN, where the $[W_2(NC_6F_5)OF_9]^-$ anion was also observed due to partial hydrolysis. Recrystallisation of this mixture from CF_3COOH afforded $[C_6F_5NH_3][W_2(NC_6F_5)_2F_9]$ as the only tungsten-containing product, which was stuided by ambient-temperature X-ray crystallography, confirming the linear nature of the imido ligand and presence of W≡N bonding.

In addition to the aforementioned syntheses of $W(NR)F_4$ derivatives via condensation reactions with primary amines and silazanes, chloroimido complexes have been prepared by Dehnicke and co-workers. Whereas $W(NCl)F_4$ was prepared via fluorination of $WNCl_3$ or $W(NCl)Cl_4$ with dilute F_2/N_2,[82] its molybdenum analogue, $Mo(NCl)F_4$, could be prepared via fluorination of $MoNCl_3$,[82] $Mo(NSCl)Cl_4$,[83] or $Mo(N_3S_2)Cl_3$.[83] Infrared spectroscopy indicated that $M(NCl)F_4$ (M = Mo, W) adopt ill-defined oligomeric structures in the solid state.[82,83] However, they react with CH_3CN to form monomeric $M(NCl)F_4(NCCH_3)$, which were characterised by IR spectroscopy and X-ray crystallography.[82,83] The reaction of $Mo(NCl)F_4$ with NaF and 15-crown-5 in CH_3CN yielded [Na(15-crown-5)][$Mo(NCl)F_5$];[84] $[W(NCl)F_5]^-$ salts were instead prepared via halogen-exchange reactions between $W(NCl)Cl_4$ and alkali-metal fluorides in the

presence of crown ethers,[85,86] as well as the reaction of $WNCl_3$ with $(CH_3)_3SnF$ and KF.[87] These salts, like their neutral parent compounds, were characterised by IR spectroscopy and X-ray crystallography.

Terminal nitrides, MNF_3, have yet to be isolated, though MNF_3 (M = Mo, W, U) were observed by IR spectroscopy in noble-gas matrices upon reaction of laser-ablated metal with NF_3; the heavier MPF_3 congeners were also observed when PF_3 was employed.[88,89] The $[As(C_6H_5)_4][MoNF_4]$ salt was prepared via reaction of the corresponding $[MoNCl_4]^-$ salt with AgF in CH_3CN,[90] whereas [Na(15-crown-5)][$MoNF_4$]·CH_3CN was prepared via fluorination of $Mo(NSCl)Cl_4$ with NaF in the presence of 15-crown-5 in CH_3CN.[91] Interestingly, crystallographic studies revealed that the former forms columns of infinitely nitrogen-bridged $[MoNF_4]^-$ anions,[90] whereas in the latter, the anion instead dimerises to adopt a fluorine-bridged $[Mo_2N_2F_8]^{2-}$ motif with terminal nitrido ligands and extensive Na···F contacts.[91]

1.1.4.3. Derivatives Containing M–N Bonds

There are comparatively fewer examples of MF_6 derivatives containing M–N bonds than those with M≡N or M=N bonds. The reaction of WF_6 with a slight molar deficiency of $(C_2H_5)_2NSi(CH_3)_3$ or $(CF_3CH_2)_2NH$ resulted in formation of $WF_5\{N(C_2H_5)_2\}$[92,93] and $WF_5\{N(CH_2CF_3)_2\}$,[94] respectively. Their ambient-temperature ^{19}F NMR spectra indicate rapid exchange of the fluorido ligands, though the crystal structure of the latter reveals a regular octahedral geometry about the tungsten centre. The reaction of WF_6 with an excess of $(CF_3CH_2)_2NH$ resulted in deprotonation of $WF_5\{N(CH_2CF_3)_2\}$, rather than the expected formation of $WF_4\{N(CH_2CF_3)_2\}_2$.[94] This resulted in the formation of

$[(CF_3CH_2)_2NH_2][WF_5\{\eta^2\text{-}CH(CF_3)N(CH_2CF_3)\}]$ containing a W–N–C three-membered metallocycle, as determined by X-ray crystallography.

The reaction of WF_6 with $(CH_3)_3SiNS(O)(CH_3)_2$ resulted in the formation of $WF_5\{NS(O)(CH_3)_2\}$ and *cis*-$WF_4\{NS(O)(CH_3)_2\}_2$, the structures of which were determined crystallographically.[95] Further substitution to *mer*-$WF_3\{NS(O)(CH_3)_2\}_3$ was achieved using $Li[NS(O)(CH_3)_2]$. Reactions of MoF_6 and WF_6 with excess $(CH_3)_3SiN_3$ in CH_3CN led to formations of homoleptic $M(N_3)_6$ (M = Mo, W),[96] whereas WF_6 was reacted with a molar deficiency of $(CH_3)_3SiN_3$ to afford $WF_5(N_3)$.[97] The crystal structures of these azidotungsten(VI) complexes were reported (despite their observed explosivity in the solid state), revealing effectively linear N_3 moieties. The attempted formation of $ReF_5(N_3)$ via an analogous route resulted in $Re^{VII}NF_4$ and a brown solid of indefinite composition, as well as numerous detonations. These products could be converted to $Re^{VII}F_5(NX)$ (X = F, Cl, Br) after treatment with XeF_2, ClF_3, or BrF_3, respectively;[98,99] treatment with ClF_3 resulted in a 1:1 mixture of the chloro- and fluoroimido products. No rhenium(VI) species were observed directly.

1.1.4.4. Derivatives Containing M=O Bonds

The most commonly observed derivative of MF_6 is MOF_4, whether deliberately or accidentally as a result of hydrolysis. Oxide tetrafluorides are known for groups 6 (including $CrOF_4$ and UOF_4) through 8; attempts to prepare $RhOF_4$, $IrOF_4$, and $PtOF_4$ resulted in reduction of the metal centre to afford $[H_3O][M^VF_6]$ or $[H_3O]_2[M^{IV}F_6]$ salts,[100] revealing instability of the metal centre towards oxidation of the oxido ligand.

The most facile preparations of MOF_4 involve direct ligand-substitution reactions of MF_6 with H_2O,[101,102] B_2O_3,[103] SiO_2/HF (indirect hydrolysis),[101,104,105] and in one

synthesis of $OsOF_4$, a reaction with OsO_4 to afford $Os^{VIII}O_2F_4 \cdot Os^{VI}OF_4$,[106] which was then decomposed *in vacuo* to yield $OsOF_4$.[107] The non-existence of CrF_6 precludes analogous synthetic routes of $CrOF_4$, which is instead best prepared via oxidation of CrO_2F_2 with KrF_2.[108] Rather than the expected MOF_4, WF_6 is hydrolysed to $[H_3O][W_2O_2F_9]$,[102] ReF_6 to a mixture of $ReOF_4$ and $[H_3O][Re_2O_2F_9]$,[102] and RuF_6 to $[H_3O][Ru^VF_6]$;[100] $RuOF_4$ was instead prepared via fluorination of RuO_2 with F_2.[109]

Due to the pentacoordination of monomeric MOF_4, they are highly prone to fluorine bridging in the solid state to achieve hexacoordinate (or in the case of UOF_4, heptacoordinate) metal centres. The only possible exception is $RuOF_4$, one modification of which has been described as monomeric (though it is perhaps better described as dimeric, considering its weak intermolecular Ru···F interactions).[107] However, while fluorine-bridging is common among the various known MOF_4 modifications, the structural features of the resultant aggregate species are diverse. Tungsten oxide tetrafluoride is tetrameric in the solid state,[110,111] whereas $CrOF_4$,[112] $MoOF_4$,[110,113] and $ReOF_4$[110] form zig-zag polymeric chains. The oxide tetrafluorides of technetium and osmium also adopt similar polymeric motifs,[107,110] though second modifications are known in both cases: for the former, a trimeric polymorph,[114,115] and for the latter, a helical polymer.[107] Ruthenium oxide tetrafluoride adopts the same helical-polymeric form that was observed for $OsOF_4$.[107] Two modifications are known for UOF_4, both of which possess pentagonal-bipyramidal uranium centres.[105,116] It has been suggested that the oxido ligand occupies an axial position in α-UOF_4[105] and an equatorial position in β-UOF_4.[116] However, these precise descriptions are dubious based on the quality of the crystallographic data reported.

The group-6 oxide tetrafluorides exhibit moderate Lewis-acid behaviour, allowing for the isolation of MOF_4 (M = Mo, W) adducts with various neutral main-group donor ligands.[60,117–119] The adducts tend to be octahedral, in which the donor ligand occupies the coordination site *trans* to the oxido ligand, as determined by X-ray crystallography and ^{19}F NMR spectroscopy. However, in the case of WOF_4, heptacoordinate adducts with C_5H_5N,[117] as well as the chelating diphosphines 1,2-bis(dimethylphosphino)ethane (dmpe) and dmpb,[120] have been reported, the crystal structures of which reveal pentagonal-bipyramidal geometries with axial oxido ligands. In the case of $WOF_4(NC_5H_5)_2$, the donor ligands occupy non-adjacent equatorial positions, whereas the bite angle of the diphosphines necessitate adjacent coordination of the phosphorus atoms in their WOF_4 adducts.

Similarly, reactions of MOF_4 with F^- donors, along with hydrolysis of MF_6 in sufficiently basic conditions, have resulted in various $[MOF_5]^-$ (M = Cr,[121,122] Mo,[123–125] W,[123,124,126] Re,[127] U[128]), $[M_2O_2F_9]^-$ (M = Mo,[129,130] W[102,123]), and $[MOF_6]^{2-}$ (M = Mo,[123] W[123,131]) salts. Crystal structures of $[WOF_5]^-$ salts typically reveal disorder of the oxido and fluorido ligands throughout the octahedral coordination sphere,[64,132–134] as did a combined neutron powder diffraction and ^{19}F NMR spectroscopic study of $Cs[UOF_5]$.[135] However, recent examples of ordered $[MOF_5]^-$ (M = Cr,[136] Mo,[136] W[136,137]) were reported. Fluorine-bridged, dioctahedral $[M_2O_2F_9]^-$ (M = Mo,[130] W[63,102,138,139]) do not exhibit such disorder due to preferential positioning of the oxido ligands *trans* to the bridging fluorido ligand. The $[WOF_6]^{2-}$ anion was found to adopt a pentagonal-bipyramidal geometry with an axial oxido ligand by ^{19}F NMR spectroscopy,[131] which is consistent with the crystal structure of isoelectronic $[Re^{VII}OF_6]^-$.[47]

Employment of the covalent F^- donors NgF_2 (Ng = Kr, Xe) in reactions with MOF_4 (M = Mo, W) resulted in chain adducts of the compositions $NgF_2 \cdot nMOF_4$ (n = 1–4), in which M–F–M bridges were observed for $n > 1$, as well as increasing $[NgF][M_nO_nF_{4n+1}]$ character with increasing n.[140–142] Recently, $NgF_2 \cdot n CrOF_4$ (n = 1, 2) were reported, representing the first neutral $CrOF_4$ adducts.[112] Unlike the heavier analogues, $NgF_2 \cdot 2CrOF_4$ do not exhibit Cr–F–Cr bridging nor $[NgF]^+$ character, but rather symmetric coordination of NgF_2 by two $CrOF_4$ molecules.

Pure transition-metal dioxide difluorides, MO_2F_2, are comparatively much rarer. Only CrO_2F_2 and MoO_2F_2 are known, and neither are prepared via ligand substitution of the parent transition-metal hexafluoride; CrO_2F_2 has been prepared by fluorination of CrO_3 or CrO_2Cl_2 using a variety of fluorinating agents (HF,[143] MoF_6,[144] WF_6,[144] etc.), whereas MoO_2F_2 was prepared via pyrolysis of $Na_2[MoO_2F_4]$ at 300 °C.[145] In contrast, UO_2F_2 can be generated in admixture with $UO_2F_2(OH_2)_2$ upon hydrolysis of UF_6.[146] The structure of MoO_2F_2 was ascertained from Rietveld refinement of the X-ray powder diffraction data, revealing cyclic, fluorine-bridged $(MoOF_2)_3$ moieties that are oxygen-bridged along the *b* axis. This results in infinite columns in which the terminal oxido and fluorido ligands are disordered.[145]

Despite their elusive natures, MoO_2F_2 and WO_2F_2 are readily synthesised as complexes with neutral donor ligands upon reactions of MF_6 with $\{(CH_3)_3Si\}_2O$ and/or H_2O in the presence of mono- or bidentate N- or O-donor ligands.[118,119] In these complexes, the metal centres prefer octahedral coordination environments, *cis*-oriented oxido ligands, and donor ligands positioned *trans* to the oxido ligands. Meanwhile, UO_2F_2 reacts with

NH_3 to afford pentagonal-bipyramidal $UO_2F_2(NH_3)_3$, in which the oxido ligands adopt a mutually *trans* orientation, occupying the axial positions.[147]

Numerous *cis*-$[MO_2F_4]^{2-}$ (M = Cr,[148] Mo,[149] W[149]) salts are known and the crystal structures of the molybdenum and tungsten compounds reveal static and/or dynamic disorder of the oxido and fluorido ligands.[149] The hypothetical $[MO_2F_3]^-$ anions are found to dimerise in $[Mo_2O_4F_6]^{2-}$ [125,150] and $[W_2O_4F_6]^{2-}$ salts,[151] resulting in structures similar to valence-isoelectronic $[Mo_2N_2F_8]^{2-}$.[91] The structural characteristics of $[CrO_2F_3]^-$ have yet to be elucidated but IR spectra of its $[NO]^+$ and $[NO_2]^+$ salts were analysed assuming *cis*-dioxo arrangements and fluorine-bridged structures.[152] Anionic derivatives of UO_2F_2 with various stoichiometries of F^- ($[UO_2F_3]^-$, $[UO_2F_4]^{2-}$, $[UO_2F_5]^{3-}$, etc.) are known.[146] Among these anions, the ubiquity of the pentagonal-bipyramidal *trans*-UO_2F_5 coordination sphere is evidenced; the trianion is monomeric[153] whereas the dianion dimerises to form $[U_2O_4F_8]^{4-}$.[154,155] Monoanionic derivatives of UO_2F_2 are subject to polymerisation to achieve local pentagonal-bipyramidal geometries, which was exploited by O'Hare and co-workers,[156–159] as well as Albrecht-Schmidt and co-workers,[160,161] in the development of variable-dimensional frameworks.

1.1.4.5. Derivatives Containing M–O Bonds

The group-6 hexafluorides are capable of undergoing reactions with a variety of main-group alkoxides or phenoxides, typically alcohols/phenols or siloxanes, yielding complexes of the general form $MF_n(OR)_{6-n}$ (M = Mo, W, U), which have been characterised primarily by ^{19}F NMR spectroscopy. The first example of such a species was $WF_5(OCH_3)$, synthesised by Noble and Winfield via reaction of WF_6 with $SO(OCH_3)_2$,[162] though $Si(CH_3)_x(OCH_3)_{4-x}$ (x = 0–3),[163–165] $P(OCH_3)_3$,[164] $B(OCH_3)_3$,[166] and $Nb(OCH_3)_5$[166]

have been similarly employed as $[OCH_3]^-$ sources in its formation. It is susceptible to slow decomposition at ambient temperature and behaves as a $[CH_3]^+$ source in the presence of $P(OCH_3)_3$ or C_6H_6.[164] The ethoxo and phenoxo derivatives can be similarly prepared; while $WF_5(OC_2H_5)$ is unstable under ambient conditions, $WF_5(OC_6H_5)$ is stable up to 180 °C.[164,165] Though $UF_5(OCH_3)_3$ was readily formed upon reaction of UF_6 with CH_3OH[167] or $(CH_3)_3SiOCH_3$,[168] $MoF_5(OCH_3)$ could not be observed, and $MoF_6/Si(CH_3)_x(OCH_3)_{4-x}$ (x = 0–3) mixtures were found to be explosive if warmed too hastily.[169]

Higher substitutions of $MF_n(OCH_3)_{6-n}$ could be prepared using increased proportions of $Si(CH_3)_x(OCH_3)_{4-x}$ (x = 0–3) with respect to MF_6. In the tungsten series, all intermediate species up to $WF(OCH_3)_5$ could be synthesised,[163] whereas $W(OCH_3)_6$ could only be observed in admixture with the lesser substituted species unless $Na[OCH_3]$ was employed.[170] Meanwhile, in the uranium series, $U(OCH_3)_6$ could be prepared readily without the harsher $[CH_3O]^-$ source,[170] though $Na[OCH_3]$ was used in one preparation.[168] Despite the instability of $MoF_5(OCH_3)$, $MoF_n(OCH_3)_{6-n}$ (n = 0–2) could be prepared as involatile liquids (n = 1, 2)[169] or a crystalline solid (n = 0).[170] Fully substituted $Re(OCH_3)_6$ was also prepared via reaction of ReF_6 with $Si(OCH_3)_4$;[170] lesser substituted derivatives have not been reported.

Lesser substituted derivatives of MoF_6 could be stabilised by the more electron-withdrawing ligands, as evidenced by the synthesis of the complete $MoF_n(OCH_2CF_3)_{6-n}$ (n = 0–6) series upon reaction of MoF_6 with $(CH_3)_3SiOCH_2CF_3$,[171] as well as $MoF_5(OC_6F_5)$ using $(CH_3)_3SiOC_6F_5/C_6F_5OH$ (*ca*. 13:1).[51] The tungsten analogues $WF_5(OCH_2CF_3)$,[94] *cis*-$WF_4(OCH_2CF_3)_4$,[94] and $WF_5(OC_6F_5)$[51] were also prepared similarly, whereas

$WF_5\{OC(CF_3)_3\}$ was instead formed using $Li[OC(CF_3)_3]$.[51] The crystal structures of $MoF_5(OC_6F_5)$[51] and *cis*-$MF_4(OCH_2CF_3)_2$ (M = Mo,[51] W[94]) establish octahedral geometries and, in the case of the disubstituted species, exclusive retention of the *cis* stereochemistry in the solid state. Like WF_6, $WF_5(OCH_2CF_3)$ is F^- accepting, forming $Cs[WF_6(OCH_2CF_3)]$ upon reaction with CsF, the crystal structure of which reveals a monocapped-octahedral anion.[94]

Reactions of MF_6 with $B(OTeF_5)_3$ allowed for the identification of $MF_n(OTeF_5)_{6-n}$ (M = W, n = 1–5; M = U, n = 1–6) by ^{19}F NMR spectroscopy.[172,173] In similar reactions with MoF_6, formation of $MoOF_3(OTeF_5)$ was observed with concomitant evolution of TeF_6,[174] whereas members of the tungsten series were found to decompose via Te=O, rather than W=O, bond formation.[172] The persubstituted compounds were accessed via oxidation of $MoCl_5$ with TeF_5OCl and disproportionation of $W(OTeF_5)_5$, respectively.[175] Their crystal structures, as well as that of $U(OTeF_5)_6$,[176] reveal regular octahedral geometries about the metal and tellurium centres.

The geometries of $MF_5(OR)$ are invariably octahedral, in which the fluorido ligands give rise to an AX_4 spin system in their ^{19}F NMR spectra corresponding to the environments *trans* (F_A) and *cis* (F_X) to the oxygen atom. Brinckman and co-workers investigated the inductive and resonance effects of the R group, specifically in terms of the *cis* and *trans* influences of OR on the chemical shifts of the fluorido ligands, by ^{19}F NMR spectroscopy. Series of haloalkoxo[177] and fluorophenoxo[178,179] derivatives of WF_6 were employed, establishing linear relationships between the electronic properties of the R group and the chemical shifts of the F_A and F_X resonances. From these studies, it was concluded that changes in the *cis* and *trans* influences of the OR groups arises almost entirely due to

changes in their π-bonding character. In addition, $MF_5(OR)$ (M = Mo, W) complexes were employed as surrogates in variable-temperature ^{19}F NMR studies concerning the stereochemical non-rigidity of MoF_6 and WF_6.[51] Their lower symmetries allowed for observation of intramolecular exchange between the F_A and F_X environments at increased temperatures and experimental estimation of the Bailar-twist enthalpies.

1.1.4.6. Derivatives Containing M=S, M–S and M=Se Bonds

Sulfide tetrafluorides are known for molybdenum, tungsten, and rhenium. They have been synthesised reactions of MF_6 with inorganic sulfides (Sb_2S_3, B_2S_3, etc.) or S_8, either neat at high temperatures (*ca*. 300 °C) or in aHF at ambient temperature.[180] The heavier group-6 analogues $MSeF_4$ (M = Mo, W) have been similarly prepared via high-temperature syntheses using Sb_2Se_3 or Se.[181–183] The crystal structures of MSF_4 (M = Mo,[184] W,[183,185] Re[183]) reveal fluorine-bridged polymeric structures similar to those of $MoOF_4$ and $ReOF_4$. Although all three crystallise in the orthorhombic space group $Pca2_1$, WSF_4 (Z = 8) is crystallographically distinct from $MoSF_4$ and $ReSF_4$ (Z = 24); preliminary X-ray photographs indicated that $WSeF_4$ is isotypic with WSF_4.[181]

Like the oxide tetrafluorides, WSF_4 is known to behave as a Lewis acid and F^- acceptor. The $WSF_4(NCCH_3)$[183,185] and $WSF_4(NC_5H_5)$[186] adducts have been isolated, as well as $[WSF_5]^-$[187,188] and $[W_2S_2F_9]^-$[188] salts, the crystal structures of which reveal nearly identical geometries to the analogous oxido complexes. It has been observed, however, that WSF_4 is a demonstrably weaker Lewis acid than WOF_4 in competitive reactions with F^-[188] and the inability to isolate $WSF_4(NC_5H_5)_2$.[186] Hydrolysis of WSF_4 or its derivatives results in initial loss of the sulfido ligand, as evidenced by the formation of $[W_2O_2S_2F_6]^{2-}$[151] and

$[W_2OSF_9]^-$;[188] the crystal structure of the former reveals that it is isostructural with $[W_2O_4F_6]^{2-}$.

Derivatives of WF_6 containing W–S bonds have only been reported in a mixture of WF_6 and $S_2(CH_3)_2$ in CH_3CN, with tentative assignments of $WF_5(SCH_3)$, $WF_4(SCH_3)_2$, $WSF_3(SCH_3)(NCCH_3)$, and $WSF_3(SCH_3)\{S_2(CH_3)_2\}$ in its ^{19}F NMR spectrum.[75] Evidently, like $WF_5(OCH_3)$, $WF_5(SCH_3)$ is susceptible to decomposition via W=S bond formation and evolution of CH_3F. Theoretical investigations of $MF_5(SCX_3)$ (M = Mo, W; X = H, F) predicted highly distorted octahedral geometries with very low differences between the energies of the octahedral ground state and trigonal-prismatic transition state (7–23 kJ mol^{-1}).[189]

1.1.4.7. Derivatives Containing M–Cl Bonds

Tungsten chloride pentafluoride was initially prepared via reaction of WF_6 with $TiCl_4$, manifesting as a yellow liquid that decomposes slowly at ambient temperature to WF_6, WCl_4F_2, WCl_5F, and WCl_6.[190,191] An alternative synthesis involved the fluorination of WCl_6 with F_2, which was also employed in the preparation of WCl_2F_4.[192] Unlike $WF_4(OR)_2$, WCl_2F_4 exists as an inseparable mixture of the *cis* and *trans* isomers that are also subject to decomposition at ambient temperature. Monitoring the reaction of WF_6 with excess $(CH_3)_3SiCl$ by ^{19}F NMR spectroscopy revealed formation of mixtures containing WCl_nF_{6-n} (n = 0–4) with eventual precipitation of a material that was presumed to contain WCl_5F and WCl_6.[192]

Members of the UCl_nF_{6-n} (n = 0–5) series were also observed by IR[193,194] and/or ^{19}F NMR[195,196] spectroscopy upon reactions of UF_6 with various main-group chlorides ($(CH_3)_3SiCl$, BCl_3, HCl, etc.), $TiCl_4$, or UCl_6 below –60 °C. However, no species were

isolated, save for the matrix isolation of $UClF_5$ in admixture with UF_6,[196] and it was observed that $UClF_5$ and UCl_2F_4 decompose above –60 °C with evolution of Cl_2.[195,197] *In-situ* generated $UClF_5$, in the presence of excess UF_6, behaves as an oxidative chlorinating and/or fluorinating agent.[196]

Neat reactions of MoF_6 and ReF_6 with excess BCl_3 below –20 °C serve as the only preparative routes to $MoCl_6$ and $ReCl_6$.[198] Their crystal structures reveal isotypicity with α-WCl_6 and regular octahedral geometries; the expected Jahn-Teller distortion of $ReCl_6$ is not observed. Rhenium chloride pentafluoride has been prepared via fluorination of $ReCl_5$ with F_2 and like $WClF_5$, slowly decomposes under ambient conditions with deposition of a black precipitate.[199]

1.2. Transition-Metal and Uranium Fluorides as Fluoride-Ion Donors

The transition-metal and actinide hexafluorides do not exhibit discrete F^--donor properties, though their increased oxidative capabilities in the presence of SbF_5 could suggest some degree of $[MF_5]^+$ or polarised $F_5M–F\cdots SbF_5$ character. The pentafluorides and various oxide fluorides, however, are well understood to exhibit discrete F^--donor properties in the solid state. This occurs commonly even in the parent compounds, in which fluorine-bridging interactions occur to satisfy octahedral coordination spheres about the metal centres (or in the case of uranium, even higher coordination numbers). Furthermore, addition of a strong F^- acceptor, principally SbF_5, allows for the generation of fluorine-bridged species with increased cationic character at the metal centres. Finally, in rare cases, ionic species free of extensive fluorine-bridging interactions can be generated by introducing stabilising donor ligands.

1.2.1. M^VF_5

The solid-state structures of the binary transition-metal and actinide pentafluorides have been reviewed previously,[200] though improved crystallographic data for CrF_5,[201] MoF_5,[202] and TaF_5[203] have since been published. They are typically found to adopt zig-zag-polymeric (VF_5 structure type; M = V, Cr, Tc, Re), planar-tetrameric (NbF_5 structure type; M = Nb, Mo, Ta, W), or distorted-tetrameric (RhF_5 structure type; M = Ru, Rh, Os, Ir, Pt) structures resulting in *cis*-fluorine-bridged MF_6 octahedra. The notable exceptions are AuF_5, which is a *cis*-fluorine-bridged dimer,[204] and UF_5, which adopts either a linear chain polymer with *trans*-fluorine-bridged UF_6 octahedra (α-UF_5)[205,206] or an extensively fluorine-bridged three-dimensional network structure with octacoordinate uranium centres.[205,207] While CrF_5 was originally thought to be crystallographically isotypic with

VF_5, TcF_5, and ReF_5, it was later determined to be distinct, though still highly similar in its structure.[201] In all cases, the fluorine-bridging interactions are such that $[MF_4][MF_6]$ character is not apparent; bridges are either completely symmetric, or asymmetric such that the coordination spheres of the metal centres are 5(+1), rather than 4(+2). However, the group-5 pentafluorides exhibit a small degree of autoionisation in the melt on the basis of conductimetric experiments, VF_5 ($\sigma = 2.4 \times 10^{-2}$ S m^{-1})[208] more so than NbF_5 or TaF_5 ($\sigma = 1.6 \times 10^{-3}$ S m^{-1});[209] MoF_5 is known to exhibit autoionisation to a considerably smaller extent ($\sigma = 1.6 \times 10^{-5}$ S m^{-1}).[210]

It is known that VF_5, CrF_5, NbF_5, TaF_5, and UF_5 react with SbF_5 under formation of fluorine-bridged adducts. The $VF_5{\cdot}SbF_5$ adduct was characterised by vibrational spectroscopy and formulated as $[VF_4][SbF_6]$ on the basis of its blue-shifted V–F stretching modes (Raman, in cm^{-1}: 852, 839, 814, 805[211]) with respect to VF_5 (833, 788, 780, 738[212]). It was described as "strongly reactive against organic compounds", though less so than $CrF_5{\cdot}2SbF_5$ (*vide infra*).[211]

The $CrF_5{\cdot}SbF_5$ adduct has been isolated as a polymer comprising alternating *cis*-fluorine-bridged CrF_6 and *trans*-fluorine-bridged SbF_6 octahedra.[201] The bridging Cr–F bonds of the adduct (2.065(2)–2.078(2) Å) are significantly elongated with respect to those of CrF_5 (1.9515(5) Å), suggesting partial ionic, i.e. $[CrF_4][SbF_6]$, character. A $CrF_5{\cdot}2SbF_5$ adduct was reported and formulated as $[CrF_4][Sb_2F_{11}]$ on the basis of its vibrational spectra,[213] but could not be reproduced; it was instead suggested that mixtures of CrF_5 with excess SbF_5 are of indefinite nature.[214] Mixtures of CrF_5 and SbF_5 were found to oxidise O_2, Xe, and C_6F_6, but not NF_3;[213,214] a mixture of CrF_5 and AsF_5 was also found to oxidise O_2, whereas neat CrF_5 does not react with O_2.[214]

Both NbF_5 and TaF_5 react with SbF_5 in neat mixtures or SO_2ClF solutions, and their ^{19}F NMR spectra revealed increasing deshielding of the F-on-Nb^V/Ta^V resonances with increasing proportion of SbF_5, suggesting more cationic character at the transition-metal nuclei.[215] Conductimetric studies on such mixtures/solutions, however, indicated lower overall conductivity ($\sigma < 1 \times 10^{-3}$ S m^{-1}) than in liquid NbF_5 and TaF_5, and the Raman spectra of $MF_5{\cdot}SbF_5$ did not reveal significant changes in the ν(MF) nor ν(SbF) frequencies.[215] The crystal structure of $NbF_5{\cdot}SbF_5$ revealed an infinite polymer with alternating, asymmetrically *cis*-fluorine-bridged NbF_6 and SbF_6 octahedra,[216] in contrast to the tetrameric structures of the parent compounds, NbF_5[217] and SbF_5.[218] The bridging Nb–F bond lengths do not differ significantly between NbF_5 (2.06(2), 2.07(2) Å) and $NbF_5{\cdot}SbF_5$ (2.16(2), 2.18(2) Å), though this could be due to the low quality of the data. Niobium and tantalum pentafluoride are also known to form mixed nNbF$_5{\cdot}$(4–n)TaF$_5$ (n = 1–3) adducts that are crystallography indistinguishable from pure NbF_5 or TaF_5.[203]

Reactions of NbF_5 and TaF_5 with mono- (B) and bidentate (B′) main-group donor ligands result in the formation of $[MF_4(B)_n][MF_6]$ (n = 2, 4) and $[MF_4(B')_2][MF_6]$ salts, which have been reviewed extensively.[219–221] Numerous crystal structures of $[MF_4(B)_4][MF_6]$ and $[MF_4(B')_2][MF_6]$ have been reported, all of which comprise well separated trigonal-dodecahedral cations and octahedral anions, as opposed to the strong fluorine-bridging interactions in $NbF_5{\cdot}SbF_5$. Niobium and tantalum pentafluoride have been employed in the selective one-electron oxidation of arenes to form $[M_2F_{11}]^-$ salts of their radical cations;[222–224] the reaction of $[TaF_4\{(OCH_3)_2C_2H_4\}_2][TaF_6]$ with $CoCp_2$ to form $[CoCp_2][TaF_6]$ could tentatively suggest that arene oxidation proceeds through transient $[MF_4]^+$ as the active oxidising agent.[225]

Gold pentafluoride is the strongest known F^--accepting binary fluoride and one of the strongest known Lewis acids with a calculated FIA[204] (in kJ mol^{-1}; AuF_5: 591, $[AuF_5]_2$: 539) higher than that of SbF_5 (*ca*. 500[141,226]). As such, it would be expected that in any adducts with other fluorine-containing compounds, it would behave as the F^- acceptor, which was corroborated via computational prediction of asymmetric fluorine bridging in favour of the gold centre in the hypothetical $[AuSbF_{11}]^-$ anion.[204]

Unlike the transition-metal pentafluorides, UF_5 forms distinguishable 1:1 and 1:2 adducts with SbF_5, the former being prepared upon thermal decomposition of the latter.[28] The crystal structure of $UF_5{\cdot}2SbF_5$ reveals an extensively fluorine-bridged three-dimensional network that is superficially similar to β-UF_5.[227] The uranium centres adopt trigonal-dodecahedral geometries with three terminal and two bridging fluorido ligands, as well as three further contacts from the SbF_6 octahedra, which are either *cis* or *mer* fluorine-bridged. There is no evidence for U–F–U nor Sb–F–Sb fluorine-bridging (i.e., formation of $[Sb_2F_{11}]^-$). The presence of $[SbF_6]^-$ anions in the 1:1 adduct could not be determined unambiguously via IR spectroscopy.[28]

1.2.2. $M^{VI}OF_4$

Upon reaction with a large excess of SbF_5, $MoOF_4$ was found to form a stable 1:1 adduct with SbF_5, as well as a possible 1:2 adduct that was unstable towards loss of SbF_5 *in vacuo*.[228] The $MoOF_4{\cdot}SbF_5$ adduct is structurally similar to $CrF_5{\cdot}SbF_5$, with alternating *cis*-fluorine-bridged $MoOF_5$ and *trans*-fluorine-bridged SbF_6 octahedra in which the bridging Mo–F bonds (2.145(6), 2.210(6) Å) are significantly elongated with respect to the intramolecular bridging Mo–F bonds of $MoOF_4$ (1.961(3) Å). Correspondingly, the Raman spectrum of $MoOF_4{\cdot}SbF_5$ exhibits a ν(MoO) band (in cm^{-1}; 1047) that was slightly blue-

shifted with respect to $MoOF_4$ (1042). The analogous reaction of WOF_4 with SbF_5 was inconclusive, and once an equimolar ratio of WOF_4 and SbF_5 had been achieved, SbF_5 could still be removed *in vacuo* at ambient temperature. The $WOF_4{\cdot}SbF_5$ adduct could not be unambiguously identified from Raman spectra or unit-cell parameters, which were equally as suggestive of superimposed WOF_4 and SbF_5.[228]

In contrast to $MoOF_4$ and WOF_4, UOF_4 forms multiple stable adducts with SbF_5, $UOF_4{\cdot}n SbF_5$ (n = 1–3).[229] Their Raman spectra exhibit blue shifts in the ν(UO) bands (in cm^{-1}; n = 1: 906, n = 2, 912, n = 3, 921) with respect to UOF_4 (895, 889, 882), indicative of stepwise withdrawal of electron density from the uranium centre as increasing equivalents of SbF_5 are introduced. However, bands attributable to discrete $[SbF_6]^-$ or $[Sb_2F_{11}]^-$ anions were not observed. The crystal structure of $UOF_4{\cdot}2SbF_5$ was found to be crystallographically isotypic with $UF_5{\cdot}2SbF_5$, though the metal centre of the UOF_4 adduct does not obviously possess the long U···F contact required for octacoordination. Instead, the structure was described as a highly distorted UOF_6 pentagonal bipyramid with axial O/F disorder, as in α-UOF_4.[105] The bridging U–F bonds (2.322(14)–2.360(15) Å) are, on average, substantially longer than in α-UOF_4 (2.25(2)–2.29(2) Å). The reactions of $UOF_4{\cdot}n SbF_5$ (n = 1, 2) with CH_3CN and $(C_6H_5)_3PO$ were reported to result in ionic species ($[SbF_6]^-$ salts) on the basis of their IR spectra.[230] While $[UOF_3(NCCH_3)_2][SbF_6]$ was suggested as a logical formulation of $UOF_4{\cdot}SbF_5{\cdot}2CH_3CN$, the precise nature of the solids with empirical composition $UOF_4{\cdot}2SbF_5{\cdot}6L$ (L = CH_3CN, $(C_6H_5)_3PO$) could not be ascertained.

1.2.3. $M^{VI}O_2F_2$ (M = Cr, U)

The only transition-metal or actinide dioxide difluorides for which F^--donor properties have been investigated are CrO_2F_2 and UO_2F_2. Chromium dioxide difluoride forms 1:1 and 1:2 adducts with SbF_5, as well as $CrO_2F_2 \cdot TaF_5$, which were formulated as $[CrO_2F][SbF_6]$, $[CrO_2F][Sb_2F_{11}]$, and $[CrO_2F][TaF_6]$ on the basis of the ν(SbF) and ν(TaF) stretching regions of their Raman spectra.[148] In superacidic HF/MF_5 (M = As, Sb, Ta) solutions of CrO_2F_2, ionic species were observed by Raman spectroscopy.[231] Computational studies later suggested that the product was $[CrO_2F(FH)]^+$, as opposed to $[CrOF_2(OH)]^+$ or free $[CrO_2F]^+$, on the basis of relative energies of the optimised geometries as well as the calculated vibrational frequencies.[232]

The uranium analogue has been found to react with AsF_5 and SbF_5, forming $UO_2F_2 \cdot AsF_5$[233] and $UO_2F_2 \cdot n SbF_5$ (n = 2, 3),[234] respectively. Their IR spectra reveal blue shifts of the $\nu_{as}(UO_2)$ band (in cm^{-1}; 1000, 1004, 1012, respectively) with respect to UO_2F_2 (990), similarly to the $UOF_4 \cdot n SbF_5$ (n = 1–3) adducts.[229] The crystal structure of $UO_2F_2 \cdot 3SbF_5$ reveals that it is best formulated as $[UO_2][SbF_6][Sb_2F_{11}]$ and contains *trans*-UO_2F_5 pentagonal bipyramids with strong interionic U···F contacts (2.33(2)–2.45(2) Å) and U=O bonds (1.66(3), 1.69(3) Å) that are insignificantly different from those of UO_2F_2 (1.74(2) Å).[234] The dissolution of UO_2F_2 in HF/AsF_5 results in the formation of HF-solvated $[UO_2]^{2+}$, likely *trans*-$[UO_2(FH)_5]^{2+}$, as determined by Raman and vibronic spectroscopy.[235]

1.2.4. ReF_7

Rhenium heptafluoride, ReF_7, acts as a discrete F^- donor towards SbF_5 to form $[ReF_6][Sb_nF_{5n+1}]$ (n = 2, 3),[236] but does not react with AsF_5; $[ReF_6]^+$ salts have been

alternatively prepared via oxidation of ReF_6 with $[KrF]^+$.[237] The Raman spectra of $[ReF_6][Sb_nF_{5n+1}]$ (n = 2, 3) suggest a regular O_h-symmetric cation, consistent with the ionic formulation.[236]

An attempt to prepare $[TcF_6][AsF_6]$ upon oxidation of $TcOF_5$ by $[KrF]^+$ was unsuccessful, instead producing $[Tc_2O_2F_9][AsF_6]$ (*vide infra*);[238] $[TcF_6]^+$ and TcF_7 remain unknown.

1.2.5. $M^{VII}OF_5$ (M = Tc, Re)

Though $TcOF_5$ exhibits negligible intermolecular interactions in the solid state,[238] both $TcOF_5$ and $ReOF_5$ react with PnF_5 (Pn = As, Sb) to form ionic products. Whereas the reaction of $ReOF_5$ with AsF_5 was found to produce a solid formulated as $[ReOF_4][AsF_6]$ on the basis of its Raman spectrum,[236] $TcOF_5$ reacts with AsF_5 in aHF to form $[Tc_2O_2F_9][AsF_6]$.[238] Reactions of MOF_5 with equimolar amounts of SbF_5 yielded $[M_2O_2F_9][Sb_2F_{11}]$ containing well separated ions, as determined by X-ray crystallography.[236,238] In the cations, the oxido ligands are positioned *trans* to the bridging fluorido ligands. The $[TcOF_4]^+$ cation could only be observed *in situ* via ^{99}Tc and ^{19}F NMR spectroscopic studies of HF/SbF_5 and SbF_5 solutions of $[Tc_2O_2F_9]^+$ salts.[238]

1.2.6. $M^{VII}O_2F_3$ (M = Tc, Re)

Technetium and rhenium dioxide trifluoride exhibit dissimilar properties in the solid state. The technetium analogue could be obtained in crystalline form upon decomposition of $[XeF_5][TcO_2F_4]$ in aHF, and consists of polymeric chains of *cis*-fluorine bridged (2.071(6)–2.106(6) Å), *cis*-TcO_2F_4 octahedra.[239] Meanwhile, ReO_2F_3 crystallises in four separate polymorphs, two of which are polymeric chains (**I** and **II**, both obtained from aHF; **II** is metastable), one of which is a cyclic trimer (**III**; obtained from $CFCl_3$ or

SO_2ClF), and the last of which is a cyclic tetramer (**IV**; obtained from SO_2ClF).[240] All four modifications consist of *cis*-fluorine-bridged, *cis*-ReO_2F_4 octahedra. However, the fluorine bridges are symmetric in **I** (2.082(7)–2.109(6) Å), **II** (2.114(5), 2.116(5) Å), and **IV** (2.087(6), 2.090(5) Å), whereas they are asymmetric in **III** (2.030(11), 2.108(11) Å).

Both TcO_2F_3 and ReO_2F_3 interact with PnF_5, yielding $MO_2F_3{\cdot}PnF_5$ polymers with alternating *cis*-fluorine-bridged *cis*-MO_2F_4 and *trans*-fluorine-bridged PnF_6 octahedra.[241] The crystal structures of the SbF_5 adducts reveal that the bridging M–F bonds (M = Tc: 2.217(4)–2.222(4) Å; M = Re: 2.200(5)–2.210(5) Å) are significantly longer than in the parent MO_2F_3 compounds. In superacidic HF/PnF_5 media, $MO_2F_3{\cdot}PnF_5$ undergo protonolysis to form [*cis*-$MO_2F_2(FH)_2$][PnF_6], as observed by Raman and ^{19}F NMR spectroscopy. In the $TcO_2F_3{\cdot}XeO_2F_2$ adduct, TcO_2F_3 and XeO_2F_2 form independent polymeric chains without notable Tc–F–Xe bridging interactions; the fluorine-bridging in the TcO_2F_3 chain (2.057(11)–2.093(13) Å) is similar to TcO_2F_3. Interestingly, XeO_2F_2 was found to undergo fluorine bridging in the co-crystal, whereas neutron-diffraction studies of solid XeO_2F_2 revealed an oxygen-bridged, two-dimensional network structure.[242] Lastly, it was found by ^{19}F NMR spectroscopy that $ReO_2F_3{\cdot}SbF_5$ is ionised in SO_2ClF and CH_3CN to [$Re_2O_4F_5$][Sb_2F_{11}] and [$ReO_2F_2(NCCH_3)_2$][SbF_6], respectively.[241]

1.2.7. $M^{VII}O_3F$ (M = Mn, Tc, Re)

The trioxide fluorides, MO_3F, are also structurally divergent in the solid state, as MnO_3F is monomeric and subject to complete disorder of the oxido and fluorido ligands,[243] TcO_3F is dimeric with asymmetric fluorine bridges (2.039(1), 2.133(1) Å),[244] and ReO_3F is a polymer of *cis*-ReO_4F_2 octahedra undergoing simultaneous asymmetric oxygen (1.865(7), 1.908(7) Å) and symmetric fluorine (2.141(6), 2.142(7) Å) bridging.[240]

Unlike the aforementioned transition-metal and actinide oxide fluorides, TcO_3F is capable of acting as a monomeric O- and F-donor ligand, coordinating to K^+ in $K[Tc_3O_9F_4]\cdot 1.5TcO_3F$.[244] The $[TcO_3]^+$ cation was originally reported to exist in aHF solutions of TcO_3F on the basis of their ^{99}Tc NMR spectra.[245] However, attempts to procure $[TcO_3]^+$ salts via F^- abstraction from TcO_3F by PnF_5 (Pn = As, Sb) in aHF were unsuccessful, instead resulting in $TcO_2F_3\cdot PnF_5\cdot 2HF$ as a result of solvolysis.[244] One HF molecule is coordinated to the technetium centre, suggesting that it is best formulated as $[TcO_2F_2(FH)][PnF_6]\cdot HF$ in which there are significant cation-anion contacts. Strongly associated $[TcO_3][O_3SF]$[246] as well as octahedral *fac*-$[MO_3]^+$ (M = Tc, Re) complexes of scorpionate ligands have been accessed, however, typically using oxides such as $[M^{VII}O_4]^-$ and $Re^{VII}_2O_7$ as metal sources.[247] Manganese trioxide fluoride exhibits no reactivity towards F^- acceptors such as AsF_5 and SbF_5,[246] and attempted F^- abstraction from ReO_3F has yet to be reported.

1.2.8. $Os^{VIII}O_2F_4$ and $Os^{VIII}O_3F_2$

While OsF_7 and OsF_8 have been reported, it is now understood that the highest-oxidation-state binary fluoride of osmium is OsF_6.[248] Osmium(VIII) fluorides are, however, accessible in the forms of OsO_3F_2 and OsO_2F_4; $OsOF_6$ was reported as well,[249] but it was revealed to have been misidentified OsO_2F_4.[250] The trioxide difluoride adopts a polymeric structure in a low-temperature monoclinic phase (α-OsO_3F_2) with symmetrically *cis*-fluorine bridged (2.108(1), 2.126(1) Å), *fac*-OsO_3F_3 octahedra. In contrast, OsO_2F_4 is monomeric in the solid state with *cis*-configured oxido ligands,[250,251] as observed in the isoelectronic $[Re^{VII}O_2F_4]^-$ anion.[252,253]

Dissolution of OsO_3F_2 in HF/PnF_5 (Pn = As, Sb) resulted in the formation of HF-solvated $[OsO_3F]^+$ salts, from which the solvent could only be removed completely in the case of $[OsO_3F][AsF_6]$ without decomposition.[254] Meanwhile, OsO_3F_2 reacted with SbF_5 under formation of $[OsO_3F][Sb_3F_{16}]$. The crystal structures of $[OsO_3F(FH)][AsF_6]\cdot HF$ and $[OsO_3F(FH)][SbF_6]$ reveal simultaneous Os···F contacts with the anions and solvent to satisfy octahedral coordination at the osmium centres. In the absence of solvent, $[OsO_3F][AsF_6]$ dimerises to achieve octahedral *fac*-OsO_3F_3 moieties via Os···F–As contacts, whereas the extremely weakly coordinating $[Sb_3F_{16}]^-$ anion stabilises tetrahedral $[OsO_3F]^+$. The attempted redissolution of $[OsO_3F][AsF_6]$ in aHF effected loss of AsF_5 and the generation of fluorine-bridged $[Os_2O_6F_3]^+$, which was only stable under the aHF supernatant. Whereas differences in Os=O bond lengths could not be observed in the crystal structures, the Raman spectra revealed gradually increasing blue shifts in the $\nu(OsO_3)$ bands of $[Os_2O_6F_3]^+$ (in cm^{-1}; 944–967), $[OsO_3F(FH)]^+$ (945–981), $[OsO_3F][PnF_6]$ (984–996), and finally $[OsO_3F][Sb_3F_{16}]$ (992, 1002), consistent with increasing Os=O bond strengths across the series.

It was determined by X-ray crystallography that the hypothetical osmium(VII) compound OsO_2F_3 actually exists as the mixed osmium(VI,VIII) compound $OsO_3F_2\cdot OsOF_4$.[106] It was found to crystallise in asymmetrically *cis*-fluorine-bridged polymeric and dimeric modifications, both of which consist of alternating *fac*-OsO_3F_3 and $OsOF_5$ octahedra. Interestingly, despite the higher oxidation state of the osmium(VIII) centre, the bridging Os^{VIII}–F bonds in both the polymeric (2.140(8), 2.142(7) Å) and dimeric (2.178(4), 2.201(4) Å) modifications are longer than the complementary Os^{VI}–F bonds (1.988(5)–2.044(8) Å). The related osmium(V,VIII) compound $OsO_3F_2\cdot OsF_5$,

which is crystallographically isotypic with dimeric $OsO_3F_2 \cdot OsOF_4$, possesses even more pronounced asymmetry in the Os^{VIII}–F–Os^{V} moieties (2.223(5), 2.252(5) vs. 1.952(5), 1.955(5) Å). This serves as a testament to the strongly electron-withdrawing nature of the fluorido ligand, which renders $OsOF_4$ and OsF_5 stronger F^- acceptors than the less fluorine-rich OsO_3F_2, despite the lower oxidation states of their metal centres.

Finally, OsO_3F_2 forms a 1:1 adduct with $XeOF_4$, in which a dimeric $(OsO_3F_2)_2$ unit is observed.[255] One fluorido ligand symmetrically bridges the two osmium atoms (2.107(4), 2.117(5) Å), and the second coordinates weakly to xenon, resulting in an elongation of this bridging Os–F bond (1.927(5) Å) with respect to the terminal Os–F bond of α-OsO_3F_2 (1.879(1) Å).[251] The adduct could be decomposed *in vacuo* at 0 °C, resulting in the removal of $XeOF_4$ with retention of the dimeric structure of $(OsO_3F_2)_2$, as determined by Raman spectroscopy.[255]

There are similar reports of OsO_2F_4 behaving as a F^- donor in HF/PnF_5 (Pn = As, Sb) media, affording $[Os_2O_4F_7][AsF_6]$ and $[OsO_4F_7][Sb_2F_{11}]$,[256] rather than the HF solvates observed for $[OsO_3F]^+$. The crystal structure of the $[Sb_2F_{11}]^-$ salt revealed a symmetrically fluorine-bridged cation with the oxido ligands lying *cis* and *trans* to the bridging ligand. Interestingly, it was observed that the Os=O bonds *cis* to the bridging fluorido ligands (1.750 Å) were elongated with respect to *cis*-OsO_2F_4 (1.674(4) Å),[251] despite the expectation of increased positive charge density at the osmium centre and, thus, contracted bonds. The overall strengthening of Os=O could, however, be realised by significant increases in the $\nu_s(OsO_2)$ stretching frequencies in the Raman spectra of $[Os_2O_4F_7][AsF_6]$[256] (in cm^{-1}; 986) and $[OsO_4F_7][Sb_2F_{11}]$[256] (984) with respect to OsO_2F_4 (943).[250] The neat reaction of OsO_2F_4 with excess SbF_5 resulted in the isolation of

$OsO_2F_4 \cdot 2SbF_5$, which is best described as $[OsO_2F_3][Sb_2F_{11}]$ containing a strong interionic Os···F–Sb contact (2.190(3) Å), resulting in an octahedral *cis*-OsO_2F_4 coordination sphere.[257] The $\nu_s(OsO_2)$ band of $[OsO_2F_3]^+$ (997) was blue-shifted to an even greater extent than in $[Os_2O_4F_7]^+$,[256] consistent with a more positively charged metal centre in the mononuclear cation. Attempts to prepare $[OsO_2F_3][SbF_6]$ were unsuccessful and it was predicted that $[Os_2O_4F_7][Sb_2F_{11}]$ was significantly more stable in the solid state (by 206 kJ mol^{-1}).[257]

1.3. Objectives and Impact of Research

The transition-metal hexafluorides have long been established to behave as Lewis acids and/or oxidising agents, with previous studies having focused predominately on these facets of their chemistry. The primary objectives of this research will be to generally expand the understood chemical behaviours of these fascinating compounds using WF_6 as a model system, due to its stability towards organic media.

The ability of WF_6 to form Lewis acid-base adducts with main-group donor ligands is of fundamental structural interest, as these complexes are heptacoordinate and their geometries are not intuitively predicted. Though there are few examples of crystallographically characterised WF_6 adducts, their geometries are not uniform; $WF_6(2\text{-}NC_5H_4F)$[60] and $WF_6\{P(CH_3)_3\}$[50] are monocapped trigonal prisms and $WF_6\{P(C_6H_5)(CH_3)_2\}$[50] is a monocapped octahedron. In Chapter 3, WF_6 adducts with pyridine, 4-methylpyridine, 4-(dimethylamino)pyridine, and 4,4'-bipyridine are synthesised and structurally characterised in order to establish possible effects of donor-ligand Lewis basicity and crystal packing on the resultant geometry.

Imidotungsten(VI) compounds are ubiquitous in inorganic and organometallic chemistry, most prominently for their roles as catalysts in olefin metathesis[258] and metal-nitrogen sources in the deposition of tungsten nitride (WN_x) and carbide nitride (WN_xC_y) thin films.[259] Despite this, there are few examples of fluorido analogues, i.e. $W(NR)F_4$ or derivatives thereof, and little investigation has been undertaken to quantify effects of the ligands and R groups on W≡N bonding. In Chapter 4 and 5, anionic and neutral derivatives of $W(NC_6F_5)F_4$ will be investigated. The reaction of $[W(NC_6F_5)F_5]^-$ with strong F^- acceptors will be explored as possible pathways to neutral $W(NC_6F_5)F_4$. Computational

studies of $[W(NR)F_5]^-$ (Chapter 4) and $W(NR)F_4$ (Chapter 5) with a series of different R groups, ranging from electron-donating to electron-withdrawing, will serve to quantify the effects of the R groups on structural properties and, in particular the nature of W≡N bonding.

The increased oxidising capabilities of MF_6 that was observed when in the presence of SbF_5 could suggest some degree of $[MF_5]^+$ or polarised $F_5M–F\cdots SbF_5$ character, though no such intermediates have been observed in oxidations performed by MF_6/SbF_5 mixtures. Stabilised and isolated $[MF_5]^+$ complexes could provide unique avenues to strong oxidising agents and Lewis acids, especially those derived from WF_6, which is the most accessible and easily handled, but weakest oxidising agent, of the transition-metal hexafluorides. Chapter 6 explores routes to the first $[WF_5]^+$ complexes, stabilised by the bidentate N-donor ligands 2,2'-bipy and 1,10-phen. Their fundamental structural and bonding properties are of crucial importance.

Lastly, the development of more strongly oxidising forms of WF_6 are of interest to access the lower tungsten fluorides, WF_4 and WF_5. In particular, WF_5 is known to be unstable towards disproportionation under ambient or slightly elevated temperatures,[260,261] its preparations are cumbersome,[260–263] and its chemical properties, such as its Lewis acidity, remain poorly understood. In Chapters 7 and 8, facile reductions of WF_6 by C_5H_5N (Chapter 7) and $P(CH_3)_3$ (Chapter 8) via donor-stabilised fluoridotungsten(VI) cations are investigated. The crystallographic and spectroscopic properties of donor-stabilised WF_5 derivatives, both neutral and cationic, will greatly expand our knowledge of structure and bonding in such d^1 fluorido complexes.

1.4. References

(1) Molski, M. J.; Seppelt, K. *Dalton Trans.* **2009**, 3379.

(2) Seppelt, K. *Chem. Rev.* **2015**, *115* (2), 1296–1306.

(3) Lucier, G.; Shen, C.; Casteel, W. J.; Chacón, L.; Bartlett, N. *J. Fluorine Chem.* **1995**, *72* (2), 157–163.

(4) Bartlett, N. *J. Fluorine Chem.* **2006**, *127* (10), 1285–1288.

(5) Malm, J. G.; Selig, H. *J. Inorg. Nucl. Chem.* **1961**, *20* (3–4), 189–197.

(6) Siegel, S.; Northrop, D. A. *Inorg. Chem.* **1966**, *5* (12), 2187–2188.

(7) Drews, T.; Supeł, J.; Hagenbach, A. and; Seppelt, K. *Inorg. Chem* **2006**, *45* (9), 3782–3788.

(8) Levy, J. H.; Taylor, J. C.; Wilson, P. W. *J. Chem. Soc., Dalton Trans.* **1976**, No. 3, 219–224.

(9) Moffitt, W.; Goodman, G. L.; Fred, M.; Weinstock, B. *Mol. Phys.* **1959**, *2* (2), 109–122.

(10) Selig, H.; Cafasso, F. A.; Gruen, D. M.; Malm, J. G. *J. Chem. Phys.* **1962**, *36* (12), 3440–3444.

(11) Craciun, R.; Long, R. T.; Dixon, D. A.; Christe, K. O. *J. Phys. Chem. A* **2010**, *114* (28), 7571–7582.

(12) Craciun, R.; Picone, D.; Long, R. T.; Li, S.; Dixon, D. A.; Peterson, K. A.; Christe, K. O. *Inorg. Chem.* **2010**, *49* (3), 1056–1070.

(13) Jong, W. A. De; Nieuwpoort, W. C. *Int. J. Quantum Chem.* **1996**, *58* (2), 203–216.

(14) Blondel, C.; Cacciani, P.; Delsart, C.; Trainham, R. *Phys. Rev. A* **1989**, *40* (7), 3698–3701.

(15) Bartlett, N.; Lohmann, D. H. *J. Chem. Soc.* **1962**, 5253.

(16) Bartlett, N. *Proc. Chem. Soc.* **1962**, 218.

(17) Graham, L.; Graudejus, O.; Jha, N. K.; Bartlett, N. *Coord. Chem. Rev.* **2000**, *197* (1), 321–334.

(18) Botkovitz, P.; Lucier, G. M.; Rao, R. P.; Bartlett, N. *Acta Chim. Slov.* **1999**, *46* (2), 141–154.

(19) Bartlett, N. *Angew. Chem. Int. Ed. Engl.* **1968**, *7* (6), 433–439.

(20) Christe, K. O.; Wilson, W. W.; Wilson, R. D. *Inorg. Chem.* **1984**, *23* (14), 2058–2063.

(21) Seidel, S.; Seppelt, K. *Angew. Chem. Int. Ed.* **2000**, *39* (21), 3923–3925.

(22) Tamadon, F.; Seidel, S.; Seppelt, K. *Acta Chim. Slov.* **2013**, *60* (3), 491–494.

(23) Padma, D. K.; Peacock, R. D. *J. Fluorine Chem.* **1981**, *17* (6), 539–541.

(24) Shorafa, H.; Mollenhauer, D.; Paulus, B.; Seppelt, K. *Angew. Chem. Int. Ed.* **2009**, *48* (32), 5845–5847.

(25) Berry, J. A.; Prescott, A.; Sharp, D. W. A.; Winfield, J. M. *J. Fluorine Chem.* **1977**, *10* (3), 247–254.

(26) McGhee, L.; Rycroft, D. S.; Winfield, J. M. *J. Fluorine Chem.* **1987**, *36* (3), 351–359.

(27) Anderson, G. M.; Winfield, J. M. *J. Chem. Soc., Dalton Trans.* **1986**, 337–341.

(28) Bougon, R.; Cearpin, P. *J. Fluorine Chem.* **1979**, *14* (3), 235–241.

(29) Paine, R. T.; Asprey, L. B.; Graham, L.; Bartlett, N. In *Inorganic Syntheses, Volume XIX*; Shriver, D. F., Ed.; 1979; pp 137–140.

(30) Moock, K.; Turowsky, L.; Seppelt, K. *J. Fluorine Chem.* **1987**, *37* (2), 253–258.

(31) Moock, K. H.; Rock, M. H. *J. Chem. Soc., Dalton Trans.* **1993**, 2459–2463.

(32) Gowik, P.; Klapötke, T. *J. Fluorine Chem.* **1990**, *47* (2), 273–281.

(33) Cameron, T. S.; Klapötke, T. M.; Schulz, A.; Valkonen, J. *J. Chem. Soc., Dalton Trans.* **1993**, No. 5, 659–662.

(34) Cameron, T. S.; Klapötke, T. M.; Schulz, A.; Valkonen, J. *J. Chem. Soc., Dalton Trans.* **1993**, 659–662.

(35) Bond, A. M.; Irvine, I.; O'Donnell, T. A. *Inorg. Chem.* **1975**, *14* (10), 2408–2412.

(36) Bond, A. M.; Irvine, I.; O'Donnell, T. A. *Inorg. Chem.* **1977**, *16* (4), 841–844.

(37) Heath, G. A.; Hefter, G. T.; Boyle, T. W.; Desjardins, C. D.; Sharp, D. W. A. *J. Fluorine Chem.* **1978**, *11* (3–4), 399–406.

(38) Sengupta, A. K.; Sharp, D. W. A.; Heath, G. A.; Brownstein, S. *J. Fluorine Chem.* **1982**, *21* (1), 38.

(39) Brownstein, S.; Heath, G. A.; Sengupta, A.; Sharp, D. W. A. *J. Chem. Soc., Chem. Commun.* **1983**, No. 12, 669–670.

(40) Macgregor, S. A.; Moock, K. H. *Inorg. Chem.* **1998**, *37* (13), 3284–3292.

(41) Christe, K. O.; Dixon, D. A.; McLemore, D.; Wilson, W. W.; Sheehy, J. A.; Boatz, J. A. *J. Fluorine Chem.* **2000**, *101* (2), 151–153.

(42) Beauchamp, J. L. *J. Chem. Phys.* **1976**, *64* (2), 718–723.

(43) Hargreaves, G. B.; Peacock, R. D. *J. Chem. Soc.* **1958**, 2170–2175.

(44) Hargreaves, G. B.; Peacock, R. D. *J. Chem. Soc.* **1958**, 4390–4393.

(45) Beuter, A.; Kuhlmann, W.; Sawodny, W. *J. Fluorine Chem.* **1975**, *6* (4), 367–378.

(46) Malta, J. G.; Selig, H.; Siegel, S. *Inorg. Chem.* **1966**, *5* (1), 130–132.

(47) Giese, S.; Seppelt, K. *Angew. Chem. Int. Ed. Engl.* **1994**, *33* (4), 461–463.

(48) Vogt, T.; Fitch, A. N.; Cockcroft, J. K. *Science* **1994**, *263* (5151), 1265–1267.

(49) Lin, Z.; Bytheway, I. *Inorg. Chem.* **1996**, *35* (3), 594–603.

(50) El-Kurdi, S.; Al-Terkawi, A.-A.; Schmidt, B.; Dimitrov, A.; Seppelt, K. *Chem. Eur. J.* **2010**, *16* (2), 595–599.

(51) Quiñones, G. S.; Hägele, G.; Seppelt, K. *Chem. Eur. J.* **2004**, *10* (19), 4755–4762.

(52) Adam, S.; Ellern, A.; Seppelt, K. *Chem. Eur. J.* **1996**, *2* (4), 398–402.

(53) Hwang, I. C.; Seppelt, K. *J. Fluorine Chem.* **2000**, *102* (1–2), 69–72.

(54) Mahjoub, A.-R.; Seppelt, K. *Angew. Chem. Int. Ed. Engl.* **1991**, *30* (7), 876–878.

(55) Peterson, S. W.; Holloway, J. H.; Coyle, B. A.; Williams, J. M. *Science* **1971**, *173* (4003), 1238–1239.

(56) Arnaudet, L.; Bougon, R.; Buu, B.; Lance, M.; Nierlich, M.; Vigner, J. *Inorg. Chem.*

1994, *33* (20), 4510–4516.

(57) Tebbe, F. N.; Muetterties, E. L. *Inorg. Chem.* **1968**, *7* (1), 172–174.

(58) Steigel, A.; Brownstein, S. *J. Am. Chem. Soc.* **1974**, *96* (19), 6227.

(59) Arnaudet, L.; Bougon, R.; Buu, B.; Lance, M.; Nierlich, M.; Thuéry, P.; Vigner, J. *J. Fluorine Chem.* **1995**, *71* (1), 123–129.

(60) Arnaudet, L.; Bougon, R.; Ban, B.; Lance, M.; Nierlich, M.; Vigner, J. *Inorg. Chem.* **1993**, *32* (7), 1142–1146.

(61) Arnaudet, L.; Bougon, R.; Ban, B.; Lance, M.; Navaza, A.; Nierlich, M.; Vigner, J. *J. Fluorine Chem.* **1994**, *67* (1), 17–25.

(62) Arnaudet, L.; Bougon, R.; Ban, B.; Charpin, P.; Isabey, J.; Lance, M.; Nierlich, M.; Vigner, J. *Can. J. Chem.* **1990**, *68* (3), 507–512.

(63) Arnaudet, L.; Bougon, R.; Ban, B.; Lance, M.; Navaza, A.; Nierlich, M.; Vigner, J. *J. Fluorine Chem.* **1992**, *59* (1), 141–152.

(64) Levason, W.; Monzittu, F. M.; Reid, G.; Zhang, W. *Chem. Commun.* **2018**, *54* (83), 11681–11684.

(65) Kleinhenz, S.; Pfennig, V.; Seppelt, K. *Chem. Eur. J.* **1998**, *4* (9), 1687–1691.

(66) Roessler, B.; Seppelt, K. *Angew. Chem. Int. Ed.* **2000**, *39* (7), 1259–1261.

(67) Shortland, A. J.; Wilkinson, G. *J. Chem. Soc., Dalton Trans.* **1973**, 872–876.

(68) Galyer, L.; Mertis, K.; Wilkinson, G. *J. Organomet. Chem.* **1975**, *85* (3).

(69) Pfennig, V.; Seppelt, K. *Science* **1996**, *271* (5249), 626–628.

(70) Köhler, K.; Herzog, A.; Steiner, A.; Roesky, H. W. *Angew. Chem. Int. Ed. Engl.* **1996**, *35* (3), 295–297.

(71) Kaupp, M. *Angew. Chem. Int. Ed. Engl.* **2001**, *40* (19), 3534–3565.

(72) Seppelt, K. *Acc. Chem. Res.* **2003**, *36* (2), 147–153.

(73) Kaupp, M. *J. Am. Chem. Soc.* **1996**, *118* (12), 3018–3024.

(74) Kaupp, M. *Chem. Eur. J.* **1998**, *4* (9), 1678–1686.

(75) Kokunov, Y. V.; Chubar, Y. D.; Bochkareva, V. A.; Buslaev, Y. A. *Koord. Khim.* **1975**, *1* (8), 1100–1105.

(76) Chambers, O. R.; Rycroft, D. S.; Sharp, D. W. A.; Winfield, J. M. *Inorg. Nucl. Chem. Lett.* **1976**, *12* (7), 559–561.

(77) Chambers, O. R.; Harman, M.; Rycroft, D. S.; Sharp, D. W. A.; Winfield, J. M. *J. Chem. Res.* **1977**, 1849–1876.

(78) Harman, M.; Sharp, D. W. A.; Winfield, J. M. *Inorg. Nucl. Chem. Lett.* **1974**, *10* (2), 183–185.

(79) Huppmann, P.; Seppelt, K. *Chem. Ber.* **1985**, *118* (2), 457–461.

(80) Seppelt, K. *Inorg. Chem.* **1973**, *12* (12), 2837–2839.

(81) Fawcett, J.; Griffith, G. A.; Peacock, R. D.; Russell, D. R. *Polyhedron* **1988**, *7* (19), 2015–2022.

(82) Rhiel, M.; Wocadlo, S.; Massa, W.; Dehnicke, K. *Z. Anorg. Allg. Chem.* **1996**, *622* (7), 1195–1199.

(83) Fenske, D.; Völp, K.; Dehnicke, K. *Z. Naturforsch. B* **1987**, *42* (11), 1398–1402.

(84) Fenske, D.; Völp, K.; Dehnicke, K. *Z. Naturforsch. B* **1988**, *43* (9), 1125–1129.

(85) Görge, A.; Dehnicke, K.; Fenske, D. *Z. Naturforsch. B* **1989**, *44* (2), 117–120.

(86) Stenger, H.; Dehnicke, K.; Hiller, W. *Z. Naturforsch. B* **1992**, *47* (7), 1054–1056.

(87) Dietrich, A.; Neumüller, B.; Dehnicke, K. *Z. Anorg. Allg. Chem.* **2000**, *626* (12), 2443–2445.

(88) Wang, X.; Andrews, L.; Lindh, R.; Veryazov, V.; Roos, B. O. *J. Phys. Chem. A* **2008**, *112* (35), 8030–8037.

(89) Andrews, L.; Wang, X.; Lindh, R.; Roos, B. O.; Marsden, C. J. *Angew. Chem. Int. Ed.* **2008**, *47* (29), 5366–5370.

(90) Fenske, D.; Liebelt, W.; Dehnicke, K. *Z. Anorg. Allg. Chem.* **1980**, *467* (1), 83–88.

(91) Völp, K.; Dehnicke, K.; Fenske, D. *Z. Anorg. Allg. Chem.* **1989**, *572* (1), 26–32.

(92) Majid, A.; McLean, R. R.; Ouellette, T. J.; Sharp, D. W. A.; Winfield, J. M. *Inorg. Nucl. Chem. Lett.* **1971**, *7* (1), 53–56.

(93) Majid, A.; McLean, R. R.; Sharp, D. W. A.; Winfield, J. M. *Z. Anorg. Allg. Chem.* **1971**, *385* (1–2), 85–91.

(94) Dimitrov, A.; Seidel, S.; Seppelt, K. *Eur. J. Inorg. Chem.* **1999**, *1999* (1), 95–99.

(95) Roesky, H. W.; Scholz, M.; Edelmann, F.; Noltemeyer, M.; Sheldrick, G. M. *Chem. Ber.* **1987**, *120* (11), 1881–1884.

(96) Haiges, R.; Boatz, J. A.; Bau, R.; Schneider, S.; Schroer, T.; Yousufuddin, M.; Christe, K. O. *Angew. Chem. Int. Ed.* **2005**, *44* (12), 1860–1865.

(97) Fawcett, J.; Peacock, R. D.; Russell, D. R. *J. Chem. Soc., Dalton Trans.* **1980**, 2294.

(98) Fawcett, J.; Peacock, R. D.; Russell, D. R. *J. Chem. Soc., Chem. Commun.* **1982**, No. 16, 958.

(99) Fawcett, J.; Peacock, R. D.; Russell, D. R. *J. Chem. Soc., Dalton Trans.* **1987**, 567.

(100) Selig, H.; Sunder, W. A.; Disalvo, F. A.; Falconer, W. E. *J. Fluorine Chem.* **1978**, *11* (1), 39–50.

(101) Paine, R. T. *Inorg. Chem.* **1973**, *12* (6), 1457–1458.

(102) Hoskins, B. F.; Linden, A.; O'Donnell, T. A. *Inorg. Chem.* **1987**, *26* (14), 2223–2228.

(103) Burns, R. C.; O'Donnell, T. A.; Waugh, A. B. *J. Fluorine Chem.* **1978**, *12* (6), 505–517.

(104) Paine, R. T.; McDowell, R. S. *Inorg. Chem.* **1974**, *13* (10), 2366–2370.

(105) Paine, R. T.; Ryan, R. R.; Asprey, L. B. *Inorg. Chem.* **1975**, *14* (5), 1113–1117.

(106) Shorafa, H.; Seppelt, K. *Inorg. Chem.* **2006**, *45* (19), 7929–7934.

(107) Shorafa, H.; Seppelt, K. *Z. Anorg. Allg. Chem.* **2007**, *633* (4), 543–547.

(108) Christe, K. O.; Wilson, W. W.; Bougon, R. A. *Inorg. Chem.* **1986**, *25* (13), 2163–2169.

(109) Sakurai, T.; Takahashi, A. *J. Inorg. Nucl. Chem.* **1977**, *39* (3), 427–429.

(110) Edwards, A. J.; Jones, G. R.; Steventon, B. R. *Chem. Commun.* **1967**, 462–463.

(111) Edwards, A. J.; Jones, G. R. *J. Chem. Soc. A* **1968**, 2074–2078.

(112) Mercier, H. P. A.; Breddemann, U.; Brock, D. S.; Bortolus, M. R.; Schrobilgen, G. J. *Chem. Eur. J.* **2019**, *25* (52), 12105–12119.

(113) Edwards, A. J.; Steventon, B. R. *J. Chem. Soc. A* **1968**, 2503.

(114) Edwards, A. J.; Jones, G. R.; Sills, R. J. C. *Chem. Commun.* **1968**, 1177–1178.

(115) Edwards, A. J.; Jones, G. R.; Sills, R. J. C. *J. Chem. Soc. A* **1970**, 2521–2523.

(116) Taylor, J. C.; Wilson, P. W. *Acta Crystallogr.* **1974**, *30* (7), 1701–1705.

(117) Arnaudet, L.; Bougon, R.; Ban, B.; Charpin, P.; Isabey, J.; Lance, M.; Nierlich, M.; Vigner, J. *Inorg. Chem.* **1989**, *28* (2), 257–262.

(118) Levason, W.; Reid, G.; Zhang, W. *J. Fluorine Chem.* **2016**, *184*, 50–57.

(119) Levason, W.; Monzittu, F. M.; Reid, G.; Zhang, W.; Hope, E. G. *J. Fluorine Chem.* **2017**, *200*, 190–197.

(120) Emsley, J. W.; Levason, W.; Reid, G.; Zhang, W.; De Luca, G. *J. Fluorine Chem.* **2017**, *197*, 74–79.

(121) Hope, E. G.; Jones, P. J.; Levason, W.; Ogden, J. S.; Tajik, M.; Turff, J. W. *J. Chem. Soc., Dalton Trans.* **1985**, No. 3, 529–533.

(122) Goettel, J. T.; Bortolus, M. R.; Stuart, D. G.; Mercier, H. P. A.; Schrobilgen, G. J. *Chem. Eur. J.* **2019**, *25* (69), 15815–15829.

(123) Bougon, R.; Bui Huy, T.; Charpin, P. *Inorg. Chem.* **1975**, *14* (8), 1822–1830.

(124) Beuter, A.; Sawodny, W. *Z. Anorg. Allg. Chem.* **1976**, *427* (1), 37–44.

(125) Kanatani, T.; Matsumoto, K.; Hagiwara, R. *Eur. J. Inorg. Chem.* **2010**, *2010* (7), 1049–1055.

(126) Matsumoto, K.; Hagiwara, R. *J. Fluorine Chem.* **2005**, *126* (7), 1095–1100.

(127) Kuhlmann, W.; Sawodny, W. *J. Fluorine Chem.* **1977**, *9* (5), 337–340.

(128) Joubert, P.; Bougon, R.; Gaudreau, B. *Can. J. Chem.* **1978**, *56* (14), 1874–1880.

(129) Beuter, A.; Sawodny, W. *Angew. Chem. Int. Ed. Engl.* **1972**, *11* (11), 1020–1021.

(130) Stene, R. E.; Scheibe, B.; Karttunen, A. J.; Petry, W.; Kraus, F. *Eur. J. Inorg. Chem.* **2019**, No. 32, 3672–3682.

(131) Sakharov, S. G.; Kokunov, Y. V.; Gustyakova, M. P.; Buslaev, Y. A. *Dokl. Akad. Nauk SSSR* **1984**, *276* (1), 148–151.

(132) Massa, W.; Hermann, S.; Dehnicke, K. *Z. Anorg. Allg. Chem.* **1982**, *493* (1), 33–40.

(133) Nuszhär, D.; Weller, F.; Dehnicke, K.; Hiller, W. *J. Alloys Compd.* **1992**, *183*, 30–44.

(134) Mazej, Z.; Gilewski, T.; Goreshnik, E. A.; Jagličić, Z.; Derzsi, M.; Grochala, W. *Inorg. Chem.* **2017**, *56* (1), 224–233.

(135) Joubert, P.; Weulersse, J.-M.; Bougon, R.; Gaudreau, B. *Can. J. Chem.* **1978**, *56* (19), 2546–2549.

(136) Bortolus, M. R.; Mercier, H. P. A.; Schrobilgen, G. J. *Chem. Eur. J.* **2020**, *26* (41), 8935–8950.

(137) Turnbull, D.; Gerken, M. *Acta. Crystallogr. E* **2020**, *76* (8), 1345–1348.

(138) Crossman, M. C.; Fawcett, J.; Hope, E. G.; Russell, D. R. *J. Organomet. Chem.* **1996**, *514* (1–2), 87–91.

(139) Stene, R. E.; Scheibe, B.; Karttunen, A. J.; Petry, W.; Kraus, F. *Eur. J. Inorg. Chem.* **2020**, No. 23, 2260–2269.

(140) Tucker, P. A.; Taylor, P. A.; Holloway, J. H.; Russell, D. R. *Acta Crystallogr.* **1975**, *31* (3), 906–908.

(141) Holloway, J. H.; Schrobilgen, G. J. *Inorg. Chem.* **1980**, *19* (9), 2632–2640.

(142) Holloway, J. H.; Schrobilgen, G. J. *Inorg. Chem.* **1981**, *20* (10), 3363–3368.

(143) Engelbrecht, A.; Grosse, A. V. *J. Am. Chem. Soc.* **1952**, *74* (21), 5262–5264.

(144) Green, P. J.; Gard, G. L. *Inorg. Chem.* **1977**, *16* (5), 1243–1245.

(145) Shorafa, H.; Ficicioglu, H.; Tamadon, F.; Girgsdies, F.; Seppelt, K. *Inorg. Chem.* **2010**, *49* (9), 4263–4267.

(146) Grenthe, I.; Drożdżyński, J.; Fujino, T.; Buck, E. C.; Albrecht-Schmitt, T. E.; Wolf, S. F. In *The Chemistry of the Actinide and Transactinide Elements*; Morss, L. R., Edelstein, N. M., Fuger, J., Eds.; Springer Netherlands: Dordrecht, Netherlands, 2008; pp 253–698.

(147) Woidy, P.; Karttunen, A. J.; Kraus, F. *Z. Anorg. Allg. Chem.* **2012**, *638* (12–13),

2044–2052.

(148) Brown, S. D.; Green, P. J.; Gard, G. L. *J. Fluorine Chem.* **1975**, *5* (3), 203–219.

(149) Laptash, N. M.; Udovenko, A. A. *J. Struct. Chem.* **2016**, *57* (2), 390–398.

(150) Veryasov, G.; Morozov, D.; Goreshnik, E.; Jesih, A. *J. Fluorine Chem.* **2013**, *156*, 240–245.

(151) Wollert, R.; Rentschler, E.; Massa, W.; Dehnicke, K. *Z. Anorg. Allg. Chem.* **1991**, *596* (1), 121–132.

(152) Green, P. J.; Gard, G. L. *Inorg. Nucl. Chem. Lett.* **1978**, *14* (4–5), 179–182.

(153) Zachariasen, W. H. *Acta Crystallogr.* **1954**, *7* (12), 783–787.

(154) Nguyen, Q. D. *Acta Crystallogr.* **1972**, *28* (7), 2011–2015.

(155) Brusset, H.; Nguyen, Q. D.; Rubinstein-Auban, A. *Acta Crystallogr.* **1972**, *28* (8), 2617–2619.

(156) Halasyamani, P. S.; Walker, S. M.; O'Hare, D. *J. Am. Chem. Soc.* **1999**, *121* (32), 7415–7416.

(157) Walker, S. M.; Halasyamani, P. S.; Allen, S.; O'Hare, D. *J. Am. Chem. Soc.* **1999**, *121* (45), 10513–10521.

(158) Allen, S.; Barlow, S.; Halasyamani, P. S.; Mosselmans, J. F. W.; O'Hare, D.; Walker, S. M.; Walton, R. I. *Inorg. Chem.* **2000**, *39* (17), 3791–3798.

(159) Ok, K. M.; Doran, M. B.; O'Hare, D. *J. Mater. Chem.* **2006**, *16* (33), 3366–3368.

(160) Almond, P. M.; Talley, C. E.; Bean, A. C.; Peper, S. M.; Albrecht-Schmitt, T. E. *J. Solid State Chem.* **2000**, *154* (2), 635–641.

(161) Talley, C. E.; Bean, A. C.; Albrecht-Schmitt, T. E. *Inorg. Chem.* **2000**, *39* (23), 5174–5175.

(162) Noble, A. M.; Winfield, J. M. *J. Chem. Soc., Chem. Commun.* **1969**, 151.

(163) Handy, L. B.; Brinckman, F. E. *J. Chem. Soc., Chem. Commun.* **1970**, 214–215.

(164) Noble, A. M.; Winfield, J. M. *J. Chem. Soc. A* **1970**, 501–506.

(165) Noble, A. M.; Winfield, J. M. *J. Chem. Soc. A* **1970**, 2574.

(166) Walker, D. W.; Winfield, J. M. *J. Inorg. Nucl. Chem.* **1972**, *34* (2), 759–762.

(167) Vergamini, P. J. *J. Chem. Soc., Chem. Commun.* **1979**, 54–55.

(168) Cuellar, E. A.; Marks, T. J. *Inorg. Chem.* **1981**, *20* (7), 2129–2137.

(169) Walker, D. W.; Winfield, J. M. *J. Fluorine Chem.* **1972**, *1* (3), 376–378.

(170) Jacob, E. *Angew. Chem. Int. Ed. Engl.* **1982**, *21* (S2), 317–330.

(171) Handy, L. B. *J. Fluorine Chem.* **1976**, *7* (6), 641–645.

(172) Leitzke, O.; Sladky, F. *Z. Anorg. Allg. Chem.* **1981**, *480* (9), 7–12.

(173) Seppelt, K. *Chem. Ber.* **1976**, *109* (3), 1046–1052.

(174) Schröder, K.; Sladky, F. *Z. Anorg. Allg. Chem.* **1981**, *477* (6), 95–100.

(175) Turowsky, L.; Seppelt, K. *Z. Anorg. Allg. Chem.* **1990**, *590* (1), 23–36.

(176) Templeton, L. K.; Templeton, D. H.; Bartlett, N.; Seppelt, K. *Inorg. Chem.* **1976**, *15* (11), 2720–2722.

(177) Brinckman, F. E.; Johannesen, R. B.; Hammerschmidt, R. F.; Handy, L. B. *J. Fluorine Chem.* **1975**, *6* (5), 427–436.

(178) Brinckman, F. E.; Johannesen, R. B.; Handy, L. B. *J. Fluorine Chem.* **1972**, *1* (4), 493–497.

(179) Handy, L. B.; Benham, C.; Brinckman, F. E.; Johannesen, R. B. *J. Fluorine Chem.* **1976**, *8* (1), 55–67.

(180) Gerken, M. In *Efficient Preparations of Fluorine Compounds*; Roesky, H. W., Ed.; John Wiley & Sons, Inc.: Hoboken, NJ, USA, 2012; pp 79–81.

(181) Atherton, M. J.; Holloway, J. H. *Inorg. Nucl. Chem. Lett.* **1978**, *14* (2–3), 121–123.

(182) Holloway, J. H.; Puddick, D. C. *Inorg. Nucl. Chem. Lett.* **1979**, *15* (2), 85–87.

(183) Holloway, J. H.; Kaučič, V.; Russell, D. R. *J. Chem. Soc., Chem. Commun.* **1983**, 1079–1081.

(184) Nieboer, J.; Mack, J. P.; Mercier, H. P. A.; Gerken, M. *Inorg. Chem.* **2010**, *49* (13), 6153–6159.

(185) Nieboer, J.; Hillary, W.; Yu, X.; Mercier, H. P. A.; Gerken, M. *Inorg. Chem.* **2009**, *48* (23), 11251–11258.

(186) Nieboer, J.; Yu, X.; Chaudhary, P.; Mercier, H. P. A.; Gerken, M. *Z. Anorg. Allg. Chem.* **2012**, *638* (3–4), 520–525.

(187) Hilbers, M.; Läge, M.; Mattes, R. *Inorg. Chim. Acta* **1992**, *201* (1), 1–3.

(188) Nieboer, J.; Haiges, R.; Hillary, W.; Yu, X.; Richardet, T.; Mercier, H. P. A.; Gerken, M. *Inorg. Chem.* **2012**, *51* (11), 6350–6359.

(189) Quiñones, G. S.; Seppelt, K. *Chem. Eur. J.* **2006**, *12* (6), 1790–1796.

(190) Cohen, B.; Edwards, A. J.; Mercer, M.; Peacock, R. D. *Chem. Commum.* **1965**, 322–323.

(191) Fraser, G. W.; Mercer, M.; Peacock, R. D. *J. Chem. Soc. A* **1967**, 1091–1092.

(192) Fraser, G. W.; Gibbs, C. J. W.; Peacock, R. D. *J. Chem. Soc. A* **1970**, 1708–1711.

(193) Maier, W. B.; Beattie, W. H.; Holland, R. F. *J. Chem. Soc., Chem. Commun.* **1983**, 598–599.

(194) Beattie, W. H.; Maier, W. B. *Polyhedron* **1983**, *2* (12), 1371–1378.

(195) Downs, A. J.; Gardner, C. J. *J. Chem. Soc., Dalton Trans.* **1984**, 2127–2132.

(196) Downs, A. J.; Gardner, C. J. *J. Chem. Soc., Dalton Trans.* **1986**, 1289–1296.

(197) Brown, D.; Berry, J. A.; Holloway, J. H.; Staunton, G. M. *J. Less-Common Met.* **1983**, *92* (1), 149–153.

(198) Tamadon, F.; Seppelt, K. *Angew. Chem. Int. Ed.* **2013**, *52* (2), 767–769.

(199) Peacock, R. D.; Stewart, D. F. *Inorg. Nucl. Chem. Lett.* **1967**, *3* (7), 255–256.

(200) Edwards, A. J. In *Advances in Inorganic Chemistry*; Academic Press, 1983; Vol. 27, pp 83–112.

(201) Shorafa, H.; Seppelt, K. *Z. Anorg. Allg. Chem.* **2009**, *635* (1), 112–114.

(202) Stene, R. E.; Scheibe, B.; Pietzonka, C.; Karttunen, A. J.; Petry, W.; Kraus, F. *J. Fluorine Chem.* **2018**, *211*, 171–179.

(203) Brewer, S. A.; Brisdon, A. K.; Fawcett, J.; Holliman, P. J.; Holloway, J. H.; Hope,

E. G.; Russell, D. R. *Z. Anorg. Allg. Chem.* **2006**, *632* (2), 325–329.

(204) Hwang, I.-C.; Seppelt, K. *Angew. Chem. Int. Ed.* **2001**, *40* (19), 3690.

(205) Zachariasen, W. H. *Acta Crystallogr.* **1949**, *2* (5), 296–298.

(206) Gary Eller, P.; Larson, A. C.; Peterson, J. R.; Ensor, D. D.; Young, J. P. *Inorg. Chim. Acta* **1979**, *37*, 129–133.

(207) Ryan, R. R.; Penneman, R. A.; Asprey, L. B.; Paine, R. T. *Acta Crystallogr.* **1976**, *32* (12), 3311–3313.

(208) Clark, H. C.; Emeléus, H. J. *J. Chem. Soc.* **1957**, 2119–2122.

(209) Fairbrother, F.; Frith, W. C.; Woolf, A. A. *J. Chem. Soc.* **1954**, 1031–1033.

(210) Opalovskii, A. A.; Khaldoyanidi, K. A. *Bull. Acad. Sci. USSR Div. Chem. Sci.* **1973**, *22* (2), 270–272.

(211) Sawodny, W.; Opferkuch, R.; Röhlke, W. *J. Fluorine Chem.* **1978**, *12* (3), 253–256.

(212) Beattie, I. R.; Livingston, K. M. S.; Ozin, G. A.; Reynolds, D. J. *J. Chem. Soc. A* **1969**, 958.

(213) Brown, S. D.; Loehr, T. M.; Gard, G. L. *J. Fluorine Chem.* **1976**, *7* (1–3), 19–32.

(214) Bougon, R.; Wilson, W. W.; Christe, K. O. *Inorg. Chem.* **1985**, *24* (14), 2286–2292.

(215) Dean, P. A. W.; Gillespie, R. J. *Can. J. Chem.* **1971**, *49* (10), 1736–1746.

(216) Edwards, A. J. *J. Chem. Soc., Dalton Trans.* **1972**, 2325–2328.

(217) Edwards, A. J. *J. Chem. Soc.* **1964**, 3714–3718.

(218) Edwards, A. J.; Taylor, P. *J. Chem. Soc., Chem. Commun.* **1971**, 1376.

(219) Marchetti, F.; Pampaloni, G. *Chem. Commun.* **2012**, *48* (5), 635–653.

(220) Benjamin, S. L.; Levason, W.; Reid, G. *Chem. Soc. Rev.* **2013**, *42* (4), 1460–1499.

(221) Levason, W.; Monzittu, F. M.; Reid, G. *Coord. Chem. Rev.* **2019**, *391*, 90–130.

(222) Marchetti, F.; Pinzino, C.; Zacchini, S.; Pampaloni, G. *Angew. Chem. Int. Ed.* **2010**, *49* (31), 5268–5272.

(223) Marchetti, F.; Pampaloni, G.; Pinzino, C. *J. Organomet. Chem.* **2011**, *696* (6), 1294–1300.

(224) Marchetti, F.; Pampaloni, G.; Pinzino, C. *Chem. Eur. J.* **2013**, *19* (41), 13962–13969.

(225) Bresciani, G.; Funaioli, T.; Zacchini, S.; Hayatifar, M.; Marchetti, F.; Pampaloni, G. *Inorg. Chim. Acta* **2018**, *482*, 498–502.

(226) Jenkins, H. D. B.; Krossing, I.; Passmore, J.; Raabe, I. *J. Fluorine Chem.* **2004**, *125* (11), 1585–1592.

(227) Sawodny, W.; Rediess, K.; Thewalt, U. *Z. Anorg. Allg. Chem.* **1980**, *469* (1), 81–86.

(228) Fawcett, J.; Holloway, J. H.; Russell, D. R. *J. Chem. Soc., Dalton Trans.* **1981**, 1212–1218.

(229) Bougon, R.; Fawcett, J.; Holloway, J. H.; Russell, D. R. *J. Chem. Soc., Dalton Trans.* **1979**, 1881–1885.

(230) Holloway, J. H.; Laycock, D.; Bougon, R. *J. Fluorine Chem.* **1984**, *26* (3), 281–293.

(231) Besida, J.; O'Donnell, T. A.; Eller, P. G. *Can. J. Chem.* **1989**, *67* (11), 2047–2051.

(232) Marsden, C. *Aust. J. Chem.* **1990**, *43* (12), 1991.

(233) Gantar, D.; Frlec, B.; Volavšek, B. *J. Chem. Soc., Dalton Trans.* **1984**, 93–94.

(234) Fawcett, J.; Holloway, J. H.; Laycock, D.; Russell, D. R. *J. Chem. Soc., Dalton Trans.* **1982**, 1355–1360.

(235) Barraclough, C. G.; Cockman, R. W.; O'Donnell, T. A. *Inorg. Nucl. Chem. Lett.* **1981**, *17* (3–4), 83–86.

(236) Schrobilgen, G. J.; Holloway, J. H.; Russell, D. R. *J. Chem. Soc., Dalton Trans.* **1984**, *43* (7), 1411–1415.

(237) Yeh, S.; Bartlett, N. *Rev. Chem. Miner.* **1986**, *23* (4–5), 676–689.

(238) LeBlond, N.; Mercier, H. P. A.; Dixon, D. A.; Schrobilgen, G. J. *Inorg. Chem* **2000**, *39* (20), 4494–4509.

(239) Mercier, H. P. A.; Schrobilgen, G. J. *Inorg. Chem.* **1993**, *32* (2), 145–151.

(240) Supeł, J.; Marx, R.; Seppelt, K. *Z. Anorg. Allg. Chem.* **2005**, *631* (15), 2979–2986.

(241) LeBlond, N.; Dixon, D. A.; Schrobilgen, G. J. *Inorg. Chem.* **2000**, *39* (12), 2473–2487.

(242) Peterson, S. W.; Willett, R. D.; Huston, J. L. *J. Chem. Phys.* **1973**, *59* (1), 453–459.

(243) Spandl, J.; Supeł, J.; Drews, T.; Seppelt, K. *Z. Anorg. Allg. Chem.* **2006**, *632* (14), 2222–2225.

(244) Supeł, J.; Abram, U.; Hagenbach, A.; Seppelt, K. *Inorg. Chem.* **2007**, *46* (14), 5591–5595.

(245) Franklin, K. J.; Lock, C. J. L.; Sayer, B. G.; Schrobilgen, G. J. *J. Am. Chem. Soc.* **1982**, *104* (20), 5303–5306.

(246) Supeł, J.; Hagenbach, A.; Abram, U.; Seppelt, K. *Z. Anorg. Allg. Chem.* **2008**, *634* (4), 646–648.

(247) Hahn, E. M.; Casini, A.; Kühn, F. E. *Coord. Chem. Rev.* **2014**, *276*, 97–111.

(248) Riedel, S.; Kaupp, M. *Coord. Chem. Rev.* **2009**, *253* (5–6), 606–624.

(249) Bougon, R. *J. Fluorine Chem.* **1991**, *53* (3), 419–427.

(250) Christe, K. O.; Dixon, D. A.; Mack, H. G.; Oberhammer, H.; Pagelot, A.; Sanders, J. C. P.; Schrobilgen, G. J. *J. Am. Chem. Soc.* **1993**, *115* (24), 11279–11284.

(251) Bougon, R.; Buu, B.; Seppelt, K. *Chem. Ber.* **1993**, *126* (6), 1331–1336.

(252) Casteel, W. J.; Dixon, D. A.; LeBlond, N.; Lock, P. E.; Mercier, H. P. A.; Schrobilgen, G. J. *Inorg. Chem.* **1999**, *38* (10), 2340–2358.

(253) Goettel, J. T.; Turnbull, D.; Gerken, M. *J. Fluorine Chem.* **2015**, *174*, 8–13.

(254) Gerken, M.; Dixon, D. A.; Schrobilgen, G. J. *Inorg. Chem.* **2002**, *41* (2), 259–277.

(255) Hughes, M. J.; Mercier, H. P. A.; Schrobilgen, G. J. *Inorg. Chem.* **2009**, *48* (10), 4478–4490.

(256) Casteel, W. J.; Dixon, D. A.; Mercier, H. P. A.; Schrobilgen, G. J. *Inorg. Chem.* **1996**, *35* (15), 4310–4322.

(257) Hughes, M. J.; Mercier, H. P. A.; Schrobilgen, G. J. *Inorg. Chem.* **2010**, *49* (1), 271–284.

(258) Schrock, R. R.; Hoveyda, A. H. *Angew. Chem. Int. Ed.* **2003**, *42* (38), 4592–4633.

(259) McElwee-White, L. *J. Chem. Soc., Dalton Trans.* **2006**, No. 45, 5327–5333.

(260) Schröder, J.; Grewe, F. J. *Angew. Chem. Int. Ed. Engl.* **1968**, *7* (2), 132–133.

(261) Schröder, J.; Grewe, F. J. *Chem. Ber.* **1970**, *103* (5), 1536–1546.

(262) O'Donnell, T. A.; Peel, T. E. *J. Inorg. Nucl. Chem.* **1976**, *28*, 61–62.

(263) Stene, R.; Scheibe, B.; Ivlev, S. I.; Karttunen, A. J.; Petry, W.; Kraus, F. *Z. Anorg. Allg. Chem.* **2020**. In press.

Chapter 2 – Experimental

2.1. General Methods

2.1.1. Standard Techniques

CAUTION! *Hydrogen fluoride (HF) is an extremely corrosive and toxic material. Elemental F_2 and the binary fluorides employed in the research reported herein evolve HF upon exposure to traces of moisture, and proper safety procedures must be implemented during their handling.*

The compounds synthesised herein, as well as many of the reagents used to prepared them, are highly moisture sensitive and must be handled under rigourously anhydrous conditions. Reactions were typically carried out in vessels constructed from heat sealed ¼"-o.d. FEP tubes affixed to Kel-F or 316-stainless-steel (Swagelok SS-1KF2) valves via flared fittings (45 or 37.5° flare, respectively). Larger-scale reactions (> 1 g) were instead conducted in ¾"-o.d. FEP reactors equipped with 316-stainless-steel valves (Swagelok SS-ORF2) and NMR-scale reactions were performed in fused ¼"-o.d./4-mm-o.d. FEP reactors. The reactors were dried under dynamic vacuum for ≥ 4 h, followed by passivation under *ca*. 800 Torr of F_2 for ≥ 8 h prior to use. Glass reaction vessels were flame-dried using a Bunsen burner under dynamic vacuum for ≥ 24 h prior to use.

Volatile materials were handled on nickel/316-stainless-steel or Pyrex vacuum lines. The quality of vacuum was achieved using high-vacuum pumps (Edwards RV8 or RV12) and verified periodically using a McLeod gauge (Labconco). Volatile materials were captured in liquid-N_2-cooled (–196 °C) Pyrex traps.

Elemental F_2 and volatile binary fluorides were handled on a nickel/316-stainless-steel vacuum line equipped with 316-stainless-steel valves and fittings (Autoclave

Engineers). Vacuum (*ca*. 10^{-4} Torr) and internal line pressures (0–1000 Torr) were monitored using absolute capacitance manometers (MKS Baratron, type 626 , 0–10 or 0–1000 Torr). Elemental F_2 and HF (*ca*. 800 Torr) were scrubbed by passing through a stainless-steel cylinder (75 cm, 17-cm o.d.) containing soda lime (EMD, 4 mesh; "rough vacuum"). Traces of F_2 (< 1 Torr) and other reactive species were scrubbed by passing through smaller stainless-steel cylinders (30 cm) containing activated charcoal ("fine vacuum"). Reactors were connected to the line using PFTE vacuum fittings (Swagelok). The metal vacuum line is illustrated in Figure 2.1.

Anhydrous HF was specifically handled in a ¼"-o.d. FEP submanifold equipped with a Kel-F valve (Figure 2.2), all of which was passivated under an atmosphere of F_2 for ≥ 4 h prior to use.

Volatile materials that do not react with glass, nor with traces of moisture to form glass-reactive species, were handled in Pyrex vacuum lines equipped with grease-free PTFE stopcocks (J. Young or Chemglass). The vacuum (*ca*. 10^{-5} Torr) was monitored using thermocouple vacuum gauges (Varian, model 531). Internal line pressures (0–1000 Torr) were measured using Be/Cu bourdon-tube pressure gauges (Heise, model CC or Ashcroft, model A4A). Reactors and distillation apparatuses were connected to the line using Ultra-Torr vacuum fittings (Swagelok). A Pyrex vacuum line is illustrated in Figure 2.3.

Solid materials were handled in a dry box (OmniLab, Vacuum Atmospheres) under an atmosphere of N_2. Volatile materials were frozen in the dry box using an evacuable well containing a sleeve of copper BBs that were cooled externally using liquid N_2 to achieve a minimum temperature of –160 °C. This cold well was also used to charge reactors with

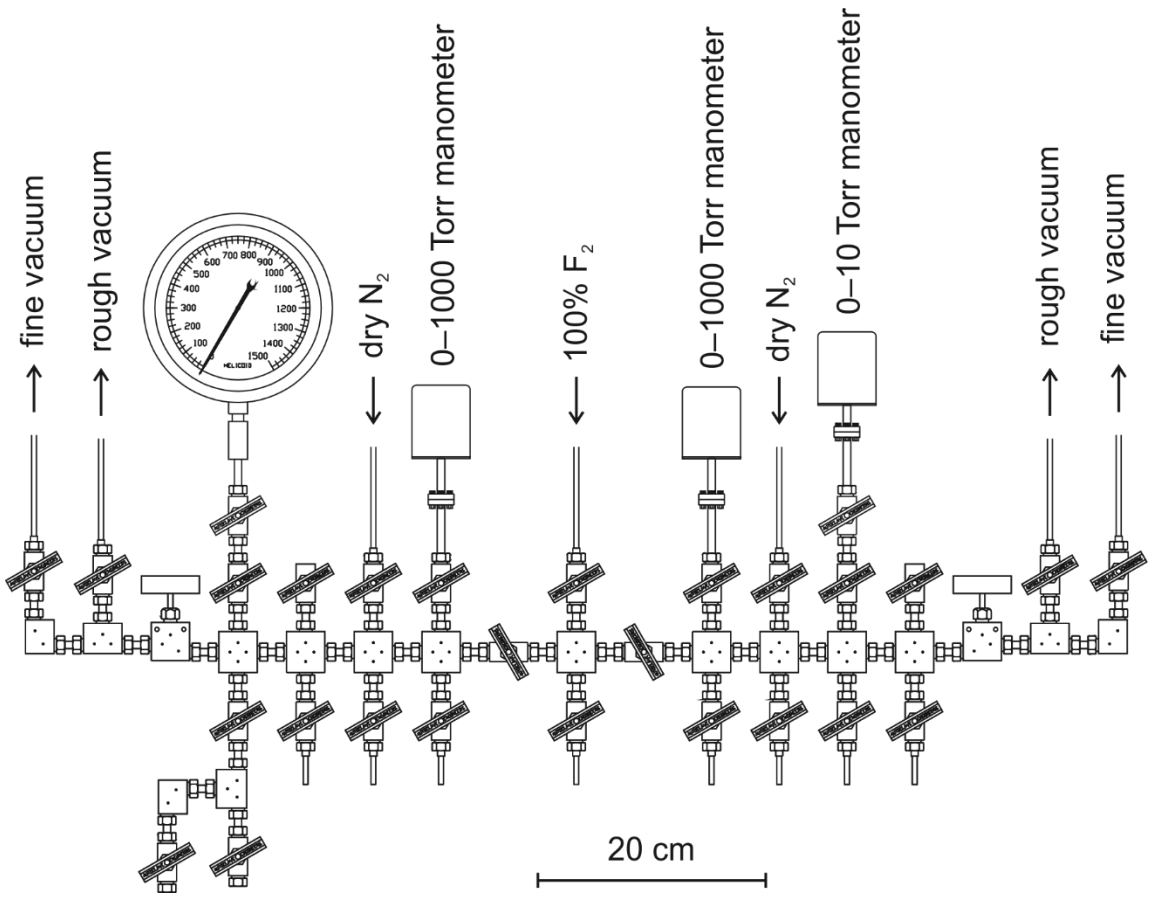

Figure 2.1. Nickel/316-stainless-steel (Autoclave Engineers) vacuum line, equipped with absolute capacitance manometers (MKS Baratron, type 626, 0–10 or 0–1000 Torr). Adapted from Jared Nieboer's M.Sc. thesis.

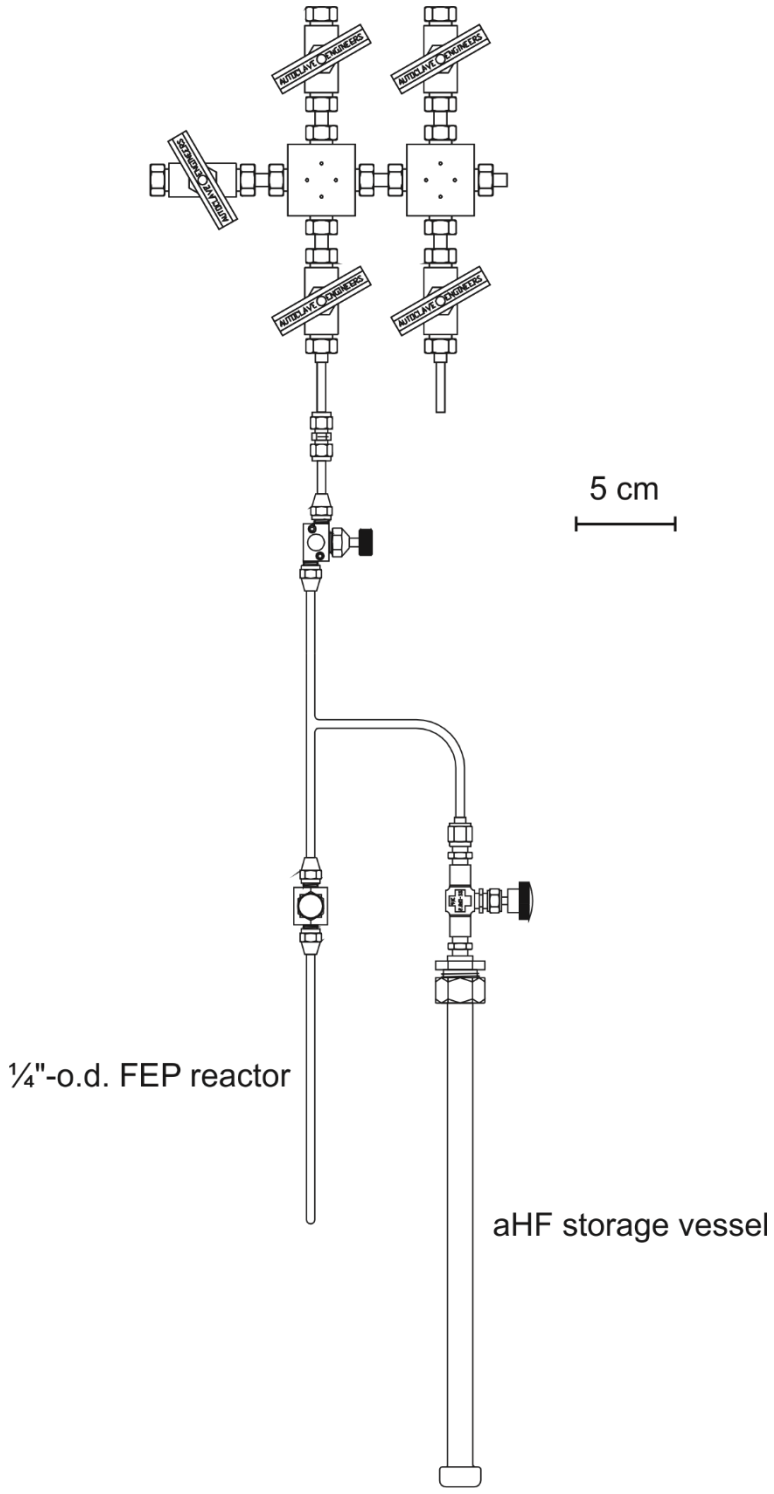

Figure 2.2. Apparatus for vacuum distillations of aHF. Adapted from Jared Nieboer's M.Sc. thesis.

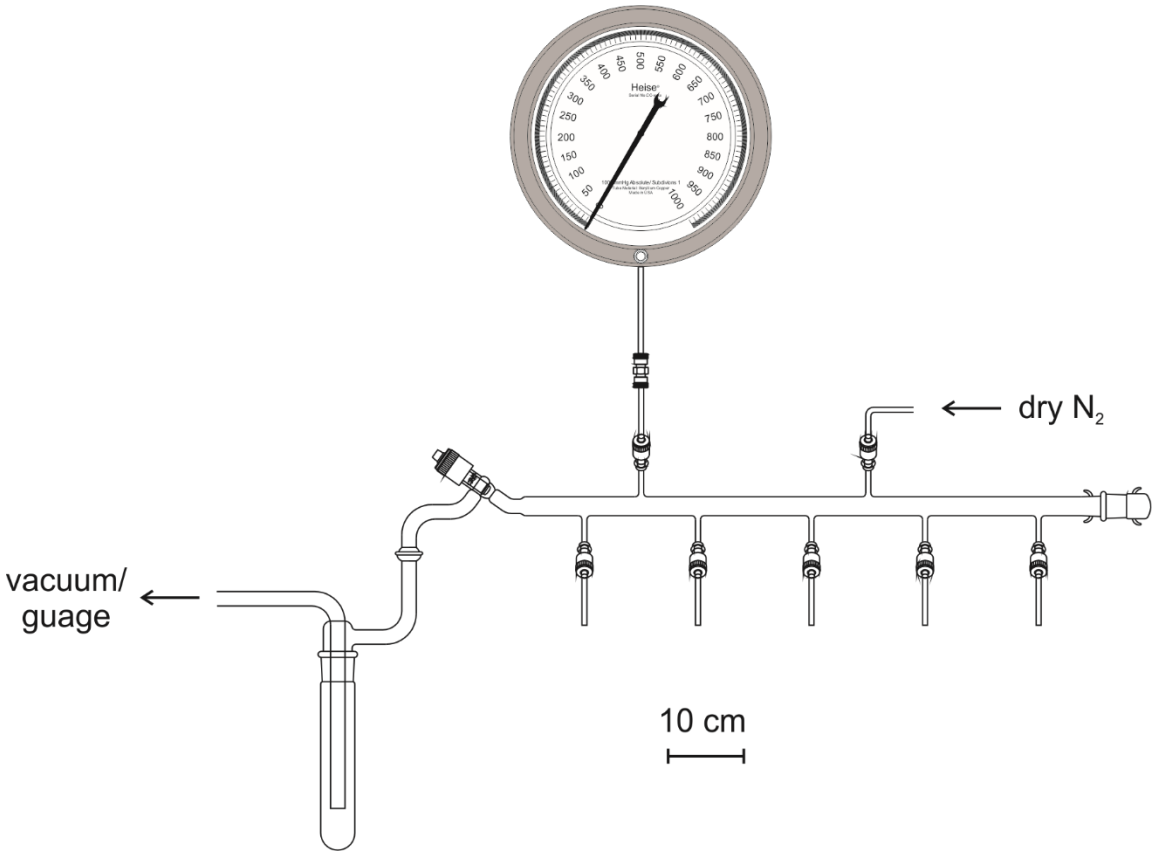

Figure 2.3. Pyrex vacuum line, equipped with grease-free PTFE stopcocks (J. Young), a thermocouple vacuum gauge (Varian, model 531), and Be/Cu bourdon-tube pressure gauge (Heise, model CC). Adapted from Jared Nieboer's M.Sc. thesis.

solid reagents that would otherwise react unfavourably in the solid state at ambient temperature. For vacuum distillations, reactors were cooled to –196 °C using liquid N_2. Otherwise, reactors were cooled below ambient temperature using anhydrous C_2H_5OH/liquid N_2 baths (min. temperature: *ca*. –120 °C). Long-term low-temperature storage (days or weeks) was achieved using an anhydrous C_2H_5OH bath that was thermostatted (Thermo NESLAB, CC-100) between –30 and –80 °C.

2.1.2. Raman Spectroscopy

Variable-temperature Raman spectra were recorded using a Bruker RFS-100 Raman spectrometer outfitted with a quartz beam splitter and liquid-N_2 cooled germanium detector. The 1064-nm line of a Nd:YAG laser was used for excitation of the sample, and backscattered (180°) radiation was sampled. The usable Stokes range of the collected data was 85–3500 cm^{-1} with a spectral resolution of 2 cm^{-1}. The laser power was typically set to 150 mW.

For materials that were thermally stable and did not attack glass, Raman spectra were recorded on flame-sealed m.p. capillaries at ambient temperature. The m.p. capillaries were dried in an oven at 140 °C for *ca*. 72 h and transferred hot into the dry box antechamber. The samples were prepared by charging the m.p. capillaries in the dry box and sealing them with Kel-F grease before flame-sealing them under the internal atmosphere of N_2 using a Bunsen burner.

For solutions, thermally unstable materials, or materials that attacked glass, Raman spectra were recorded on FEP reactors in a low-temperature-mounting apparatus at either ambient temperature or –100 °C. The lower temperature was achieved using a resistive liquid N_2 boiler, passing cold N_2 gas over a glass Dewar flask containing the sample.

2.1.3. NMR Spectroscopy

Variable-temperature NMR spectra were recorded using a Bruker Avance II spectrometer (7.05 T; 300.16 MHz for ^{1}H, 282.43 MHz for ^{19}F, 121.51 MHz for ^{31}P, 75.48 MHz for ^{13}C) equipped with a 5-mm BBFO probe and referenced externally to $CFCl_3$ (^{19}F), $Si(CH_3)_4$ (^{1}H and $^{13}C\{^{1}H\}$), or 85% H_3PO_4 (^{31}P) at 20 °C.

Samples were typically prepared as 4-mm-o.d. FEP inserts by heat-sealing fused ¼"-o.d./4-mm-o.d. FEP reactors under dynamic vacuum, during which the contents of the reactor were frozen in liquid N_2 at –196 °C. Spectra were recorded on these samples sheathed in 5-mm-o.d. glass NMR tubes, unlocked, at temperatures between –80 °C and 20 °C. Low temperatures were achieved using a resistive liquid N_2 boiler, passing cold N_2 gas over the sample. The exception is a sample of $[W(NC_6F_5)F_4]_x$ in CH_2Cl_2, which was prepared in a flame-sealed 5-mm-o.d. glass NMR tube; the tube was flame dried under dynamic vacuum for *ca*. 24 h prior to use.

Spectral simulations were performed using MestreNova (version 9.0)[1] and SpinWorks (version 4.2.7).[2]

2.1.4. X-ray Crystallography

2.1.4.1. Crystal Growth and Mounting

Crystals were invariably grown from solutions and isolated in ¼"-o.d. FEP reactors. The crystal mounting apparatus consists of an aluminium trough that is positioned in a silvered-glass Dewar sleeve, all of which is simultaneously dried and cooled to temperatures between –40 and –80 °C by passing N_2 gas through a 10.5-L Dewar of liquid N_2 (Figure 2.4). The ¼"-o.d. FEP reactors containing the crystals were placed in the trough and cut, and the crystals were transferred onto the trough. Crystals were selected for

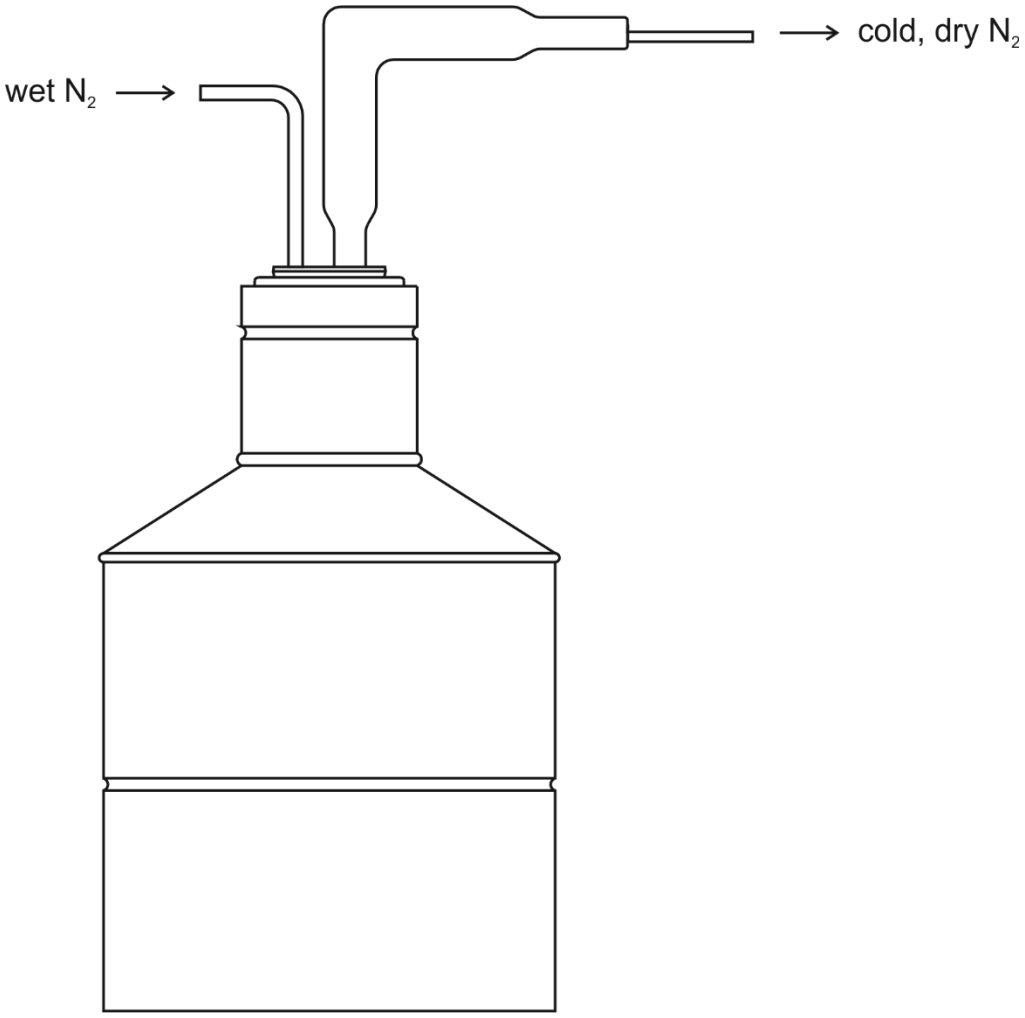

Figure 2.4. Low-temperature crystal-mounting apparatus, consisting of a 10.5-L Dewar equipped with a glass N_2 inlet, mirrored-glass Dewar sleeve, and aluminium trough.

mounting using a microscope and affixed to a Nylon cryo-loop (Hampton) using perfluorinated polyether oil (Fomblin Z-25) before being quickly transferred and affixed to the goniometer head.

In almost all cases, the goniometer head was pre-cooled to –173 °C. However, in the case of $[WF_4(NC_5H_5)_4][O_3SCF_3]\cdot 1.5CH_3CN$, powdering occurred upon mounting at this temperature due to thermal shock. This was avoided by suspending the crystals in Fomblin Z-15 oil at –40 °C, mounting them at that temperature, and cooling the goniometer head to –173 °C at a rate of 320 °C h^{-1}.

2.1.4.2. Data Collection and Reduction

The crystals were centered on a Rigaku SuperNova diffractometer equipped with a Dectris Pilatus 3R 200K-A hybrid-pixel-array detector, a four-circle κ goniometer, an Oxford Cryostream 800, and sealed MoKα and CuKα X-ray sources. Data were collected using the MoKα source (λ = 0.71073 Å) between –163 °C and −173 °C. Crystals were screened for quality before a pre-experiment was run to determine the unit cell, and a data-collection strategy was calculated based on the determined unit cell and intensity of the preliminary data. This strategy was optimised to collect five-fold redundant data at a resolution of 0.77 Å. The data were processed using CrysAlisPro,[3] which applied necessary Lorentz and polarisation corrections to the integrated data and scaled the data. A numerical (Gaussian-grid) absorption correction was generated based upon the indexed faces of the crystal.

In the case of $W(NC_6F_5)F_4(NCCH_3)$, a twin component (rotated by 180° about [0 1 0] in the real lattice) was found using the Ewald reciprocal space viewer, resulting in two

components in a ratio of 0.52:0.48. The data for these twin components were reduced separately.

2.1.4.3. Structure Solution and Refinement

Atom positions were determined using the intrinsic phasing method (ShelXT)[4] and were refined using least-squares refinement (ShelXL).[5] Non-hydrogen atoms were refined anisotropically and recommended weights for the atoms were determined before hydrogen atoms were introduced using a riding model (HFIX). The positions of hydrogen atoms involved in significant intermolecular interactions were refined without positional restraints after either being located directly in the difference Fourier map or introduced using the riding model. The maximum and minimum electron density in the difference Fourier maps were located near the tungsten atom in all cases. Structure solution and refinement were performed with the aid of Olex2 (version 1.2).[6]

Structures that have been published were deposited in the Cambridge Crystallographic Data Centre (CCDC). Compounds the crystal structures of which have been elucidated, their internal and CCDC identification codes, as well as their CCDC deposition numbers are given in Table 2.1. The data can be accessed in .cif format from https://www.ccdc.cam.ac.uk free of charge.

Table 2.1. Internal and CCDC Identification Codes and CCDC Deposition Numbers for Crystal Structures Reported Herein

	Identification Code		CCDC
	Internal	**CCDC**	
$WF_6(NC_5H_5)$	MG16038c	ODUDUP	1853269
$WF_6(4\text{-}NC_5H_4CH_3)$	MG18002	ODUFAX	1853270
$WF_6\{4\text{-}NC_5H_4N(CH_3)_2\}$	MG17029	ODUFEB	1853271
$[C_5H_5NH][W(NC_6F_5)F_5]$	MG16042	DECQEK01	1566648
$[N(CH_3)_4][W(NC_6F_5)F_5]$	MG16014	DECQIO01	1566649
$[C_5H_5NH][W_2(NC_6F_5)_2F_9]$	MG17016	DECQOU01	1566650
$W(NC_6F_5)F_4(NCCH_3)$	MG16045	ROGQEM	1899538
$W(NC_6F_5)F_4(NC_5H_5)$	MG16046	ROGQIQ	1899539
$WOF_4(NC_5H_5)$	MG18011b	SAJCIP01	1899540
$WOF_4(NC_5H_5)_2$	MG18010	SAJCOV01	1899541
$[WF_5(2,2'\text{-bipy})][Sb_2F_{11}]$	MG18023	JOMXUH	1918937
$[WF_5(1,10\text{-phen})][Sb_2F_{11}]$	MG19003	JOMYAO	1918938
$[WF_5(1,10\text{-phen})][SbF_6]\cdot SO_2$	MG19002	JOMYES	1918939
$WF_5(NC_5H_5)_2$	MG18015b	ZUTDAW	1979285
$[WF_4(NC_5H_5)_4][O_3SCF_3]\cdot 1½CH_3CN$	MG19022b		
$[WF_4\{P(CH_3)_3\}_4][O_3SCF_3]$	MG19023		

2.2. Preparation and Purification of Reagents

2.2.1. Fluorine and Binary Fluorides

Elemental F_2 (Linde, 100%) and MoF_6 (Ozark-Mahoning) were used without further purification. Hydrogen fluoride (Air Products, 99.9%) was dried under an atmosphere of F_2 for *ca*. 2 weeks before being distilled onto $K_2[NiF_6]$ (Fluka). Tungsten hexafluoride (Ozark-Mahoning) and SbF_5 (Ozark-Mahoning) were purified by distillation. Arsenic trifluoride was prepared via reaction of As_2O_3 with CaF_2 in H_2SO_4 and stored over NaF.[7] Arsenic pentafluoride was subsequently prepared as described previously via fluorination of AsF_3 with F_2.[7]

2.2.2. Common Solvents

Sulfur dioxide (Matheson) was purified by distillation and stored over CaH_2. Dichloromethane was dispensed from a solvent purification system (M. Braun MB-SPS) onto 3-Å molecular sieves before being distilled onto fresh sieves. Toluene was dispensed from a solvent purification system, distilled onto sodium metal, and finally stored over Na/K alloy. Trichlorofluoromethane (Aldrich, 99+%) was dried over CaH_2 and purified by distillation.

2.2.3. Volatile Bases

Acetonitrile (Baker 99.8%) was purified using P_4O_{10} and 4-Å molecular sieves, as described previously.[8] Pyridine (Sigma-Aldrich, 99.8%) was dried over 3-Å molecular sieves and distilled onto fresh sieves. 4-Methylpyridine (Sigma-Aldrich) was dried over potassium metal and distilled onto 4-Å molecular sieves. The phosphines $P(CH_3)_3$ and $P(C_2H_5)_3$ were gifted from Dr. Paul G. Hayes and purified by distillation onto 3-Å molecular sieves.

2.2.4. Trimethylsilyl Reagents

Hexamethyldisiloxane (Sigma-Aldrich, ≥ 98%) was purified by distillation and stored over 3-Å molecular sieves. Trimethylsilyl triflate (Alfa Aesar, 99%) was purified by distillation. The $[(CH_3)_3Si(NC_5H_5)][O_3SCF_3]$ salt was prepared via reaction of $(CH_3)_3SiO_3SCF_3$ with excess C_5H_5N, either neat or in CH_2Cl_2.[9]

2.2.5. Solid Bases

4-(Dimethylamino)pyridine (Sigma-Aldrich, 99%), 4,4′-bipyridine (Sigma-Aldrich, 98%), and $C_6F_5NH_2$ (Sigma-Aldrich, 99%) were used without further purification. 2,2′-Bipyridine (Sigma-Aldrich, ≥ 99%) was dried under dynamic vacuum for *ca*. 16 h at ambient temperature. 1,10-Phenanthroline (Sigma-Aldrich, ≥ 99%) and $[N(CH_3)_4]F{\cdot}4H_2O$ (Fluka, 98%) were dried via recrystallisation from $(CH_3)_2CHOH$ (Sigma-Aldrich, 99.5%) that was dried over sodium metal.[10]

2.2.6. Tungsten Oxide Tetrafluoride

Tungsten oxide tetrafluoride was prepared via reaction of WF_6 with quartz wool (Perkin Elmer) in aHF and purified by sublimation, as described previously.[11]

2.2.7. Main-Group and Transition-Metal Fluoride Adducts

The materials listed were prepared as described previously. The $WF_6(NC_5H_5)_n$ (n = 1, 2) adducts were prepared via reactions of WF_6 with C_5H_5N (1 or 2 molar equivalents) in CH_2Cl_2,[12] whereas $[N(CH_3)_4][WF_7]$ was prepared using $[N(CH_3)_4]F$ and excess WF_6 in CH_2Cl_2.[13] The $WOF_4(NCCH_3)$ adduct was prepared via reaction of WF_6 with $\{(CH_3)_3Si\}_2O$ in CH_3CN.[14] The $WOF_4(NC_5H_5)_n$ (n = 1, 2) adducts were prepared via reactions of WOF_4 with C_5H_5N in CH_2Cl_2 (n = 1) or excess C_5H_5N (n = 2).[15] The $SbF_5(OSO)$ adduct was prepared via dissolution of SbF_5 in SO_2.[16]

2.3. Synthesis and Crystal Growth

2.3.1. Heptacoordinate WF_6 Adducts with C_5H_5N and Derivatives Thereof

2.3.1.1. $WF_6(NC_5H_5)$

Tungsten hexafluoride (2.979 g, 10.00 mmol) was distilled into a ¾”-o.d. FEP reactor, followed by CH_2Cl_2 (2 mL) and C_5H_5N (0.655 g, 8.28 mmol). The reactor was warmed to ambient temperature and agitated until all solid dissolved, resulting in a colourless solution from which colourless blocks crystallised over the course of 1 h at ambient temperature. The volatile materials were removed under dynamic vacuum at −60 °C for 2 h and at ambient temperature for 20 min, yielding $WF_6(NC_5H_5)$ (3.114 g, 8.26 mmol) as a fine, white powder in nearly quantitative yield.

NMR (ppm, CH_3CN, 20 °C, unlocked): $\delta(^{19}F)$ 166 (s, br). $\delta(^{1}H)$ 9.08 (H_o, dd, $^{3}J(H_o–H_m)$ = 6.6 Hz, $^{4}J(H_o–H_p)$ = 1.4 Hz); 8.29 (H_p, tt, $^{3}J(H_p–H_m)$ = 7.6 Hz); 7.82 (H_m, dd). $\delta(^{13}C\{^{1}H\})$ 145.84 (C_o), 144.12 (C_p), 127.32 (C_m).

Colourless plates of $WF_6(NC_5H_5)$ crystallised from CH_3CN in a ¼”-o.d. FEP reactor upon cooling the bottom of the reactor to −196 °C to effect rapid crystallisation of a small amount of the solute, followed by submerging the reactor in an ethanol bath cooled to −10 °C and slowly cooling to −40 °C thereafter. Alternatively, crystals could be grown from SO_2 upon cooling to –70 °C or CH_2Cl_2 as described previously. However, in the latter case, the crystals were observed to decompose readily at ambient temperature, despite adopting the same phase as those grown from CH_3CN.

2.3.1.2. $WF_6(4\text{-}NC_5H_4CH_3)$

4-Methylpyridine (0.064 g, 0.69 mmol) and CH_2Cl_2 (0.695 g) were distilled into a ¼”-o.d. FEP reactor at −196 °C, after which the reactor was kept below −50 °C.

Subsequently, WF_6 (0.280 g, 0.940 mmol) was distilled into the reactor at −196 °C and the mixture was warmed to −50 °C, upon which a white solid immediately precipitated from solution. The reactor was allowed to warm further to ambient temperature, resulting in dissolution of the solid to afford a colourless solution. The volatile materials were removed under dynamic vacuum at −60 °C for 1 h and at ambient temperature for 10 min, affording $WF_6(4\text{-}NC_5H_4CH_3)$ (0.251 g, 0.642 mmol, 93% with respect to 4-methylpyridine) as a white powder.

NMR (ppm, CH_3CN, 20 °C, unlocked): $\delta(^{19}F)$ 168 (s, br). $\delta(^{1}H)$ 8.98 (H_o, d, $^{3}J(H_o–H_m)$ = 7.7 Hz); 7.61 (H_m, d); 2.49 (CH_3, s). $\delta(^{13}C\{^{1}H\})$ 145.58 (C_o), 127.66 (C_m), 21.35 (CH_3). Impurities of $[WF_7]^-$ (3 mol%, $\delta(^{19}F)$ = 143.42 ppm) and various oxidotungsten(VI) species (trace, $\delta(^{19}F)$ = 61–78 ppm) were observed by ^{19}F NMR spectroscopy.

Colourless blocks of $WF_6(4\text{-}NC_5H_4CH_3)$ could be crystallised by slowly cooling a concentrated SO_2 solution to −70 °C in a ¼”-o.d. FEP reactor.

2.3.1.3. $WF_6\{4\text{-}NC_5H_4N(CH_3)_2\}$

In the dry box, a ¼”-o.d. FEP reactor was charged with 4-(dimethylamino)pyridine (0.060 g, 0.49 mmol). Dichloromethane (0.767 g) was distilled into the reactor at −196 °C, followed by WF_6 (0.179 g, 0.601 mmol). Upon warming the reactor to −60 °C, a dark red suspension formed immediately. The reactor was warmed to ambient temperature, then briefly to 45 °C, with agitation to ensure reaction completion. The volatile materials were removed under dynamic vacuum at −70 °C for 2 h and at ambient temperature for 5 min, affording $WF_6\{4\text{-}NC_5H_4N(CH_3)_2\}$ (0.208 g, 0.495 mmol, 100% yield with respect to 4-(dimethylamino)pyridine) as a dark red powder.

NMR (ppm, CH_3CN, 20 °C, unlocked): δ(^{19}F) 164 (s, br). δ(^{1}H) 8.58 (H_o, d, $^{3}J(H_o–H_m)$ = 7.7 Hz); 6.68 (H_m, d); 3.10 (CH_3, s). δ(^{13}C{^{1}H}) 145.61 (C_o), 106.74 (C_m), 39.88 (CH_3). Impurities of $[WF_7]^-$ (6 mol%, δ(^{19}F) = 143.55 ppm) and WOF_4{4-$NC_5H_4N(CH_3)_2$} (trace, δ(^{19}F) = 61.09 ppm, ^{1}J (F–^{183}W) = 63.5 Hz) were observed by ^{19}F NMR spectroscopy.

Red-orange needles of WF_6{4-$NC_5H_4N(CH_3)_2$} were grown by keeping a dilute CH_3CN solution at –40 °C for 1 h in a ¼”-o.d. FEP reactor.

2.3.1.4. $F_6W(4,4'\text{-bipy})WF_6$

In the dry box, a ¼”-o.d. FEP reactor was charged with 4,4′-bipyridine (0.029 g, 0.19 mmol). Dichloromethane (0.415 g) was distilled into the reactor at −196 °C, followed by WF_6 (0.231 g, 0.776 mmol). Upon warming the reactor to ambient temperature, a large amount of white solid precipitated from the solution; brief heating to 45 °C or agitation in an ultrasonic bath did not effect any noticeable dissolution. The reactor was left to stand at ambient temperature for 2 h with occasional agitation before the volatile materials were removed under dynamic vacuum at −70 °C for 30 min and at ambient temperature for 2 min, affording $F_6W(4,4'\text{-bipy})WF_6$ (0.141 g, 0.188 mmol, 100% yield with respect to 4,4′-bipy) as a white powder. The sample could not be characterised by ^{19}F NMR spectroscopy due to its insolubility in the solvents employed herein.

2.3.2. $[W(NC_6F_5)F_5]^-$ and $[W_2(NC_6F_5)_2F_9]^-$ Salts

2.3.2.1. $[C_5H_5NH][W(NC_6F_5)F_5]$

In the dry box, a ¼”-o.d. FEP reactor was charged with $WF_6(NC_5H_5)$ (0.568 g, 1.51 mmol) and $C_6F_5NH_2$ (0.291 g, 1.59 mmol) at ambient temperature, causing immediate formation of an orange substance upon contact of the solids; the reactor was kept at −80

°C to curtail further solid-state reactions. Dichloromethane (1.097 g) was distilled into the reactor at −196 °C and warmed to ambient temperature, resulting in the formation of an orange solution. Volatile materials were removed under dynamic vacuum at ambient temperature (with constant agitation) for 1 h and at 45 °C for 30 min, yielding $[C_5H_5NH][W(NC_6F_5)F_5]$ (0.809 g, 1.50 mmol, 99.4% yield with respect to $WF_6(NC_5H_5)$) as a coarse yellow powder.

NMR (ppm, CH_3CN, 20 °C, unlocked): $\delta(^1H)$ 13.78 (s, H_N), 8.73 (d, H_o, $^3J(H_o-H_m)$ ≈ 6 Hz), 8.60 (t, H_p, $^3J(H_m-H_p)$ ≈ 8 Hz), 8.05 (t, H_m). Fluorine-19 NMR spectroscopic data are provided in Tables 4.5 and 4.6. An impurity of $[WOF_5]^-$ (1 mol %) was observed by ^{19}F NMR spectroscopy.

Long, yellow plates of $[C_5H_5NH][W(NC_6F_5)F_5]$ were grown by cooling a CH_2Cl_2 solution to −35 °C, followed by slow removal of the solvent under dynamic vacuum at that temperature.

2.3.2.2. $[N(CH_3)_4][W(NC_6F_5)F_5]$

In the dry box, a ¼”-o.d. FEP reactor was charged with $[N(CH_3)_4][WF_7]$ (0.2324 g, 0.594 mmol) and $C_6F_5NH_2$ (0.1150 g, 0.628 mmol) at ambient temperature; no reaction between the solids was observed. Acetonitrile (0.300 g) was distilled into the reactor at −196 °C and warmed to ambient temperature, resulting in the formation of an orange solution. Volatile materials were removed under dynamic vacuum at ambient temperature (with constant agitation) for 30 min and at 45 °C for 30 min, yielding $[N(CH_3)_4][W(NC_6F_5)F_5]$ (0.317 g, 0.594 mmol, 100% yield with respect to $[N(CH_3)_4][WF_7]$) as a coarse yellow powder.

NMR (ppm, CH_3CN, 20 °C, unlocked): δ(^{1}H) 3.07 (s, CH_3). Fluorine-19 NMR spectroscopic data are provided in Tables 4.5 and 4.6. Impurities of $[WOF_5]^-$ (1 mol %), $C_6F_5NH_2$ (2 mol %), $[W_2(NC_6F_5)_2F_9]^-$ (trace), and HF (trace) were observed by ^{19}F NMR spectroscopy.

Yellow blocks of $[(CH_3)_4N][W(NC_6F_5)F_5]$ were grown from a CH_3CN solution by slow removal of the solvent under dynamic vacuum at −40 °C.

2.3.2.3. $[C_5H_5NH][W_2(NC_6F_5)_2F_9]$

In the dry box, the straight arm of a T-shaped ¼”-o.d. reactor was charged with $[C_5H_5NH][W(NC_6F_5)F_5]$ (0.383 g, 0.709 mmol). Anhydrous HF (0.136 g, 6.80 mmol) was distilled into the reactor at −196 °C and warmed to ambient temperature, resulting in the formation of a deep red solution. Cooling the solution to −25 °C resulted in the precipitation of yellow crystals; the solution was then decanted from these crystals into the side arm of the reactor, and the HF was partially condensed back into the straight arm at −196 °C. This was repeated five times, resulting in yellow crystals remaining in the straight arm and a red solution in the side arm. Volatile materials were removed under dynamic vacuum at −70 °C for 2 h and at ambient temperature over 30 min, yielding $[C_5H_5NH][W_2(NC_6F_5)_2F_9]$ (0.266 g, 0.271 mmol, 76.5% yield with respect to $[C_5H_5NH][W(NC_6F_5)F_5]$) in the straight arm as a yellow powder.

NMR (ppm, CH_3CN, 20 °C, unlocked): δ(^{1}H) 13.18 (tt, H_N, $^1J(H–^{14}N)$ = 68.4 Hz), 8.71 (t, H_o, $^3J(H_N–H_o) \approx {}^3J(H_o–H_m) \approx 6$ Hz), 8.61 (tt, H_p, $^3J(H_m–H_p) \approx 8$ Hz, $^5J(H_N–H_p) \approx 1$ Hz), 8.05 (t, H_m). Fluorine-19 NMR spectroscopic data are provided in Tables 4.5 and 4.6. Impurities of $[W(NC_6F_5)F_5]^-$ (3−5 mol %), $[W_2(NC_6F_5)OF_9]^-$ (2 mol %), $C_6F_5NH_2$

(1−2 mol %), and HF (trace) were observed by ^{19}F NMR spectroscopy (the impurity of $[W(NC_6F_5)F_5]^-$ is in addition to that generated by solvolysis of the product in CH_3CN).

The side arm contained a yellow-orange powder that consisted of $[C_5H_5NH][W(NC_6F_5)F_5]$ and $[C_5H_5NH][F(HF)_n]$, as determined by Raman spectroscopy.

Thin, yellow plates of $[(CH_3)_4N][W(NC_6F_5)F_5]$ were grown from a CH_3CN solution by slow removal of the solvent under dynamic vacuum at −40 °C.

2.3.3. $[W(NC_6F_5)F_4]_x$ and Adducts Thereof with N-Donor Ligands

2.3.3.1. $[W(NC_6F_5)F_4]_x$

In a typical synthesis, a ¼”-o.d. FEP reactor was charged with $[C_5H_5NH][W(NC_6F_5)F_5]$ (0.823 g, 1.52 mmol) in the dry box. Dichloromethane (1.327 g) was then distilled into the reactor at −196 °C and warmed to ambient temperature, resulting in an orange solution. Subsequently, AsF_5 (0.272 g, 1.60 mmol) was distilled into the reactor at −196 °C. Upon warming to −50 °C, the top of the CH_2Cl_2 solution, at its interface with AsF_5, turned dark red. The reactor was further warmed to ambient temperature and briefly agitated in an ultrasonic bath, resulting in a homogeneous orange suspension. The volatile materials were removed under dynamic vacuum at −65 °C for 2 h, at ambient temperature with constant agitation for 10 min, and at 45 °C for 20 min, affording a pale orange solid mixture along with a small amount of an involatile, yellow film that coated the reactor walls (1.102 g, 1.08 g expected for 1:1 mixture of $[W(NC_6F_5)F_4]_x$ and $[C_5H_5NH][AsF_6]$).

The mixture was transferred into the side arm of a glass Y-shaped decanting vessel equipped with a PTFE valve (J. Young), and $CFCl_3$ (*ca.* 2 mL) was distilled onto the solid at −196 °C, resulting in the formation of a yellow solution above undissolved yellow-

orange solid upon warming to ambient temperature, followed by agitating for several minutes. The solution was decanted into the straight arm of the decanting vessel, and the $CFCl_3$ was condensed back into the side arm at −10 °C, resulting in the solution in the straight arm becoming dark red. This was repeated five times, until only a faint yellow colour remained in the solution in the side arm. The solvent was then removed under dynamic vacuum at −80 °C for 1 h, and at ambient temperature for 45 min, affording $[W(NC_6F_5)F_4]_x$ (0.568 g, 1.29 mmol, 84.5% yield with respect to $[C_5H_5NH][W(NC_6F_5)F_5]$) as an orange solid in the straight arm and a mixture of white and yellow-orange solids in the side arm.

Due to the complicated nature of the ^{19}F NMR spectrum of $[W(NC_6F_5)F_4]_x$ in CH_2Cl_2, the purity of a sample was ascertained by ^{19}F NMR spectroscopy in CH_3CN, which typically gave rise to signals corresponding to $W(NC_6F_5)F_4(NCCH_3)$ (Tables 5.1 and 5.2) along with impurities of $[C_5H_5NH][AsF_6]$ (3–4 mol%) and trace amounts of various imido- and oxidotungsten(VI) complexes including $WOF_4(NCCH_3)$, $[W_2(NC_6F_5)OF_9]^-$, and $[W_2(NC_6F_5)_2F_9]^-$.

2.3.3.2. $W(NC_6F_5)F_4(NCCH_3)$

In the dry box, a ¼”-o.d. FEP reactor was charged with $[W(NC_6F_5)F_4]_x$ (0.030 g, 0.068 mmol), onto which CH_3CN (0.123 g) was distilled at −196 °C. The reactor was warmed to −40 °C, resulting in an orange solution that lightened to yellow upon further warming to ambient temperature and letting stand for several minutes. The CH_3CN was removed under dynamic vacuum at ambient temperature with constant agitation for 5 min, affording $W(NC_6F_5)F_4(NCCH_3)$ (0.033 g, 0.068 mmol) as a yellow, microcrystalline solid in quantitative yield.

NMR (ppm, CH_3CN, 20 °C, unlocked): $\delta(^1H)$ 2.39 (CH_3). Fluorine-19 NMR spectroscopic data are provided in Tables 5.1 and 5.2.

Yellow blocks of $W(NC_6F_5)F_4(NCCH_3)$ were grown from a solution of $[W(NC_6F_5)F_4]_x$ in CH_3CN (0.05 mL) by slow removal of the solvent under dynamic vacuum at –40 °C.

2.3.3.3. $W(NC_6F_5)F_4(NC_5H_5)$

In the dry box, a ¼"-o.d. FEP reactor was charged with $[W(NC_6F_5)F_4]_x$ (0.062 g, 0.14 mmol), into which CH_3CN (0.206 g) was then distilled, resulting in an orange solution that lightened to yellow over the course of several minutes at ambient temperature. Subsequently, C_5H_5N (0.020 g, 0.25 mmol) was distilled into the reactor from a graduated glass weighing vessel. Upon warming the reactor to –40 °C and washing the C_5H_5N from the reactor walls with CH_3CN, the solution turned orange. The reactor was briefly warmed to ambient temperature and agitated to ensure reaction completion. Finally, the volatile materials were removed under dynamic vacuum at –40 °C for 1 h, at ambient temperature for 15 min, and at 45 °C for 1 h, affording $W(NC_6F_5)F_4(NC_5H_5)$ (0.072 g, 0.14 mmol) as an orange-brown powder in quantitative yield.

NMR (ppm, CH_3CN, 20 °C, unlocked): $\delta(^1H)$ 8.77 (H_o, $^3J(H_o–H_m)$ = 6.5 Hz, $^4J(H_o–H_p)$ = 1.6 Hz); 8.16 (H_p, $^3J(H_p–H_m)$ = 7.7 Hz); 7.72 (H_m). $\delta(^{13}C\{^1H\})$ 147.91 (C_o), 142.51 (C_p), 126.68 (C_m). Fluorine-19 NMR spectroscopic data are provided in Tables 5.1 and 5.2.

Yellow plates of $W(NC_6F_5)F_4(NC_5H_5)$ were grown from a solution of $[W(NC_6F_5)F_4]_x$ in C_5H_5N/CH_2Cl_2 (*ca*. 1:1; 0.1 mL) by slow removal of the solvent under dynamic vacuum at –35 °C.

2.3.3.4. *$W(NC_6F_5)F_4(NC_5H_5)_2$*

Pyridine (0.206 g, 2.60 mmol) was distilled into a reactor containing freshly prepared $W(NC_6F_5)F_4(NCCH_3)$ (0.057 g, 0.12 mmol), after which the reactor was warmed to −40 °C and agitated for several minutes, resulting in a pale-orange suspension. The reactor was then warmed to ambient temperature and agitated briefly, before being cooled to −40 °C again. The volatile materials were removed under dynamic vacuum at −35 °C for 3 h, affording $W(NC_6F_5)F_4(NC_5H_5)_2$ (0.072 g, 0.12 mmol) as an off-white powder in quantitative yield.

NMR (ppm, CH_2Cl_2, –80 °C, unlocked): $\delta(^1H)$ 7.86 (H_o, $^3J(H_o–H_m)$ = 5.7 Hz); 6.86 (H_p, $^3J(H_p–H_m)$ = 6.8 Hz); 6.44 (H_m). $\delta(^{13}C\{^1H\})$ 147.57 (C_o), 144.57 (C_p), 125.29 (C_m). Fluorine-19 NMR spectroscopic data are provided in Tables 5.1 and 5.2.

2.3.4. Adducts of WF_6 and $[WF_5]^+$ with Bidentate N-Donor Ligands

2.3.4.1. *WF_6(2,2′-bipy)*

In the dry box, a ¼”-o.d. FEP reactor was charged with $WF_6(NC_5H_5)$ (0.1586 g, 0.4208 mmol) and 2,2′-bipy (0.0655 g, 0.419 mmol) at ambient temperature. The reactor was kept below –50 °C until CH_2Cl_2 (0.655 g) was distilled in at –196 °C, resulting in the formation of a yellow suspension upon slow warming to ambient temperature. After agitating the reactor for several minutes at ambient temperature, the reactor was cooled to –30 °C and volatile materials were removed under dynamic vacuum at that temperature for 30 min. Afterwards the reactor was warmed to ambient temperature for 10 min to remove any trace of solvent, and then to 100 °C, resulting in colorless crystals of 2,2′-bipy subliming onto the reactor walls, and involatile WF_6(2,2′-bipy) remaining in the bottom of the reactor. The product was isolated by cutting the reactor in the dry box below the point

at which the 2,2′-bipy was sublimed, resulting in WF_6(2,2′-bipy) (0.185 g, 0.407 mmol, 97.1% yield w.r.t. 2,2′-bipy) as a yellow powder. The Raman spectrum revealed only traces of $[2,2'\text{-bipy-H}]^+$ (1016 and 995 cm^{-1})[17] and $[WF_7]^-$ (706 cm^{-1})[18] as impurities.

2.3.4.2. WF_6(1,10-phen)

In the dry box, a ¼”-o.d. FEP reactor was charged with $WF_6(NC_5H_5)$ (0.0821 g, 0.218 mmol) and 1,10-phen (0.0385 g, 0.0214 mmol) at ambient temperature. The reactor was then kept below –50 °C until CH_2Cl_2 (0.413 g) was distilled in at –196 °C, resulting in the formation of a beige suspension upon warming to ambient temperature. The volatile materials were removed under dynamic vacuum at –50 °C for 1 h, at ambient temperature for 30 min, and at 45 °C for 30 min, resulting in WF_6(1,10-phen) (0.100 g, 0.209 mmol, 97.7% yield w.r.t. 1,10-phen) as a beige powder. The Raman spectrum revealed only traces of $[1,10\text{-phen-H}]^+$ (1043 cm^{-1})[19] and $[WF_7]^-$ (705 cm^{-1})[18] as impurities.

2.3.4.3. $[WF_5(2,2'\text{-bipy})][Sb_2F_{11}]$

In the dry box, a ¼”-o.d. FEP reactor was charged with WF_6(2,2′-bipy) (0.0484 g, 0.107 mmol) and SbF_5(OSO) (0.0599 g, 0.213 mmol) at *ca.* –100 °C. The reactor was kept below –80 °C until SO_2 (0.544 g) was distilled in at –196 °C, resulting in the formation of an orange solution above undissolved black and orange solids upon warming to –70 °C. Further warming to ambient temperature resulted in the solution rapidly turning dark brown before lightening to yellow over the course of 16 h. The reactor was cooled to –70 °C and volatile materials were removed under dynamic vacuum at that temperature for 1 h and at ambient temperature for 10 min, resulting in $[WF_5(2,2'\text{-bipy})][Sb_2F_{11}]$ (0.095 g, 0.21 mmol, 100% yield w.r.t. SbF_5(OSO)) as a crystalline yellow solid.

NMR (ppm, SO_2, 20 °C, unlocked): δ(^{19}F) 206 (s, WF_5), –91 (s, $[Sb_2F_{11}]^-$, F_b), –111 (s, $[Sb_2F_{11}]^-$, F_c), –133 (s, $[Sb_2F_{11}]^-$, F_t). δ(^{1}H) 10.15 (d, H1; ^3J(H1–H2) = 6.3 Hz), 9.37 (m, H2/H4), 8.83 (td, H3; ^3J(H3–H2/H4) = 6.6 Hz; ^4J(H3–H1) = 1.8 Hz). δ(^{13}C{^{1}H}) 152.58 (C5), 149.95 (C4), 148.41 (C2), 131.31 (C3), 126.92 (C1). Atom labels are as in Figure 2.5a. The sample was found to contain traces of $[WF_4(2,2'\text{-bipy})_2]^{2+}$ (154.04 ppm, s; $^1J(^{19}F–^{183}W)$ = 27.2 Hz),[20,21] WOF_4(OSO) (73.87 ppm, s), and unknown impurities (likely hydrolysis or solvolysis products) by ^{19}F NMR spectroscopy in SO_2. A small impurity of $[2,2'\text{-bipy-H}]^+$ was observed by ^{1}H NMR spectroscopy, likely carried over from the WF_6(2,2′-bipy) used.

Yellow blocks of $[WF_5(2,2'\text{-bipy})][Sb_2F_{11}]$ suitable for X-ray crystallography were recovered from the initial reaction mixture.

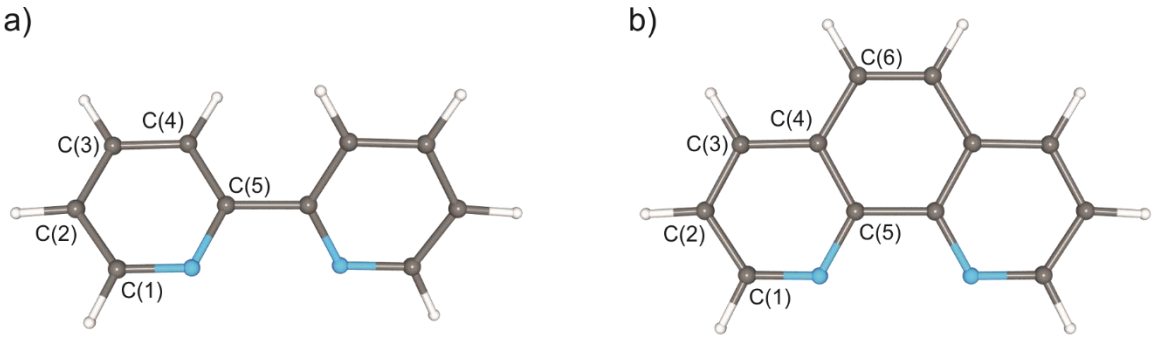

Figure 2.5. Atom-labelling schemes for a) 2,2'-bipy and b) 1,10-phen. Labels for hydrogen are analogous to those shown for carbon.

2.3.4.4. [WF_5(1,10-phen)][Sb_2F_{11}]

In the dry box, a ¼”-o.d. FEP reactor was charged with WF_6(1,10-phen) (0.0336 g, 0.0703 mmol) and SbF_5(OSO) (0.0392 g, 0.140 mmol) at *ca*. –100 °C. The reactor was kept below –80 °C until SO_2 (0.478 g) was distilled in at –196 °C, resulting in the formation of an orange solution upon warming to –70 °C. Further warming to ambient temperature resulted in the solution rapidly darkening to orange-brown before lightening to orange over the course of 16 h. The reactor was cooled to –70 °C and volatile materials were removed under dynamic vacuum at that temperature for 1 h and at ambient temperature for 10 min, resulting in [WF_5(1,10-phen)][Sb_2F_{11}] (0.063 g, 0.14 mmol, 100% yield w.r.t. SbF_5(OSO)) as a microcrystalline orange solid.

NMR (ppm, SO_2, 20 °C, unlocked): $\delta(^{19}F)$ 204 (s, WF_5), –91 (s, $[Sb_2F_{11}]^-$, F_b), –112 (s, $[Sb_2F_{11}]^-$, F_c), –133 (s, $[Sb_2F_{11}]^-$, F_t). $\delta(^1H)$ 10.53 (dd, H1; ^3J(H1–H2) = 5.7 Hz; ^4J(H1–H3) = 1.0 Hz), 9.88 (dd, H3; 3J(H3–H2) = 8.1 Hz), 9.14 (s, H6), 9.11 (dd, H2). $\delta(^{13}C\{^1H\})$ 150.92 (C1), 147.48 (C6), 142.43 (C3), 133.62 (C4), 130.24 (C5), 128.72 (C2). Atom labels are as in Figure 2.5b. The sample was found to contain traces of [WF_4(1,10-phen)$_2$]$^{2+}$ (151.82, s), WOF_4(OSO) (73.67 ppm, s), and unknown impurities (likely hydrolysis or solvolysis products) by ^{19}F NMR spectroscopy in SO_2. A small impurity of [1,10-phen-H]$^+$ was observed by ^1H NMR spectroscopy, likely carried over from the WF_6(1,10-phen) used.

Large, orange blocks of [WF_5(1,10-phen)][Sb_2F_{11}] were grown by suspending the microcrystalline material (*ca*. 0.015 g) in a small amount of CH_2Cl_2 (*ca*. 0.1 mL) in a ¼”-o.d. FEP reactor and then adding a minimum amount of SO_2 (*ca*. 0.02 mL total) such that

the solid completely dissolved at ambient temperature. The solution was then stored at –70 °C for 16 h.

2.3.4.5. $[WF_5(1,10\text{-phen})][SbF_6]\cdot SO_2$

In the dry box, a ¼”-o.d. FEP reactor was charge with WF_6(1,10-phen) (0.0366 g, 0.0766 mmol) and SbF_5(OSO) (0.0215 g, 0.0766 mmol) at *ca*. –100 °C. The reactor was kept below –80 °C until SO_2 (0.476 g) was distilled in at –196 °C, resulting in a pale orange solution above undissolved black and orange solids upon warming to –70 °C; agitation of the reactor at –70 °C caused an immediate disappearance of the black colour. The resultant orange suspension was warmed to ambient temperature before volatile materials were removed with constant agitation for 10 min and for 30 min further without agitation, yielding $[WF_5(1,10\text{-phen})][SbF_6]\cdot SO_2$ (0.056 g, 0.074 mmol, 96% yield w.r.t. SbF_5(OSO)) as a crystalline orange solid.

NMR (ppm, SO_2, 20 °C, unlocked): δ(^{19}F) 203 (s, WF_5); –115 (m, $[SbF_6]^-$; ^1J(F–^{121}Sb) = 980 Hz, ^1J(F–^{123}Sb = 1940 Hz). In addition to resonances corresponding to $[WF_5(1,10\text{-phen})][SbF_6]$, traces of WF_6 (166.64 ppm, s; $^1J(^{19}F–^{183}W)$ = 43.4 Hz), $[WF_4(1,10\text{-phen})_2]^{2+}$ (151.35, s; $^1J(^{19}F–^{183}W)$ = 30.2 Hz), and unknown impurities were observed by ^{19}F NMR spectroscopy, though the overall purity could not be ascertained due to the low solubility of the product in SO_2. After heating to 45 °C for *ca*. 10 min, the signals corresponding to WF_6 and $[WF_4(1,10\text{-phen})_2]^{2+}$ increased in intensity at the expense of $[WF_5(1,10\text{-phen})]^+$.

Orange blocks of $[WF_5(1,10\text{-phen})][SbF_6]\cdot SO_2$ suitable for X-ray crystallography were recovered from the initial reaction mixture.

2.3.4.6. Decomposition of [WF_5(2,2′-bipy)][SbF_6] in SO_2

In the dry box, a 4-mm-o.d. FEP reactor was charged with WF_6(2,2′-bipy) (0.0222 g, 0.0489 mmol) and SbF_5(OSO) (0.0148 g, 0.0527 mmol) while submerged at *ca*. –100 °C. The reactor was kept below –80 °C until SO_2 (*ca*. 0.3 mL) was distilled in at –196 °C and the reactor was heat sealed. Warming the heat-sealed FEP tube to ambient temperature resulted in the formation of a yellow suspension; brief agitation resulted in the complete dissolution of the precipitate to afford a yellow solution, which was studied by ^{19}F NMR spectroscopy at 20 °C. A second sample was prepared similarly, containing WF_6(2,2′-bipy) (0.0122 g, 0.0269 mmol) and SbF_5(OSO) (0.0080 g, 0.028 mmol), and was left at ambient temperature for 24 h before being studied by ^{19}F NMR spectroscopy at 20 °C.

2.3.5. Adducts of $[WF_5]^+$ and WF_5 with C_5H_5N

2.3.5.1. [$WF_5(NC_5H_5)_3$][O_3SCF_3]

In the dry box, ¼”-o.d. FEP reactor was charged with $WF_6(NC_5H_5)_2$ (0.0401 g, 0.0879 mmol) and [$(CH_3)_3Si(NC_5H_5)$][O_3SCF_3] (0.0265 g, 0.0879 mmol) at –160 °C. The solids were kept below –80 °C before CH_2Cl_2 (0.3 mL) was distilled onto the solid mixture at –196 °C. The reactor was warmed to –60 °C, resulting in a white suspension, before being slowly warmed until all solid dissolved to affording a colourless solution, after which the solution was quickly re-cooled to –60 °C. Volatile materials were removed under dynamic vacuum at ambient temperature for 3 h, affording [$WF_5(NC_5H_5)_3$][O_3SCF_3] (0.058 g, 0.087 mmol, 99% yield w.r.t. $WF_6(NC_5H_5)_2$) as a transparent, colourless solid. Trace impurities of $[WF_4(NC_5H_5)_4]^{2+}$ and $WF_6(NC_5H_5)_2$ were observed by ^{19}F NMR spectroscopy.

NMR (ppm, CH_2Cl_2, –100 °C, unlocked): ^{19}F 161 (tdd, F_A; $^2J(F_A–F_B)$ = 25 Hz, $^2J(F_A–F_C)$ = 180 Hz, $^2J(F_A–F_D)$ = 55 Hz, [1F]), 140 (ddd, F_B; $^2J(F_B–F_C)$ = 145 Hz, $^2J(F_B–F_D)$ = 65 Hz, [2F]), 107 (dtd, F_C; $^2J(F_C–F_D)$ = 75 Hz, [1F]), 106 (qn, F_D, [1F]), –80.07 (s, CF_3; $^1J(F–^{13}C)$ = 320.6 Hz, [3F]). ^1H 7.83 (d, H_o(Y); $^3J(H_o–H_m$ = 4.2 Hz, [2H]), 7.56 (d, H_o(Z); $^3J(H_o–H_m$ = 6.0 Hz, [2H]) 7.52 (d, H_o(Z); $^3J(H_o–H_m$ = 4.4 Hz, [2H]), 6.82 (t, H_p; $^3J(H_p–H_m)$ = 6.0 Hz, [3H]), 6.40 (t, H_m(Y), [2H]), 6.34 (t, H_m(Z), [4H]). Atom labels for fluorido ligands are as in Figure 7.2.

2.3.5.2. Decomposition of $[WF_5(NC_5H_5)_3][O_3SCF_3]$ in C_5H_5N

General procedure: In the dry box, a fused ¼"-o.d./4-mm o.d. FEP reactor was charged with $WF_6(NC_5H_5)$ (1 equiv., ca. 0.05 mmol) and $[(CH_3)_3Si(NC_5H_5)][O_3SCF_3]$ (1 or 1.5 equiv.) at –160 °C. The solids were kept below –80 °C before CH_2Cl_2 (0.3 mL) was distilled onto the solid mixture and the 4-mm portion of the reactor was heat-sealed under dynamic vacuum. The sealed tubes were then heated to ambient temperature and agitated until all solid had dissolved before NMR spectra were recorded at 20 °C.

NMR (ppm, C_5H_5N, 20 °C, unlocked) [4-pypy][O_3SCF_3]: ^{19}F –77.19 (s, CF_3; $^1J(F–^{13}C)$ = 322.1 Hz). ^1H 9.31 (s, br, [2H]), 8.57 (s, br, [2H]), 8.41 (s, br, [1H]), 8.03 (s, br, [2H]), 7.73 (s, br, [2H]). $(CH_3)_3SiF$: ^{19}F –156.23 (s, br; $^1J(F–^{29}Si)$ = 273.7 Hz). ^1H 0.51 (s, br; $^1J(H–^{13}C)$ = 117.4 Hz).

2.3.5.3. $WF_5(NC_5H_5)_2$

In the dry box, one arm of a flame-dried two-arm glass decanting vessel in which the two arms are separated by a PTFE valve (Figure 2.6), was charged with $WF_6(NC_5H_5)$ (0.4237 g, 1.124 mmol). Pyridine (2 mL) was then distilled onto the solid at –196 °C, followed by $(CH_3)_3SiO_3SCF_3$ (0.270 g, 1.22 mmol). Upon warming to ambient

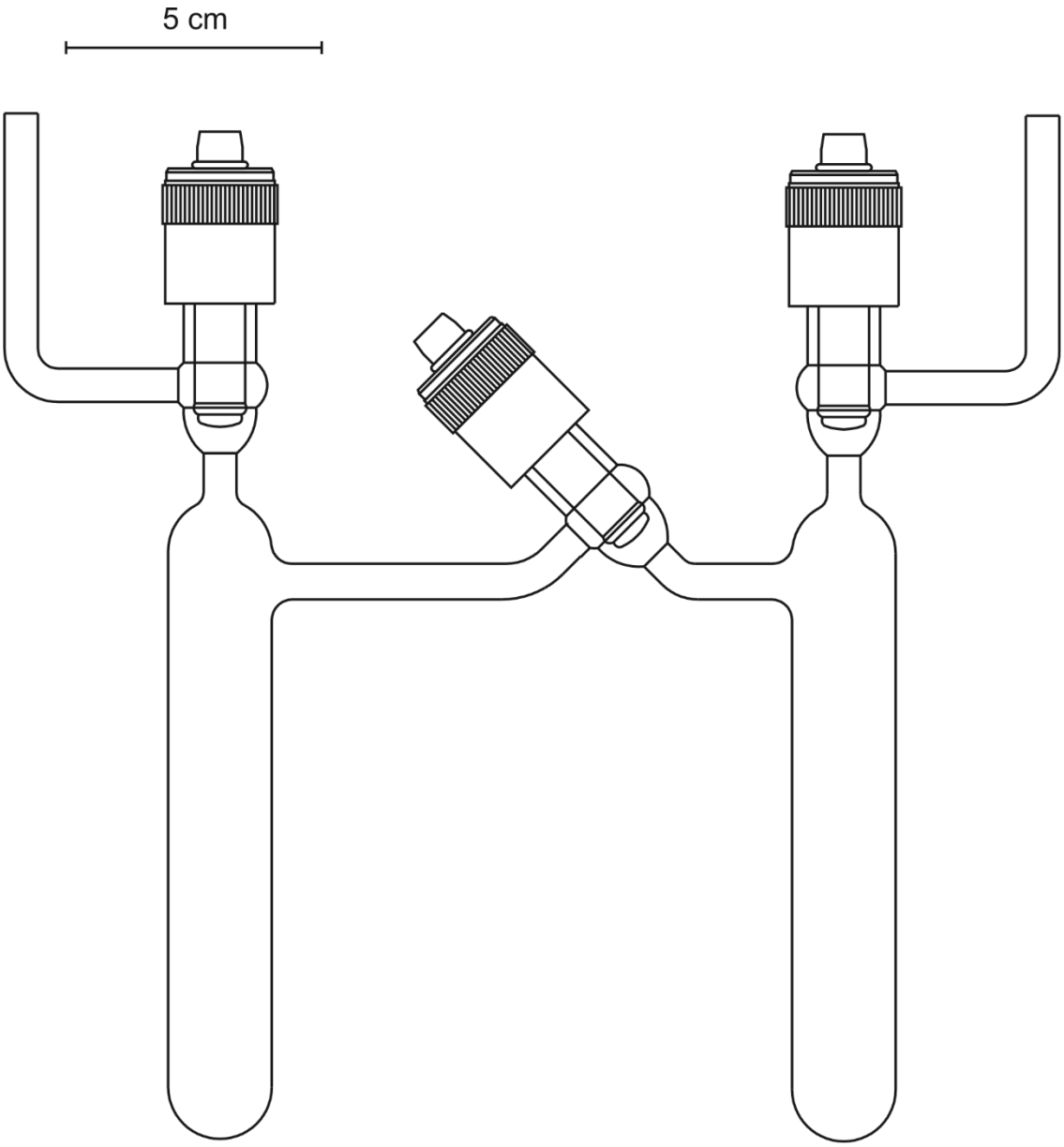

Figure 2.6. Two-armed glass decanting vessel equipped with PTFE stopcocks (J. Young). Adapted from Jared Nieboer's M.Sc. thesis.

temperature, a yellow suspension formed; agitation in an ultrasonic bath for *ca*. 2 min resulted in dissolution of the solids to afford a yellow solution that quickly changed to dark brown during sonication. The solution was kept at ambient temperature for 20 h, during which red-orange blocks crystallised. The solution was briefly (< 60 s) agitated in an ultrasonic bath and kept at ambient temperature for 28 h further before CH_2Cl_2 (2 mL) was condensed onto the mixture at –40 °C. The supernatant was decanted into the second arm, after which the solvent was back-distilled onto the crystals under static vacuum at –40 °C. This was repeated five times until the wash appeared very pale yellow in colour. The residual solvent was distilled from the crystals into the second arm at –196 °C and the central stopcock was closed to isolate the dried crystals. In the dry box, the crystals were transferred into a FEP jar, yielding $WF_5(NC_5H_5)_2$ (0.2758 g, 0.06311 mmol, 56.15% yield with respect to $WF_6(NC_5H_5)$) as a red-orange crystalline solid. The product was found to contain a trace impurity of $WF_6(NC_5H_5)_2$[12] by Raman spectroscopy.

Single crystals suitable for X-ray crystallography were grown by heating a suspension of $WF_5(NC_5H_5)_2$ (*ca*. 0.01 g) in CH_3CN (*ca*. 0.1 mL) to 60 °C and allowing the solution to cool to ambient temperature. The crystals obtained from the mother liquor were found to be the same phase as those obtained after recrystallisation, but considerable residual electron density was observed along the W–F bonds in those cases.

2.3.5.4. Decomposition of $[WF_5(NC_5H_5)_2][Sb_2F_{11}]$ in SO_2

In the dry box, a fused ¼”-o.d./4-mm o.d. FEP reactor was charged with $WF_6(NC_5H_5)_2$ (0.209 g, 0.0458 mmol) and $SbF_5(OSO)$ (0.090 mmol) at –160 °C. The reactor was kept below –80 °C before SO_2 (0.3 mL) was distilled onto the solid mixture and the 4-mm portion of the reactor was heat-sealed under dynamic vacuum. It should be

noted that a small amount of $WF_6(NC_5H_5)_2$ remained above the sealed portion of the reactor. The sealed tube was briefly (< 60 s) warmed to –50 °C, resulting in a yellow solution, before NMR spectra were recorded at that temperature. Intermittent warming to ambient temperature for 60–180 s intervals between NMR experiments resulted in dissipation of the yellow colour to afford a colourless solution (after *ca*. 5 min total at ambient temperature).

2.3.6. Adducts of $[WF_4]^+$ with N- and P-Donor Ligands

2.3.6.1. $[WF_4(NC_5H_5)_4][O_3SCF_3]$

In the dry box, a ¼"-o.d. FEP reactor was charged with $WF_5(NC_5H_5)_2$ (0.0232 g, 0.0531 mmol) and $[(CH_3)_3Si(NC_5H_5)][O_3SCF_3]$ (0.0160 g, 0.0531 mmol) at –160 °C. The reactor was kept below –50 °C until C_5H_5N was distilled in at –196 °C. The reactor was warmed to –35 °C, resulting in a red-brown suspension, and slowly warmed to ambient temperature until all solid dissolved, after which it was promptly re-cooled to –35 °C. Volatile materials were removed under dynamic vacuum at that temperature for –35 °C for 2 h and at ambient temperature for 1 h, yielding $[WF_4(NC_5H_5)_4][O_3SCF_3]$ (0.038 g, 0.053 mmol) as a brown powder in quantitative yield.

Orange needles of $[WF_4(NC_5H_5)_4][O_3SCF_3]\cdot 1.5CH_3CN$ were upon cooling a violet CH_3CN (*ca*. 0.1 mL) solution of the salt (*ca*. 0.020 g) to –40 °C and storing at that temperature for 1 h.

2.3.6.2. $[WF_4\{P(CH_3)_3\}_4][O_3SCF_3]$

Tungsten hexafluoride (0.218 g, 0.732 mmol) was distilled into a ¼"-o.d. FEP reactor at –196 °C, followed by CH_2Cl_2 (*ca*. 0.2 mL) and $(CH_3)_3SiO_3SCF_3$ (0.160 g, 0.720 mmol). The reactor was warmed to ambient temperature, resulting in a colourless solution,

before being re-cooled to –196 °C. Trimethylphosphine (*ca*. 0.2 mL) was then distilled into the reactor, resulting in an orange colouration at the interface between the $P(CH_3)_3$ and CH_2Cl_2 phases. Upon warming to ambient temperature, the phases were mixed in an ultrasonic bath, immediately resulting in a viscous, red-violet suspension. Volatile materials were removed under dynamic vacuum from –70 °C to –50 °C over 3 h, and at ambient temperature for 30 min, yielding $[WF_4\{P(CH_3)_3\}_4][O_3SCF_3]$ (0.516 g, 0.723 mmol) as a red-violet powder in quantitative yield. The material was determined to be pure by Raman spectroscopy.

Red blocks of $[WF_4\{P(CH_3)_3\}_4][O_3SCF_3]$ suitable for X-ray crystallography were grown by layering $P(CH_3)_3$ (< 0.1 mL) onto a CH_2Cl_2 (*ca*. 0.1 mL) solution of the salt (*ca*. 0.010 g) at –196 °C, followed by slowly warming to –70 °C and storing at that temperature for 16 h.

2.3.6.3. Reaction of WF_6 with $(CH_3)_3SiO_3SCF_3$ in $P(CH_3)_3/CH_2Cl_2$

General procedure: Tungsten hexafluoride (1 equiv., *ca*. 0.05 mmol) was distilled into a fused ¼”-o.d./4-mm o.d. FEP reactor at –196 °C, followed by CH_2Cl_2 (*ca*. 0.2 mL) and $(CH_3)_3SiO_3SCF_3$ (1 equiv.). The mixture was briefly warmed until all WF_6 dissolved, then re-frozen and $P(CH_3)_3$ (*ca*. 0.1 mL) distilled onto it before the 4-mm portion of the reactor was heat-sealed under dynamic vacuum. The sealed tubes were then heated to ambient temperature, resulting in red-violet suspensions, and NMR spectra were recorded at 20 °C or –50 °C.

NMR (ppm, C_5H_5N, –50 °C, unlocked) $WF_6\{P(CH_3)_3\}_2$: ^{19}F 25 (s, br). ^{31}P 92.9 (st). $P(CH_3)F_2$: ^{19}F –6.96 (d, $^1J(F–^{31}P)$ = 529.0 Hz, $^3J(^1F–^1H)$ = 11.4 Hz). ^{31}P: –14.50 ($^2J(P–^1H)$

= 16.0 Hz). ^{1}H: 0.38 (d). $[P(CH_3)_3F]^+$: ^{19}F –136.75 (d, ^{1}J(F–^{31}P) = 945.5 Hz), ^{31}P: 144.17 (d). $(CH_3)_3SiF$: ^{19}F –156.23 (s, br; ^{1}J(F–^{29}Si) = 271.2 Hz). ^{1}H –1.16 (d, ^{1}J(F–^{1}H) = 6.8 Hz).

2.4. Computational Methods

In Chapters 3–5, the B3LYP functional, as implemented in Gaussian[22] (09, revision D.01) was employed. The Stuttgart basis set[23] augmented by one *f*-type polarisation function (α_f = 0.823)[24] and associated relativistic pseudopotentials were used for tungsten, whereas the aug-cc-pVTZ or cc-pVTZ basis sets were used for the lighter atoms. This combined basis set is referred to as sVTZ when referring to cases wherein aug-cc-pVTZ was used, and VTZ when cc-pVTZ was used instead. The $WF_6(NC_5H_5)$ adduct was studied at the B3LYP/sVTZ and B3LYP/VTZ levels of theory, revealing minimal differences in calculated bond lengths (Table 2.2), vibrational frequencies (Table 2.3), and various NBO data (Table 2.4) including natural-population-analysis (NPA) charges, Wiberg valences, and Wiberg bond indices (WBIs).

In Chapters 6–8, the B3LYP functional, as implemented in Gaussian[22] (16, revision B.01) was employed. The aug-cc-pVTZ-PP basis set as developed by Peterson and co-workers,[25] with associated pseudopotentials, was used for tungsten along with the cc-pVTZ basis set for carbon and hydrogen and the aug-cc-pVTZ basis set for the remaining atoms. This combined basis set is referred to as aVTZ. The SMD implicit solvent model was used for thermochemical investigations in solution.

Geometries were optimised in the gas phase and vibrational frequencies were calculated on the optimised geometries, returning all real frequencies unless otherwise specified. Whenever possible, geometries determined via X-ray crystallography were used as input geometries prior to optimisation. Generally, at the levels of theory described,

excellent agreement was observed between experimental and calculated geometries and frequencies. Geometry optimisations with implicit solvation were performed using the optimised gas-phase geometries as input. Molecular orbitals were calculated for, and NBO[26] (version 6.0) analyses performed on, the optimised geometries. GaussView[27] (versions 5.0 and 6.0) was used to visualise vibrational modes and aid in their description. GaussView and Avogadro[28] (version 1.2) were used to visualise the geometries and MOs. Optimised atomic coordinates are provided in Appendices A–F.

For thermochemical investigations, zero-point vibrational corrections and thermal corrections to enthalpy and Gibbs energy were derived from the calculated vibrational data and applied to the zero-point energies.

Table 2.2. Comparison of Calculated Bond Lengths (Å) and Angles (°) of $WF_6(NC_5H_5)$ at Various Levels of Theory

	B3LYP/ sVTZ	**B3LYP/ VTZ**		**B3LYP/ sVTZ**	**B3LYP/ VTZ**
W−F(1)	1.868	1.870	F(1)−W−F(2)	76.3	76.4
W−F(2)	1.868	1.870	F(1)−W−F(3)	79.3	79.3
W−F(3)	1.877	1.879	F(1)−W−F(4)	127.8	127.8
W−F(4)	1.877	1.879	F(1)−W−F(5)	79.3	79.3
W−F(5)	1.877	1.879	F(1)−W−F(6)	127.8	127.8
W−F(6)	1.877	1.879	F(2)−W−F(3)	127.8	127.8
W−N	2.343	2.340	F(2)−W−F(4)	79.3	79.3
N−C(1)	1.338	1.338	F(2)−W−F(5)	127.8	127.8
C(1)−C(2)	1.384	1.384	F(2)−W−F(6)	79.3	79.3
C(2)−C(3)	1.388	1.388	F(3)−W−F(4)	80.6	80.5
C(3)−C(4)	1.388	1.388	F(3)−W−F(5)	90.9	90.9
C(4)−C(5)	1.384	1.384	F(3)−W−F(6)	148.4	148.4
C(5)−N	1.338	1.338	F(4)−W−F(5)	148.4	148.4
			F(4)−W−F(6)	90.9	90.9
			F(5)−W−F(6)	80.6	80.5
			F(1)−W−N	141.9	141.8
			F(2)−W−N	141.9	141.8
			F(3)−W−N	74.2	74.2
			F(4)−W−N	74.2	74.2
			F(5)−W−N	74.2	74.2
			F(6)−W−N	74.2	74.2
			W−N−C(1)	120.3	120.3
			N−C(1)−C(2)	121.9	121.9
			C(1)−C(2)−C(3)	119.0	119.0
			C(2)−C(3)−C(4)	118.8	118.8
			C(3)−C(4)−C(5)	119.0	119.0
			C(4)−C(5)−N	121.9	121.9
			C(5)–N–C(1)	119.4	119.5
			C(5)−N−W	120.3	120.3
			F(1)–W–N–C(1)	0.0	0.0

Table 2.3. Comparison of Calculated Vibrational Frequencies (cm^{-1}) of $WF_6(NC_5H_5)$ at Various Levels of Theory

B3LYP/sVTZ	B3LYP/VTZ	B3LYP/sVTZ	B3LYP/VTZ
3229(158)[5]	3233(147)[5]	669(1)[71]	669(2)[57]
3226(1)[<0.1]	3230(2)[<0.1]	659(1)[99]	659(1)[91]
3208(156)[1]	3210(164)[1]	658(4)[145]	657(3)[156]
3204(87)[2]	3205(90)[3]	645(<0.1)[176]	644(<0.1)[175]
3185(73)[3]	3186(76)[3]	641(1)[96]	640(1)[101]
1654(10)[27]	1657(8)[26]	591(2)[0]	588(2)[0]
1621(11)[2]	1623(10)[2]	559(1)[3]	558(1)[3]
1530(3)[3]	1532(2)[4]	476(<1)[4]	477(<1)[5]
1488(0)[35]	1490(<0.1)[37]	423(1)[<0.1]	422(1)[<0.1]
1398(0)[2]	1401(0)[2]	400(<0.1)[0]	400(<1)[0]
1294(<1)[3]	1295(<1)[3]	356(1)[2]	355(1)[2]
1250(6)[19]	1253(7)[18]	332(1)[61]	332(1)[62]
1181(2)[4]	1185(2)[3]	329(1)[22]	329(1)[23]
1109(<1)[1]	1111(<1)[1]	304(1)[7]	303(1)[7]
1096(<1)[19]	1098(<1)[20]	302(1)[0]	303(1)[0]
1064(21)[6]	1064(21)[5]	293(<1)[21]	292(<1)[23]
1041(51)[7]	1042(41)[7]	270(1)[3]	271(1)[3]
1036(<0.1)[<1]	1036(<0.1)[<0.1]	217(1)[<0.1]	217(2)[<0.1]
1016(0)[0]	1013(<0.1)[0]	170(<0.1)[3]	170(<1)[4]
982(<1)[<1]	980(<0.1)[<0.1]	161(3)[4]	162(2)[4]
889(<1)[0]	887(<0.1)[0]	81(1)[0]	81(2)[<1]
786(<0.1)[23]	786(<1)[22]	81(2)[<1]	81(<1)[0]
710(<0.1)[71]	709(<0.1)[75]	79(<0.1)[1]	80(<0.1)[1]
702(47)[52]	698(44)[51]	48(3)[0]	47(4)[0]

Table 2.4. Comparison of NPA Charges, Wiberg Valences, and WBIs of $WF_6(NC_5H_5)$ at Various Levels of Theory

	Charge		Valence			WBI	
	B3LYP/sVTZ	**B3LYP/VTZ**	**B3LYP/sVTZ**	**B3LYP/VTZ**		**B3LYP/sVTZ**	**B3LYP/VTZ**
W	+2.74	+2.66	4.78	4.88	W−F(1)	0.76	0.77
F(1)	−0.48	−0.47	0.94	0.96	W−F(2)	0.76	0.77
F(2)	−0.48	−0.47	0.94	0.96	W−F(3)	0.72	0.73
F(3)	−0.51	−0.50	0.90	0.91	W−F(4)	0.72	0.73
F(4)	−0.51	−0.50	0.90	0.91	W−F(5)	0.72	0.73
F(5)	−0.51	−0.50	0.90	0.91	W−F(6)	0.72	0.73
F(6)	−0.51	−0.50	0.90	0.91	W−N(1)	0.36	0.37
N(1)	−0.46	−0.45	3.35	3.36	N(1)−C(1)	1.36	1.36
C(1)	+0.09	+0.09	3.91	3.91	C(1)−C(2)	1.44	1.44
C(2)	–0.23	–0.23	3.96	3.96	C(2)−C(3)	1.44	1.44
C(3)	–0.13	–0.13	3.96	3.96	C(3)−C(4)	1.44	1.44
C(4)	–0.23	–0.23	3.96	3.96	C(4)−C(5)	1.44	1.44
C(5)	+0.09	+0.09	3.91	3.91	C(5)−N(1)	1.36	1.36

2.5. References

(1) Willcott, M. R. *J. Am. Chem. Soc.* **2014**, *131* (36), 13180–13180.

(2) SpinWorks, version 4.2.7. Marat, K. University of Manitoba, Winnipeg, MB, CA, **2017**.

(3) CrysAlisPro. Agilent Technologies, Ltd.: Yarnton, Oxfordshire, England **2014**.

(4) Sheldrick, G. M. *Acta Crystallogr. A* **2015**, *71* (1), 3–8.

(5) Sheldrick, G. M. *Acta Crystallogr. C* **2015**, *71* (1), 3–8.

(6) Dolomanov, O. V.; Bourhis, L. J.; Gildea, R. J.; Howard, J. A. K.; Puschmann, H. *J. Appl. Crystallogr.* **2009**, *42* (2), 339–341.

(7) Paine, R. T.; Asprey, L. B. *Inorg. Chem.* **1974**, *13* (6), 1529–1531.

(8) Emara, A. A. A.; Lehmann, J. F.; Schrobilgen, G. J. *J. Fluorine Chem.* **2005**, *126* (9–10), 1373–1376.

(9) Winfield, J. M. *J. Fluorine Chem.* **1984**, *25* (1), 91–98.

(10) Robertson, A. P. M.; Chitnis, S. S.; China, S.; Cortes S., H. J.; Patrick, B. O.; Jenkins, H. A.; Burford, N. *Can. J. Chem.* **2016**, *94* (4), 424–429.

(11) Christe, K. O.; Wilson, W. W.; Wilson, R. D.; Bau, R.; Feng, J. A. *J. Am. Chem. Soc.* **1990**, *112* (21), 7619–7625.

(12) Hoskins, B. F.; Linden, A.; O'Donnell, T. A. *Inorg. Chem.* **1987**, *26* (14), 2223–2228.

(13) Arnaudet, L.; Bougon, R.; Buu, B.; Lance, M.; Nierlich, M.; Thuéry, P.; Vigner, J. *J. Fluorine Chem.* **1995**, *71* (1), 123–129.

(14) Levason, W.; Reid, G.; Zhang, W. *J. Fluorine Chem.* **2016**, *184*, 50–57.

(15) Arnaudet, L.; Bougon, R.; Ban, B.; Charpin, P.; Isabey, J.; Lance, M.; Nierlich, M.; Vigner, J. *Inorg. Chem.* **1989**, *28* (2), 257–262.

(16) Minkwitz, R.; Molsbeck, W.; Preut, H. *Z. Naturforsch. B* **1989**, *44* (12), 1581–1583.

(17) Barker, D. J.; Summers, L. A.; Cooney, R. P. *J. Mol. Struct.* **1987**, *159* (3–4), 249–254.

(18) Beuter, A.; Kuhlmann, W.; Sawodny, W. *J. Fluorine Chem.* **1975**, *6* (4), 367–378.

(19) Krishnan, K.; Plane, R. A. *Spectrochim. Acta A* **1969**, *25* (4), 831–837.

(20) Arnaudet, L.; Bougon, R.; Ban, B.; Lance, M.; Navaza, A.; Nierlich, M.; Vigner, J. *J. Fluorine Chem.* **1992**, *59* (1), 141–152.

(21) Arnaudet, L.; Bougon, R.; Ban, B.; Lance, M.; Navaza, A.; Nierlich, M.; Vigner, J. *J. Fluorine Chem.* **1994**, *67* (1), 17–25.

(22) Gaussian 16, revision B.01. Frisch, M. J.; Trucks, G. W.; Schlegel, H. B.; Scuseria, G. E.; Robb, M. A.; Cheeseman, J. R.; Scalmani, G.; Barone, V.; Petersson, G. A.; Nakatsuji, H.; Li, X.; Caricato, M.; Marenich, A. V.; Bloino, J.; Janesko, B. G.; Gomperts, R.; Mennucci, B.; Hratchian, H. P.; Ortiz, J. V.; Izmaylov, A. F.; Sonnenberg, J. L.; Williams-Young, D.; Ding, F.; Lipparini, F.; Egidi, F.; Goings, J.; Peng, B.; Petrone, A.; Henderson, T.; Ranasinghe, D.; Zakrzewski, V. G.; Gao, J.; Rega, N.; Zheng, G.; Liang, W.; Hada, M.; Ehara, M.; Toyota, K.; Fukuda, R.; Hasegawa, J.; Ishida, M.; Nakajima, T.; Honda, Y.; Kitao, O.; Nakai, H.; Vreven, T.; Throssell, K.; Montgomery, J. A., Jr.; Peralta, J. E.; Ogliaro, F.; Bearpark, M. J.; Heyd, J. J.; Brothers, E. N.; Kudin, K. N.; Staroverov, V. N.; Keith, T. A.; Kobayashi, R.; Normand, J.; Raghavachari, K.; Rendell, A. P.; Burant, J. C.; Iyengar, S. S.; Tomasi, J.; Cossi, M.; Millam, J. M.; Klene, M.; Adamo, C.; Cammi, R.; Ochterski, J. W.; Martin, R. L.; Morokuma, K.; Farkas, O.; Foresman, J. B.; Fox, D. J. Gaussian, Inc.: Wallingford, CT, USA **2016**.

(23) Andrae, D.; Häußermann, U.; Dolg, M.; Stoll, H.; Preuß, H. *Theor. Chim. Acta* **1990**, *77* (2), 123–141.

(24) Ehlers, A. W.; Böhme, M.; Dapprich, S.; Gobbi, A.; Höllwarth, A.; Jonas, V.; Köhler, K. F.; Stegmann, R.; Veldkamp, A.; Frenking, G. *Chem. Phys. Lett.* **1993**, *208* (1–2), 111–114.

(25) Figgen, D.; Peterson, K. A.; Dolg, M.; Stoll, H. *J. Chem. Phys.* **2009**, *130* (16), 164108.

(26) NBO, version 6.0. Glendening, E. D.; Badenhoop, J. K.; Reed, A. E.; Carpenter, J. E.; Bohmann, J. A.; Morales, C. M.; Landis, C. R.; Weinhold, F. Theoretical Chemistry Institute, University of Wisconsin: Madison, WI, USA **2013**.

(27) GaussView, version 6.0. Dennington, R.; Keith, T. A.; Millam, J. M. Semichem, Inc.: Shawnee Mission, KS, USA **2016**.

(28) Hanwell, M. D.; Curtis, D. E.; Lonie, D. C.; Vandermeerschd, T.; Zurek, E.; Hutchison, G. R. *J. Cheminform.* **2012**, *4* (8), 1–17.

Chapter 3 – Lewis-Acid Behaviour of WF_6 Towards C_5H_5N and Derivatives Thereof*

3.1. Introduction

Tungsten hexafluoride is well understood to behave as a moderate Lewis acid and F^- acceptor, resulting in the formation of hepta- and octacoordinate complexes (see section 1.1.3). In the case of the heptacoordinate complexes, their structural properties are of fundamental interest due to the three most probable geometries—the pentagonal bipyramid, monocapped octahedron, and monocapped trigonal prism—possessing highly similar energies. It has been discovered that the size of the Lewis base can effect changes in the overall structure, as $WF_6\{P(CH_3)_3\}$ is monocapped-trigonal-prismatic, whereas $WF_6\{P(C_6H_5)(CH_3)_2\}$ is monocapped-octahedral.[1] However, there has been little investigation into the effect of ligand basicity on structure in these systems, despite previous attribution of the structural differences between $WF_6(2\text{-}NC_5H_4F)$ and $[WF_7]^-$ to differences in ligand basicity.[2]

In this chapter, the syntheses and structural characterisation of heptacoordinate WF_6 adducts with 4-methylpyridine and 4-(dimethylamino)pyridine, as well as a dinuclear 2:1 adduct with 4,4′-bipyridine (4,4′-bipy), are detailed. In addition, the crystal structure of previously reported $WF_6(NC_5H_5)$ is elucidated. Complementary DFT (B3LYP) studies have been conducted, including geometry optimisations, calculations of the vibrational frequencies and MOs, and NBO analyses. The effects of ligand basicity on structure and bonding in Lewis acid-base adducts of WF_6 are discussed.

* Based on the following publication: Turnbull, D.; Kostiuk, N.; Wetmore, S. D.; Gerken, M. *J. Fluorine Chem.* **2018**, *215*, 1–9.

3.2. Results and Discussion

3.2.1. Syntheses and Properties of $WF_6(4\text{-}NC_5H_4R)$ (R = H, CH_3, $N(CH_3)_2$) and $F_6W(4,4'\text{-bipy})WF_6$

The $WF_6(4\text{-}NC_5H_4R)$ (R = H, CH_3, $N(CH_3)_2$) and $F_6W(4,4'\text{-bipy})WF_6$ adducts are conveniently prepared by the reaction of the corresponding pyridine derivative with a slight excess of WF_6 in CH_2Cl_2 at ambient temperature (Eqs. 3.1 and 3.2), as described previously for $WF_6(NC_5H_5)$.[3] Upon removal of the solvent and excess WF_6 under dynamic vacuum up to ambient temperature, the adducts are obtained as fine white powders, with the exception of $WF_6\{4\text{-}NC_5H_4N(CH_3)_2\}$, which instead has an intense red-orange colour. The mononuclear adducts are soluble to varying degrees in CH_3CN, CH_2Cl_2, and SO_2, whereas $F_6W(4,4'\text{-bipy})WF_6$ is insoluble in these solvents.

$$WF_6 + 4\text{-}NC_5H_4R \xrightarrow{CH_2Cl_2} WF_6(4\text{-}NC_5H_4R) \quad (3.1)$$

$$2WF_6 + 4,4'\text{-bipy} \xrightarrow{CH_2Cl_2} F_6W(4,4'\text{-bipy})WF_6 \quad (3.2)$$

The pyridine and 4-methylpyridine adducts have been found to volatilise slowly *in vacuo* at ambient temperature, and as such can only be held under such conditions for brief periods. Although $WF_6(NC_5H_5)$ is seemingly indefinitely stable if stored under an inert atmosphere of N_2, it appears to slowly sublime over extended periods without decomposition. The $WF_6(4\text{-}NC_5H_4CH_3)$ adduct decomposes within weeks in the solid state, or hours in CH_3CN, at ambient temperature to afford a brown material. The adducts are highly reactive towards traces of moisture and HF, leading to cleavage of the W–F and W–N bonds, respectively (Eqs. 3.3 and 3.4). As HF is formed as a hydrolysis product, it is typical to observe traces of both impurities in the sample simultaneously.

$$WF_6(B) + H_2O \rightarrow WOF_4(B) + 2HF \quad (3.3)$$

$$WF_6(B) + HF \rightarrow [BH][WF_7] \quad (3.4)$$

Attempts to synthesise $WF_6(NC_5H_5)$ in CH_3CN invariably resulted in contamination of the product with an unidentified brown material, signalling the occurrence of side reactions. However, if the excess WF_6 is removed before the introduction of CH_3CN, no such side reactions occur. Thus, it appears that the WF_6-CH_3CN system is a stronger oxidant than WF_6 alone and is capable of oxidising the nitrogen bases employed in this study. The enhanced oxidising capabilities of WF_6 in the presence of CH_3CN have been observed previously in its reactions with iron[4] and tungsten,[5] which do not typically proceed under mild conditions. Analogous reactions performed in SO_2 resulted in increased contamination by WOF_4 derivatives, which is attributed to O/F exchange between WF_6 and SO_2 (Eq. 3.5) as similar side reactions have been observed previously.[6]

$$WF_6 + SO_2 \rightarrow WOF_4 + SOF_2 \quad (3.5)$$

3.2.2. Molecular Geometries

The solid-state structures of $WF_6(4\text{-}NC_5H_4R)$ (R = H, CH_3, $N(CH_3)_2$) were elucidated by X-ray crystallography at –173 °C. In addition, gas-phase geometries were optimised for these adducts along with $F_6W(4,4'\text{-bipy})WF_6$ and previously reported $WF_6(2\text{-}NC_5H_4F)$. The experimental geometries of the adducts were used as starting points whenever possible. Selected experimental and calculated geometric parameters are given in Table 3.1. Crystallographic data collection and refinement parameters are provided in the Appendix (Table A.1).

Table 3.1. Selected Experimental and Calculated Bond Lengths (Å) and Angles (°) in $WF_6(4\text{-}NC_5H_4R)$ (R = H, CH_3, $N(CH_3)_2$) and $F_6W(4,4'\text{-bipy})WF_6$

	$WF_6(NC_5H_5)$		$WF_6(4\text{-}NC_5H_4CH_3)$		$F_6W(4,4'\text{-bipy})WF_6$		$WF_6\{4\text{-}NC_5H_4N(CH_3)_2\}^c$		
					calcd[b]				
	exptl	calcd[a]	exptl	calcd[a]	θ = 0.2°	θ = 89.9°		exptl	calcd[a]
W–F(1)	1.880(6)	1.868	1.875(2)	1.868	1.867	1.866	W–F(1)	1.8711(14)	1.873
W–F(2)	1.875(5)	1.868	1.868(2)	1.868	1.867	1.866			
W–F(3)	1.861(5)	1.877	1.859(2)	1.878	1.878	1.879	W–F(2)	1.8696(14)	1.880
W–F(4)	1.864(5)	1.877	1.858(2)	1.878	1.878	1.879	W–F(3)	1.8628(14)	1.880
W–F(5)	1.843(5)	1.877	1.858(2)	1.878	1.878	1.879			
W–F(6)	1.868(5)	1.877	1.867(2)	1.878	1.878	1.879			
W–N	2.251(7)	2.343	2.250(3)	2.339	2.351	2.357	W–N(1)	2.214(3)	2.301
F(1)–W–F(2)	75.1(3)	76.3	75.70(10)	76.3	76.5	76.6	F(1)–W–F(1)^i	75.49(9)	76.2
F(1)–W–F(3)	77.4(2)	79.3	78.94(11)	79.2	79.5	79.5	F(1)–W–F(2)	77.69(7)	78.9
F(1)–W–F(4)	124.1(3)	127.8	126.35(11)	127.4	128.1	127.9	F(1)–W–F(3)	124.96(7)	127.3
F(3)–W–F(4)	81.6(3)	80.5	80.53(11)	80.1	80.5	79.9	F(2)–W–F(3)	81.36(6)	80.7
F(3)–W–F(5)	90.5(3)	90.9	91.72(10)	91.7	90.7	91.4	F(2)–W–F(3)^i	91.77(6)	91.4
F(3)–W–F(6)	149.6(2)	148.4	151.21(10)	149.0	148.9	148.3	F(2)–W–F(2)^i	150.86(10)	149.6
F(1)–W–N	143.2(3)	141.9	143.20(10)	141.8	141.8	141.7	F(1)–W–N(1)	142.25(5)	142.0
F(3)–W–N	74.8(3)	74.2	75.74(11)	74.5	73.9	74.1	F(2)–W–N(1)	75.43(5)	74.8
F(1)–W–N–C(1)	–3.6(9)	0.0	90.0(3)	90.0	0.2	89.9	F(1)–W–N(1)–C(1)^i	3.3(2)	0.0

[a]Calculated at the B3LYP/sVTZ level of theory. [b]Calculated at the B3LYP/VTZ level of theory. Theta (θ) is defined as the F(1)–W–N–C(1) dihedral angle. [c]Symmetry transformation: i = 1 – x, y, 1.5 – z.

The $WF_6(NC_5H_5)$ adduct crystallises in the triclinic space group $P\bar{1}$, whereas its methyl and dimethylamino derivatives crystallise in the monoclinic space groups $P2_1/n$ and $C2/c$, respectively. The compounds manifest as discrete molecular entities with no significant intermolecular contacts. In the pyridine and 4-methylpyridine adducts, all atoms are crystallographically unique. In $WF_6\{4\text{-}NC_5H_4N(CH_3)_2\}$, the molecule possesses crystallographically imposed C_2 symmetry.

The adducts adopt monocapped-trigonal-prismatic geometries with the pyridyl ligands in the capping positions (Figure 3.1), resulting in approximately C_{2v}-symmetric structures. Interestingly, $WF_6(4\text{-}NC_5H_4CH_3)$ adopts a geometry in which the plane of the pyridyl ligand is orthogonal to the opposing edge of the trigonal prism formed by F(1) and F(2), resulting in a F(1)–W–N–C(1) dihedral angle (θ) of 90.0(3)°. This contrasts with the other adducts, which are structurally similar to $WF_6(2\text{-}NC_5H_4F)$ ($\theta \approx 0°$).[7] The invariant observation of a monocapped-trigonal-prismatic geometry in these complexes, despite significant differences in the BF_3 affinities (i.e., Lewis basicities) of 2-fluoropyridine (97 kJ mol^{-1}), pyridine (128 kJ mol^{-1}), 4-methylpyridine (134 kJ mol^{-1}), and 4-(dimethylamino)pyridine (152 kJ mol^{-1}),[8] suggest that this geometry best assuages the steric demands of the pyridyl ligand. However, even 4-(dimethylamino)pyridine is predicted to be a significantly weaker Lewis base than "naked F^-", which affords monocapped-octahedral $[WF_7]^-$,[2] as the FIA of BF_3 (344 kJ mol^{-1}) and BF_3 affinity of F^- should be considered equivalent.

The dative W–N bonds are of equal length in the pyridine and 4-methylpyridine adducts, whereas that of $WF_6\{4\text{-}NC_5H_4N(CH_3)_2\}$ is slightly shorter and that of $WF_6(2\text{-}NC_5H_4F)$[7] slightly longer (Table 3.2). The W–N bonds in these adducts are significantly

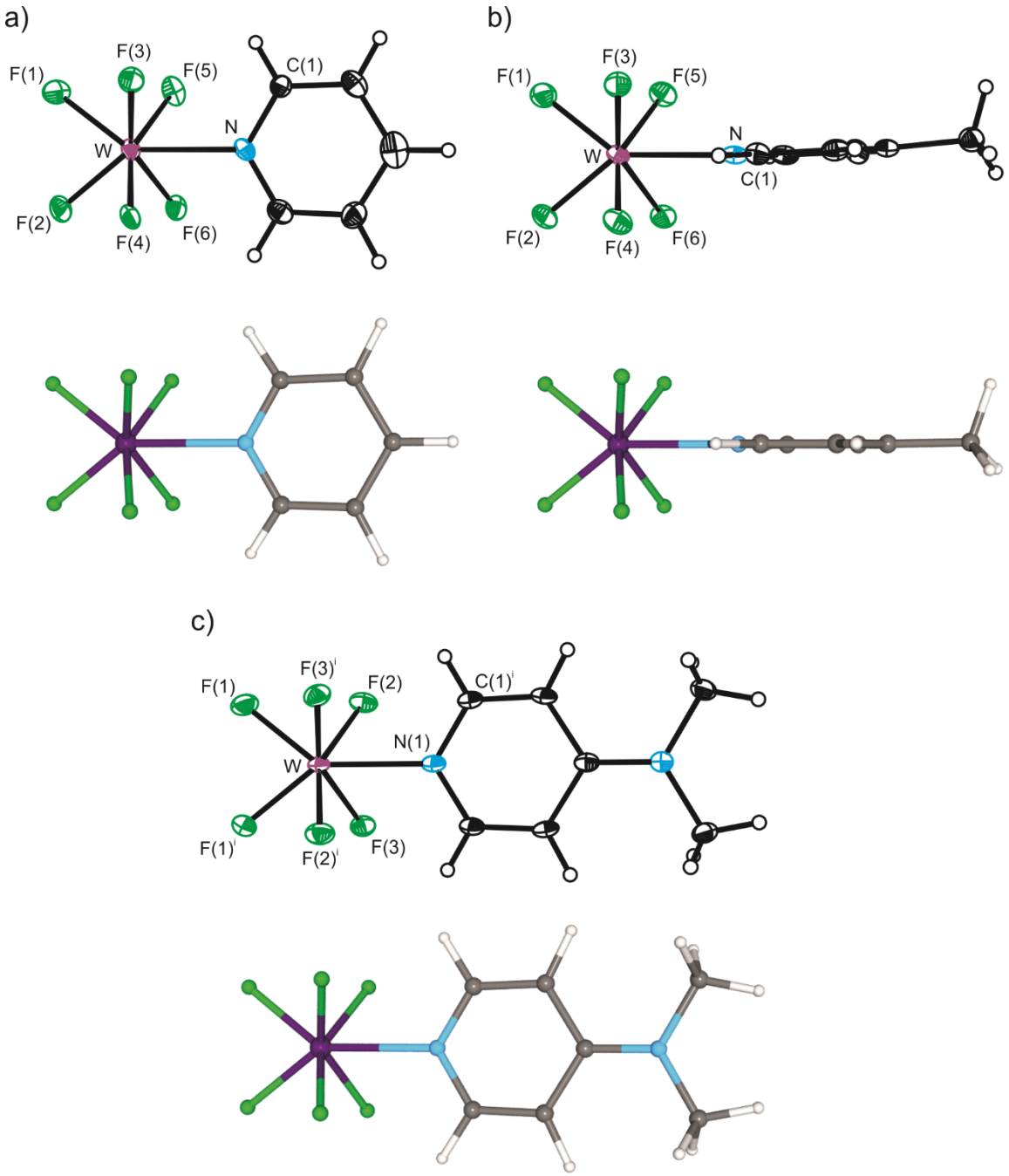

Figure 3.1. Thermal ellipsoid plots (50% probability level, top) and optimised gas-phase geometries (bottom) of $WF_6(4\text{-}NC_5H_4R)$: a) R = H, b) R = CH_3, c) R = $N(CH_3)_2$. Symmetry transformation: *i* = 1 – x, y, 1.5 – z.

Table 3.2. Selected Experimental and Calculated Bond Lengths (Å) and Normalised Contacts[a] in WF_6 and Its Adducts with Various Pnictogen (Pn) Bases

Base	W–F (average)		W–Pn			
	exptl	calcd[b]	exptl		calcd[b]	
—[c]	1.8264	1.845	—			
NC_5H_5	1.865	1.874	2.251(7)	[0.633]	2.343	[0.659]
4-$NC_5H_4CH_3$	1.864	1.875	2.250(3)	[0.633]	2.339	[0.658]
4-$NC_5H_4N(CH_3)_2$	1.8678	1.878	2.214(3)	[0.622]	2.301	[0.647]
4,4′-bipy[d]	—	1.874	—		2.351	[0.661]
2-NC_5H_4F[e]	1.84	1.865	2.294(9)	[0.645]	2.418	[0.680]
$P(CH_3)_3$[f]	1.86	—	2.598(9)	[0.657]	—	
$P(C_6H_5)(CH_3)_2$[f]	1.878	—	2.564(1)	[0.648]	—	
PH_3[f]	—	1.857	—		2.706	[0.761]

[a]Given in square brackets. Defined as the ratio of the bond length to the sum of the van der Waals radii (r) of the bonded atoms[9] (r(W) = 2.007[10]; r(P) = 1.95[11]; r(N) = 1.55[12]). [b]Calculated at the B3LYP/sVTZ level of theory, unless otherwise noted. [c]Crystallographic bond lengths from reference 10. [d]Calculated at the B3LYP/VTZ level of theory. θ = 89.9° [e]Crystallographic bond lengths from reference 7. [f]From reference 1.

shorter than the W–P bonds in analogous adducts with tertiary phosphines (2.564(1)–2.598(9) Å),[1] which is not surprising considering that phosphorus is larger than nitrogen. The trend in W–Pn (Pn = N, P) bond strengths is more directly compared by their normalised contacts (Table 3.2).[9] The normalised W–N contact of $WF_6\{4\text{-}NC_5H_4N(CH_3)_2\}$ is the shortest (0.622), indicating that its W–Pn bond is the strongest of the series. Conversely, the 2-fluoropyridine (0.645) and tertiary phosphine (0.648–0.657) adducts possess larger normalised W–Pn contacts, reflecting weaker bonds.

The W–F bonds in $WF_6(4\text{-}NC_5H_4R)$ (R = H, CH_3, $N(CH_3)_2$) and $WF_6\{P(C_6H_5)(CH_3)_2\}$ are, on average, significantly elongated relative to crystalline WF_6 (1.8261(13)–1.8266(19) Å).[13] In the $WF_6(4\text{-}NC_5H_4CH_3)$ adduct, the W−F(1) and W–F(2) bonds are longer than those of the fluorido ligands that form the capped face, but are predicted to be slightly shorter. The other adducts exhibit differences of lesser to no significance in crystallographic bond lengths. The contraction or elongation of the opposing and adjacent W–F bonds, respectively, is possibly a consequence of crystal packing.

As inferred from the adducts having crystallised in different space groups, the $WF_6(4\text{-}NC_5H_4R)$ (R = H, CH_3, $N(CH_3)_2$) adducts exhibit highly dissimilar packing motifs despite their similar compositions and molecular structures. The $WF_6(NC_5H_5)$ adduct crystallises such that the pyridyl ligands of adjacent molecules are π-stacked, which was also observed in the crystal structure of the 2-fluoropyridine adduct.[7] However, in the former, adjacent pyridyl ligands are rotated 180° relative to one another (Figure 3.2a) and in the latter, adjacent molecules are rotated by approximately 120° relative to one another. Contrastingly, no such interactions occur in $WF_6(4\text{-}NC_5H_4CH_3)$ (Figure 3.2b), while in

$WF_6\{4\text{-}NC_5H_4N(CH_3)_2\}$, the neutral ligands overlap in such a way as to maximise stacking interactions between the entire delocalised π systems (Figure 3.2c).

Optimisation of the gas-phase geometries of $WF_6(4\text{-}NC_5H_4R)$ (R = H, CH_3, $N(CH_3)_2$) and $WF_6(2\text{-}NC_5H_4F)$ using the experimental geometries from the crystal structures as starting points resulted in C_{2v}- or C_s-symmetric structures, in excellent agreement with the experimental data. The largest discrepancies are slight overestimations of the W–N bond lengths (Table 3.1). As such, in the absence of crystallographic data, two gas-phase geometries were optimised for $F_6W(4,4'\text{-bipy})WF_6$ as global (θ = 89.9°) and local (θ = 0.2°) energy minima with monocapped-trigonal-prismatic geometries at the tungsten centres, in which the planes of the two pyridyl rings intersect at an angle of 37.7–38.0° (Figure 3.3). The W–F and W–N bonds in $F_6W(4,4'\text{-bipy})WF_6$ appear similar in strength to those in the pyridine and 4-methylpyridine adducts.

Given the different conformation of $WF_6(4\text{-}NC_5H_4CH_3)$ observed in its crystal structure, relaxed potential-energy-surface (PES) scans were conducted on $WF_6(NC_5H_5)$ and $WF_6(4\text{-}NC_5H_4CH_3)$ to ascertain the possible effect of the 4-methyl group on the overall geometry of the complex. In both cases, it was determined that the orthogonal configuration (θ = 90°) observed in the crystal structure of $WF_6(4\text{-}NC_5H_4CH_3)$ was *ca*. 4 kJ mol^{-1} lower in energy than the co-planar configuration, with an overall energy barrier for rotation about the W–N bond of *ca*. 11 kJ mol^{-1} (Figure 3.4). Thus, the presence of a methyl group in $WF_6(4\text{-}NC_5H_4CH_3)$ has no intrinsic effect on the energy of the adduct regarding the orientation of the pyridyl ligand and such minimal differences in energy could easily be overcome during crystal formation in favour of maximising packing efficiency.

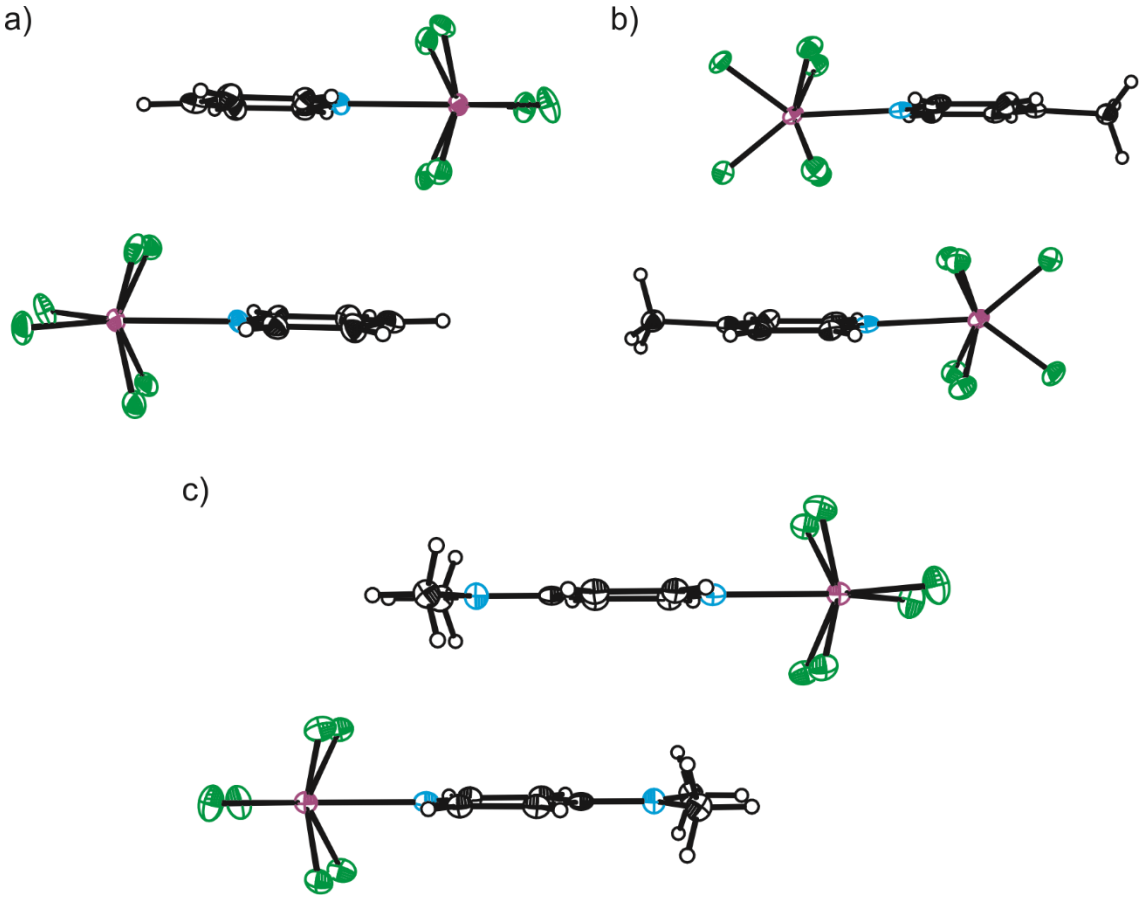

Figure 3.2. Thermal ellipsoid plots (50% probability level) of intermolecular π-stacking interactions in crystalline $WF_6(4\text{-}NC_5H_4R)$: a) R = H, b) R = CH_3, c) R = $N(CH_3)_2$.

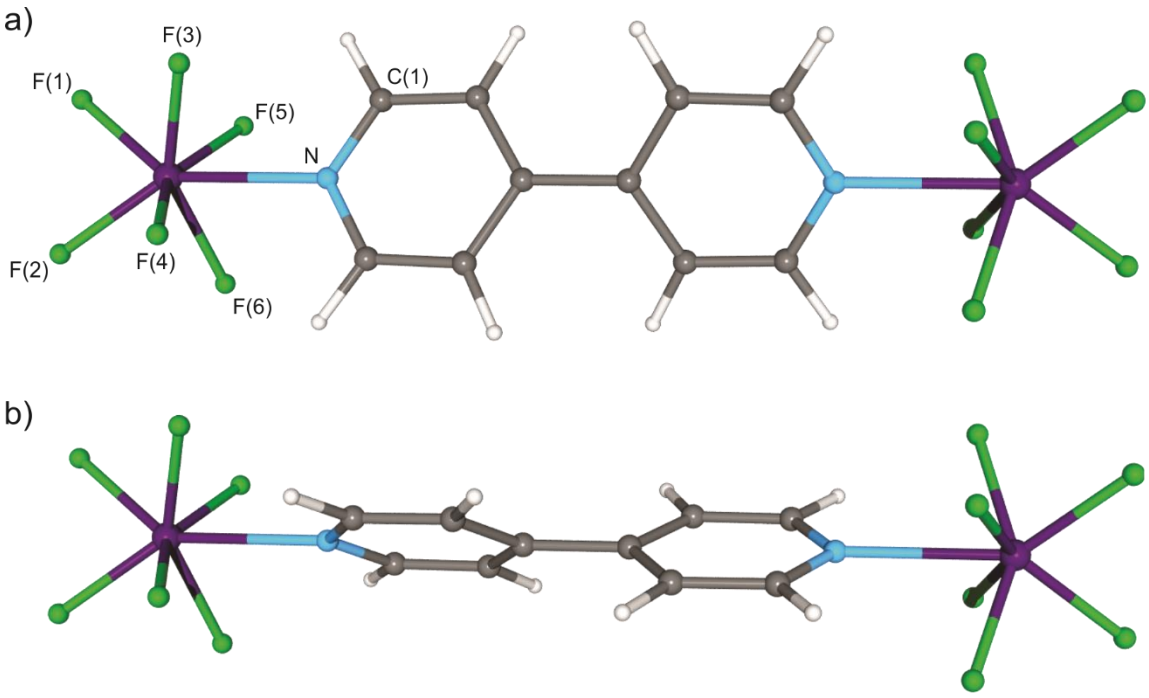

Figure 3.3. Optimised gas-phase geometries: of $F_6W(4,4'\text{-bipy})WF_6$: a) θ = 0.2°, b) θ = 89.9°.

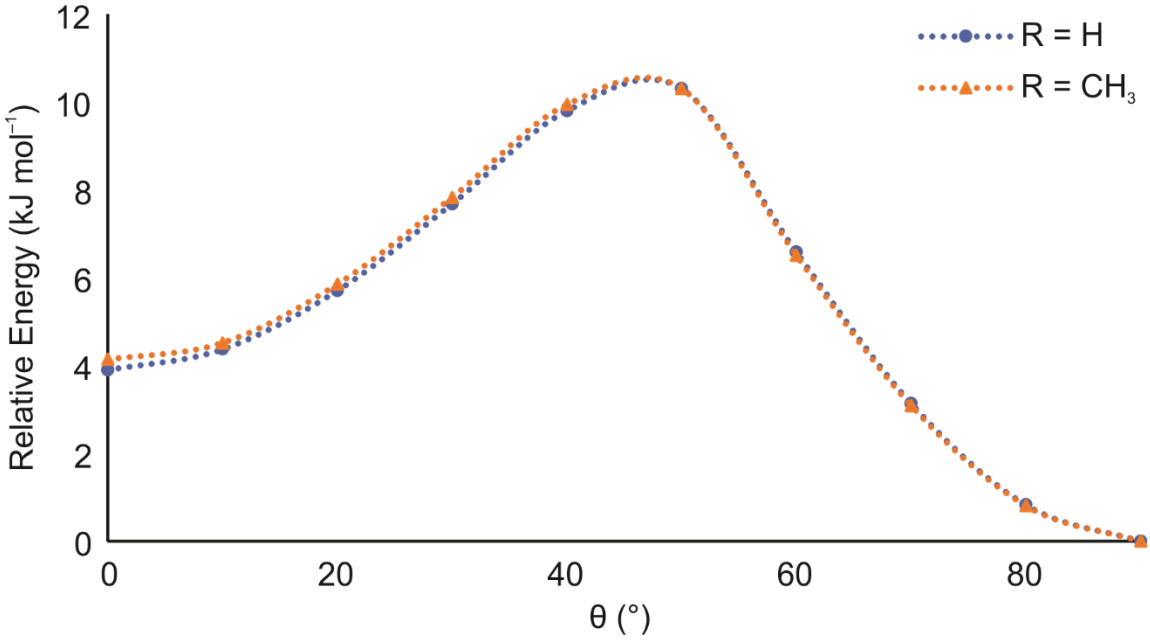

Figure 3.4. Relaxed PES scans of the F(1)–W–N–C(1) dihedral angle (θ) in $WF_6(4\text{-}NC_5H_4R)$ (R = H, CH_3) from 0 to 90°.

Considering that in $F_6W(4,4'\text{-bipy})WF_6$, the conformation of the pyridyl ligand does not cause any significant changes to other geometric properties of the adduct, further computational studies have been conducted based on those structures that best simulate their experimental counterparts. In the case of $F_6W(4,4'\text{-bipy})WF_6$, for which the actual geometry remains uncertain, the orthogonal conformation ($\theta = 89.9°$) is discussed as it is, predictably, 8 kJ mol^{-1} lower in energy.

3.2.3. Raman Spectroscopy

The Raman spectrum of solid $WF_6(NC_5H_5)$ (Figure 3.5) is in excellent agreement with that reported previously.[3] The transfer of electron density from the pyridyl ligand to the tungsten centre causes weakening of the W–F bonds, accompanied by strengthening of the C–C and C–N bonds. Thus, bands corresponding to the pyridyl ligand tend to increase in frequency relative to those of free pyridine, while those corresponding to WF_6 decrease relative to free WF_6 (Table 3.3). The previous assignment of the symmetric W−F stretching mode to the band at 705 cm^{-1} (vs. 771 cm^{-1} in free WF_6) is confirmed by frequency calculations. The band of the ring-breathing mode ($\nu_s(NC_5)$) is correspondingly blue-shifted to 1024 cm^{-1} from 990 cm^{-1} in free pyridine. The Raman spectra of the 4-methyl (Figure 3.6), 4-dimethylamino (Figure 3.7), 4-(4′-pyridyl) (Figure 3.8), and 2-fluoro[7] derivatives exhibit very similar general features to that of $WF_6(NC_5H_5)$ (Table 3.3). Experimental and calculated vibrational frequencies, with assignments, for WF_6 and its adducts are detailed in the Appendix (Tables A.2–A.7).

The W–N stretching modes of adducts are assigned to bands that occur at *ca*. 150–200 cm^{-1}, which are higher in frequency than their predicted counterparts due to overestimation of the W–N bond lengths in the optimised geometries. The trend in

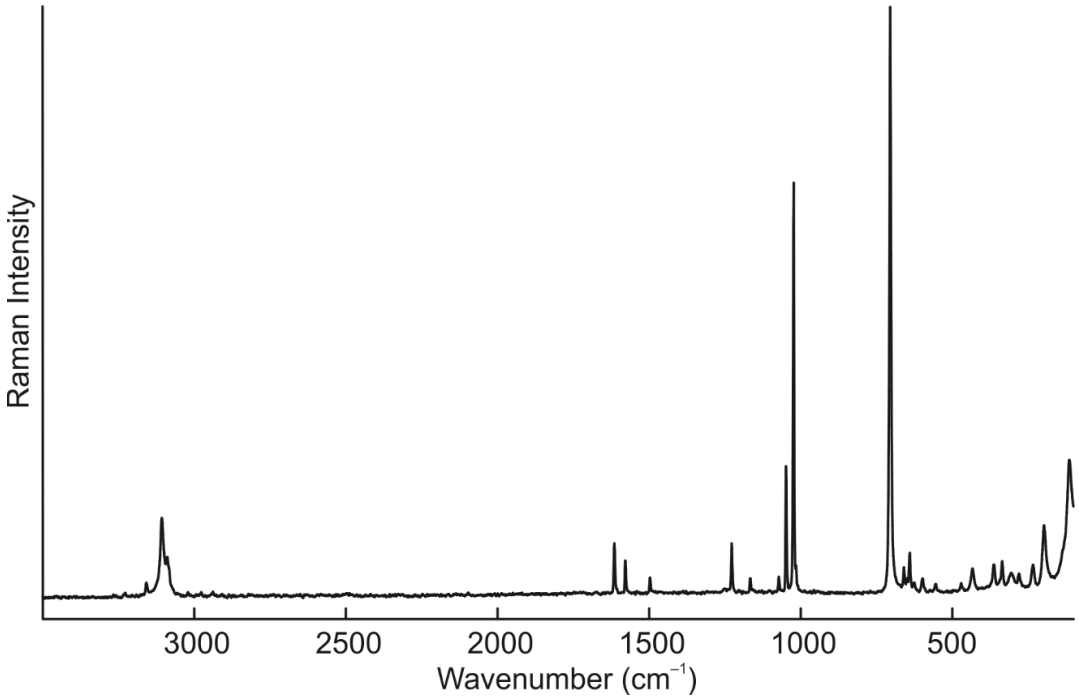

Figure 3.5. Raman spectrum of solid $WF_6(NC_5H_5)$, recorded at ambient temperature.

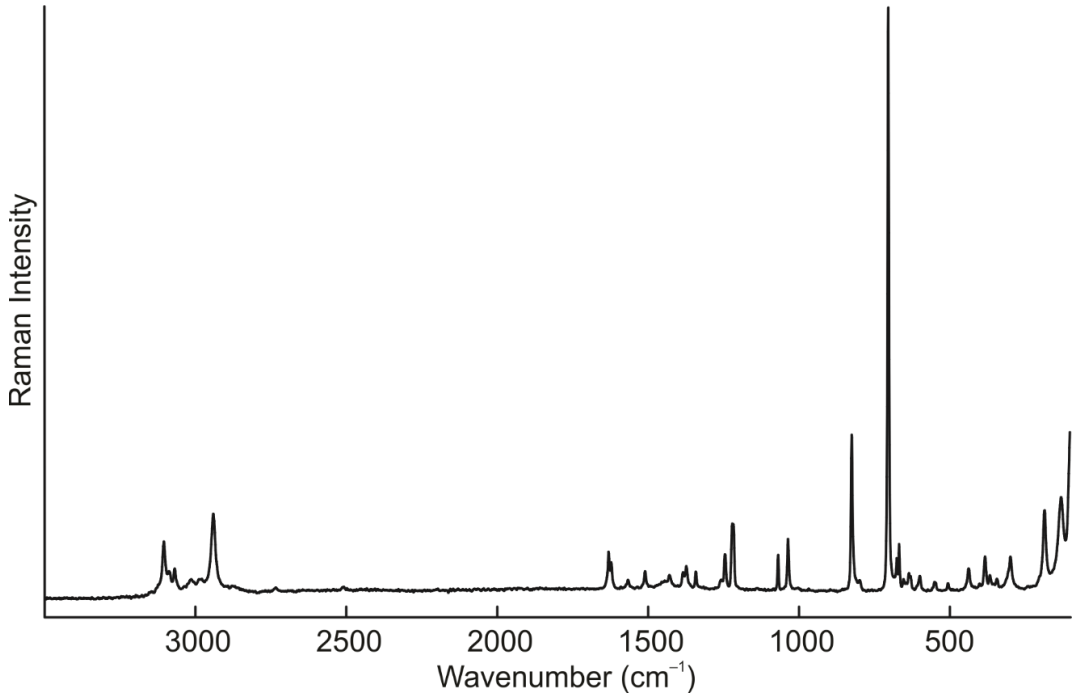

Figure 3.6. Raman spectrum of solid $WF_6(4\text{-}NC_5H_4CH_3)$, recorded at ambient temperature.

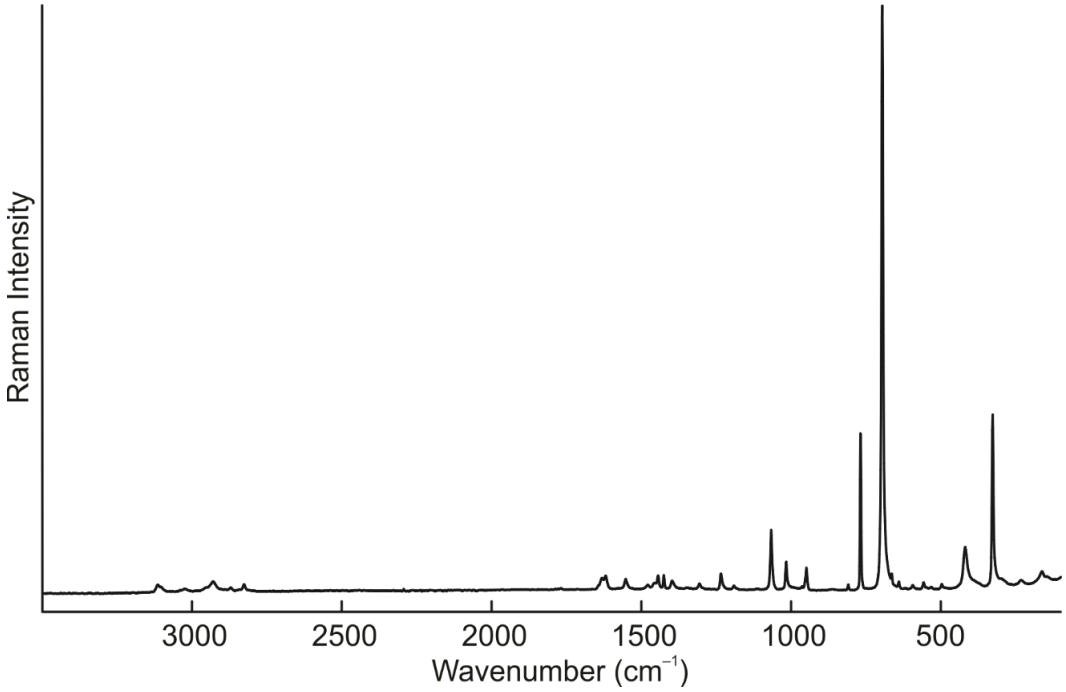

Figure 3.7. Raman spectrum of solid $WF_6\{4\text{-}NC_5H_4N(CH_3)_2\}$, recorded at ambient temperature.

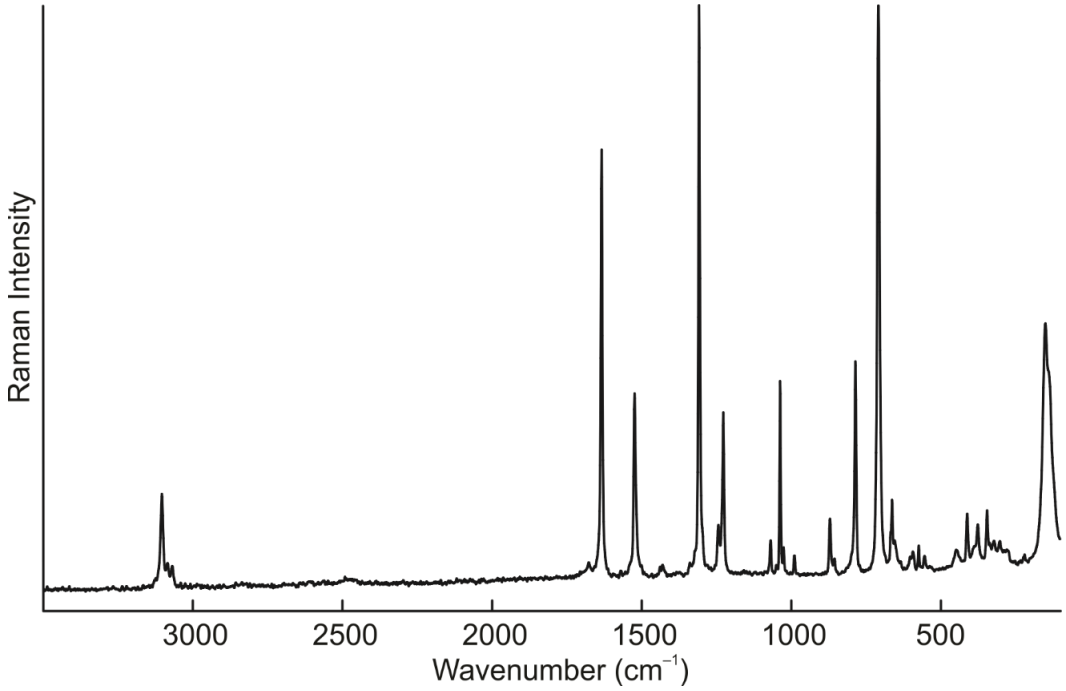

Figure 3.8. Raman spectrum of solid $F_6W(4,4'\text{-bipy})WF_6$, recorded at ambient temperature.

Table 3.3. Selected Experimental and Calculated[a] Vibrational Frequencies (cm^{-1}) of WF_6 and Its Adducts with Various Nitrogen Bases

Base	**$\nu_s(WF_6)$**		**$\nu_s(NC_5)$**		**$\nu(WN)$**	
—	771	[755]	—		—	
NC_5H_5	705	[702]	1024	[1041]	198	[161]
4-$NC_5H_4CH_3$	704	[701]	1036	[1047]	185	[157]
4-$NC_5H_4N(CH_3)_2$	697	[696]	1018	[1039]	164	[140]
4,4′-bipy[b]	708	[700]	1037	[1050]	—	[154/65]
2-NC_5H_4F[c]	712	[709]	1029	[1080]	171	[126]

[a]Given in square brackets. Calculated at the B3LYP/sVTZ level of theory, unless otherwise noted. [b]Calculated at the B3LYP/VTZ level of theory. θ = 89.9°. [c]Experimental data from reference 7

frequencies of these bands does not correspond to the strength of the W–N bond, but rather the size of the pyridyl ligand. As such, the W–N stretching band in WF_6{4-$NC_5H_4N(CH_3)_2$} is the lowest in frequency, despite it being predicted to possess the strongest W–N bond.

The Raman spectrum of $F_6W(4,4'$-bipy)WF_6 is much like those of the mononuclear adducts, suggesting a common geometry at the tungsten centres. This is further corroborated by the excellent agreement between the experimental and calculated Raman bands, though the calculated vibrational frequencies for the two conformations are too similar to deduce the true geometry of the adduct using vibrational spectroscopy (Table A.5). The two $WF_6(NC_5H_4)$ moieties are predicted to be, in general, weakly vibrationally coupled such that splittings caused by symmetric and antisymmetric combinations of their vibrational modes could not be resolved. The symmetrically and antisymmetrically coupled W–N stretching modes are predicted to occur at *ca*. 60 and 150 cm^{-1}, respectively, but could not be positively identified in the experimental Raman spectrum, consistent with their low calculated intensities.

3.2.4. Computational Results

3.2.4.1. Molecular Orbitals

The three degenerate LUMOs of WF_6 are comprised entirely of antibonding d_π-p_π interactions between the tungsten centre and fluorido ligands. In the adducts, the LUMOs retain this antibonding character, as illustrated for $WF_6(NC_5H_5)$ (Figure 3.9) though they are significantly higher in energy than in free WF_6 (Table 3.4), which should serve to quench the sensitivity of the metal centre towards reduction.

Table 3.4. Selected MO Energies (eV) and HOMO-LUMO Gaps (ΔE) WF_6 and Its Adducts with Various Nitrogen Bases[a]

Base	E_{MO}				ΔE	
	LUMO	HOMO	HOMO – 1	HOMO – 2	eV	nm
—	–4.91					
NC_5H_5	–3.64	–8.56	–9.34	–9.75	4.92	252
4-$NC_5H_4CH_3$	–3.35	–8.68	–8.89	–9.95	5.33	232
4-$NC_5H_4N(CH_3)_2$	–3.26	–6.95	–8.17	–9.50	3.69	336
4,4′-bipy[b]	–4.08	–9.09	–9.11	–9.21	5.15	247
2-NC_5H_4F	–3.73	–8.44	–9.54	–9.98	4.71	263

[a]Calculated at the B3LYP/sVTZ level of theory, unless otherwise noted. [b]Calculated at the B3LYP/VTZ level of theory. θ = 89.9°.

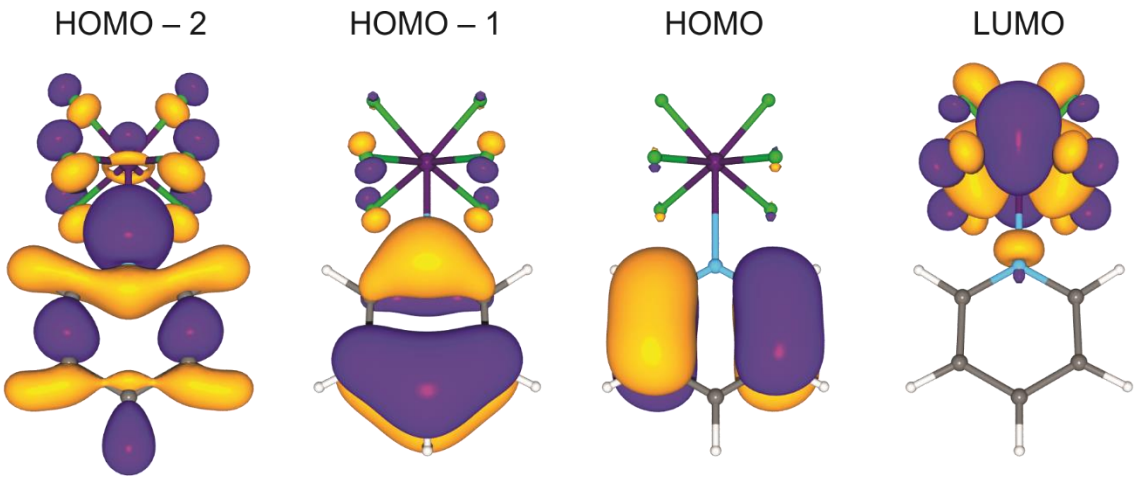

Figure 3.9. Selected MOs of $WF_6(NC_5H_5)$. Isosurfaces are drawn at 0.04 e $Å^{-3}$

The HOMOs and HOMOs – 1 of the adducts are π-bonding in nature, with the electron density localised primarily on the pyridyl ligands, rendering the HOMO-LUMO transition LMCT in nature. This is readily apparent in the case of boldly coloured WF_6{4-$NC_5H_4N(CH_3)_2$}, for which the increase in the energy of the HOMO is brought on by the dimethylamino group causing a significant decrease of the HOMO-LUMO gap (Table 3.4). The d_σ-p_σ interactions that comprise the dative W–N bonds involve the d_{z^2} orbital on tungsten and are observed in the HOMOs – 2. The W−F interactions in the HOMOs − 2 are strongly antibonding in nature, corroborating the elongation of the W−F bonds upon adduct formation, though this is potentially exacerbated by steric crowding induced by a seventh ligand.

3.2.4.2. NBO Analyses

Upon coordination of the nitrogen base to the tungsten centre, its natural-population-analysis (NPA) charge decreases slightly in the mononuclear adducts in comparison to that in free WF_6 (Table 3.5). This coincides with a slight decrease in the Wiberg bond indices (WBIs, Table 3.6) of the W−F bonds, more prevalently in those adjacent to (0.71−0.72) than opposite (0.75−0.77) the pyridyl ligand. The dative W−N bonds (WBI: 0.31−0.40) are approximately half as strong as the W−F bonds, indicating significant covalent character, with that of WF_6(2-NC_5H_4F) being the weakest. Surprisingly, the same WBI was calculated for the W–N bonds of the 4-methylpyridine and 4-(dimethylamino)pyridine adducts, despite the stronger W–N bond in the latter, as well as the difference in Lewis basicities of the parent nitrogen bases. The charges and WBIs of F_6W(4,4′-bipy)WF_6 are of a similar magnitude to those of the mononuclear adducts, and differences between the two conformations are effectively indiscernible.

Table 3.5. Natural-Population-Analysis Charges and Wiberg Valences[a] for WF_6 and Its Adducts with Various Nitrogen Bases[b]

	Base					
	—	**NC_5H_5**	**4-$NC_5H_4CH_3$**	**4-$NC_5H_4N(CH_3)_2$**	**4,4′-bipy[c]**	**2-NC_5H_4F**
W	+2.80 [4.71]	+2.74 [4.78]	+2.74 [4.79]	+2.74 [4.79]	+2.66 [4.89]	+2.76 [4.78]
F(1)	−0.47 [0.98]	−0.48 [0.94]	−0.49 [0.93]	−0.48 [0.94]	–0.47 [0.96]	–0.48 [0.95]
F(2)	−0.47 [0.98]	−0.48 [0.94]	−0.49 [0.93]	−0.51 [0.89]	–0.47 [0.96]	–0.47 [0.95]
F(3)	−0.47 [0.98]	−0.51 [0.90]	−0.51 [0.90]	−0.51 [0.89]	–0.50 [0.92]	–0.52 [0.89]
F(4)	−0.47 [0.98]	−0.51 [0.90]	−0.51 [0.90]		–0.50 [0.92]	–0.49 [0.93]
F(5)	−0.47 [0.98]	−0.51 [0.90]	−0.51 [0.90]		–0.50 [0.92]	–0.52 [0.89]
F(6)	−0.47 [0.98]	−0.51 [0.90]	−0.51 [0.90]		–0.50 [0.92]	–0.49 [0.95]
N(1)		−0.46 [3.35]	–0.47 [3.35]	−0.51 [3.33]	–0.44 [3.36]	–0.50 [3.30]
C_o		+0.09 [3.91]	+0.13 [3.92]	+0.11 [3.91]	+0.13 [3.92]	+0.09 [3.83]
C_m		–0.23 [3.96]	–0.23 [3.96]	−0.31 [3.95]	–0.20 [3.96]	–0.29 [3.95]
C_p		–0.13 [3.96]	+0.11 [4.01]	+0.24 [3.97]	+0.04 [4.01]	–0.12 [3.95]
H[d]		+0.23 [0.95]	+0.21 [0.95]	+0.21 [0.95]	+0.23 [0.95]	+0.23 [0.95]
C_{Me}			–0.61 [3.87]	−0.37 [3.82]		
N_p				−0.42 [3.39]		
F_o						–0.29 [1.09]

[a]Given in square brackets. [b]Calculated at the B3LYP/sVTZ level of theory, unless otherwise noted. Atom labels are as in Figure 3.1. [c]Calculated at the B3LYP/VTZ level of theory. No significant difference between $\theta = 0.2$ and 89.9°. Atom labels are as in Figure 3.3. [d]Averaged value.

Table 3.6. Wiberg Bond Indices for WF_6 and Its Adducts with Various Nitrogen Bases

	Base					
	—	**NC_5H_5**	**4-$NC_5H_4CH_3$**	**4-$NC_5H_4N(CH_3)_2$**	**4,4′-bipy**[b]	**2-NC_5H_4F**
W−F(1)	0.78	0.76	0.75	0.75	0.77	0.76
W−F(2)		0.76	0.75	0.71	0.77	0.77
W−F(3)		0.72	0.71	0.71	0.73	0.71
W−F(4)		0.72	0.71		0.73	0.75
W−F(5)		0.72	0.71		0.73	0.71
W−F(6)		0.72	0.71		0.73	0.75
W−N(1)		0.36	0.40	0.40	0.39	0.31
N(1)−C_o		1.36	1.33	1.31	1.34	1.36
C_o−C_m		1.44	1.47	1.51	1.46	1.37
C_m−C_p		1.44	1.39	1.29	1.37	1.47
C–H[c]		0.92	0.93	0.92	0.91	0.91
C_p–C_{Me}			1.04			
C_p–N_p				1.21		
N_p–C_{Me}				0.96		
C_p–C_p'					1.06	
C_o−F_o						0.93

[a]Calculated at the B3LYP/sVTZ level of theory, unless otherwise noted. Atom labels are as in Figure 3.1. [b]Calculated at the B3LYP/VTZ level of theory. No significant difference between θ = 0.2 and 89.9°. Atom labels are as in Figure 3.3. [c]Averaged value.

3.3. Conclusions

The Lewis-acid behaviour of WF_6 towards pyridine and several derivatives thereof has been investigated systematically. The monocapped-trigonal-prismatic geometries of the mononuclear adducts have been elucidated by low-temperature X-ray crystallography, and a combination of Raman spectroscopic and computational studies has been employed to suggest this geometry for dinuclear $F_6W(4,4'\text{-bipy})WF_6$ as well. The crystal structures revealed two distinct conformations, which represent the two minima on the potential energy surface with small calculated energy differences (4 kJ mol^{-1} for $WF_6(NC_5H_5)$) that describe the rotation of the pyridyl ligand with respect to the WF_6 trigonal prism. Bonding in the adducts was explored via MO calculations and NBO analyses, which established that the dative W–N bonds, though weak, are largely covalent in nature.

3.4. References

(1) El-Kurdi, S.; Al-Terkawi, A.-A.; Schmidt, B.; Dimitrov, A.; Seppelt, K. *Chem. Eur. J.* **2010**, *16* (2), 595–599.

(2) Giese, S.; Seppelt, K. *Angew. Chem. Int. Ed. Engl.* **1994**, *33* (4), 461–463.

(3) Arnaudet, L.; Bougon, R.; Buu, B.; Lance, M.; Nierlich, M.; Thuéry, P.; Vigner, J. *J. Fluorine Chem.* **1995**, *71* (1), 123–129.

(4) Barbour, C. J.; Cameron, J. H.; Winfield, J. M. *J. Chem. Soc., Dalton Trans.* **1980**, 2001–2005.

(5) Bao, N.; Winfield, J. M. *J. Fluorine Chem.* **1990**, *50* (3), 339–343.

(6) Wilson, W. W.; Christe, K. O. *Inorg. Chem.* **1981**, *20* (12), 4139–4143.

(7) Arnaudet, L.; Bougon, R.; Ban, B.; Lance, M.; Nierlich, M.; Vigner, J. *Inorg. Chem.* **1993**, *32* (7), 1142–1146.

(8) Laurence, C.; Gal, J.-F. In *Lewis Basicity and Affinity Scales: Data and Measurement*; John Wiley, 2010; pp 85–109.

(9) Scilabra, P.; Terraneo, G.; Resnati, G. *J. Fluorine Chem.* **2017**, *203*, 62–74.

(10) Batsanov, S. S. *J. Mol. Struct.* **1999**, *468* (1–2), 151–159.

(11) Batsanov, S. S. *Inorg. Mater.* **2001**, *37* (9), 871–885.

(12) Bondi, A. *J. Phys. Chem.* **1964**, *68* (3), 441–451.

(13) Drews, T.; Supeł, J.; Hagenbach, A. and; Seppelt, K. *Inorg. Chem* **2006**, *45* (9), 3782–3788.

Chapter 4 – Fluoride-Ion-Acceptor Behaviour of $W(NC_6F_5)F_4$ and Computational Studies of $[W(NR)F_5]^-$ (R = H, F, CH_3, CF_3, C_6H_5, C_6F_5)*

4.1. Introduction

A number of methods for the preparation of $[W(NR)F_5]^-$ anions, including substitution reactions with WF_6 and $W(NCl)Cl_4$ (see section 1.1.4.2), as well as a synthesis of $[C_6F_5NH_3][W_2(NC_6F_5)_2F_9]$,[1] have been reported. However, to our knowledge, a systematic study is lacking in regards to the structural and bonding properties of related $[W(NR)F_5]^-$ and $[W_2(NR)_2F_9]^-$ anions. The R group could confer highly variable electronic effects onto the metal centres, allowing for tunability of the structural and chemical properties of the anions. As such, these anions could represent diverse alternatives to known fluorine-containing weakly coordination anions (e.g., $[BF_4]^-$, $[AsF_6]^-$).

In this chapter, the synthesis and characterisation of $[Cat][W(NC_6F_5)F_5]$ ($[Cat]^+$ = $[C_5H_5NH]^+$, $[N(CH_3)_4]^+$) and $[C_5H_5NH][W_2(NC_6F_5)_2F_9]$ are reported. Complementary DFT (B3LYP) studies on the aforementioned anions, as well as $[W(NR)F_5]^-$ (R = H, F, CH_3, CF_3, C_6H_5) have been conducted, including geometry optimisations, calculations of the vibrational frequencies and MOs, and NBO analyses.

* Based on the following publication: Turnbull, D.; Wetmore, S. D.; Gerken, M. *Inorg. Chem.* **2017**, *56* (20), 12581–12593.

4.2. Results and Discussion

4.2.1. Syntheses and Properties of $[W(NC_6F_5)F_5]^-$ and $[W_2(NC_6F_5)_2F_9]^-$ Salts

While the reaction of WF_6 with $C_6F_5NH_2$ produces a mixture of products,[1] substituting $WF_6(NC_5H_5)$ for WF_6 results in the quantitative formation of $[C_5H_5NH][W(NC_6F_5)F_5]$ (Eq. 4.1), which can then be isolated as a yellow powder from CH_2Cl_2 by the removal of volatile materials under dynamic vacuum. This salt is highly soluble in CH_2Cl_2, CH_3CN, and SO_2.

$$WF_6 \cdot NC_5H_5 + C_6F_5NH_2 \rightarrow [C_5H_5NH][W(NC_6F_5)F_5] + HF \quad (4.1)$$

The $[N(CH_3)_4][W(NC_6F_5)F_5]$ salt can be isolated in a similar fashion by reacting $[N(CH_3)_4][WF_7]$ with $C_6F_5NH_2$ in SO_2 or CH_3CN solvent at ambient temperature (Eq. 4.2), followed by the removal of volatile materials under dynamic vacuum. The reaction must be conducted over several hours in SO_2 to ensure completion, though it is effectively instantaneous in CH_3CN. While thermally stable and highly soluble in CH_3CN and SO_2 like its $[C_5H_5NH]^+$ analogue, the $[N(CH_3)_4]^+$ salt is insoluble in CH_2Cl_2.

$$[N(CH_3)_4][WF_7] + C_6F_5NH_2 \rightarrow [N(CH_3)_4][W(NC_6F_5)F_5] + 2HF \quad (4.2)$$

The $[C_5H_5NH][W(NC_6F_5)F_5]$ salt can be solvolysed in aHF to afford $[C_5H_5NH][W_2(NC_6F_5)_2F_9]$, which contains a fluorine-bridged, dinuclear $[W_2(NC_6F_5)_2F_9]^-$ anion (Eq. 4.3). This is analogous to previously reported preparations of $[W_2Ch_2F_9]^-$ salts by the solvolysis of $[WChF_5]^-$ (Ch = O, S) in aHF.[2–4] As with the preparation of $[W_2O_2F_9]^-$ salts,[2,3] the reaction exists in equilibrium, as direct removal of aHF from the product mixture causes substantial reversion to the mononuclear anion. However, decanting the

solvent from the product allows for the isolation of $[C_5H_5NH][W_2(NC_6F_5)_2F_9]$ containing a small impurity of $[C_5H_5NH][W(NC_6F_5)F_5]$.

$$2[W(NC_6F_5)F_5]^- + n\text{HF} \rightleftharpoons [W_2(NC_6F_5)_2F_9]^- + [F(HF)_n]^- \quad (4.3)$$

The $[C_5H_5NH][W_2(NC_6F_5)_2F_9]$ salt is highly soluble in CH_3CN and SO_2, but only slightly soluble in CH_2Cl_2. At ambient temperature, the anion is partially solvolysed by CH_3CN to afford $[W(NC_6F_5)F_5]^-$ and $W(NC_6F_5)F_4(NCCH_3)$, as determined by ^{19}F NMR spectroscopy (Eq. 4.4).

$$[W_2(NC_6F_5)_2F_9]^- + CH_3CN \rightleftharpoons [W(NC_6F_5)F_5]^- + W(NC_6F_5)F_4(NCCH_3) \quad (4.4)$$

These $[W(NC_6F_5)F_5]^-$ and $[W_2(NC_6F_5)_2F_9]^-$ salts manifest as yellow powders, forming vibrant yellow solutions that then proceed to darken to orange upon concentration under dynamic vacuum. These salts are stable at ambient temperature and highly moisture sensitive; contact with even trace amounts of moisture results in the formation of $[WOF_5]^-$ and $[W_2(NC_6F_5)OF_9]^-$, respectively.

4.2.2. Molecular Geometries

The $[C_5H_5NH][W(NC_6F_5)F_5]$, $[N(CH_3)_4][W(NC_6F_5)F_5]$, and $[C_5H_5NH][W_2(NC_6F_5)_2F_9]$ salts were studied by X-ray crystallography at –173 °C. Crystallographic data collection and refinement parameters are given in the Appendix (Table B.1). In addition, the geometries of $[W(NC_6F_5)F_5]^-$ and $[W_2(NC_6F_5)_2F_9]^-$ were optimised using DFT methods (B3LYP), resulting in stationary points whose geometries are in excellent agreement with the crystallographic data. Selected experimental and calculated geometric parameters are given in Tables 4.1 and 4.2.

Table 4.1. Select Experimental and Calculated Bond Lengths (Å) and Angles (°) in $[W(NC_6F_5)F_5]^{-}$[a]

	exptl		calcd[b]
	$[C_5H_5NH]^+$ salt	**$[N(CH_3)_4]^+$ salt**	
W−N(1)	1.747(2)	1.755(4)	1.797
W−F(1)	2.0212(13)	1.973(3)	1.941
W−F(2)	1.8873(14)	1.8901(19)	1.898
W−F(3)	1.8770(13)	1.8866(18)	1.898
W−F(4)	1.8850(12)		1.898
W−F(5)	1.8846(14)		1.898
F(1)···N(2)	2.688(2)		
W−N(1)−C(1)	175.58(17)	178.5(3)	180.0
N(1)−W−F(1)	179.42(7)	179.75(15)	180.0
N(1)−W−F(2)	96.68(8)	96.57(10)	95.1
N(1)−W−F(3)	97.20(3)	95.84(10)	95.1
N(1)−W−F(4)	97.16(8)		95.1
N(1)−W−F(5)	97.65(8)		95.1
F(1)−W−F(2)	83.61(6)	83.61(9)	85.0
F(1)−W−F(3)	83.31(6)	83.98(9)	85.0
F(1)−W−F(4)	82.56(6)		85.0
F(1)−W−F(5)	81.85(6)		85.0
F(2)−W− $F(2)^i$/F(5)	89.63(7)	88.50(12)	89.8
F(2)−W−F(3)	87.43(7)	89.24(9)	89.8
F(2)−W− $F(3)^i$/F(4)	166.13(6)	167.56(8)	169.9
F(3)−W− $F(3)^i$/F(4)	90.03(6)	90.35(12)	89.8
F(3)−W−F(5)	165.10(7)		169.9
F(4)−W−F(5)	89.34(6)		89.8
N(2)−H(2)···F(1)	169(3)		

[a]Symmetry transformation: i = x, 1.5 − y, z. [b]Calculated at the B3LYP/sVTZ level of theory.

Table 4.2. Select Experimental and Calculated Bond Lengths (Å) and Angles (°) in $[C_5H_5NH][W_2(NC_6F_5)_2F_9]$[a]

	exptl	calcd[b]
W−N(1)	1.724(7)	1.759
W−F(1)	2.1013(17)	2.120
W−F(2)	1.855(5)	1.883
W−F(3)	1.858(6)	1.883
W−F(4)	1.859(5)	1.883
W−F(5)	1.866(6)	1.883
F(4)···N(2)	2.958(11)	
$F(3)^{j}$···N(2)	3.046(13)	
$F(3)^{k}$···N(2)	3.082(13)	
W−F(1)−W^{i}	156.0(4)	180.0
W−N(1)−C(1)	176.4(6)	180.0
N(1)−W−F(1)	179.8(3)	180.0
N(1)−W−F(2)	98.6(3)	97.8
N(1)−W−F(3)	99.5(3)	97.7
N(1)−W−F(4)	98.5(3)	97.8
N(1)−W−F(5)	98.3(3)	97.7

[a]Symmetry transformations: i = 1.5 − x, y, 0.5 – z; j = 0.5 − x, y, 1.5 − z; k = −1 + x, y, z.
[b]Calculated at the B3LYP/VTZ level of theory.

Long, yellow plates of $[C_5H_5NH][W(NC_6F_5)F_5]$ were grown by cooling a CH_2Cl_2 solution to −35 °C, whereas $[N(CH_3)_4][W(NC_6F_5)F_5]$ crystallised as yellow blocks from a CH_3CN solution at −40 °C. The $[C_5H_5NH]^+$ salt crystallises in the monoclinic space group $P2_1/c$ with four formula units per unit cell and one ion pair in the asymmetric unit. Meanwhile, the $[N(CH_3)_4]^+$ salt crystallises in the orthorhombic space group *Pnma* with four formula units per unit cell and one half of an ion pair in the asymmetric unit, as the ions are reflected across *b* mirror planes.

In both $[W(NC_6F_5)F_5]^-$ salts, the anion adopts a pseudo-octahedral geometry with the imido ligand in an axial position (Figure 4.1). In the $[N(CH_3)_4]^+$ salt, the W−F_{ax} bond (1.973(3) Å) is elongated relative to the W−F_{eq} bonds (1.8866(18)−1.8901(19) Å) due to a *trans* influence from the imido ligand. The equatorial fluorido ligands distort from the ideal WF_4 plane towards the axial fluorido ligand due to repulsion by the imido ligand (F(1)−W−F_{eq} = 83.61(9)−83.98(9)°). The W−N−C bond angle is approximately linear (178.5(3)°), as was observed previously for the W−N−Cl angle in $[W(NCl)F_5]^-$ salts (170.7(5)−176.1(5)°).[5–7]

The anion in the $[C_5H_5NH]^+$ salt exhibits a similar distortion of the WF_4 moiety from planarity (F(1)−W−F = 81.85(6)−83.61(6)°) and approximate linearity in the W−N−C bond angle (175.58(17)°). The elongation of the W−F_{ax} bond (2.0212(13) Å) relative to the W−F_{eq} bonds (1.8770(13)−1.8873(14) Å) is more dramatic than in the $[N(CH_3)_4]^+$ salt due to N−H···F_{ax} hydrogen bonding between the cation and anion (Figure 4.1a); the W≡N and W−F_{eq} bond lengths are not significantly affected by this interaction. A conformational difference between the salts is also observed (Figure 4.1d), presumably as a result of crystal packing. In the $[C_5H_5NH]^+$ salt, the anion adopts a nearly eclipsed C_1 geometry, whereas

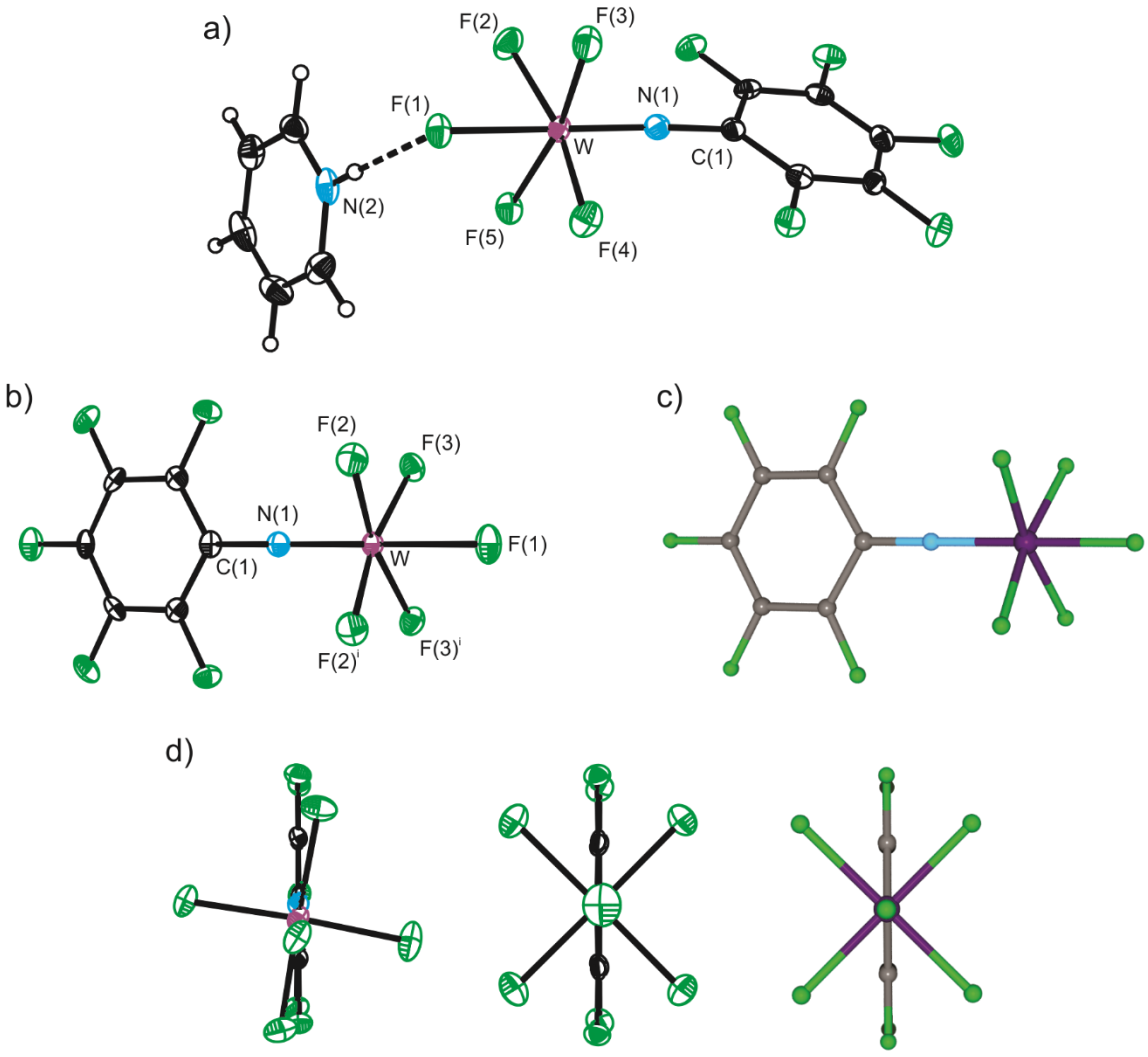

Figure 4.1. Thermal ellipsoid plots (50% probability level) of a) $[C_5H_5NH][W(NC_6F_5)F_5]$ and b) the anion in $[N(CH_3)_4][W(NC_6F_5)F_5]$, with c) the optimised gas-phase geometry (B3LYP/sVTZ) of $[W(NC_6F_5)F_5]^-$ and d) end-on views of the anions in a), b), and c).

in the $[N(CH_3)_4]^+$ salt, it adopts a staggered geometry approximating C_{2v} symmetry.

The predicted C_{2v}-symmetric gas-phase geometry is in excellent agreement with that determined crystallographically for the $[N(CH_3)_4]^+$ salt (Figures 4.1b and c), where the primary discrepancies are a slight overestimation of the predicted W≡N bond length (1.797 vs. 1.755(4) Å) and a corresponding underestimation of the W−F_{ax} bond length (1.941 vs. 1.973(3) Å).

Yellow plates of $[C_5H_5NH][W_2(NC_6F_5)_2F_9]$ were crystallised from a CH_3CN solution upon removal of the solvent at −40 °C. The plates were very thin and fractured easily such that a very small crystal had to be used to acquire adequate data. The $[C_5H_5NH][W_2(NC_6F_5)_2F_9]$ salt crystallises in the monoclinic space group *P*2/*n* with two formula units per unit cell and one half of a crystallographically unique ion pair in the asymmetric unit, as the F(1) atom is located on a twofold axis. The unit cell consists of double layers within the *ac* plane in which the cations and anions alternate along the *c* axis (Figure 4.2). While very weak N−H···F_{eq} hydrogen bonds are observed within the double layers, no such interactions between the double layers are observed, explaining the facile cleaving of the crystals during their selection and mounting.

The $[W_2(NC_6F_5)_2F_9]^-$ anion adopts a bent, pseudo-dioctahedral geometry with a symmetric fluorine bridge (Figure 4.3) in which the W−F_{ax}−W angle (156.1(4)°) is intermediate between those observed in the $[C_6F_5NH_3]^+$ salt (150.8(12)−170.4(19)°). The anion possesses crystallographically imposed C_2 symmetry and each $W(NC_6F_5)F_5$ moiety exhibits approximate C_{2v} symmetry. The C_6F_5 groups are staggered relative to the adjacent WF_4 moieties, and the WF_4 moieties are also staggered relative to one another (Figures 4.3b and c), thus differing from the crystallographically unique conformations observed in

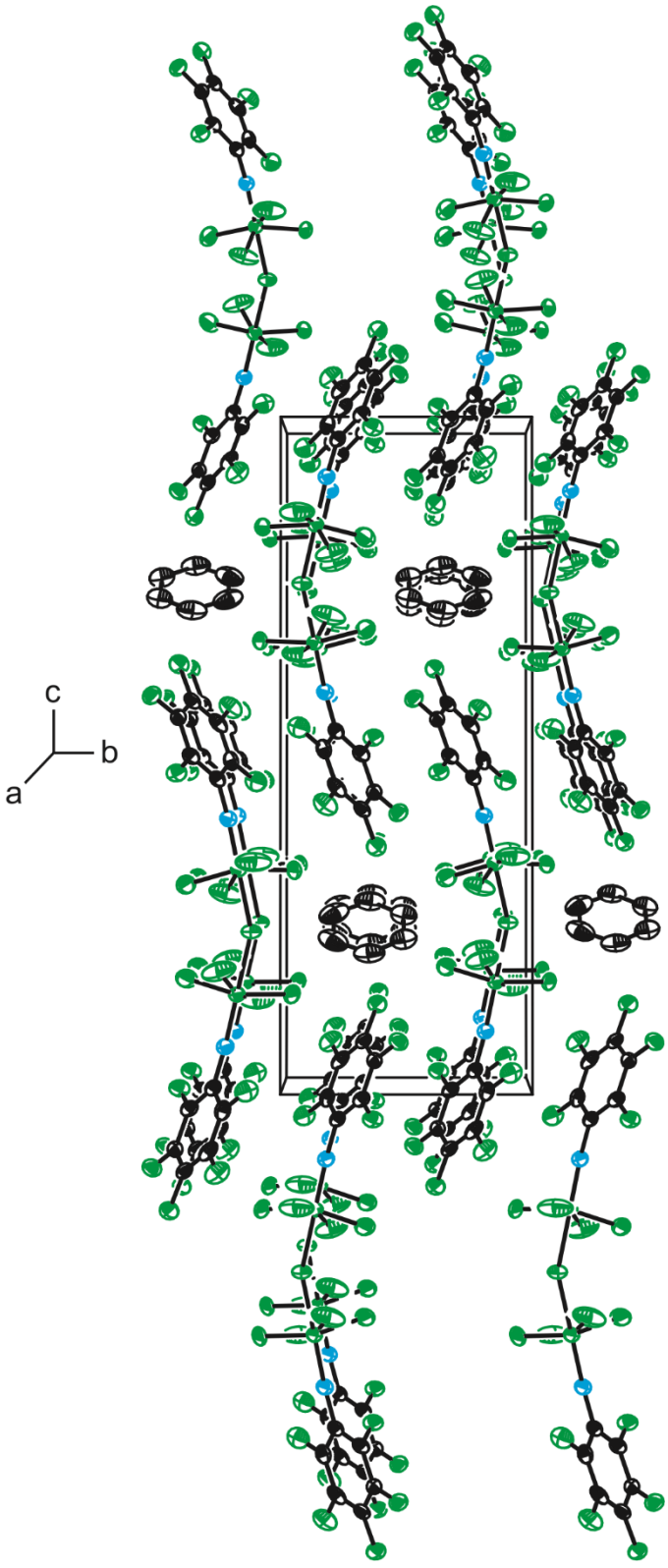

Figure 4.2. Crystal packing diagram of $[C_5H_5NH][W_2(NC_6F_5)_2F_9]$. Hydrogen atoms are omitted for clarity.

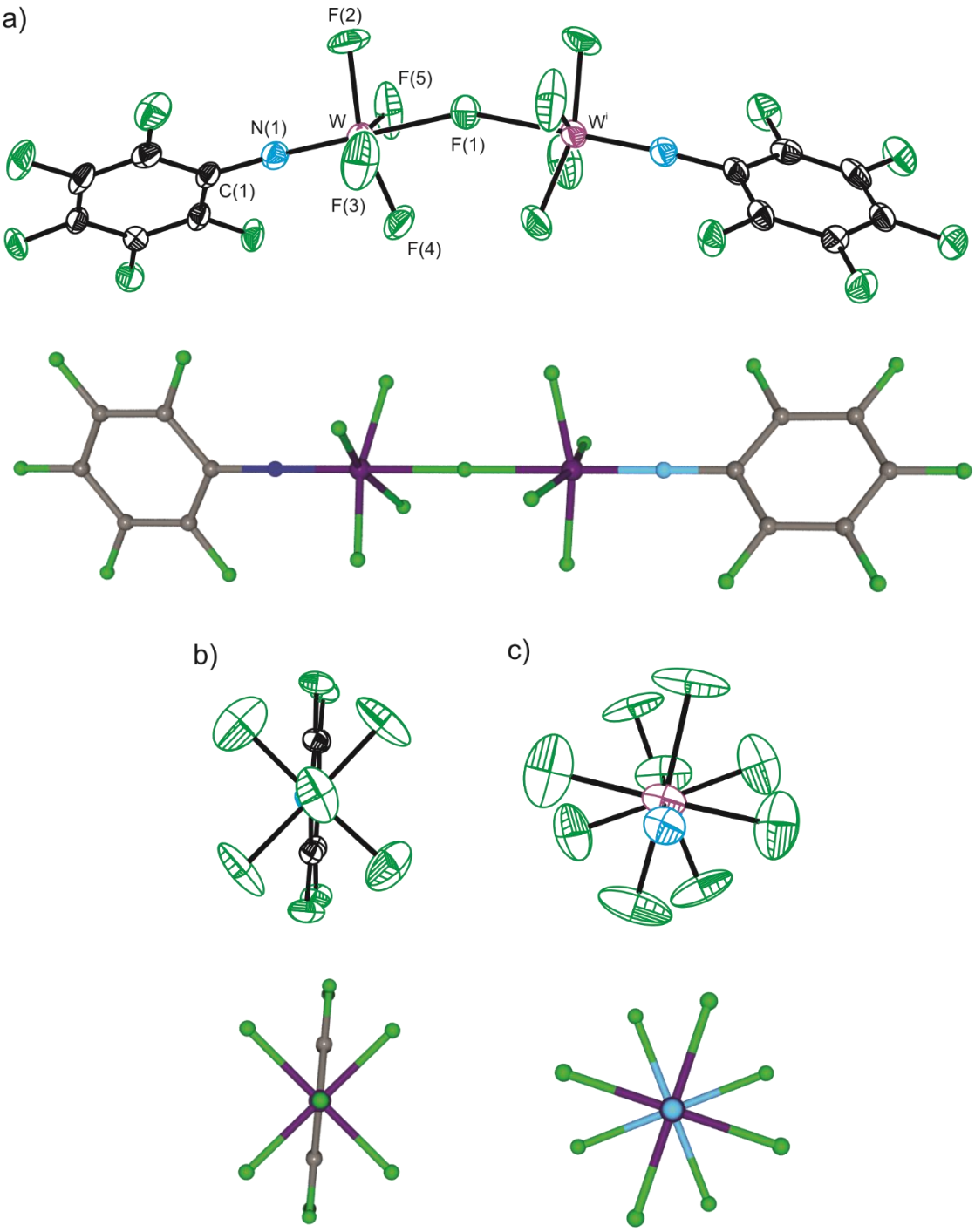

Figure 4.3. Thermal ellipsoid plot (50% probability level, top) and optimised gas-phase geometry (B3LYP/VTZ, bottom) of a) the anion in $[C_5H_5NH][W_2(NC_6F_5)_2F_9]$ with end-on views of the b) $W(NC_6F_5)F_5$ and c) W_2N_2F9 moieties.

the $[C_6F_5NH_3]^+$ salt, in which the WF_4 moieties are essentially eclipsed in both cases.[1] This suggests that the conformation of the anion is susceptible to crystal packing effects.

The W−F_{ax} bond is elongated relative to the W−F_{eq} bonds (2.1010(17) Å vs. 1.854(5)−1.867(6) Å). It is also longer than the W−F_{ax} bond observed in either salt of the mononuclear anion due to the coordination of the axial fluorido ligand to two tungsten centres and the resultant W−F_{ax} bonds possessing greater ionic character. As a consequence, the W−F_{eq} bonds in the dinuclear anion are shorter than those observed in the mononuclear anion. While the W≡N bond is slightly shorter than that observed in $[N(CH_3)_4][W(NC_6F_5)F_5]$ (1.724(7) vs. 1.755(4) Å), it is not significantly different from that observed in $[C_5H_5NH][W(NC_6F_5)F_5]$ (1.747(2) Å). The equatorial fluorido ligands distort from the ideal WF_4 plane towards the axial fluorido ligand (F(1)−W−F: 80.7(2)−81.6(3)°) to a slightly greater extent than in the mononuclear anion, which is expected due to the decreased repulsion by the axial fluorido ligand. As expected, the W−N−C angle is approximately linear (176.3(6)°).

The cation-anion interactions are much weaker in $[C_5H_5NH][W_2(NC_6F_5)_2F_9]$ (N(2)−F = 2.958(11)−3.082(13) Å) than in $[C_5H_5NH][W(NC_6F_5)F_5]$ (N(2)−F(1) = 2.688(2) Å) and have no significant effect on the W−F_{eq} bond lengths, reflecting a greater degree of weakly coordinating character in the dinuclear anion.

The predicted D_2-symmetric geometry of the dinuclear anion agrees well with the structure of the anion in the $[C_5H_5NH]^+$ salt (Figure 4.3), save for the prediction of a linear W−F_{ax}−W angle, which appears to be highly susceptible to crystal packing effects. Unlike for the $[W_2S_2F_9]^-$ anion,[4] no stable optimisation of a bent geometry was found, and the linear geometry was obtained even if the input was bent. Differences in the calculated

W−F_{ax}−W angle, however, were not found to significantly influence other geometric properties of the anion.

4.2.3. Raman Spectroscopy

Raman spectra were recorded on solid samples of $[C_5H_5NH][W(NC_6F_5)F_5]$, $[N(CH_3)_4][W(NC_6F_5)F_5]$, and $[C_5H_5NH][W_2(NC_6F_5)_2F_9]$ at ambient temperature (Figures 4.4–4.6). Bands corresponding to the $[C_5H_5NH]^+$ and $[N(CH_3)_4]^+$ cations were identified based on previous assignments,[8–10] as well as by comparison of the Raman spectra of the $[W(NC_6F_5)F_5]^-$ salts. Vibrational frequencies were calculated for $[W(NC_6F_5)F_5]^-$ and $[W_2(NC_6F_5)_2F_9]^-$, revealing no imaginary frequencies and excellent agreement with the experimental Raman spectra. As such, assignments of the experimental Raman bands for the anions were made on the bases of C_{2v} and D_2 symmetry, respectively. Selected experimental and calculated vibrational frequencies for the anions are given in Tables 4.3 and 4.4. More complete descriptions of the vibrational frequencies for these anions are given in the Appendix (Tables B.2–B.4).

The Raman spectra of the $[W(NC_6F_5)F_5]^-$ salts (Figures 4.4 and 4.5) are highly similar in regards to bands corresponding to the anion, with the majority of observed anion bands being within 2 cm^{-1} of one another and possessing comparable relative intensities. The experimental and predicted Raman frequencies are in excellent agreement with one another. While the 48 vibrational modes are all expected to be Raman-active, the Raman intensities of 16 modes were predicted to be < 1 $Å^4$ u^{-1}, and no obvious experimental counterparts are observed in these cases. The $\nu_s(WF_5)$ mode is found at a higher frequency in the $[C_5H_5NH]^+$ salt (661 cm^{-1}) than the $[N(CH_3)_4]^+$ salt (650 cm^{-1}), which is attributed to the hydrogen bond in the former decreasing the covalent character the W−F_{ax} bond and

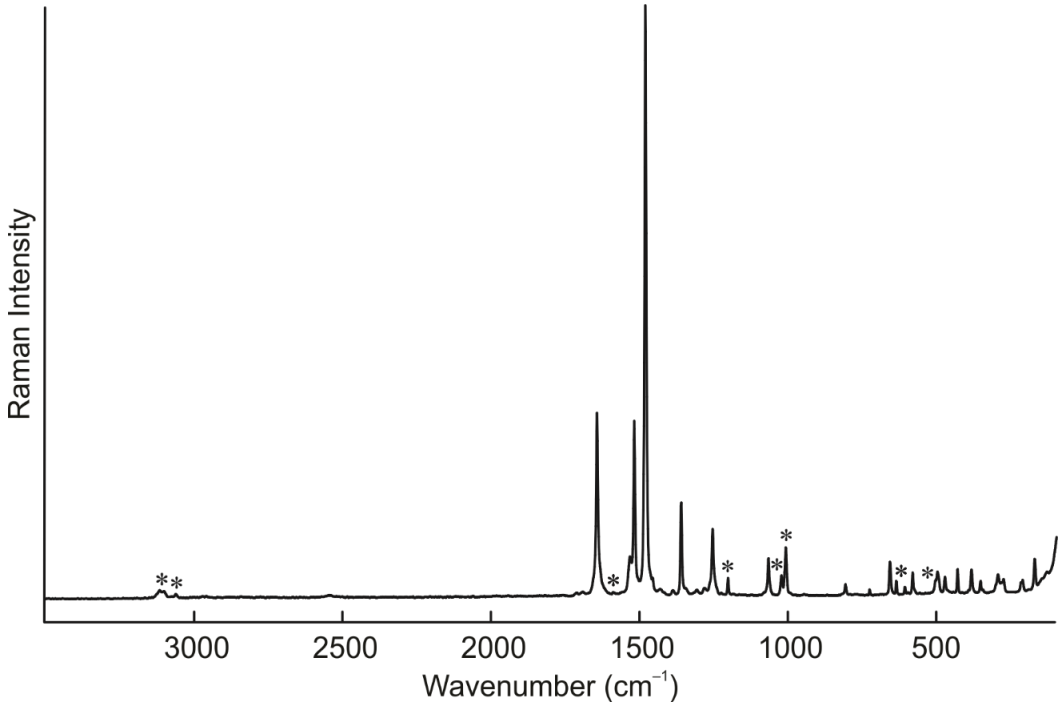

Figure 4.4. Raman spectrum of solid $[C_5H_5NH][W(NC_6F_5)F_5]$, recorded at ambient temperature. Asterisks (*) denote $[C_5H_5NH]^+$ bands.

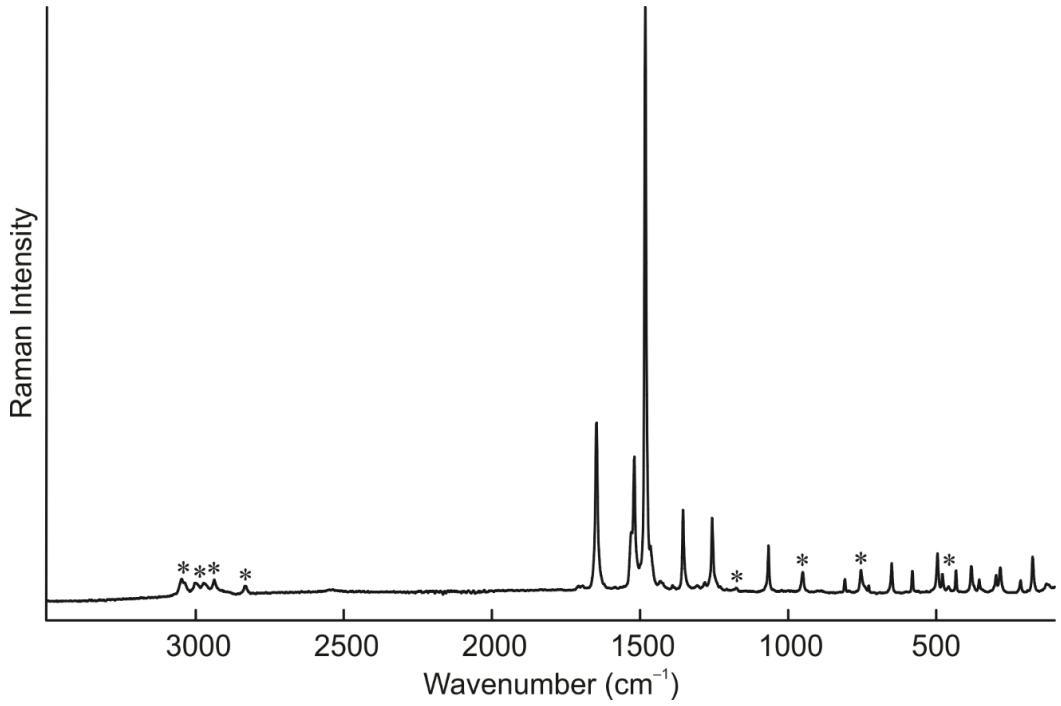

Figure 4.5. Raman spectrum of solid $[N(CH_3)_4][W(NC_6F_5)F_5]$, recorded at ambient temperature. Asterisks (*) denote $[N(CH_3)_4]^+$ bands.

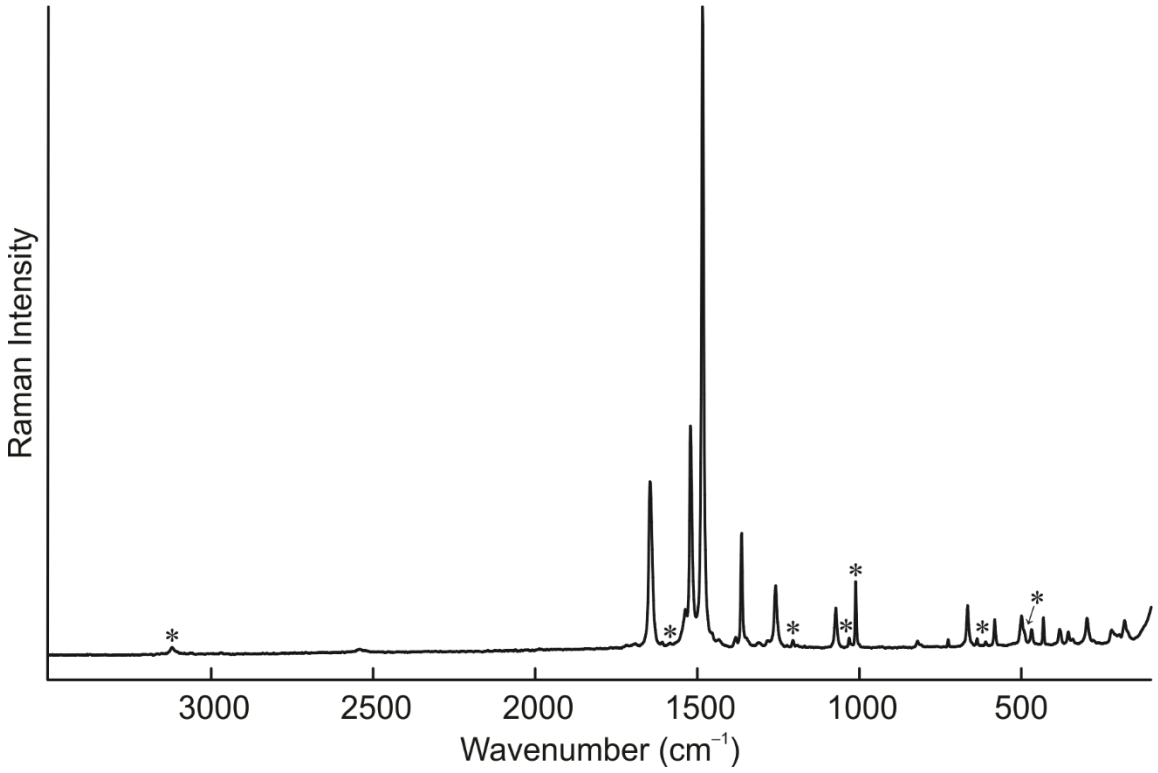

Figure 4.6. Raman spectrum of solid $[C_5H_5NH][W_2(NC_6F_5)_2F_9]$, recorded at ambient temperature. Asterisks (*) denote $[C_5H_5NH]^+$ bands.

Table 4.3. Selected Vibrational Frequencies (cm^{-1}) for $[W(NC_6F_5)F_5]^-$

exptl[a]		calcd[d]	Assignment (C_{2v})[e]
$[C_5H_5NH]^+$ salt[b]	$[N(CH_3)_4]^+$ salt[c]		
1362(17)	1353(14)	1358(37)[91]	A_1, ν(WN) − ν(NC) + $\nu(C_oF_o)$ + $\nu(C_pF_p)$
1256(12)	1255(12)	1240(38)[117]	A_1, ν(WN) − ν(NC) + $\nu(C_mF_m)$ − (C_pF_p)
1069(7)	1066(8)	1063(45)[290]	A_1, ν(WN) − $\nu(C_oF_o)$ + $\nu(C_pF_p)$
810(2)	808(2)	801(13)[<1]	A_1, ν(WN) + ν(NC) − $\nu(C_mF_m)$
661(6)	650(5)	647(19)[287]	A_1, $\nu_s(WF_5)$
		607(<1)[269]	B_2, $\nu_{as}(WF_5)$ (2 + 3 – 4 − 5)
		606(<1)[247]	B_1, $\nu_{as}(WF_5)$ (2 – 3 – 4 + 5)
585(4)	581(4)	579(19)[10]	A_1, ν(WN) + $\delta(C_oC_iC_o)$ + $\delta_s(C_oC_mC_p)$
		575(3)[0]	A_2, $\nu_{as}(WF_5)$ (2 – 3 + 4 – 5)
		548(<1)[165]	A_1, $\nu(WF_{ax})$
501(4)	496(6)	497(35)[8]	A_1, ν(WN) − $\delta(C_oC_iC_o)$−$\delta(C_mC_pC_m)$
356(2)	355(2)	353(7)[9]	A_1, ν(WN) + $\delta_s(C_iC_oF_o)$
298(3)	299(3)	294(6)[41]	A_1, $\delta_s(WF_{eq})$

[a]Normalised Raman intensities are given in parentheses. [b]Cation bands are observed at 3115(4), 3100(4), 3060(2), 1591(1), 1205(5), 1026(6), 1011(13), 639(4), 610(3), 504(4), and 96(11) cm^{-1}. [c]Cation bands are observed at 3044(3), 3033(2), 2999(2), 2970(2), 2934(3), 2831(2), 1176(1), 950(4), 754(5), and 458(2) cm^{-1}. [d]Calculated at the B3LYP/sVTZ level of theory. Absolute Raman intensities (in $Å^4\ u^{-1}$) are given in parentheses and absolute IR intensities (in km mol^{-1}) are given in square brackets. [e]Symbols and abbreviations denote stretch (ν), bend (δ), symmetric (s), antisymmetric (as), axial (ax), and equatorial (eq). Atom labels for fluorido ligands are as in Figure 4.1a.

Table 4.4. Selected Vibrational Frequencies (cm^{-1}) for $[W_2(NC_6F_5)_2F_9]^-$

exptl[a]	calcd[b]	Assignment (D_2)[c]
1364(18)	1379(167)[0]	A, ν(WN) − ν(NC) + ν(C_oF_o) + ν(C_pF_p) (s)
1259(9)	1266(126)[0]	A, ν(WN) − ν(NC) + ν(C_mF_m) − (C_pF_p) (s)
1074(6)	1083(104)[0]	A, ν(WN) − ν(C_oF_o) + ν(C_pF_p) (s)
821(2)	824(31)[0]	A, ν(WN) + ν(NC) − ν(C_mF_m) (s)
667(7)	665(45)[0]	A, $\nu_s(WF_5)$ (s)
	646(0)[420]	B_3, $\nu_{as}(WF_5)$ (2 + 3 – 4 − 5) (s)
	629(<1)[<1]	B_3, $\nu_{as}(WF_5)$ (2 – 3 – 4 + 5) (s)
	598(3)[0]	A, $\nu_{as}(WF_5)$ (2 – 3 + 4 – 5) (s)
584(5)	582(34)[0]	A, ν(WN) + δ($C_oC_iC_o$) + δ_s($C_oC_mC_p$) (s)
501(6)	502(67)[0]	A, ν(WN) − δ($C_oC_iC_o$) − δ($C_mC_pC_m$) (s)
	464(<0.1)[576]	B_1, $\nu_{as}(F_{ax}W_2)$
299(6)	296(17)[0]	A, $\delta_s(WF_{eq})$ (s)

[a]Normalised Raman intensities are given in parentheses. Cation bands are observed at 3120(2), 1586(1), 1206(2), 1033(2), 1012(10), 638(2), 611(1), and 494(4), and 98(7) cm^{-1}. [b]Calculated at the B3LYP/sVTZ level of theory. Absolute Raman intensities (in $Å^4\ u^{-1}$) are given in parentheses and absolute IR intensities (in km mol^{-1}) are given in square brackets. [c]Symbols and abbreviations denote stretch (ν), bend (δ), symmetric (s), antisymmetric (as), axial (ax), and equatorial (eq). Atom labels for fluorido ligands are as in Figure 4.2a. Mode descriptions are based on the vibration of one $W(NC_6F_5)F_5$ moiety, and the mode is then described as a symmetric (s) or antisymmetric (as) combination of the vibrations of the two moieties.

thereby increasing the covalent character of adjacent bonds. As expected, the predicted frequency for this mode (647 cm^{-1}) agrees more closely with the $[N(CH_3)_4]^+$ salt. Calculation of the vibrational frequencies reveals extensive coupling of the W≡N stretching vibrations with vibrations of the C_6F_5 group, and as there is no characteristic ν(WN) mode, the nature of the W≡N bond cannot be elucidated easily by consideration of the relative frequencies.

The Raman spectrum of $[C_5H_5NH][W_2(NC_6F_5)_2F_9]$ (Figure 4.6) is highly similar to those of the $[W(NC_6F_5)F_5]^-$ salts in terms of the frequencies and relative intensities of the anion bands. The experimental and calculated Raman frequencies are in excellent agreement; the decrease from calculated D_2 symmetry to experimentally observed C_2 symmetry likely does not significantly affect mode descriptions, as alteration of the W−F_{ax}−W angle in the $[W_2S_2F_9]^-$ anion only affected low-frequency modes involving the fluorine bridge.[4] Due to the weak nature of the fluorine bridge, splittings due to vibrational coupling of the halves are typically predicted to be negligible and cannot be discerned experimentally. Coordination of the axial fluorido ligand to two tungsten centres causes an increase in the covalent character of the adjacent bonds, and the $\nu_s(WF_5)$ mode (667 cm^{-1}) is subsequently higher in frequency than in either $[W(NC_6F_5)F_5]^-$ salt. The W≡N stretching vibrations of the dinuclear anion are also extensively coupled to vibrations of the C_6F_5 group in manners identical to those observed for the mononuclear anion.

4.2.4. Fluorine-19 NMR Spectroscopy

The nature of the $[W(NC_6F_5)F_5]^-$ and $[W_2(NC_6F_5)_2F_9]^-$ anions in solution has been investigated by ^{19}F NMR spectroscopy in CH_3CN at ambient temperature. Spectroscopic data for the fluorine-on-tungsten regions of $[C_5H_5NH][W(NC_6F_5)F_5]$, $[N(CH_3)_4][W(NC_6F_5)F_5]$, and $[C_5H_5NH][W_2(NC_6F_5)_2F_9]$, along with an impurity of $W(NC_6F_5)F_4(NCCH_3)$ that was observed in a solution of $[C_5H_5NH][W_2(NC_6F_5)_2F_9]$, are given in Table 4.5.

In the ^{19}F NMR spectra of the $[W(NC_6F_5)F_5]^-$ salts, the WNF_5 moieties give rise to AX_4 spin systems with ^{183}W satellites (Figures 4.7a and b). Furthermore, the F_{ax} multiplets, expected to be quintets, are broadened by partially quadrupole-collapsed coupling to ^{14}N (I = 1, 99.636% natural abundance) at ambient temperature. Resolution enhancement of the spectra allowed for the $^2J(^{19}F_{ax}–^{14}N)$ coupling constants to be ascertained. In the $[C_5H_5NH]^+$ salt, the outer transitions of the equal-intensity triplets were broadened to the extent that the $^2J(^{19}F_{ax}–^{14}N)$ coupling constant could only be estimated in the range of 37−40 Hz and the ^{183}W satellites could not be observed. However, in the $[N(CH_3)_4]^+$ salt, splittings due to $^2J(^{19}F_{ax}–^{14}N)$ and $^1J(^{183}W–^{19}F_{ax})$ coupling could be resolved (Figure 4.8). The observation of $^2J(^{19}F_{ax}–^{14}N)$ coupling corroborates the approximately linear F−W≡N−C skeleton that is observed crystallographically, which results in a small apparent electric-field gradient around the nitrogen atom. Geminal $^2J(^{19}F_{ax}–^{14}N)$ coupling constants of similar magnitude have been observed previously in $[CH_3NH_3][W(NCH_3)F_5]$ (40 Hz) and $[C_2H_5NH_3][W(NC_2H_5)F_5]$ (36 Hz).[11,12]

Table 4.5. Fluorine-19 NMR Spectroscopic Data for the Fluorine-on-Tungsten Resonances of $[W(NC_6F_5)F_5]^-$, $[W_2(NC_6F_5)_2F_9]^-$, and $W(NC_6F_5)F_4(NCCH_3)$[a]

	$\delta(^{19}F)$ (ppm)[b]	*J* (Hz)		
		$^2J(^{19}F–^{19}F)$	$^2J(^{19}F–^{14}N)$	$^1J(^{19}F–^{183}W)$
$[C_5H_5NH][W(NC_6F_5)F_5]$	51.49 (F_{eq}, d)	64.9		42.2
	−61.02 (F_{ax}, m)		37−40	n.o.
$[N(CH_3)_4][W(NC_6F_5)F_5]$	50.93 (F_{eq}, d)	65.1		42.8
	−44.96 (F_{ax}, m)		47.1	68.3
$[C_5H_5NH][W_2(NC_6F_5)_2F_9]$	61.66 (F_{eq}, d)	64.2		41.2
	−110.92 (F_{ax}, n)			n.o.
$W(NC_6F_5)F_4(NCCH_3)$	61.50 (s)			38.1

[a]Recorded in CH_3CN at 20 °C. [b]Abbreviations denote singlet (s), doublet (d), nonet (n), multiplet (m), axial (ax), and equatorial (eq).

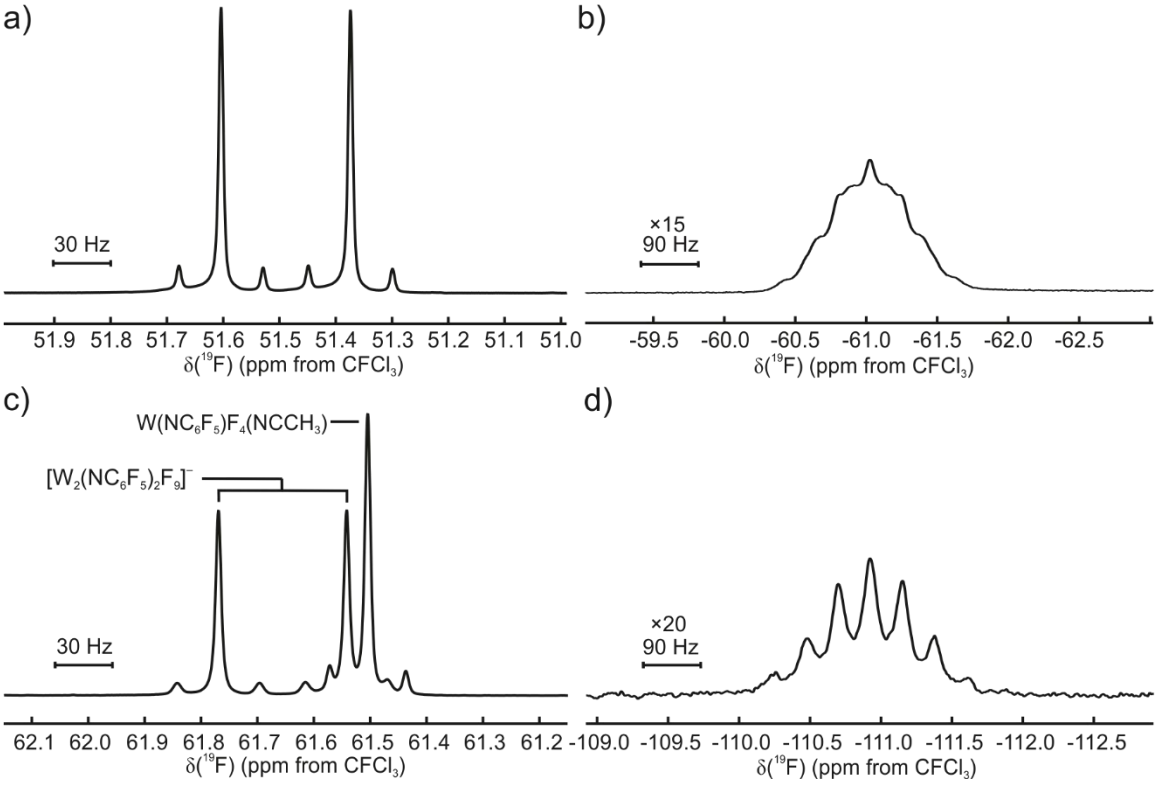

Figure 4.7. Fluorine-19 NMR spectra of the $[W(NC_6F_5)F_5]^-$ and $[W_2(NC_6F_5)_2F_9]^-$ anions, recorded in CH_3CN at 20 °C: a) F_{eq} doublet in $[C_5H_5NH][W(NC_6F_5)F_5]$; b) F_{ax} multiplet in $[C_5H_5NH][W(NC_6F_5)F_5]$; c) F_{eq} doublet in $[C_5H_5NH][W_2(NC_6F_5)_2F_9]$, including the $W(NC_6F_5)F_4(NCCH_3)$ impurity; d) F_{ax} nonet in $[C_5H_5NH][W_2(NC_6F_5)_2F_9]$.

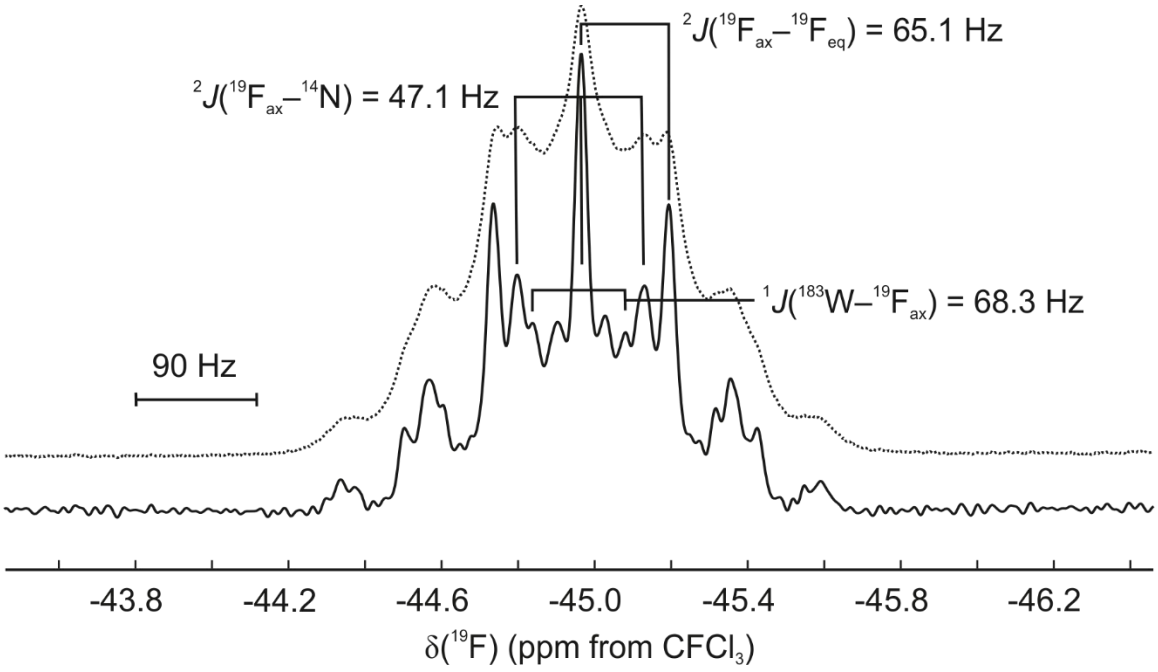

Figure 4.8. Resolution-enhanced (exponential multiplication = −20 Hz; Gaussian multiplication = 10 Hz; solid trace) and unenhanced (dotted trace) ^{19}F NMR spectra of the F_{ax} multiplet in $[N(CH_3)_4][W(NC_6F_5)F_5]$, recorded in CH_3CN at 20 °C.

The contribution of $^{2}J(^{19}F_{ax}–^{14}N)$ coupling to the F_{ax} multiplet, which is poorly resolved at ambient temperature, was confirmed experimentally by variable-temperature NMR spectroscopy, where the expected collapse of the $^{2}J(^{19}F_{ax}–^{14}N)$ coupling at decreased temperatures was observed due to hastened quadrupolar relaxation of the ^{14}N nucleus (Figure 4.9). The behaviour of the $[C_5H_5NH]^+$ and $[N(CH_3)_4]^+$ salts are effectively identical in this regard. It was observed in both cases that the chemical shift of the F_{ax} resonance is linearly temperature-dependent, $\Delta\delta(^{19}F_{ax})$ = 0.0375T – 72.33 (R^2 = 0.994) for the $[C_5H_5NH]^+$ salt and 0.0335T – 54.85 (R^2 = 0.984) for the $[N(CH_3)_4]^+$ salt, where T is the temperature in kelvin. The inferior fit of the data for the latter to a linear equation is likely due to crystallisation of a small amount of the solute at −40 °C subtly influencing the chemical shift at that temperature, as crystals were observed upon removal of the sample from the spectrometer.

In the $[N(CH_3)_4]^+$ salt, the $^{1}J(^{183}W–^{19}F_{ax})$ coupling constant (68.3 Hz) is significantly higher in magnitude than the $^{1}J(^{183}W–^{19}F_{eq})$ coupling constant (42.2 Hz), despite the more ionic nature of the W−F_{ax} bond. While this phenomenon is counterintuitive based on the relative W−F bond strengths, it was observed previously for the $[WSF_5]^-$ anion and can be attributed to varying contributions from multiple scalar coupling mechanisms of different signs.[4]

The ^{19}F chemical shifts and coupling constants for the F_{eq} doublet are in excellent agreement with those reported previously for the $[C_6F_5NH_3]^+$ salt ($\delta(^{19}F_{eq})$ = 52.5 ppm, $^{2}J(^{19}F_{eq}–^{19}F_{ax})$ = 64.7 Hz, $^{1}J(^{183}W–^{19}F_{eq})$ = 41.8 Hz).[1] These doublets are much higher in chemical shift than the corresponding F_{ax} multiplets due to a strongly shielding *trans* influence from the imido ligand. The chemical shift for the F_{ax} multiplet appears lower for

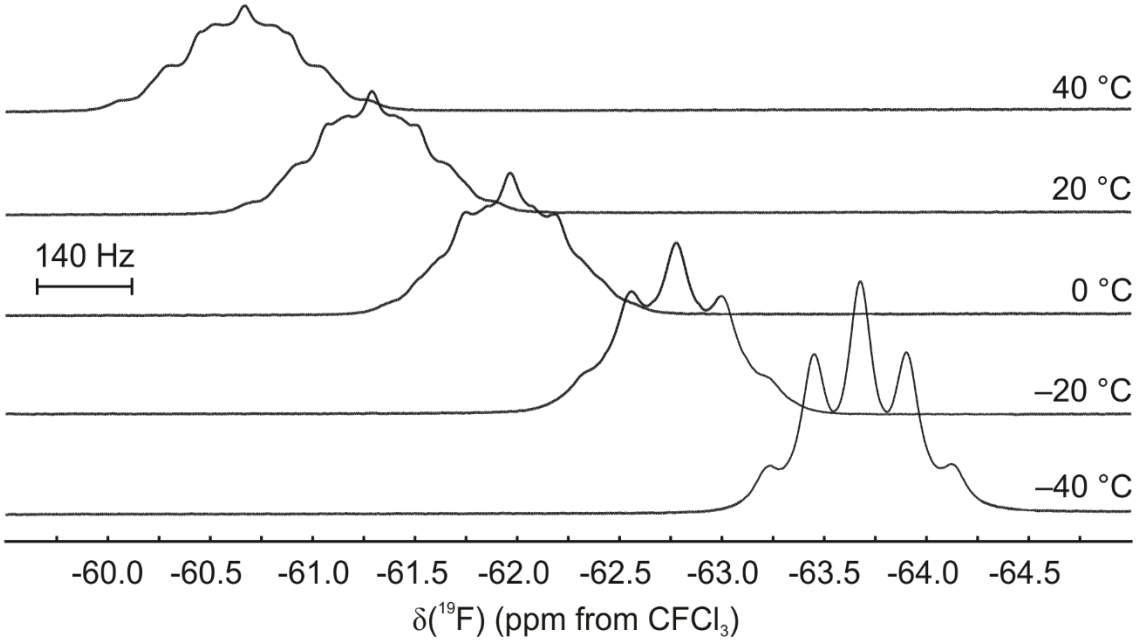

Figure 4.9. Fluorine-19 NMR spectra of the F_{ax} multiplet in $[C_5H_5NH][W(NC_6F_5)F_5]$, recorded in CH_3CN at various temperatures between –40 and 40 °C.

the $[C_5H_5NH]^+$ salt (−61.02 ppm) than the $[N(CH_3)_4]^+$ salt (−44.96 ppm), suggesting that the hydrogen bond in the $[C_5H_5NH]^+$ salt persists in solution. The F_{ax} resonance was observed at −63 ppm for the $[C_6F_5NH_3]^+$ salt,[1] suggesting the presence of a similar hydrogen bond there as well. The F_{eq} and F_{ax} resonances for $[W(NC_6F_5)F_5]^-$ are found to be considerably higher in chemical shift than those for $[W(NCH_3)F_5]^-$ ($\delta(^{19}F_{eq})$ = 28.0, $\delta(^{19}F_{ax})$ = −101.5 ppm), $[W(NC_2H_5)F_5]^-$ ($\delta(^{19}F_{eq})$ = 27.6, $\delta(^{19}F_{ax})$ = −99.5 ppm), and $[W(NC_4H_9)F_5]^-$ ($\delta(^{19}F_{eq})$ = 28.7, $\delta(^{19}F_{ax})$ = −101 ppm).[11,12] This illustrates the electron-withdrawing nature of the C_6F_5 group, which deshields the nuclei and apparently weakens the trans influence of the imido ligand.

In the ^{19}F NMR spectrum of $[C_5H_5NH][W_2(NC_6F_5)_2F_9]$, the $W_2N_2F_9$ moiety gives rise to an AX_8 spin system with ^{183}W satellites being observed for the F_{eq} doublet (Figure 4.7c), in excellent agreement with the ^{19}F NMR spectrum of the $[C_6F_5NH_3]^+$ salt ($\delta(^{19}F_{eq})$ = 61.9, $\delta(^{19}F_{ax})$ = −110 ppm; $^2J(^{19}F_{eq}–^{19}F_{ax})$ = 64.7, $^1J(^{183}W–^{19}F_{eq})$ = 39 Hz).[1] The F_{ax} nonet is broadened to the extent that the outer transitions are not observed, likely due to partially quadrupole-collapsed coupling to the two ^{14}N nuclei (Figure 4.7d). The $^1J(^{183}W–^{19}F_{ax})$ and/or $^2J(^{19}F_{ax}–^{14}N)$ coupling constants could not be extracted by resolution enhancement or variable-temperature experiments. The fluorido ligands in $W(NC_6F_5)F_4(NCCH_3)$, which is a product of solvolysis of $[W_2(NC_6F_5)_2F_9]^-$ by CH_3CN, were observed as a singlet with ^{183}W satellites that overlapped partially with the F_{eq} doublet of the dinuclear anion (Figure 4.7c).

The C_6F_5 groups of these complexes give rise to the expected AA′MM′X spin systems with ^{13}C satellites (Table 4.6). The $J(^{19}F–^{19}F)$ coupling constants were ascertained via spectral simulation, first for $[C_5H_5NH][W(NC_6F_5)F_5]$ (Figure 4.10), and vary only subtly

Table 4.6. Fluorine-19 NMR Spectroscopic Data for the Fluorine-on-Carbon Resonances of $[W(NC_6F_5)F_5]^-$, $[W_2(NC_6F_5)_2F_9]^-$, and $W(NC_6F_5)F_4(NCCH_3)$[a]

	$\delta(^{19}F)$ (ppm)[b]	J (Hz)[c]			
		$^3J(^{19}F–^{19}F_m)$	$^4J(^{19}F–^{19}F')$	$^5J(^{19}F–^{19}F_m')$	$^1J(^{19}F–^{13}C)$
$[C_5H_5NH][W(NC_6F_5)F_5]$	−148.80 (F_o, m)	21.4	2.8	−6.5	251.2
	−156.73 (F_p, t)	20.4			253.7
	−164.44 (F_m, m)		1.8		249.2
$[N(CH_3)_4][W(NC_6F_5)F_5]$	−149.01 (F_o, m)	21.4	2.6	−6.4	250.4
	−157.50 (F_p, t)	20.4			252.9
	−164.51 (F_m, m)		1.9		248.8
$[C_5H_5NH][W_2(NC_6F_5)_2F_9]$	−147.31 (F_o, m)	21.4	4.2	−6.1	252.7
	−153.39 (F_p, t)	20.4			255.7
	−163.28 (F_m, m)		1.6		256.2
$W(NC_6F_5)F_4(NCCH_3)$	−146.55 (F_o, m)	21.4	2.7	−6.4	n.o.
	−151.28 (F_p, t)	20.4			n.o.
	−162.80 (F_m, m)		2.0		n.o.

[a]Recorded in CH_3CN at 20 °C. [b]Abbreviations denote triplet (t) and multiplet (m). [c]$J(^{19}F–^{19}F)$ coupling constants were determined by spectral simulations using MestreNova.

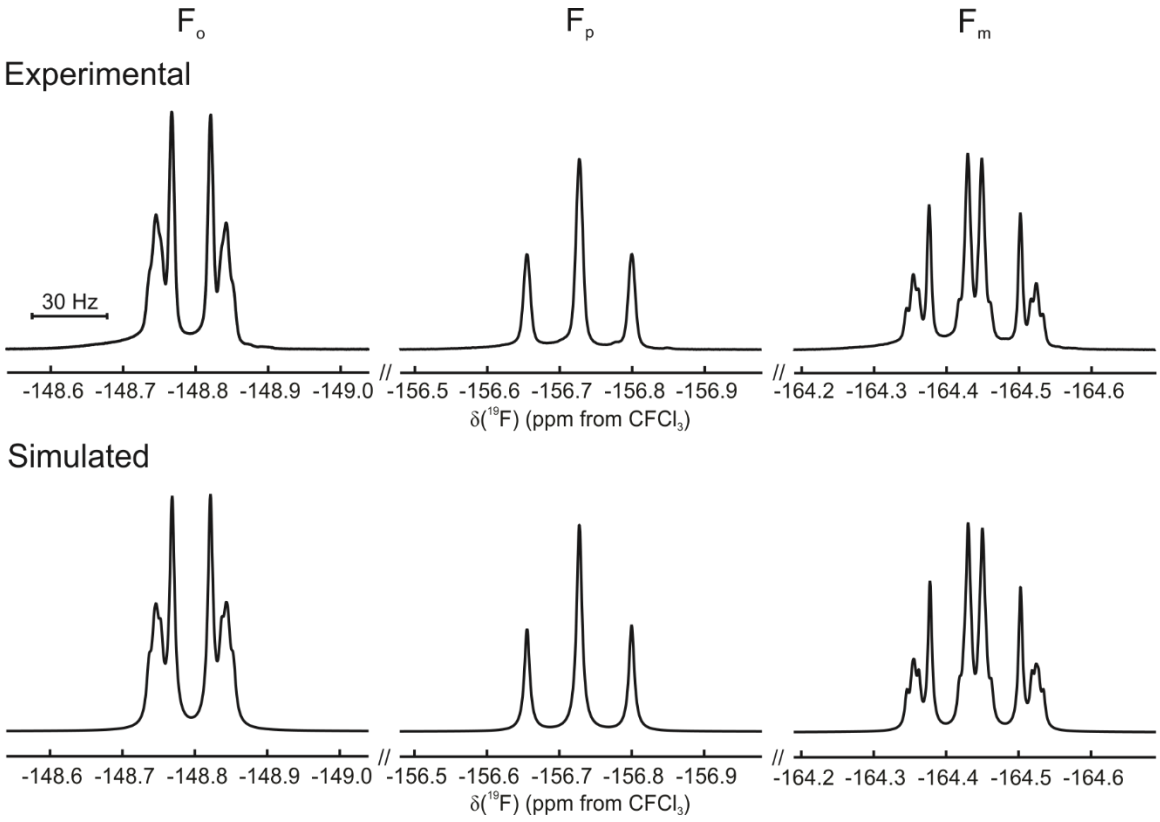

Figure 4.10. Experimental (top) and simulated (bottom) fluorine-on-carbon resonances in the ^{19}F NMR spectrum of $[C_5H_5NH][W(NC_6F_5)F_5]$, recorded in CH_3CN at 20 °C.

between complexes. The magnitudes and signs of the coupling constants agree well with those observed previously for organic compounds containing NC_6F_5 moieties.[13]

4.2.5. Computational Results

4.2.5.1. Optimised Geometries

Selected calculated geometric parameters for $[W(NR)F_5]^-$ (R = H, F, CH_3, CF_3, C_6H_5) are given in Table 4.7. The $[W(NR)F_5]^-$ anions are isostructural (geometric aspects of the R group notwithstanding) resulting in pseudo-octahedral geometries with linear or near-linear W−N−X (X = H, F, C) angles (Figure 4.11). Interestingly, in $[W(NCH_3)F_5]^-$, the CH_3 group adopts an eclipsed conformation relative to the WF_4 moiety, whereas the CF_3 group is staggered in $[W(NCF_3)F_5]^-$. Generally, anions containing fluorinated imido ligands possess shorter W−F bonds, with the exception being that the $W-F_{eq}$ bonds in $[W(NF)F_5]^-$ (1.911 Å) are the second longest in the series, behind only those of $[W(NCH_3)F_5]^-$ (1.914−1.915 Å). There is no obvious division between fluorinated and non-fluorinated imido ligands regarding the W≡N bond length, as this bond length is primarily affected by conjugation with the R group (*vide infra*).

4.2.5.2. Vibrational Frequencies

Selected calculated vibrational frequencies for $[W(NR)F_5]^-$ (R = H, F, CH_3, CF_3, C_6H_5) are given in Table 4.8, and complete vibrational frequencies, with assignments, are provided in the Appendix (Tables B.5–B.9**).** The $[W(NR)F_5]^-$ anions are predicted to exhibit very similar vibrational patterns corresponding to their WNF_5 octahedra; the primary differences manifest in the vibrational coupling between the W≡N stretch and other vibrations. Vibrational coupling is observed in all cases except $[W(NH)F_5]^-$, which exhibits a discrete ν(WN) mode at 967 cm^{-1}. However, the nature of the vibrational coupling

Table 4.7. Selected Calculated Bond Lengths (Å) and Angles (°) of $[W(NR)F_5]^-$ (R = H, F, CH_3, CF_3, C_6H_5)[a]

	R				
	H	**F**	**CH_3**	**CF_3**	**C_6H_5**
W−N	1.764	1.763	1.762	1.793	1.783
W−F_{ax}	1.968	1.935	1.969	1.940	1.955
W−F_{eq}	1.909	1.911	1.914−1.915	1.894	1.906
W−N−R	180.0	180.0	178.7	179.8	180.00
N−W−F_{ax}	180.0	180.0	179.4	179.9	180.00
F_{ax}−W−F_{eq}	84.2	84.4	84.3−89.3	84.7−84.8	84.8

[a]Calculated at the B3LYP/sVTZ level of theory.

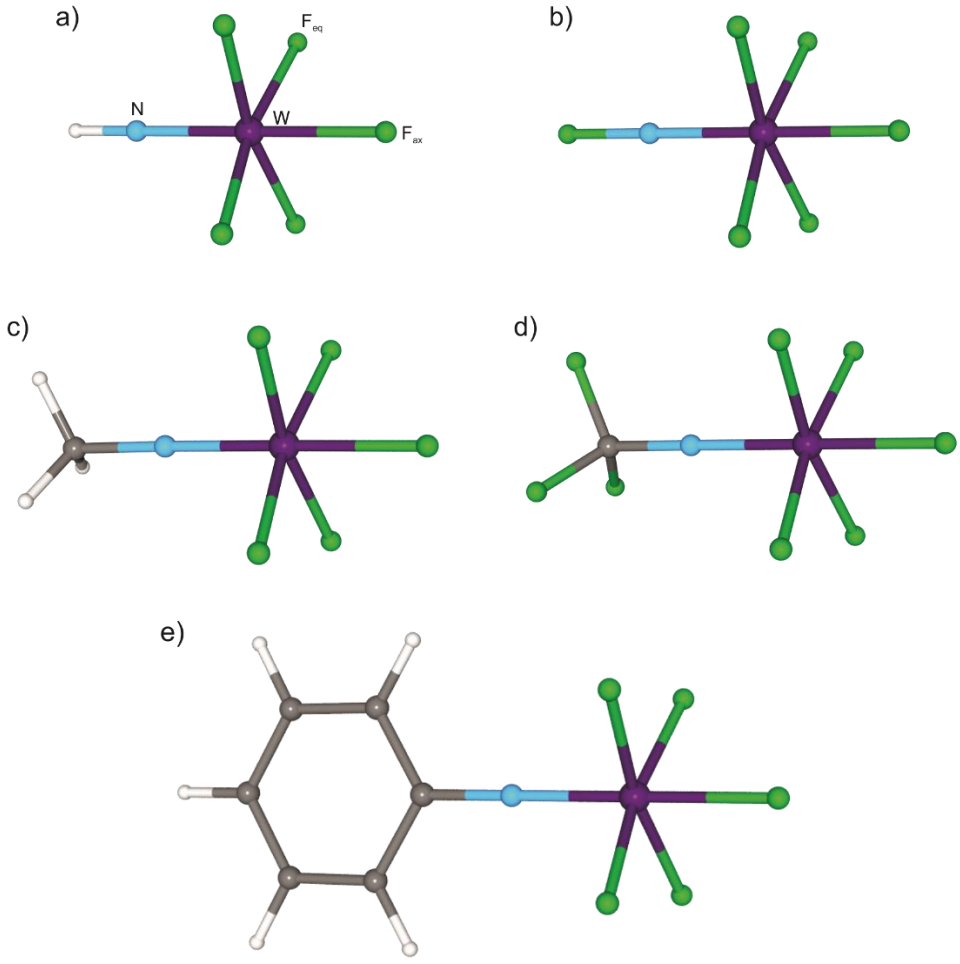

Figure 4.11. Optimised gas-phase geometries (B3LYP/sVTZ) of $[W(NR)F_5]^-$: R = a) H, b) F, c) CH_3, d) CF_3, e) C_6H_5.

Table 4.8. Selected Calculated Vibrational Frequencies of $[W(NR)F_5]^-$ (R = H, F, CH_3, CF_3, C_6H_5)

	calcd[a]	Assignment[b]
$[W(NH)F_5]^-$	967(69)[172]	ν(WN)
	639(11)[93]	$\nu_s(WF_5)$
	518(1)[125]	$\nu(WF_{ax})$
$[W(NF)F_5]^-$	1371(1)[58]	ν(WN) – ν(NF)
	648(24)[64]	$\nu_s(WF_5)$
	552(1)[163]	$\nu(WF_{ax})$
	535(18)[86]	ν(WN) + ν(NF)
$[W(NCH_3)F_5]^-$	1368(219)[257]	ν(WN) – ν(NC) + $\delta_s(CH_3)$
	634(16)[84]	$\nu_s(WF_5)$
	600(17)[83]	ν(WN) + ν(NC)
	518(1)[132]	$\nu(WF_{ax})$
$[W(NCF_3)F_5]^-$	1409(108)[1503]	ν(WN) – ν(NC)
	1059(5)[242]	ν(WN) + ν(NC) − $\delta_s(CF_3)$
	712(23)[4]	ν(WN) + ν(NC) + $\delta_s(CF_3)$
	653(12)[200]	$\nu_s(WF_5)$
	548(1)[138]	$\nu(WF_{ax})$
$[W(NC_6H_5)F_5]^-$	1047(32)[25]	ν(WN) − $\nu_s(C_pC_m)$ + $\nu_s(C_iC_o)$
	1025(56)[32]	ν(WN) + $\delta(C_mC_pC_m)$ − $\delta(C_oC_iC_o)$
	686(30)[6]	ν(WN) − $\delta(C_mC_pC_m)$ − $\delta(C_oC_iC_o)$
	636(8)[273]	$\nu_s(WF_5)$
	533(<1)[169]	$\nu(WF_{ax})$
	231(5)[1]	ν(WN)+ν(NC)+$\delta_s(WF_{eq})$+$\delta(C_oC_iC_o)$

[a]Calculated at the B3LYP/sVTZ level of theory. Absolute Raman intensities (in $Å^4\ u^{-1}$) are given in parentheses and absolute IR intensities (in km mol^{-1}) are given in square brackets. [b]Symbols and abbreviations denote stretch (ν), bend (δ), symmetric (s), axial (ax), and equatorial (eq).

in the anions is different depending on the R group and cannot be described generally. Thus, differences between the W≡N bond strengths in the $[W(NR)F_5]^-$ anions cannot be discerned based on their vibrational frequencies. The $[W(NF)F_5]^-$ anion exhibits antisymmetric and symmetric coupling of the ν(WN) and ν(NF) vibrations at 1371 and 535 cm^{-1}, respectively. The $[W(NCH_3)F_5]^-$ and $[W(NCF_3)F_5]^-$ anions exhibit coupling between the ν(WN), ν(NC) and $\delta_s(CX_3)$ (X = H, F) vibrations. Interestingly, the bending vibration couples only with the higher-energy ν(WN) – ν(NC) vibration in $[W(NCH_3)F_5]^-$, and only with the lower-energy ν(WN) + ν(NC) vibration in $[W(NCF_3)F_5]^-$. In $[W(NC_6H_5)F_5]^-$, the ν(WN) vibration exhibits extensive vibrational coupling with various C−C stretches and ring deformations, as it does in the perfluorinated analogue.

The bands at 1347 and 718 cm^{-1} in the Raman spectrum of $[CH_3NH_3][W(NCH_3)F_5]$ had been assigned tentatively as "ν(CNW)",[12] which should correspond to the ν(WN) – ν(NC) + $\delta_s(CH_3)$ and ν(WN) + ν(NC) modes in the predicted spectrum, respectively. It should be noted that while the calculated frequency for the former mode (1368 cm^{-1}) agrees with the experimental value (1347 cm^{-1}), the latter mode is predicted to be significantly lower in frequency (600 cm^{-1}) than that determined experimentally (718 cm^{-1}). Given the agreement observed between experimental and calculated spectra for the $[W(NC_6F_5)F_5]^-$ salts, this could suggest an incorrect assignment of the lower-frequency ν(CNW) mode in $[CH_3NH_3][W(NCH_3)F_5]$.

The trend in predicted frequencies of the $\nu(WF_{ax})$ mode correlates inversely with the trend in predicted W−F_{ax} bond lengths. For instance, $[W(NF)F_5]^-$ has the shortest W−F_{ax} bond (1.935 Å) and the highest frequency $\nu(WF_{ax})$ mode (552 cm^{-1}), and $[W(NCH_3)F_5]^-$ has the longest bond (1.969 Å) and lowest frequency mode (518 cm^{-1}).

Overall, the series of $\nu(WF_{ax})$ frequencies descends in the order $[W(NF)F_5]^-$ > $[W(NCF_3)F_5]^-$ = $[W(NC_6F_5)F_5]^-$ > $[W(NC_6H_5)F_5]^-$ > $[W(NH)F_5]^-$ = $[W(NCH_3)F_5]^-$. The relative frequencies of the $\nu_s(WF_5)$ mode, however, do not correlate with the W−F_{eq} bond lengths, likely because this mode possesses differing proportions of ν(WN), $\nu_s(WF_{eq})$, and $\nu(WF_{ax})$ character, depending on the anion.

4.2.5.3. Molecular Orbitals

The two highest-occupied molecular orbitals in the $[W(NR)F_5]^-$ anions consist of the $\pi(d_{xz/yz}(W)$-$p_{x/y}(N))$ interactions that comprise the π components of the W≡N bond, along with $\pi^*(d(W)$-$p(F_{eq}))$ and π-antibonding N−R interactions. The energies of the MOs containing these interactions, along with the LUMO energies, are given in Table 4.9. In $[W(NR)F_5]^-$ (R = H, F, CH_3, CF_3), the occupied MOs are degenerate or pseudodegenerate, whereas in $[W(NC_6H_5)F_5]^-$ and $[W(NC_6F_5)F_5]^-$, these MOs are considerably different in energy due to the W≡N π system interacting with the aromatic π system in the HOMOs and the sp^2-hybridised σ system of the rings in the HOMOs − 1 (Figure 4.12).

The LUMOs of the anions are dominated by π-antibonding interactions. In $[W(NR)F_5]^-$ (R = H, F, CH_3, CF_3), the LUMO consists of out-of-phase W−F_{eq} interactions, whereas in $[W(NC_6H_5)F_5]^-$ and $[W(NC_6F_5)F_5]^-$, the LUMO consists of out-of-phase W−F_{eq}, W−N and C−C interactions (Figure 4.12). The HOMO/LUMO gap is smaller in $[W(NC_6H_5)F_5]^-$ and $[W(NC_6F_5)F_5]^-$ than in their non-aromatic counterparts as a result of the π-antibonding interactions involving the aromatic rings in the HOMO and LUMO. The 4.44-eV HOMO/LUMO gap predicted for $[W(NC_6F_5)F_5]^-$ corresponds to a 280-nm absorption, indicating that the difference in energies is slightly overestimated based on the observed yellow colour of the $[W(NC_6F_5)F_5]^-$ salts.

Table 4.9. Selected MO Energies (eV) and MO Gaps (ΔE, eV) of $[W(NR)F_5]^-$ (R = H, F, CH_3, CF_3, C_6H_5, C_6F_5) and $[W_2(NC_6F_5)_2F_9]^-$[a]

	E_{MO}			ΔE	
	LUMO	**HOMO**	**HOMO − 1**	**HOMO /HOMO − 1**	**HOMO /LUMO**
$[W(NH)F_5]^-$	1.70	–3.90	-		5.60
$[W(NF)F_5]^-$	1.45	–3.92	-		5.38
$[W(NCH_3)F_5]^-$	1.80	–3.50	–3.50	0	5.29
$[W(NCF_3)F_5]^-$	0.82	–4.81	–3.50	0	5.63
$[W(NC_6H_5)F_5]^-$	1.35	–3.10	−4.00	0.90	4.45
$[W(NC_6F_5)F_5]^-$	0.80	–3.64	−4.64	1.00	4.44
$[W_2(NC_6F_5)_2F_9]^-$[b]	–0.19	–4.72	–4.72	0	4.53

[a]Calculated at the B3LYP/sVTZ level of theory, unless otherwise noted. [b]Calculated at the B3LYP/VTZ level of theory.

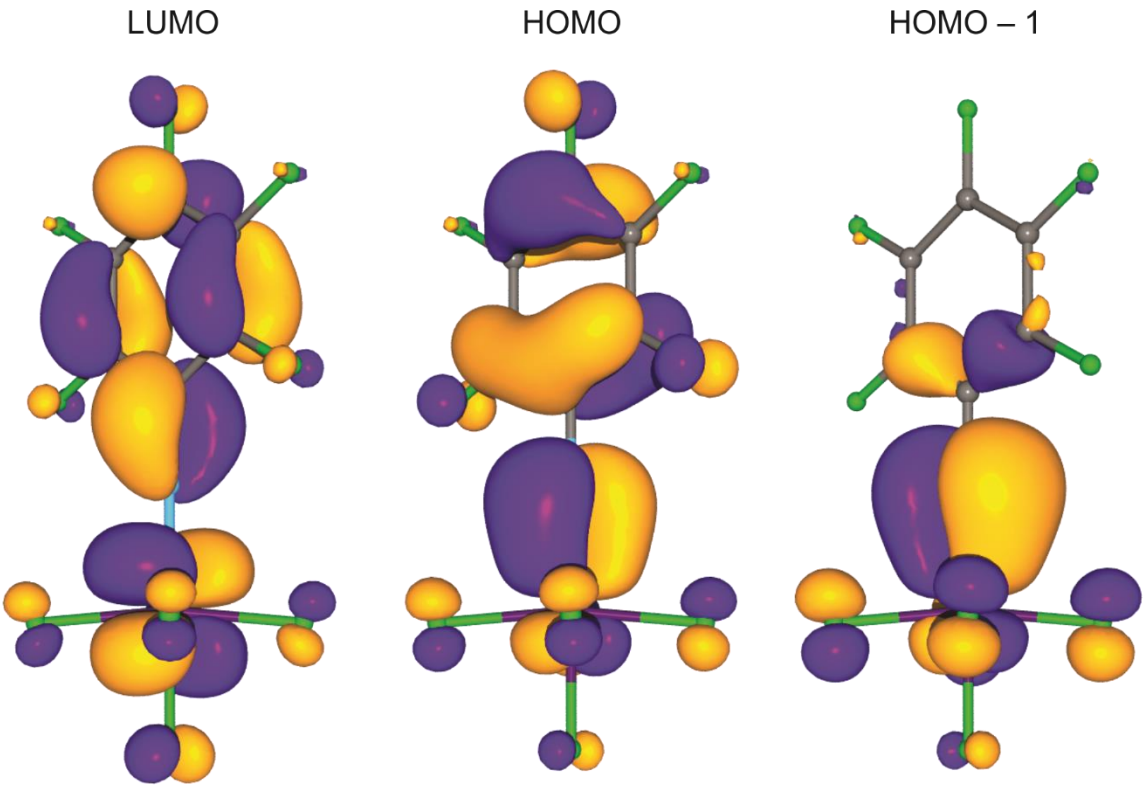

Figure 4.12. Selected MOs of $[W(NC_6F_5)F_5]^-$. Isosurface values are drawn at 0.04 e $Å^{-3}$.

Meanwhile, the HOMO and HOMO − 1 of $[W_2(NC_6F_5)_2F_9]^-$ are pseudo-degenerate and analogous to the HOMO of $[W(NC_6F_5)F_5]^-$, whereas the HOMO − 4 and HOMO − 5 are analogous to the HOMO − 1 of the mononuclear anion; the LUMOs of the anions are comparable. The HOMO/HOMO − 4 gap is slightly higher in energy than the HOMO/HOMO − 1 gap in $[W(NC_6F_5)F_5]^-$ (1.28 vs. 1.00 eV), and the HOMO/LUMO gaps are predictably similar in energy (4.44 vs. 4.53 eV).

4.2.5.4. Natural-Bond-Orbital Analyses

The NBO analyses of $[W(NR)F_5]^-$ and $[W_2(NC_6F_5)_2F_9]^-$ reveal the effects of the R group on the electron density at the tungsten centres, as well as the W≡N and W−F bonds. Natural-population-analysis charges and Wiberg valences are given in Table 4.10. Wiberg bond indices are given in Table 4.11. Selected donor-acceptor interaction energies as per the NBO second-order perturbation analyses are given in Tables 4.12–4.17.

Generally, the WBIs of the W≡N bonds are more than twice those of the $W-F_{eq}$ bonds, corroborating the experimental observation of triple-bond character in imidotungsten(VI) species herein and in previous studies.[5,14] In fact, the WBI of the W≡N bond in $[W(NH)F_5]^-$ (1.90) is almost exactly triple that of the $W-F_{eq}$ bonds (0.64). Multiple resonance structures (Figure 4.13) can be invoked to describe the bonding in the W≡N−R

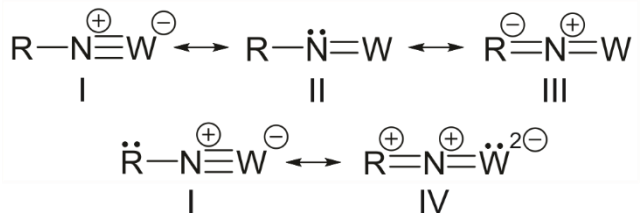

Figure 4.13. Resonance structures contributing to bonding in the W≡N−R moiety of the $[W(NR)F_5]^-$ (R = H, F, CH_3, CF_3, C_6H_5, C_6F_5) and $[W_2(NC_6F_5)_2F_9]^-$ anions.

Table 4.10. Natural-Population-Analysis Charges and Wiberg Valences[a] of $[W(NR)F_5]^-$ (R = H, F, CH_3, CF_3, C_6H_5, C_6F_5) and $[W_2(NC_6F_5)_2F_9]^{-b}$

	$[W(NH)F_5]^-$	**$[W(NF)F_5]^-$**	**$[W(NCH_3)F_5]^-$**	**$[W(NCF_3)F_5]^-$**	**$[W(NC_6H_5)F_5]^-$**	**$[W(NC_6F_5)F_5]^-$**	**$[W_2(NC_6F_5)_2F_9]^{-c}$**
W	+2.39 [4.93]	+2.31 [4.96]	+2.38 [4.93]	+2.47 [4.91]	+2.41 [4.92]	+2.45 [4.92]	+2.36 [5.00]
F_{ax}	–0.63 [0.69]	–0.61 [0.75]	–0.64 [0.69]	–0.60 [0.76]	–0.62 [0.72]	–0.60 [0.75]	–0.61 [0.74]
F_{eq}	–0.57 [0.80]	–0.57 [0.80]	–0.57 [0.79]	–0.54 [0.85]	–0.56 [0.81]	–0.55 [0.84]	–0.52 [0.89]
N	–0.85 [3.13]	–0.21 [3.15]	–0.61 [3.30]	–0.74 [3.18]	–0.65 [3.30]	–0.67 [3.26]	–0.55 [3.34]
X_N	+0.36 [0.88]	–0.21 [1.12]					
C_i			–0.40 [3.88]	+1.11 [3.72]	+0.25 [3.98]	+0.13 [3.99]	+0.02 [3.86]
C_o					−0.24 [3.99]	+0.32 [3.87]	+0.38 [3.86]
C_m					−0.21 [3.97]	+0.27 [3.85]	+0.28 [3.86]
C_p					−0.25 [3.97]	+0.27 [3.85]	+0.29 [4.00]
X_i			+0.19 [0.97]	–0.36 [0.99]			
X_o					+0.21 [0.97]	–0.31 [1.06]	–0.30 [1.07]
X_m					+0.19 [0.97]	–0.32 [1.04]	–0.31 [1.05]
X_p					+0.19 [0.97]	–0.32 [1.04]	–0.30 [1.06]

[a]Given in square brackets. [b]Calculated at the B3LYP/sVTZ level of theory, unless otherwise noted. X = H, F. [c]Calculated at the B3LYP/VTZ level of theory.

Table 4.11. Wiberg Bond Indices of $[W(NR)F_5]^-$ (R = H, F, CH_3, CF_3, C_6H_5, C_6F_5) and $[W_2(NC_6F_5)_2F_9]^{-a}$

	$[W(NH)F_5]^-$	**$[W(NF)F_5]^-$**	**$[W(NCH_3)F_5]^-$**	**$[W(NCF_3)F_5]^-$**	**$[W(NC_6H_5)F_5]^-$**	**$[W(NC_6F_5)F_5]^-$**	**$[W_2(NC_6F_5)_2F_9]^{-b}$**
W−N	1.90	1.81	1.85	1.61	1.69	1.59	1.76
$W-F_{ax}$	0.48	0.51	0.47	0.54	0.50	0.53	0.27
$W-F_{eq}$	0.64	0.63	0.63	0.67	0.64	0.66	0.70
$N-X_N$	0.86	0.97					
$N-C_i$			1.08	1.14	1.19	1.22	1.19
C_i-C_o					1.32	1.28	1.29
C_o-C_m					1.47	1.38	1.37
C_m-C_p					1.42	1.34	1.34
C_i-X_i			0.93	0.85			
C_o-X_o					0.92	0.92	0.93
C_m-X_m					0.93	0.91	0.92
C_p-X_p					0.93	0.91	0.92

[a]Calculated at the B3LYP/sVTZ level of theory, unless otherwise noted. X = H, F. [b]Calculated at the B3LYP/VTZ level of theory.

Table 4.12. Energies ($E^{(2)}$, kJ mol^{-1}) of Interactions Between π(WN) and *p*(F_N) NBOs in $[W(NF)F_5]^{-a}$

	π(WN)→R*	**R→π*(WN)**
$p(F_N)_1 \rightarrow \pi^*(WN)_1$		41.25
$p(F_N)_1 \rightarrow \pi^*(WN)_2$		15.48
$p(F_N)_2 \rightarrow \pi^*(WN)_1$		18.03
$p(F_N)_2 \rightarrow \pi^*(WN)_2$		35.31
Σ		110.08

[a]Calculated at the B3LYP/sVTZ level of theory.

Table 4.13. Energies ($E^{(2)}$, kJ mol^{-1}) of Interactions Between π(WN) and *σ*(CH) NBOs in $[W(NCH_3)F_5]^{-a}$

	π(WN)→R*	**R→π*(WN)**
$\pi(WN)_1 \rightarrow \sigma^*(CH)_1$	7.20	
$\pi(WN)_1 \rightarrow \sigma^*(CH)_2$	7.15	
$\pi(WN)_1 \rightarrow \sigma^*(CH)_3$	21.84	
$\pi(WN)_2 \rightarrow \sigma^*(CH)_1$	19.37	
$\pi(WN)_2 \rightarrow \sigma^*(CH)_2$	19.37	
$\sigma(CH)_1 \rightarrow \pi^*(WN)_1$		3.39
$\sigma(CH)_2 \rightarrow \pi^*(WN)_2$		12.76
$\sigma(CH)_1 \rightarrow \pi^*(WN)_1$		3.39
$\sigma(CH)_2 \rightarrow \pi^*(WN)_2$		12.76
$\sigma(CH)_3 \rightarrow \pi^*(WN)_1$		23.05
Σ	74.94	55.35

[a]Calculated at the B3LYP/sVTZ level of theory.

Table 4.14. Energies ($E^{(2)}$, kJ mol^{-1}) of Interactions Between π(WN) and *σ*(CF) NBOs in $[W(NCF_3)F_5]^{-a}$

	π(WN)→R*	**R→π*(WN)**
$\pi(WN)_1 \rightarrow \sigma^*(CF)_1$	47.57	
$\pi(WN)_1 \rightarrow \sigma^*(CF)_2$	53.89	
$\pi(WN)_1 \rightarrow \sigma^*(CF)_3$	15.02	
$\pi(WN)_2 \rightarrow \sigma^*(CF)_1$	15.23	
$\pi(WN)_2 \rightarrow \sigma^*(CF)_2$	71.25	
$\sigma(CF)_1 \rightarrow \pi^*(WN)_1$		3.89
$\sigma(CF)_2 \rightarrow \pi^*(WN)_1$		3.14
$\sigma(CF)_3 \rightarrow \pi^*(WN)_2$		4.27
Σ	202.97	11.30

[a]Calculated at the B3LYP/sVTZ level of theory.

Table 4.15. Energies ($E^{(2)}$, kJ mol^{-1}) of Interactions Between π(WN) and σ/π(CC) NBOs in $[W(NC_6H_5)F_5]^{-a}$

	π(WN)→R*	**R→π*(WN)**
$\pi(WN)_1 \rightarrow \sigma^*(CC)_1$	21.59	
$\pi(WN)_2 \rightarrow \sigma^*(CC)_2$	21.59	
$\pi(WN)_1 \rightarrow \pi^*(CC)_1$	95.23	
$\sigma(CC)_1 \rightarrow \pi^*(WN)_1$		10.96
$\sigma(CC)_2 \rightarrow \pi^*(WN)_1$		10.96
$\pi(CC)_1 \rightarrow \pi^*(WN)_2$		81.30
Σ	138.41	103.22

[a]Calculated at the B3LYP/sVTZ level of theory.

Table 4.16. Energies ($E^{(2)}$, kJ mol^{-1}) of Interactions Between π(WN) and σ/π(CC) NBOs in $[W(NC_6F_5)F_5]^{-a}$

	π(WN)→R*	**R→π*(WN)**
$\pi(WN)_1 \rightarrow \sigma^*(CC)_1$	28.87	
$\pi(WN)_2 \rightarrow \sigma^*(CC)_2$	28.87	
$\pi(WN)_1 \rightarrow \pi^*(CC)_1$	120.04	
$\sigma(CC)_1 \rightarrow \pi^*(WN)_1$		9.33
$\sigma(CC)_2 \rightarrow \pi^*(WN)_1$		9.33
$\pi(CC)_1 \rightarrow \pi^*(WN)_2$		68.70
Σ	177.78	87.36

[a]Calculated at the B3LYP/sVTZ level of theory.

Table 4.17. Energies ($E^{(2)}$, kJ mol^{-1}) of Interactions Between π(WN) and σ/π(CC) NBOs in $[W_2(NC_6F_5)_2F_9]^{-a}$

	π(WN)→R*	**R→π*(WN)**
$\pi(WN)_1 \rightarrow \sigma^*(CC)_1$	28.12	
$\pi(WN)_2 \rightarrow \sigma^*(CC)_2$	28.12	
$\pi(WN)_1 \rightarrow \pi^*(CC)_1$	105.60	
$\sigma(CC)_1 \rightarrow \pi^*(WN)_1$		9.29
$\sigma(CC)_2 \rightarrow \pi^*(WN)_1$		9.29
$\pi(CC)_1 \rightarrow \pi^*(WN)_2$		74.14
Σ	161.84	92.72

[a]Calculated at the B3LYP/VTZ level of theory.

moiety of $[W(NR)F_5]^-$. For the parent $[W(NH)F_5]^-$ anion, resonance structure I clearly predominates and the W≡N bond possesses essentially triple-bond character, inferred from the relative WBIs and the linearity of the W≡N−H moiety. Resonance structure II, which is the only structure without formal charges, does not seem to play a significant role for any of the studied anions, as they are all predicted to exhibit linear (or near-linear) W≡N−R moieties.

In $[W(NR)F_5]^-$ (R = F, CF_3, C_6H_5, C_6F_5), conjugation is observed, resulting in a decrease in the WBIs of the W≡N bond (1.59−1.81) relative to $[W(NH)F_5]^-$. Conjugation between the W≡N bond and R group can manifest due to π-electron withdrawal (resonance structure III) or donation (resonance structure IV) by the R group, weakening the W≡N bond in both cases. The WBIs of the W≡N bonds and predicted W≡N bond lengths are, as expected, inversely correlated. However, this is only obvious in the anions with the highest degrees of conjugation (R = CF_3, C_6H_5, C_6F_5); the W≡N bond lengths of the remaining anions (R = H, F, CH_3) are practically indistinguishable (1.762−1.764 Å).

In $[W(NCF_3)F_5]^-$ and $[W(NC_6F_5)F_5]^-$, the π-electron-accepting nature of the CF_3 and C_6F_5 groups favors the invocation of resonance structure III as contributing to the decrease in the W≡N bond order. This is corroborated by the higher positive charges on tungsten in these anions (+2.45 to +2.47) than in $[W(NH)F_5]^-$ (+2.39). The NBO second-order perturbation analyses reveal substantial energies for interactions between the W≡N bonds and the π-accepting groups (CF_3: 203 kJ mol^{-1}, C_6F_5: 178 kJ mol^{-1}). The converse is true for $[W(NF)F_5]^-$, which contains the mildly π-electron-donating nitrogen-bound fluorine atom. An interaction energy of 110 kJ mol^{-1} is calculated for π-electron donation from the fluorine atom to the W≡N bond, resulting in a slight decrease in W≡N bond order

and lowering of the positive charge on tungsten (+2.31), consistent with a contribution from resonance structure IV. The C_6H_5 group may act as a π-electron donor and acceptor, and the NBO second-order perturbation analysis returns a slightly larger interaction energy for π-electron withdrawal (138 kJ mol^{-1}) versus donation (103 kJ mol^{-1}). As such, resonance structures III and IV likely contribute to the nature of the W≡N−R moiety of $[W(NC_6H_5)F_5]^-$, explaining why the charge on tungsten (+2.41) is similar to that in $[W(NH)F_5]^-$.

Finally, in $[W_2(NC_6F_5)_2F_9]^-$, the WBI of the W−F_{ax} bond (0.27) is approximately half that predicted for $[W(NC_6F_5)F_5]^-$ (0.53), consistent with the change from a terminal to bridging coordination environment decreasing the covalent character of the W−F_{ax} bonds. The positive charge on each tungsten centre in the dinuclear anion (+2.36) is lower than in the mononuclear anion despite the decreased covalent character of the W−F_{ax} bonds, which is seemingly due to overcompensatory donation from the imido ligand. The WBI of the W≡N bond (1.76) is higher in the dinuclear anion than the mononuclear anion (1.59).

4.3. Conclusions

Convenient routes to $[W(NC_6F_5)F_5]^-$ and $[W_2(NC_6F_5)_2F_9]^-$ salts have been reported, which have been fully characterised in the solid state and in solution. The structural properties of these anions are somewhat dependent on the cation. Cation-anion interactions in $[C_5H_5NH][W(NC_6F_5)F_5]$ affect structure and bonding in the anion, which is observed crystallographically and spectroscopically in the solid state and in solution. Meanwhile, the $[W_2(NC_6F_5)_2F_9]^-$ anion is highly susceptible to conformational distortions in the solid state, as inferred from the variations between the crystal structures of the $[C_5H_5NH]^+$ and previously reported $[C_6F_5NH_3]^+$ salts.[1] The Raman spectra of $[W(NC_6F_5)F_5]^-$ and $[W_2(NC_6F_5)_2F_9]^-$ salts reveal extensive coupling of the W≡N stretching vibration with symmetric vibrations of the C_6F_5 group, and these bands have been assigned unambiguously with the aid of DFT calculations.

To complement the experimental studies, a suite of $[W(NR)F_5]^-$ anions has been studied by DFT methods. The calculations reveal that the R group can have substantial effects on the structural and electronic properties of the anion. The calculated $W-F_{ax}$ bond lengths suggest that the tungsten centre is more electrophilic in anions containing fluorinated R groups than in their hydrogen-containing analogues. The calculated W≡N bond lengths, MOs, and NBO analyses further validate the designation of a triple bond between tungsten and nitrogen, although conjugation between the W≡N bond and the R group can considerably decrease the W≡N bond order.

4.4. References

(1) Fawcett, J.; Griffith, G. A.; Peacock, R. D.; Russell, D. R. *Polyhedron* **1988**, *7* (19), 2015–2022.

(2) Wilson, W. W.; Christe, K. O. *Inorg. Chem.* **1981**, *20* (12), 4139–4143.

(3) Katayama, Y.; Hagiwara, R.; Ito, Y. *J. Fluorine Chem.* **1995**, *74* (1), 89–95.

(4) Nieboer, J.; Haiges, R.; Hillary, W.; Yu, X.; Richardet, T.; Mercier, H. P. A.; Gerken, M. *Inorg. Chem.* **2012**, *51* (11), 6350–6359.

(5) Görge, A.; Dehnicke, K.; Fenske, D. *Z. Naturforsch. B* **1989**, *44* (2), 117–120.

(6) Stenger, H.; Dehnicke, K.; Hiller, W. *Z. Naturforsch. B* **1992**, *47* (7), 1054–1056.

(7) Dietrich, A.; Neumüller, B.; Dehnicke, K. *Z. Anorg. Allg. Chem.* **2000**, *626* (12), 2443–2445.

(8) Cook, D. *Can. J. Chem.* **1961**, *39* (10), 2009–2024.

(9) Foglizzo, R.; Novak, A. *J. Chem. Phys.* **1969**, *50* (12), 5366–5373.

(10) Kabisch, G. *J. Raman Spectrosc.* **1980**, *9* (5), 279–285.

(11) Chambers, O. R.; Rycroft, D. S.; Sharp, D. W. A.; Winfield, J. M. *Inorg. Nucl. Chem. Lett.* **1976**, *12* (7), 559–561.

(12) Chambers, O. R.; Harman, M.; Rycroft, D. S.; Sharp, D. W. A.; Winfield, J. M. *J. Chem. Res.* **1977**, 1849–1876.

(13) Hogben, M. G.; Graham, W. A. G. *J. Am. Chem. Soc.* **1969**, *91* (2), 283–291.

(14) Harman, M.; Sharp, D. W. A.; Winfield, J. M. *Inorg. Nucl. Chem. Lett.* **1974**, *10* (2), 183–185.

Chapter 5 – Lewis-Acid Behaviour of $W(NC_6F_5)F_4$ Towards N-Donor Ligands and Computational Studies of $W(NR)F_4$ (R = H, F, CH_3, CF_3, C_6H_5, C_6F_5)*

5.1. Introduction

As a complement to the potential versatility of $[W(NR)F_5]^-$ and $[W_2(NR)_2F_9]^-$ as weakly coordinating anions, their parent Lewis acid, $W(NR)F_4$, should also demonstrate a high degree of tunability via modulation of the R group. However, $W(NR)F_4$ compounds are rare, as substitutions with primary amines, RNH_2, result in anionic complexes, whereas silazanes, $RN\{Si(CH_3)_3\}_2$, only react appreciably with WF_6 in donor solvents, such as CH_3CN (see section 1.1.4.2). However, $W(NCl)F_4$ was prepared upon fluorination of $WNCl_3$ or $W(NCl)Cl_4$ with F_2.[1] It was found to adopt an ill-defined oligomeric or polymeric structure and react with CH_3CN under formation of monomeric $W(NCl)F_4(NCCH_3)$, the crystal structure of which as acquired, revealing a *trans* orientation of the nitrogen atoms.

In this chapter, the synthesis of a new parent $W(NR)F_4$ Lewis acid, $[W(NC_6F_5)F_4]_x$, as well as its reactions with the nitrogen bases CH_3CN and C_5H_5N to afford $W(NC_6F_5)F_4(NCCH_3)$ and $W(NC_6F_5)F_4(NC_5H_5)_n$ (n = 1, 2), are reported. These species have been conclusively characterised, including crystal structures of $W(NC_6F_5)F_4(NCCH_3)$ and $W(NC_6F_5)F_4(NC_5H_5)$ as well as improved structures of $WOF_4(NC_5H_5)_n$ (n = 1, 2) for the purposes of comparison. Furthermore, DFT (B3LYP) calculations have been performed on monomeric $WChF_4$ (Ch = O, S) and $W(NR)F_4$ (R = H, F, CH_3, CF_3, C_6H_5, C_6F_5) to compare their structural, electronic, and Lewis-acid properties, including FIAs.

* Based on the following publication: Turnbull, D.; Wetmore, S. D.; Gerken, M. *Inorg. Chem.* **2019**, *58* (9), 6363–6375.

5.2. Results and Discussion

5.2.1. Syntheses and Properties of $[W(NC_6F_5)F_4]_x$, $W(NC_6F_5)F_4(NCCH_3)$, and $W(NC_6F_5)F_4(NC_5H_5)_n$ (n = 1, 2)

While the reaction of $[C_5H_5NH][W(NC_6F_5)F_5]$ with aHF resulted in partial F^- abstraction and the formation of $[C_5H_5NH][W_2(NC_6F_5)_2F_9]$ (see Chapter 4), introduction of the stronger F^- acceptor AsF_5 resulted in quantitative F^- abstraction, thereby affording a mixture of $[W(NC_6F_5)F_4]_x$ and $[C_5H_5NH][AsF_6]$ (Eq. 5.1). Neutral $[W(NC_6F_5)F_4]_x$ demonstrated high solubility in $CFCl_3$, resulting in deep orange-to-red solutions, and could subsequently be separated from the insoluble $[C_5H_5NH][AsF_6]$ by decantation. Removal of the $CFCl_3$ under dynamic vacuum yielded $[W(NC_6F_5)F_4]_x$ as transparent, red-orange shards. Despite their crystalline appearance, attempts at X-ray crystallography revealed that they were completely non-diffracting and $[W(NC_6F_5)F_4]_x$ prepared as such exists in an amorphous phase.

$$[C_5H_5NH][W(NC_6F_5)F_5] + AsF_5 \rightarrow 1/x[W(NC_6F_5)F_4]_x + [C_5H_5NH][AsF_6] \quad (5.1)$$

The dissolution of $[W(NC_6F_5)F_4]_x$ in CH_3CN resulted in an orange solution at −40 °C which lightened to yellow upon warming to ambient temperature over several minutes. Removal of CH_3CN under dynamic vacuum yielded $W(NC_6F_5)F_4(NCCH_3)$ as a microcrystalline, yellow solid (Eq. 5.2). The gradual dissipation of the orange colour in solution suggests that the reaction of $[W(NC_6F_5)F_4]_x$ with CH_3CN upon dissolution is slow. The CH_3CN adduct was observed *in situ* by ^{19}F NMR spectroscopy upon solvolysis of $[W_2(NC_6F_5)_2F_9]^-$ by CH_3CN (see section 4.2.4).

$$1/x[W(NC_6F_5)F_4]_x + CH_3CN \xrightarrow{CH_3CN} W(NC_6F_5)F_4(NCCH_3) \quad (5.2)$$

Conversely, $[W(NC_6F_5)F_4]_x$ is only very slightly soluble in C_5H_5N at −35 °C, and dissolution could only be achieved at that temperature by the addition of CH_2Cl_2 as a co-solvent. Upon removal of the volatile materials, yellow crystals of $W(NC_6F_5)F_4(NC_5H_5)$ were obtained, which could alternatively be prepared in quantitative yield by the reaction of $[W(NC_6F_5)F_4]_x$ with a sub-twofold excess of C_5H_5N in CH_3CN (Eq. 5.3). The dissolution of $W(NC_6F_5)F_4(NCCH_3)$ in a large (> 20-fold) excess of C_5H_5N at −35 °C instead resulted in a yellow-orange solution from which $W(NC_6F_5)F_4(NC_5H_5)_2$ promptly precipitated as an off-white powder that could not be dissolved upon warming to ambient temperature (Eq. 5.4). This 1:2 adduct is only very slightly soluble in CH_2Cl_2 and CH_3CN at low temperatures and attempts to warm the suspensions towards ambient temperature to increase solubility resulted in dissociation to the 1:1 adduct (Eq. 5.5). The formation of an isolable 1:2 adduct indicates that $W(NC_6F_5)F_4$ is qualitatively similar in Lewis acidity to WOF_4.[2,3]

$$1/x[W(NC_6F_5)F_4]_x + C_5H_5N \xrightarrow{CH_3CN} W(NC_6F_5)F_4(NC_5H_5) \quad (5.3)$$

$$W(NC_6F_5)F_4(NCCH_3) + 2C_5H_5N \xrightarrow{C_5H_5N} W(NC_6F_5)F_4(NC_5H_5)_2 + CH_3CN \quad (5.4)$$

$$W(NC_6F_5)F_4(NC_5H_5)_2 \rightarrow W(NC_6F_5)F_4(NC_5H_5) + C_5H_5N \quad (5.5)$$

Tungsten (pentafluorophenyl)imide tetrafluoride and its adducts with CH_3CN and C_5H_5N, though thermally stable in the solid state, are highly moisture sensitive; exposure to traces of moisture results in the fast formation of WOF_4 adducts or $[WOF_5]^-$ salts. The $W(NC_6F_5)F_4(NC_5H_5)_2$ adduct was observed to visibly decompose to an orange-brown material under an inert atmosphere of N_2 at ambient temperature over the course of months, likely due to dissociation to the 1:1 adduct. Like $WF_6(NC_5H_5)$ and its derivatives (see

Chapter 3), exposure of $W(NC_6F_5)F_4(NC_5H_5)_n$ (n = 1, 2) to HF results in cleavage of the W–N, yielding $[C_5H_5NH][W(NC_6F_5)F_5]$.

5.2.2. Fluorine-19 NMR Spectroscopy

5.2.2.1. $[W(NC_6F_5)F_4]_x$

The ^{19}F NMR spectrum of $[W(NC_6F_5)F_4]_x$ in CH_2Cl_2 is complex (Figure 5.1), giving rise to a multitude of resonances within three distinct regions that range from 50 to 150 ppm, –60 to –120 ppm, and –140 to –160 ppm with relative integrations of 3:1:5. The first two regions are assigned to terminal (F_t) and bridging (F_b) fluorine-on-tungsten environments, respectively, within oligomeric and/or polymeric $[W(NC_6F_5)F_4]_x$. It appears that, like its oxide and sulfide analogues, $W(NC_6F_5)F_4$ aggregates via fluorine bridges such that the incoming fluorido ligand is exclusively positioned *trans* to the multiply bound ligand. This would explain the difference in chemical shift between the regions, as the imido ligand was observed to exhibit a strongly shielding *trans* influence in $[W(NC_6F_5)F_5]^-$ and $[W_2(NC_6F_5)_2F_9]^-$.[4]

The individual resonances within the fluorine-on-tungsten regions can differ in their relative integrations by several orders of magnitude, indicating that there is no single unique structure of $[W(NC_6F_5)F_4]_x$. Furthermore, though the lowest-frequency region is attributed to the C_6F_5 group, the signals are broad and the expected AA′MM′X spin system is not observed. This is attributed to the presence of large, slowly tumbling aggregate structure(s) in solution causing chemical-shift anisotropies and dipole-dipole interactions not to average out completely.

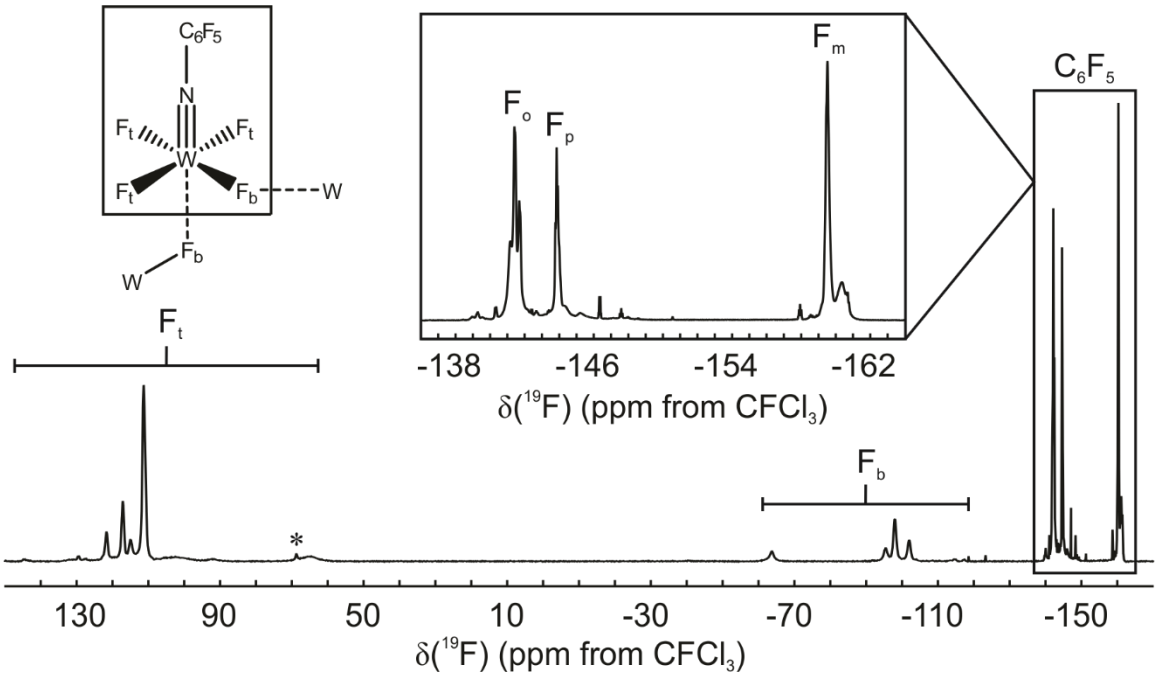

Figure 5.1. Fluorine-19 NMR spectrum of $[W(NC_6F_5)F_4]_x$, recorded in CH_2Cl_2 at 20 °C. Asterisk (*) denotes an impurity of WOF_4.

5.2.2.2. $W(NC_6F_5)F_4(NCCH_3)$ and $W(NC_6F_5)F_4(NC_5H_5)$

The ^{19}F NMR spectra of the 1:1 adducts are simple in comparison to that of $[W(NC_6F_5)F_4]_x$. The fluorine-on-tungsten regions consist of singlets with ^{183}W satellites due to the chemical equivalence of the fluorido ligands (Table 5.1, Figures 5.2 and 5.3), in excellent agreement with the previously reported spectroscopic data for $W(NC_6F_5)F_4(NCCH_3)$.[4] The chemical shifts of these singlets (59.14–61.57 ppm) are slightly lower than those reported for the analogous WOF_4 adducts (62.9–67.4 ppm)[2,5] and significantly lower than the WSF_4 adducts (81.8[6]–85.4[7] ppm). The fluorine-on-carbon environments consist of AA′MM′X spin systems that are highly characteristic of the NC_6F_5 moiety (Table 5.2), with coupling constants similar to those of $[W(NC_6F_5)F_5]^-$ and $[W_2(NC_6F_5)_2F_9]^-$ (see section 4.2.4).

5.2.2.3. $W(NC_6F_5)F_4(NC_5H_5)_2$

Due to the prompt decomposition of $W(NC_6F_5)F_4(NC_5H_5)_2$ in solution at ambient temperature, its ^{19}F NMR spectra were recorded on a saturated CH_2Cl_2 solution at variable temperatures. At –80 °C, an A_2MX spin system is observed, which has been observed previously for $WOF_4(NC_5H_5)_2$ under similar conditions.[3] The observation of the same spin system in both adducts provides evidence that they share a common geometry, which is a pentagonal bipyramid in which the imido ligand occupies an axial position and the pyridyl ligands are in non-adjacent equatorial positions (Figure 5.4). Unlike in $WOF_4(NC_5H_5)_2$, the F_A resonance is a triplet rather than a doublet of doublets, due to the $^2J(F_A–F_M)$ and $^2J(F_A–F_X)$ coupling constants being of coincidentally similar magnitude (53.5 and 57.3 Hz, ΔJ = 3.8 Hz) and the linewidth ($\Delta\nu_{½}$ = 23 Hz) not allowing for resolution of the individual couplings. No coupling to ^{183}W was observed for any of the three resonances. The ^1H and

Table 5.1. Fluorine-19 NMR Spectroscopic Data for the Fluorine-on-Tungsten Resonances of $W(NC_6F_5)F_4(NCCH_3)$ and $W(NC_6F_5)F_4(NC_5H_5)_n$ (n = 1, 2)

	$\delta(^{19}F)$ (ppm)[a]	J (Hz)			
		$^2J(F_A–F_M)$	$^2J(F_A–F_X)$	$^2J(F_M–F_X)$	$^1J(F–^{183}W)$
$W(NC_6F_5)F_4(NCCH_3)$[b]	61.57 (s)				38.3
$W(NC_6F_5)F_4(NC_5H_5)$[b]	59.14 (s)				35.5
$W(NC_6F_5)F_4(NC_5H_5)_2$[c]	–9.15 (F_A, t)	55.5[d]	55.5[d]		
	–26.37 (F_M, dt)	53.5		83.9	
	–48.26 (F_X, dt)		57.3		

[a]Abbreviations denote singlet (s), triplet (t), and doublet of triplets (dt). [b]Recorded in CH_3CN at 20 °C. [c]Recorded in CH_2Cl_2 at –80 °C. [d]Couplings were not resolved in F_A pseudo-triplet.

Table 5.2. Fluorine-19 NMR Spectroscopic Data for the Fluorine-on-Carbon Resonances of $W(NC_6F_5)F_4(NCCH_3)$ and $W(NC_6F_5)F_4(NC_5H_5)_n$ (n = 1, 2)

	$\delta(^{19}F)$ (ppm)[a]	J (Hz)[b]				
		$^3J(^{19}F–^{19}F_m)$	$^4J(^{19}F–^{19}F_p)$	$^4J(^{19}F–^{19}F')$	$^5J(^{19}F–^{19}F_m')$	$^1J(^{19}F–^{13}C)$
$W(NC_6F_5)F_4(NCCH_3)$[c]	–146.59 (F_o, m)	21.4		2.7	–6.4	n.o.[e]
	–151.35 (F_p, t)	20.4				n.o.[e]
	–162.85 (F_m, m)			2.0		n.o.[e]
$W(NC_6F_5)F_4(NC_5H_5)$[c]	–146.69 (F_o, m)	21.4	1.3	4.6	–6.5	253.1
	–152.00 (F_p, t)	20.3				257.2
	–163.19 (F_m, m)			1.4		250.1
$W(NC_6F_5)F_4(NC_5H_5)_2$[d]	–146.07 (F_o, dd)	~23			~6	~260
	–151.93 (F_p, t)	22.2				n.o.
	–162.36 (F_m, td)					n.o.

[a]Abbreviations denote triplet (t), doublet of doublets (dd), triplet of doublets (td), and multiplet (m). [b]$J(^{19}F–^{19}F)$ coupling constants were determined by spectral simulations using MestreNova. [c]Recorded in CH_3CN at 20 °C. [d]Recorded in CH_2Cl_2 at –80 °C. [e]Obscured by traces of NC_6F_5-containing impurities.

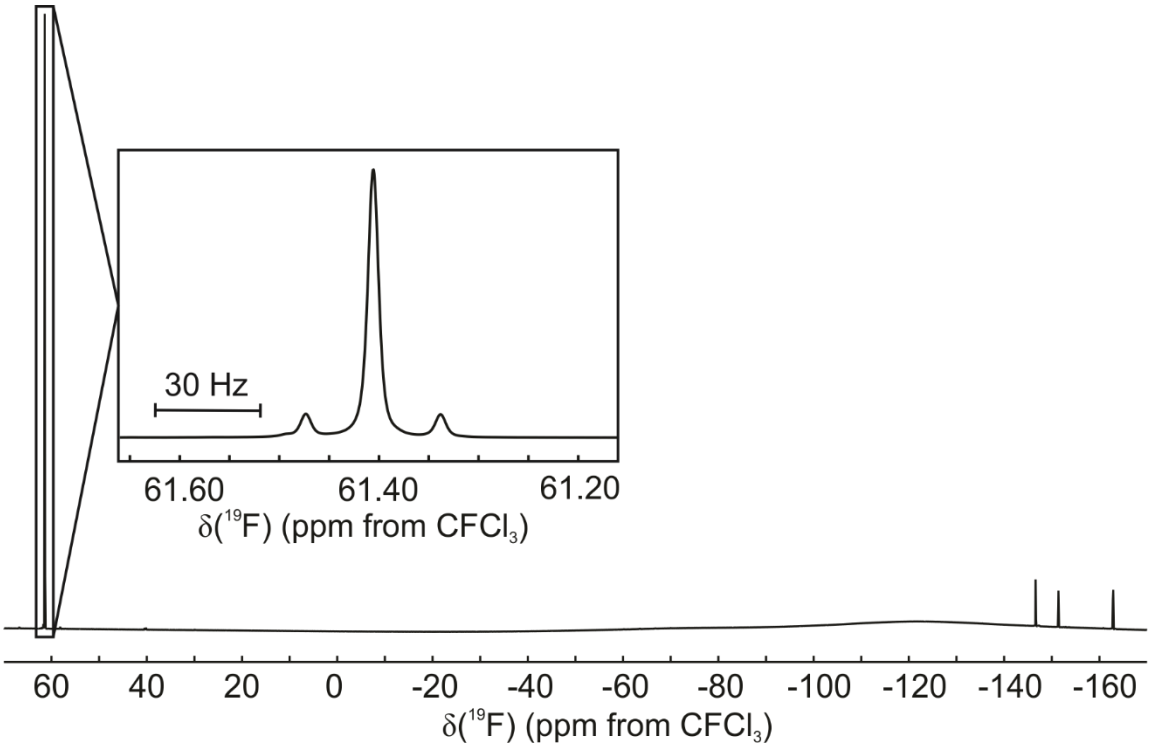

Figure 5.2. Fluorine-19 NMR spectrum of $W(NC_6F_5)F_4(NCCH_3)$, recorded in CH_3CN at 20 °C.

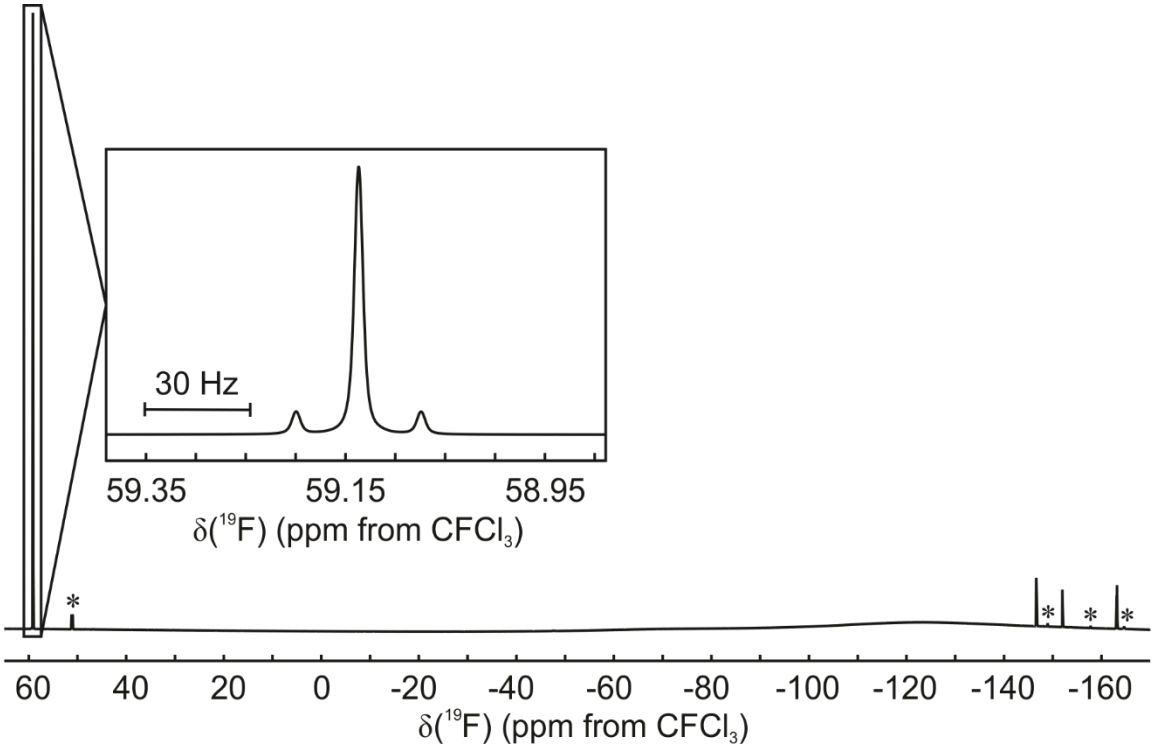

Figure 5.3. Fluorine-19 NMR spectrum of $W(NC_6F_5)F_4(NC_5H_5)$, recorded in CH_3CN at 20 °C. Asterisks (*) denote an impurity of $[W(NC_6F_5)F_5]^-$.

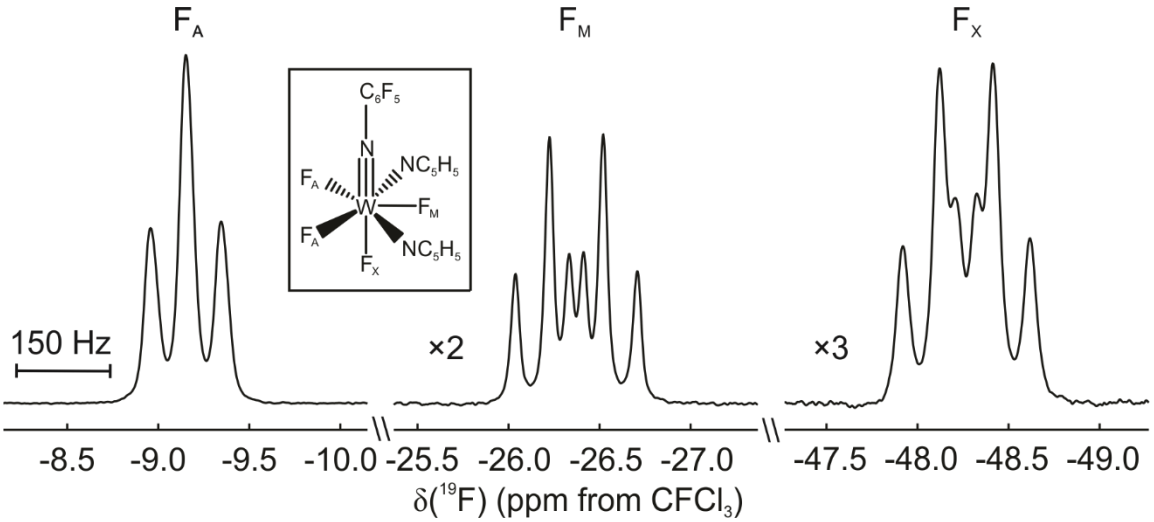

Figure 5.4. Fluorine-on-tungsten resonances in the ^{19}F NMR spectrum of $W(NC_6F_5)F_4(NC_5H_5)_2$, recorded in CH_2Cl_2 at –80 °C.

$^{13}C\{^{1}H\}$ NMR spectra each exhibit one set of resonances corresponding to the pyridyl ligands, corroborating their expected stereochemical equivalence (see section 2.3.3.4).

Upon gradual warming to –20 °C, the F_A and F_M signals simplified to broad singlets and the F_X signal, formerly a doublet of triplets, became a quartet. The axial ligand thus appears to remain rigid at this temperature, allowing it to couple to the now rapidly exchanging equatorial fluorido ligands ($^{2}J(F_{ax}–F_{eq})$ = *ca*. 70 Hz). Above this temperature, irreversible decomposition began, and the adduct was observed to have dissociated almost entirely upon standing at 0 °C for less than five minutes. Regardless of temperature, the fluorine-on-carbon environment maintains the characteristic AA′MM′X spin system observed in the 1:1 adducts, though the signals are broadened such that that ^{4}J coupling could not be observed (Table 5.2).

5.2.3. Molecular Geometries

The structures of $W(NC_6F_5)F_4(NCCH_3)$, $W(NC_6F_5)F_4(NC_5H_5)$, and $WOF_4(NC_5H_5)_n$ (n = 1, 2) were elucidated by X-ray crystallography. Crystallographic data collection and refinement parameters are provided in the Appendix (Tables C.1 and C.2). In addition, gas-phase geometries were optimised for $W(NC_6F_5)F_4(NCCH_3)$ and $W(NC_6F_5)F_4(NC_5H_5)_n$ (n = 1, 2) using DFT (B3LYP) methods.

5.2.3.1. $W(NC_6F_5)F_4(NCCH_3)$ and $W(NC_6F_5)F_4(NC_5H_5)$

Single crystals of $W(NC_6F_5)F_4(NCCH_3)$ and $W(NC_6F_5)F_4(NC_5H_5)$ were obtained from solutions of $W(NC_6F_5)F_4$ in CH_3CN and C_5H_5N/CH_2Cl_2, respectively, upon slow removal of the solvents at low temperature. Selected experimental and calculated geometric parameters are given in Table 5.3. They crystallise in the triclinic space group $P\bar{1}$ with two molecules per unit cell. The γ angle of unit cell in the CH_3CN adduct is

Table 5.3. Selected Experimental and Calculated[a] Bond Lengths (Å) and Angles (°) of $W(NCl)F_4(NCCH_3)$, $W(NC_6F_5)F_4(NCCH_3)$, and $W(NC_6F_5)F_4(NC_5H_5)_n$ (n = 1, 2)

	$W(NCl)F_4(NCCH_3)$	**$W(NC_6F_5)F_4(NCCH_3)$**		**$W(NC_6F_5)F_4(NC_5H_5)_n$**		
				***n* = 1**		***n* = 2**
	exptl[b]	**exptl**	**calcd**	**exptl**	**calcd**	**calcd**
$W-F_{eq}$	1.878(4)–1.894(4)	1.873(6)–1.880(6)	1.882–1.884	1.8767(14)–1.8836(14)	1.886–1.889	1.913–1.944
$W-F_{ax}$						1.946
W−N(1)	1.722(8)	1.728(6)	1.743	1.738(2)	1.752	1.782
W−N(2)	2.267(9)	2.278(6)	2.375	2.2854(19)	2.366	2.232
W–N(3)						2.237
W–N(1)–C(1)	178.6(6)[c]	174.7(4)	180.0	171.69(18)	180.0	178.9
$N(1)-W-F_{eq}$	98.6(3)–99.1(2)	98.2(3)–99.5(3)	100.0–100.3	96.51(8)–100.77(8)	99.6–99.9	92.3–96.8
$N(1)-W-F_{ax}$						174.1
N(1)−W−N(2)	179.9(4)	178.7(4)	180.0	175.74(8)	180.0	93.0
N(1)−W−N(3)						93.6
N(2)−W−N(3)						140.4

[b]Calculated at the B3LYP/VTZ level of theory. [b]From reference 37. [c]Defined as W–N(1)–Cl.

approximately 90° and the crystal is consequently twinned by pseudomerohedry.

The geometries of the 1:1 adducts are comparable, consisting of an octahedral coordination sphere about the tungsten centre in which the nitrogen bases are coordinated *trans* to the imido ligand (Figures 5.5 and 5.6). The W–N(1)–C(1) angles of the CH_3CN and C_5H_5N adducts deviate from linearity by only 5.3 and 8.3°, respectively, suggesting significant triple-bond character in the W≡N bond of the imido ligand via donation of the lone pair on nitrogen to the electron-poor tungsten centre.

The C_6F_5 groups adopt staggered conformations relative to the WF_4 moieties, and it is observed that the fluorido ligands deviate from the ideal WF_4 plane towards the nitrogen base (N(1)–W–F_{eq}: 96.51(8)–100.77(8)°) to a similar extent to the analogous WSF_4 adducts (99.05(5)–100.74(6) Å)[6,7] and $WOF_4(NC_5H_5)$ (98.43(15)–98.95(15) Å, *vide infra*). The W–N(1), W–F, and (where applicable) dative W−N(2) bond lengths do not differ significantly between the $W(NC_6F_5)F_4$ adducts nor from those of $W(NCl)F_4(NCCH_3)$[1] (Table 5.3), as well as $[W(NC_6F_5)F_5]^-$ and $[W_2(NC_6F_5)_2F_9]^-$ (see Chapter 4). The coordination environments about the tungsten centres are consistent with previously reported WOF_4[2,5,8,9] and WSF_4[6,7] adducts whose crystal structures have been elucidated.

The optimised gas-phase geometries of the adducts are in excellent agreement with the experimentally determined structures. They adopt (pseudo-)C_2-symmetric geometries with the C_6F_5 groups staggered relative to the WF_4 moieties; while the C_5H_5N adduct conforms to the C_2 point group, the CH_3CN adduct is C_1-symmetric overall as a consequence of the local C_{3v} symmetry of the CH_3CN ligand. The only notable discrepancies are that the calculated W–N(2) bond lengths are somewhat overestimated

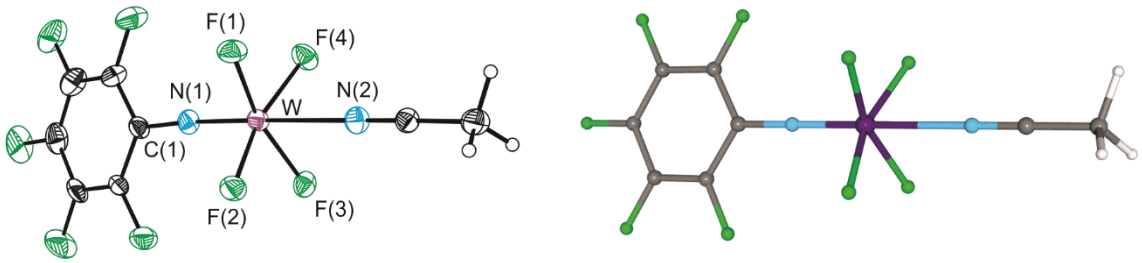

Figure 5.5. Thermal ellipsoid plot (50% probability level, left) and optimised gas-phase geometry (B3LYP/VTZ, right) of $W(NC_6F_5)F_4(NCCH_3)$.

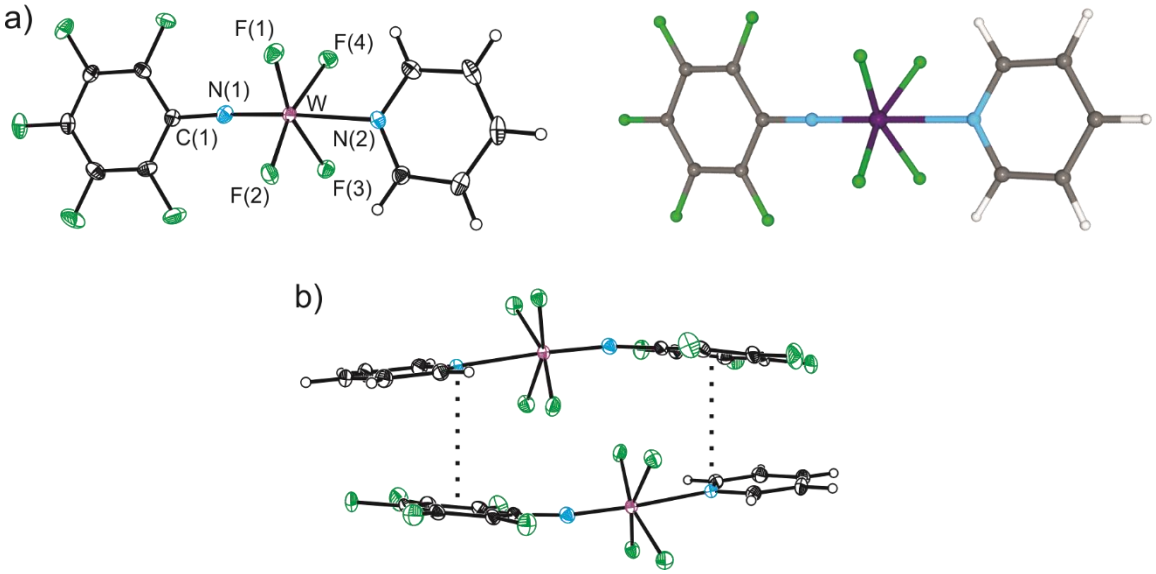

Figure 5.6. Thermal ellipsoid plot (50% probability level, left) and optimised gas-phase geometry (B3LYP/VTZ, right) of a) $W(NC_6F_5)F_4(NC_5H_5)$ with b) intramolecular π-stacking interactions in $W(NC_6F_5)F_4(NC_5H_5)$.

(*ca*. 0.1 Å), as they were for $WSF_4(NCCH_3)$ (exptl.: 2.369(3), calcd.: 2.494 Å)[7] and $WSF_4(NC_5H_5)$ (exptl.: 2.319(2), calcd.: 2.439 Å)[6] at a similar level of theory. It should be noted that the dative W–N bonds of the $W(NC_6F_5)F_4$ adducts are calculated to differ by only 0.009 Å, which is consistent with the observed overlap of errors (within 2σ) in the experimentally determined W–N(2) bond lengths of the CH_3CN (2.278(6) Å) and C_5H_5N (2.2854(19) Å) adducts.

In the crystal structure of $W(NC_6F_5)F_4(NC_5H_5)$, the W−N(1)−C(1) (171.69(18)°) and N(1)−W−N(2) (175.74(8)°) angles deviate further from linearity than in the CH_3CN adduct. This likely arises from the antiparallel-displaced π-stacking interactions between adjacent molecules causing them to flex towards one another (Figure 5.6b). It appears that these interactions are facilitated via electron-poor C_6F_5 groups centering over the relatively electron-rich nitrogen atoms of adjacent pyridyl ligands. This distortion of the C(1)–N(1)–W–N(2) skeleton in the C_5H_5N adduct was not reproduced computationally, further suggesting that its origin lies in solid-state interactions.

5.2.3.2. ***$W(NC_6F_5)F_4(NC_5H_5)_2$***

Attempts to crystallise $W(NC_6F_5)F_4(NC_5H_5)_2$ from C_5H_5N and mixtures thereof with CH_3CN and CH_2Cl_2 did not return crystals suitable for X-ray crystallography, whereas when additional C_5H_5N was not present in the solvent, the 1:1 adduct crystallised instead. As such, in the absence of crystallographic data, the geometry of the 1:2 adduct was optimised based on that determined for $WOF_4(NC_5H_5)_2$ (Figure 5.7),[2,3] given the similarities between their low-temperature ^{19}F NMR spectra. This pentagonal-bipyramidal geometry is ubiquitous in high-valent fluorido complexes of tungsten(VI) and rhenium(VII) containing multiply bound ligands, considering that known heptacoordinate

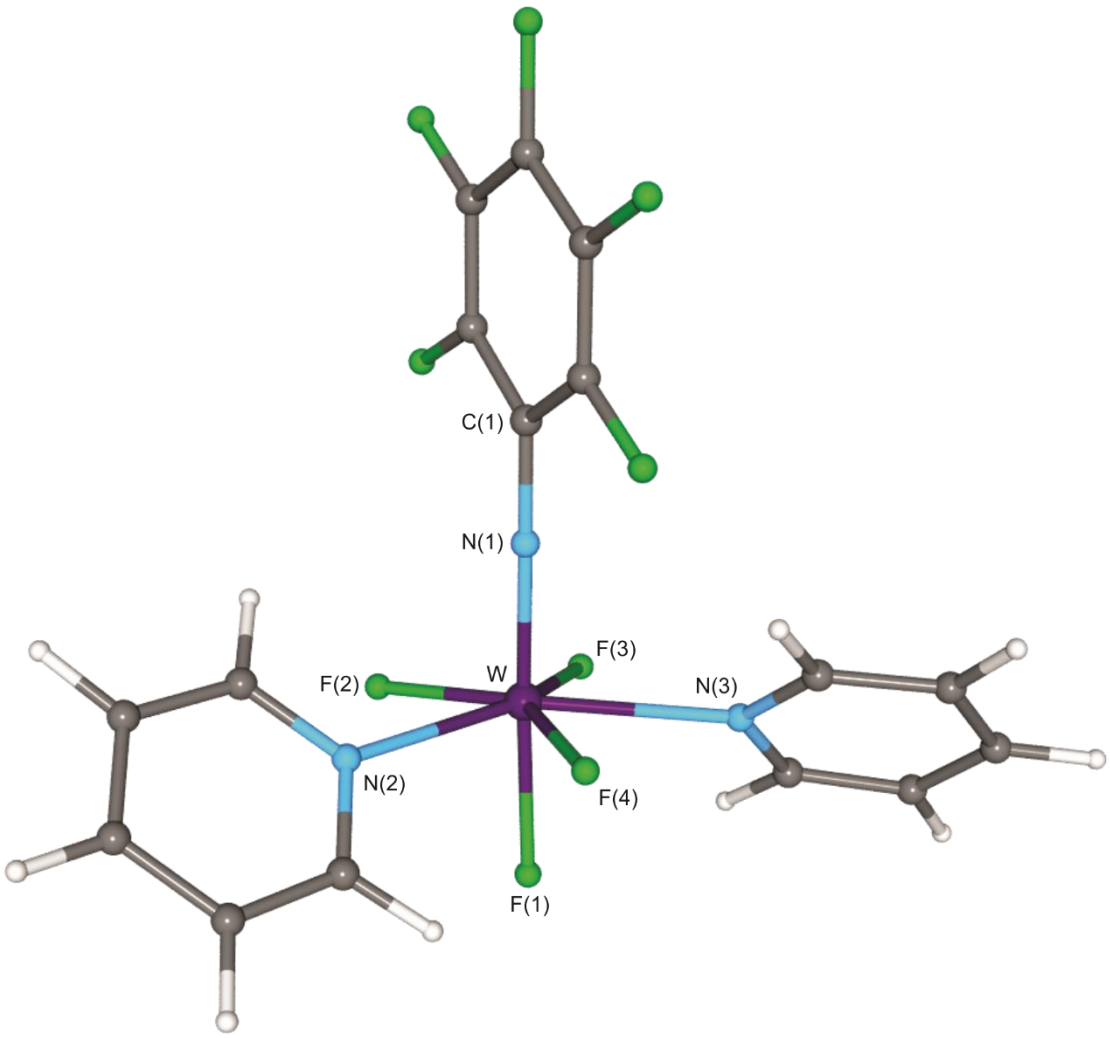

Figure 5.7. Optimised gas-phase geometry (B3LYP/VTZ) of $W(NC_6F_5)F_4(NC_5H_5)_2$.

WOF_4 adducts,[2,10] as well as the $[WOF_6]^{2-}$[11] and $[ReOF_6]^{-}$[12] anions, have all been found to adopt such a geometry.

Interestingly, while the W–N(1) and W–F bonds of $W(NC_6F_5)F_4(NC_5H_5)_2$ are significantly longer than those predicted for the 1:1 adducts, reflecting the decrease in covalent character of those bonds caused by the coordination of a second pyridyl ligand, the dative W–N bonds of the 1:2 adduct (2.332−2.337 Å) are significantly shorter than those calculated for $W(NC_6F_5)F_4(NC_5H_5)$ (2.366 Å). This is attributed to the *trans* influence of the imido ligand weakening the W–N(2) bond in the 1:1 adduct, which instead affects the W–F(1) bond in the 1:2 adduct.

5.2.3.3. $WOF_4(NC_5H_5)_n$ (n = 1, 2)

It was thought that salient inferences of the Lewis acidity of $W(NC_6F_5)F_4$ relative to WOF_4 and WSF_4 could be made by comparing the dative W–N bond lengths in the nitrogen-base adducts. Indeed, the significantly shorter bonds in $W(NC_6F_5)F_4(NCCH_3)$ (2.278(6) Å) and $W(NC_6F_5)F_4(NC_5H_5)$ (2.2854(19) Å) in comparison to the analogous WSF_4 adducts (2.369(3)[7] and 2.319(2)[6] Å, respectively) would suggest that $W(NC_6F_5)F_4$ is the stronger Lewis acid. Unfortunately, the large errors in the reported crystal structure of $WOF_4(NC_5H_5)$[2] precluded similar comparisons to WOF_4 and an improved crystal structure of the adduct was sought. Selected geometric parameters are given in Table 5.4, along with those for the related 1:2 adduct.

The crystallisation of $WOF_4(NC_5H_5)$ (Figure 5.8a) from CH_2Cl_2 at –80 °C resulted in an orthorhombic phase (*Pcbn*), which is pseudo-isomorphic with the closely related $WSF_4(NC_5H_5)$ adduct (*Pcba*).[6] This differs from the monoclinic space group ($P2_1/c$) assigned to the previously reported crystal structure, though the two adopt highly similar

Table 5.4. Selected Bond Lengths (Å) and Angles (°) of $WOF_4(NC_5H_5)_n$ (n = 1, 2)[a]

	***n* = 1**	***n* = 2**
W–F_{eq}	1.859(3)–1.868(3)	1.9132(19)–1.917(2)
W–F_{ax}		1.834(2)[b]
W–O	1.690(3)	1.834(2)[b]
W–N	2.344(3)	2.223(2)
O–W–F_{eq}	98.45(15)–98.85(15)	86.80(7)–93.96(10)
O–W–F_{ax}		173.60(13)
O–W–N	179.73(16)	87.74(10)–90.25(10)
N–W–N^i		143.43(14)

[a]Symmetry transformation: i = 1 – x, y, 0.5 – z. [b]Equivalent due to 50/50 disorder between O and F(1).

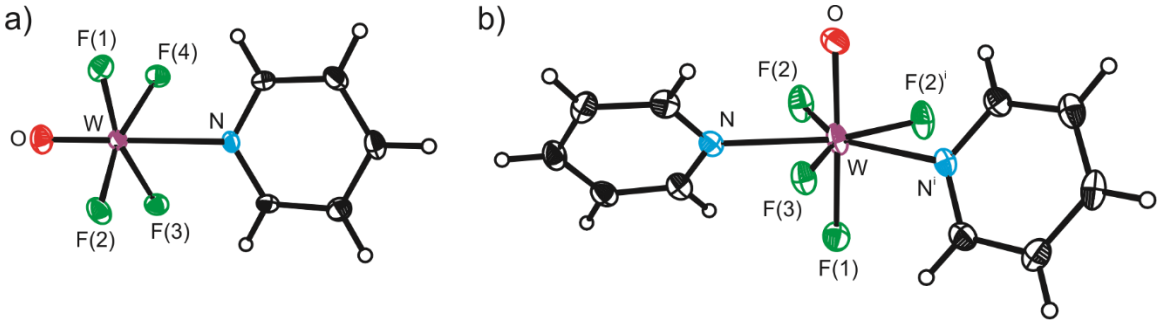

Figure 5.8. Thermal ellipsoid plots (50% probability level) of a) $WOF_4(NC_5H_5)$ and b) $WOF_4(NC_5H_5)_2$.

crystal-packing motifs (Figures 5.9 and 5.10). The newly reported W=O (1.690(3) Å) and W–F (1.859(3)–1.868(3)) bond lengths are of substantially superior quality and are found to be insignificantly different from those of $WOF_4\{OP(C_6H_5)_3\}$ (W=O: 1.682(5); W–F: 1.857(3)–1.871(3) Å).[5] However, it was also observed that the W–N bond (2.344(3) Å) is, in fact, longer than in the WSF_4 adduct (2.319(2) Å).[6] This is despite WOF_4 being the stronger Lewis acid as demonstrated by competitive reactions with F^-,[13] vitiating the notion that the relative Lewis acidities of the parent compounds could be ascertained by comparisons of the dative W–N bond lengths in their C_5H_5N adducts.

During our reinvestigation of the crystal structure of $WOF_4(NC_5H_5)$, crystals of $WOF_4(NC_5H_5)_2$ (Figure 5.8b) grew fortuitously and were thus studied by low-temperature X-ray crystallography. Due to the higher accuracy in the geometric parameters in both adducts, it was clearly observed that the W–F bonds were elongated upon coordination of the second pyridyl ligand, while the W–N bonds were significantly contracted (Table 5.4), as predicted in the optimised geometries of $W(NC_6F_5)F_4(NC_5H_5)_n$ (n = 1, 2). Despite the low temperature and improved quality of the data, the axial O/F disorder in $WOF_4(NC_5H_5)_2$, which is imposed crystallographically by a twofold axis along the W–F(3) bond, could not be parsed.

5.2.4. Raman Spectroscopy

Raman spectra were recorded on solid samples of $[W(NC_6F_5)F_4]_x$, $W(NC_6F_5)F_4(NCCH_3)$, and $W(NC_6F_5)F_4(NC_5H_5)_n$ (n = 1, 2) at ambient temperature. Vibrational frequencies were calculated for the optimised geometries, resulting in excellent agreement between experimental and calculated data; as such, assignments were made on

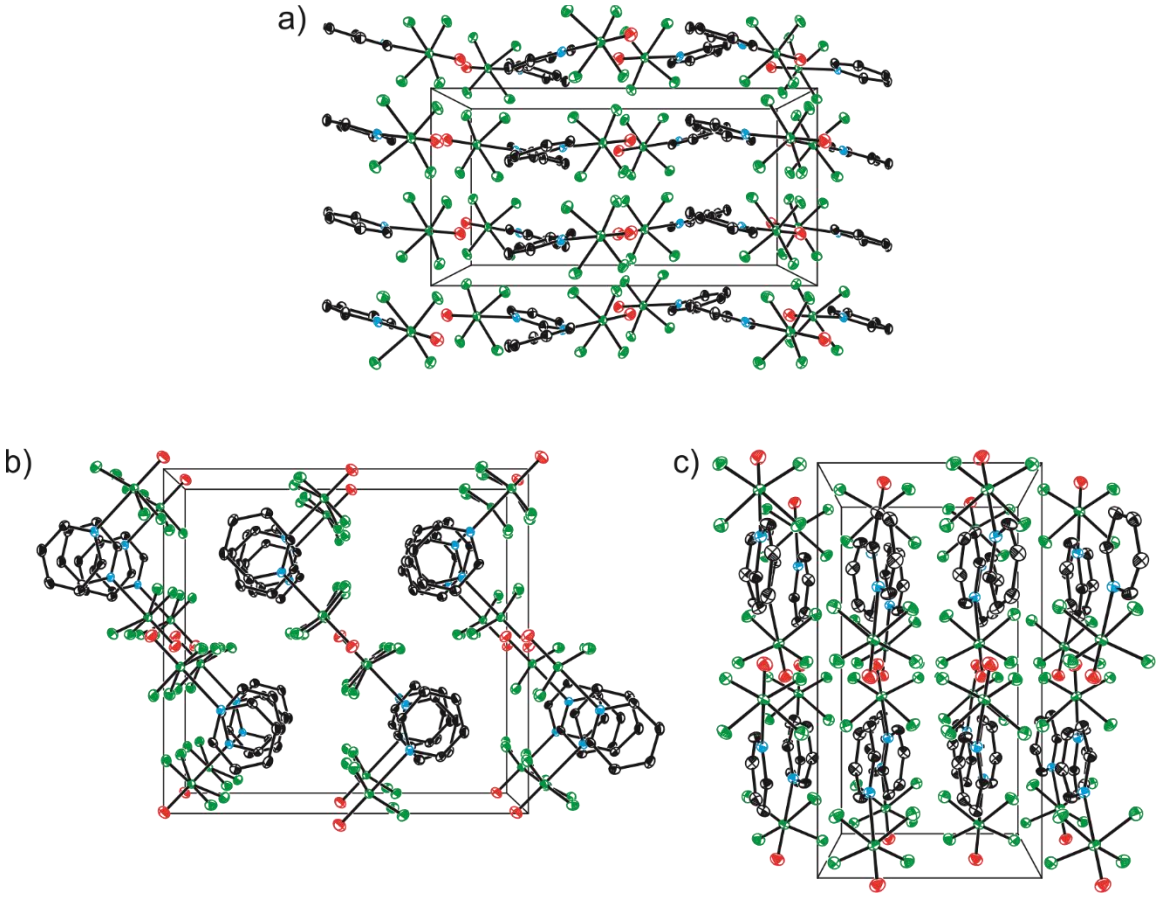

Figure 5.9. Crystal packing diagrams of $WOF_4(NC_5H_5)$ (*Pcbn*) along the a) *a*, b) *b*, and c) *c* axes. Thermal ellipsoids are drawn at the 50% probability level and hydrogen atoms are omitted for clarity.

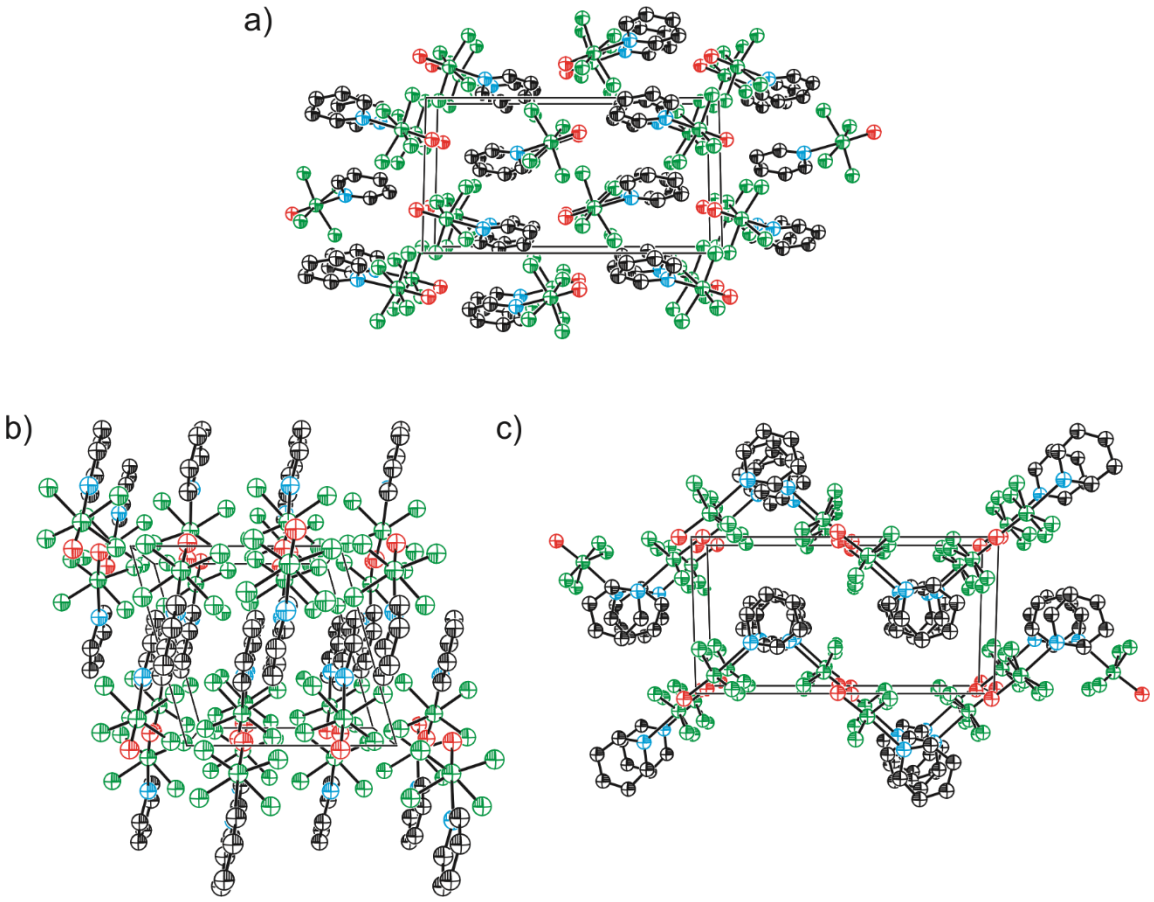

Figure 5.10. Crystal packing diagrams of $WOF_4(NC_5H_5)$ ($P2_1/c$) along the a) *a*, b) *b*, and c) *c* axes. Thermal ellipsoids are drawn at the 50% probability level and hydrogen atoms are omitted for clarity. Crystallographic data are from reference 2.

the basis of these calculations. In the case of $[W(NC_6F_5)F_4]_x$, the Raman spectrum was compared to the calculated vibrational frequencies of monomeric $W(NC_6F_5)F_4$, which agreed well with the experimental data. Selected vibrational frequencies are given in Table 5.5, and complete accounts of the vibrational spectroscopic data, with assignments, are provided in the Appendix (Tables C.3–C.6).

In the Raman spectra of $[W(NC_6F_5)F_4]_x$ and its derivative adducts (Figures 5.11–5.14), the bands corresponding to each $W(NC_6F_5)F_4$ moiety are highly similar to one another and to those of $[W(NC_6F_5)F_5]^-$ and $[W_2(NC_6F_5)_2F_9]^-$ (see Chapter 4), both in frequency and relative intensity. This suggests that the vibrational coupling between the W≡N stretch in these species is identical to the anions, which was verified by the frequency calculations. In the Raman spectrum of $[W(NC_6F_5)F_4]_x$, one broad W–F stretching band is observed, as opposed to the numerous sharp W–F stretching bands of WOF_4[14,15] and WSF_4,[7,16] likely due to the amorphous nature of the solid and the presence of several oligomeric and/or polymeric modifications.

The frequency of the symmetric W–F stretching mode correlates directly with the degree of electron donation from the nitrogen base(s) to the tungsten centre. As such, the frequency of this band (in cm^{-1}) decreases in the series $[W(NC_6F_5)F_4]_x$ (693) > $W(NC_6F_5)F_4(NCCH_3)$ (676) > $W(NC_6F_5)F_4(NC_5H_5)$ (666, 642) > $W(NC_6F_5)F_4(NC_5H_5)_2$ (585). The symmetric W–F stretching vibration of $W(NC_6F_5)F_4(NC_5H_5)$ is predicted to be split due to vibrational coupling to in-plane deformations of the pyridyl ligand, which agrees excellently with the observed splitting of the experimental Raman spectrum in this region.

Table 5.5. Selected Experimental[a] and Calculated[b] Frequencies (cm^{-1}) of $[W(NC_6F_5)F_4]_x$, $W(NC_6F_5)F_4(NCCH_3)$, and $W(NC_6F_5)F_4(NC_5H_5)_n$ (n = 1, 2)

	$\nu_s(WF_4)$		$\nu(WN(1))^c$		$\nu(WN(2))$	
	exptl	**calcd**	**exptl**	**calcd**	**exptl**	**calcd**
$[W(NC_6F_5)F_4]_x$ [d]	693(6)	698(29)	1373(17)	1384(70)		
$W(NC_6F_5)F_4(NCCH_3)$	676(6)	668(29)	1368(10)	1384(96)	224(2)	194(10)
$W(NC_6F_5)F_4(NC_5H_5)$	666(7) 642(4)	665(19) 649(23)	1359(19)	1381(152)	196(5)	187(9)
$W(NC_6F_5)F_4(NC_5H_5)_2$	585(5)[e]	605(25)[e]	1351(11)	1370(117)	190(2)	176(3)

[a]Normalised Raman intensities are given in parentheses. [b]Calculated at the B3LYP/VTZ level of theory, unless otherwise noted. Absolute Raman intensities ($Å^4\ u^{-1}$) are given in parentheses. [c]Highest frequency mode containing ν(WN(1)) character, fully described as $\nu(WN(1) + C_oF_o + C_o'F_o' + C_pF_p)$. [d]Calculated for monomeric $W(NC_6F_5)F_4$ at the B3LYP/sVTZ level of theory. [e]Fully described as ν(WF(1) + WF(3) + WF(4)). Atoms are labelled as in Figure 5.7.

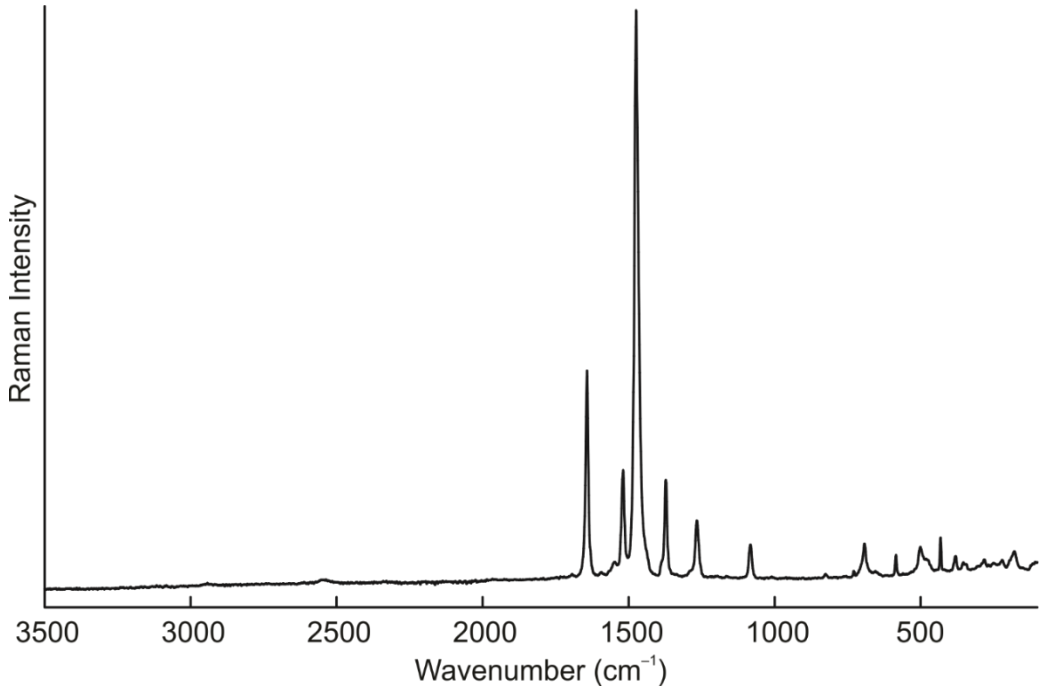

Figure 5.11. Raman spectrum of solid $[W(NC_6F_5)F_4]_x$, recorded at ambient temperature.

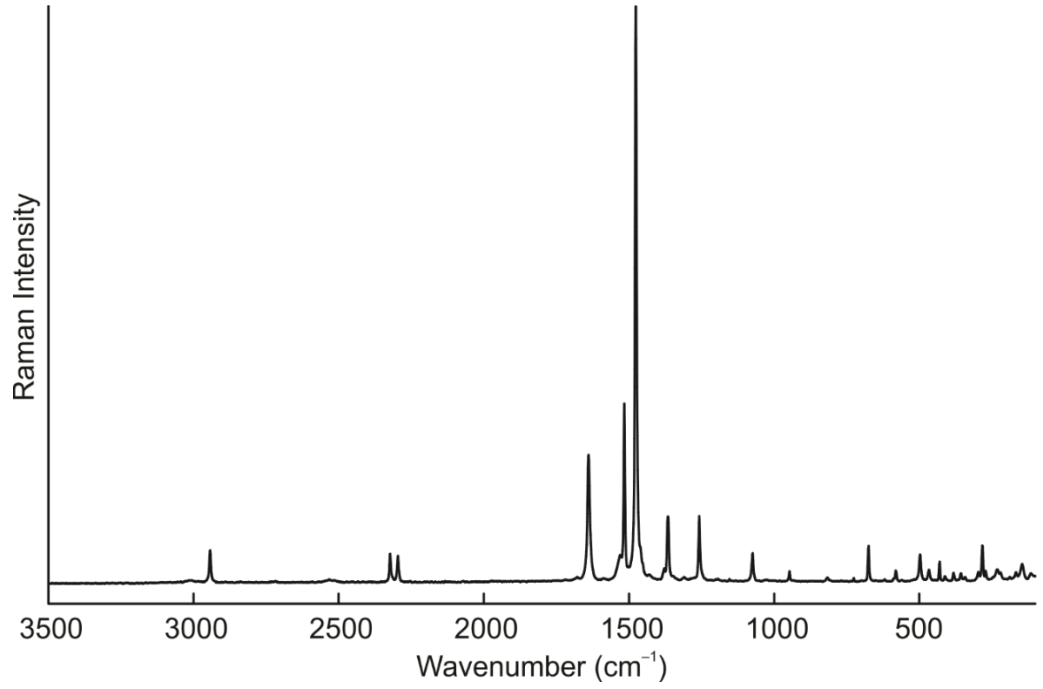

Figure 5.12. Raman spectrum of solid $W(NC_6F_5)F_4(NCCH_3)$, recorded at ambient temperature.

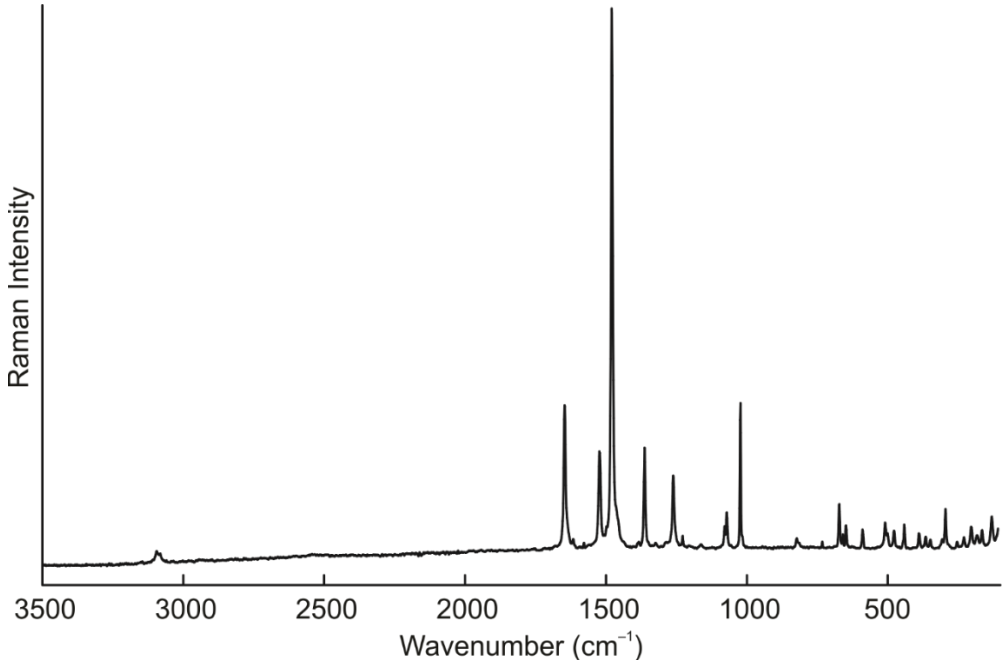

Figure 5.13. Raman spectrum of solid $W(NC_6F_5)F_4(NC_5H_5)$, recorded at ambient temperature.

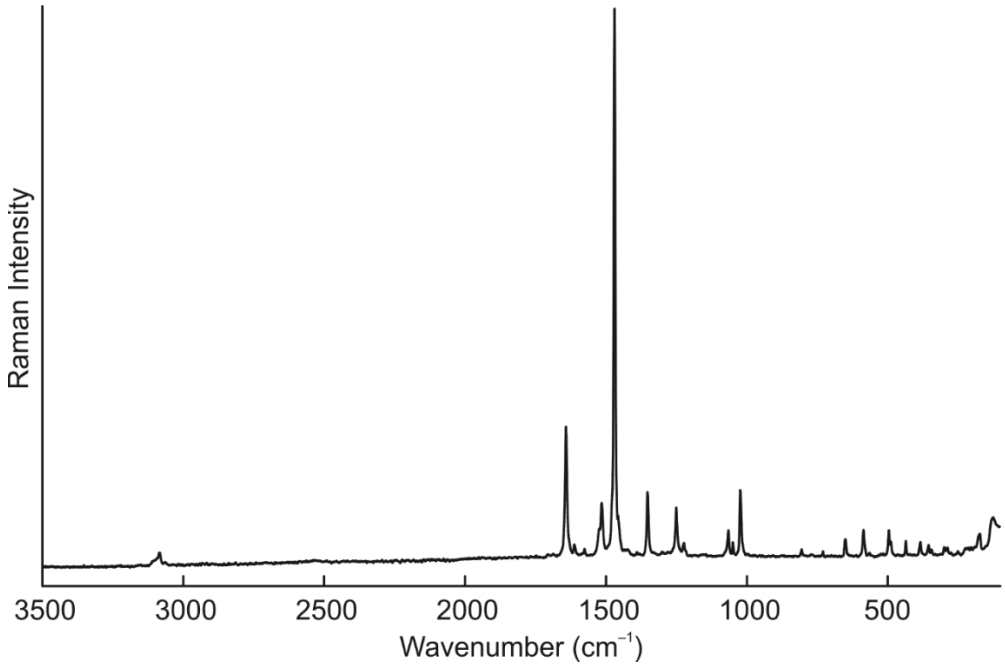

Figure 5.14. Raman spectrum of solid $W(NC_6F_5)F_4(NC_5H_5)_2$, recorded at ambient temperature.

In the cases of the adducts, there is also a complementary increase in frequency for characteristic bands corresponding to the nitrogen bases. In $W(NC_6F_5)F_4(NCCH_3)$, bands corresponding to the C≡N stretching mode are blue-shifted to 2328 and 2300 cm^{-1} from 2293 and 2253 cm^{-1} in free CH_3CN, whereas in the C_5H_5N adducts, the ring-breathing mode is shifted to 1018 (n = 1) and 1022 cm^{-1} (n = 2), respectively, from 990 cm^{-1} in free C_5H_5N (*cf.* $WOF_4(NC_5H_5)_n$: 1020 (n = 1), 1022 cm^{-1} (n =2)).[5] The W–N stretching modes exhibit greater dependence on the size of the neutral ligand, and therefore the reduced mass of the vibration, than the strength of the bond, hence that of the CH_3CN adduct being higher in frequency than either C_5H_5N adduct. A similar phenomenon was observed for a series of WF_6 adducts with various C_5H_5N derivatives (see Chapter 3). Comparison of the C≡N stretching frequency (in cm^{-1}) of $W(NC_6F_5)F_4(NCCH_3)$ (2328, 2300) with those determined previously for the analogous WOF_4 (IR: 2319)[5] and WSF_4 (Raman: 2313, 2286)[7] adducts suggests again that $W(NC_6F_5)F_4$ is comparable in its Lewis acidity to WOF_4, both of which are stronger than WSF_4.

Coupling is observed between the W≡N stretching vibration and various vibrations of the C_6F_5 group in manners identical to $[W(NC_6F_5)F_5]^-$ and $[W_2(NC_6F_5)_2F_9]^-$ (see section 4.2.3). However, comparisons of the bands that possess W≡N stretching character reveal patterns in relative frequency similar to, though lesser in magnitude than, that of the symmetric W–F stretching frequencies. It is possible that this trend arises due to weakening of the W≡N bond, but the significant degree of vibrational coupling obfuscates its true origin.

5.2.5. Computational Results

5.2.5.1. Optimised Geometries and Vibrational Frequencies of W(NR)F$_4$ (R = H, F, CH$_3$, CF$_3$, C$_6$H$_5$, C$_6$F$_5$)

Consistent with the experimentally determined structures of WChF$_4$ (Ch = O,[17] S,[18] Se[19]) in the gas phase, W(NR)F$_4$ (R = H, F, CH$_3$, CF$_3$, C$_6$H$_5$, C$_6$F$_5$) optimise to square-pyramidal geometries with the multiply bonded ligands occupying the apical positions (Figures 5.15 and 5.16). Selected geometric parameters are given in Table 5.6.

Potential-energy minima could not be found for W(NCH$_3$)F$_4$ or W(NC$_6$H$_5$)F$_4$, and the conformations that resemble those of their derivative [W(NR)F$_5$]$^-$ anions exist as transition states for which the imaginary frequencies correspond to rotations of the R group relative to the WF$_4$ moiety. Potential-energy-surface scans of the rotation about the C–N bond revealed that there is a negligible energy barrier (<0.1 kJ mol^{-1}) and no obvious minimum, hence the difficulty in ascertaining the true ground-state geometries. In the case of W(NC$_6$F$_5$)F$_4$, while a ground-state geometry was found, it is not staggered and C_{2v}-symmetric like [W(NC$_6$F$_5$)F$_5$]$^-$, but rather C_2-symmetric and nearly eclipsed in its conformation with a dihedral angle of 3.8° between the C$_6$F$_5$ group and the W–F(1) bond (Figure 5.16). Otherwise, the geometric parameters predicted for these compounds in the gas phase are highly similar to those calculated for the corresponding [W(NR)F$_5$]$^-$ anions (see section 4.2.5.1). The most prominent differences that arise upon removal of the axial fluorido ligand are slight contractions of the W≡N and W–F bonds (*ca*. 0.05 Å) and increases in the N≡W–F angles (*ca*. 10°) to better accommodate the mild steric repulsion between the imido and fluorido ligands.

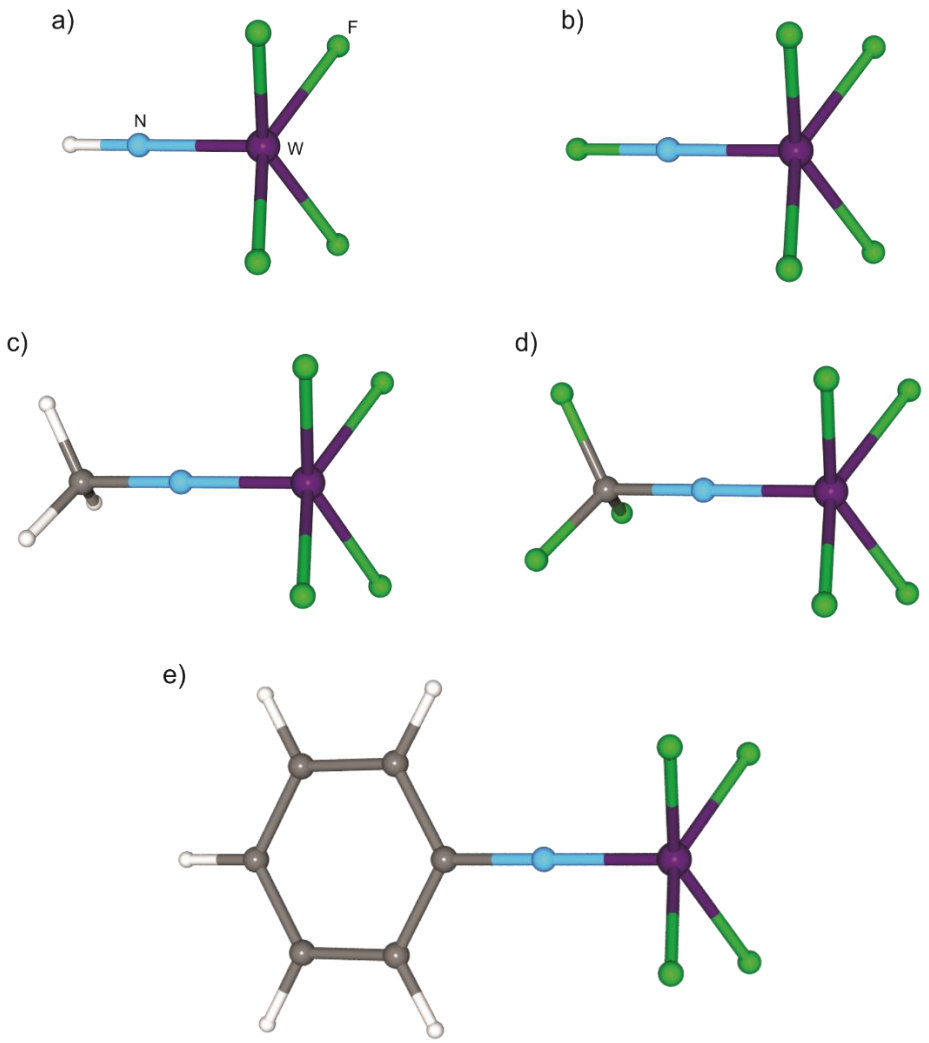

Figure 5.15. Optimised gas-phase geometries (B3LYP/sVTZ) of $W(NR)F_4$: R = a) H, b) F, c) CH_3, d) CF_3, e) C_6H_5.

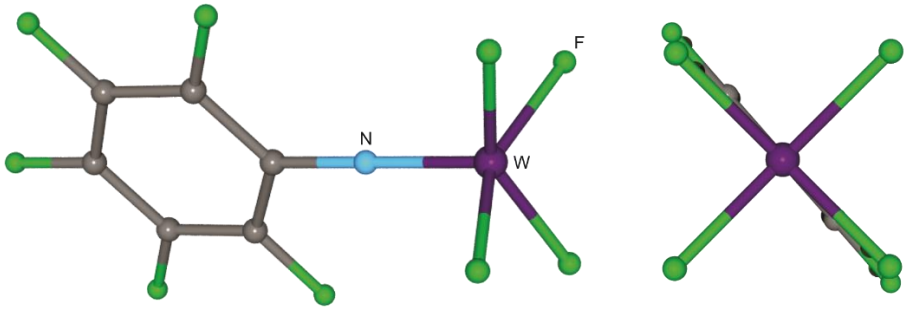

Figure 5.16. Side-on (left) and end-on (right) views of the optimised gas-phase geometry (B3LYP/sVTZ) of $W(NC_6F_5)F_4$.

Table 5.6. Selected Calculated Bond Lengths (Å) and Angles (°) in $W(NR)F_4$ (R = H, F, CH_3, CF_3, C_6H_5, C_6F_5)[a]

R	W≡N	W–F	N≡W–F
H	1.713	1.869	105.4
F	1.719	1.870	105.2
CH_3	1.712	1.877	104.6–104.8
CF_3	1.727	1.861	105.3–105.5
C_6H_5	1.723	1.876	104.6
C_6F_5	1.731	1.863–1.874	103.2–106.7

[a]Calculated at the B3LYP/sVTZ level of theory.

Their calculated vibrational spectra also exhibit characteristics much like those of their anionic counterparts, and the vibrational coupling of the W≡N stretch with vibrations of the R groups can be described in manners effectively identical to the anions (see section 4.2.5.2). It is generally observed that the W≡N and W–F stretching modes increase in frequency upon removal of the axial fluorido ligand. This is evidenced most clearly in $W(NH)F_4$, for which the discrete W≡N and W–F stretches are shifted to 1080 and 704 cm^{-1}, respectively, from 967 and 639 cm^{-1} in the $[W(NH)F_5]^-$ anion. Vibrational frequencies, with assignments, for $W(NR)F_4$ (R = H, F, CH_3, CF_3, C_6H_5) are provided in the Appendix (Tables C.7–C.11).

5.2.5.2. Fluoride-Ion Affinities of $W(NR)F_4$ (R = H, F, CH_3, CF_3, C_6H_5, C_6F_5)

Given the difficulty in measuring the gas-phase FIAs of Lewis acids experimentally, which requires the generation of free F^- using an ion cyclotron resonance spectrometer, a reliable and accurate method for calculating the FIAs of main-group compounds was introduced by Christe, Dixon, and co-workers.[20] In this method, the pseudo-isodesmic reactions of various Lewis acids (A) with the $[COF_3]^-$ anion were studied (Eq. 5.6). The resulting reaction enthalpies, which can be considered the FIAs of A relative to COF_2, were then made absolute by adding the experimentally determined FIA of COF_2 (209 kJ mol^{-1}).[45]

$$A_{(g)} + [COF_3]^-_{(g)} \rightarrow [AF]^-_{(g)} + COF_{2(g)} \qquad (5.6)$$

Herein, a similar approach is used in which the reaction of monomeric $W(NR)F_4$ with the $[WF_7]^-$ anion (Eq. 5.7) is considered. The resultant FIA of $W(NR)F_4$ relative to WF_6 is then corrected by the FIA of WF_6 (327 kJ mol^{-1}), previously calculated using *ab initio* (CCSD(T)) methods and corrected for zero-point energy and core-valence electron

correlation, as well as relativistic and spin-orbit effects.[46] For these calculations, three geometries were predicted for the $[WF_7]^-$ anion using B3LYP: pentagonal-bipyramidal (D_{5h}), monocapped-octahedral (C_{3v}), and monocapped-trigonal-prismatic (C_{2v}). Of the three, the C_{2v}-symmetric geometry was the lowest in energy and was employed in the FIA determinations.

$$W(NR)F_{4(g)} + [WF_7]^-_{(g)} \rightarrow [W(NR)F_5]^-_{(g)} + WF_{6(g)} \quad (5.7)$$

It is evident from the range of calculated FIAs (Table 5.7) that the R group has drastic effects on the Lewis acidity of the tungsten centre, with the strongest Lewis acids possessing highly electron-withdrawing, fluorinated R groups. Coincidentally, the FIA (in kJ mol^{-1}) of the weakest Lewis acid of the series, $W(NCH_3)F_4$ (345) is comparable in its strength to the archetypal Lewis acid BF_3 (344), whereas the strongest, $W(NCF_3)F_4$ (426) approaches the strength of AsF_5 (443).[20] The FIA of $W(NC_6F_5)F_4$ (411) is predicted to be greater than those of WOF_4 (382) and WSF_4 (362). However, it should be noted that the C_6F_5 group is strongly π-accepting, complementing the π-donating behaviour of the incoming F^- and potentially favouring the formation of dative W–F bonds over other dative bonds with predominantly σ character. As such, the expected superiority of $W(NC_6F_5)F_4$ as a F^- acceptor should not be generalised to all Lewis bases.

5.2.5.3. Molecular Orbitals

The HOMOs of $W(NR)F_4$ consist of the $d_{xz/yz}$–$p_{x/y}$ bonding interactions that comprise the W≡N π bonds, as do the HOMOs – 1 of $W(NCH_3)F_4$ and $W(NCF_3)F_4$ along with the HOMOs – 2 of $W(NC_6H_5)F_4$ and $W(NC_6F_5)F_4$. The HOMOs and HOMOs – 1 of the methyl derivatives are pseudo-degenerate, whereas the HOMOs and HOMOs – 2 of the

Table 5.7. Calculated FIAs (kJ mol^{-1}) of $W(NR)F_4$ (R = H, F, CH_3, CF_3, C_6H_5, C_6F_5) and $WChF_4$ (Ch = O, S)[a]

	FIA
$W(NH)F_4$	353
$W(NF)F_4$	417
$W(NCH_3)F_4$	345
$W(NCF_3)F_4$	426
$W(NC_6H_5)F_4$	367
$W(NC_6F_5)F_4$	411
WOF_4	382
WSF_4	362

[a]Calculated at the B3LYP/sVTZ level of theory.

phenyl derivatives are disparate due to different interactions of the inorganic moiety with delocalised σ and π systems in the R groups. Energies for selected MOs for $W(NR)F_4$ are given in Table 5.8 and depicted for $W(NC_6F_5)F_4$ in Figure 5.17.

The LUMOs consist of π*(WF) interactions involving the $d_{x^2-y^2}$ orbital on tungsten and do not contain any interaction between the WF_4 moieties and R groups. The nature of the LUMOs as such does not allow for appropriate orbital overlap with an incoming Lewis base. Instead, the LUMOs + 1, + 2, and + 3 incorporate the d_{xz}, d_{yz}, and d_{z^2} orbitals such that they are available to accept electron density from either σ- (d_{z^2}) or π-donors (d_{xz} and d_{yz}). The π-accepting MOs are typically lower in energy with the notable exception of $W(NF)F_4$, which is attributed to the combined σ-withdrawing and π-donating properties of the nitrogen-bound fluorine atom. The "acidic" MOs are antibonding with respect to the W≡N and W–F bonds, consistent with the indiscriminate elongation of these bonds upon formation of $[W(NR)F_5]^-$.

5.2.5.4. Natural-Bond-Orbital Analyses

Natural-population-analysis charges and Wiberg valences of $W(NR)F_4$ (R = H, F, CH_3, CF_3, C_6H_5, C_6F_5), as well as $W(NC_6F_5)F_4(NCCH_3)$ and $W(NC_6F_5)F_4(NC_5H_5)_n$ (n = 1, 2) are given in Tables 5.9 and 5.10, whereas WBIs are given in Tables 5.11 and 5.12. It is observed that the WBIs of the W≡N bonds are found to be somewhat less than triple those of the W–F bonds, with the exception of $W(NH)F_4$, for which the ratio of WBIs is 3.0. The lowest ratios of WBIs are observed for $W(NCF_3)F_4$ (2.6) and $W(NC_6F_5)F_4$ (2.7) due to conjugation of the W≡N bond with the strongly π-accepting R groups, which was described in detail previously for $[W(NR)F_5]^-$ (see Chapter 4).

Table 5.8. Selected MO Energies (eV) of $W(NR)F_4$ (R = H, F, CH_3, CF_3, C_6H_5, C_6F_5)[a]

R	HOMO – 2	HOMO – 1	HOMO	LUMO	LUMO + 1	LUMO + 2	LUMO + 3
H		–9.80		–3.76	–2.16 (π)		–1.82 (σ)
F		–9.63		–4.04	–3.45 (σ)	–2.28 (π)	
CH_3		–9.01[b]		–3.41	–1.77[b] (π)		–1.52 (σ)
CF_3		–10.33[b]		–4.34	–3.00[b] (π)		–2.41 (σ)
C_6H_5	–9.12		–7.31	–3.43	–2.51 (π)	–1.87 (π)	–1.49 (σ)
C_6F_5	–9.86		–7.84	–3.89	–3.20 (π)	–2.38 (π)	–2.06 (σ)

[a]Calculated at the B3LYP/sVTZ level of theory. Sigma (σ) and pi (π) denote the MO character at the open coordination site of the W^{VI} centre. [b]Molecular orbitals are pseudodegenerate due to the overall C_s symmetry of the compounds.

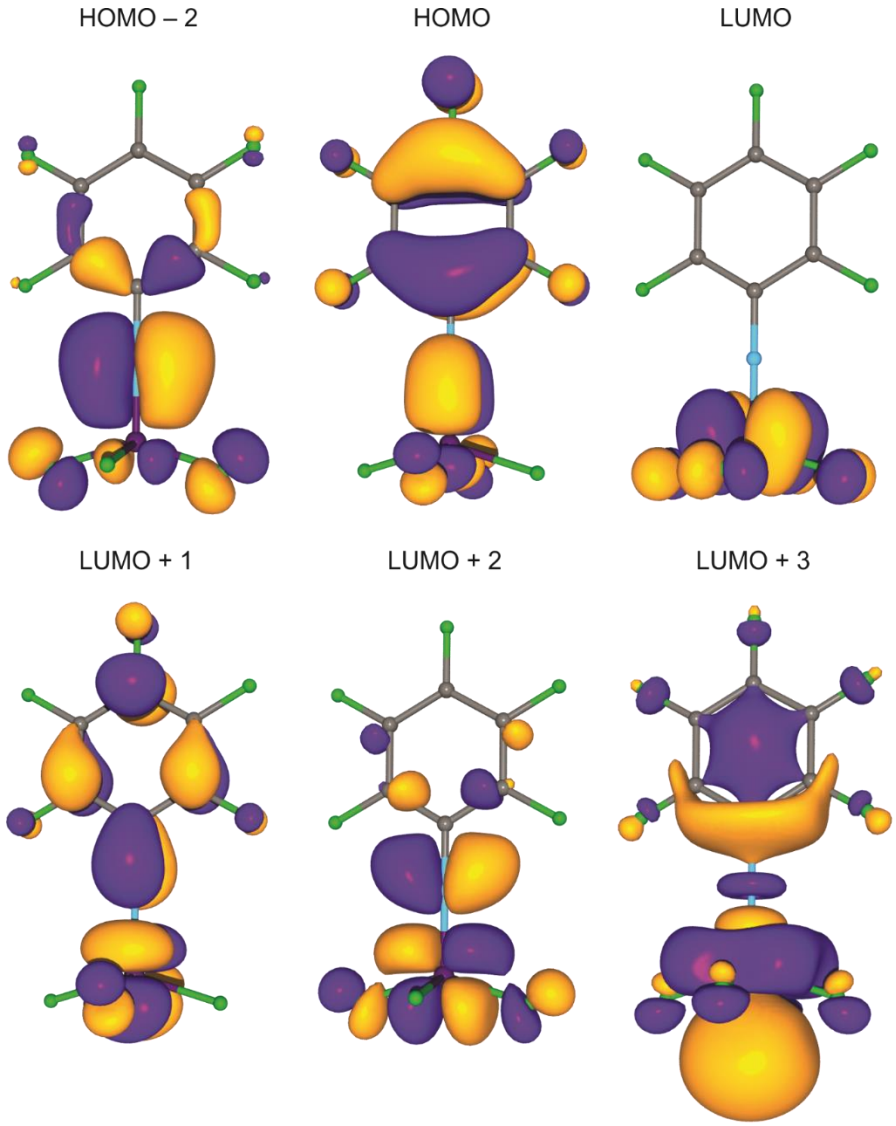

Figure 5.17. Selected MOs of $W(NC_6F_5)F_4$. Isosurface values are drawn at 0.04 e $Å^{-3}$.

Table 5.9. Natural-Population-Analysis Charges and Wiberg Valences[a] of $W(NR)F_4$ (R = H, F, CH_3, CF_3, C_6H_5)[b]

	R									
	H		**F**		**CH_3**		**CF_3**		**C_6H_5**	
W	+2.47	[4.83]	+2.40	[4.84]	+2.44	[4.83]	+2.52	[4.81]	+2.44	[4.82]
F(1)	–0.52	[0.88]	–0.52	[0.89]	–0.53	[0.86]	–0.51	[0.91]	–0.53	[0.86]
F(2)	–0.52	[0.88]	–0.52	[0.89]	–0.53	[0.86]	–0.51	[0.91]	–0.53	[0.86]
F(3)	–0.52	[0.88]	–0.52	[0.89]	–0.53	[0.86]	–0.51	[0.91]	–0.53	[0.86]
F(4)	–0.52	[0.88]	–0.52	[0.89]	–0.53	[0.86]	–0.51	[0.91]	–0.53	[0.86]
N	–0.79	[3.21]	–0.19	[3.27]	–0.55	[3.40]	–0.68	[3.28]	–0.58	[3.41]
X_N	+0.42	[0.83]	–0.13	[1.20]						
C_i					–0.42	[3.84]	+1.12	[3.73]	+0.19	[3.98]
C_o									–0.22	[3.98]
C_m									–0.19	[3.97]
C_p									–0.19	[3.97]
X_i					+0.22	[0.95]	–0.32	[1.05]		
X_o									+0.22	[0.96]
X_m									+0.21	[0.96]
X_p									+0.21	[0.96]

[a]Given in square brackets. [b]Calculated at the B3LYP/sVTZ level of theory.

Table 5.10. Natural-Population-Analysis Charges and Wiberg Valences[a] of $W(NC_6F_5)F_4$, $W(NC_6F_5)F_4(NCCH_3)$, and $W(NC_6F_5)F_4(NC_5H_5)_n$ (n = 1, 2)

	$W(NC_6F_5)F_4$[b]		**$W(NC_6F_5)F_4(NCCH_3)$[c]**		**$W(NC_6F_5)F_4(NC_5H_5)_n$[c]**			
					***n* = 1**		***n* = 2[d]**	
W	+2.48	[4.81]	+2.28	[5.01]	+2.28	[5.01]	+2.15	[5.16]
F(1)	–0.51	[0.89]	–0.52	[0.89]	–0.52	[0.88]	–0.58	[0.78]
F(2)	–0.52	[0.88]	–0.51	[0.89]	–0.52	[0.87]	–0.57	[0.78]
F(3)	–0.52	[0.88]	–0.52	[0.89]	–0.52	[0.88]	–0.53	[0.86]
F(4)	–0.51	[0.89]	–0.51	[0.89]	–0.52	[0.87]	–0.53	[0.86]
N	–0.60	[3.37]	–0.50	[3.40]	–0.50	[3.39]	–0.56	[3.30]
C_i	+0.07	[3.98]	+0.00	[3.99]	+0.00	[3.99]	+0.01	[4.00]
C_o	+0.34	[3.88]	+0.37	[3.86]	+0.37	[3.86]	+0.35	[3.86]
C_m	+0.29	[3.87]	+0.28	[3.86]	+0.28	[3.86]	+0.28	[3.86]
C_p	+0.31	[3.87]	+0.31	[3.86]	+0.31	[3.86]	+0.30	[3.86]
F_o	–0.29	[1.08]	–0.29	[1.08]	–0.29	[1.08]	–0.31	[1.06]
F_m	–0.29	[1.07]	–0.29	[1.07]	–0.29	[1.07]	–0.30	[1.06]
F_p	–0.29	[1.08]	–0.29	[1.08]	–0.29	[1.08]	–0.29	[1.07]
N_L			–0.41	[3.21]	–0.51	[3.25]	–0.43	[3.37]
$C_{o/N}$			+0.47	[3.93]	+0.08	[3.92]	+0.09	[3.92]
$C_{m/Me}$			–0.70	[3.83]	–0.23	[3.96]	–0.24	[3.96]
C_p					–0.13	[3.96]	–0.14	[3.96]
H_o					+0.22	[0.95]	+0.22	[0.95]
$H_{m/Me}$			+0.26	[0.93]	+0.22	[0.95]	+0.22	[0.95]
H_p					+0.22	[0.96]	+0.21	[0.96]

[a]Given in square brackets. [b]Calculated at the B3LYP/sVTZ level of theory. [c]Calculated at the B3LYP/VTZ level of theory [d]Data for one pyridyl ligand given.

Table 5.11. Wiberg Bond Indices of $W(NR)F_4$ (R = H, F, CH_3, CF_3, C_6H_5)[a]

	R				
	H	**F**	**CH_3**	**CF_3**	**C_6H_5**
W–N	2.05	1.93	2.03	1.87	1.93
W–F	0.69	0.69	0.67	0.71–0.72	0.68
N–X_N	0.82	1.02			
N–C			1.05	1.01	1.11
C–X			0.92	0.90	0.92
C_i–C_o					1.35
C_o–C_m					1.46
C_m–C_p					1.43

[a]Calculated at the B3LYP/sVTZ level of theory.

Table 5.12. Wiberg Bond Indices of $W(NC_6F_5)F_4$, $W(NC_6F_5)F_4(NCCH_3)$, and $W(NC_6F_5)F_4(NC_5H_5)_n$ (n = 1, 2)

	$W(NC_6F_5)F_4$ [a]	**$W(NC_6F_5)F_4(NCCH_3)$[b]**	**$W(NC_6F_5)F_4(NC_5H_5)_n$[b]**	
			***n* = 1**	***n* = 2[c]**
W–F(1)	0.71	0.69	0.69	0.54
W–F(2)	0.69	0.69	0.68	0.59
W–F(3)	0.71	0.69	0.69	0.66
W–F(4)	0.69	0.69	0.68	0.65
W–N(1)	1.85	1.84	1.83	1.71
N(1)–C_i	1.14	1.17	1.17	1.19
C_i–C_o	1.30	1.29	1.29	1.28
C_o–C_m	1.37	1.37	1.37	1.37
C_m–C_p	1.34	1.34	1.34	1.34
C_o–F_o	0.93	0.93	0.93	0.92
C_m–F_m	0.93	0.93	0.93	0.93
C_p–F_p	0.94	0.94	0.94	0.93
W–N_L		0.27	0.24	0.38
N_L–$C_{o/N}$		2.79	1.37	1.36
$C_{o/N}$–$C_{m/Me}$		1.10	1.44	1.45
C_m–C_p			1.44	1.43
C_o–H_o			0.91	0.91
$C_{m/Me}$–$H_{m/Me}$		0.90	0.92	0.92
C_p–H_p			0.92	0.92

[a]Calculated at the B3LYP/sVTZ level of theory. [b]Calculated at the B3LYP/VTZ level of theory [c]Data for one pyridyl ligand given.

In comparison to free, monomeric $W(NC_6F_5)F_4$, its 1:1 adducts possess less positively charged tungsten centres but no significant changes in the strengths of W–F and W≡N bonds. In the 1:2 adduct with C_5H_5N, however, marked decreases in the charge on the metal centre and WBIs of the W≡N bond are observed. The most notable difference between the adducts is in the strength of the dative W–N bonds. The WBIs of these bonds in $W(NC_6F_5)F_4(NC_5H_5)_2$ (0.38) are comparable to that of $WF_6(NC_5H_5)$ (0.40),[38] and indicate a significant degree of covalent character. Meanwhile, those of the 1:1 adducts (0.21–0.24) are approximately one-third the WBIs of the W–F bonds (0.68–0.69), suggesting a greater degree of polarisation towards the neutral ligands inflicted by the *trans* influence of the imido ligand. Comparing the NPA charges of the pyridyl ligands in the C_5H_5N adducts corroborates this notion, as the nitrogen atom (–0.50) and entire pyridyl ligand (+0.17) in the 1:1 adduct are less positively charged than in the 1:2 adduct (–0.43 and +0.25, respectively). This is further evidenced by the predicted contraction of the W–N bonds upon coordination of a second pyridyl ligand.

5.3. Conclusions

A synthetic route to $[W(NC_6F_5)F_4]_x$ via F^- abstraction from $[C_5H_5NH][W(NC_6F_5)F_5]$ has been developed. Though amorphous in the solid state, it is thought to aggregate by asymmetric fluorine bridges much like WOF_4 and WSF_4, forming various oligo- or polymeric modifications. In addition, it readily forms stable adducts upon reaction with CH_3CN and C_5H_5N. With C_5H_5N, a stable, heptacoordinate 1:2 adduct could be isolated, which was determined to adopt a pentagonal-bipyramidal geometry by low-temperature ^{19}F NMR spectroscopy. These adducts have been comprehensively characterised in the solid state and in solution, revealing that $W(NC_6F_5)F_4$ possesses a Lewis acidity similar to that of WOF_4. Lastly, DFT (B3LYP) studies of the $W(NR)F_4$ series revealed that these compounds are expected to exhibit a wide range of Lewis acidities, with $W(NCH_3)F_4$ being the weakest in the series and $W(NCF_3)F_4$ the strongest ($R = CF_3 > F > C_6F_5 >> C_6H_5 > H > CH_3$). In particular, it was found that the FIA (in kJ mol^{-1}) of $W(NC_6F_5)F_4$ (411) is higher than those of WOF_4 (382) and WSF_4 (362).

5.4. References

(1) Rhiel, M.; Wocadlo, S.; Massa, W.; Dehnicke, K. *Z. Anorg. Allg. Chem.* **1996**, *622* (7), 1195–1199.

(2) Arnaudet, L.; Bougon, R.; Ban, B.; Charpin, P.; Isabey, J.; Lance, M.; Nierlich, M.; Vigner, J. *Inorg. Chem.* **1989**, *28* (2), 257–262.

(3) Arnaudet, L.; Bougon, R.; Buu, B. *J. Fluorine Chem.* **1995**, *74* (2), 223–225.

(4) Fawcett, J.; Griffith, G. A.; Peacock, R. D.; Russell, D. R. *Polyhedron* **1988**, *7* (19), 2015–2022.

(5) Levason, W.; Reid, G.; Zhang, W. *J. Fluorine Chem.* **2016**, *184*, 50–57.

(6) Nieboer, J.; Yu, X.; Chaudhary, P.; Mercier, H. P. A.; Gerken, M. *Z. Anorg. Allg. Chem.* **2012**, *638* (3–4), 520–525.

(7) Nieboer, J.; Hillary, W.; Yu, X.; Mercier, H. P. A.; Gerken, M. *Inorg. Chem.* **2009**, *48* (23), 11251–11258.

(8) Arnaudet, L.; Bougon, R.; Ban, B.; Lance, M.; Nierlich, M.; Vigner, J. *Inorg. Chem.* **1993**, *32* (7), 1142–1146.

(9) Tucker, P. A.; Taylor, P. A.; Holloway, J. H.; Russell, D. R. *Acta Crystallogr.* **1975**, *31* (3), 906–908.

(10) Emsley, J. W.; Levason, W.; Reid, G.; Zhang, W.; De Luca, G. *J. Fluorine Chem.* **2017**, *197*, 74–79.

(11) Sakharov, S. G.; Kokunov, Y. V.; Gustyakova, M. P.; Buslaev, Y. A. *Dokl. Akad. Nauk SSSR* **1984**, *276* (1), 148–151.

(12) Giese, S.; Seppelt, K. *Angew. Chem. Int. Ed. Engl.* **1994**, *33* (4), 461–463.

(13) Nieboer, J.; Haiges, R.; Hillary, W.; Yu, X.; Richardet, T.; Mercier, H. P. A.; Gerken, M. *Inorg. Chem.* **2012**, *51* (11), 6350–6359.

(14) Beattie, I. R.; Reynolds, D. J. *Chem. Commun.* **1968**, 1531–1532.

(15) Alexander, L. E.; Beattie, I. R.; Bukovszky, A.; Jones, P. J.; Marsden, C. J.; Schalkwyk, G. J. Van. *J. Chem. Soc., Dalton Trans.* **1974**, 81.

(16) Atherton, M. J.; Holloway, J. H. *J. Chem. Soc., Chem. Commun.* **1977**, 424.

(17) Robiette, A. G.; Hedberg, K.; Hedberg, L. *J. Mol. Struct.* **1977**, *37* (1), 105–112.

(18) Rice, D. A.; Hagen, K.; Hedberg, L.; Hedberg, K.; Staunton, G. M.; Holloway, J. H. *Inorg. Chem.* **1984**, *23* (13), 1826–1828.

(19) Hagen, K.; Rice, D. A.; Holloway, J. H.; Kaučič, V. *J. Chem. Soc., Dalton Trans.* **1986**, 1821–1823.

(20) Christe, K. O.; Dixon, D. A.; McLemore, D.; Wilson, W. W.; Sheehy, J. A.; Boatz, J. A. *J. Fluorine Chem.* **2000**, *101* (2), 151–153.

Chapter 6 – Stabilisation of $[WF_5]^+$ by Bidentate N-Donor Ligands*

6.1. Introduction

Transition-metal hexafluorides (MF_6, M = Mo, W, Tc, and Re) behave as moderate-strength Lewis acids and F^- acceptors, forming $[MF_7]^-$ and $[MF_8]^{2-}$ salts.[1–3] Conversely, they are not expected to behave as F^- donors, which is exemplified by the use of WF_6 as an inert solvent for reactions between the strong acceptors SbF_5 and BiF_5.[4,5] Cationic derivatives of the transition-metal hexafluorides (i.e. $[MF_5]^+$) or fluorine-bridged, polarised species (i.e. $F_5M–F\cdots SbF_5$), however, may play important roles in their chemistry. For instance, the oxidation of C_6F_6 by OsF_6 to afford $[C_6F_6][Os_2F_{11}]$ is catalysed by SbF_5,[6] and while the neat oxidation of xenon by IrF_6 to form $[XeF][IrF_6]$ only occurs at an appreciable rate upon heating to 45 °C, the addition of SbF_5 allows for the low-temperature preparation of $[XeF][IrSbF_{11}]$.[7]

There are few examples of cationic derivatives of MF_6, prepared by the ligand-induced autoionisation of WF_6 in the presence of bidentate Lewis bases (B′) to form $[WF_4(B')_2]^{2+}$ salts.[8–10] Similar autoionisation in the presence of mono- and bidentate Lewis bases is well documented for NbF_5 and TaF_5.[11–13] A monocationic derivative of a transition-metal hexafluoride, $[MF_5]^+$, or donor-stabilised complexes thereof have not been reported previously. In this chapter, the first examples of such species, in the form of $[WF_5]^+$ stabilised by the bidentate N-donor ligands 2,2′-bipy and 1,10-phen, are reported and their properties discussed.

* Based on the following publication: Turnbull, D.; Wetmore, S. D.; Gerken, M. *Angew. Chem. Int. Ed.* **2019**, *58* (37), 13035–13038.

6.2. Results and Discussion

6.2.1. Syntheses and Properties of $WF_6(L)$ and $[WF_5(L)]^+$ (L = 2,2′-bipy, 1,10-phen) Salts

To access $[WF_5(L)]^+$ salts, octacoordinate $WF_6(L)$ adducts were employed as precursors, which are readily prepared by the reaction of $WF_6(NC_5H_5)$ with L in CH_2Cl_2 (Eq. 6.1). The WF_6(2,2′-bipy) adduct was prepared previously via reaction of WF_6 with one molar equivalent of 2,2′-bipy,[9] and we have found that using a solid synthetic equivalent to gaseous WF_6 allows for more facile control of the stoichiometry. These adducts are completely insoluble in SO_2 and compatible organic solvents, and during the preparation of WF_6(2,2′-bipy), the product was invariably contaminated by free ligand, suggesting that it is unstable towards dissociation in the presence of solvent. Upon removal of the solvent, no further dissociation was observed and the impurity could be sublimed *in vacuo* at 100 °C. The 1,10-phen adduct demonstrated no such instability, likely due to the stronger chelate effect of 1,10-phen.

$$WF_6(NC_5H_5) + L \rightarrow WF_6(L) + C_5H_5N \qquad (6.1)$$

The $WF_6(L)$ adducts react with two molar equivalents of $SbF_5(OSO)$ in SO_2 at ambient temperature, yielding $[WF_5(L)][Sb_2F_{11}]$ as yellow (L = 2,2′-bipy) or orange (L = 1,10-phen) solids upon removal of the volatile materials *in vacuo* (Eq. 6.2). Whereas the equimolar reaction of WF_6(1,10-phen) and $SbF_5(OSO)$ in SO_2 yielded $[WF_5$(1,10-phen)$][SbF_6]\cdot SO_2$ as an orange solid upon isolation (Eq. 6.3), the analogous reaction using WF_6(2,2′-bipy) was not found to afford a single, isolable product based on ^{19}F NMR spectroscopy in SO_2 (*vide infra*).

$$WF_6(L) + 2SbF_5(OSO) \rightarrow [WF_5(L)][Sb_2F_{11}] + 2SO_2 \quad (6.2)$$

$$WF_6(1,10\text{-phen}) + SbF_5(OSO) \rightarrow [WF_5(1,10\text{-phen})][SbF_6]\cdot SO_2 \quad (6.3)$$

An incipient black material was observed in the incompletely reacted solid mixtures of $WF_6(L)$ and $SbF_5(OSO)$ after the introduction of solvent and warming to –70 °C. In the 1:1 reactions, this colour disappeared immediately upon brief agitation at low temperature, but in the 1:2 reactions, it persisted in solution and dissipated over *ca*. 16 h at ambient temperature. The ^{19}F NMR spectrum of a freshly prepared solution of $[WF_5(2,2'\text{-bipy})][Sb_2F_{11}]$ revealed a small singlet at 235 ppm that disappeared in conjunction with the loss of colour, suggesting that its source could be an intermediate tungsten(VI) complex undergoing intense ligand-to-metal charge transfer (LMCT).

6.2.2. Molecular Geometries

6.2.2.1. $WF_6(L)$ (L = 2,2′-bipy, 1,10-phen)

Due to their indiscriminate insolubility, the geometries of $WF_6(L)$ were investigated computationally using DFT (B3LYP) methods. Those of $WF_6(NC_5H_5)_2$ and $[WF_4(2,2'\text{-bipy})_2]^{2+}$, the crystal structures of which have been reported previously,[8,9,14] were also optimised for comparative purposes. Overall, excellent agreement was observed between the experimental and calculated data for the reference compounds, with only minor overestimations of the W–N bond lengths (*ca*. 0.1 Å). Thus, the data for $WF_6(L)$ are believed to be accurate. Selected experimental and calculated bond lengths and angles are given in Table 6.1.

The $WF_6(L)$ adducts are found to adopt C_2- (L = 2,2′-bipy) and C_{2v}-symmetric (L = 1,10-phen) geometries that are best described as heavily distorted dodecahedra, more similar to $[WF_4(2,2'\text{-bipy})_2]^{2+}$ than $WF_6(NC_5H_5)_2$ (Figure 6.1). The WF_6N_2 moieties are

Table 6.1. Selected Experimental and Calculated[a] Bond Lengths (Å) and Angles (°) of $WF_6(NC_5H_5)_2$, WF_6(2,2′-bipy), WF_6(1,10-phen), and $[WF_4(2,2'\text{-bipy})_2]^{2+}$

	$WF_6(NC_5H_5)_2$		WF_6(2,2′-bipy)	WF_6(1,10-phen)	$[WF_4(2,2'\text{-bipy})_2]^{2+}$	
	exptl[b]	calcd	calcd	calcd	exptl[c]	calcd
W–F(1)	1.885(6)	1.885	1.885	1.885	1.836(4)	1.851
W–F(2)	1.883(6)	1.885	1.885	1.885	1.836(4)	1.851
W–F(3)	1.898(5)	1.884	1.869	1.870	1.836(4)	1.851
W–F(4)	1.900(5)	1.884	1.869	1.870	1.836(4)	1.851
W–F(5)	1.898(5)	1.884	1.887	1.887		
W–F(6)	1.900(5)	1.884	1.887	1.887		
W–N	2.344(6)	2.480	2.547	2.545	2.263(7)	2.320
F(1)–W–F(2)	90.3(3)	85.8	131.6	131.4	96.07(9)	95.7
F(1)–W–F(3)	85.0(2)	85.6	97.1	94.6	142.1(3)	143.1
F(1)–W–F(4)	142.7(2)	141.2	92.1	94.6	96.07(9)	95.7
F(1)–W–F(5)	84.9(2)	85.6	75.9	76.0		
F(1)–W–F(6)	142.7(2)	141.2	152.4	152.7		
F(1)–W–N(1)	71.5(2)	70.6	68.8	69.6	73.9(2)	73.5
F(2)–W–N(1)	71.4(2)	70.6	70.5	69.6	75.3(2)	75.0
F(3)–W–N(1)	72.0(2)	70.8	69.3	68.9	144.3(2)	143.4
F(4)–W–N(1)	72.1(2)	70.8	133.1	133.4	73.7(2)	75.0
F(5)–W–N(1)	139.6(2)	139.7	129.2	131.5		
F(6)–W–N(1)	139.7(2)	139.7	134.3	131.5		
N(1)–W–N(2)	126.3(3)	126.2	64.0	64.5	70.7(3)	69.9

[a]Calculated at the B3LYP/aVTZ level of theory. [b]From reference 14. [c]From reference 8.

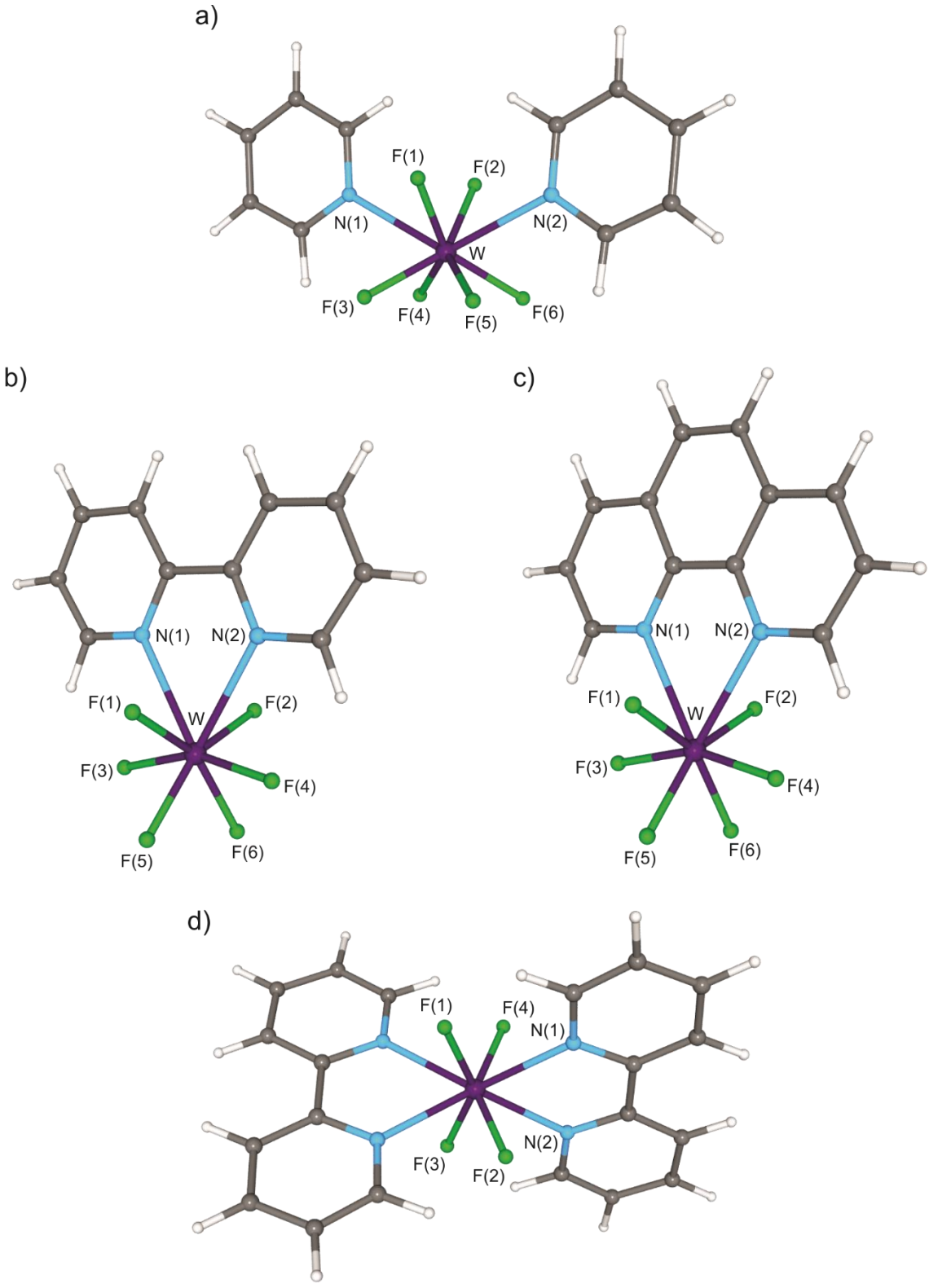

Figure 6.1. Optimised gas-phase geometries (B3LYP/aVTZ) of a) $WF_6(NC_5H_5)_2$, b) WF_6(2,2′-bipy), c) WF_6(1,10-phen), and d) $[WF_4(2,2'\text{-bipy})_2]^{2+}$

effectively identical, with negligible differences between analogous bond lengths and angles. The N(1)–W–N(2) angles in $WF_6(L)$ are constrained by the bite angle of the bidentate ligands (64.0–64.5°), resulting in geometries that differ from that of $WF_6(NC_5H_5)_2$, which is bicapped-trigonal-prismatic and possesses a wide N(1)–W–N(2) angle (calcd. 126.2°).

The W–F bonds in $WF_6(L)$ (1.869–1.887 Å) are predicted to be similar in length to $WF_6(NC_5H_5)_2$ (calcd. 1.884–1.885 Å) as well as $WF_6(NC_5H_5)$ and its derivatives (calcd. 1.866–1.880 Å, see Chapter 3) but are considerably elongated relative to free WF_6 (calcd. 1.839 Å) as well as $[WF_4(2,2'\text{-bipy})_2]^{2+}$ (calcd. 1.851 Å). The calculated W–N bonds (2.545–2.547 Å) in $WF_6(L)$ are longer than in any of the aforementioned WF_6 derivatives, whether neutral or cationic (calcd. 2.290–2.480 Å). This arises due to the steric strain imposed by the bite angles of the bidentate ligands combined with the inferior Lewis acidity of neutral WF_6 relative to the cationic tungsten centres.

6.2.2.2. $[WF_5(L)]^+$ (L = 2,2′-bipy, 1,10-phen)

The geometries of the $[WF_5(L)]^+$ cations, as determined by X-ray crystallography, can be described as monocapped octahedra, in which F(1) is capping and F(5), N(1), and N(2) form the trigonal base (Figures 6.2–6.4). Alternatively, they can, perhaps more accurately, be described as 4:3 polyhedra in which four fluorido ligands form the square face and F(3), N(1), and N(2) form the triangular face (see Figure 6.5 and Section 6.2.2.3), similar to the structure of $[Mo^{II}(CNCH_3)_7]^{2+}$.[15] Gas-phase geometry optimisations reproduced the experimental geometries with only minor overestimations of the W–N bond lengths (Table 6.2). The crystal structures show weak W···F cation-anion contacts (3.085(4)–3.244(3) Å; $\Sigma_r(vdW) = 1.47(F)$[16] + 2.007(W)[17] = 3.48 Å). These contacts cap the

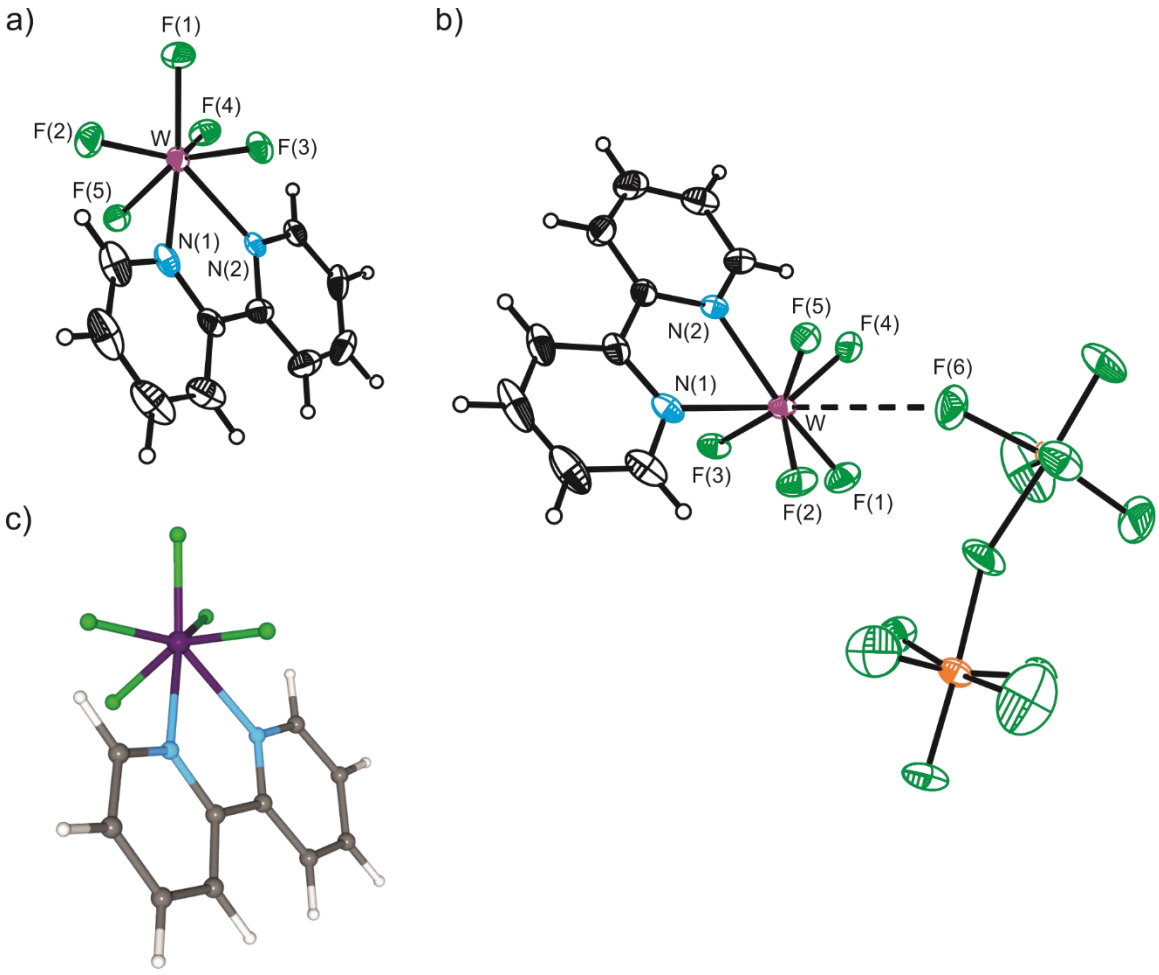

Figure 6.2. Thermal ellipsoid plots (50% probability level) of the a) cation and b) ion pair in $[WF_5(2,2'\text{-bipy})][Sb_2F_{11}]$, with c) the optimised gas-phase geometry (B3LYP/aVTZ) of $[WF_5(2,2'\text{-bipy})]^+$.

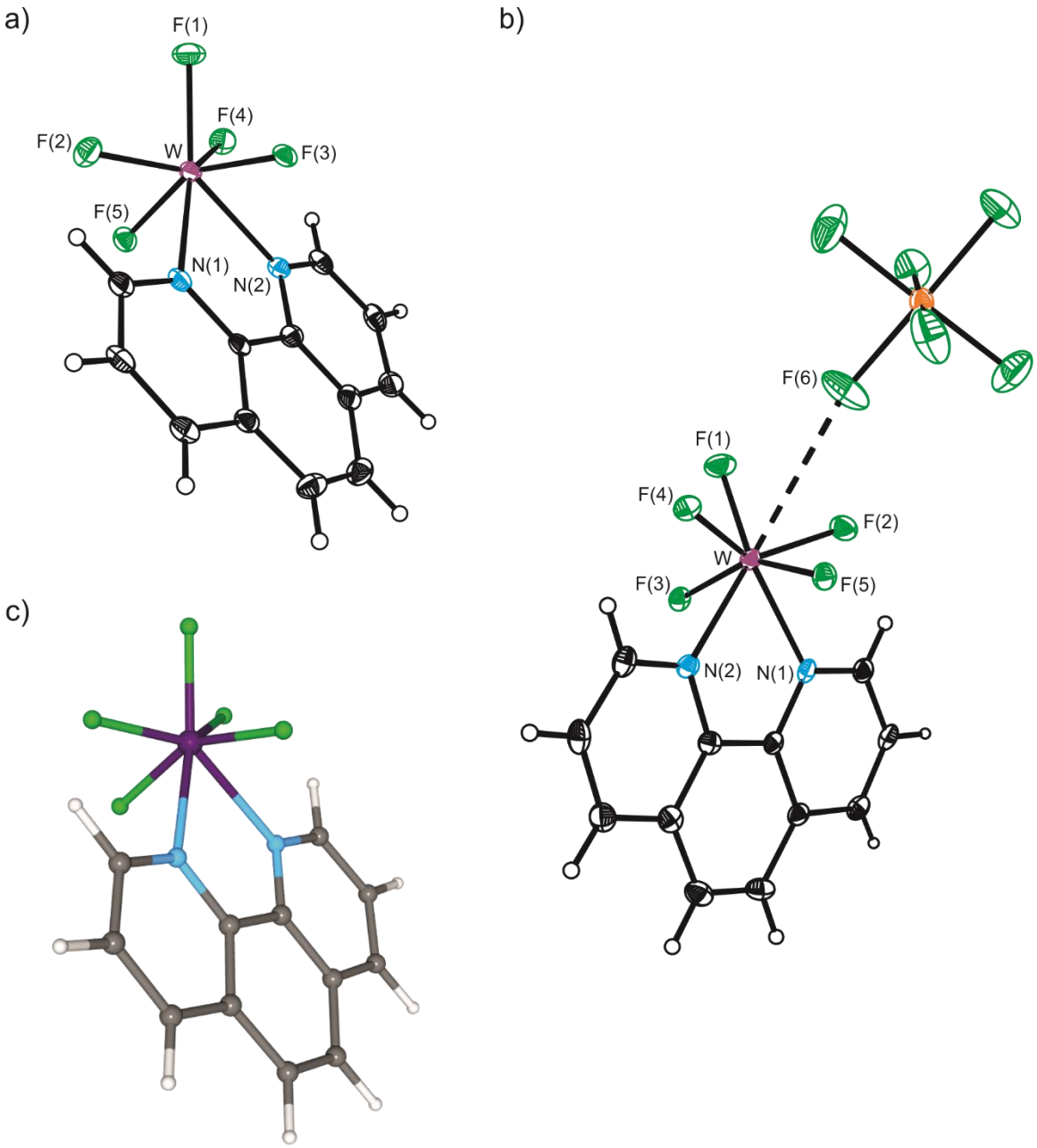

Figure 6.3. Thermal ellipsoid plots (50% probability level) of the a) cation and b) ion pair in $[WF_5(1,10\text{-phen})][SbF_6]\cdot SO_2$, with c) the optimised gas-phase geometry (B3LYP/aVTZ) of $[WF_5(1,10\text{-phen})]^+$.

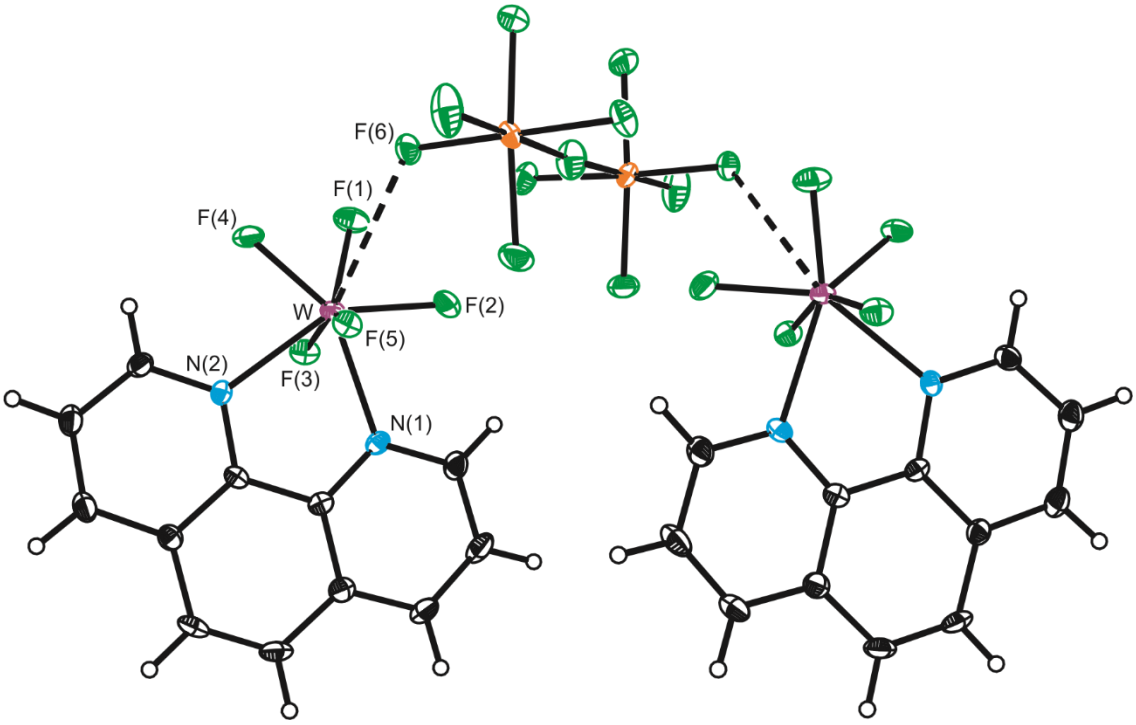

Figure 6.4. Thermal ellipsoid plot (50% probability level) of the $[\{WF_5(1,10\text{-phen})\}_2(\mu\text{-}Sb_2F_{11})]^+$ unit in $[WF_5(1,10\text{-phen})][Sb_2F_{11}]$.

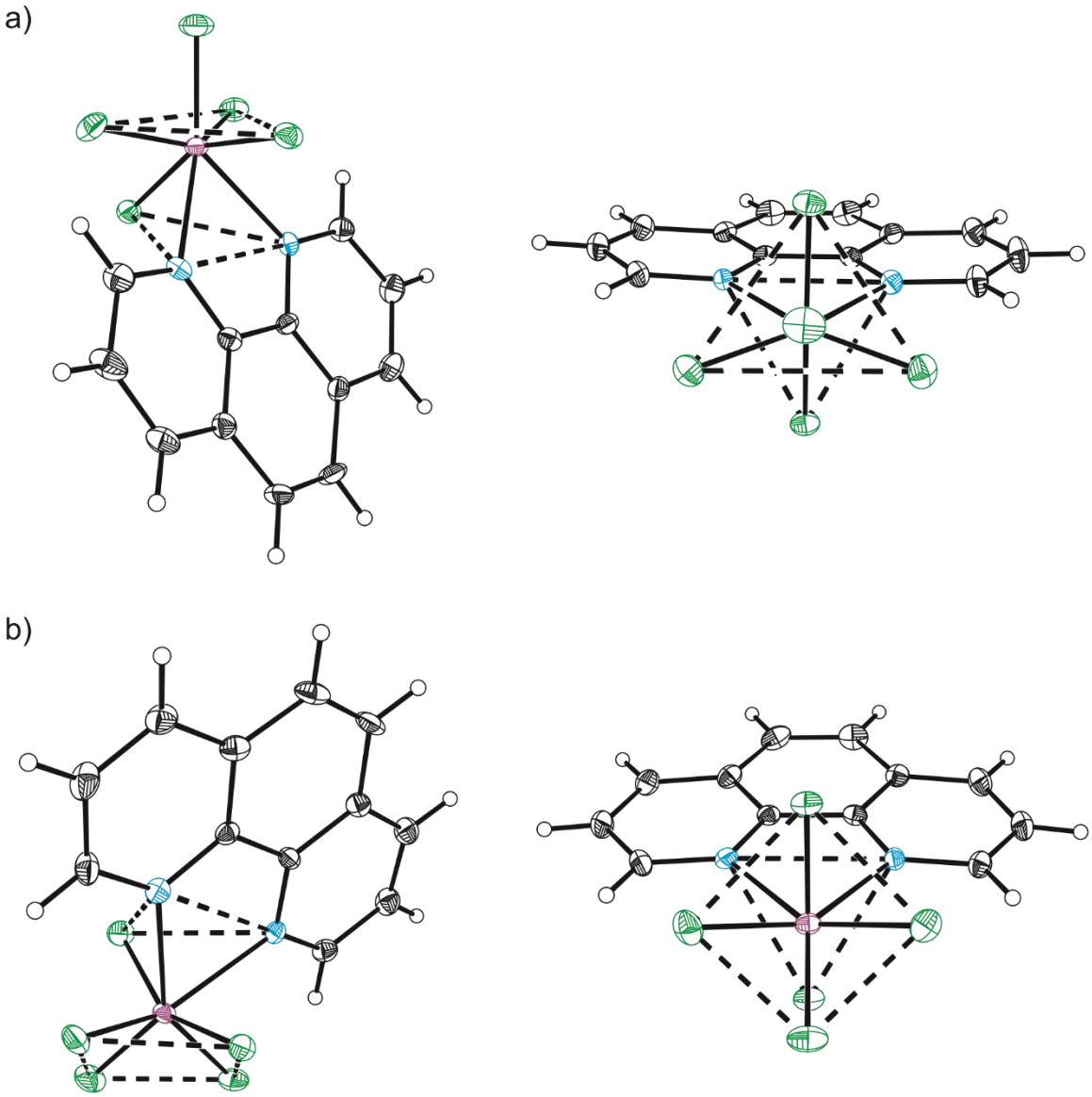

Figure 6.5. Side-on (left) and top-down (right) views of the $[WF_5(1,10\text{-phen})]^+$ cation in a) monocapped-octahedral and b) 4:3 configurations. Characteristic polygons within these configurations are drawn with dashed lines (---).

Table 6.2. Selected Experimental and Calculated[a] Bond Lengths (Å) and Angles (°) of $[WF_5(2,2'\text{-bipy})]^+$ and $[WF_5(1,10\text{-phen})]^+$

	$[WF_5(2,2'\text{-bipy})]^+$		**$[WF_5(1,10\text{-phen})]^+$**		
	exptl	**calcd**	**exptl[b]**	**exptl[c]**	**calcd**
W–F(1)	1.854(3)	1.844	1.860(2)	1.861(3)	1.844
W–F(2)	1.842(3)	1.846	1.842(2)	1.844(3)	1.848
W–F(3)	1.842(3)	1.844	1.8377(19)	1.853(2)	1.843
W–F(4)	1.838(3)	1.846	1.852(2)	1.832(3)	1.848
W–F(5)	1.850(3)	1.850	1.8459(18)	1.856(2)	1.848
W–N(1)	2.234(4)	2.290	2.240(3)	2.223(4)	2.294
W–N(2)	2.224(4)	2.290	2.230(3)	2.229(3)	2.294
W···F(6)	3.085(4)		3.167(2)	3.244(3)	
F(1)–W–F(2)	77.56(15)	77.7	77.64(10)	77.95(12)	77.6
F(1)–W–F(3)	80.71(14)	82.7	80.54(9)	80.17(11)	83.2
F(1)–W–F(4)	78.14(15)	77.7	76.99(10)	78.52(12)	77.6
F(1)–W–F(5)	129.41(14)	126.9	128.78(9)	129.91(11)	125.9
F(1)–W–N(1)	136.61(16)	138.1	137.30(10)	133.24(12)	138.2
F(1)–W–N(2)	136.65(16)	138.1	136.14(10)	137.42(12)	138.2
F(2)–W–N(1)	75.35(16)	74.9	74.75(10)	74.75(12)	74.2
F(3)–W–N(1)	75.89(14)	76.1	76.70(9)	75.65(11)	76.2
F(4)–W–N(1)	144.27(15)	143.1	144.72(10)	146.74(12)	143.1
F(5)–W–N(1)	79.02(14)	79.8	79.29(9)	82.09(12)	80.2
N(1)–W–N(2)	71.53(15)	70.4	72.30(10)	72.45(13)	70.9

[a]Calculated at the B3LYP/aVTZ level of theory. [b]From $[WF_5(1,10\text{-phen})][Sb_2F_{11}]$. [c]From $[WF_5(1,10\text{-phen})][SbF_6]\cdot SO_2$.

square face of the 4:3 polyhedron, resulting in a "monocapped-4:3" coordination sphere that does not otherwise conform to the archetypal octacoordinate geometries.[18] Crystallographic data collection and refinement parameters are provided in the Appendix (Table D.1).

While discrete ion pairs with zero net charge are found in $[WF_5(2,2'\text{-bipy})][Sb_2F_{11}]$ and $[WF_5(1,10\text{-phen})][SbF_6]\cdot SO_2$ (Figures 6.2 and 6.3), in $[WF_5(1,10\text{-phen})][Sb_2F_{11}]$, the ions aggregate to form $[\{WF_5(1,10\text{-phen})\}_2(\mu\text{-}Sb_2F_{11})]^+$ units (Figure 6.4) with one equivalent of non-coordinated $[Sb_2F_{11}]^-$ acting as the counterion. The bridging anion adopts a pseudo-D_{4h}-symmetric geometry. Similar coordination motifs for $[Sb_nF_{5+n}]^-$ (n = 1, 2) have been observed in crystallographic studies of Brønsted-superacidic systems; pseudo-D_{4h}-symmetric, bridging $[Sb_2F_{11}]^-$ anions were observed in $[H_3F_2][Sb_2F_{11}]$[19] while $[(CH_3)_2COH\cdots SbF_6\cdots HOC(CH_3)_2]^+$ units were observed in $[(CH_3)_2COH][SbF_6]$.[20]

The bonds and angles within the WF_5N_2 moieties differ only marginally, if at all, beyond experimental error (3σ) between the cations and any such differences are likely a consequence of crystal packing effects. The W–F bond lengths lie, on average (*ca*. 1.84 Å), between those of crystalline WF_6 (1.8261(13)–1.8266(19) Å)[21] and the known heptacoordinate WF_6 adducts (*ca*. 1.87 Å),[22] illustrating a compromise between increased Lewis acidity at the cationic tungsten centre and increased steric repulsion with respect to WF_6. Comparisons to $[WF_4(2,2'\text{-bipy})_2]^{2+}$ (1.836(4) Å)[9] and $[WF_4(dmpb)_2]^{2+}$ (1.91(4)–1.93(4) Å) reveal no appreciable differences in W−F bond lengths,[10] though these bonds are significantly elongated in the arsenic analogue, $[WF_4(dmab)_2]^{2+}$ (2.114(6) Å).[10] The W–N bonds, meanwhile, are similar to those of $WF_6(NC_5H_5)$ and its derivatives (*ca*. 2.25 Å, see Chapter 3) and $[WF_4(2,2'\text{-bipy})_2]^{2+}$ (2.263(7) Å),[9] but much shorter than in

$WF_6(NC_5H_5)_2$ (2.344(6) Å).[14] The calculated W–F (*ca*. 1.85 Å) and W–N (*ca*. 2.29 Å) bond lengths of $[WF_5(L)]^+$ are contracted with respect to those of $WF_6(L)$.

The crystal structure of $[WF_5(1,10\text{-phen})][SbF_6]\cdot SO_2$ consists of $[WF_5(1,10\text{-phen})][SbF_6]$ ions that pair in a similar manner to those of $[WF_5(2,2'\text{-bipy})][Sb_2F_{11}]$, as well as discrete SO_2 molecules. The solvent molecules are encapsulated between the cations and anions such that there exist weak S···F contacts (2.892, 2.912, 3.094 Å; Σ_r(vdW) = 1.80(S) + 1.47(F) = 3.27 Å).[16] These contacts seemingly serve to secure its position within the crystal lattice such that the solvate is stable even at ambient temperature *in vacuo*.

6.2.2.3. Monocapped-Octahedral vs. 4:3 Geometries in $[WF_5(L)]^+$

Deviations from the ideal monocapped octahedron are conventionally quantified by measuring the angles α and β, which define the angle between the apical and equatorial (α) or apical and basal (β) environments (Figure 6.6a). The ideal monocapped octahedron was originally derived from $[WBr_3(CO)_4]^-$, for which α = 74.1° and β = 125.5°,[23] though more relevant comparisons to the $[WF_5(L)]^+$ cations could be made by employing $[MoF_7]^-$ and $[WF_7]^-$, for which α = 75.5(2)° and β = 131.8(2)° in both cases.[24] There is seemingly no such model 4:3 compound to make judgments of ideality.

Additional criteria can be considered, however, which are various vertex angles (θ) of polygons (internal or facial)within the complex, as well as the angle between the planes of these polygons (γ). For instance, in the ideal monocapped octahedron, which conforms to C_{3v} symmetry, the equatorial and basal ligands form parallel equilateral triangles (T_e and T_b, respectively) that are staggered (Figure 6.6b; $\theta(T_e) = \theta(T_b) = 60°$, $\gamma = 0°$). The polygons that represent the ideal 4:3 polyhedron are, more obviously, the parallel square

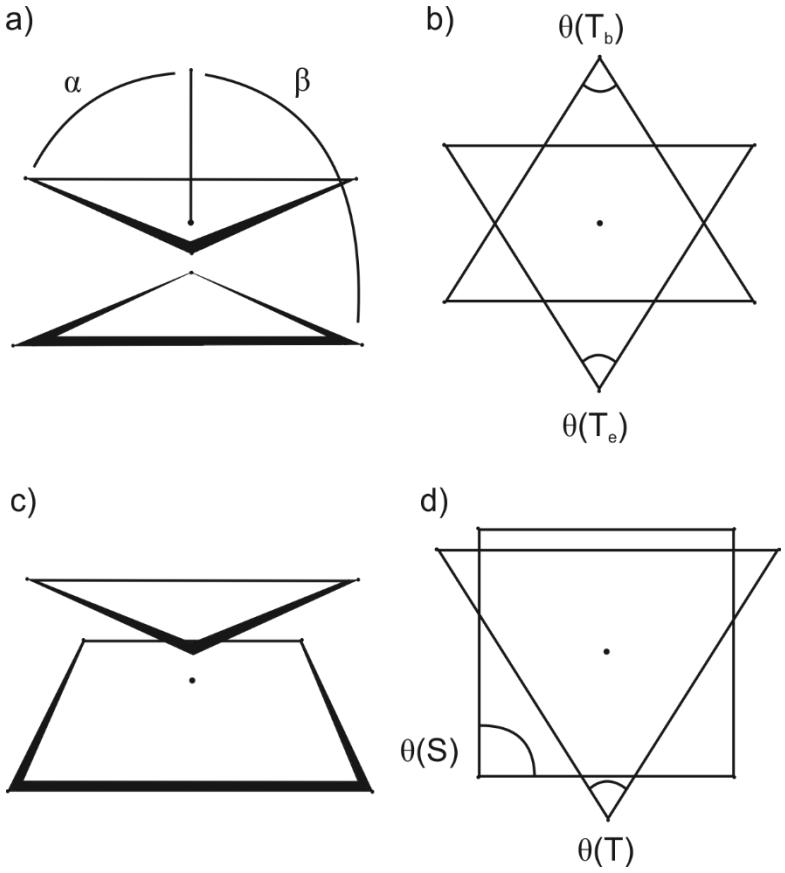

Figure 6.6. Model geometries with definitions of characteristic angles: a) monocapped octahedron, side-on; b) monocapped octahedron, top-down; c) 4:3, side-on; d) 4:3, top-down.

(S) and triangular (T) faces (Figure 6.6d; θ(S) = 90°, θ(T) = 60°, γ = 0°). An additional consideration that is specific to the 4:3 case is the degree of deviation of the fluorido ligands from the ideal square plane (σ). However, the crystal structures reveal that F(1), F(2), F(4), and F(5) reasonably approximate this plane (σ < 0.0301 Å).

Characteristic angles of the monocapped-octahedral and 4:3 configurations are provided in Tables 6.4 and 6.5, respectively. It is observed that the average α (exptl. 77.81–78.80°, calcd. 79.4–79.5°) and β (exptl. 133.52–134.22°, calcd. 134.1–134.4°) angles of the cations are slightly larger than those of the $[MoF_7]^-$ and $[WF_7]^-$ anions, but are otherwise similar to the ranges observed for a series of homoleptic complexes (α = 72–77°, β = 117–137°),[25] as well as those derived from extended-Hückel MO calculations (α = 70–84°, β = 127–138°).[26] There is little variability in the α angles, resulting in a small Δα value (see Table 6.3). However, it should be noted that in the β angles, the F(1)–W–F(5) angles (exptl. 128.78(9)–129.91(11)°, calcd. 125.9–126.9°) are appreciably less obtuse than the F(1)–W–N angles (exptl. 133.24(12)–137.42(12)°, calcd. 138.1–138.2°), resulting in a larger Δβ value.

In all structures considered, the T_e polygon formed by the equatorial ligands within the monocapped-octahedral arrangement is that which is most significantly distorted. This is most clearly illustrated by its wide F(2)–F(3)–F(4) angle (exptl. 67.5–69.4°, calcd. 69.5–70.3°), which is compensated by contractions of the other θ(T_e) angles (exptl. 54.8–57.8°, calcd. 54.8–55.2°). The T_b polygon, as well as the triangular face of the 4:3 polyhedron, reasonably approximate equilateral triangles (θ = 60 ± 2°). In addition, the γ angles in the monocapped octahedra deviate much further from parallel (exptl. 8.84(18)–9.2(2)°, calcd. 10.9–11.1°) than those of the 4:3 polyhedra (exptl. 2.3(2)–2.6(3)°, calcd. 1.9–2.0°).

Table 6.3. Characteristic Angles (°) in $[WF_5(2,2'\text{-bipy})]^+$ and $[WF_5(1,10\text{-phen})]^+$ (Monocapped-Octahedral Configuration)

	$[WF_5(2,2'\text{-bipy})]^+$		**$[WF_5(1,10\text{-phen})]^+$**		
	exptl	**calcd[a]**	**exptl[b]**	**exptl[c]**	**calcd[a]**
α[d]	78.80	79.4	78.39	77.81	79.5
$\Delta\alpha$[e]	3.15	5.0	3.55	2.22	5.6
β[f]	134.22	134.4	134.07	133.52	134.1
$\Delta\beta$[e]	7.20	11.2	8.52	7.51	12.3
F(2)–F(3)–F(4)	68.3	69.5	69.4	67.5	70.3
F(3)–F(4)–F(2)	55.3	55.2	54.6	57.8	54.8
F(4)–F(2)–F(3)	56.4	55.2	56.1	54.8	54.8
F(5)–N(1)–N(2)	60.5	60.4	59.8	58.8	60.3
N(1)–N(2)–F(5)	59.9	60.4	59.8	61.8	60.3
N(2)–F(5)–N(1)	59.6	59.1	60.3	59.4	59.3
γ[g]	9.2(2)	11.1	9.57(15)	8.84(18)	10.9

[a]Calculated at the B3LYP/aVTZ level of theory. [b]From $[WF_5(1,10\text{-phen})][Sb_2F_{11}]$. [c]From $[WF_5(1,10\text{-phen})][SbF_6]\cdot SO_2$. [d]The average of the F(1)–W–F(2), F(1)–W–F(3), and F(1)–W–F(4) angles. [e]Difference between largest and smallest angle that contribute to the average α or β value. [f]The average of the F(1)–W–F(5), F(1)–W–N(1), and F(1)–W–N(2) angles. [g]The angle between the planes formed by {F(2), F(3), F(4)} and {F(5), N(1), N(2)}.

Table 6.4. Characteristic Angles (°) in $[WF_5(2,2'\text{-bipy})]^+$ and $[WF_5(1,10\text{-phen})]^+$ (4:3 Configuration)

	$[WF_5(2,2'\text{-bipy})]^+$		**$[WF_5(1,10\text{-phen})]^+$**		
	exptl	**calcd[a]**	**exptl[b]**	**exptl[c]**	**calcd[a]**
F(1)–F(2)–F(5)	90.0	88.3	88.9	90.6	87.6
F(2)–F(5)–F(4)	87.7	88.7	87.6	87.7	89.0
F(5)–F(4)–F(1)	89.7	88.3	89.6	90.3	87.6
F(4)–F(1)–F(2)	92.5	94.3	93.7	91.3	95.1
σ^d	0.0178		0.0301	0.0097	
F(3)–N(1)–N(2)	59.2	60.4	59.8	58.2	60.3
N(1)–N(2)–F(3)	58.8	60.4	59.8	58.6	60.3
N(2)–F(3)–N(1)	62.0	59.1	60.3	63.2	59.3
γ^e	2.6(3)	1.9	2.61(16)	2.3(2)	2.0

*a*Calculated at the B3LYP/aVTZ level of theory. *b*From $[WF_5(1,10\text{-phen})][Sb_2F_{11}]$. *c*From $[WF_5(1,10\text{-phen})][SbF_6]\cdot SO_2$. *d*Root-mean-squared deviations from least-squares plane formed by F(1), F(2), F(4), and F(5). *e*The angle between the planes formed by {F(1), F(2), F(4), F(5)} and {F(3), N(1), N(2)}.

As such, the geometries of the $[WF_5(L)]^+$ cations are best described as monocapped octahedra that distort into 4:3 polyhedra, with the square faces being loosely capped by fluorido ligands of the $[Sb_nF_{5n+1}]^-$ (n = 1, 2) counterions.

6.2.3. Raman Spectroscopy

Ambient-temperature Raman spectra were recorded on solid samples of $WF_6(L)$ (Figures 6.7 and 6.8) and the $[WF_5(1,1,0\text{-phen})]^+$ salts (Figures 6.9 and 6.10), whereas that of $[WF_5(2,2'\text{-bipy})][Sb_2F_{11}]$ was recorded in SO_2 solution (*ca*. 0.8 M) as the solid was observed to fluoresce prohibitively (Figure 6.11). Assignments were made based on the calculated vibrational frequencies of the adducts and cations in addition to those of free 2,2′-bipy and 1,10-phen. Bands corresponding to $[SbF_6]^-$[27–29] and $[Sb_2F_{11}]^-$[30] were identified based on previous assignments. Generally, reasonably good agreement was observed between the experimental and calculated frequencies corresponding to the WF_6 moieties (better for the cations than the neutral adducts), whereas those of the organic moieties, including the free ligands, were typically overestimated. Complete descriptions of the vibrational frequencies are provided in the Appendix (Tables D.2–D.5).

The Raman spectra of $WF_6(L)$ exhibit characteristics similar to other octacoordinate fluoridotungsten(VI) complexes, most notably in terms of the symmetric W–F stretching frequencies (in cm^{-1}; $WF_6(2,2'\text{-bipy})$: exptl. 665, 647; calcd. 692, 661; $WF_6(1,10\text{-phen})$: exptl. 658, calcd. 688; *cf*. $WF_6(NC_5H_5)_2$: exptl. 661,[14] calcd. 673; $[WF_4(2,2'\text{-bipy})_2]^{2+}$: exptl. 678, 645;[9] calcd. 684, 650). The frequencies of these bands are invariably lower than that of free WF_6 (exptl. 771,[31] calcd. 759). In $WF_6(2,2'\text{-bipy})$, two modes with $\nu_s(WF_6)$ character are observed due to in-phase and out-of-phase coupling with an in-plane deformation of 2,2′-bipy, which was also observed for $[WF_4(2,2'\text{-bipy})_2]^{2+}$ and

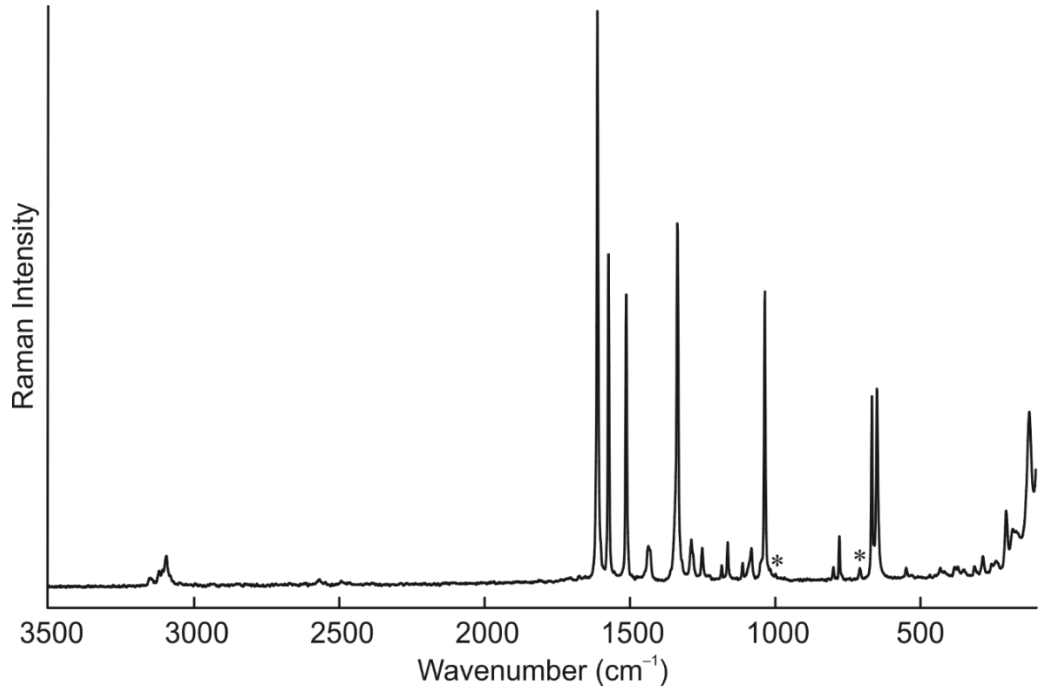

Figure 6.7. Raman spectrum of solid WF_6(2,2′-bipy), recorded at ambient temperature. Asterisks (*) denote an impurity of [2,2′-bipy-H][WF_7].

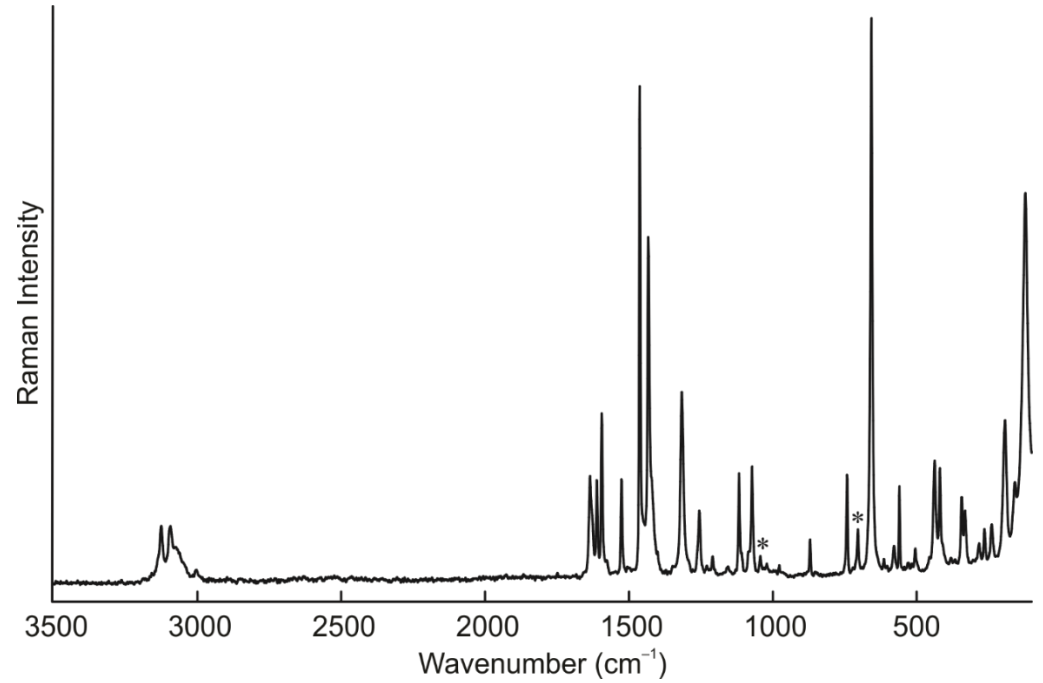

Figure 6.8. Raman spectrum of solid WF_6(1,10-phen), recorded at ambient temperature. Asterisks (*) denote an impurity of [1,10-phen-H][WF_7].

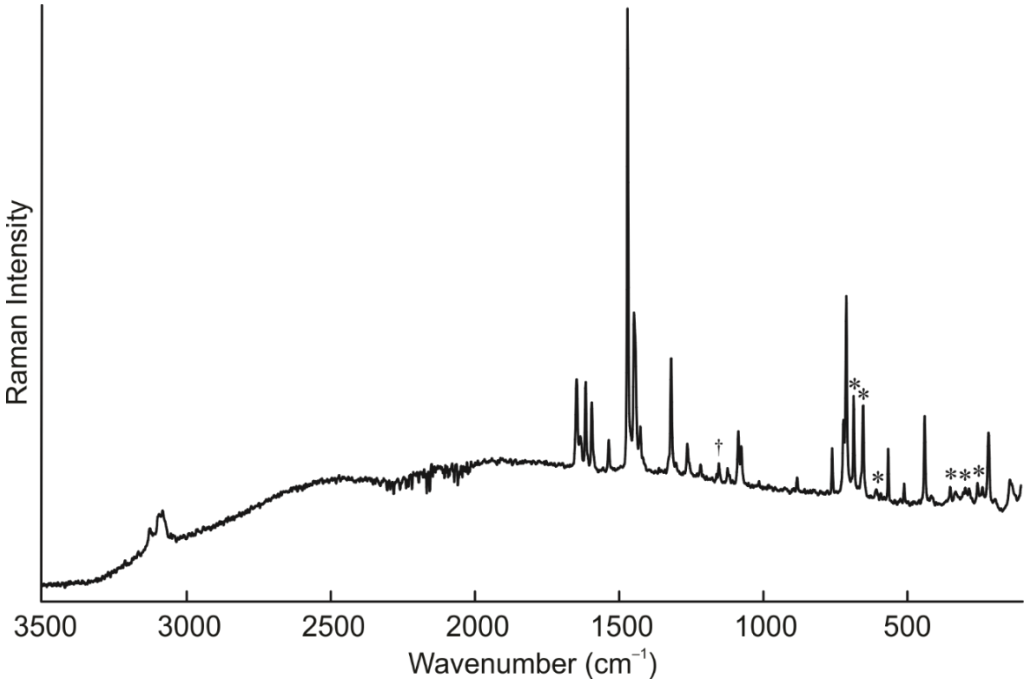

Figure 6.9. Raman spectrum of $[WF_5(1,10\text{-phen})][Sb_2F_{11}]$, recorded at ambient temperature. Asterisks (*) and dagger (†) denote bands corresponding to the $[Sb_2F_{11}]^-$ anion and residual SO_2, respectively.

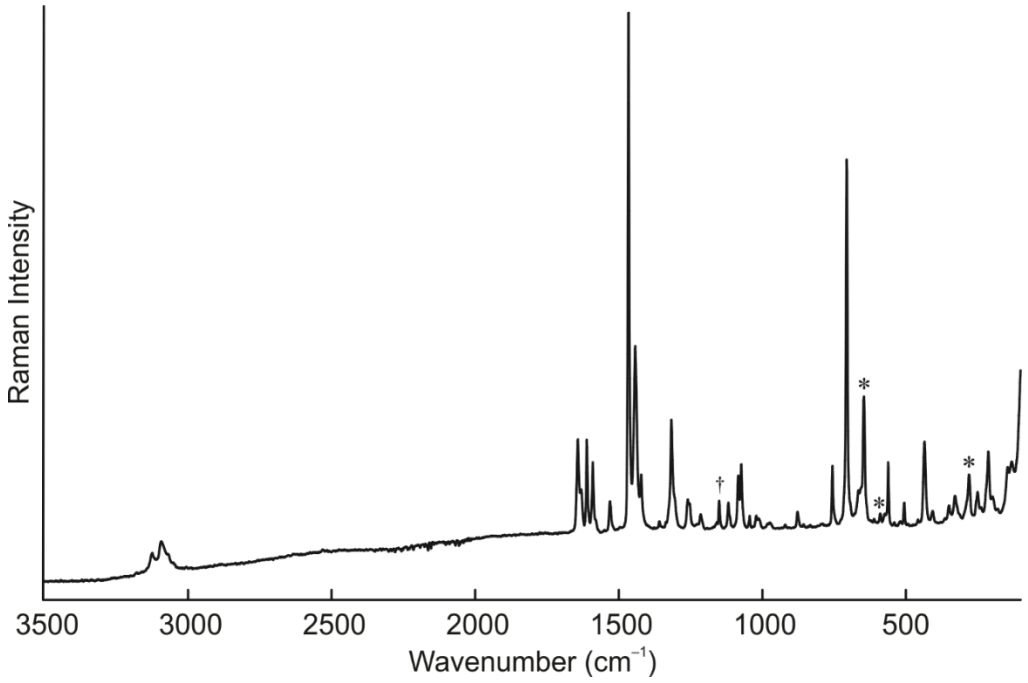

Figure 6.10. Raman spectrum of $[WF_5(1,10\text{-phen})][SbF_6]\cdot SO_2$, recorded at ambient temperature. Asterisks (*) and dagger (†) denote bands corresponding to the $[SbF_6]^-$ anion and SO_2, respectively.

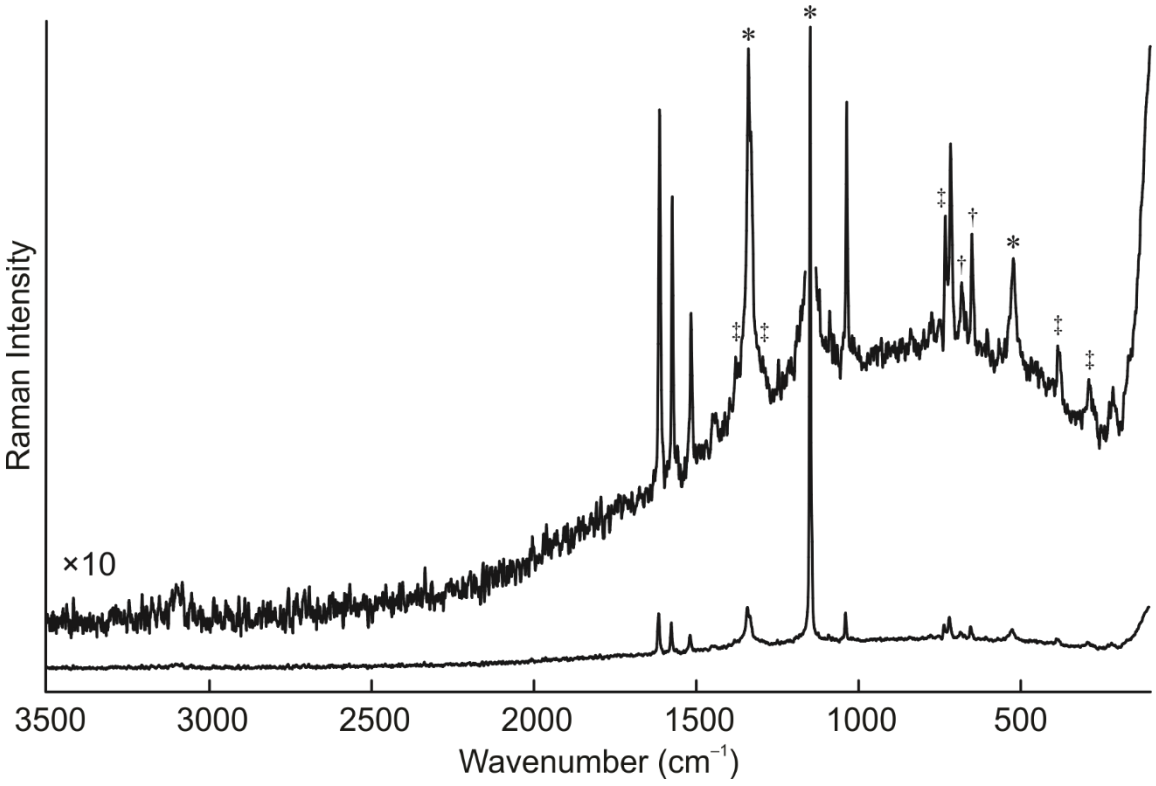

Figure 6.11. Raman spectrum of $[WF_5(2,2'\text{-bipy})][Sb_2F_{11}]$ (*ca*. 0.8 M in SO_2), recorded at ambient temperature. Asterisks (*), daggers (†), and double daggers (‡) denote bands corresponding to SO_2, the $[Sb_2F_{11}]^-$ anion, and the FEP sample tube, respectively.

verified by assignment of the calculated vibrational frequencies. However, the observed equal-intensity distribution of these bands was not reproduced computationally, suggesting a disparity between the actual and predicted degrees of vibrational coupling between the WF_6 and 2,2′-bipy moieties. For WF_6(1,10-phen), significant vibrational coupling between the WF_6 and 1,10-phen moieties was not predicted nor observed, and the symmetric W–F stretching band is distinct.

The systematic overestimation of $\nu_s(WF_6)$ in the calculations suggests that the W–F bond lengths are underestimated. This can be rationalised by a complementary overestimation of the W–N bonds, which was observed for the compounds whose structures are known experimentally (Table 6.1). The weaker W–N interactions in the predicted geometries resulted in less polarisation of the W–F bonds and therefore stretching frequencies that are higher than in the experimental spectra.

In the solid-state Raman spectra of $[WF_5(1,10\text{-phen})][Sb_2F_{11}]$ and $[WF_5(1,10\text{-phen})][SbF_6]\cdot SO_2$, as well as that of $[WF_5(2,2'\text{-bipy})][Sb_2F_{11}]$ in SO_2 solution, bands corresponding to $\nu_s(WF_5)$ are observed in the region typical for W–F stretching in heptacoordinate fluoridotungsten(VI) complexes (*cf*. $WF_6(NC_5H_5)$: exptl. 705, calcd. 702)[22] and are heavily red-shifted in comparison to the symmetric W–F stretching frequencies of free $[WF_5]^+$ (calcd. 814) and WF_6. In $[WF_5(1,10\text{-phen})][SbF_6]\cdot SO_2$, a single band attributed to $\nu_s(WF_5)$ is observed at 707 cm^{-1} (calcd. 720), whereas in solvated $[WF_5(2,2'\text{-bipy})][Sb_2F_{11}]$, the band is observed at 716 cm^{-1} (calcd. 724). In $[WF_5(1,10\text{-phen})][Sb_2F_{11}]$, two bands are observed at 717 and 707 cm^{-1}, which is attributed to vibrational coupling between the two WF_5 moieties within the $[\{WF_5(1,10\text{-phen})\}_2(\mu\text{-}Sb_2F_{11})]^+$ unit of the crystal structure. The splitting of several other bands in the Raman

spectrum of $[WF_5(1,10\text{-phen})][Sb_2F_{11}]$ is similarly attributed to vibrational coupling between cations.

The stretching modes of 2,2′-bipy and 1,10-phen, most notably the symmetric ring-breathing modes, are blue-shifted in both the neutral and cationic complexes with respect to the free ligands. In $WF_6(2,2'\text{-bipy})$, this mode is observed at 1033 cm^{-1} (calcd 1033), which is shifted from 995 cm^{-1} (calcd. 1010) in the free ligand. Interestingly, despite the stronger W–N bond in $[WF_5(2,2'\text{-bipy})]^+$, the difference in frequencies for the ring-breathing mode between the two complexes is effectively negligible (exptl. 1036, calcd. 1048). The same trends are observed for the 1,10-phen analogues (WF_6(1,10-phen): exptl. 1085, 1073; calcd. 1084; $[WF_5(1,10\text{-phen})]^+$: exptl. 1083, 1072; calcd. 1097). It should be noted that the symmetric ring-breathing modes of the 1,10-phen complexes and free 1,10-phen (exptl. 1039, 1035; calcd. 1058) are invariably split in the experimental Raman spectra, the origin of which is not fully understood.

A band attributable to the W–N stretching modes could only be identified for $[WF_5(1,10\text{-phen})][SbF_6]\cdot SO_2$ at 214 cm^{-1} (calcd. 198, 195). The W–N stretching frequencies of $WF_6(NC_5H_5)$ and its derivatives were also observed to be underestimated as a result of an overestimation of the corresponding bond lengths.

6.2.4. Fluorine-19 NMR Spectroscopy

The ^{19}F NMR spectra of $[WF_5(L)][Sb_2F_{11}]$ and $[WF_5(1,10\text{-phen})][SbF_6]$ in SO_2 are comprised of broad singlets at 206 (L = 2,2′-bipy; $\Delta\nu_{½}$ = 15 Hz) and 204 ppm (Figure 6.12; L = 1,10-phen; $\Delta\nu_{½}$ = 140 Hz). These are much higher in frequency than free WF_6 (167 ppm), consistent with highly electron-poor tungsten centres and a fluxional coordination environment. Cooling to –70 °C did not suppress exchange, though $[WF_5(1,10\text{-phen})]^+$ was

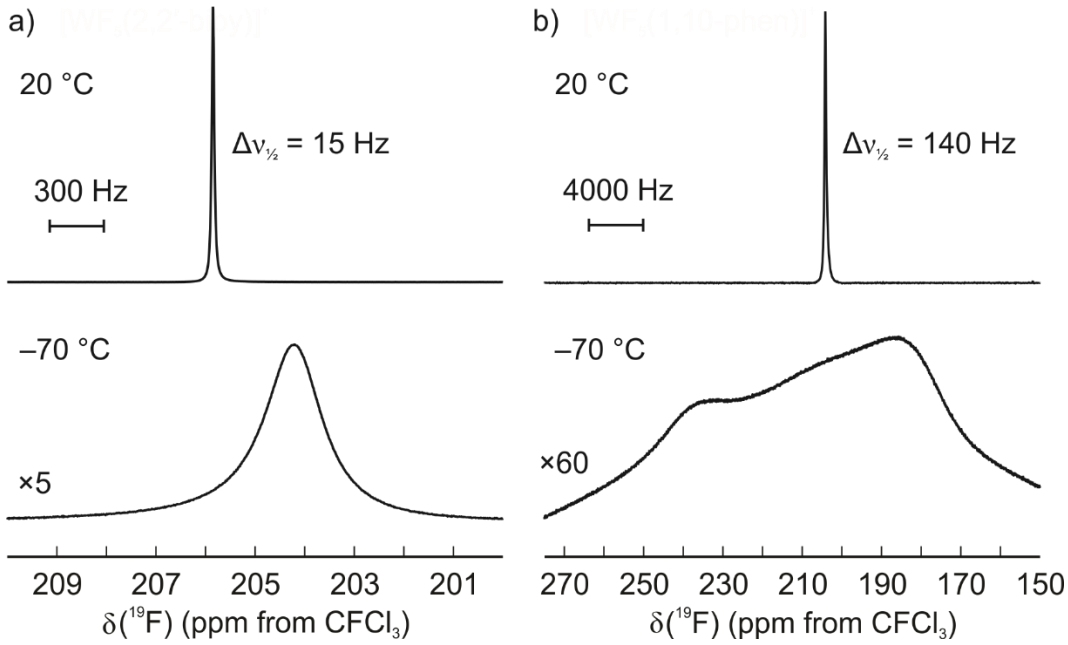

Figure 6.12. Fluorine-on-tungsten resonances in the ^{19}F NMR spectra of a) $[WF_5(2,2'\text{-bipy})][Sb_2F_{11}]$ and b) $[WF_5(1,10\text{-phen})][Sb_2F_{11}]$, recorded in SO_2 at 20 (top) and −70 °C (bottom).

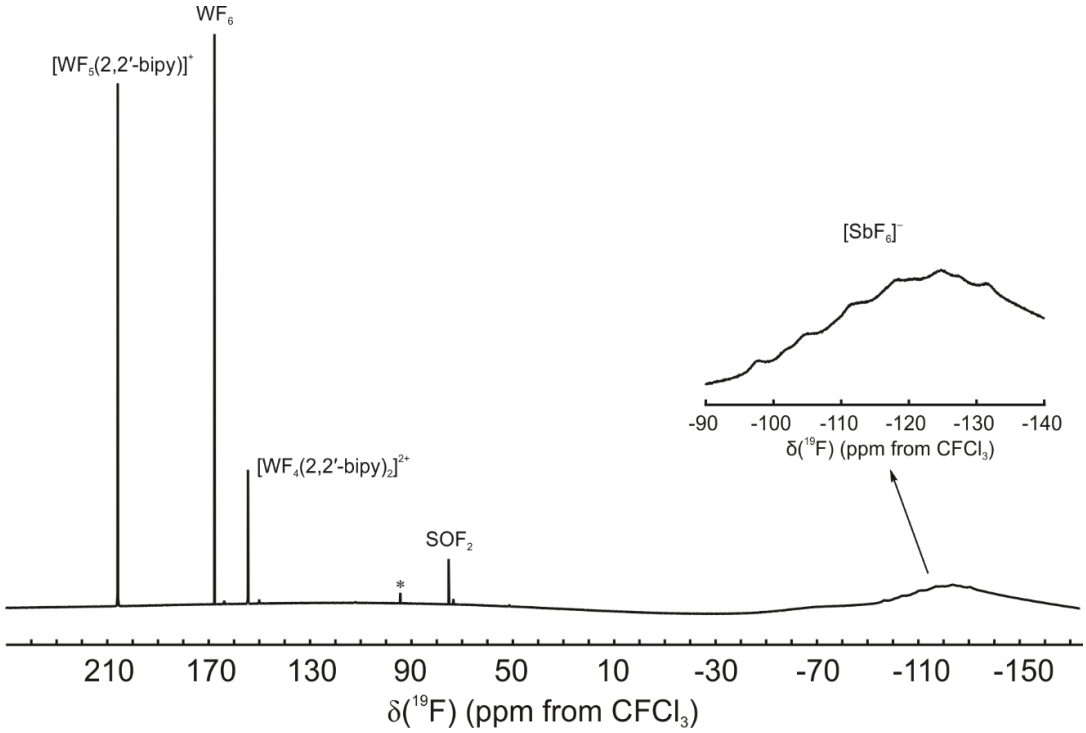

Figure 6.13. Fluorine-19 NMR spectrum of WF_6(2,2′-bipy) and SbF_5(OSO) (1.0:1.1), recorded in SO_2 at 20 C. Asterisk (*) denotes an unknown impurity.

observed to reach the coalescence point (Figure 6.12b).

The fluorine-on-tungsten regions in the ^{19}F NMR spectra of *ca*. 1:1 mixtures of WF_6(2,2′-bipy) and SbF_5(OSO) in SO_2 consist of varying proportions of $[WF_5(2,2'\text{-bipy})]^+$, WF_6, and $[WF_4(2,2'\text{-bipy})_2]^{2+}$ (Figure 6.13 and Eq. 6.4). The equilibrium between these three species is established quickly and does not change after 24 h at ambient temperature nor 1 h at 45 °C. In a sample containing the reagents in a molar ratio of 1.0:1.0, the relative molar ratio of $[WF_5(2,2'\text{-bipy})]^+$:$WF_6$:$[WF_4(2,2'\text{-bipy})_2]^{2+}$ was found to be 1.00:0.73:0.95, respectively. The loss of WF_6 is due to solvolysis over the course of 24 h to afford 0.23 molar equivalents each of WOF_4(OSO) and SOF_2 with respect to $[WF_5(2,2'\text{-bipy})]^+$ (Eq. 6.5). The slight excess of WF_6 with respect to $[WF_4(2,2'\text{-bipy})_2]^{2+}$ could be due to the impurity of $[WF_7]^-$ in the WF_6(2,2′-bipy), from which F^- would be readily abstracted by SbF_5(OSO) (Eq. 6.6). If the reagents are present in a ratio of 1.0:1.1, then the distribution of the three primary products was found to be 1.00:0.20:0.18 (Figure 6.13), reflecting increased stabilisation of $[WF_5(2,2'\text{-bipy})]^+$ by the partial formation of $[Sb_2F_{11}]^-$.

$$2[WF_5(2,2'\text{-bipy})]^+ \rightleftharpoons WF_4(2,2'\text{-bipy})_2]^{2+} + WF_6 \quad (6.4)$$

$$WF_6 + 2SO_2 \rightarrow WOF_4(OSO) + SOF_2 \quad (6.5)$$

$$[WF_7]^- + SbF_5(OSO) \rightarrow WF_6 + [SbF_6]^- + SO_2 \quad (6.6)$$

While a suspension of sparingly soluble $[WF_5(1,10\text{-phen})][SbF_6]\cdot SO_2$ in SO_2 reveals only small amounts of $[WF_4(1,10\text{-phen})_2]^{2+}$ and WF_6 at ambient temperature (Figure 6.14), heating to 45 °C results in increased proportions of the dismutation products. This indicates that the dismutation of $[WF_5(2,2'\text{-bipy})]^+$ is facilitated by the lability of 2,2′-bipy via rotation about the C–C′ bond, and that $[WF_5(1,10\text{-phen})]^+$ is better stabilised by the increased rigidity of 1,10-phen.

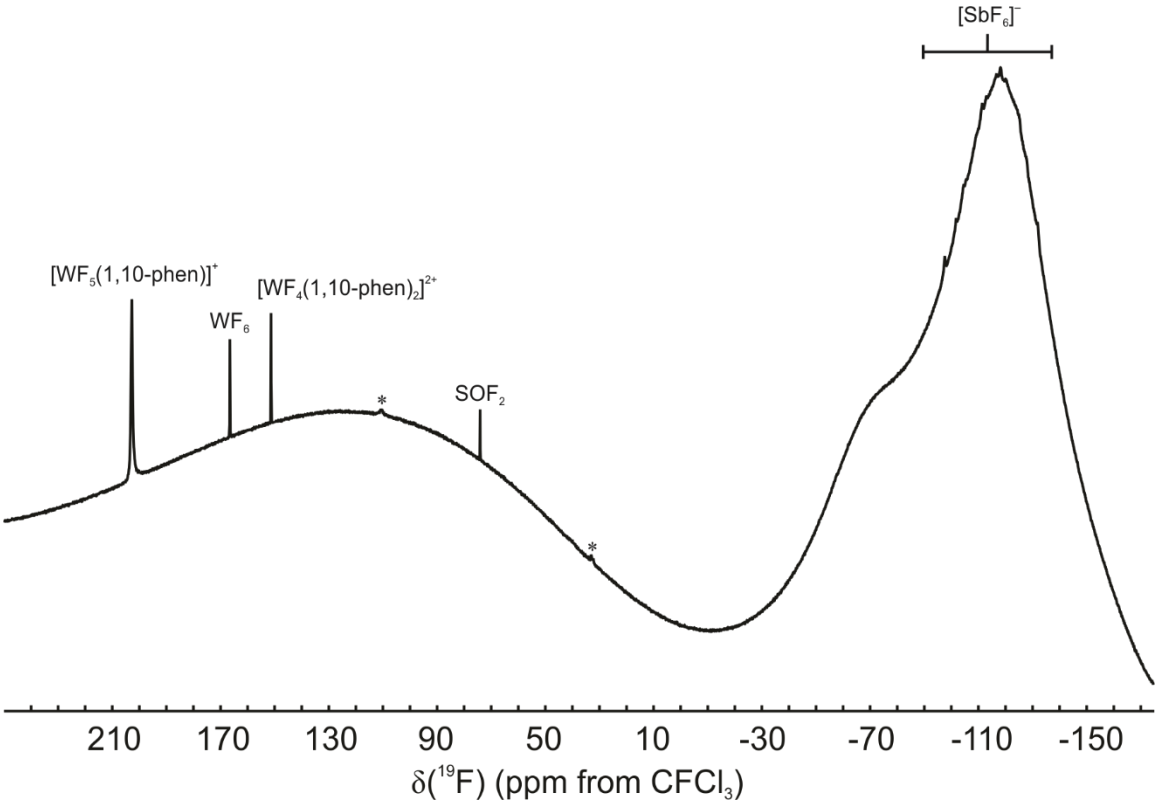

Figure 6.14. Fluorine-19 NMR spectrum of $[WF_5(1,10\text{-phen})][SbF_6]\cdot SO_2$, recorded in SO_2 at 20 °C. Asterisks (*) denote unknown impurities.

$$2[WF_5(2,2'\text{-bipy})]^+ \rightleftharpoons WF_4(2,2'\text{-bipy})_2]^{2+} + WF_6 \quad (6.4)$$

As such, it is postulated that $[WF_5(B')]^+$ is formed as an intermediate in the ligand-induced autoionisation of WF_6, but is destabilised by the relatively fluorobasic $[WF_7]^-$ anion, resulting in quantitative conversion to $[WF_4(B')_2]^{2+}$. Substitution of $[WF_7]^-$ with $[SbF_6]^-$ is sufficient to achieve a stable equilibrium between the mono- and dications, whereas $[Sb_2F_{11}]^-$ is required to fully stabilise the monocation.

6.2.5. Computational Results

6.2.5.1. Optimised Geometries of $[WF_5]^+$

Two geometries of $[WF_5]^+$ without stabilising ligands were optimised (Figure 6.15): trigonal-bipyramidal (D_{3h}) and square-pyramidal (C_{4v}). It was found that the C_{4v}-symmetric stereoisomer is 9 kJ mol^{-1} higher in energy, illustrating a low energy barrier for the Berry pseudorotation of D_{3h}-symmetric $[WF_5]^+$ (*cf*. PF_5: 16 ± 2 kJ mol^{-1},[32] $[Co(CO)_5]^+$: 8.5 kJ mol^{-1}).[33] The W–F bonds of the ground-state geometry (calcd. F_{eq}: 1,782, F_{ax}: 1.810 Å) are significantly contracted with respect to free WF_6 (calcd. 1.839 Å).

6.2.5.2. Molecular Orbitals

Molecular-orbital calculations reveal that the HOMO-LUMO transitions of $WF_6(L)$ and $[WF_5(L)]^+$ are LMCT in nature (Table 6.5, Figures 6.16–6.19). Meanwhile, the LUMO of free, trigonal-bipyramidal $[WF_5]^+$ consists of $\pi(d_{xz/yz}(W)\text{-}p_{x/y}(F))$ interactions that are antibonding in nature and the HOMO is non-bonding (Figure 6.20). Like that observed for $[W(NC_6F_5)F_5]^-$, the HOMO-LUMO transition energies seem to be minorly overestimated based on the observed colours of the complexes. In addition, the relative LUMO energies indicate that while $WF_6(L)$ are weaker oxidising agents than free WF_6, the cations are significantly stronger. The W–N bonding MOs comprise $\sigma(d(W)\text{-}p(N))$ interactions in

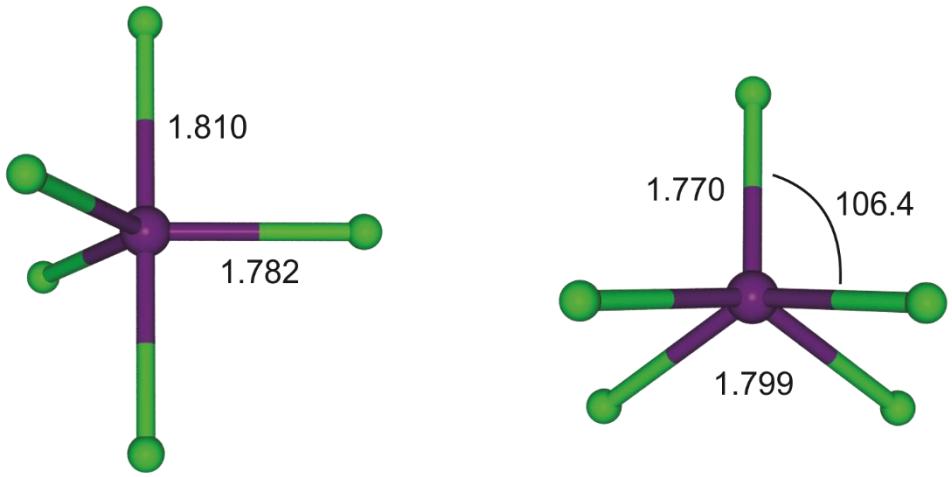

Figure 6.15. Optimised gas-phase geometries (B3LYP/aVTZ) of D_{3h}- (left) and b) C_{4v}-symmetric (right) $[WF_5]^+$. Bond lengths and angles are given in Ångstroms and degrees, respectively.

Table 6.5. Selected MO Energies (eV), HOMO-LUMO Energy Gaps (ΔE), and Colours of Various Fluoridotungsten(VI) Complexes[a]

	E_{HOMO}	E_{LUMO}	ΔE		Colour
			eV	nm	
WF_6	–12.49	–4.83	7.66	162	colourless
$[WF_5]^+$ (D_{3h})	–19.05	–11.20	7.85	158	—
$[WF_5]^+$ (C_{4v})	–18.58	–11.18	7.40	168	—
$WF_6(NC_5H_5)_2$	–7.89	–2.81	5.08	244	colourless
WF_6(2,2′-bipy)	–7.77	–2.96	4.81	258	yellow
WF_6(1,10-phen)	–7.59	–2.94	4.65	267	beige
$[WF_5$(2,2′-bipy)$]^+$	–11.42	–7.50	3.92	316	yellow
$[WF_5$(1,10-phen)$]^+$	–11.09	–7.43	3.66	339	orange
$[WF_4(2,2'\text{-bipy})_2]^{2+}$	–13.21	–10.02	3.19	389	orange

[a]Calculated at the B3LYP/aVTZ level of theory.

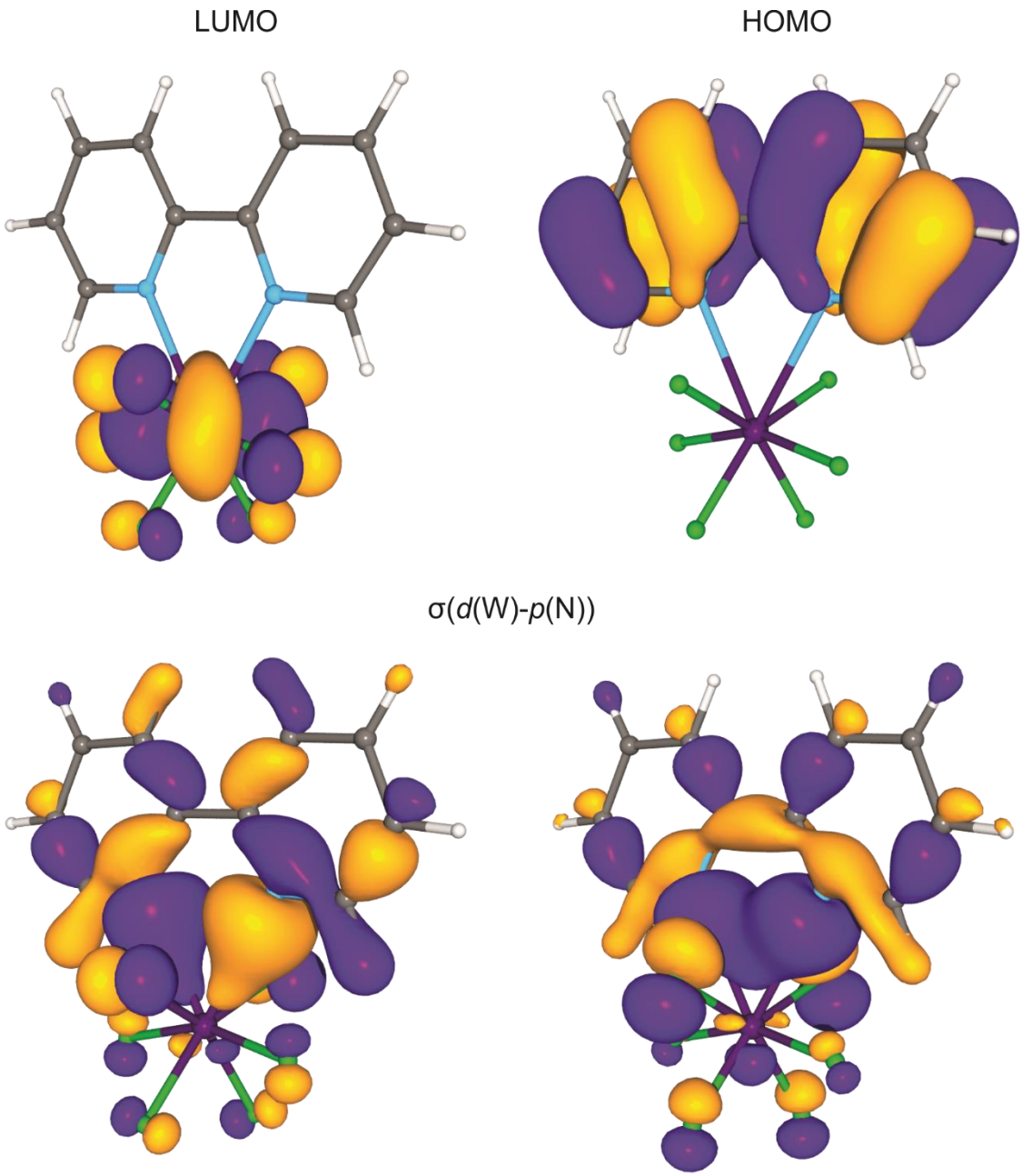

Figure 6.16. Selected MOs of WF_6(2,2′-bipy). Isosurface values are drawn at 0.04 e $Å^{-3}$.

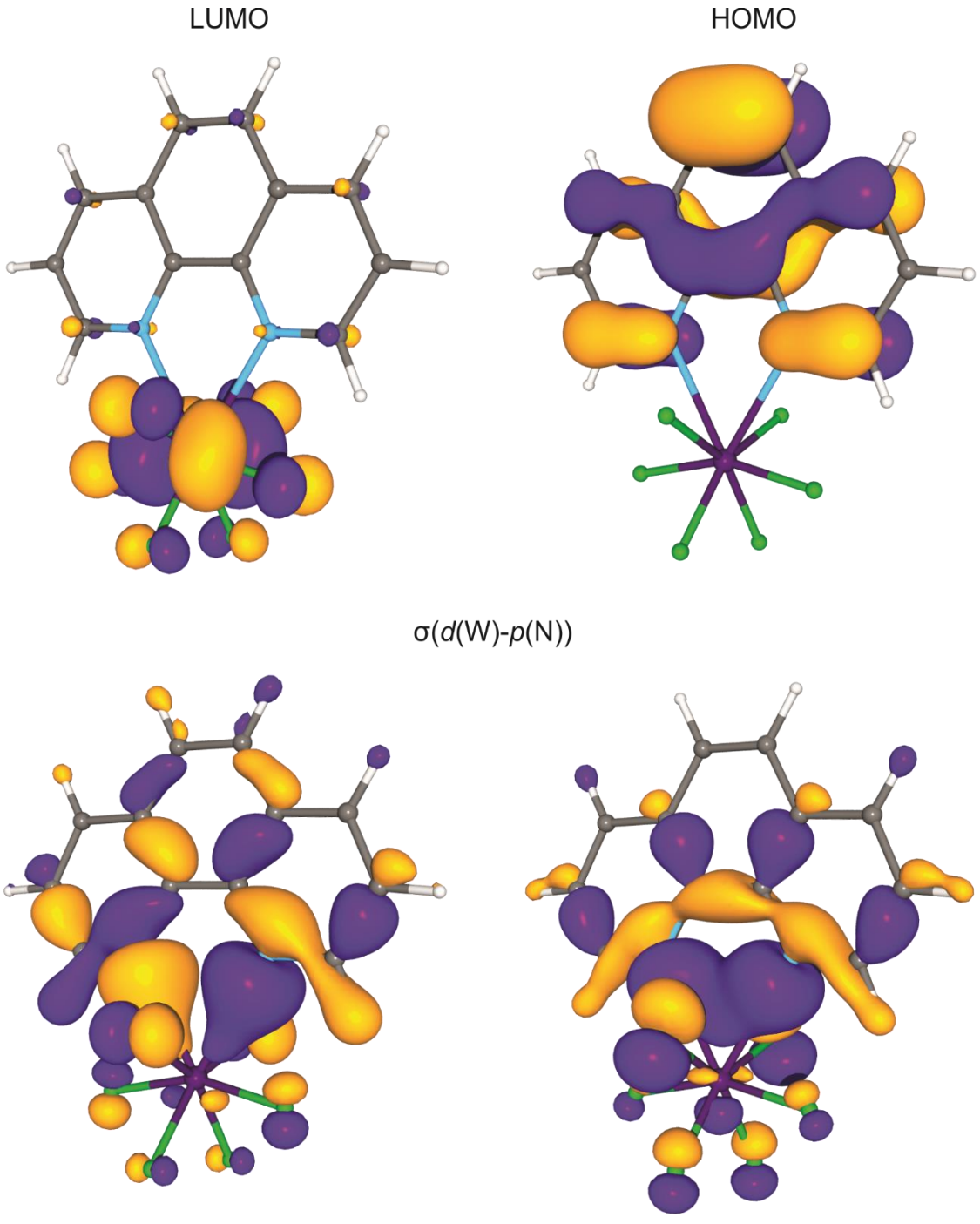

Figure 6.17. Selected MOs of WF_6(1,10-phen). Isosurface values are drawn at 0.04 e $Å^{-3}$.

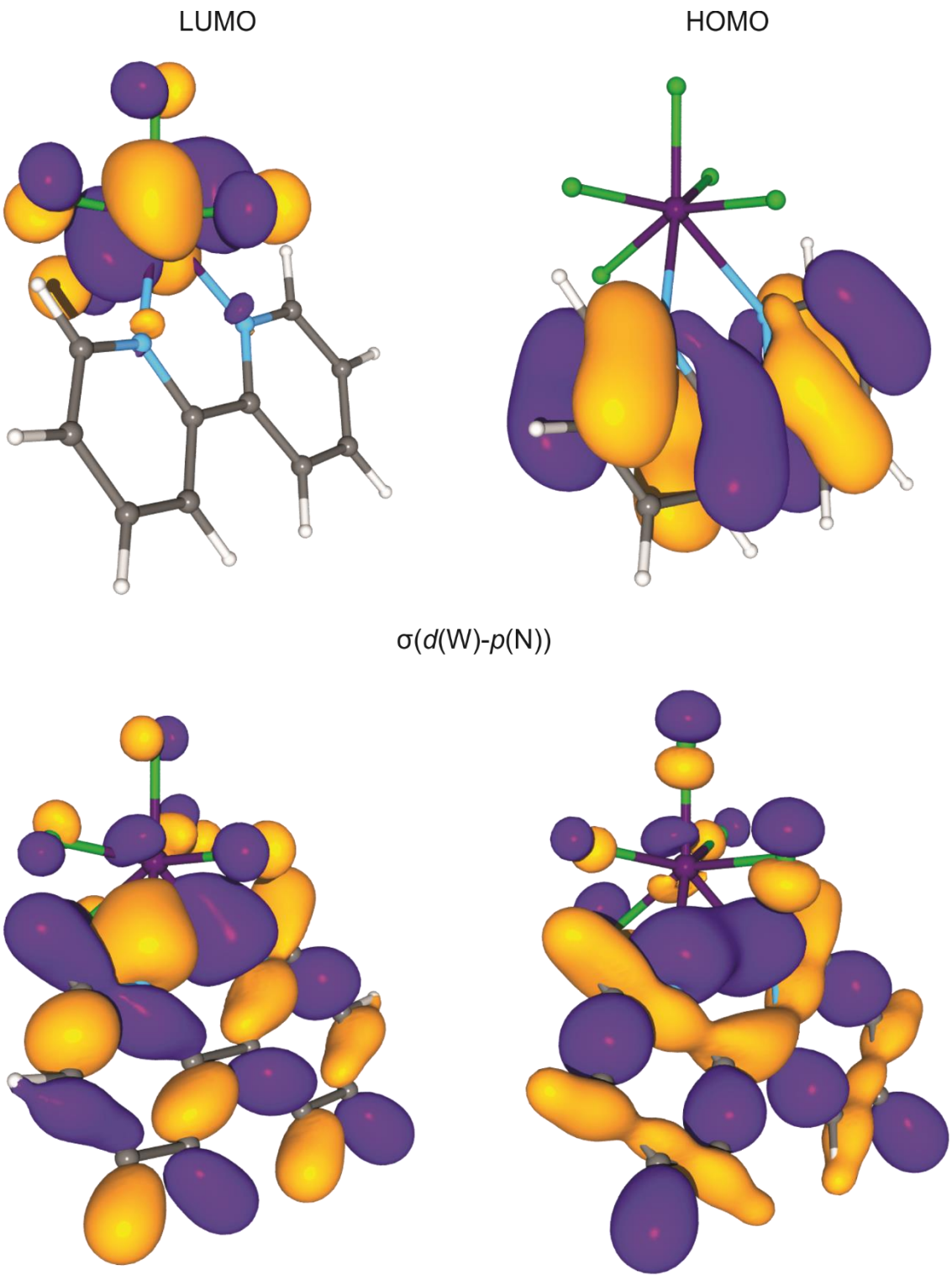

Figure 6.18. Selected MOs of $[WF_5(2,2'\text{-bipy})]^+$. Isosurface values are drawn at 0.04 e $Å^{-3}$.

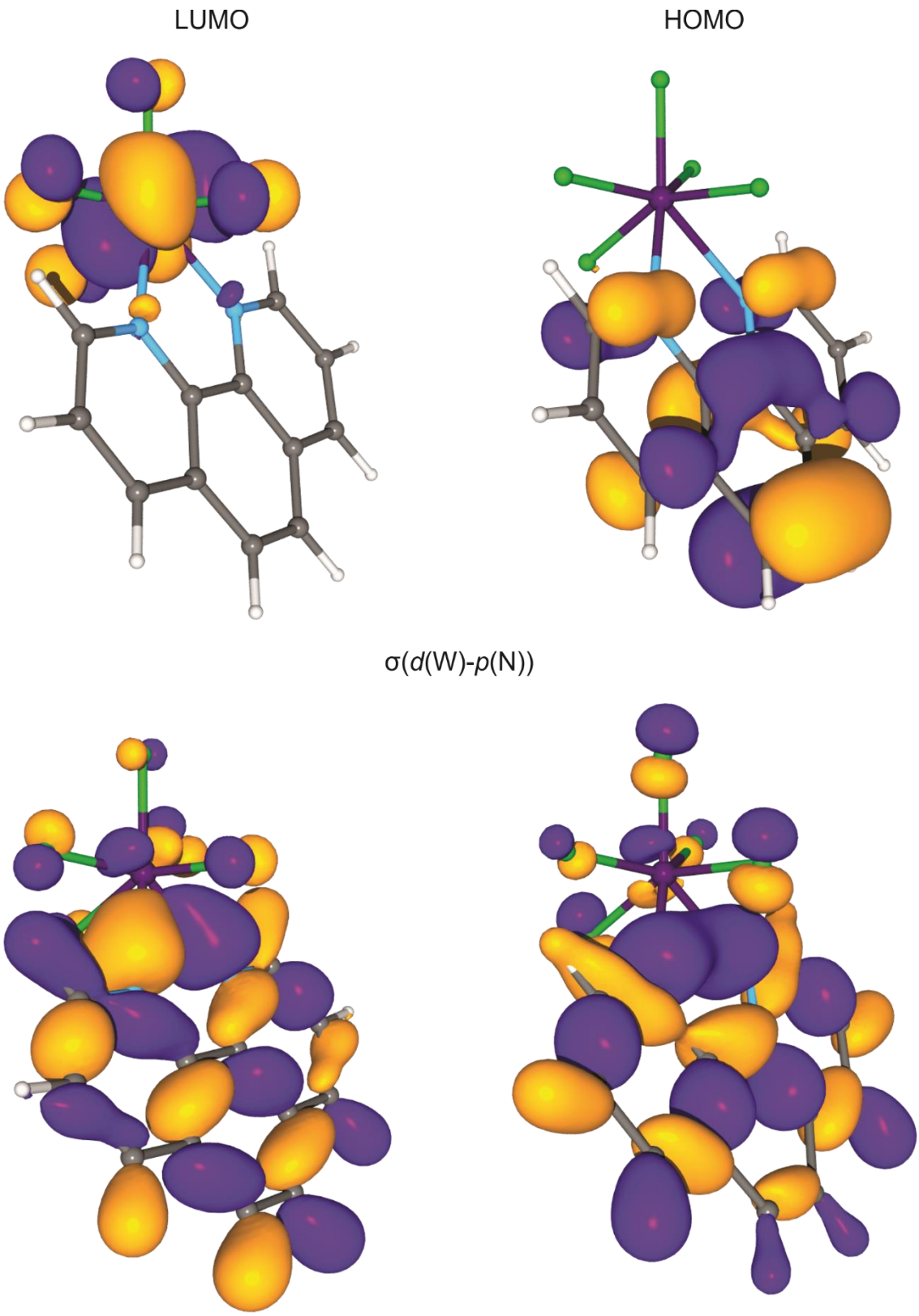

Figure 6.19. Selected MOs of $[WF_5(1,10\text{-phen})]^+$. Isosurface values are drawn at 0.04 e $Å^{-3}$.

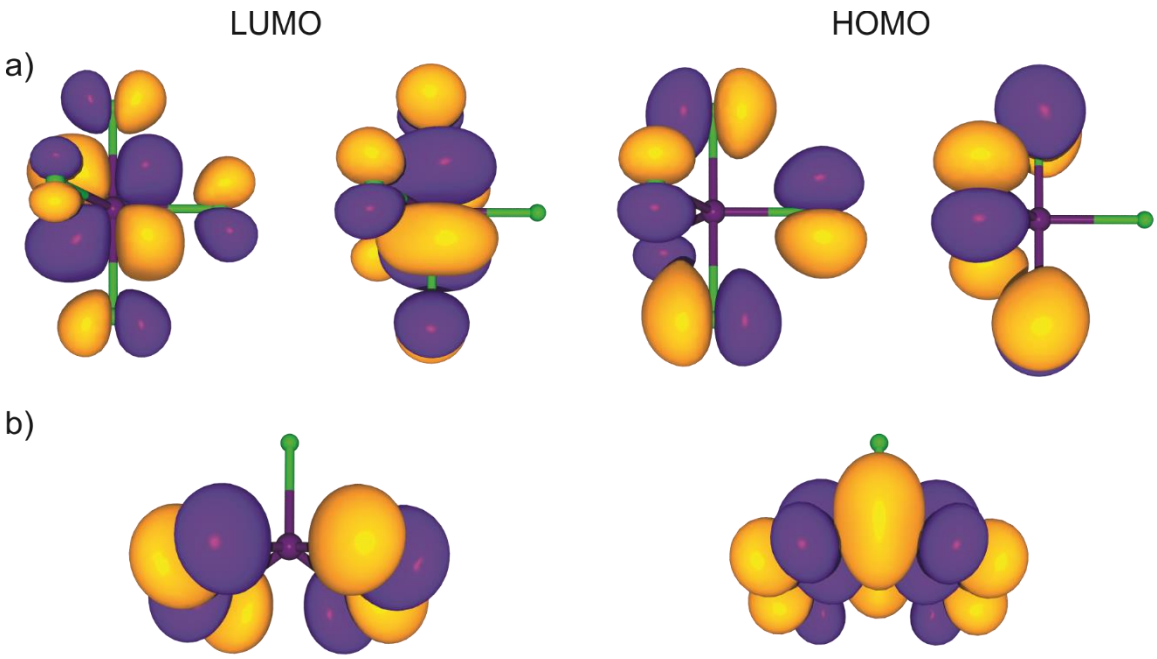

Figure 6.20. Selected MOs of a) D_{3h}- and b) C_{4v}-symmetric $[WF_5]^+$. Isosurface values are drawn at 0.04 e Å^{-3}.

which the *p* orbitals on the nitrogen atoms are in or out of phase.

6.2.5.3. Natural-Bond-Orbital Analyses

The NBO analyses reveal that upon F^- abstraction from $WF_6(L)$ to form $[WF_5(L)]^+$, a slight increase in the energies is observed for π(lp(F)→lv(W)) (lp = lone pair, lv = lone valence) interactions (Tables 6.6 and 6.7). More so, there is a substantial increase in the total σ(lp(N)→lv(W)) interaction energies, indicating that the positive charge introduced to the tungsten centre is stabilised by compensatory electron donation from the surrounding ligands, especially the N-donor ligands. This is paralleled by the NPA charges on tungsten (Table 6.8) hardly increasing upon F^- abstraction from $WF_6(L)$ (+2.57) to $[WF_5(L)]^+$ (+2.59), and even decreasing to $[WF_4(2,2'\text{-bipy})_2]^{2+}$ (+2.39), for which the σ(lp(N)→lv(W)) interactions are strongest. Correspondingly, the NPA charges residing on the ligands increase in the order $WF_6(L) < [WF_5(L)]^+ < [WF_4(2,2'\text{-bipy})_2]^{2+}$. Furthermore, there is a significant increase in the WBIs from $WF_6(L)$ to the cations in the polar-covalent W–F and dative W–N bonds (Table 6.9). Whereas the W−N bonds in $WF_6(L)$ are predicted to be approximately one-third the order of the W−F bond, this proportion increases to more than one half in the cations. To contrast, the absence of N-donor ligands in free $[WF_5]^+$ results in highly covalent W–F bonds (F_{eq}: 0.95; F_{ax}: 0.90) and a highly positively charged tungsten centre (+2.82).

Table 6.6. Energies ($E^{(2)}$, kJ mol^{-1}) of W–N and W–F Interactions in WF_6(L) (L = 2,2′-bipy, 1,10-phen) with Total π-Interaction Energies (Σ_π), Total $E^{(2)}$ (Σ_t), and Proportion of π-Interaction Energies to the Total $E^{(2)}$ ($P(\pi)$)[a]

	σ(lp(N)→lv(W))	σ(lp(F)→lv(W))	π_1(lp(F)→lv(W))	π_2(lp(F)→lv(W))	Σ_π(lp(F)→lv(W))	Σ_t(lp(F)→lv(W))	$P(\pi)$
WF_6(2,2′-bipy)							
W–N(1)	406						
W–N(2)	406						
W–F(1)		1031	179	202	381	1412	0.27
W–F(2)		1031	179	202	381	1412	0.27
W–F(3)		957	211	198	409	1366	0.30
W–F(4)		957	211	198	409	1366	0.30
W–F(5)		1125	219	221	440	1564	0.28
W–F(6)		1125	219	221	440	1564	0.28
Average	406	1038	203	207	410	1447	0.28
Total	812	6226	1218	1242	2460	8684	
WF_6(1,10-phen)							
W–N(1)	410						
W–N(2)	410						
W–F(1)		1021	187	218	405	1426	0.28
W–F(2)		1021	187	218	405	1426	0.28
W–F(3)		938	208	210	418	1356	0.31
W–F(4)		938	208	210	418	1356	0.31
W–F(5)		1114	220	231	450	1564	0.29
W–F(6)		1114	220	231	450	1564	0.29
Average	410	1024	205	220	424	1449	0.29
Total	820	6146	1230	1318	2546	8692	

[a]Calculated at the B3LYP/aVTZ level of theory. Abbreviations denote lone pair (lp) and lone valence (lv).

Table 6.7. Energies ($E^{(2)}$, kJ mol^{-1}) of W–N and W–F Interactions in $[WF_5(L)]^+$ (L = 2,2′-bipy, 1,10-phen) and $[WF_4(2,2'\text{-bipy})_2]^{2+}$ with Total π-Interaction Energies (Σ_π), Total $E^{(2)}$ (Σ_t), and Proportion of π-Interaction Energies to the Total $E^{(2)}$ ($P(\pi)$)[a]

	σ(lp(N)→lv(W))	σ(lp(F)→lv(W))	π_1(lp(F)→lv(W))	π_2(lp(F)→lv(W))	Σ_π(lp(F)→lv(W))	Σ_t(lp(F)→lv(W))	$P(\pi)$
				$[WF_5(2,2'\text{-bipy})]^+$			
W–N(1)	847						
W–N(2)	847						
W–F(1)		1220	235	237	472	1692	0.28
W–F(2)		1015	206	242	448	1464	0.31
W–F(3)		941	232	244	475	1416	0.34
W–F(4)		1015	206	242	448	1464	0.31
W–F(5)		1001	210	266	476	1478	0.32
Average	847	1038	218	246	464	1503	0.31
Total	1694	5192	1089	1231	2319	7514	
				$[WF_5(1,10\text{-phen})]^+$			
W–N(1)	848						
W–N(2)	848						
W–F(1)		1222	234	236	470	1692	0.28
W–F(2)		1021	204	242	446	1467	0.30
W–F(3)		940	232	243	475	1415	0.34
W–F(4)		1021	204	242	446	1467	0.30
W–F(5)		997	211	269	480	1477	0.33
Average	848	1040	217	246	463	1504	0.31
Total	1696	5201	1085	1232	2317	7518	
				$[WF_4(2,2'\text{-bipy})_2]^{2+}$			
W–N (×4)	928						
W–F (×4)		1064	180	227	407	1470	0.28
Total	3712	4256	720	908	1628	5880	

[a]Calculated at the B3LYP/aVTZ level of theory. Abbreviations denote lone pair (lp) and lone valence (lv).

Table 6.8. Natural-Population-Analysis Charges and Wiberg Valences[a] of Various Fluoridotungsten(VI) Complexes[b]

	WF_6	$[WF_5]^+$ (D_{3h})	$[WF_5]^+$ (C_{4v})	$WF_6(NC_5H_5)_2$	WF_6(2,2′-bipy)	WF_6(1,10-phen)	$[WF_5$(2,2′-bipy)$]^+$	$[WF_5$(1,10-phen)$]^+$	$[WF_4$(2,2′-bipy)$_2]^{2+}$
W	+2.69 [4.81]	+2.82 [4.65]	+2.83 [4.65]	+2.58 [4.96]	+2.57 [4.96]	+2.57 [4.96]	+2.59 [4.90]	+2.59 [4.90]	+2.39 [5.06]
F(1)		–0.38 [1.12]	–0.34 [1.16]	–0.52 [0.88]	–0.50 [0.91]	–0.50 [0.91]	–0.42 [1.04]	–0.42 [1.04]	
F(2)		–0.35 [1.15]	–0.37 [1.12]	–0.52 [0.88]	–0.50 [0.91]	–0.50 [0.91]	–0.45 [1.00]	–0.45 [0.99]	–0.45 [1.00]
F(3)	–0.45 [1.01]	–0.35 [1.15]	–0.37 [1.12]	–0.50 [0.91]	–0.49 [0.93]	–0.49 [0.93]	–0.45 [1.00]	–0.45 [1.00]	
F(4)		–0.35 [1.15]	–0.37 [1.12]	–0.50 [0.91]	–0.49 [0.93]	–0.49 [0.93]	–0.45 [1.00]	–0.45 [0.99]	
F(5)		–0.38 [1.12]	–0.37 [1.12]	–0.50 [0.91]	–0.48 [0.93]	–0.48 [0.93]	–0.46 [0.99]	–0.45 [0.99]	
F(6)				–0.50 [0.91]	–0.48 [0.93]	–0.48 [0.93]			
N(1)				–0.43 [3.34]	–0.42 [3.32]	–0.42 [3.32]	–0.48 [3.36]	–0.48 [3.37]	–0.46 [3.41]
C(1)				+0.09 [3.91]	+0.09 [3.90]	+0.11 [3.90]	+0.11 [3.89]	+0.13 [3.88]	+0.10 [3.89]
C(2)				–0.24 [3.96]	–0.22 [3.96]	–0.22 [3.96]	–0.19 [3.95]	–0.21 [3.95]	–0.19 [3.95]
C(3)				–0.14 [3.96]	–0.14 [3.96]	–0.12 [3.96]	–0.10 [3.94]	–0.07 [3.94]	–0.09 [3.93]
C(4)				–0.24 [3.96]	–0.20 [3.96]	–0.07 [4.01]	–0.19 [3.96]	–0.06 [4.01]	–0.18 [3.95]
C(5)				+0.09 [3.92]	+0.20 [3.99]	+0.19 [3.99]	+0.21 [3.98]	+0.19 [3.98]	+0.20 [3.98]
C(6)						–0.17 [3.96]		–0.15 [3.96]	
H(1)				+0.23 [0.95]	+0.24 [0.95]	+0.24 [0.95]	+0.24 [0.94]	+0.24 [0.94]	+0.24 [0.94]
H(2)				+0.22 [0.95]	+0.22 [0.95]	+0.22 [0.95]	+0.25 [0.94]	+0.24 [0.94]	+0.25 [0.94]
H(3)				+0.21 [0.95]	+0.22 [0.96]	+0.21 [0.96]	+0.24 [0.94]	+0.23 [0.95]	+0.25 [0.94]
H(4)				+0.22 [0.96]	+0.21 [0.96]		+0.23 [0.95]		+0.23 [0.95]
H(5)				+0.21 [0.96]					
H(6)						+0.21 [0.96]		+0.23 [0.94]	
Σ(L)[c]				+0.44 (total)	+0.38	+0.39	+0.62	+0.62	+0.71 (each)

[a]Given in square brackets. [b]Calculated at the B3LYP/aVTZ level of theory. Values are given for one half of the 2,2′-bipy and 1,10-phen ligands as the two halves are related by C_s or C_2 (or higher) symmetry. Atom labelling for N, C and H is as in **Error! Reference source not found.**. [c]Total NPA charge of the C_5H_5N, 2,2′-bipy, or 1,10-phen ligands.

Table 6.9. Wiberg Bond Indices of Various Fluoridotungsten(VI) Complexes[a]

	WF_6	$[WF_5]^+$ (D_{3h})	$[WF_5]^+$ (C_{4v})	$WF_6(NC_5H_5)_2$	WF_6(2,2′-bipy)	WF_6(1,10-phen)	$[WF_5$(2,2′-bipy)$]^+$	$[WF_5$(1,10-phen)$]^+$	$[WF_4$(2,2′-bipy)$_2]^{2+}$
W–F(1)	0.80	0.90	0.98	0.69	0.71	0.71	0.82	0.83	0.76
W–F(2)		0.95	0.92	0.69	0.71	0.71	0.79	0.79	
W–F(3)		0.95	0.92	0.72	0.73	0.73	0.80	0.80	
W–F(4)		0.95	0.92	0.72	0.73	0.73	0.79	0.79	
W–F(5)		0.90	0.92	0.72	0.74	0.74	0.79	0.79	
W–F(6)				0.72	0.74	0.74			
W–N				0.32	0.27	0.27	0.42	0.42	0.46
N–C				1.38	1.34–1.40	1.29–1.46	1.28–1.35	1.24–1.40	1.28–1.34
C–C				1.43–1.44	1.38–1.44 (1.05)[b]	1.15–1.53	1.40–1.43 (1.06)[b]	1.17–1.51	1.40–1.43 (1.07)[b]
C–H				0.91–0.92	0.90–0.92	0.90–0.92	0.90–0.91	0.90–0.91	0.90–0.91

[a]Calculated at the B3LYP/aVTZ level of theory. [b]Wiberg bond index for the C–C′ bond.

6.3. Conclusions

The $[WF_5(L)]^+$ cations have been stabilised by the bidentate N-donor ligands 2,2′-bipy and 1,10-phen, resulting in the first isolated complexes of $[MF_5]^+$ cations (for any transition metal M). They have been found to adopt distorted monocapped-octahedral or, alternatively, 4:3 geometries in the solid state, though in solution these geometries are fluxional on the NMR timescale. Fluorine-19 NMR studies revealed the thermodynamic instability of the $[SbF_6]^-$ salts, thus implicating heptacoordinate $[WF_5]^+$ complexes as reactive intermediates in the ligand-induced autoionisation of WF_6. The positive charges of the cations are stabilised primarily by increased σ-electron donation from the N-donor ligands.

6.4. References

(1) Craciun, R.; Long, R. T.; Dixon, D. A.; Christe, K. O. *J. Phys. Chem. A* **2010**, *114* (28), 7571–7582.

(2) Craciun, R.; Picone, D.; Long, R. T.; Li, S.; Dixon, D. A.; Peterson, K. A.; Christe, K. O. *Inorg. Chem.* **2010**, *49* (3), 1056–1070.

(3) Molski, M. J.; Seppelt, K. *Dalton Trans.* **2009**, 3379.

(4) Chen, G. S. H.; Passmore, J.; Taylor, P.; Whidden, T. K. *Inorg. Nucl. Chem. Lett.* **1976**, *12* (12), 943–948.

(5) Chen, G. S. H.; Passmore, J.; Taylor, P.; Whidden, T. K.; White, P. S. *J. Chem. Soc., Dalton Trans.* **1985**, No. 1, 9–16.

(6) Shorafa, H.; Mollenhauer, D.; Paulus, B.; Seppelt, K. *Angew. Chem. Int. Ed.* **2009**, *48* (32), 5845–5847.

(7) Tamadon, F.; Seidel, S.; Seppelt, K. *Acta Chim. Slov.* **2013**, *60* (3), 491–494.

(8) Arnaudet, L.; Bougon, R.; Ban, B.; Lance, M.; Navaza, A.; Nierlich, M.; Vigner, J. *J. Fluorine Chem.* **1992**, *59* (1), 141–152.

(9) Arnaudet, L.; Bougon, R.; Ban, B.; Lance, M.; Navaza, A.; Nierlich, M.; Vigner, J. *J. Fluorine Chem.* **1994**, *67* (1), 17–25.

(10) Levason, W.; Monzittu, F. M.; Reid, G.; Zhang, W. *Chem. Commun.* **2018**, *54* (83), 11681–11684.

(11) Marchetti, F.; Pampaloni, G. *Chem. Commun.* **2012**, *48* (5), 635–653.

(12) Benjamin, S. L.; Levason, W.; Reid, G. *Chem. Soc. Rev.* **2013**, *42* (4), 1460–1499.

(13) Levason, W.; Monzittu, F. M.; Reid, G. *Coord. Chem. Rev.* **2019**, *391*, 90–130.

(14) Arnaudet, L.; Bougon, R.; Buu, B.; Lance, M.; Nierlich, M.; Thuéry, P.; Vigner, J. *J. Fluorine Chem.* **1995**, *71* (1), 123–129.

(15) Brant, P.; Cotton, F. A.; Sekutowski, J. C.; Wood, T. E.; Walton, R. A. *J. Am. Chem. Soc.* **1979**, *101* (22), 6588–6593.

(16) Bondi, A. *J. Phys. Chem.* **1964**, *68* (3), 441–451.

(17) Batsanov, S. S. *J. Mol. Struct.* **1999**, *468* (1–2), 151–159.

(18) Drew, M. G. B. *Coord. Chem. Rev.* **1977**, *24* (2–3), 179–275.

(19) Mootz, D.; Bartmann, K. *Angew. Chem. Int. Ed. Engl.* **1988**, *27* (3), 391–392.

(20) Stuart, D.; Wetmore, S. D.; Gerken, M. *Angew. Chem. Int. Ed.* **2017**, *56* (51), 16380–16384.

(21) Drews, T.; Supeł, J.; Hagenbach, A. and; Seppelt, K. *Inorg. Chem* **2006**, *45* (9), 3782–3788.

(22) Turnbull, D.; Kostiuk, N.; Wetmore, S. D.; Gerken, M. *J. Fluorine Chem.* **2018**, *215*, 1–9.

(23) Drew, M. G. B. In *Progress in Inorganic Chemistry*, *Volume 23*; Lippard, S. J., Ed.; John Wiley & Sons, Ltd, 1977; pp 67–210.

(24) Giese, S.; Seppelt, K. *Angew. Chem. Int. Ed. Engl.* **1994**, *33* (4), 461–463.

(25) Casanova, D.; Alemany, P.; Bofill, J. M.; Alvarez, S. *Chem. Eur. J.* **2003**, *9* (6), 1281–1295.

(26) Hoffmann, R.; Beier, B. F.; Muetterties, E. L.; Rossi, A. R. *Inorg. Chem.* **1977**, *16* (3), 511–522.

(27) Qureshl, A. M.; Aubke, F. *Can. J. Chem.* **1970**, *48* (20), 3117–3123.

(28) Christe, K. O. *Inorg. Chem.* **1975**, *14* (9), 2230–2233.

(29) Hohorst, F. A.; Stein, L.; Gebert, E. *Inorg. Chem.* **1975**, *14* (9), 2233–2236.

(30) Benkič, P.; Brooke Jenkins, H. D.; Ponikvar, M.; Mazej, Z. *Eur. J. Inorg. Chem.* **2006**, *2006* (5), 1084–1092.

(31) Claassen, H. H.; Selig, H. *Isr. J. Chem.* **1969**, *7* (4), 499–504.

(32) Marsden, C. J. *J. Chem. Soc., Chem. Commun.* **1984**, 401–402.

(33) Meier, S. C.; Himmel, D.; Krossing, I. *Chem. Eur. J.* **2018**, *24* (72), 19348–19360.

Chapter 7 – Stabilisation of $[WF_5]^+$ and WF_5 by Pyridine: Facile Access to $[WF_5(NC_5H_5)_3]^+$ and $WF_5(NC_5H_5)_2$*

7.1. Introduction

Until the syntheses of $[WF_5(2,2'\text{-bipy})][Sb_2F_{11}]$ and $[WF_5(1,10\text{-phen})][Sb_nF_{5n+1}]$ (n = 1, 2) via reactions of $WF_6(L)$ (L = 2,2′-bipy, 1,10-phen) with $SbF_5(OSO)$ in SO_2, no discrete $[MF_5]^+$ cation, free or complexed, had been reported (see Chapter 6). Donor-stabilised $[WF_5]^+$ complexes are predicted to behave as significantly stronger oxidising agents than WF_6. Their reduction could serve as an alternative synthetic route to thermally unstable WF_5, the cumbersome preparations of which involve reduction of WF_6 with tungsten wires at 500–700 °C in a cold (–50 to –60 °C) quartz vessel,[1,2] F^- abstraction from $[WF_6]^-$ in HF/SbF_5 and sublimation at 0°C,[3] and photochemical reduction of WF_6 by CO in the presence of Hg as a sensitiser.[4]

In this chapter, it is demonstrated that F^- abstraction from WF_6 in the presence of C_5H_5N can be achieved under relatively mild conditions using $(CH_3)_3SiO_3SCF_3$, and that decomposition of the resultant $[WF_5(NC_5H_5)_3]^+$ cation in C_5H_5N results in controlled reduction to $WF_5(NC_5H_5)_2$.

* Based on the following publication: Turnbull, D.; Hazendonk, P.; Wetmore, S. D.; Gerken, M. *Chem. Eur. J.* **2020**, *26* (30), 6879–6886.

7.2. Results and Discussion

7.2.1. Syntheses and Physical Properties of $[WF_5(NC_5H_5)_3][O_3SCF_3]$ and $WF_5(NC_5H_5)_2$

The reaction of $WF_6(NC_5H_5)_2$ with one molar equivalent of $[(CH_3)_3Si(NC_5H_5)][O_3SCF_3]$ in CH_2Cl_2 at –60 °C resulted in F^- abstraction, quantitatively yielding $[WF_5(NC_5H_5)_3]^+$ (Eq. 7.1). The $[WF_5(NC_5H_5)_3][O_3SCF_3]$ salt was isolated as a colourless solid upon removal of the volatile materials under dynamic vacuum. It is highly soluble in SO_2ClF, SO_2 and CH_2Cl_2, (though the solutions turn brown over several hours at ambient temperature due to decomposition) whereas it is insoluble in $CFCl_3$.

$$WF_6(NC_5H_5)_2 + [(CH_3)_3Si(NC_5H_5)]^+ \rightarrow [WF_5(NC_5H_5)_3]^+ + (CH_3)_3SiF \qquad (7.1)$$

Attempts to prepare $[WF_5(NC_5H_5)_2][O_3SCF_3]$ via reaction of $WF_6(NC_5H_5)$ and $[(CH_3)_3Si(NC_5H_5)][O_3SCF_3]$, or $[WF_5(NC_5H_5)_2][Sb_2F_{11}]$ via reaction of $WF_6(NC_5H_5)_2$ with $SbF_5(OSO)$ in SO_2 did not yield a sole, identifiable product. Monitoring the attempted preparation of $[WF_5(NC_5H_5)_2][Sb_2F_{11}]$ by ^{19}F NMR spectroscopy revealed its instability in solution (*vide infra*).

The attempted preparation of $[WF_5(NC_5H_5)_3][O_3SCF_3]$ in excess C_5H_5N resulted in the formation of a pale yellow solution, which over time darkened to red-brown. After 16–24 h at ambient temperature, red-orange crystals settled from what had become an intractable oil. These crystals were isolated after washing with CH_2Cl_2 and found to consist of $WF_5(NC_5H_5)_2$ by X-ray crystallography (Eq. 7.2), though their Raman spectrum revealed significant contamination by $WF_6(NC_5H_5)_2$. This impurity could be minimised by employing a slight excess of $(CH_3)_3SiO_3SCF_3$ (1.1 equivalents), agitating the mixture after 16–24 h at ambient temperature, allowing to settle for an additional 24 h, and subsequently washing with CH_2Cl_2. Under these conditions, $WF_5(NC_5H_5)_2$ could be obtained in *ca.* 60%

yield. If 1.5 molar equivalents of $(CH_3)_3SiO_3SCF_3$ were employed, the yield was drastically reduced (< 20%). The $WF_5(NC_5H_5)_2$ adduct was found to be slightly soluble in CH_2Cl_2, C_5H_5N and CH_3CN.

Both $[WF_5(NC_5H_5)_3][O_3SCF_3]$ and $WF_5(NC_5H_5)_2$ are thermally stable in the solid state under an atmosphere of dry N_2. This is especially noteworthy for $WF_5(NC_5H_5)_2$, as it contrasts with the proclivity of WF_5 to disproportionate at ambient or slightly elevated temperatures.[1,2] They are, however, hydrolytically sensitive. In the latter case, exposure to air, H_2O, or aqueous NaOH results in blue/violet discolouration due to the formation of mixed-oxidation-state tungsten oxides.[5]

7.2.2. Molecular Geometries

7.2.2.1. $WF_5(NC_5H_5)_2$

The $WF_5(NC_5H_5)_2$ adduct was found to crystallise from the mother liquor during preparation and could also be recrystallised from hot CH_3CN, allowing for determination of its structure via X-ray crystallography at –161 °C. In addition, its geometry was optimised in the gas phase at the B3LYP/aVTZ level of theory. Selected experimental and calculated geometric parameters are given in Table 7.1. Crystallographic data collection and refinement parameters are provided in the Appendix (Table E.1).

The $WF_5(NC_5H_5)_2$ adduct crystallises in the monoclinic space group $C2/c$ (a = 8.1621(4) Å, b = 11.1419(5) Å, c = 13.6465(7) Å, β = 107.055(6)°, Z = 4, R_1 = 0.0099, wR_2 = 0.0234), adopting a pentagonal-bipyramidal geometry with crystallographically imposed C_2 symmetry, in which the nitrogen atoms occupy non-adjacent, equatorial positions (Figure 7.1). The pentagonal plane is nearly ideal, with only small displacements from the least-squares plane (< 0.08 Å), an ideal sum of internal angles (exptl. 360.3°,

Table 7.1. Selected Bond Lengths (Å) and Angles (°) of $WF_5(NC_5H_5)_2$[a]

	exptl	calcd[b]
W–F(1)	1.8936(14)	1.904
W–F(2)	1.9088(12)	1.920
W–F(3)	1.9191(11)	1.902
W–N	2.2206(15)	2.294
$N–C_o$[c]	1.348(2)	1.339
$C_o–C_m$[c]	1.382(3)	1.385
$C_m–C_p$[c]	1.387(3)	1.388
F(1)–W–F(2)	87.49(3)	85.9
F(1)–W–F(3)	143.14(3)	142.1
F(1)–W–N	72.14(4)	71.3
$F(2)–W–F(2)^i$	174.98(7)	171.9
F(2)–W–F(3)	89.79(5)	90.8
$F(2)–W–F(3)^i$	94.23(5)	95.6
F(2)–W–N	90.91(5)	90.3
$F(2)–W–N^i$	87.54(5)	87.1
$F(3)–W–F(3)^i$	73.72(7)	75.8
F(3)–W–N	71.16(5)	71.0
$F(3)–W–N^i$	144.47(5)	146.4
$N–W–N^i$	144.27(7)	142.5

[a]Symmetry transformation: i = 1 – x, y, ½ – z. [b]Calculated at the B3LYP/aVTZ level of theory. [c]Averaged value.

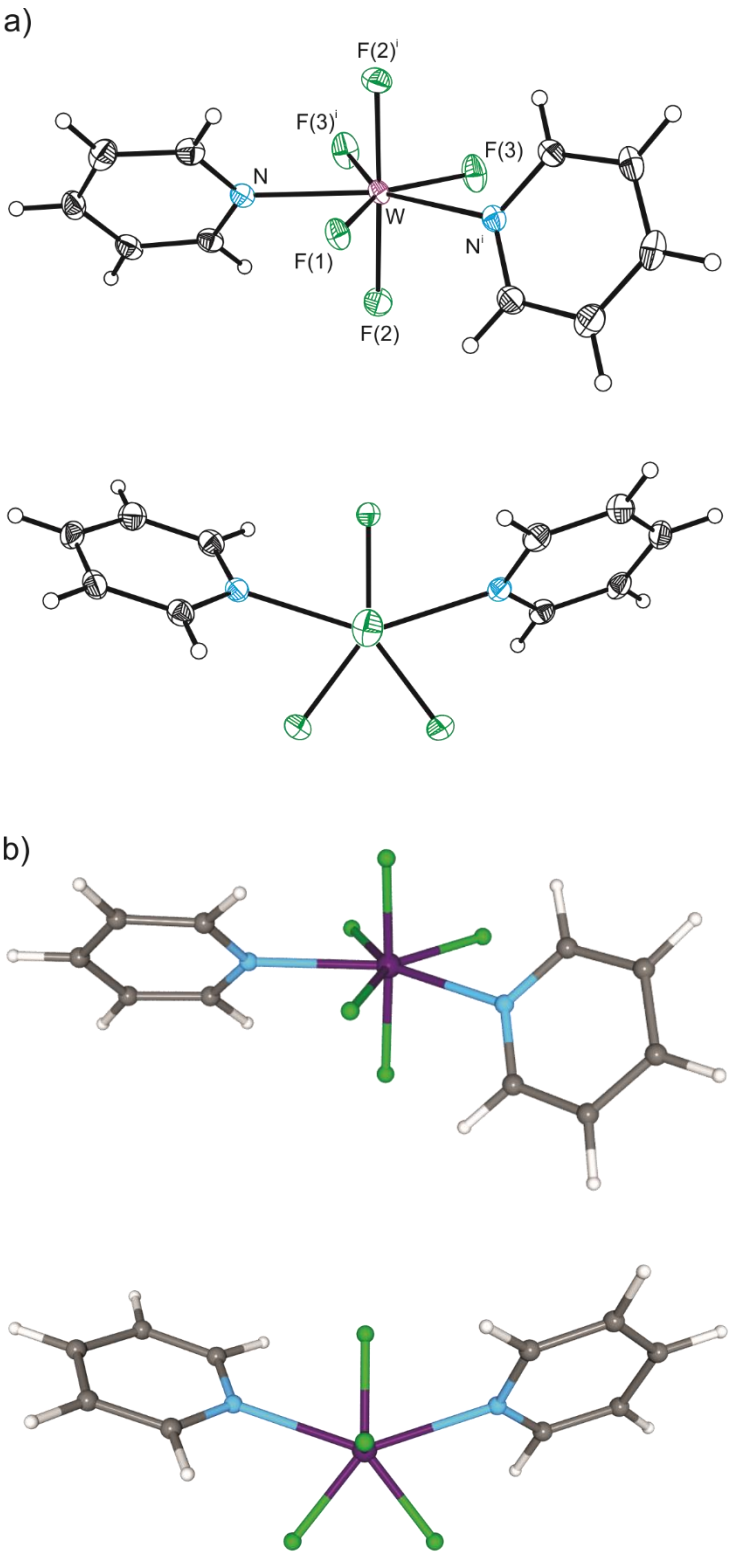

Figure 7.1. Side-on (top) and top-down (bottom) views of a) thermal ellipsoid plots (50% probability level) and b) optimised gas-phase geometries (B3LYP/aVTZ) of $WF_5(NC_5H_5)_2$.

calcd. 360.4°), and no displacement of the tungsten centre from the plane. A similar coordination geometry has been observed for the adducts of WOF_4[6] and $W(NC_6F_5)F_4$ (see Chapter 5) with two molar equivalents of C_5H_5N. Adducts of WOF_4 with chelating diphosphines are also pentagonal-bipyramidal; however, the donor atoms occupy adjacent sites in the pentagonal plane.[7] The $WXF_4(NC_5H_5)_2$ (X = O, F) adducts are isomorphic, but can be distinguished by their unit-cell parameters ($WOF_4(NC_5H_5)_2$: a = 8.2014(5) Å, b = 11.1972(5) Å, c = 13.5387(9) Å, β = 107.256(7)°) and disorder between the axial W=O and W–F bonds in $WOF_4(NC_5H_5)_2$ resulting in an averaged bond length (1.834(2) Å, see Chapter 5). To our knowledge, only one other heptacoordinate fluoridotungsten(V) complex is known, $K_2[WF_7]$, in which the anion is found to adopt an edge-disordered, monocapped-trigonal-prismatic geometry.[8]

Comparison of $WF_5(NC_5H_5)_2$ and $[WF_7]^{2-}$ reveal insignificant differences between their W–F bond lengths (1.8936(14)–1.9191(11) and 1.882(16)–1.943(19) Å),[8] respectively), though larger errors in the latter prevent more precise analysis. In addition, the W–F bonds are typically elongated relative to those of comparable heptacoordinate tungsten(VI) complexes such as $WF_6(NC_5H_5)$ and its derivatives (1.803(8)–1.880(6) Å)[9] as well as $[WF_5(L)]^+$ (L = 2,2′-bipy, 1,10-phen; 1.8377(19)–1.861(3) Å). In contrast, the W–N bonds (2.2206(15) Å) in $WF_5(NC_5H_5)_2$ are insignificantly different from, or even slightly shorter than, those of the aforementioned tungsten(VI) complexes (2.214(3)–2.294(9) Å).

In comparison to the most closely related neutral tungsten(V) adduct, *trans*-$WF_4\{N(CH_2CF_3)_2\}\{P(C_6H_5)_3\}$, the W–F bonds in $WF_5(NC_5H_5)_2$ (1.8936(14)–1.9191(11) Å) are elongated in relation to those of the bent WF_2 moiety (1.845(3)–1.859(3) Å), but differ

insignificantly from those of its linear WF_2 moiety (1.884(3)–1.912(3) Å).[10] The W^V–Pn (Pn = N, P) normalised contacts[11] in $WF_5(NC_5H_5)_2$ (0.624) and *trans*-$WF_4\{N(CH_2CF_3)_2\}\{P(C_6H_5)_3\}$ (0.682) suggest stronger W–Pn bonds in the former, a trend which was also observed between WF_6 adducts with N- and P-donor ligands.[12]

The optimised gas-phase geometry of $WF_5(NC_5H_5)_2$ agrees excellently with the geometry observed in the crystal structure (Figure 7.1), in which the largest discrepancy is a minor overestimation of the W–N bond length (2.2206(15) vs. 2.294 Å). Whereas the longest W–F bonds in the crystal structure are W–F(3)/F(3)^i, these are the shortest W–F bonds in the optimised geometry.

The $WF_5(NC_5H_5)_2$ adduct represents the first heptacoordinate adduct of a transition-metal pentafluoride; NMR spectroscopic[13,14] and crystallographic[15] studies of $MF_5{\cdot}2C_5H_5N$ (M = Nb, Ta) revealed that MF_5 undergo quantitative ligand-induced autoionisation to the ionic coordination isomers, $[MF_4(NC_5H_5)_4][MF_6]$, upon reaction with C_5H_5N. Furthermore, the observation of ionic species upon reactions of MF_5 with excess monodentate donor ligand, or stoichiometric amounts of bidentate ligand, is ubiquitous.[16,17] Uranium pentafluoride, however, forms a monocapped-trigonal-prismatic adduct with 2,2′-bipy;[18] $UF_5{\cdot}2HCN$ instead manifests as a one-dimensional coordination polymer with trigonal-dodecahedral uranium(V) centres.[19]

7.2.2.2. $[WF_5(NC_5H_5)_n]^+$ (n = 2, 3)

While attempts to grow crystals of $[WF_5(NC_5H_5)_3][O_3SCF_3]$ were unsuccessful, the geometry of the cation was determined unambiguously by variable-temperature ^{19}F NMR spectroscopy (see section 7.2.4). In addition, the gas-phase geometries of $[WF_5(NC_5H_5)_n]^+$ (n = 2, 3) were optimised in the gas-phase, resulting in monocapped-trigonal-prismatic and

trigonal-dodecahedral geometries, respectively (Figure 7.2). In $[WF_5(NC_5H_5)_3]^+$, the nitrogen atoms and one fluorido ligand occupy the "A" coordination sites of the trigonal dodecahedron and the remaining fluorido ligands correspondingly occupy the "B" (equatorial) sites (Figure 7.2a).[20] This was achieved even when a bicapped-trigonal-prismatic geometry derived from the crystal structure of $WF_6(NC_5H_5)_2$ was input as the starting geometry for the optimisation. The cation possesses C_1 symmetry, though the WF_5N_3 moiety loosely approximates C_s symmetry. In contrast, complexes of octacoordinate ReH_5 adducts with monodentate ligands are inverted such that the donor ligands occupy "B" sites of the trigonal dodecahedron.[21,22]

In $[WF_5(NC_5H_5)_2]^+$, the geometry is monocapped-trigonal-prismatic in which the nitrogen atoms occupy the capping position and one vertex opposite the capping position, resulting in overall C_s symmetry (Figure 7.2b). This geometry contrasts with those of the $[WF_5(L)]^+$ (L = 2,2′-bipy, 1,10-phen) cations, in which the presence of bidentate ligands yields monocapped-octahedral or 4:3-polyhedral geometries. An attempt to optimise a pentagonal-bipyramidal (C_2-symmetric) stereoisomer based on that of $WF_5(NC_5H_5)_2$ resulted in a transition state that is 6 kJ mol^{-1} higher in energy, in which the imaginary frequency corresponds to a distortion towards the ground-state geometry.

Optimised geometric parameters are given in Table 7.2. The W–F bond lengths are predicted to be significantly longer in $[WF_5(NC_5H_5)_3]^+$ (1.863–1.878 Å) than in $[WF_5(NC_5H_5)_2]^+$ (1.846–1.856 Å) and $[WF_5(L)]^+$, though not as long as in $WF_5(NC_5H_5)_2$. Similarly, the W–N bonds in $[WF_5(NC_5H_5)_3]^+$ (2.356–2.398 Å) are significantly longer than in any of the aforementioned heptacoordinate complexes, including $WF_5(NC_5H_5)_2$. These trends in W–F and W–N bond lengths are attributed primarily to significantly

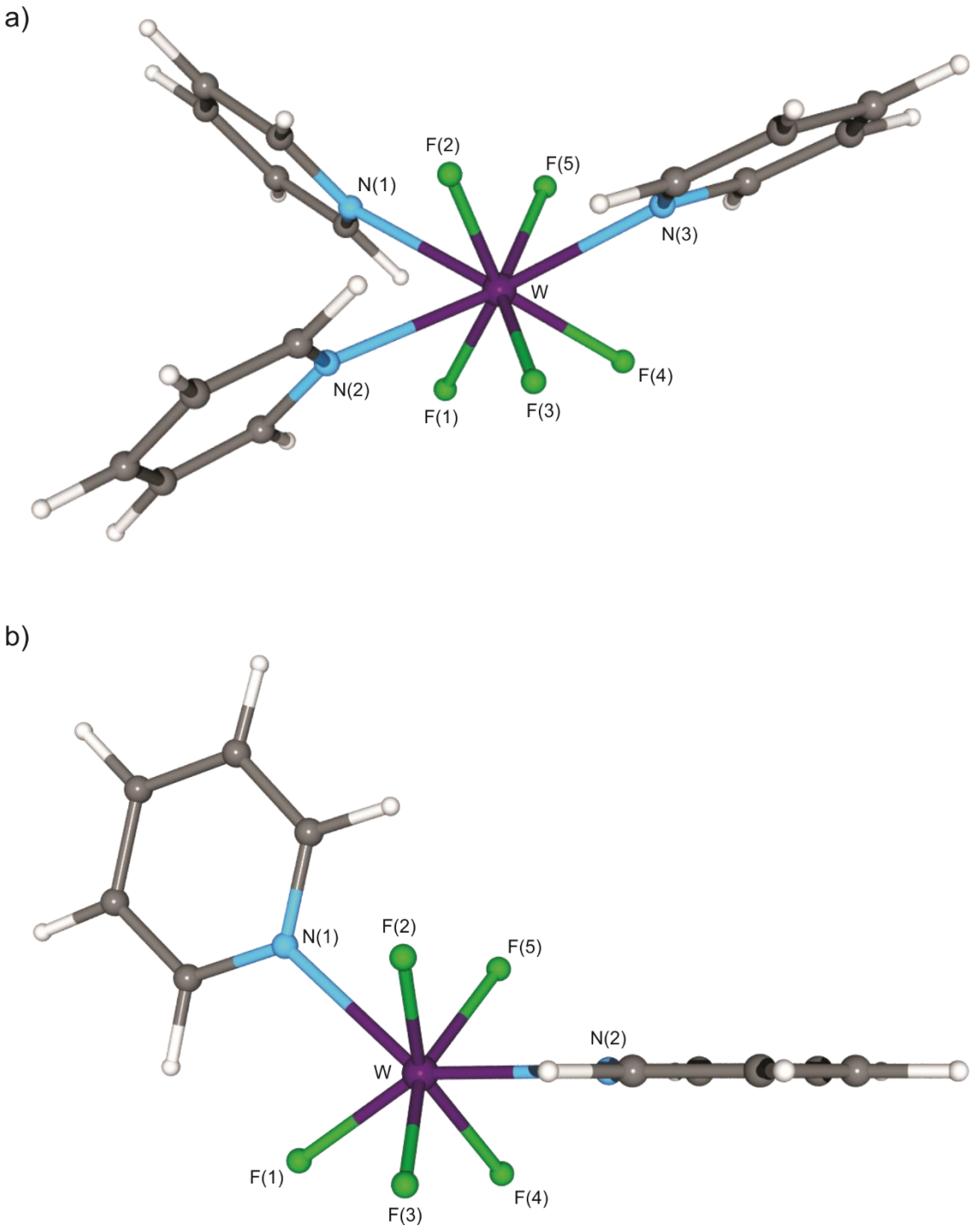

Figure 7.2. Optimised gas-phase geometries (B3LYP/aVTZ) of a) $[WF_5(NC_5H_5)_3]^+$ and b) $[WF_5(NC_5H_5)_2]^+$.

Table 7.2. Selected Calculated Bond Lengths (Å) and Angles (°) of $[WF_5(NC_5H_5)_n]^+$ (n = 2, 3)[a]

	***n* = 2**	***n* = 3**
W–F(1)	1.846	1.867
W–F(2)	1.859	1.878
W–F(3)	1.848	1.863
W–F(4)	1.848	1.864
W–F(5)	1.859	1.878
W–N(1)	2.293	2.398
W–N(2)	2.276	2.382
W–N(3)		2.356
N–C_o[b]	1.347	1.341
C_o–C_m[b]	1.382	1.384
C_m–C_p[b]	1.388	1.388
F(1)–W–F(2)	123.3	140.7
F(1)–W–F(3)	81.2	102.4
F(1)–W–F(4)	81.2	75.6
F(1)–W–F(5)	123.3	98.6
F(1)–W–N(1)	73.8	73.4
F(1)–W–N(2)	147.2	73.3
F(1)–W–N(3)		147.4
N(1)–W–N(2)	138.9	71.0
N(1)–W–N(3)		131.6
N(2)–W–N(3)		129.6

[a]Calculated at the B3LYP/aVTZ level of theory. [b]Averaged value.

increased steric crowding caused by octacoordination. As expected, the W–F and W–N bond lengths are comparable between $[WF_5(NC_5H_5)_2]^+$ and $[WF_5(L)]^+$.

7.2.3. Raman Spectroscopy

The ambient-temperature Raman spectra of solid $[WF_5(NC_5H_5)_3][O_3SCF_3]$ (Figure 7.3) and $WF_5(NC_5H_5)_2$ (Figure 7.4) were obtained and vibrational frequencies were calculated for the optimised geometries, resulting in excellent agreement between the experimental and calculated data. Experimental and calculated vibrational frequencies, with assignments, are given in the Appendix (Tables E.2 and E.3). Bands corresponding to $[O_3SCF_3]^-$ were identified by comparison to those of aqueous HO_3SCF_3.[23]

In $[WF_5(NC_5H_5)_3][O_3SCF_3]$, the $\nu_s(WF_5)$ frequency (in cm^{-1}; exptl. 667, calcd. 679) is consistent with octacoordinate tungsten(VI) complexes such as $WF_6(NC_5H_5)_2$ (exptl. 661,[24] calcd. 673), $WF_6(L)$ (L = 2,2′-bipy, 1,10-phen; exptl. 647–665, calcd. 661–692), and $[WF_4(2,2'\text{-bipy})_2]^{2+}$ (exptl. 645, 687;[25] calcd. 650, 684). Two $\nu_s(NC_5)$ modes with significant Raman activity were predicted, one corresponding to the symmetric coupling of the N(1)- and N(2)-pyridyl ligands (1036), and the other to that of the N(3)-pyridyl ligand (1038). Due to their highly similar frequencies, only one $\nu_s(NC_5)$ band was observed experimentally. The $\nu_s(NC_5)$ modes (exptl. 1022; calcd. 1036, 1038) are blue-shifted from that of free C_5H_5N (exptl. 990, calcd. 1013) to a similar extent as in $WF_6(NC_5H_5)$ (exptl. 1024,[24] calcd. 1041) and $WF_6(NC_5H_5)_2$ (exptl. 1026,[24] calcd. 1036). Three distinct W–N stretching modes, $\nu_{as}(WN_3)$ (168), $\nu_s(WN_3)$ (151), and $\nu_{as}(WN_2)$ (130) are predicted, the last of which is tentatively assigned to a band at 175 cm^{-1} (*cf.* $WF_6(NC_5H_5)$: exptl. 198, calcd. 161).

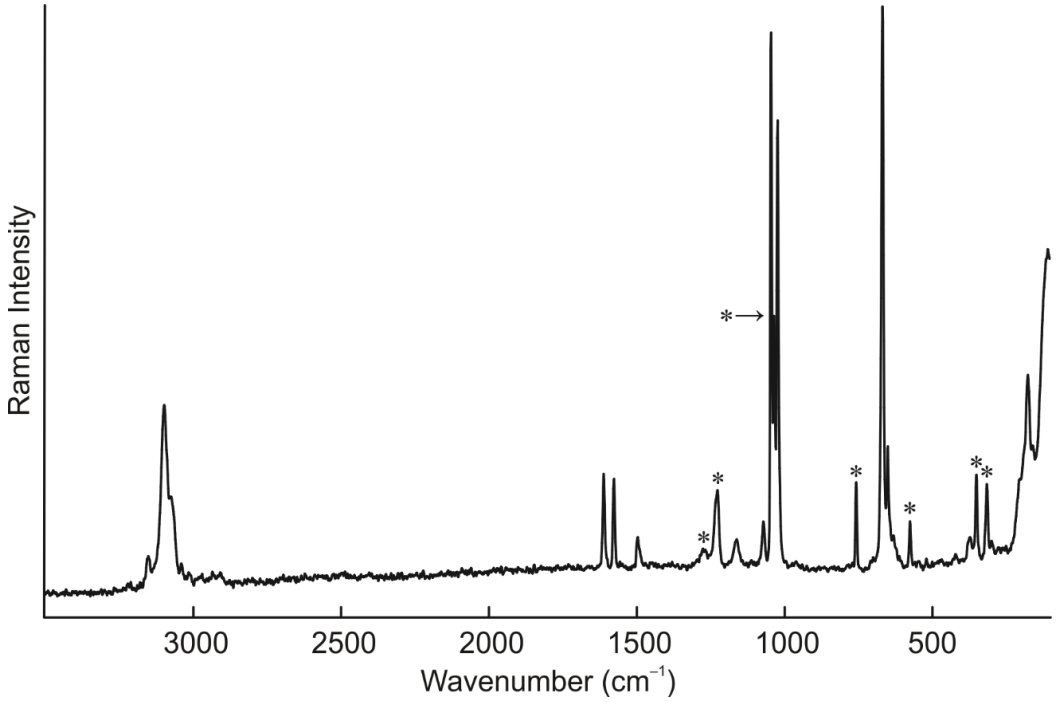

Figure 7.3. Raman spectrum of solid $[WF_5(NC_5H_5)_3][O_3SCF_3]$, recorded at ambient temperature. Asterisks (*) denote $[O_3SCF_3]^-$ bands.

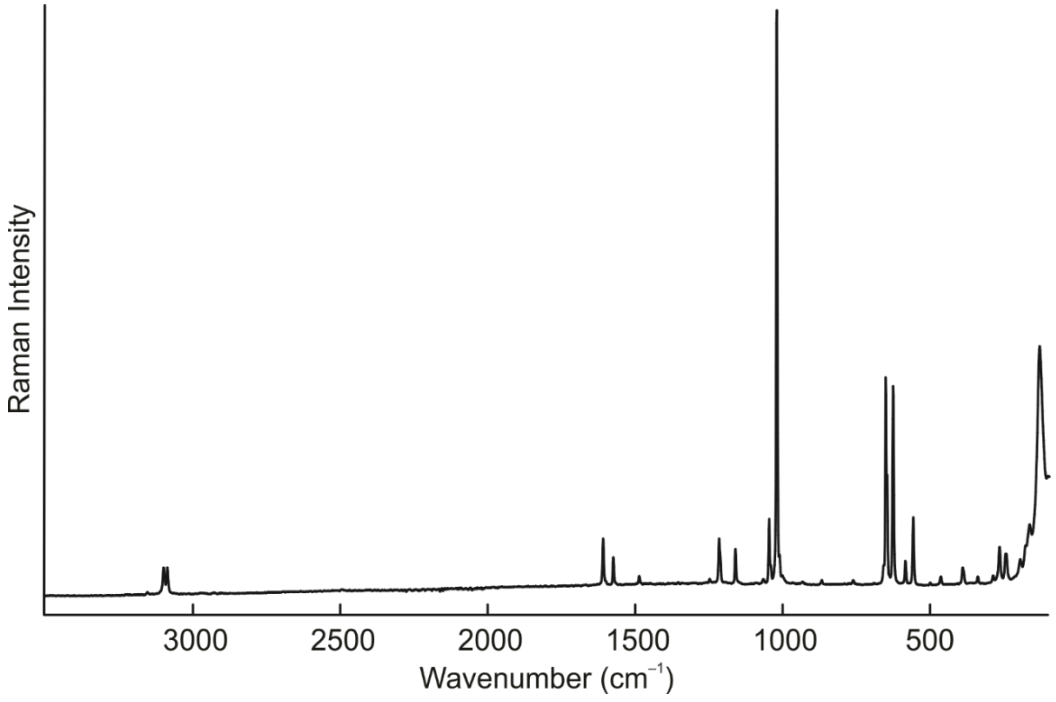

Figure 7.4. Raman spectrum of solid $WF_5(NC_5H_5)_2$, recorded at ambient temperature.

In $WF_5(NC_5H_5)_2$, several bands are observed between 500 and 660 cm^{-1} that are attributed to W–F stretching vibrations, assigned by comparison to the calculated vibrational frequencies. The $\nu_s(WF_5)$ stretch and in-plane deformations of the pyridyl ligands are coupled, resulting in two bands (exptl. 655, 630, calcd. 660, 636). The symmetric W–F_{ax} stretch, $\nu_s(WF_{2,ax})$, couples with stretching vibrations of the W–F_{eq} bonds, resulting in two further bands (exptl. 588, 562, calcd. 607, 555). The $\nu_s(WF_5)$ modes are similar in frequency to the $\nu_s(WF_7)$ modes of $M_2[WF_7]$[8] (M = K: 642; M = Rb: 637) but are considerably lower than the symmetric W–F stretching modes of heptacoordinate WF_6 or $[WF_5]^+$ complexes (*ca*. 700). The symmetrically (s) and antisymmetrically (as) coupled $\nu_s(NC_5)$ modes of the pyridyl ligands (exptl. 1024 (s), 1016 (as); calcd. 1040 (s), 1038 (as)) are also significantly blue-shifted. The tentatively assigned symmetric W–N stretching mode (exptl. 167, calcd. 154) is predicted to be similar to $WF_6(NC_5H_5)$.

7.2.4. NMR Spectroscopy

7.2.4.1. $[WF_5(NC_5H_5)_3][O_3SCF_3]$

The solution-phase structure of $[WF_5(NC_5H_5)_3]^+$ was investigated by variable-temperature ^{19}F and ^1H NMR spectroscopy in CH_2Cl_2 (Figures 7.5 and 7.6, respectively). At –100 °C, the fluorine-on-tungsten (F-on-W^{VI}) region in the ^{19}F NMR spectrum of $[WF_5(NC_5H_5)_3][O_3SCF_3]$ gives rise to an AB_2CD spin system, which was simulated and optimised (Table 7.3 and Figure 7.7). The F_A resonance corresponds to F(1), F_B to F(3) and F(5), F_C to F(2), and F_D to F(4). Traces of $[WF_4(NC_5H_5)_4]^{2+}$ (158.63 ppm, *cf*. $[WF_4(2,2'\text{-bipy})_2]^{2+}$: 155 ppm[25,26]) and $WF_6(NC_5H_5)_2$[24] (122.58, 74.49 ppm) were observed at the start of the reaction, which is attributed to twofold F^- abstraction from $WF_6(NC_5H_5)_2$ causing retention of some unreacted educt (Eq. 7.2). The ^1H NMR spectrum reveals two

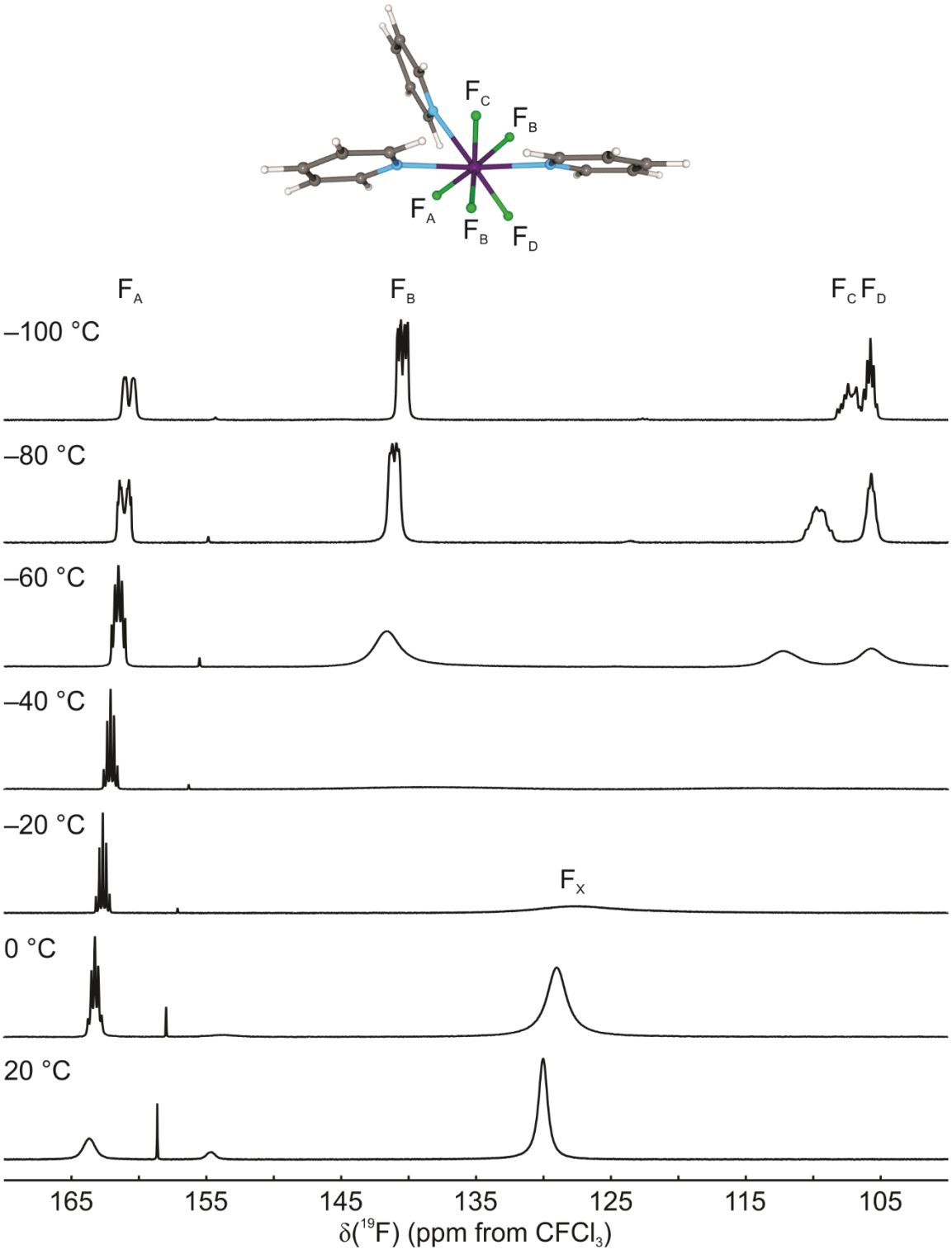

Figure 7.5. Fluorine-on-tungsten region in the ^{19}F NMR spectra of $[WF_5(NC_5H_5)_3][O_3SCF_3]$, recorded in CH_2Cl_2 at various temperatures from from –100 to 20 °C.

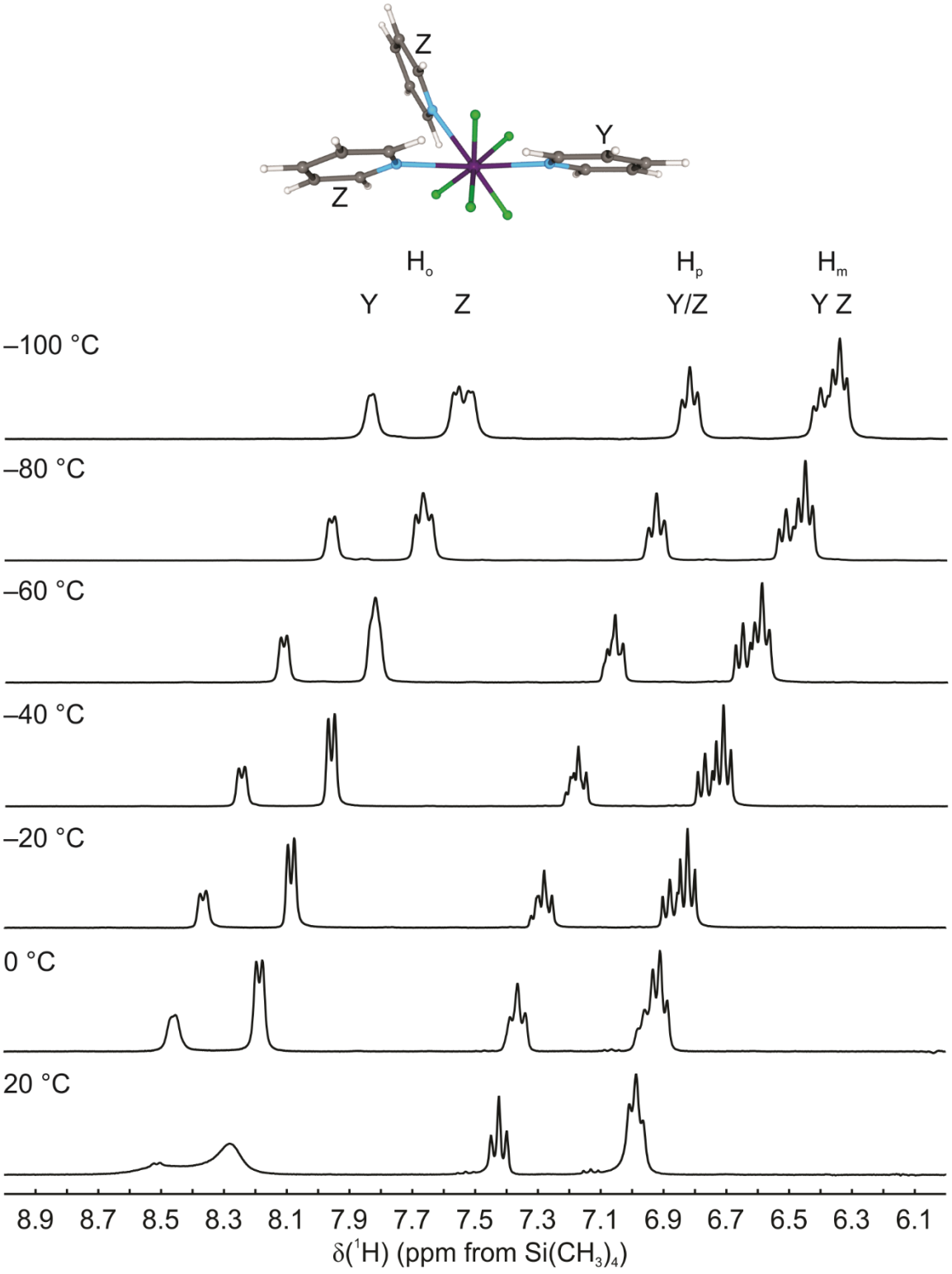

Figure 7.6. Aromatic-proton region in the ^{1}H NMR spectra of $[WF_5(NC_5H_5)_3][O_3SCF_3]$, recorded in CH_2Cl_2 at various temperatures from –100 to 20 °C.

Table 7.3. Fluorine-19 NMR Spectroscopic Data for $[WF_5(NC_5H_5)_3]^{+a}$

	$\delta(^{19}F)$ (ppm)	J (Hz)[b]		
		$^2J(F–F_B)$	$^2J(F–Fc)$	$^2J(F–F_D)$
F_A	160.70	20.9(3)	180.7(3)	53.9(4)
F_B	140.42		143.2(3)	65.4(3)
F_C	107.17			76.2(4)
F_D	105.74			

*a*Recorded in CH_2Cl_2 at –100 °C. *b*Determined via spectral simulations and optimisations using SpinWorks (version 4.2.7).[27]

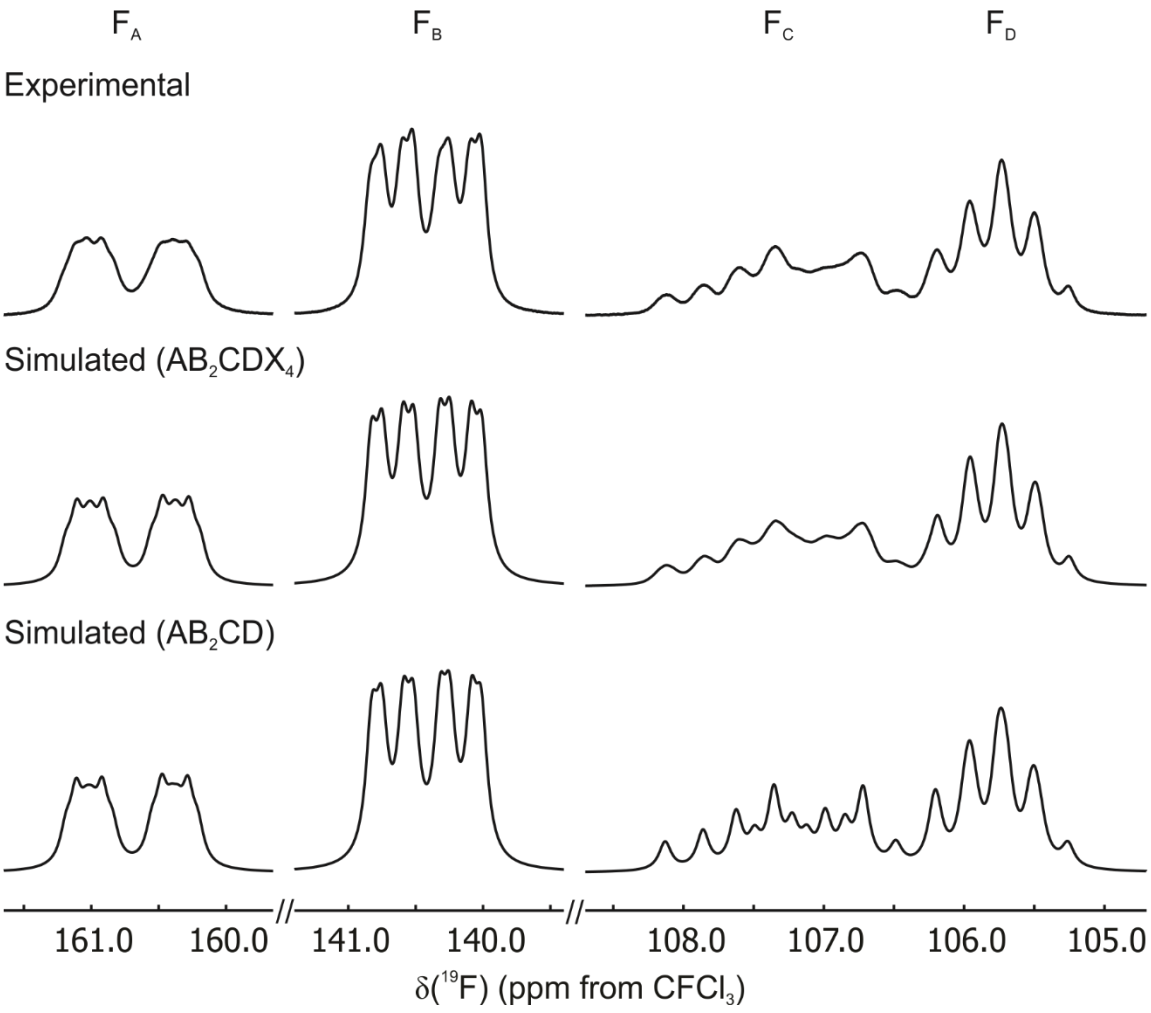

Figure 7.7. Experimental (top) and simulated (NUMMRIT, middle and bottom) fluorine-on-tungsten regions in the ^{19}F NMR spectrum of $[WF_5(NC_5H_5)_3][O_3SCF_3]$, recorded in CH_2Cl_2 at –100 °C. The middle trace includes through-space $F–H_o(Z)$ coupling; the bottom trace does not.

distinct environments for the three pyridyl ligands (Y and Z, Figure 7.6). Through-space F_A–H_o(Z) (2.5 Hz) and F_C–H_o(Z) (14.0 Hz) couplings via the π systems of the Z pyridyl ligands were simulated, resulting in a heteronuclear AB_2CDX_4 spin system. The latter coupling is well resolved and gives rise to the H_o(Z) doublet of doublets (Figure 7.6).

$$WF_6(NC_5H_5)_2 + 2[(CH_3)_3Si(NC_5H_5)]^+ \rightarrow [WF_4(NC_5H_5)_4]^{2+} + 2(CH_3)_3SiF \qquad (7.2)$$

Upon warming to –60 °C, coupling information within the F_B, F_C, and F_D resonances is lost and F_A collapses into a pseudo-quintet. Between –40 and –20 °C, the F_B, F_C, F_D resonances coalesce into a broad singlet (F_X) and F_A collapses to a binomial quintet with an averaged $^2J(F_A–F_X)$ (71.1 Hz), representing a pseudo-AX_4 spin system. At 20 °C, all coupling information in the F_A resonance is lost, though the F_A and F_X environments remain distinct. The coalescence event is accompanied by ^{19}F decoupling in the ^1H NMR spectrum at –60 °C such that through-space coupling is no longer observed.

At or above 0 °C, decomposition of $[WF_5(NC_5H_5)_3]^+$ is indicated by formation of a broad resonance at 155 ppm in the ^{19}F NMR spectrum along with increasing amounts of $[WF_4(NC_5H_5)_4]^{2+}$. The broad resonance is tentatively attributed to $[WF_5(NC_5H_5)_2]^+$ that undergoes rapid exchange with $[WF_5(NC_5H_5)_3]^+$ and $WF_6(NC_5H_5)_2$, and interacts with $[O_3SCF_3]^-$. Intermolecular exchange occurs to such an extent that $WF_6(NC_5H_5)_2$ is no longer observed. This explains its difference in chemical shift from the related $[WF_5(L)]^+$ cations, which are stabilised by the more weakly coordinating $[Sb_nF_{5n+1}]^-$ (n = 1, 2) anions. The small amounts of additional $[WF_4(NC_5H_5)_4]^{2+}$ are likely generated upon dismutation of $[WF_5(NC_5H_5)_2]^+$ (Eq. 7.3) and/or $[WF_5(NC_5H_5)_3]^+$ (Eq. 7.4)

$$[WF_5(NC_5H_5)_2]^+ \rightleftharpoons \tfrac{1}{2}[WF_4(NC_5H_5)_4]^{2+} + \tfrac{1}{2}WF_6 \qquad (7.3)$$

$$[WF_5(NC_5H_5)_3]^+ \rightleftharpoons \tfrac{1}{2}[WF_4(NC_5H_5)_4]^{2+} + \tfrac{1}{2}WF_6(NC_5H_5)_2 \quad (7.4)$$

Reaction rates for the four-site exchange process observed in the ^{19}F NMR spectra between –100 °C and 0 °C were determined via dynamic NMR simulations (Table 7.4 and Figure 7.8), the Eyring plot of which (Figure 7.9) yielded precise values for $\Delta H^{\ddagger}$ (37.8(6) kJ mol^{-1}) and $\Delta S^{\ddagger}$ (0(3) J mol^{-1} K^{-1}). The process is entropically neutral, suggesting unimolecular exchange that is best described as a rotation of the F_X square face with respect to the triangular face formed by F_A and the Z pyridyl ligands. This mechanism is corroborated by the prediction of such a rotation as a low-frequency vibrational mode (86 cm^{-1}) and would be consistent with the observed averaging of all ^2J coupling to F_A along with loss of through-space coupling from H_o to F_C. As the F_X square face is capped by the Y pyridyl ligand, the proposed exchange mechanism invokes the "monocapped-4:3" coordination sphere used to describe the solid-state geometries of the $[WF_5(L)]^+$ salts. This mechanism is similar to the "turnstile" mechanism of trigonal-dodecahedral ReH_5 adducts in which an H_3 triangular rotates with respect to the remainder of the trigonal dodecahedron.[21,22]

In order to investigate the possibility of a two-site exchange process between two distinct $H_o(Z)$ environments in the variable-temperature ^1H NMR spectra, their dynamic behaviour was simulated. The chemical-shift difference between the $H_o(Z)$ doublets was set to 14.0 Hz with $^3J(H_o–H_m)$ = 6.9 Hz at −100 °C. The dynamic simulations show that the two doublets broaden while maintaining an envelope of *ca.* 24 Hz, eventually coalescing into a single resonance at a rate of 20 s^{-1}. Beyond the coalescence point, a broad doublet emerges at a rate of 130 s^{-1}. Beyond a rate of 300 s^{-1}, the linewidth converges rapidly to the natural width. At no point do the envelopes resemble the pseudo-triplets

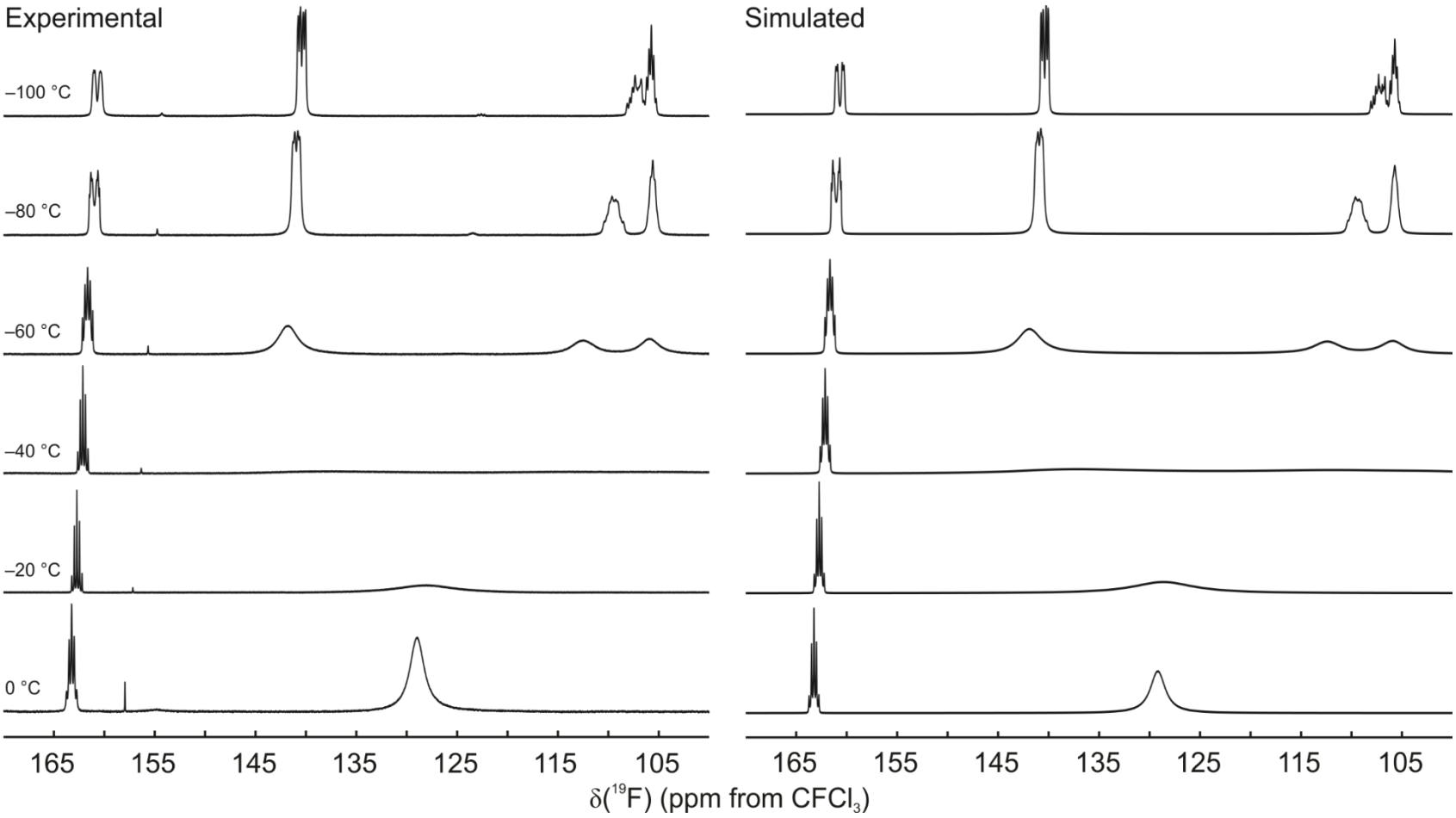

Figure 7.8. Experimental (left) and simulated (MEXICO, right) fluorine-on-tungsten regions in the ^{19}F NMR spectra of $[WF_5(NC_5H_5)_3][O_3SCF_3]$, recorded in CH_2Cl_2 at various temperatures from –100 to 20 °C.

Table 7.4. Rate Constants for Intramolecular Ligand Exchange in $[WF_5(NC_5H_5)_3]^{+a}$

T (K)	k (s^{-1})[b]
173	15
153	200
133	2 300
113	13 000
93	85 000
73	350 000

[a]Recorded in CH_2Cl_2. [b]Simulated using MEXICO (version 3.0).[11,12]

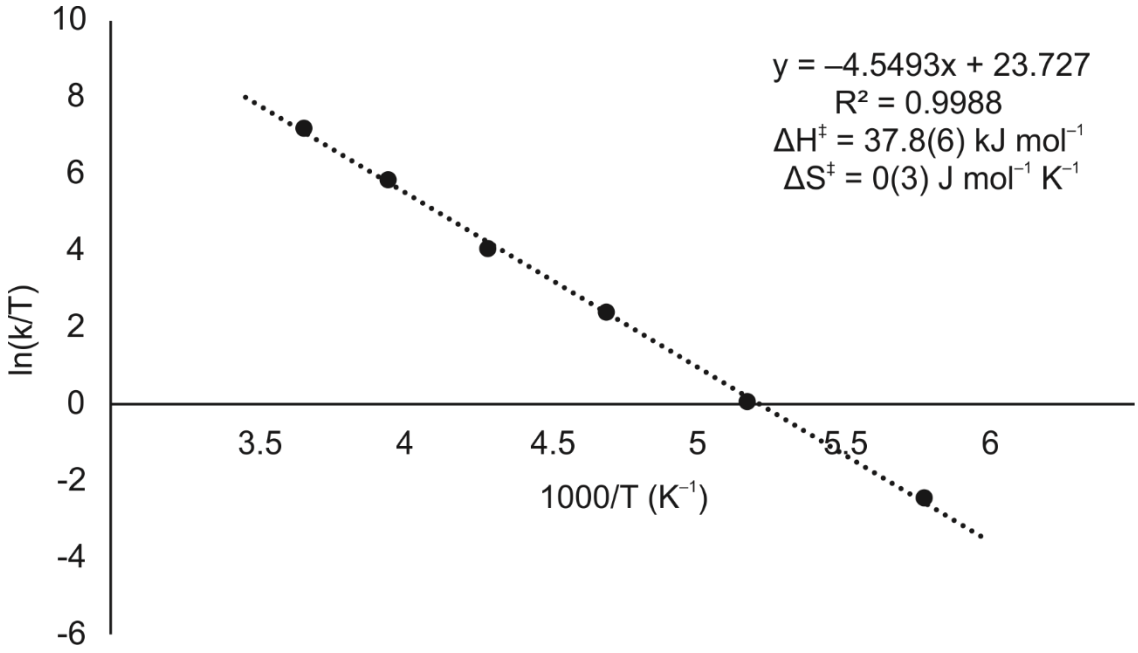

Figure 7.9. Eyring plot of the intramolecular ligand exchange in $[WF_5(NC_5H_5)_3]^+$.

observed from –60 to –80 °C, and the linewidths at rates of 10–200 s^{-1} are consistently broader than those observed experimentally (7 Hz at −100 °C and 4.5 Hz at 20 °C). Therefore, two-site exchange of the $H_o(Z)$ environments was rejected and the through-space F_C–$H_o(Z)$ coupling included in the final simulation, which also produced better agreement between the experimental and simulated ^{19}F NMR spectra.

7.2.4.2. Decomposition of $[WF_5(NC_5H_5)_3][O_3SCF_3]$ in C_5H_5N

Monitoring the reaction of equimolar WF_6 and $(CH_3)_3SiO_3SCF_3$ in C_5H_5N by ambient-temperature ^{19}F NMR spectroscopy reveals immediate formation of equimolar amounts of $(CH_3)_3SiF$ and $[O_3SCF_3]^-$, along with $[WF_5(NC_5H_5)_3]^+$ and small amounts of $WF_6(NC_5H_5)_2$. After quantitative F^- abstraction, the ratio of the combined integrals of the F-on-W^{VI} resonances, i.e., those for $[WF_5(NC_5H_5)_3]^+$ (165, 129 ppm) and $WF_6(NC_5H_5)_2$ (114 ppm[24]), to the integral of $[O_3SCF_3]^-$ is expected to be 5:3. A ratio of 4.80:3 was observed after *ca*. 15 min, which gradually decreased over time (4.65:3 after *ca*. 30 min; 4.14:3 after *ca*. 90 min), indicating slow reduction to NMR-silent tungsten(V). After *ca*. 16 h, only $WF_6(NC_5H_5)_2$ was observed.

The $WF_6(NC_5H_5)_2$ adduct is retained due to consumption of $(CH_3)_3SiO_3SCF_3$ via twofold F^- abstraction from WF_6 to form $[WF_4(NC_5H_5)_4]^{2+}$ (Eq. 7.2) and/or generated by dismutation of $[WF_5(NC_5H_5)_n]^+$ (n = 2, 3; Eqs. 7.3 and 7.4). The $[WF_4(NC_5H_5)_4]^{2+}$ and $[WF_5(NC_5H_5)_2]^+$ cations are not observed directly, which is attributed to their rapid reduction in C_5H_5N. This was corroborated by monitoring a reaction employing 1.5 molar equivalents of $(CH_3)_3SiO_3SCF_3$. Whereas $WF_6(NC_5H_5)_2$ is gradually formed over the course of *ca*. 90 min in the 1:1 reaction as a result of dismutation (Figure 7.10), in the 1:1.5 reaction, this formation is suppressed, consistent with Eq. 7.2 suppressing Eqs. 7.3 and/or

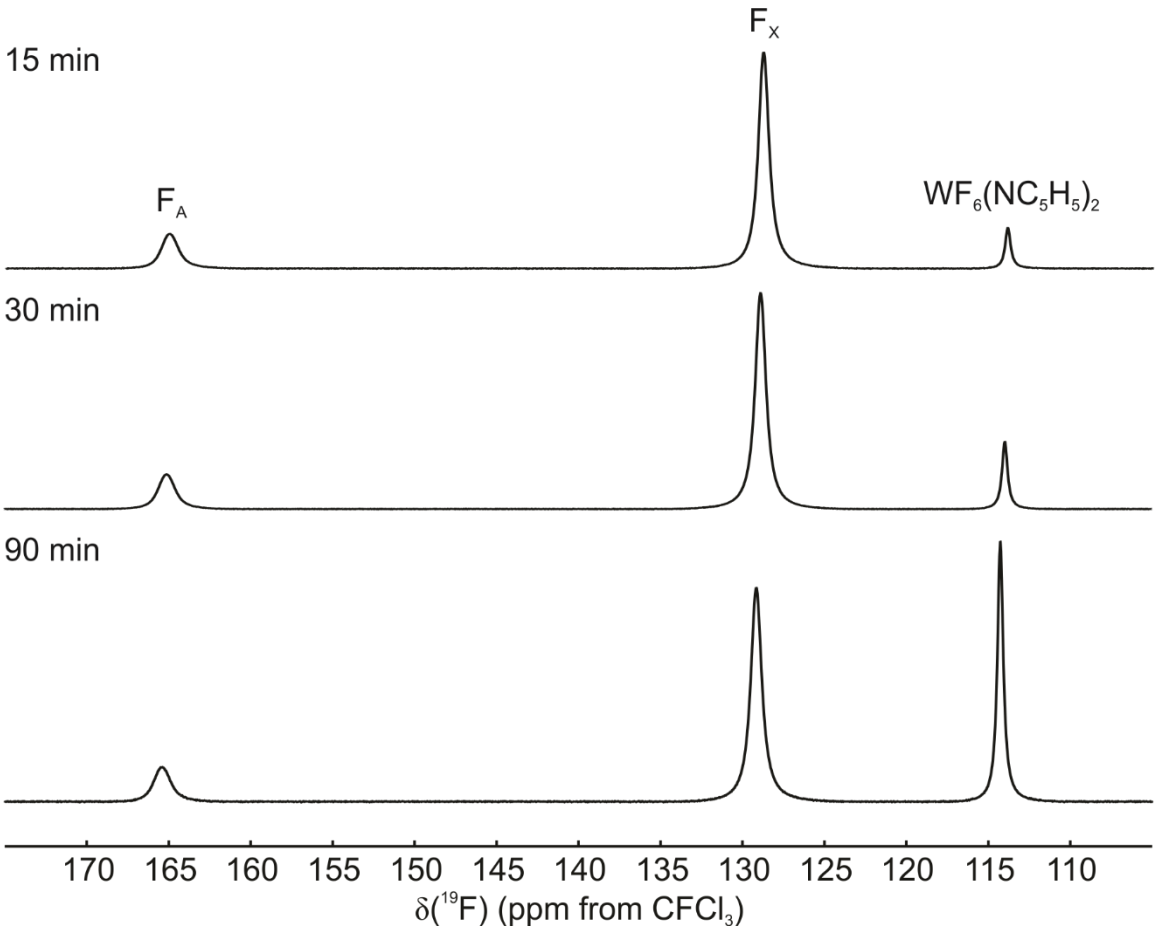

Figure 7.10. Fluorine-on-tungsten region in the ^{19}F NMR spectra of $[WF_5(NC_5H_5)_3][O_3SCF_3]$ after 15–90 min at ambient temperature, recorded in C_5H_5N at 20 °C.

7.4, while a more significant decrease in cumulative F-on-W^{VI} signal intensity is observed (1.62:3 with respect to $[O_3SCF_3]^-$ after *ca*. 30 min). The dication is apparently not reduced to $WF_5(NC_5H_5)_2$, as the latter did not crystallise appreciably from this solution. It is possible that a monocationic species that remains dissolved in the inextricable oil, e.g. $[WF_4(NC_5H_5)_4]^+$, is formed. This is reinforced by the observed loss of yield when 1.5 molar equivalents of $(CH_3)_3SiO_3SCF_3$ were used in a preparation of $WF_5(NC_5H_5)_2$. The more pronounced dismutation of $[WF_5(NC_5H_5)_n]^+$ (n = 2, 3) in C_5H_5N than in CH_2Cl_2 is apparently driven by rapid consumption of the dication via reduction.

The ^{1}H NMR spectra revealed formation of $(CH_3)_3SiF$ and the *N*-(4-pyridyl)pyridinium cation ([4-pypy]$^+$); no additional species developed after 16–24 h at ambient temperature (Figure 7.11). Formation of [4-pypy]$^+$ has been observed previously upon reduction of MX_5 (M = Nb, Ta; X = Cl, Br),[28] WBr_5,[29] and WCl_6[29] by C_5H_5N (Eq. 7.5). Notably, the reduction of these transition-metal halides is proposed to proceed via $[MX_4(NC_5H_5)_2]^+$ cations as reactive intermediates.[28] The absence of $[C_5H_5NH]^+$ in the ^{1}H NMR spectrum reported herein is attributed to rapid exchange of the nitrogen-bound proton between solvent molecules.

$$MX_5 + 3½C_5H_5N \rightarrow MX_4(NC_5H_5)_2 + ½[4\text{-pypy}]X + ½[C_5H_5NH]X \qquad (7.5)$$

7.2.4.3. Attempted Synthesis of $[WF_5(NC_5H_5)_2][Sb_2F_{11}]$ in SO_2

An attempt to prepare $[WF_5(NC_5H_5)_2][Sb_2F_{11}]$ via reaction of $WF_6(NC_5H_5)_2$ with $SbF_5(OSO)$ in SO_2 (Eq. 7.6) resulted in formation of a yellow solution, in which $[WF_5(NC_5H_5)_2]^+$ was observed by ^{19}F NMR spectroscopy at –50 °C (Figure 7.12). The $[WF_5(NC_5H_5)_2]^+$ cation, however, is highly susceptible to decomposition, preventing its isolation. In addition to a broad resonance corresponding to the expected cation (205 ppm,

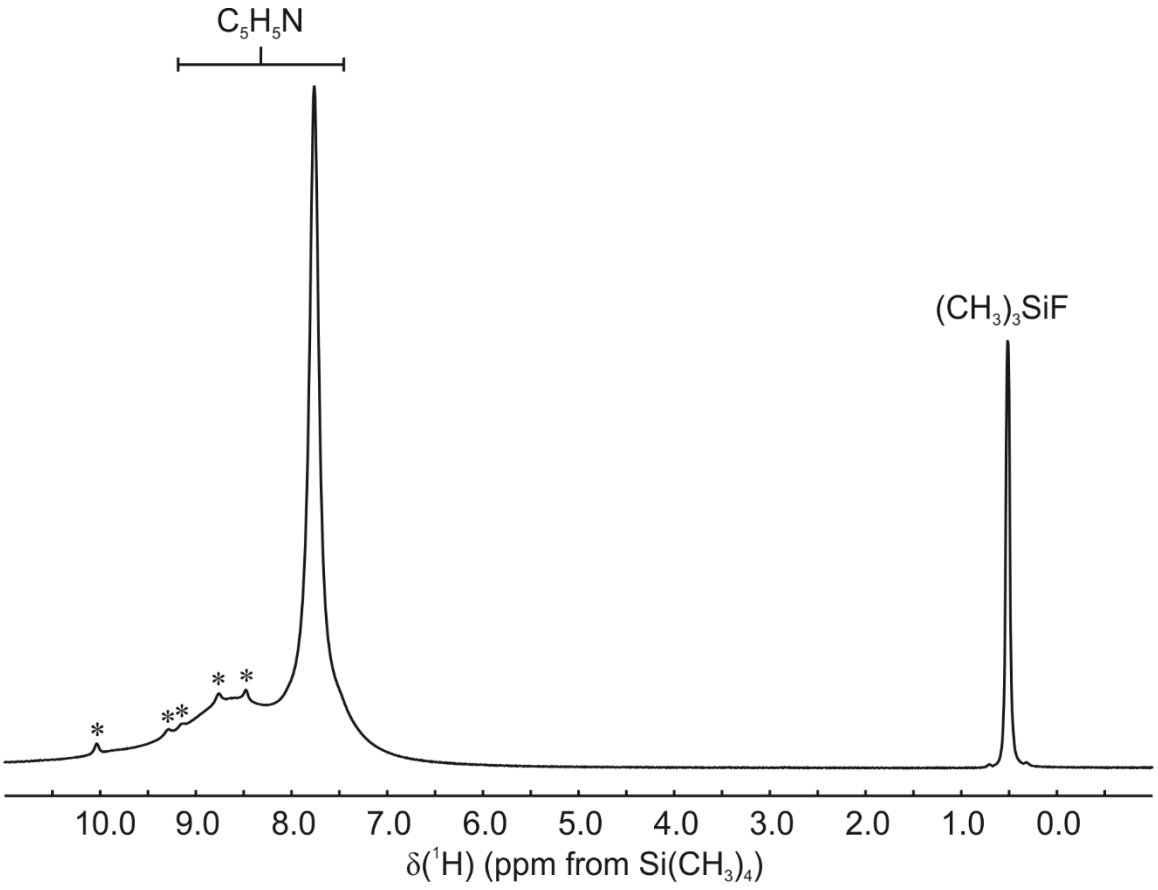

Figure 7.11. Proton NMR spectrum of a mixture of $WF_6(NC_5H_5)_2$ and $[(CH_3)_3Si(NC_5H_5)][O_3SCF_3]$ (molar ratio *ca*. 1:1.5), recorded in C_5H_5N at 20 °C. Asterisks (*) denote $[4\text{-pypy}]^+$.

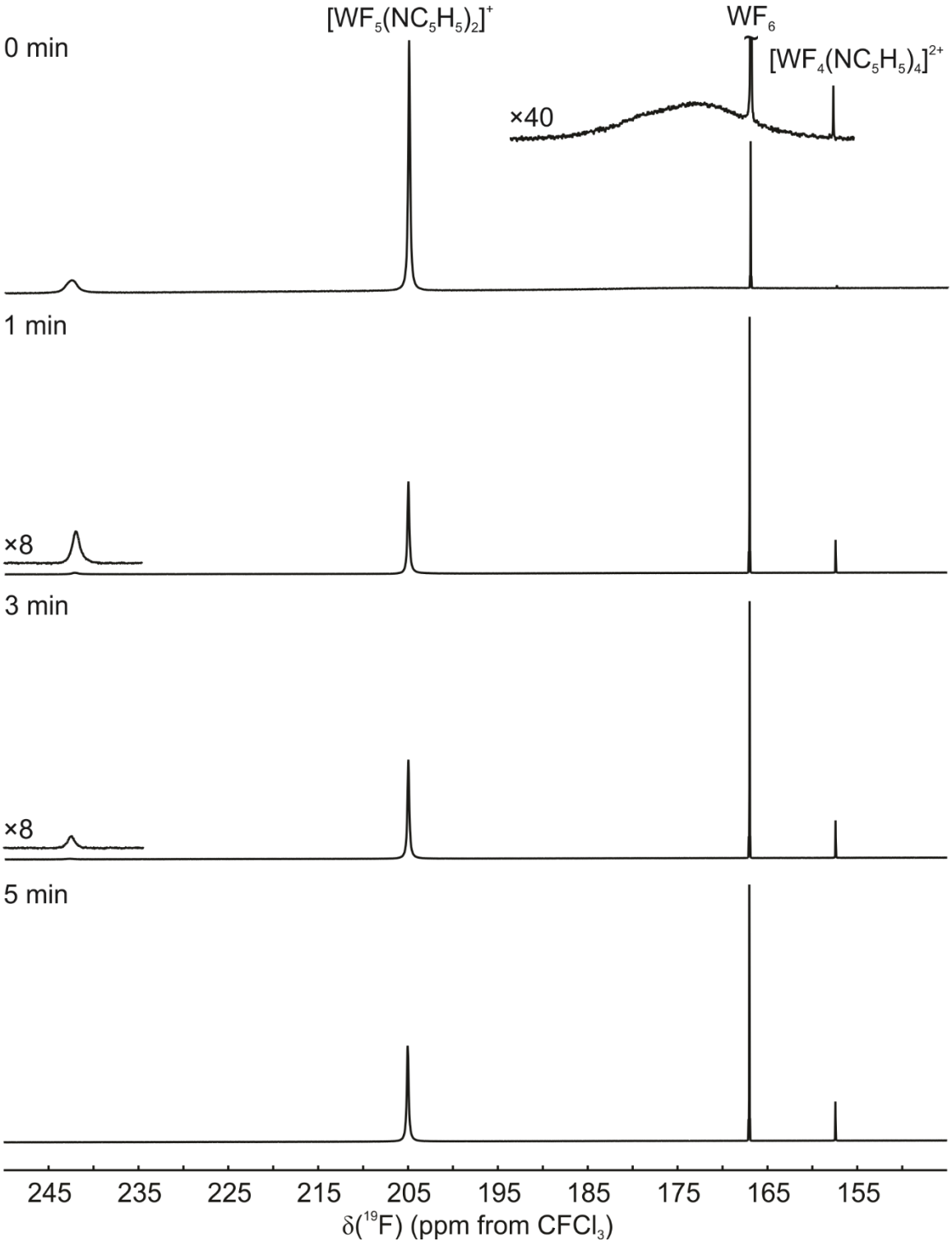

Figure 7.12. Fluorine-on-tungsten region in the ^{19}F NMR spectra of a mixture of $WF_6(NC_5H_5)_2$ and $SbF_5(OSO)$ (molar ratio *ca.* 1:2) after 0–5 min at ambient temperature, recorded in SO_2 at –50 °C.

cf. $[WF_5(L)]^+$: 204–206 ppm), significant amounts of WF_6 (166.96 ppm) and traces of $[WF_4(NC_5H_5)_4]^{2+}$ (157.43 ppm) were observed, along with broad resonances at 243 and 175 ppm that are attributed to unidentified fluoridotungsten(VI) cations. A similar dark brown impurity was observed at 235 ppm in the ^{19}F NMR spectrum of $[WF_5(2,2'\text{-bipy})]^+$, which could be removed by keeping the solution at ambient temperature for *ca*. 16 h. However, while intermittently warming the $[WF_5(NC_5H_5)_2]^+$ solution to ambient temperature resulted in depletion of the broad resonances and complete loss of colour, increased proportions of $[WF_4(NC_5H_5)_4]^{2+}$ and WF_6 were generated at the expense of $[WF_5(NC_5H_5)_2]^+$, revealing its much greater susceptibility to dismutation than $[WF_5(L)]^+$, which are stable as their $[Sb_2F_{11}]^-$ salts.

$$WF_6(NC_5H_5)_2 + 2SbF_5(OSO) \rightarrow [WF_5(NC_5H_5)_2][Sb_2F_{11}] + 2SO_2 \qquad (7.6)$$

The proportion of WF_6 with respect to $[WF_4(NC_5H_5)_4]^{2+}$ increased after several minutes at ambient temperature such that its formation could not be accounted for entirely by dismutation of $[WF_5(NC_5H_5)_2]^+$. This suggests that C_5H_5N abstraction from $WF_6(NC_5H_5)_2$ by $SbF_5(OSO)$ occurs as an additional side reaction (Eq. 7.7). However, $SbF_5(NC_5H_5)$ could not be unambiguously identified due to possible overlap between resonances that would correspond to it (assuming similarities to $SbF_5(NCR)$ adducts[30]), $SbF_5(OSO)$,[31] and $[Sb_2F_{11}]^-$[31] (Figure 7.13).

$$WF_6(NC_5H_5)_2 + 2SbF_5(OSO) \rightarrow WF_6 + 2SbF_5(NC_5H_5) + 2SO_2 \qquad (7.7)$$

It should be noted that there was no evidence for formation of $[4\text{-pypy}]^+$ or $[C_5H_5NH]^+$ in the attempted synthesis of $[WF_5(NC_5H_5)_2][Sb_2F_{11}]$, nor discolouration of the

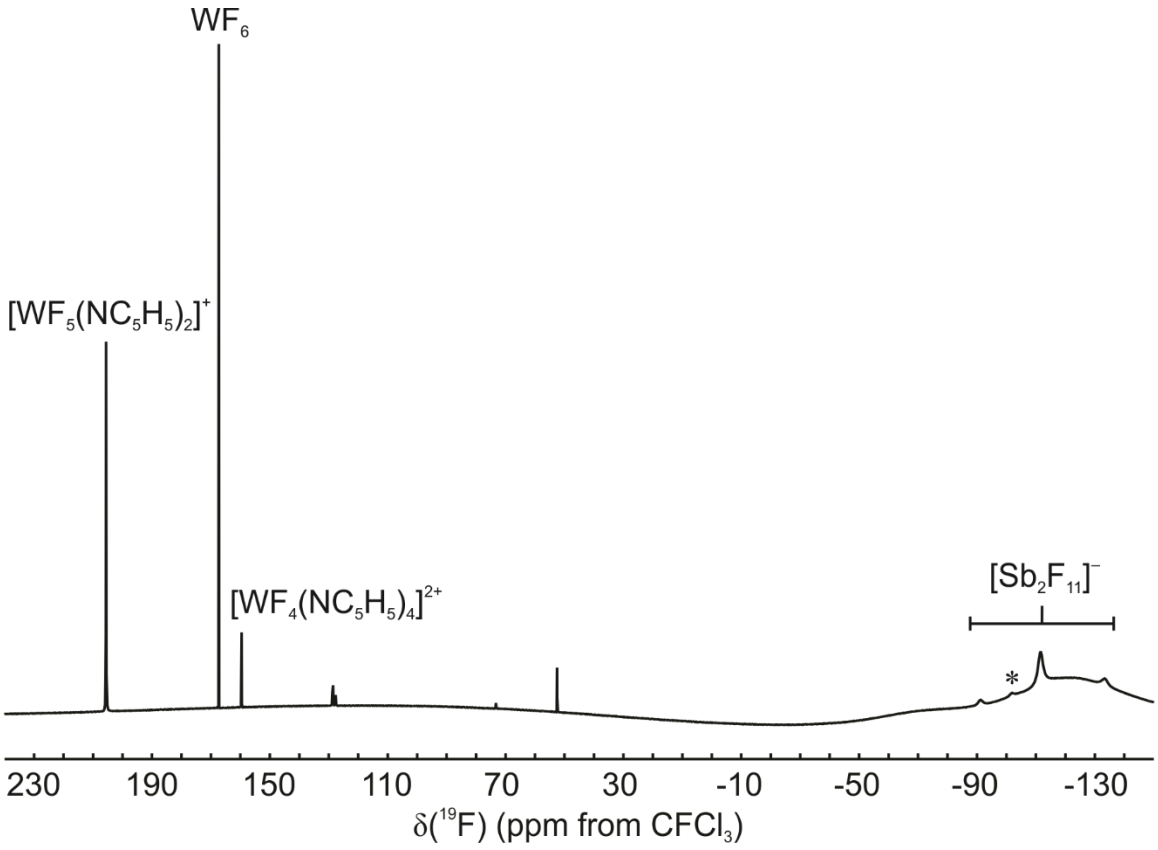

Figure 7.13. Fluorine-19 NMR spectrum of a mixture of $WF_6(NC_5H_5)_2$ and $SbF_5(OSO)$ (molar ratio *ca*. 1:2) after 30 min at ambient temperature, recorded in SO_2 at 20 °C. Asterisk (*) denotes the F_{eq} resonance of $SbF_5(OSO)$ and/or $SbF_5(NC_5H_5)$.

sample even after storage at ambient temperature for 24 h. This illustrates the necessity of free C_5H_5N for reduction of the cation to occur.

7.2.5. Computational Results

7.2.5.1. Molecular Orbitals and Natural-Bond-Orbital (NBO) Analysis of $[WF_5(NC_5H_5)_n]^+$ (n = 2, 3) and $WF_5(NC_5H_5)_2$

The HOMO-LUMO transitions of $[WF_5(NC_5H_5)_n]^+$ (n = 2, 3) are predicted to be LMCT in nature (Figure 7.14a and b). However, in the LUMO of $[WF_5(NC_5H_5)_2]^+$, there is also substantial $p_\pi(C_o)$ and $p_\pi(C_p)$ character on the non-capping pyridyl ligand. The HOMO-LUMO gaps of the cations (n = 2: 3.76 eV; n = 3: 4.09 eV) are comparable to those calculated for $[WF_5(L)]^+$ (L = 2,2′-bipy, 1,10-phen; 3.66–3.92 eV) at the same level of theory,[32] despite the difference in colour between the cations bearing bidentate (yellow-orange) vs. monodentate ligands (colourless). The LUMO energy of $[WF_5(NC_5H_5)_2]^+$ (–7.63 eV) is significantly lower than that of $[WF_5(NC_5H_5)_3]^+$ (–6.60 eV), suggesting a much greater susceptibly of the former to reduction. For comparison, the difference in LUMO energies is similar to the difference in E_{ea} values between MoF_6 (4.23 eV[33]) and WF_6 (3.16 eV[34]); the former is capable of oxidising NO to $[NO]^+$, whereas the latter is not.[35] The SOMO of $WF_5(NC_5H_5)_2$, like the LUMO of its parent cation, possesses $\pi^*(d(W)–p(F))$ and $p_\pi(C)$ character (Figure 7.14c). The absence of $\sigma^*(d(W)–p(N))$ interactions explains the observed insignificant change in the W–N bond lengths in $WF_5(NC_5H_5)_2$ while the W–F bonds are elongated upon comparison to related tungsten(VI) complexes.

Natural-bond-orbital (NBO) analyses were performed, providing natural-population-analysis (NPA) charges, Wiberg valences, and Wiberg bond indices (WBIs) for

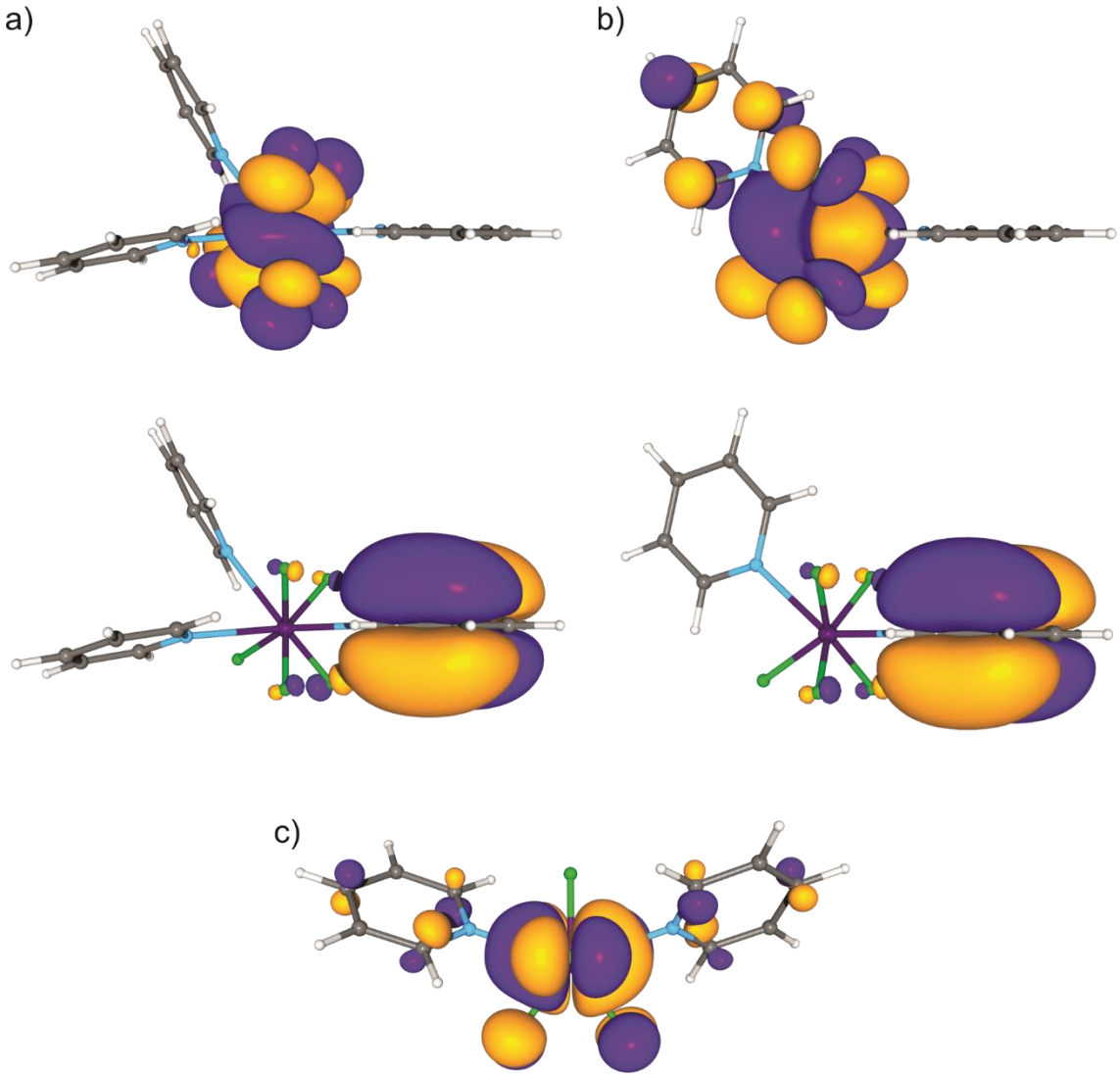

Figure 7.14. LUMO (top) and HOMO (bottom) of a) $[WF_5(NC_5H_5)_3]^+$ and b) $[WF_5(NC_5H_5)_2]^+$, with c) the SOMO of $WF_5(NC_5H_5)_2$. Isosurface values are drawn at 0.04 e $Å^{-3}$.

$[WF_5(NC_5H_5)_n]^+$ (n = 2, 3) and $WF_5(NC_5H_5)_2$ (Tables 7.5 and 7.6). There is a large degree of compensatory electron donation from the pyridyl ligands to stabilise the electron-poor tungsten(VI) centres of $[WF_5(NC_5H_5)_n]^+$ (n = 2, 3), as evidenced by the cumulative NPA charges on the ligands, which in the case of $[WF_5(NC_5H_5)_3]^+$ (+0.92), accounts for nearly all of the overall charge of the complex. Correspondingly, the NPA charge on the tungsten(VI) centre decreases only slightly upon reduction to +5 (+2.57 → +2.31). The WBIs of the W–F and W–N bonds in $[WF_5(NC_5H_5)_2]^+$ (n = 2, 3) are similar to $[WF_5(L)]^+$ (W–F: 0.79–0.83, W–N: 0.42), with the W–F bonds being slightly weaker and the W–N bonds slightly stronger. Meanwhile, those of $[WF_5(NC_5H_5)_3]^+$ are more similar to $WF_6(NC_5H_5)$ and derivatives thereof (W–F: 0.71–0.77, W–N: 0.31–0.40). In the case of both $[WF_5(NC_5H_5)_n]^+$ cations, the W−N bonds strengths are somewhat more than half those of the W−F bonds (W–N/W–F: 0.53–0.61).

The WBIs of $WF_5(NC_5H_5)_2$ suggest proportional weakening of the W–F and W–N bonds (W–N/W–F: 0.56–0.58) with respect to $[WF_5(NC_5H_5)_2]^+$. Significant σ(lp(N)→lv(W)) (lp = lone pair, lv = lone valence) bonding (324 kJ mol^{-1} per ligand) is predicted for $WF_5(NC_5H_5)_2$ as per second-order perturbation analysis of the NBO donor-acceptor interactions, whereas there exists negligible synergic bonding in the form of π(lp(W)→π*(NC)) interactions (< 5 kJ mol^{-1} per ligand), consistent with the highly positive NPA charge on the electron-poor tungsten(V) centre (+2.31).

7.2.5.2. Thermodynamics of the Reduction of $[WF_5(NC_5H_5)_2]^+$

Considering that nucleophilic attack at a pyridyl ligand is the proposed first step for the reduction of transition-metal halides by C_5H_5N[28] and the LUMO of $[WF_5(NC_5H_5)_2]^+$

Table 7.5. NPA Charges, Wiberg Valences, and WBIs of $[WF_5(NC_5H_5)_3]^+$, $[WF_5(NC_5H_5)_2]^+$, and $WF_5(NC_5H_5)_2$[a]

	$[WF_5(NC_5H_5)_3]^+$		$[WF_5(NC_5H_5)_2]^+$		$WF_5(NC_5H_5)_2$	
W	+2.48	[5.02]	+2.57	[4.91]	+2.31	[4.17]
F(1)	–0.48	[0.95]	–0.45	[1.00]	–0.55	[0.82]
F(2)	–0.51	[0.90]	–0.47	[0.96]	–0.57	[0.79]
F(3)	–0.47	[0.97]	–0.44	[1.00]	–0.54	[0.85]
F(4)	–0.47	[0.95]	–0.44	[1.00]		
F(5)	–0.47	[0.96]	–0.47	[0.96]		
N(1)	–0.46	[3.38]	–0.50	[3.38]	–0.46	[3.35]
N(2)	–0.46	[3.38]	–0.48	[3.39]		
N(3)	–0.45	[3.40]				
C_o[b]	+0.09	[3.91]	+0.09	[3.90]	+0.10	[3.91]
C_m[b]	–0.22	[3.96]	–0.22	[3.96]	–0.23	[3.96]
C_p[b]	–0.12	[3.95]	–0.10	[3.94]	–0.14	[3.96]
H_o[b]	+0.23	[0.95]	+0.23	[0.95]	+0.23	[0.95]
H_m[b]	+0.23	[0.95]	+0.24	[0.94]	+0.22	[0.95]
H_p[b]	+0.23	[0.95]	+0.23	[0.95]	+0.21	[0.96]
$\Sigma(C_5H_5N(1))$	+0.29		+0.35		+0.23	
$\Sigma(C_5H_5N(2))$	+0.30		+0.36			
$\Sigma(C_5H_5N(3))$	+0.32					

[a]Calculated at the B3LYP/aVTZ level of theory. [b]Averaged value.

Table 7.6. Wiberg Bond Indices of $[WF_5(NC_5H_5)_3]^+$, $[WF_5(NC_5H_5)_2]^+$, and $WF_5(NC_5H_5)_2$[a]

	$[WF_5(NC_5H_5)_3]^+$	$[WF_5(NC_5H_5)_2]^+$	$WF_5(NC_5H_5)_2$
		WBI	
W–F(1)	0.73	0.78	0.65
W–F(2)	0.69	0.75	0.65
W–F(3)	0.75	0.80	0.68
W–F(4)	0.74	0.80	
W–F(5)	0.75	0.75	
W–N(1)	0.40	0.46	0.38
W–N(2)	0.40	0.45	
W–N(3)	0.42		
N–C_o	1.35	1.33	1.36
C_o–C_m	1.45	1.46	1.44
C_m–C_p	1.44	1.43	1.44
C_o–H_o	0.91	0.91	0.91
C_m–H_m	0.91	0.91	0.92
C_p–H_p	0.91	0.91	0.92

[a]Calculated at the B3LYP/aVTZ level of theory.

could facilitate such an attack, the thermodynamic feasibility of a similar route for the reduction of $[WF_5(NC_5H_5)_2]^+$ was investigated at the B3LYP/aVTZ level of theory. The reactions characterised for the reduction of $[WF_5(NC_5H_5)_2]^+$ by C_5H_5N are illustrated in Figure 7.15, with geometries and Gibbs energies calculated in implicit C_5H_5N solvent (SMD solvent model) at 25 °C. Gas-phase thermochemical data are given in Table 7.7 and Gibbs energies and enthalpies of solvation are given in Table 7.8.

The Gibbs energy and enthalpy of solvation ($\Delta_{solv}G$ and $\Delta_{solv}H$, respectively) are strictly defined herein as the Gibbs energy or enthalpy of the dissolution of a gaseous species (X) in C_5H_5N at 25 °C (Eq. 7.8). In the case of C_5H_5N, $\Delta_{solv}H$ is equivalent to the negative of the enthalpy of vaporisation ($\Delta_{vap}H$, Eq. 7.9) if "solvated, gaseous" C_5H_5N and liquid C_5H_5N are considered to be equivalent. The calculated $\Delta_{solv}H$ (–25 kJ mol^{-1}) agrees reasonably well with the reported $\Delta_{vap}H$ at 25 °C (40.2(1) kJ mol^{-1}).[36]

$$X_{(g)} \xrightarrow{C_5H_5N} X_{(solv)} \quad (7.8)$$

$$C_5H_5N_{(l)} \rightarrow C_5H_5N_{(g)} \quad (7.9)$$

First, it was established that dissociation of C_5H_5N from $[WF_5(NC_5H_5)_3]^+$ (Eq. 7.10) is thermodynamically favourable (Δ_rG = –33 kJ mol^{-1}, Δ_rH = +13 kJ mol^{-1}), which is consistent with the ^{19}F NMR spectroscopic studies. Furthermore, an attempt to optimise the intermediate complex formed upon nucleophilic attack at a *para* carbon atom in $[WF_5(NC_5H_5)_3]^+$ was unsuccessful, as the C_p–N bond of the intermediate preferentially dissociated to regenerate the parent cation and free C_5H_5N. These observations corroborate the notion that $[WF_5(NC_5H_5)_3]^+$ is not directly involved in the redox process.

$$[WF_5(NC_5H_5)_3]^+ \rightleftharpoons [WF_5(NC_5H_5)_2]^+ + C_5H_5N \quad (7.10)$$

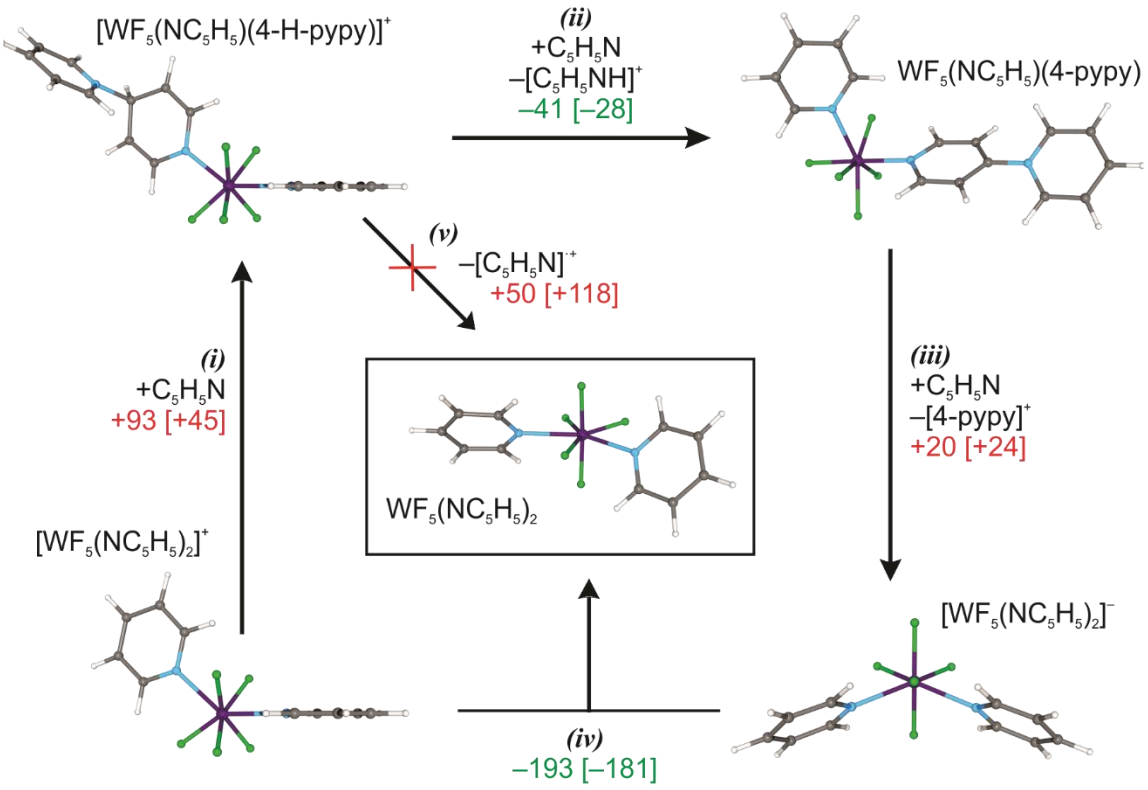

Figure 7.15. Proposed routes for the reduction of $[WF_5(NC_5H_5)_2]^+$ in C_5H_5N, with optimised geometries and calculated Gibbs energies [enthalpies] (kJ mol^{-1}) in C_5H_5N at 25 °C (B3LYP/aVTZ).

Table 7.7. Gas-Phase Thermochemical Data ($\Delta_r G$ and $\Delta_r H$, kJ mol^{-1}) for the Decomposition of $[WF_5(NC_5H_5)_3]^+$ in C_5H_5N at 25 °C[a]

Reaction[b]	$\Delta_r G$	$\Delta_r H$
(8)	+4	+59
(9)	+13	–7
(i)	+84	+35
(ii)	+72	+80
(iii)	+404	+404
(iv)	–535	–532
(v)	+142	+200

[a]Calculated at the B3LYP/aVTZ level of theory. [b]Labels correspond to those in the main text, with Roman-numerical labels corresponding to Scheme 1.

Table 7.8. Gibbs Energies and Enthalpies of Solvation ($\Delta_{solv}G$ and $\Delta_{solv}H$, kJ mol^{-1}) of Compounds Involved in the Decomposition of $[WF_5(NC_5H_5)_3]^+$ in C_5H_5N at 25 °C[a]

	$\Delta_{solv}G$	$\Delta_{solv}H$
$[W^{VI}F_5(NC_5H_5)_3]^+$	–210	–210
$[W^{VI}F_5(NC_5H_5)_2]^+$	–222	–232
$[W^{VI}F_5(NC_5H_5)(4\text{-H-pypy})]^+$	–238	–247
$W^{IV}F_5(NC_5H_5)(4\text{-pypy})$	–124	–128
$[W^{IV}F_5(NC_5H_5)_2]^-$	–290	–289
$W^{V}F_5(NC_5H_5)_2$	–85	–85
$[4\text{-pypy}]^+$	–243	–244
$[C_5H_5NH]^+$	–251	–251
$[C_5H_5N]^{\bullet+}$	–244	–244
C_5H_5N	–25	–25

[a]Calculated at the B3LYP/aVTZ level of theory using the SMD implicit solvent model.

Nucleophilic attack at the activated *para* carbon atom of $[WF_5(NC_5H_5)_2]^+$, meanwhile, is predicted to result in an intermediate 4-hydro-4-(1′-pyridyl)pyridyl (4-H-pypy) complex (Figure 7.15, (i)). The optimised gas-phase geometry of this intermediate reveals that the coordination geometry of the tungsten centre does not change. However, complete dearomatisation of the attacked pyridyl ligand results in a semiquinoidal complex with a W=N bond, causing significant contraction of the W–N (2.108 Å) and C_o–C_m bonds (1.344, 1.345 Å) and complementary elongation of the C_o–N (1.352, 1.359 Å) and C_m–C_p (1.397, 1.403 Å) bonds with respect to $[WF_5(NC_5H_5)_2]^+$ (Table 7.2). The formation of a W=N bond indicates that 4-H-pypy is redox non-innocent, whereas the ligand-centred HOMOs of $[WF_5(NC_5H_5)_n]^+$ (n = 2, 3; Figure 7.14a and b) suggest innocence from the pyridyl ligands.

The reduction of $[WF_5(NC_5H_5)_2]^+$ could proceed through $[WF_5(NC_5H_5)(4\text{-H-pypy})]^+$ as a reactive intermediate, despite its thermodynamic unfavourability, assuming rapid deprotonation of 4-H-pypy by free C_5H_5N (Figure 7.15, (ii)). This results in concomitant rearomatisation of 4-H-pypy to $[4\text{-pypy}]^+$ and formal two-electron reduction to afford a zwitterionic tungsten(IV) complex, $WF_5(NC_5H_5)(4\text{-pypy})$. This complex is predicted to adopt a pentagonal-bipyramidal geometry in which the $[4\text{-pypy}]^+$ ligand occupies an axial position, in contrast to the co-equatorial positions of the pyridyl ligands in $WF_5(NC_5H_5)_2$.

Following reduction from +6 to +4, substitution of the $[4\text{-pypy}]^+$ ligand with C_5H_5N is expected to occur (Figure 7.15, (iii)), after which a highly exergonic and exothermic comproportionation of the resultant $[WF_5(NC_5H_5)_2]^-$ with $[WF_5(NC_5H_5)_2]^+$ would yield the final product (Scheme 1, (iv)). The overall one-electron reduction of $[WF_5(NC_5H_5)_2]^+$ to

$WF_5(NC_5H_5)_2$ via the proposed route (Eq. 7.11) is predicted to be thermodynamically favourable (Δ_rG = –60 kJ mol^{-1}, Δ_rH = –70 kJ mol^{-1}).

$$[W^{VI}F_5(NC_5H_5)_2]^+ + 1½C_5H_5N \rightarrow W^{V}F_5(NC_5H_5)_2 + ½[C_5H_5NH]^+ + ½[4\text{-pypy}]^+ \quad (7.11)$$

In lieu of the multi-step mechanism described, direct reduction from tungsten(VI) to tungsten(IV) could be envisioned via homolysis of the C_p–N bond in $[WF_5(NC_5H_5)(4\text{-H-pypy})]^+$ (Figure 7.15, (v)). However, this reaction is unfavourable with respect to the already unstable intermediate and especially with respect to $[WF_5(NC_5H_5)_2]^+$ in C_5H_5N (Figure 7.15, (i) + (v); Δ_rG = +143 kJ mol^{-1}, Δ_rH = +163 kJ mol^{-1}). In addition, it is inconsistent with the observed ^{1}H NMR spectrum; a radical-substitution reaction of C_5H_5N with $[C_5H_5N]^{\bullet+}$ would necessarily be termolecular in nature and expected to result in a mixture of isomers (Eq. 7.12), as was observed during analogous reactions of C_5H_5N with 2-$C_6H_4R^{\bullet}$ (R = H, CH_3, NO_2).[37]

$$2[C_5H_5N]^{\bullet+} + C_5H_5N \rightarrow [x\text{-pypy}]^+ + [C_5H_5NH]^+ \ (x = 2, 3, 4) \quad (7.12)$$

7.2.5.3. Ligand-Induced Autoionisation of MF_5 (M = Nb, Mo, Ta, W) by C_5H_5N

The isolation of molecular $WF_5(NC_5H_5)_2$ is unique, considering the susceptibility of NbF_5 and TaF_5 to autoionise in the presence of mono- and bidentate main-group donor ligands. Thus, the isomerisation of $MF_5(NC_5H_5)_2$ (M = Mo, Nb, Ta, W; Eq. 7.13) was investigated in the gas phase and in solution to elucidate a possible thermodynamic basis for this observed difference in Lewis-acid behaviour.

$$2MF_5(NC_5H_5)_2 \rightarrow [MF_4(NC_5H_5)_4][MF_6] \quad (7.13)$$

The geometries of $MF_5(NC_5H_5)_2$ (M = Nb, Ta) were predicted to be isostructural with $[WF_5(NC_5H_5)_2]^+$, whereas $MoF_5(NC_5H_5)_2$ is isostructural with $WF_5(NC_5H_5)_2$. The $[MF_4(NC_5H_5)_4]^+$ cations are in excellent agreement with the reported crystal structures,[15] as is $[WF_4(NC_5H_5)_4]^+$ (see Chapter 8); the complexes are again isostructural within each group. Meanwhile, the $[MF_6]^-$ anions possess slightly elongated bonds (M = Nb: 1.915 Å; M = Ta: 1.914 Å) in comparison to the crystal structures (*ca*. 1.88–1.89 Å).[15] While their group-6 analogues are expected to be D_{3d}-symmetric in the gas phase due to a t_{2g} Jahn-Teller distortion, a stable ground state did not persist in calculations that included solvation. As such, contracted, D_{4h}-symmetric structures with imaginary frequencies (M = Mo; 244*i* cm^{-1}; M = W: 195*i* cm^{-1}) were optimised instead in the gas phase and with solvation. The Mo–F bonds (1.864, 1.914 Å) are also somewhat elongated with respect to those in crystal structures of alkali-metal $[MoF_6]^-$ salts (*ca*. 1.84–1.87 Å).[38] Gibbs energies and enthalpies of solvation are given in Table 7.9.

It was determined that, irrespectively of the metal centre, $MF_5(NC_5H_5)_2$ are the thermodynamic products (Table 7.10). The relative stability is greater for the group-6 transition metals. This could suggest that the disparity is due to the kinetic stabilisation of $[MF_4(NC_5H_5)_4][MF_6]$. Niobium and tantalum pentafluoride are susceptible to a small degree of spontaneous autoionisation in the melt (< 1%; Eq. 7.14)[39,40] as determined by conductimetric experiments. Thus, it is possible that a strongly Lewis-acidic $[M_nF_{5n-1}]^+$ cation is reactive towards C_5H_5N in solution, rather than neutral MF_5 (Eq. 7.15). The resultant salt is then kinetically stable towards isomerisation to molecular $MF_5(NC_5H_5)_2$. This is corroborated by the observed formation of molecular $TaF_5(NH_3)$ upon displacement of F^- from $[TaF_6]^-$ (i.e., a non-ionising source of TaF_5) by NH_3.[41]

Table 7.9. Gibbs Energies and Enthalpies of Solvation of Compounds Involved in the Isomerisation of $MF_5(NC_5H_5)_2$ at 25 °C

M	In C_5H_5N	In CH_3CN	In C_5H_5N	In CH_3CN	In C_5H_5N	In CH_3CN
	$MF_5(NC_5H_5)_2$		$[MF_4(NC_5H_5)_4]^+$		$[MF_6]^-$	
Nb	–89 [–95]	–96 [–103]	–195 [–200]	–205 [–208]	–192 [–190]	–204 [–201]
Mo	–85 [–55]	–90 [–90]	–202 [–200]	–209 [–207]	–188 [–188]	–210 [–194]
Ta	–94 [–98]	–103 [–107]	–197 [–201]	–208 [–208]	–192 [–190]	–204 [–202]
W	–85 [–85]	–91 [–90]	–198 [–201]	–205 [–208]	–192 [–191]	–204 [–203]

[a]Given in square brackets. [b]Calculated at the B3LYP/aVTZ level of theory using the SMD solvent model.

Table 7.10. Gibbs Energies and Enthalpies[a] of Isomerisation of $MF_5(NC_5H_5)_2$ at 25 °C

M	Gas-phase	In C_5H_5N	In CH_3CN
Nb	240 [227]	31 [27]	22 [24]
Mo	278 [259]	57 [41]	39 [38]
Ta	237 [222]	36 [27]	31 [25]
W	282 [264]	62 [42]	54 [34]

[a]Given in square brackets. [b]Calculated at the B3LYP/aVTZ level of theory using the SMD solvent model.

$$x\mathrm{MF_5} \rightleftharpoons [\mathrm{M}_y\mathrm{F5}_{y-1}][\mathrm{M}_z\mathrm{F}_{5z+1}] \quad (7.14)$$

$$[\mathrm{M}_y\mathrm{F}_{5y-1}]^+ + 4\mathrm{C_5H_5N} \rightarrow [\mathrm{MF_4(NC_5H_5)_4}]^+ + (y-1)\mathrm{MF_5} \quad (7.15)$$

The synthetic route employed herein alternatively eschews autoionisation of the parent WF_5 by instead exploiting the reduction of $[WF_5]^+$. However, MoF_5 is 100-fold less conductive than NbF_5 and TaF_5 in the melt.[42] and though similar studies could not be conducted for WF_5 due to its thermal instability, it is possible that it too does not ionise appreciably in the melt or in solution. Therefore, the reaction of WF_5 with C_5H_5N could afford a direct route to $WF_5(NC_5H_5)_2$, provided the development of an improved synthesis of the parent pentafluoride is developed.

7.3. Conclusions

Though $[WF_5(NC_5H_5)_2]^+$ was found to be much less stable towards dismutation than $[WF_5(L)]^+$ (L = 2,2′-bipy, 1,10-phen), the $[O_3SCF_3]^-$ salt of trigonal-dodecahedral $[WF_5(NC_5H_5)_3]^+$ could be stabilised at ambient temperature in the solid state and below 0 °C in solution. Above this temperature, the cation is prone to dissociation of a pyridyl ligand in solution that, in the presence of excess C_5H_5N, results in the rapid reduction of transiently generated $[WF_5(NC_5H_5)_2]^+$ to $WF_5(NC_5H_5)_2$, as determined by ^{19}F and ^1H NMR spectroscopy. The $WF_5(NC_5H_5)_2$ adduct is the first unambiguously characterised WF_5 adduct and heptacoordinate MF_5 adduct (for any transition metal M), the pentagonal-bipyramidal geometry of which was confirmed by X-ray crystallography. The thermal stability of this adduct suggests an accessible point of entry into the chemistry of tungsten(V) fluorides, considering the difficulty in preparing and isolating the parent WF_5. Computational studies affirmed that whereas $[WF_5(NC_5H_5)_3]^+$ is reductively resistant towards C_5H_5N, $[WF_5(NC_5H_5)_2]^+$ undergoes two-electron reduction via activation of the *para* carbon atom of a pyridyl ligand, followed by comproportionation to tungsten(V).

7.4. References

(1) Schröder, J.; Grewe, F. J. *Angew. Chem. Int. Ed. Engl.* **1968**, *7* (2), 132–133.

(2) Schröder, J.; Grewe, F. J. *Chem. Ber.* **1970**, *103* (5), 1536–1546.

(3) O'Donnell, T. A.; Peel, T. E. *J. Inorg. Nucl. Chem.* **1976**, *28*, 61–62.

(4) Stene, R.; Scheibe, B.; Ivlev, S. I.; Karttunen, A. J.; Petry, W.; Kraus, F. *Z. Anorg. Allg. Chem.* **2020**. In press.

(5) Lassner, E.; Schubert, W.-D. *Int. J. Refract. Met. Hard Mater.* **1995**, *13* (1–3), 111–117.

(6) Arnaudet, L.; Bougon, R.; Ban, B.; Charpin, P.; Isabey, J.; Lance, M.; Nierlich, M.; Vigner, J. *Inorg. Chem.* **1989**, *28* (2), 257–262.

(7) Emsley, J. W.; Levason, W.; Reid, G.; Zhang, W.; De Luca, G. *J. Fluorine Chem.* **2017**, *197*, 74–79.

(8) Eklund, S. E.; Chambers, J. Q.; Mamantov, G.; Diminnie, J.; Barnes, C. E. *Inorg. Chem.* **2001**, *40* (4), 715–722.

(9) Arnaudet, L.; Bougon, R.; Ban, B.; Lance, M.; Nierlich, M.; Vigner, J. *Inorg. Chem.* **1993**, *32* (7), 1142–1146.

(10) El-Kurdi, S.; Al-Terkawi, A.-A.; Schmidt, B.; Dimitrov, A.; Seppelt, K. *Chem. Eur. J.* **2010**, *16* (2), 595–599.

(11) Scilabra, P.; Terraneo, G.; Resnati, G. *J. Fluorine Chem.* **2017**, *203*, 62–74.

(12) Turnbull, D.; Kostiuk, N.; Wetmore, S. D.; Gerken, M. *J. Fluorine Chem.* **2018**, *215*, 1–9.

(13) Moss, K. C. *J. Chem. Soc. A* **1970**, 1224–1226.

(14) Howell, J. A. S.; Moss, K. C. *J. Chem. Soc. A* **1971**, 2483–2487.

(15) Haiges, R.; Deokar, P.; Christe, K. O. *Z. Anorg. Allg. Chem.* **2014**, *640* (8–9), 1568–1575.

(16) Marchetti, F.; Pampaloni, G. *Chem. Commun.* **2012**, *48* (5), 635–653.

(17) Levason, W.; Monzittu, F. M.; Reid, G. *Coord. Chem. Rev.* **2019**, *391*, 90–130.

(18) Arnaudet, L.; Bougon, R.; Buu, B.; Lance, M.; Nierlich, M.; Vigner, J. *Inorg. Chem.* **1994**, *33* (20), 4510–4516.

(19) Scheibe, B.; Rudel, S. S.; Buchner, M. R.; Karttunen, A. J.; Kraus, F. *Chem. Eur. J.* **2017**, *23* (2), 291–295.

(20) Burdett, J. K.; Hoffmann, R.; Fay, R. C. *Inorg. Chem.* **1978**, *17* (9), 2553–2568.

(21) Lee, J. C.; Yao, W.; Crabtree, R. H.; Rüegger, H. *Inorg. Chem.* **1996**, *35* (3), 695–699.

(22) Bosque, R.; Maseras, F.; Eisenstein, O.; Patel, B. P.; Yao, W.; Crabtree, R. H. *Inorg. Chem.* **1997**, *36* (24), 5505–5511.

(23) Sampoli, M.; Marziano, N. C.; Tortato, C. *J. Phys. Chem.* **1989**, *93* (20), 7252–7257.

(24) Arnaudet, L.; Bougon, R.; Buu, B.; Lance, M.; Nierlich, M.; Thuéry, P.; Vigner, J. *J. Fluorine Chem.* **1995**, *71* (1), 123–129.

(25) Arnaudet, L.; Bougon, R.; Ban, B.; Lance, M.; Navaza, A.; Nierlich, M.; Vigner, J. *J. Fluorine Chem.* **1994**, *67* (1), 17–25.

(26) Arnaudet, L.; Bougon, R.; Ban, B.; Lance, M.; Navaza, A.; Nierlich, M.; Vigner, J. *J. Fluorine Chem.* **1992**, *59* (1), 141–152.

(27) Marat, K. Winnipeg, Manitoba, Canada 2017.

(28) McCarley, R. E.; Hughes, B. G.; Boatman, J. C.; Torp, B. A. In *Reactions of Coordinated Ligands and Homogeneous Catalysis*; American Chemical Society, 1963; pp 243–255.

(29) McCarley, R. E.; Brown, T. M. *Inorg. Chem.* **1964**, *3* (9), 1232–1236.

(30) Saal, T.; Christe, K. O.; Haiges, R. *Dalton Trans.* **2019**, *48* (1), 99–106.

(31) Bacon, J.; Dean, P. A. W.; Gillespie, R. J. *Can. J. Chem.* **1969**, *47* (10), 1655–1659.

(32) Turnbull, D.; Wetmore, S. D.; Gerken, M. *Angew. Chem. Int. Ed.* **2019**, *58* (37), 13035–13038.

(33) Craciun, R.; Long, R. T.; Dixon, D. A.; Christe, K. O. *J. Phys. Chem. A* **2010**, *114* (28), 7571–7582.

(34) Craciun, R.; Picone, D.; Long, R. T.; Li, S.; Dixon, D. A.; Peterson, K. A.; Christe, K. O. *Inorg. Chem.* **2010**, *49* (3), 1056–1070.

(35) Geichman, J. R.; Smith, E. A.; Trond, S. S.; Ogle, P. R. *Inorg. Chem.* **1962**, *1* (3), 661–665.

(36) Chirico, R. D.; Steele, W. V.; Nguyen, A.; Klots, T. D.; Knipmeyer, S. E. *J. Chem. Thermodyn.* **1996**, *28* (8), 797–818.

(37) Abramovitch, R. A.; Saha, J. G. *J. Chem. Soc.* **1964**, 2175–2187.

(38) Stene, R. E.; Scheibe, B.; Petry, W.; Kraus, F. *Eur. J. Inorg. Chem.* **2020**.

(39) Fairbrother, F.; Frith, W. C.; Woolf, A. A. *J. Chem. Soc.* **1954**, 1031–1033.

(40) Fairbrother, F.; Grundy, K. H.; Thompson, A. *J. Chem. Soc.* **1965**, 761.

(41) Baer, S. A.; Lozinšek, M.; Kraus, F. *Z. Anorg. Allg. Chem.* **2013**, *639* (14), 2586–2588.

(42) Opalovskii, A. A.; Khaldoyanidi, K. A. *Bull. Acad. Sci. USSR Div. Chem. Sci.* **1973**, *22* (2), 270–272.

Chapter 8 – Stabilisation of $[WF_4]^+$ by N- and P-Donor Ligands: Second-Order Jahn-Teller Effects in Octacoordinate d^1 Complexes

8.1. Introduction

Tungsten hexafluoride is the weakest oxidising agent of the transition-metal hexafluorides, uniquely among them being unable to oxidise NO or Si. Thus, it is unsurprising that preparations of WF_5 are cumbersome and that its chemical properties remain largely unknown.[1–4] This is exacerbated further by its disproportionation under ambient conditions or upon slight warming.[1,2] Nevertheless, it is known to adopt a fluorine-bridged, tetrameric structure in the solid state[5] and its F^--acceptor and Lewis-acid behaviour have been observed indirectly per syntheses of $[WF_{5+n}]^{n-}$ (n = 1–3) salts,[6] as well as a preliminary account of $WF_5(NCCH_3)$,[7] via reduction of WF_6.

In Chapters 6 and 7, it was demonstrated that WF_6, which does not typically behave as a F^- donor, relinquishes F^- to strong acceptors in the presence of N-donor ligands to yield donor-stabilised $[WF_5]^+$ complexes. These complexes are significantly stronger oxidising agents than WF_6, demonstrated by the facile reduction of $[WF_5(NC_5H_5)_2]^+$ to $WF_5(NC_5H_5)_2$ in C_5H_5N, representing a comparatively facile route to a neutral WF_5 derivative. Unlike WF_5, $WF_5(NC_5H_5)_2$ is stable towards disproportionation.

Interestingly, the molecular nature of $WF_5(NC_5H_5)_2$ contrasts with the group-5 analogues, the crystal structures of which reveal the ionic coordination isomers, $[MF_4(NC_5H_5)_4][MF_6]$ (M = Nb, Ta),[8] demonstrating a fundamental difference in Lewis-acid behaviour. The ligand-induced autoionisation of MF_5 by mono- and bidentate main-group donor ligands to afford octacoordinate $[MF_4]^+$ cations is ubiquitous[9–11] and various

$[MCl_4]^+$ analogues with bidentate Pn-donor (Pn = P, As) ligands are also known.[12–14] In these cases, the cations are trigonal-dodecahedral (TD), in which the neutral donor atoms occupy the "A" sites and the halido ligands the "B" sites (Figure 8.1).[15]

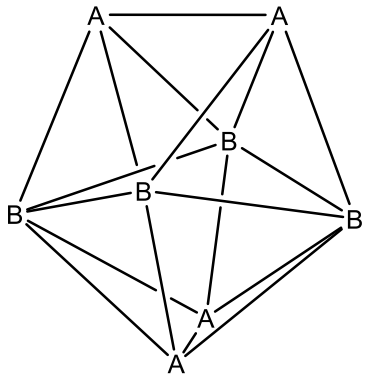

Figure 8.1. Trigonal dodecahedron with "A" and "B" ligand sites.

Interestingly, however, upon reduction of the metal centre, analogous MCl_4 complexes are found to adopt either TD or square-antiprismatic (SA) geometries.[13,16] The coincidence of these geometries remains enigmatic but has been attributed to: the similar energies of the coordination polyhedra,[17] an indirect steric effect of the *d* electron (via changes in bond-length ratios causing preference for the SA), and the SA geometry better accommodating metal-to-ligand π bonding.[13]

In this chapter, redox and non-redox synthetic routes to octacoordinate $[WF_4]^+$ complexes with C_5H_5N and $P(CH_3)_3$ are reported, which were characterised as their $[O_3SCF_3]^-$ salts. Furthermore, DFT (B3LYP) methods were employed to elucidate the nature of the observed geometric dissimilarities in analogous octacoordinate d^0 and d^1 complexes of the early transition metals, which are caused by a second-order Jahn-Teller (SOJT) distortion upon occupation of a *d* orbital on the metal centre.

8.2. Results and Discussion

8.2.1. Syntheses and Physical Properties

The $[WF_4(NC_5H_5)_4]^+$ cation was prepared via F^- abstraction from $WF_5(NC_5H_5)_2$ using $[(CH_3)_3Si(NC_5H_5)]^+$ in C_5H_5N (Eq. 8.1) and was isolated as its $[O_3SCF_3]^-$ salt upon removal of the volatile materials under dynamic vacuum. It is a yellow solid that is adhered together by a small amount of tacky, dark brown oil. The presence of the oil is attributed to the reduction of trace $WF_6(NC_5H_5)_2$ in the starting material. The salt is soluble in CH_2Cl_2, C_5H_5N, and CH_3CN.

$$WF_5(NC_5H_5)_2 + [(CH_3)_3Si(NC_5H_5)]^+ + C_5H_5N \rightarrow [WF_4(NC_5H_5)_4]^+ (CH_3)_3SiF \qquad (8.1)$$

Meanwhile, the $[WF_4\{P(CH_3)_3\}_4]^+$ cation was synthesised in quantitative yield upon reduction of WF_6 by excess $P(CH_3)_3$ in the presence of one molar equivalent of $(CH_3)_3SiO_3SCF_3$ (Eq. 8.2). The salt is highly soluble in CH_2Cl_2 and insoluble in $P(CH_3)_3$. The generation of $P(CH_3)_3F_2$ was verified by NMR spectroscopy (see section 8.2.4), which revealed electrophilic fluorination, rather than oxidative dimerisation as was the case with C_5H_5N.

$$WF_6 + 3½P(CH_3)_3 + [(CH_3)_3Si\{P(CH_3)_3\}]^+ \rightarrow$$
$$[WF_4\{P(CH_3)_3\}_4]^+ + ½P(CH_3)F_2 + (CH_3)_3SiF \qquad (8.2)$$

Octacoordinate complexes of monodentate, tertiary phosphines are rare, exclusively being reserved for hydrides of the early transition metals.[18] Apparently, fluorine is sufficiently small to accommodate the steric demands of the ligands in $[WF_4\{P(CH_3)_3\}_4]^+$ such that dissociation was not observed even after heating to 45 °C *in vacuo* for several hours. However, contact of the solid with glass resulted in small amounts

of decomposition, as determined by Raman spectroscopy (see section 8.2.3). No such decomposition was observed in FEP after several days at ambient temperature, suggesting that glass catalyses the loss of one or two phosphine ligands. Similar behaviour was possibly exhibited during the ligand-induced autoionisation of TaF_5 by $P(CH_3)_3$, which was performed in a dried glass vessel and yielded hexacoordinate $[TaF_4\{P(CH_3)_3\}_2]^+$ as its $[TaF_6]^-$ salt.[19]

8.2.2. Molecular Geometries

8.2.2.1. $[WF_4(L)_4]^+$ ($L = C_5H_5N$, $P(CH_3)_3$)

Orange needles of $[WF_4(NC_5H_5)_4][O_3SCF_3]\cdot 1.5CH_3CN$ were grown from a CH_3CN solution of crude $[WF_4(NC_5H_5)_4][O_3SCF_3]$, whereas red blocks of $[WF_4\{P(CH_3)_3\}_4][O_3SCF_3]$ salt were obtained from a $P(CH_3)_3/CH_2Cl_2$ solvent mixture. As such, the structures of the $[WF_4(L)_4]^+$ ($L = C_5H_5N$, $P(CH_3)_3$) salts were elucidated by X-ray crystallography at –173 °C. In $[WF_4(NC_5H_5)_4][O_3SCF_3]\cdot 1.5CH_3CN$, two crystallographic unique ion pairs (I and II) co-crystallise with three molecules of CH_3CN, whereas in the $P(CH_3)_3$ analogue, only one ion pair exists in the asymmetric unit. In both cases, no significant cation-anion interactions are observed, testifying to the coordinative saturation and low charge density of the metal centres. As well, the geometries of the cations were optimised in the gas phase, which returned structures that are generally in excellent agreement with the crystallographic data (Table 8.1). Crystallographic data collection and refinement parameters are provided in the Appendix (Table F.1).

The cations are found to adopt SA geometries of approximately D_2 symmetry about the WF_4Pn_4 (Pn = N, P) moieties, in which the donor ligands occupy the opposing vertices of each square face (Figure 8.2; see next section). The W–F bond lengths are significantly

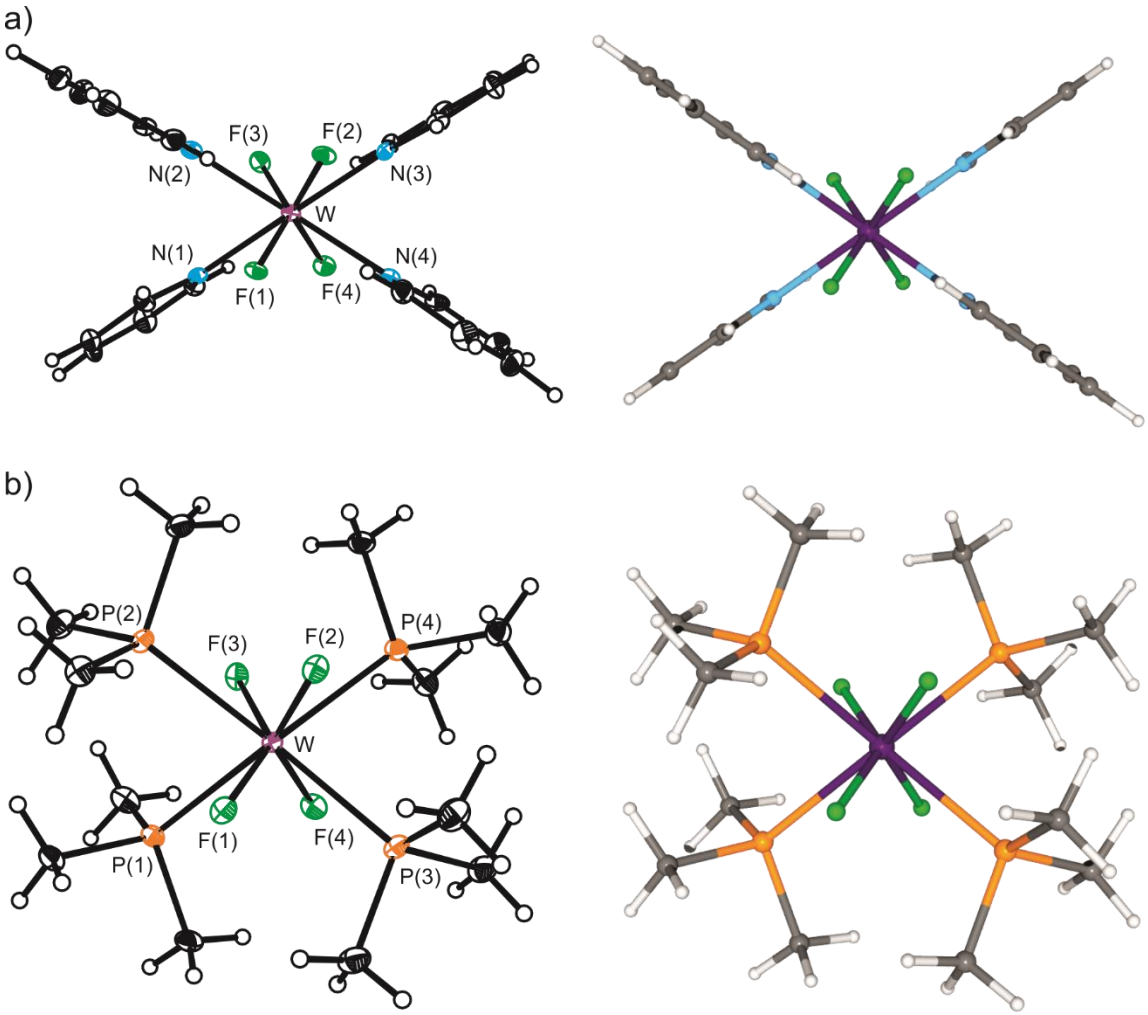

Figure 8.2. Thermal ellipsoid plots (50% probability level, left) and optimised gas-phase geometries (B3LYP/aVTZ, right) of a) $[WF_4(NC_5H_5)_4]^+$ (I) and b) $[WF_4\{P(CH_3)_3\}_4]^+$.

Table 8.1. Selected Experimental and Calculated[a] Bond Lengths (Å) and Angles (°) of $[WF_4(L)_4]^+$

	L = C_5H_5N[b]			**L = $P(CH_3)_3$[c]**	
	exptl		**calcd**	**exptl**	**calcd**
	I	**II**			
W–F(1)	1.926(3)	1.930(3)	1.917	1.9723(14)	1.966
W–F(2)	1.925(3)	1.924(3)		1.9880(14)	
W–F(3)	1.918(3)	1.924(3)		1.9873(13)	
W–F(4)	1.920(3)	1.925(3)		1.9809(13)	
W–Pn(1)	2.292(4)	2.290(4)	2.350	2.5958(7)	2.690
W–Pn(2)	2.281(4)	2.276(4)		2.5916(6)	
W–Pn(3)	2.302(4)	2.276(4)		2.5947(6)	
W–Pn(4)	2.282(4)	2.275(4)		2.5922(7)	
F(1)–W–F(2)	77.46(11)	79.66(12)	77.7	76.79(6)	77.2
F(1)–W–F(3)	142.38(12)	143.20(11)	139.0	141.75(6)	138.7
F(1)–W–F(4)	114.62(11)	112.25(12)	117.2	118.00(6)	118.1
F(1)–W–Pn(1)	73.53(13)	74.59(14)	73.1	73.99(4)	73.2
F(1)–W–Pn(2)	77.00(13)	75.79(13)	75.7	77.75(4)	77.1
F(1)–W–Pn(3)	74.21(13)	73.48(13)	74.0	71.23(4)	71.2
F(1)–W–Pn(4)	141.57(13)	142.31(13)	144.5	143.99(4)	146.5
Pn(1)–W–Pn(2)	74.87(14)	74.54(14)	79.5	83.60(2)	87.0
Pn(1)–W–Pn(3)	117.43(13)	120.28(15)	114.0	107.82(2)	107.1
Pn(1)–W–Pn(4)	142.41(14)	139.83(15)	140.8	140.65(2)	139.2

[a]Calculated at the B3LYP/aVTZ level of theory. [b]Pn = N. [c]Pn = P.

shorter in the C_5H_5N complex (1.918(3)–1.926(3) Å) than its $P(CH_3)_3$ analogue (1.9723(14)–1.9880(14) Å), whereas the W–P bond lengths in the latter (2.5916(6)–2.5958(7) Å) are insignificantly different from those of $[WCl_4(dmpe)_2]^+$ (2.575(7)–2.590(7) Å; dmpe = (1,2-bis(dimethylphosphino)ethane)).[20] Comparison of the W–Pn normalised contacts[21] (r(vdW): W = 2.001,[22] P = 1.90,[23] N = 1.66[23]) reveals that the W–Pn bonds are stronger in $[WF_4(NC_5H_5)_4]^+$ (0.623–0.629) than $[WF_4\{P(CH_3)_3\}_4]^+$ (0.664–0.665). The W–Pn bonds in both cations are weaker than those of $WF_5(NC_5H_5)_2$ (0.603) and $[WF_4(2,2'\text{-bipy})_2]^{2+}$ (0.609–0.618)[24,25] due to increased steric repulsion in octa- vs. heptacoordinate complexes and decreased Lewis acidity upon reduction of the tungsten centre, respectively.

8.2.2.2. Trigonal Dodecahedron vs. Square Antiprism

To rigourously determine the best description for the geometries of $[WF_4(L)_4]^+$, the least-squared planes of a) the intersecting A_2B_2 trapezoids of the TD (referring to the "A" and "B" sites of an ideal TD) and b) the square faces of the SA were measured during crystal structure refinement. According to Lippard and Russ,[26] both the degree of deviation of the square faces and trapezoids from the least-squared planes (σ_S and σ_T, respectively) as well as the dihedral angle of the A_2B_2 trapezoids (θ_T) are diagnostic; the TD requires a θ_T of 90° to conform to D_{2d} symmetry, whereas in the ideal SA, it contracts to 77.4°. However, assessing the geometries of $[WF_4(L)_4]^+$ by these methods yield contradictory results, as the deviations from the least-squared planes clearly indicate SA geometries, while the θ_T values instead indicate TD (Table 8.2).

Thus, this approach was modified slightly. The TD → SA isomerisation results in counter-rotation of the A–A and B–B edges within each A_2B_2 trapezoid (Figure 8.3; averaging of various A–W–A and B–W–B angles to form the regular square faces also

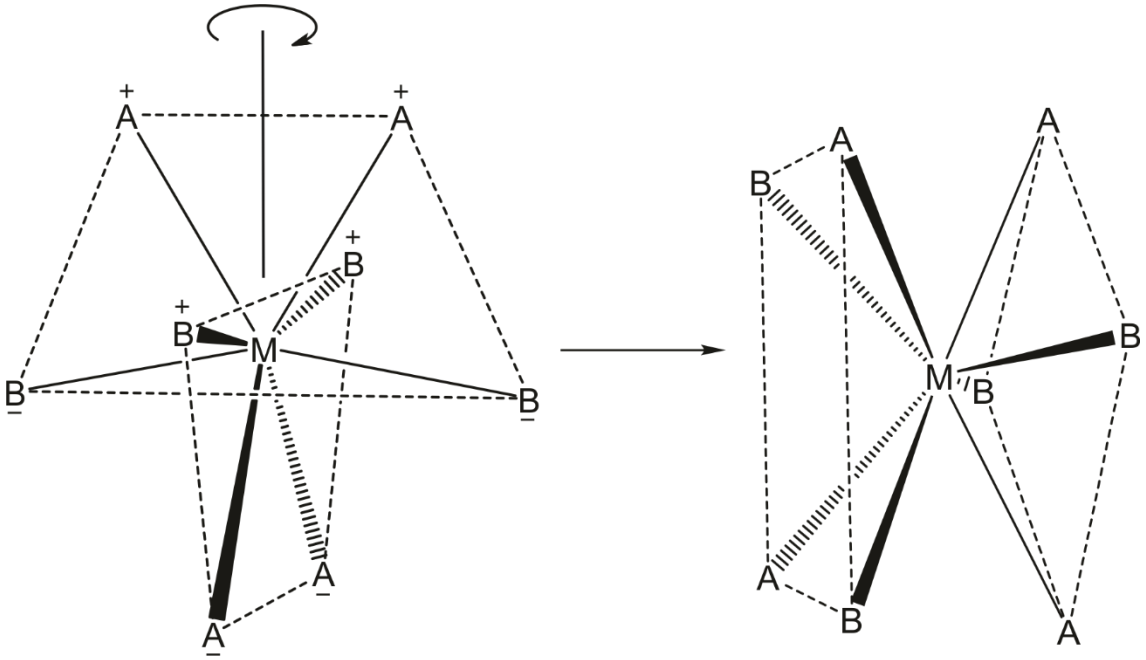

Figure 8.3. Counter-rotation within A_2B_2 trapezoidal planes during isomerisation of TD to SA. Plus (+) and minus (–) represent equal but opposite rotations about the defined axis. Dashed lines (---) denote the characteristic planes within each polyhedron.

Table 8.2. Characteristic Geometric Parameters for Determination of Coordination Polyhedra of $[WF_4(L)_4]^+$

L	σ_S (Å)[a]	σ_T (Å)[b]	θ_S (°)[c]	θ_T (°)[d]	α_A (°)[e]	α_B (°)[f]
C_5H_5N (I)	0.077(2)–0.078(2)	0.271(2)–0.368(2)	0.24(2)	86.16(6)	63.46(11)	68.96(6)
C_5H_5N (II)	0.024(2)–0.029(2)	0.216(2)–0.295(2)	0.58(4)	85.82(8)	69.49(14)	72.10(12)
$P(CH_3)_3$	0.2096(6)–0.2570(6)	0.3861(6)–0.4340(6)	0.71(7)	87.82(3)	59.26(2)	67.94(8)

[a]Displacement of atoms from least-squared planes formed by {F(1), F(4), Pn(1), Pn(3)} and {F(2), F(3), Pn(2), Pn(4)} (square planes). [a]Displacement of atoms from least-squared planes formed by {F(1), F(3), Pn(3), Pn(4)} and {F(2), F(4), Pn(1), Pn(2)} (trapezoidal planes). [c]Angle between square planes. [d]Angle between trapezoidal planes. [e]Angle between planes formed by {W, Pn(1), Pn(2)} and {W, Pn(3), Pn(4)}. [f]Angle between planes formed by {W, F(1), F(3)} and {W, F(2), F(4)}.

occurs). These trapezoids are necessarily orthogonal under the D_{2d} symmetry of the TD, but conversion to SA results in a twist of the A–A edges with respect to one another, resulting in a contraction of the dihedral angle (α_A), which is also true for the B–B edges (α_B). Though observation of orthogonal trapezoids ($\alpha_A = \alpha_B = 90°$) in truly TD complexes is perhaps somewhat obvious, the degree of contraction upon conversion to SA is obscure; analysis of the crystal structure of $Cs[Re^{VII}F_8]$,[27] containing the SA $[Re^{VII}F_8]^-$ anion, returns $\alpha_A = 61.9°$ and $\alpha_B = 69.6°$. Considering that these dihedral angles distort to different extents and that the TD → SA isomerisation is continuous, this method provides two independent values for assessing whether complexes are TD, SA, or intermediate in nature, rather than the combined θ_T parameter of Lippard of Russ.

Measurement of α_A and α_B in the crystal structures of the $[WF_4(L)_4]^+$ salts reveals unambiguous SA character (Table 8.2). The SA designation is further supported upon comparison of the F–W–F (L = C_5H_5N: 114.62(11)–115.91(11)°, L = $P(CH_3)_3$: 114.85(6)–118.00(6)°) and Pn–W–Pn (L = C_5H_5N: 117.43(13)–118.06(14)°, L = $P(CH_3)_3$: 107.82(2)–109.53(2)°) angles within each square face to those of an ideal SA (114–120°), as well as the coplanarity of the square faces (θ_S = 0.24(2)–0.71(7)°). The slightly contracted P–W–P angles in $[WF_4\{P(CH_3)_3\}_4]^+$ can be attributed to steric repulsion between edge-sharing $P(CH_3)_3$ ligands.

A survey of α_A and α_B parents in a series of related d^0 and d^1 halido complexes of the group-5 and 6 transition metals largely supports the notion that d^0 complexes and those containing dmpb and dmab co-ligands (regardless of electron configuration) are TD (Table 8.3), whereas d^1 complexes with ethylene-bridged ligands are closer to SA. This trend persists irrespectively of crystallographically imposed symmetry and the denticity of the

Table 8.3. Crystallographic Symmetries and Geometries, with α_A and α_B (°), of Various Octacoordinate d^0 and d^1 Complexes[a]

	Configuration	Symmetry	Geometry[b]	α_A[c]	α_B[c]
$[NbF_4(NC_5H_5)_4]^{+}$[d]	d^0	C_1	TD	87.6	89.5
$[NbF_4(dmpb)_2]^{+}$[d]	d^0	C_1	TD	84.3	88.7
$[NbF_4(dmab)_2]^{+}$[d]	d^0	D_{2d}	TD	90.0	90.0
$[NbCl_4(dmpb)_2]^{+}$[d]	d^0	C_s	TD	90.0	90.0
		C_1	TD	86.9	88.8
$[NbCl_4(dmab)_2]^{+}$[e]	d^0	C_1	TD	87.8	89.2
$[NbBr_4(dmpe)_2]^{+}$[f]	d^0	S_4	TD	90.0	90.0
$NbCl_4(dmpb)_2$[e]	d^1	D_{2d}	TD	90.0	90.0
$NbCl_4(dmpe)_2$[e]	d^1	C_2	SA	71.2	79.4
$NbCl_4(depe)_2$[e]	d^1	C_1	I	80.5	83.0
$NbBr_4(dmpe)_2$[f]	d^1	C_1	SA	70.2	80.0
$[MoCl_4(dmab)_2]^{+}$[g]	d^1	C_1	TD	87.2	87.5
$[TaF_4(NC_5H_5)_4]^{+}$[d]	d^0	C_1	TD	87.5	89.4
$[TaF_4(dmpb)_2]^{+}$[e]	d^0	C_1	TD	83.4	88.5
$[TaCl_4(dmpe)_2]^{+}$[h]	d^0	D_{2d}	TD	90.0	90.0
$TaCl_4(dmpe)_2$[h]	d^1	C_2	SA	70.1	78.3
$[WF_4(2,2'\text{-bipy})_2]^{2+}$	d^0	S_4[i]	TD	90.0	90.0
		C_1[i]	TD	87.1	89.2
		C_1[j]	TD	89.8	89.3
		C_1[j]	TD	89.7	89.1
$[WF_4(dmpb)_2]^{2+}$[k]	d^0	C_1	TD	88.5	89.7
$[WF_4(dmab)_2]^{2+}$[k]	d^0	D_2	SA	71.7	76.7
$[WF_4(NC_5H_5)_4]^{+}$ (I)	d^1	C_1	SA	63.5	69.0
$[WF_4(NC_5H_5)_4]^{+}$ (I)	d^1	C_1	SA	69.5	72.1
$[WF_4\{P(CH_3)_3\}_4]^{+}$	d^1	C_1	SA	59.3	67.9
$[WCl_4(dmpe)_2]^{+}$[l]	d^1	C_1	I	78.2	84.1

[a]Complexes with d^1 electron configuration are highlighted. [b]Abbreviations denote trigonal dodecahedron (TD), square antiprism (SA), and intermediate (I). [c]Obtained using Mercury (version 2020.1).[28] [d]From reference 7. [e]From reference 13. [f]From reference 15. [g]From reference 41. [h]From reference 12. [i]From reference 24. [j]From reference 23. [k]From reference 28. [l]From reference 19.

donor ligand. However, it is found that $[W^{VI}F_4(dmab)_2]^{2+}$ (α_A = 71.7°, α_B = 76.7°)[29] is perhaps better described as SA, whereas $[W^{V}Cl_4(dmpe)_2]^{+}$ (α_A = 78.2°, α_B = 84.1°)[20] and $Nb^{IV}Cl_4(depe)_2$ (depe = 1,2-bis(diethylphosphino)ethane; α_A = 80.5°, α_B = 83.0°)[16] seem to possess intermediate geometries. The cations were described as TD in their original reports and $NbCl_4(depe)_2$ was described as SA. It should be noted that the d^1 complexes surveyed invariably include bidentate donor ligands, which is expected to result in a slight energetic preference for TD to better minimise interligand repulsion in the presence of an imposed bite angle.[30]

8.2.3. Raman Spectroscopy

The Raman spectra of solid $[WF_4(L)_4][O_3SCF_3]$ (Figures 8.4 and 8.5) were recorded at ambient temperature and the vibrational frequencies of the cations were calculated at the B3LYP/aVTZ level of theory, resulting in excellent agreement between the experimental and calculated spectroscopic data. Complete assignments of the vibrational frequencies are provided in the Appendix (Tables F.2 and F.3). Bands corresponding to $[O_3SCF_3]^-$ were assigned by comparison to those of aqueous HO_3SCF_3[31] and the low-intensity bands at 614 and 604 cm^{-1} in the Raman spectrum of $[WF_4\{P(CH_3)_3\}_4][O_3SCF_3]$ are tentatively attributed to $\nu_s(WF_4)$ modes in traces of $[WF_4\{P(CH_3)_3\}_n]^+$ (n = 2 or 3).

The $\nu_s(WF_4)$ mode is higher in frequency for $[WF_4(NC_5H_5)_4]^+$ (in cm^{-1}; exptl. 580, calcd. 587) than $[WF_4\{P(CH_3)_3\}_4]^+$ (exptl. 519, calcd. 529), consistent with the significantly elongated W–F bonds in the latter. These modes are lower in frequency than the $\nu_s(WF_8)$ modes of $[WF_8]^{3-}$ salts (595–614 cm^{-1}),[32] which represent the only other well characterised examples of octacoordinate fluoridotungsten(V) complexes, and even more

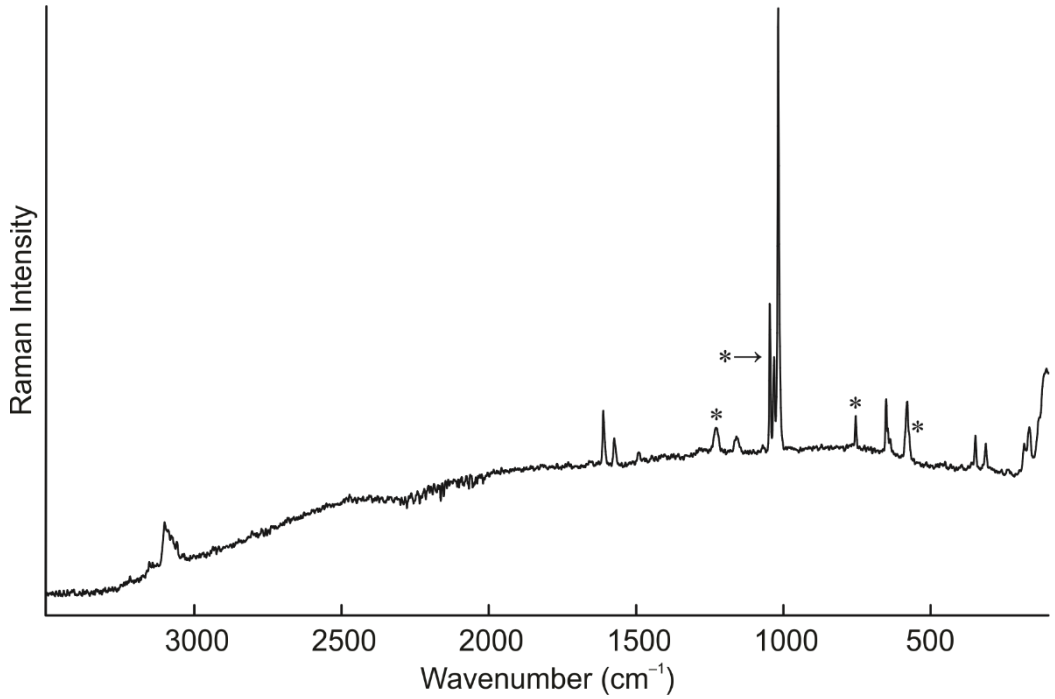

Figure 8.4. Raman spectrum of solid $[WF_4(NC_5H_5)_4][O_3SCF_3]$, recorded at ambient temperature. Asterisks (*) denote $[O_3SCF_3]^-$ bands.

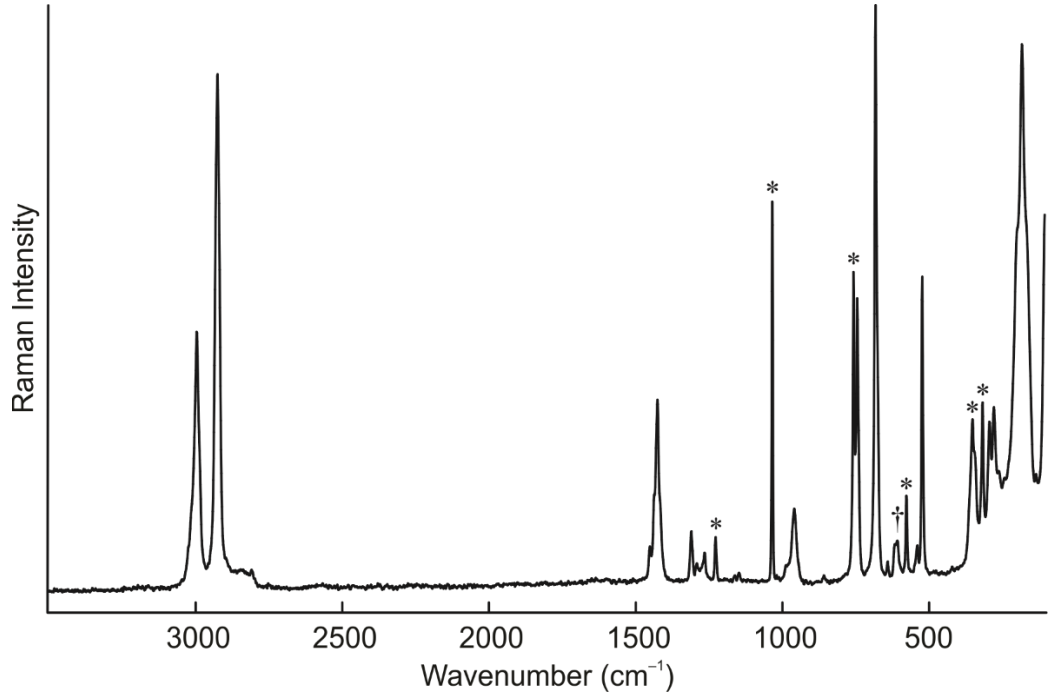

Figure 8.5. Raman spectrum of solid $[WF_4\{P(CH_3)_3\}_4][O_3SCF_3]$, recorded at ambient temperature. Asterisks (*) denote $[O_3SCF_3]^-$ bands and dagger (†) denotes a trace impurity.

substantially red-shifted with respect to $[WF_4(2,2'\text{-bipy})_2]^{2+}$ (exptl. 678, 645;[25] calcd. 684, 650). The $\nu_s(NC_5)$ bands of the pyridyl ligands in $[WF_4(NC_5H_5)_4]^+$ are blue-shifted (1018 vs. 990 in free C_5H_5N) to a similar extent as in other adducts of tungsten(VI) fluorides (*ca.* 1020; see Chapters 3, 5, and 7). The $\nu_s(PC_3)$ mode of $P(CH_3)_3$ is comparably shifted in $[WF_4\{P(CH_3)_3\}_4]^+$ (678 vs. 653).

8.2.4. NMR Spectroscopy

The reduction of WF_6 by $P(CH_3)_3$ in the presence of $(CH_3)_3SiO_3SCF_3$ was monitored by multinuclear NMR spectroscopy, from which it was determined that the reduction mechanism is dissimilar from when C_5H_5N is employed as the reducing agent (see Chapter 7). Though F^- abstraction seems to be rapid and quantitative, resulting in the precipitation of a large amount of red-violet solid, hitherto unreported $WF_6\{P(CH_3)_3\}_2$ (^{19}F: 24 ppm, s; ^{31}P: 93.9 ppm, st; $^1J(^{31}P–^{19}F)$ = 84 Hz at –50 °C) was observed as the only appreciable tungsten(VI) species in solution, identified by the binomial septet in the ^{31}P NMR (Figure 8.6) and integration of the resonances with respect to $P(CH_3)_3F_2$ (6:2 F:P). Both the ^{31}P and ^{19}F resonances are shifted to much lower frequency than the 1:1 adduct (^{19}F: 133.6 ppm, d; ^{31}P: 115.5 ppm, m; $^1J(^{31}P–^{19}F)$ = 74 Hz).[33,34] Only a single, broadened $P(CH_3)_3$ resonance could be observed in the ^{1}H NMR spectrum. This would suggest that unlike $[WF_5(NC_5H_5)_n]^+$, $[WF_5\{P(CH_3)_3\}_n]^+$ (n = 2, 3) are prone to dismutation (Eqs. 8.3 and 8.4) at faster rate than reduction, and that, e.g., $[WF_4\{P(CH_3)_3\}_4]^{2+}$ acts as an oxidising agent, possibly in addition to a $[WF_5]^+$ complex. Broad singlets in the ^{19}F and ^{31}P NMR spectra are attributed to a second, unknown tungsten(VI) species (^{19}F: 30 ppm, s; ^{31}P: 89 ppm, s) that exists as a minor component.

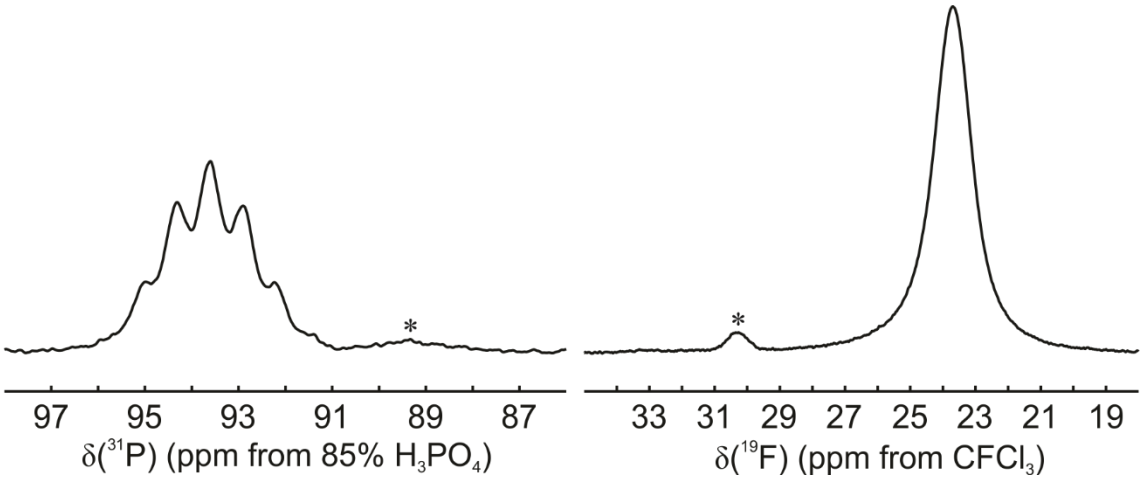

Figure 8.6. Phosphorus-31 (left) and ^{19}F (right) NMR spectra of $WF_6\{P(CH_3)_3\}_2$, recorded in $CH_2Cl_2/P(CH_3)_3$ at –50 °C. Asterisks (*) denote an unknown tungsten(VI) impurity.

$$2[WF_5\{P(CH_3)_3\}_2]^+ \rightarrow [WF_4\{P(CH_3)_3\}_4]^{2+} + WF_6 \quad (8.3)$$

$$2[WF_5\{P(CH_3)_3\}_3]^+ \rightarrow [WF_4\{P(CH_3)_3\}_4]^{2+} + WF_6\{P(CH_3)_3\}_2 \quad (8.4)$$

Furthermore, while small amounts of $WF_6(NC_5H_5)_2$ were present during the analogous reduction in C_5H_5N, it persisted as an impurity in the isolated $WF_5(NC_5H_5)_2$. In the $P(CH_3)_3$ system, the neutral adduct is slowly but completely consumed over 16–48 h with a corresponding increase in $P(CH_3)_3F_2$, which is the only appreciable oxidation product observed (Figures 8.7 and 8.8). Ultimately, tungsten(VI) is quantitatively reduced to $[W^{V}F_4\{P(CH_3)_3\}_4]^+$, as verified by mass balance and Raman spectroscopy, while $P(CH_3)_3F_2$ and $(CH_3)_3SiF$ are the major by-products observable by NMR spectroscopy. In one sample, traces of $[P(CH_3)_3F]^+$ were also observed, though this could be due to $F^–$ abstraction from $P(CH_3)_3F_2$ by a slight excess of $(CH_3)_3SiO_3SCF_3$.[35]

Given the stability of $[WF_4(dmpb)_2]^{2+}$,[29] the reduction is not expected to be unimolecular. Thus, it could involve outer-sphere single-electron transfer (SET) from $P(CH_3)_3$ to $[W^{VI}F_4\{P(CH_3)_3\}_4]^{2+}$, forming $[P(CH_3)_3]^{\cdot+}$, which would dimerise to known $[(CH_3)_3PP(CH_3)_3]^{2+}$ (Eqs. 8.5 and 8.6).[36] This would be followed by sequential $F^–$ transfer steps from $WF_6\{P(CH_3)_3\}_2$ to phosphorus (Eqs. 8.7 and 8.8). The disproportionation of $[(CH_3)_3PP(CH_3)_3]^{2+}$ in the presence of $F^–$ has been observed previously.[35]

$$[W^{VI}F_4\{P(CH_3)_3\}_4]^{2+} + P(CH_3)_3 \rightarrow [W^{V}F_4\{P(CH_3)_3\}_4]^{+} + [P(CH_3)_3]^{\cdot+} \quad (8.5)$$

$$[P(CH_3)_3]^{\cdot+} \rightarrow [(CH_3)_3PP(CH_3)_3]^{2+} \quad (8.6)$$

$$W^{VI}F_6\{P(CH_3)_3\}_2 + ½[(CH_3)_3PP(CH_3)_3]^{2+} \rightarrow W^{V}F_5\{P(CH_3)_3\}_2 + [P(CH_3)_3F]^{+} \quad (8.7)$$

$$W^{V}F_5\{P(CH_3)_3\}_2 + [P(CH_3)_3F]^{+} \rightarrow [W^{V}F_4\{P(CH_3)_3\}_4]^{+} + P(CH_3)_3F_2 \quad (8.8)$$

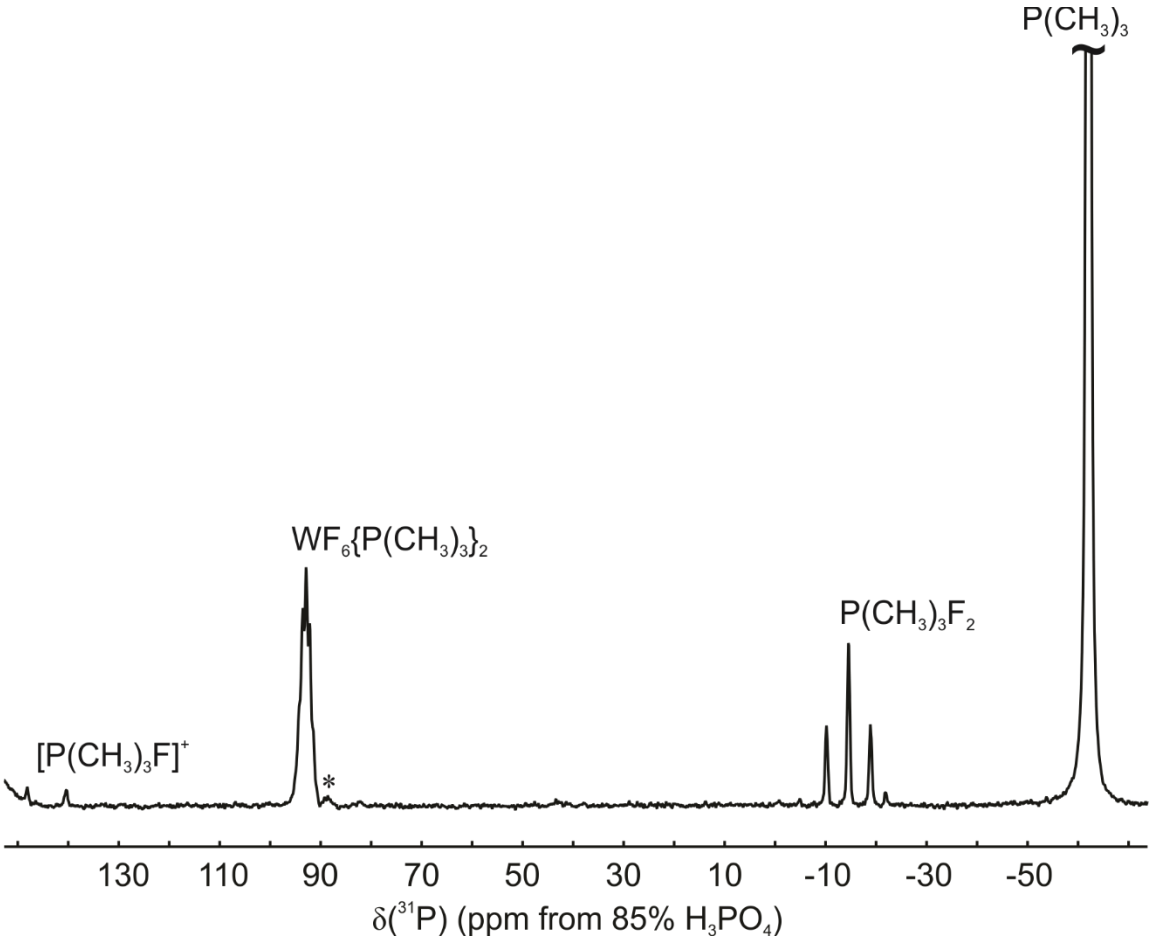

Figure 8.7. Phosphorus-31 NMR spectrum of WF_6 and $(CH_3)_3SiO_3SCF_3$ (1:1), recorded in $P(CH_3)_3/CH_2Cl_2$ at –50 °C after *ca*. 1 h a ambient temperature. Asterisk (*) could denote an unknown tungsten(VI) impurity.

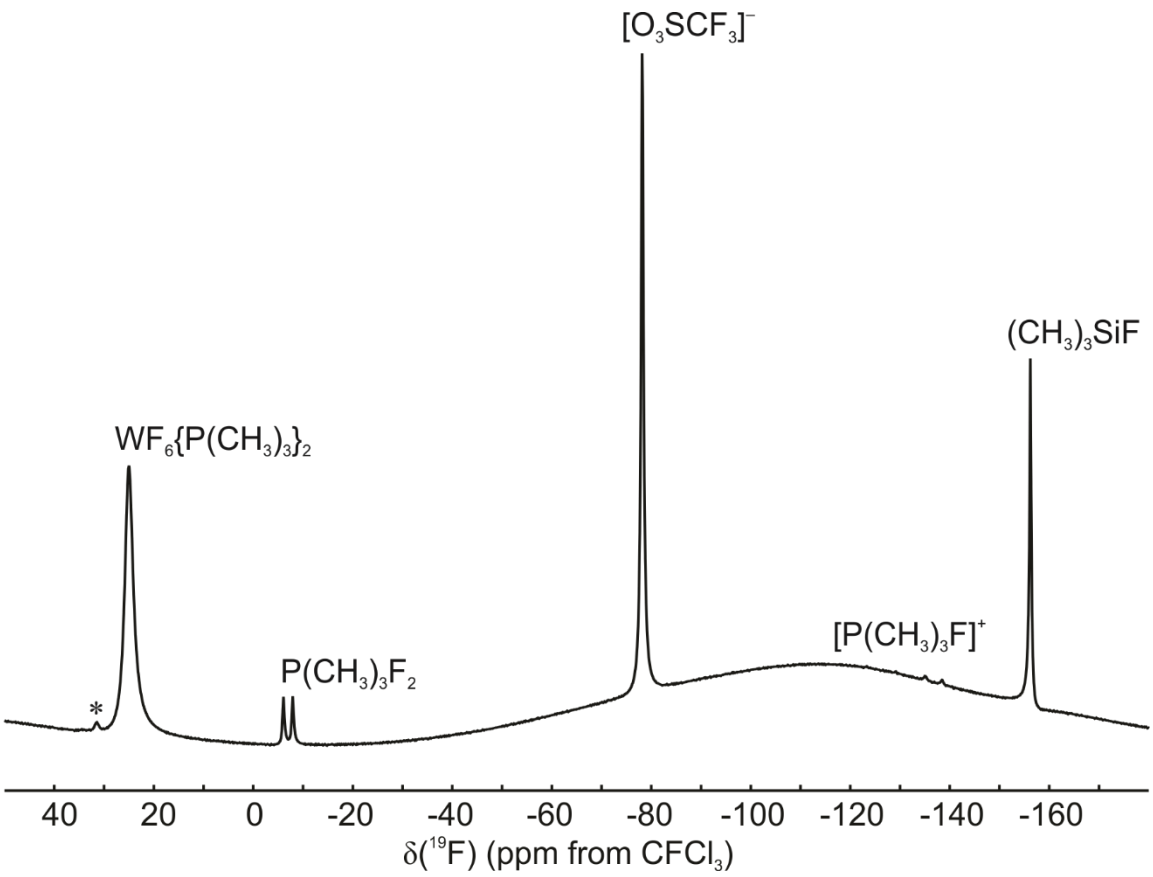

Figure 8.8. Fluorine-19 NMR spectrum of WF_6 and $(CH_3)_3SiO_3SCF_3$ (1:1), recorded in $P(CH_3)_3/CH_2Cl_2$ at –50 °C after *ca*. 1 h at ambient temperature. Asterisk (*) could denote an unknown tungsten(VI) impurity.

8.2.5. Computational Results

8.2.5.1. Molecular Orbitals and Natural-Bond-Orbital Analyses

The SOMO and LUMO of $[WF_4\{P(CH_3)_3\}_4]^+$ both appear to possess d_{z^2} character but are rotated about the *x* and *y* axes, respectively, corresponding to linear combinations of the $d_{x^2-y^2}$ and d_{z^2} orbitals (Figure 5). This is corroborated by NBO analyses of the canonical MOs, in which the SOMO and LUMO are described as $d_{x^2-y^2} + d_{z^2}$ and $d_{x^2-y^2} - d_{z^2}$, respectively (the NBOs involved have effectively pure *d* character). The same is true of the SOMO and LUMO + 1 of $[WF_4(NC_5H_5)_4]^+$, whereas the LUMO is ligand-based and insignificantly different in energy from the LUMO + 1 (–4.421 vs. –4.414 eV). The calculated SOMO to LUMO ($[WF_4(NC_5H_5)_4]^+$: 4.10 eV, 303 nm; $[WF_4\{P(CH_3)_3\}_4]^+$: 4.23 eV, 293 nm) and SOMO – 1 to SOMO ($[WF_4(NC_5H_5)_4]^+$: 1.87 eV, 664 nm; $[WF_4\{P(CH_3)_3\}_4]^+$: 1.26 eV, 985 nm) transitions would suggest that the latter, which is smaller and possesses LMCT character in both cases, is responsible for the intense colours of the complexes.

The NPA charges and Wiberg valences are given in Table 8.4, and WBIs are provided in Table 8.5. The NBO analyses reveal that there is a much greater degree of charge delocalisation from the tungsten centre in $[WF_4\{P(CH_3)_3\}_4]^+$ than in the corresponding C_5H_5N complex due to the greater electropositivity of the phosphorus atoms. This is evidenced in the decreased NPA charge on tungsten (+1.28 vs. +2.17) and increase in the total NPA charge of each ligand (+0.51 vs. +0.27) and results in a slight weakening of the W–F bonds (WBI: 0.57 vs. 0.63), as observed in the crystal structures. However, the W–P bonds are predicted to be significantly stronger than the W–N bonds (WBI: 0.56 vs. 0.40) despite the shorter normalised contacts of the latter. This could be

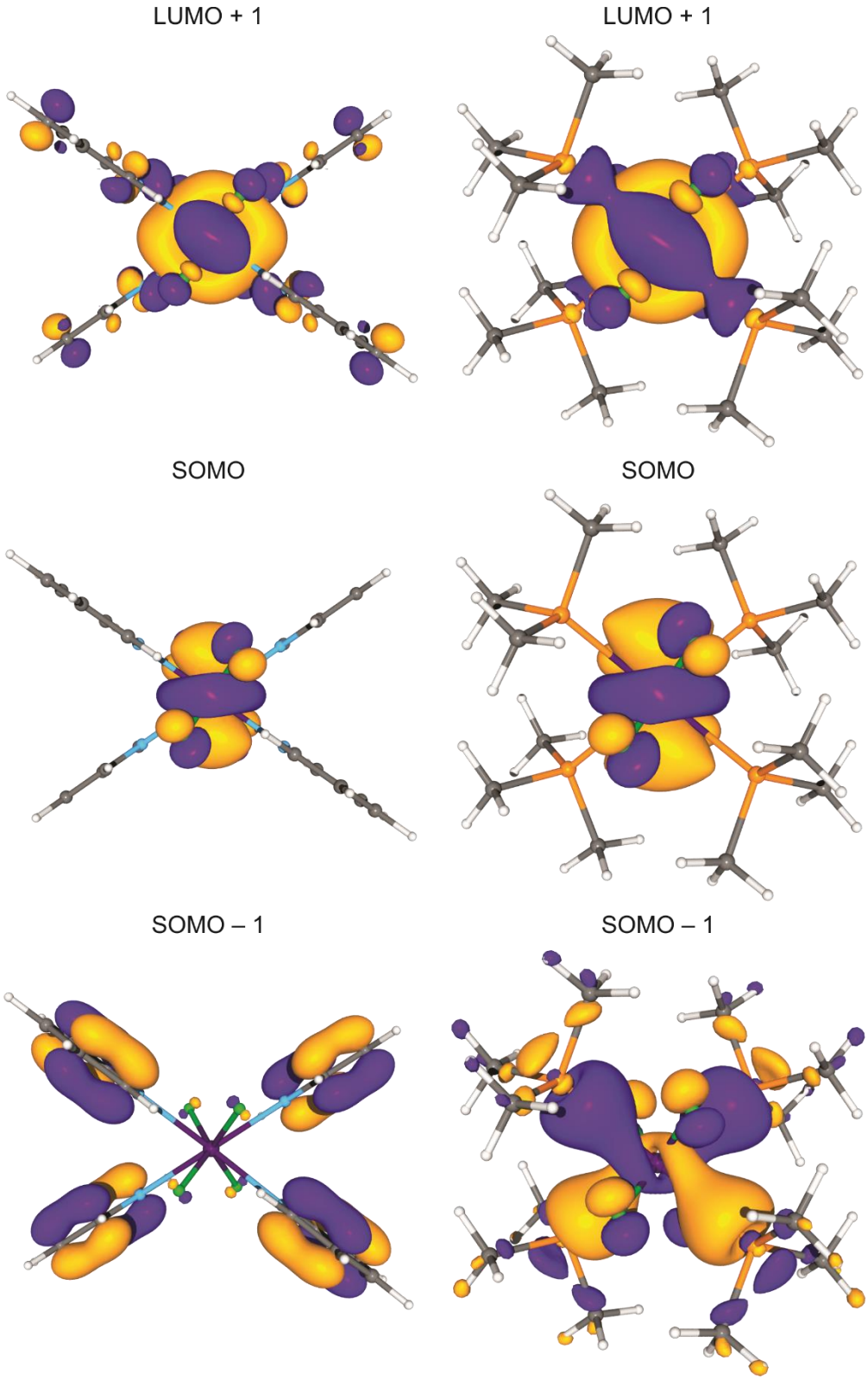

Figure 8.9. Selected MOs of $[WF_4(NC_5H_5)_4]^+$ (left) and $[WF_4\{P(CH_3)_3\}_4]^+$ (right). Isosurface values are drawn at 0.04 e $Å^{-3}$.

Table 8.4. Natural-Population-Analysis Charges and Wiberg Valences[a] of $[WF_4(L)_4]^{+b}$

	L	
	$P(CH_3)_3$	**C_5H_5N**
W	+1.28 [4.76]	+2.17 [4.36]
F	–0.58 [0.78]	–0.56 [0.81]
Pn	+1.03 [3.69]	–0.47 [3.36]
C_{Me}[c]	–0.89 [3.81]	
H_{Me}[c]	+0.24 [0.95]	
C_o		+0.09 [3.91]
C_m		–0.23 [3.96]
C_p		–0.12 [3.95]
H_o		+0.23 [0.95]
H_m		+0.23 [0.95]
H_p		+0.22 [0.95]
Σ(L)	+0.51[d]	+0.27[d]

[a]Given in square brackets. [b]Calculated at the B3LYP/aVTZ level of theory. [c]Averaged value. [d]For each ligand.

Table 8.5. Wiberg Bond Indices of $[WF_4(L)_4]^{+a}$

	L	
	$P(CH_3)_3$	**C_5H_5N**
W–F	0.57	0.63
W–Pn	0.56	0.40
P–C_{Me}	0.96	
C_{Me}–H_{Me}	0.93	
N–C_o		1.34
C_o–C_m		1.45
C_m–C_p		1.44
C_o–H_o		0.91
C_m–H_m		0.92
C_p–H_p		0.92

[b]Calculated at the B3LYP/aVTZ level of theory.

attributed to a greater degree of electrostatic contribution to bonding in $[WF_4(NC_5H_5)_4]^+$, resulting in overall stronger bonds with a lesser orbital component; the greater NPA charge on tungsten would fortify this notion.

8.2.5.2. Second-Order Jahn-Teller Effects in $[WF_4(PH_3)_4]^+$

As discussed, the geometric differences observed between octacoordinate d^0 complexes and their d^1 analogues, such as those reported herein, are not well understood. Therefore, the nature of this disparity was investigated computationally using $[WF_4(PH_3)_4]^{n+}$ (n = 1, 2) as model cations, revealing that there is a preference for SA in certain d^1 complexes due to a SOJT distortion from TD.

The SOJT effect has been discussed in detail by Bader[37,38] and Pearson,[39,40] and dictates that the mixing of ground and low-lying excited states may cause an energetically favourable vibration or distortion (Q). However, the direct product of irreducible representations of the ground (Γ_0) and excited (Γ_i) states under the initial point group of the system must be the same as the distortion in question (Eq. 8.11).

$$\Gamma_0 \times \Gamma_i = \Gamma_Q \tag{8.11}$$

This is because the Hamiltonian operator is invariant to symmetry operations applied to the system (i.e., totally symmetric). If a system is perturbed, its Hamiltonian operator ($\hat{H}$), energy (E), and wavefunction (ψ) can be described as per second-order perturbation theory by Eqs. 8.12–8.14, in which U is the potential energy and i defines some excited state. From Eq. 8.12, it is established that ($\delta U/\delta Q$) has the same symmetry as Q to achieve a totally symmetric second term. Furthermore, ($\delta^2 U/\delta Q^2$) must be totally symmetric, as Q^2 is.

$$\hat{H} = \hat{H}_0 + Q\left(\frac{\partial U}{\partial Q}\right) + \frac{Q^2}{2}\left(\frac{\partial^2 U}{\partial Q^2}\right) \tag{8.12}$$

$$E = E_0 + Q\langle\psi_0\left|\frac{\partial U}{\partial Q}\right|\psi_0\rangle + \frac{Q^2}{2}\langle\psi_0\left|\frac{\partial^2 U}{\partial Q^2}\right|\psi_0\rangle + Q^2\sum_i \frac{\left[\langle\psi_0\left|\frac{\partial U}{\partial Q}\right|\psi_i\rangle\right]^2}{(E_0 - E_i)} \tag{8.13}$$

$$\psi = \psi_0 + Q\,\psi_i \sum_i \frac{\langle\psi_0\left|\frac{\partial U}{\partial Q}\right|\psi_i\rangle}{(E_0 - E_i)} \tag{8.14}$$

The occurrence of the SOJT effect is dependent on the terms that are quadratic with respect to Q. The first quadratic term in Eq. 8.13 can be seen as a "restoring force" that is always non-zero (i.e., totally symmetric) and positive due to the symmetry of $(\delta^2U/\delta Q^2)$ and $\psi_0 \times \psi_0$. Meanwhile, the second quadratic term is a "stabilising force" that is always zero or negative as $|E_0| < |E_i|$. It is only non-zero if the integral $\langle\psi_0|\delta U/\delta Q|\psi_i\rangle$ is totally symmetric, or rather, if the symmetries of $\psi_0 \times \psi_i$ and $(\delta U/\delta Q)$ are equal. As discussed, the symmetry of $(\delta U/\delta Q)$ is equal to that of Q, hence Eq. 8.11.

In terms of MO theory, the symmetry of the distortion must be the same as the direct product of symmetries of interacting occupied (o) and unoccupied (uo) MOs ($\Gamma_o \times \Gamma_{uo}$). In addition, the MOs must be sufficiently close in energy (originally thought to be within 4 eV,[39] though recent computational studies indicate a possible limit as high as 12 eV[41]). Beyond a critical threshold, the destabilising or "restoring" term of the SOJT effect will begin to predominate; the smaller the initial MO gap, the more stabilising the effect. The effect ultimately manifests as a structural distortion that stabilises the occupied MO and destabilises the unoccupied MO while rendering the symmetries of the interacting MOs equal under the new point group.

The d^0 $[WF_4(PH_3)_4]^{2+}$ cation is predicted to adopt a TD geometry with true D_{2d} symmetry. The lowest-lying *d* orbitals, the LUMO ($d_{x^2-y^2}$) and LUMO + 1 (d_{z^2}), are b_1- and

a_1-symmetric, respectively, such that the direct product of their symmetries is b_1 (Eq. 8.15). Upon reduction to d^1 $[WF_4(PH_3)_4]^+$, i.e., occupation of the b_1-symmetric LUMO, a distortion of b_1 symmetry would be energetically favourable via the SOJT effect due to mixing of the b_1 SOMO and a_1 LUMO (Eqs. 8.15 and 8.16). Optimisation of D_{2d}-symmetric $[WF_4(PH_3)_4]^+$ reveals that it exists as a transition state with a single imaginary frequency ($\nu(B_1)$, 195*i* cm^{-1}), the vibrational mode corresponding to the TD → SA isomerisation. As expected, ground-state $[WF_4(PH_3)_4]^+$ is distorted to SA and D_2-symmetric (Table 8.6 and Figure 8.10a), 37 kJ mol^{-1} lower in energy than the transition state.

$$b_1 \times a_1 = b_1 \quad (8.15)$$

$$b_1 \times b_1 = a_1 \text{ (totally symmetric)} \quad (8.16)$$

The distortion results in stabilisation of the SOMO and corresponding destabilisation of the LUMO (Figure 8.11). Descent from D_{2d} to D_2 symmetry also results in the SOMO, LUMO, and distortion becoming totally symmetric (a) under the D_2 point group. As well, the same mixing of SOMO and LUMO occurs as was predicted for the C_5H_5N and $P(CH_3)_3$ complexes. These observations are completely consistent with an SOJT distortion.

The structural distortion results in a slight increase of the NPA charge on the tungsten centre of $[WF_4(PH_3)_4]^+$ (+1.32 → +1.37) along with strengthening of the W–F (WBI: 0.58 → 0.62) and weakening of the W–P (0.59 → 0.55) bonds, evidenced by changes in the WBIs (Table 8.7). The second-order perturbation analysis of the NBO donor-acceptor interactions reveals improved $sp^2_\sigma(F) \rightarrow d_\sigma(W)$ and $s_\sigma(P) \rightarrow d_\sigma(W)$ bonding at the expense of $p_\pi(F) \rightarrow d_\pi(W)$ bonding (Table 8.8). The overall weakening of the W–P bonds

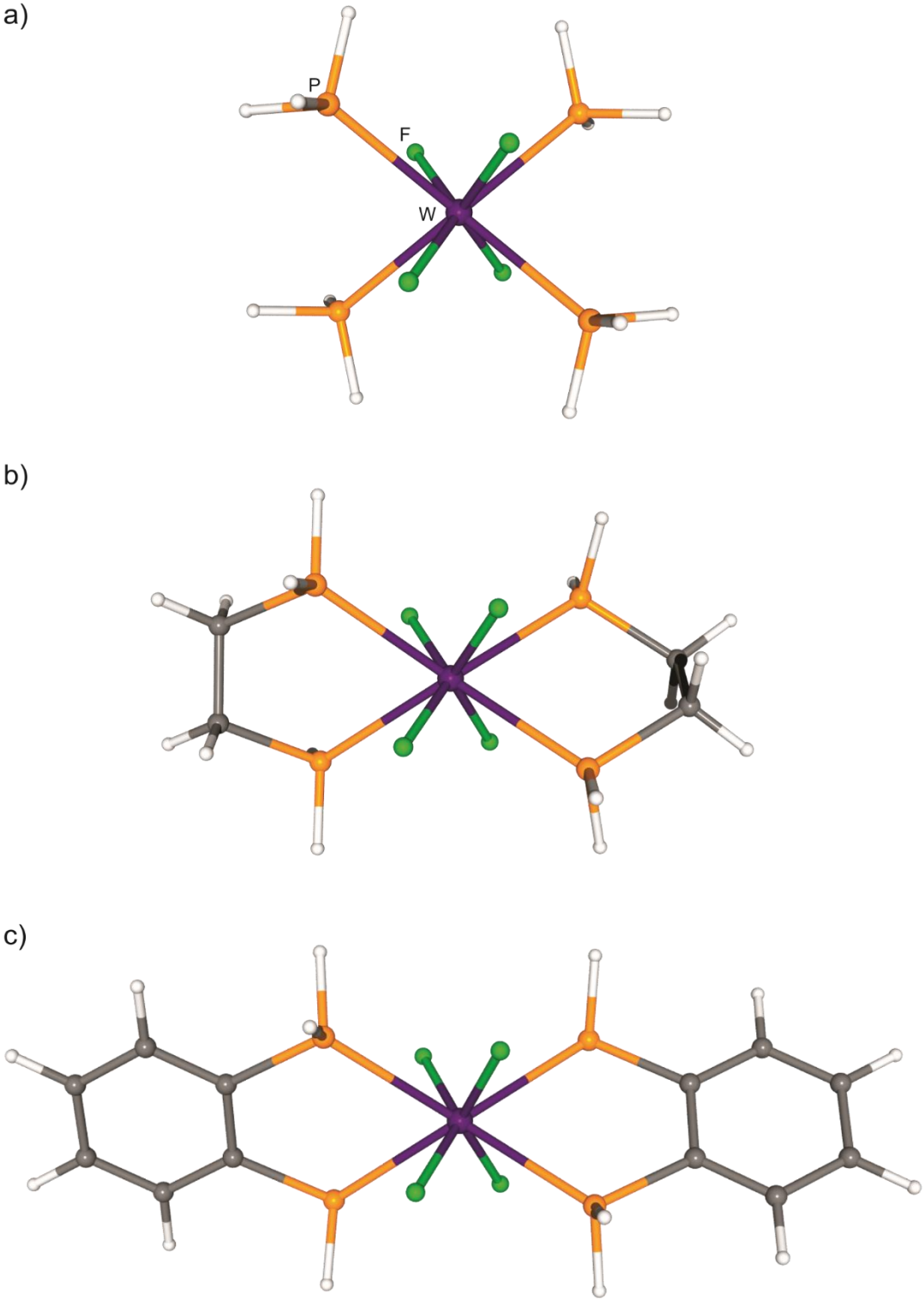

Figure 8.10. Optimised gas-phase ground-state geometries (B3LYP/aVTZ) of a) $[WF_4(PH_3)_4]^+$, b) $[WF_4(dpe)_2]^+$ (C_2), and c) $[WF_{4(}dpb)_2]^+$.

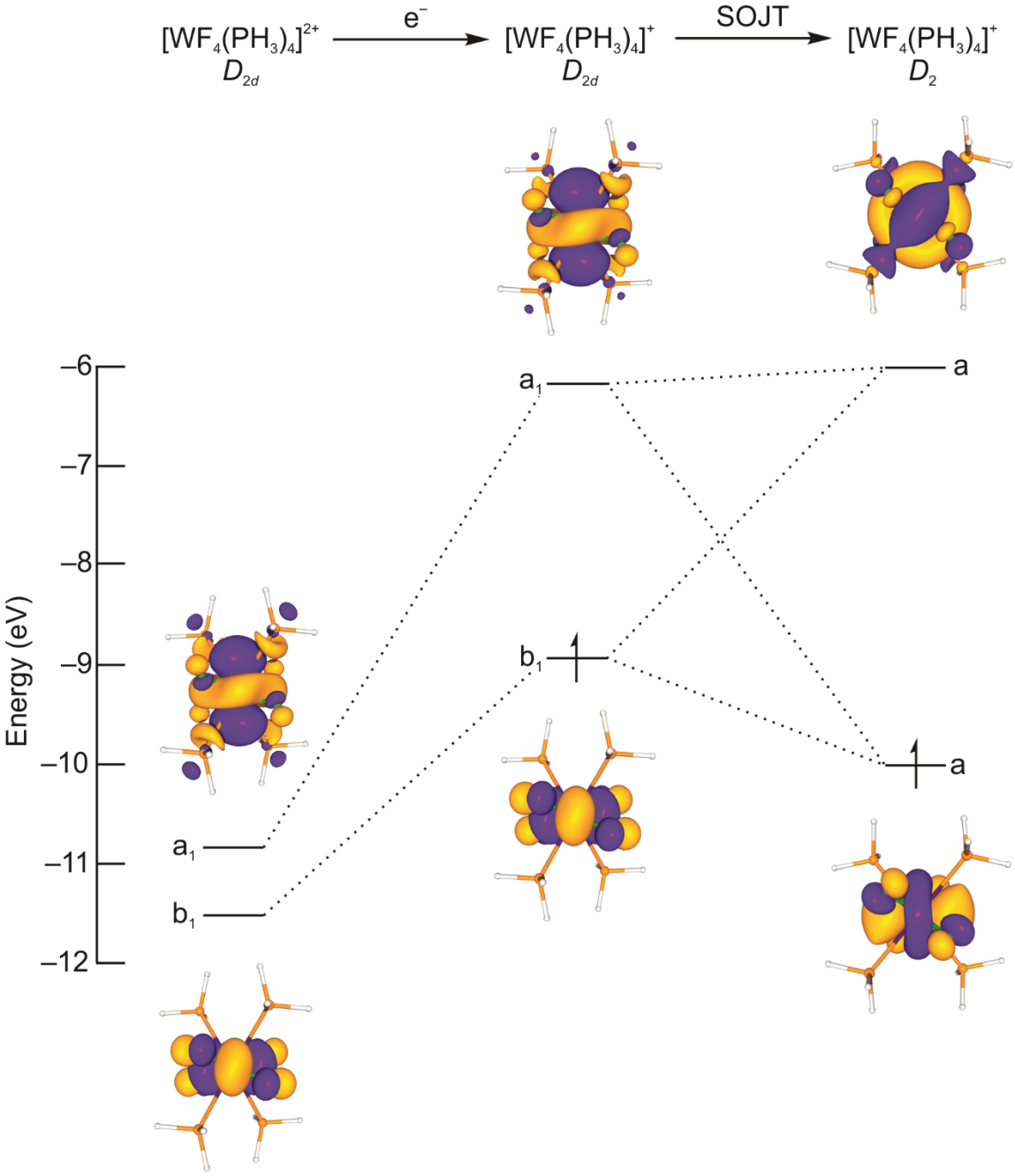

Figure 8.11. Selected MOs of $[WF_4(PH_3)_4]^{n+}$ (n = 1, 2). Isosurface values are drawn at 0.04 e Å^{-3}.

Table 8.6. Calculated SOJT Stabilisation Energies (kJ mol^{-1}), MO Energies (eV), SOMO-LUMO Gaps (eV), ν(B_1) Frequencies **(**cm^{-1}), and α_A and α_B (°)[a] of Various Octacoordinate d^1 Complexes[b]

	Symmetry	E_{SOJT}	E_{LUMO}	E_{SOMO}	ΔE	ν(B_1)	α_A	α_B
$[WF_4(PH_3)_4]^+$	D_{2d}	37	–6.33	–8.98	2.65	195*i*		
	D_2		–6.00	–10.00	4.00	52	59.7	67.2
$[WF_4(dpe)_2]^+$	S_4	26	–5.50	–8.30	2.80	169*i*		
	C_2		–5.25	–9.18	3.93	73	62.5	69.3
$[WF_4(dpb)_2]^+$	D_{2d}	19	–5.18	–8.05	2.87	155*i*		
	D_2		–4.95	–8.79	3.84	59	67.5	71.1
$[WCl_4(PH_3)_4]^+$	D_{2d}	3	–6.63	–9.81	3.17	43*i*		
	D_2		–6.51	–9.94	3.43	55	71.3	79.9
$[WCl_4(dpe)_2]^+$	S_4	0	–5.80	–9.25	3.44	59		
	D_2	N/A	–5.75	–9.28	3.53	70	77.7	84.3
$[WCl_4(dpb)_2]^+$	D_{2d}	0	–5.53	–9.00	3.47	52		
$TaCl_4(dpe)_2$	S_4	0	–6.36	–10.69	4.33	81		

[a]D_{2d}- and S_4-symmetric complexes have $\alpha_A = \alpha_B = 90°$. [b]Calculated at the B3LYP/aVTZ level of theory.

despite improved σ-bonding interactions is attributed to increased *cis* and *trans* effects from the fluorido ligands resulting in overcompensatory σ*(WP) character. Negligible synergic bonding in the form of d_π(W)→π*(PC) interactions is estimated (< 1 kJ mol^{-1} per ligand), corroborating the prediction by Levason and co-workers that an electron-poor d^1 metal centre would not behave as a π donor.[16]

8.2.5.3. Influence of Chelating Ligands on SOJT Effect

While the SOJT treatment elegantly describes the structural distortion observed in SA $[WF_4(L)_4]^+$ complexes with monodentate ligands, this geometry is not ubiquitous among its valence-isoelectronic brethren, namely the TD complexes of MCl_4 (M = Nb, Ta)[12,16] and $[MoCl_4]^{+}$[42] with dmpb and/or dmab, as well as the intermediate geometry of $[WCl_4(dmpe)_2]^+$.[20] As such, the 1,2-diphosphinoethane (dpe) and 1,2-diphosphinobenzene (dpb) ligands were employed in $[WF_4(dpe)_2]^{n+}$ and $[WF_4(dpb)_2]^{n+}$ (n = 1, 2) model systems to simulate the geometric constraints of chelating ligands.

The parent dications were found to adopt TD geometries about the tungsten centres. While $[WF_4(dpb)_2]^{2+}$ possesses true D_{2d} symmetry, its dpe analogue can achieve either D_2 or S_4 symmetry, depending on the relative orientation of the ethylene backbones of the donor ligands. The stereoisomers of the ground states are negligibly different in energy, so reduction of the S_4-symmetric system from d^0 to d^1 was studied (a descent in symmetry upon SOJT distortion aids in the determination of a stable transition state). After reduction without descent in symmetry, both $[WF_4(L')_2]^+$ cations manifest as TD transition states with imaginary vibrations along the coordinate of the TD → SA isomerisation (Table 8.8). However, the stabilisation energies are less than in $[WF_4(PH_3)_4]^+$ (L′ = dpb: 19 kJ mol^{-1}; L′ = dpe: 26 kJ mol^{-1}), with the decrease being slightly greater for the more rigid dpb

Table 8.7. NPA Charges, Wiberg Valences, and WBIs of D_{2d}- and D_2-Symmetric $[WF_4(PH_3)_4]^{+a}$

	D_{2d}		D_2			D_{2d}	D_2
	Charge	**Valence**	**Charge**	**Valence**		**WBI**	
W	+1.32	4.78	+1.37	4.76	W–F	0.58	0.62
F	–0.57	0.80	–0.55	0.84	W–P	0.59	0.55
P	+0.32	3.70	+0.29	3.66	P–H[b]	0.97	0.97
H[b]	+0.05	1.00	+0.06	1.00			

[a]Calculated at the B3LYP/aVTZ level of theory. [b]Averaged value.

Table 8.8. Energies ($E^{(2)}$, kJ mol^{-1}) of W–F and W–P Interactions in D_{2d}- and D_2-Symmetric $[WF_4(PH_3)_4]^{+[a]}$

	D_{2d}	D_2
sp^x_σ(F)→d_σ(W)	544[b]	582[c]
p_π(F)→d_π(W)	131	87
sp^y_σ(P)→d_σ(W)	837[d]	999[e]
d_π(W)→π^*(PC)	< 1	< 1

[a]Calculated at the B3LYP/aVTZ level of theory. Per ligand. [b]x = 2.01 [c]x = 2.09 [d]y = 0.34 [e]y = 0.42

complex. This is attributed to a combination of a steric effect, wherein the constraints of the chelating ligands result in a preference for TD to minimise interligand repulsion,[30] and electronic mitigation of the SOJT effect due to expanded SOMO–LUMO gaps in the TD transition states (Table 8.8).

8.2.5.4. Influence of Halido Ligands on SOJT Effect

Substituting the fluorido ligands with chlorido ligands results in more appreciable effects on the SOJT stabilisation energies. The $[WCl_4(PH_3)_4]^+$ cation was only predicted to be 3 kJ mol^{-1} more stable as its SA stereoisomer and is distorted towards SA to a lesser degree than the fluorido complexes (Table 8.8). Meanwhile, D_{2d}-symmetric $[WCl_4(dpb)_2]^+$ already represents a minimum-energy geometry. The dpe complex is interesting in that under D_2 symmetry, both the corresponding mono- and dication adopt intermediate geometries with no obvious SOJT effect. The stereochemistry of D_2-symmetric $[WCl_4(dpe)_2]^+$ (α_A = 77.7°, α_B = 84.3°) is in excellent agreement with the crystal structure of $[WCl_4(dmpe)_2][SbCl_6]$ (α_A = 78.2°, α_B = 84.1°).[20] Meanwhile, S_4-symmetric $[WCl_4(dpe)_2]^+$ represents an undistorted minimum-energy geometry. Like the chelating ligands, the chlorido ligands seemingly serve to expand the SOMO-LUMO gaps in the TD stereoisomers, resulting in less SOJT stabilisation.

8.2.5.5. Influence of Metal Centre on SOJT Effect

Lastly, in addition to the influence of the ligands, there is an evident effect of the metal centre on the nature of the SOJT distortion, considering that $MCl_4(dmpe)$ (M = Nb, Ta) and $[WCl_4(dmpe)_2]^+$ are valence-isoelectronic, but not isostructural. Thus, the SOJT stabilisation energies for $TaCl_4(dpe)_2$ were calculated. However, it was found that the $[WCl_4]^+$ and $TaCl_4$ systems behave identically at the B3LYP/aVTZ level of theory. On the

basis of the reported crystal structures, in tandem with the calculations for the fluorine-containing systems, it seems most likely that the known dmpb and dmab complexes remain TD due to the aforementioned steric and electronic effects. For the less rigid dmpe systems, the SOJT distortion is still sufficiently stabilising to overcome this energetic preference, save for the $[WCl_4]^+$ complex, in which crystal-packing effects seemingly predominate. However, the SOMO–LUMO gap is likely overpredicted in the TD transition state at the level of theory used, artificially diminishing the SOJT effect of the chlorine-containing systems.

8.3. Conclusions

Facile syntheses of $[WF_4]^+$ complexes with N- and P-donor ligands have been developed using WF_6 and $WF_5(NC_5H_5)_2$ as reagents. Their crystal structures reveal SA geometries at the tungsten(V) centres, unlike analogous d^0 complexes of the group-5 and 6 transition metals, which are known to be TD. Extensive computational studies elucidated that this disparity arises due to an SOJT distortion of the d^1 complexes, serving to improve the σ-bonding orbital overlap of all eight ligands with the metal centre. This provides a definitive justification for a phenomenon that has been long observed in crystallographic studies, but for which only speculative explanations have been given. However, the extent, or even occurrence, of the SOJT effect is dependent on the properties of the ligands, resulting in the expectation of both TD and SA d^1 complexes.

8.4. References

(1) Schröder, J.; Grewe, F. J. *Angew. Chem. Int. Ed. Engl.* **1968**, *7* (2), 132–133.

(2) Schröder, J.; Grewe, F. J. *Chem. Ber.* **1970**, *103* (5), 1536–1546.

(3) O'Donnell, T. A.; Peel, T. E. *J. Inorg. Nucl. Chem.* **1976**, *28*, 61–62.

(4) Stene, R.; Scheibe, B.; Ivlev, S. I.; Karttunen, A. J.; Petry, W.; Kraus, F. *Z. Anorg. Allg. Chem.* **2020**. In press.

(5) Edwards, A. J. *J. Chem. Soc. A* **1969**, 909.

(6) Mazej, Z.; Hagiwara, R. *J. Fluorine Chem.* **2007**, *128* (4), 423–437.

(7) Bao, N.; Winfield, J. M. *J. Fluorine Chem.* **1990**, *50* (3), 339–343.

(8) Haiges, R.; Deokar, P.; Christe, K. O. *Z. Anorg. Allg. Chem.* **2014**, *640* (8–9), 1568–1575.

(9) Marchetti, F.; Pampaloni, G. *Chem. Commun.* **2012**, *48* (5), 635–653.

(10) Benjamin, S. L.; Levason, W.; Reid, G. *Chem. Soc. Rev.* **2013**, *42* (4), 1460–1499.

(11) Levason, W.; Monzittu, F. M.; Reid, G. *Coord. Chem. Rev.* **2019**, *391*, 90–130.

(12) Dewan, J. C.; Kepert, D. L.; Raston, C. L.; White, A. H. *J. Chem. Soc., Dalton Trans.* **1975**, No. 20, 2031–2038.

(13) Cotton, F. A.; Falvello, L. R.; Najjar, R. C. *Inorg. Chem.* **1983**, *22* (5), 770–774.

(14) Levason, W.; Light, M. E.; Reid, G.; Zhang, W. *Dalton Trans.* **2014**, *43* (25), 9557–9566.

(15) Burdett, J. K.; Hoffmann, R.; Fay, R. C. *Inorg. Chem.* **1978**, *17* (9), 2553–2568.

(16) Benjamin, S. L.; Chang, Y. P.; Hector, A. L.; Jura, M.; Levason, W.; Reid, G.; Stenning, G. *Dalton Trans.* **2016**, *45* (19), 8192–8200.

(17) Kepert, D. L. In *Progress in Inorganic Chemistry, Volume 24*; 1978; pp 179–249.

(18) Hlatky, G. G.; Crabtree, R. H. *Coord. Chem. Rev.* **1985**, *65* (C), 1–48.

(19) Levason, W.; Reid, G.; Zhang, W. *J. Fluorine Chem.* **2015**, *172*, 62–67.

(20) Saboonchian, V.; Wilkinson, G.; Hussain-Bates, B.; Hursthouse, M. B. *Polyhedron* **1991**, *10* (6), 595–603.

(21) Scilabra, P.; Terraneo, G.; Resnati, G. *J. Fluorine Chem.* **2017**, *203*, 62–74.

(22) Batsanov, S. S. *J. Mol. Struct.* **1999**, *468* (1–2), 151–159.

(23) Alvarez, S. *Dalton Trans.* **2013**, *42* (24), 8617–8636.

(24) Arnaudet, L.; Bougon, R.; Ban, B.; Lance, M.; Navaza, A.; Nierlich, M.; Vigner, J. *J. Fluorine Chem.* **1992**, *59* (1), 141–152.

(25) Arnaudet, L.; Bougon, R.; Ban, B.; Lance, M.; Navaza, A.; Nierlich, M.; Vigner, J. *J. Fluorine Chem.* **1994**, *67* (1), 17–25.

(26) Lippard, S. J.; Russ, B. J. *Inorg. Chem.* **1968**, *7* (8), 1686–1688.

(27) Hwang, I. C.; Seppelt, K. *J. Fluorine Chem.* **2000**, *102* (1–2), 69–72.

(28) Macrae, C. F.; Sovago, I.; Cottrell, S. J.; Galek, P. T. A.; McCabe, P.; Pidcock, E.; Platings, M.; Shields, G. P.; Stevens, J. S.; Towler, M.; et al. *J. Appl. Crystallogr.* **2020**, *53* (1), 226–235.

(29) Levason, W.; Monzittu, F. M.; Reid, G.; Zhang, W. *Chem. Commun.* **2018**, *54* (83), 11681–11684.

(30) Blight, D. G.; Kepert, D. L. *Inorg. Chem.* **1972**, *11* (7), 1556–1561.

(31) Sampoli, M.; Marziano, N. C.; Tortato, C. *J. Phys. Chem.* **1989**, *93* (20), 7252–7257.

(32) Eklund, S. E.; Chambers, J. Q.; Mamantov, G.; Diminnie, J.; Barnes, C. E. *Inorg. Chem.* **2001**, *40* (4), 715–722.

(33) Tebbe, F. N.; Muetterties, E. L. *Inorg. Chem.* **1968**, *7* (1), 172–174.

(34) El-Kurdi, S.; Al-Terkawi, A.-A.; Schmidt, B.; Dimitrov, A.; Seppelt, K. *Chem. Eur. J.* **2010**, *16* (2), 595–599.

(35) Chitnis, S. S.; Robertson, A. P. M.; Burford, N.; Weigand, J. J.; Fischer, R. *Chem. Sci.* **2015**, *6* (4), 2559–2574.

(36) Weigand, J. J.; Riegel, S. D.; Burford, N.; Decken, A. *J. Am. Chem. Soc.* **2007**, *129* (25), 7969–7976.

(37) Bader, R. F. W. *Mol. Phys.* **1960**, *3* (2), 137–151.

(38) Bader, R. F. W. *Can. J. Chem.* **1962**, *40* (6), 1164–1175.

(39) Pearson, R. G. *Proc. Natl. Acad. Sci.* **1975**, *72* (6), 2104–2106.

(40) Pearson, R. G. *J. Mol. Struct.* **1983**, *103* (C), 25–34.

(41) Wedler, H. B.; Wendelboe, P.; Tantillo, D. J.; Power, P. P. *Dalton Trans.* **2020**, *49* (16), 5175–5182.

(42) Drew, M. G. B.; Egginton, G. M.; Wilkins, J. D. *Acta Crystallogr.* **1974**, *30* (8), 1895–1900.

Chapter 9 – Conclusions and Future Work

9.1. Conclusions

The Lewis acidity of WF_6 towards N-donor ligands has been exploited in order to access new tungsten(VI) and (V) systems and explore their Lewis-acid behaviours. The reactions of WF_6 with C_5H_5N and derivatives thereof were investigated in detail, and $WF_6(NC_5H_5)$ was subsequently employed as a synthetic equivalent to WF_6 in the development of novel transition-metal fluoride complexes. This allowed for the syntheses of various $W(NR)F_4$, $[WF_5]^+$, WF_5, and $[WF_4]^+$ complexes with N- and P-donor ligands as well as the elucidation of their fundamental structural and bonding characteristics using a suite of crystallographic, spectroscopic, and computational techniques.

In Chapter 3, the $WF_6(NC_5H_5)$ adduct and its *para*-substituted derivatives were synthesised and characterised in the solid state, invariably revealing monocapped-trigonal-prismatic geometries about the tungsten centres. The utility of the parent adduct as a synthetic equivalent to WF_6 was demonstrated in facile syntheses of $[C_5H_5NH][W(NC_6F_5)F_5]$ (Chapter 4), WF_6(2,2′-bipy) and WF_6(1,10-phen) (Chapter 6), and $W^VF_5(NC_5H_5)_2$ (Chapter 7).

The synthesis of pure $[C_5H_5NH][W(NC_6F_5)F_5]$ from $WF_6(NC_5H_5)$ permitted a systematic study of the $F^–$-acceptor and Lewis-acid properties of $W(NC_6F_5)F_4$, which were bolstered by computational studies of diverse $[W(NR)F_5]^–$ and $W(NR)F_4$ series (Chapters 4 and 5). These investigations established, in a quantitative fashion, the tunability of the electronic properties of the tungsten centre upon modulation of the R group, which could aid in the development of new weakly coordinating anions and Lewis acids.

Meanwhile, F^- abstraction from WF_6(2,2′-bipy) and WF_6(1,10-phen) was achieved to afford stable, heptacoordinate $[WF_5]^+$ complexes, demonstrating the discrete F^--donor capabilities of WF_6 in the presence of stabilising donor ligands (Chapter 6). These salts are the first isolated examples of $[MF_5]^+$ complexes (for any transition metal M). The dismutation of $[WF_5(L)]^+$ to $[WF_4(L)_2]^{2+}$ and WF_6 was also observed, suggesting the generation of intermediate $[WF_5]^+$ complexes during the ligand-induced autoionisation of WF_6. The calculated LUMO energies of these cations suggest that they could be employed as strong oxidising agents developed from the most accessible of the transition-metal hexafluorides, WF_6.

The first octacoordinate $[WF_5]^+$ complex, $[WF_5(NC_5H_5)_3]^+$, was stabilised in the absence of excess C_5H_5N, and its intramolecular exchange mechanism in solution was elucidated by variable-temperature NMR spectroscopy and dynamic NMR simulations (Chapter 7). In demonstrations of the reactivity of $[WF_5]^+$ complexes, F^- abstraction from WF_6 allowed for controlled reduction to $W^VF_5(NC_5H_5)_2$ (Chapter 7) and $[W^VF_4\{P(CH_3)_3\}_4]^+$ (Chapter 8) in the presence of excess C_5H_5N and $P(CH_3)_3$, respectively. These, in addition to $[W^VF_4(NC_5H_5)_4]^+$, represent rare derivatives of thermally unstable WF_5, including the first examples of $[W^VF_4]^+$ complexes. Interestingly, NMR spectroscopic studies indicate highly disparate redox processes when C_5H_5N and $P(CH_3)_3$ are employed as reducing agents.

Crystallographic studies of octacoordinate $[W^VF_4(L)_4]^+$ revealed square-antiprismatic geometries, contrasting with their trigonal-dodecahedral tungsten(VI) analogues, and the nature of this difference was investigated computationally (Chapter 8). The occurrence of SOJT distortions in the d^1 complexes that are absent in their d^0 brethren

was revealed, explaining the long observed, but ill understood, structural dissimilarities between d^0 and d^1 complexes of the group-5 and 6 halides.

Furthermore, the coordination numbers seven and eight are unique in their potential for structural diversity, with several geometries being of similarly favourable energy in both cases. Herein, this diversity was realised, as new examples for the three model heptacoordinate geometries were characterised: the monocapped octahedron (e.g. $[WF_5(2,2'\text{-bipy})]^+$), monocapped trigonal prism (e.g. $WF_6(NC_5H_5)$), and pentagonal bipyramid (e.g. $WF_5(NC_5H_5)_2$). The $[WF_5(2,2'\text{-bipy})]^+$ and $[WF_5(1,10\text{-phen})]^+$ cations also represent rare examples of 4:3 complexes, as their geometries may be interpreted either as monocapped octahedra or 4:3 polyhedra. Examples of both trigonal-dodecahedral (e.g. $[WF_5(NC_5H_5)_3]^+$) and square-antiprismatic (e.g. $[WF_4(NC_5H_5)_4]^+$) complexes were characterised, and a robust method for differentiating these eight-vertex coordination polyhedra were established.

9.2. Future Work

The $[W(NC_6F_5)F_5]^-$ and $[W_2(NC_6F_5)_2F_9]^-$ anions show promise as templates for weakly coordinating anions, and greater versatility could be achieved upon further substitution of the fluorido ligands with sterically demanding groups, such as OC_6F_5 or $OTeF_5$. These groups could possibly be introduced by direct reactions of the anions with C_6F_5OH and TeF_5OH, condensing HF. With larger substituents, Lewis acids that are potentially susceptible to frustrated Lewis pair chemistry,[1] as well as larger and even more weakly coordinating anions, could be envisioned. Of special interest would be fluorine-bridged dinuclear anions, e.g. $[W_2(NC_6F_5)_2(\mu\text{-}F)(OC_6F_5)_8]$. These would be expected to exhibit very weakly coordinating behaviour by analogy with known fluorine-bridged dialuminate anions supporting perfluoroalkoxy substituents.[2]

Furthermore, whereas the greatest Lewis acidity was predicted for $W(NF)F_4$ and $W(NCF_3)F_4$ complexes in the $W(NR)F_4$ series, a more reasonably synthesised $W(NR)F_4$ Lewis acid could be $W(NTeF_5)F_4$. This could be accessed via TeF_5NH_2 or $TeF_5NH\{Si(CH_3)_3\}$ as $NTeF_5$ sources, which are known to be stable,[3] unlike CF_3NH_2[4] and (unknown) FNH_2.

The stabilisation of $[WF_5]^+$ by numerous N-donor ligands illustrates the possible tolerance of main-group donor ligands by strongly oxidising transition-metal centres. As such, fundamental Lewis-acid behaviour for the more strongly oxidising transition-metal hexafluorides, such as MoF_6 and ReF_6, should be explored. Low-temperature Raman and NMR spectroscopic studies could elucidate the presence of adduct formation in the solid state and solution and demonstrate new non-redox chemistry for the transition-metal hexafluorides beyond WF_6.

While C_5H_5N and $P(CH_3)_3$ have served as model reducing agents to demonstrate the oxidising and fluorinating capabilities of $[WF_5]^+$ complexes, the general applicability of such complexes in desirable organic oxidations, e.g. electrophilic fluorination, remains unknown. It has recently been demonstrated that a palladium(IV) fluoride complex exhibits different electrophilically fluorinating behaviour than the prototypical agent SelectFluor^{TM},[5] and the use of $[WF_5]^+$ complexes in similar reactions could be investigated. As well, the LMCT HOMO-LUMO transition in each of these complexes suggests the possibility of oxidation of the donor ligands by the metal centre under photochemical conditions. This could possibly allow for oxidations via non-innocent, cationic donor ligands, as opposed to metal-mediated electron transfer. As such, the redox behaviour of these complexes under both photochemical and non-photochemical conditions should be investigated.

Finally, while it was demonstrated that octacoordinate $[W^{V}F_4]^+$ complexes are square-antiprismatic due to SOJT distortions from trigonal dodecahedra, the only known $[WCl_4]^+$ complex, $[WCl_4(dmpe)_2]^+$, possesses an intermediate geometry that is not adequately described by either archetypal polyhedron. Further $[WCl_4]^+$ complexes could possibly be accessed via halide substitution of $[WF_4]^+$ complexes with $(CH_3)_3SiCl$, driven enthalpically by formation of the Si–F bond. Their crystallographic study would substantiate whether structural dissimilarities from valence-isoelectronic $NbCl_4$ and $TaCl_4$ derivatives are systemic.

9.3. References

(1) Stephan, D. W.; Erker, G. *Angew. Chemie - Int. Ed.* **2010**, *49* (1), 46–76.

(2) Riddlestone, I. M.; Kraft, A.; Schaefer, J.; Krossing, I. *Angew. Chem. Int. Ed.* **2018**, *57* (43), 13982–14024.

(3) Seppelt, K. *Inorg. Chem.* **1973**, *12* (12), 2837–2839.

(4) Kloeter, G.; Seppelt, K. *J. Am. Chem. Soc.* **1979**, *101* (2), 347–349.

(5) Brandt, J. R.; Lee, E.; Boursalian, G. B.; Ritter, T. *Chem. Sci.* **2014**, *5* (1), 169–179.

Appendix A – Supporting Information for Chapter 3

Table A.1. Crystallographic Data Collection and Refinement Parameters for $WF_6(4\text{-}NC_5H_4R)$ (R = H, CH_3, $N(CH_3)_2$)

	$WF_6(NC_5H_5)$	**$WF_6(4\text{-}NC_5H_4CH_3)$**	**$WF_6\{4\text{-}NC_5H_4N(CH_3)_2\}$**
Identification code	MG16038c	MG18002	MG17029
Empirical formula	$C_5H_5F_6NW$	$C_6H_7F_6NW$	$C_7H_{10}N_2F_6W$
Formula weight	376.95	390.98	420.02
Temperature/K	99.98(17)	100.6(8)	100.0(3)
Crystal system	triclinic	monoclinic	monoclinic
Space group	P-1	$P2_1/n$	C2/c
a/Å	6.8162(3)	9.0570(4)	11.4523(5)
b/Å	7.9414(3)	8.7114(3)	12.2477(5)
c/Å	8.0005(3)	11.5124(4)	7.7085(3)
α/°	70.630(4)	90	90
β/°	81.142(4)	97.253(3)	108.970(5)
γ/°	78.213(3)	90	90
Volume/$Å^3$	398.19(3)	901.05(6)	1022.50(8)
Z	2	4	4
$\rho_{calc}g/cm^3$	3.144	2.882	2.728
μ/mm^{-1}	14.56	12.875	11.358
F(000)	340	712	776
Crystal size/mm^3	0.148 × 0.121 × 0.078	0.221 × 0.145 × 0.119	0.227 × 0.043 × 0.042
Goodness-of-fit on F^2	1.214	1.056	1.069
Final R indexes [I>=2σ (I)]	R_1 = 0.0360, wR_2 = 0.0927	R_1 = 0.0208, wR_2 = 0.0484	R_1 = 0.0131, wR_2 = 0.0307
Final R indexes [all data]	R_1 = 0.0381, wR_2 = 0.0935	R_1 = 0.0254, wR_2 = 0.0500	R_1 = 0.0137, wR_2 = 0.0308
Largest diff. peak/hole / e $Å^{-3}$	2.98/-1.72	1.49/-1.13	0.51/-0.69

[a] $R_1 = \sum||F_o| - |F_c||/\sum|F_o|$. [b] $wR_2 = [\sum[w(F_o^2 - F_c^2)^2]/\sum w(F_o^4)]^{1/2}$.

.**Table A.2.** Vibrational Frequencies (cm^{-1}) for NC_5H_5 and $WF_6(NC_5H_5)$

NC_5H_5[a]		$WF_6(NC_5H_5)$		Assignment[d]
exptl[b]	calcd[c]	exptl[b]	calcd[c]	
3173(1)		3266(1)		C−H stretching modes, combination bands, and overtones
3145(3)		3228(1)		
3091(5)		3158(2)		
3056(39)	3194(280)[7]	3107(11)	3229(158)[5]	
3036 sh	3186(36)[24]		3226(1)[<0.1]	
3025 sh	3170(94)[5]	3089(5)	3208(156)[1]	
2988(5)	3148(86)[4]	3022(1)	3204(87)[2]	
2955(5)	3146(95)[27]	2978(1)	3185(73)[3]	
2908(1)		2941(1)		
2871(1)				
2453(1)				
1597(5)		1615(8)	1654(10)[27]	C–C/C–N stretching modes and in-plane ring deformations
1581(9)	1624(16)[23] 1618(9)[10]	1579(5)	1621(11)[2]	
1573(7)				
1482(3)	1516(2)[2]	1497(2)	1530(3)[3]	
	1474(<1)[26]		1488(0)[35]	
	1389(<1)[<1]		1398(0)[2]	
	1282(1)[<0.1]		1294(<1)[3]	
1217(8)	1241(8)[4]	1228(8)	1250(6)[19]	
1146(2)	1170(2)[3]	1167(2)	1181(2)[4]	

	1095(2)[3]		1109(<1)[1]	C–C/C–N stretching modes and in-plane ring deformations
1068(2)	1078(<1)[<0.1]	1072(2)	1096(<1)[19]	
1030(75)	1051(41)[7]	1048(21)	1064(21)[6]	δ_{ip}(CCC)/δ_{ip}(CNC)
990(100)	1012(32)[5]	1024(70)	1041(51)[7]	NC_5 ring-breathing mode
980(5)		1019(4)		
	1025(<0.1)[<0.1]		1036(<0.1)[<1]	out-of-plane ring deformations
	1014(<0.1)[0]		1016(0)[0]	
	966(<1)[<0.1]		982(<1)[<1]	
	902(<1)[0]		889(<1)[0]	
	768(<0.1)[8]		786(<0.1)[23]	
	722(<0.1)[63]		710(<0.1)[71]	
		705(100)	702(47)[52]	$\nu_s(WF_6)$
		660(4)	669(1)[71]	$\nu_{as}(WF_6)$ [1 − 2 + 3 − 4 + 5 – 6] − δ_{ip}(NC1C2) − δ_{ip}(C3C4C5)
652(5)	670(3)[<1]	650(2)	659(1)[99]	$\nu_{as}(WF_6)$ [1 + 2 – 3 − 4 – 5 – 6] + δ_{ip}(NC1C2) + δ_{ip}(C3C4C5)
		641(6)	658(4)[145]	$\nu_{as}(WF_6)$ [1 − 2 + 3 − 4 + 5 – 6] + δ_{ip}(NC1C2) + δ_{ip}(C3C4C5)
			645(<0.1)[176]	$\nu_{as}(WF_4)$ [3 + 4 − 5 – 6]
603(3)	617(2)[4]	626(2)	641(1)[96]	$\nu_{as}(WF_6)$ [1 + 2 – 3 − 4 – 5 – 6] – δ_{ip}(NC1C2) – δ_{ip}(C3C4C5)
		598(2)	591(2)[0]	$\nu_{as}(WF_4)$ [3 – 4 − 5 + 6]
		555(1)	559(1)[3]	$\nu_{as}(WF_6)$ [1 – 2 – 3 + 4 − 5 + 6]
		471(1)	476(<1)[4]	out-of-plane ring deformation
		433(3)	423(1)[<0.1]	δ(F1WF2) + δ(F3WF4) + δ(F5WF6)
406(1)	421(<1)[4]		400(<0.1)[0]	τ(C1NC5)–τ(C2C3C4)
	385(<0.1)[0]			
		363(3)	356(1)[2]	δ(F1WF3) + δ(F2WF4) − δ(F1WF5) − δ(F2WF6)
		336(3)	332(1)[61]	δ(F1WF2) − δ(F3WF4) − δ(F5WF6)

	329(1)[22]	ρ(F1WF2) + ω(F3WF5) − ω(F4WF6)
306(2)	304(1)[7]	δ(F3WF4) + δ(F5WF6)
	302(1)[0]	τ(F1WF2) + τ(F3WF4) + τ(F5WF6)
	293(<1)[21]	ω(F1WF2) + δ(F3WF4) − δ(F5WF6)
280(2)	270(1)[3]	
234(3)	217(1)[<0.1]	rocking modes
	170(<0.1)[3]	
198(10)	161(3)[4]	ν(WN)
114(21)		
	81(1)[0]	
	81(2)[<1]	rocking, twisting, and lattice modes
	79(<0.1)[1]	
	48(3)[0]	

[a]From Nieboer, J.; Yu, X.; Chaudhary, P.; Mercier, H. P. A.; Gerken, M. *Z. Anorg. Allg. Chem.* **2012**, *638* (3–4), 520–525. [b]Recorded in a flame-sealed m.p. capillary at ambient temperature. Normalised Raman intensities are given in parentheses. [c]Calculated at the B3LYP/sVTZ level of theory. Absolute Raman intensities (in $Å^4\ u^{-1}$) are given in parentheses and absolute infrared intensities (in km mol^{-1}) are given in square brackets. [d]Symbols and abbreviations denote stretch (ν), bend (δ), rock (ρ), twist (τ), wag (ω), symmetric (s), antisymmetric (as), in-plane (ip), and out-of-plane (op). Numbers in square brackets denote the fluorine atoms involved in the antisymmetric stretching mode. Atom labels are as in Figure 3.1a.

Table A.3. Vibrational Frequencies (cm^{-1}) for 4-$NC_5H_4CH_3$ and WF_6(4-$NC_5H_4CH_3$)

4-$NC_5H_4CH_3$[a]		WF_6(4-$NC_5H_4CH_3$)		Assignment[d]
exptl[b]	calcd[c]	exptl[b]	calcd[c]	
3049(92)	3172(288)[1]	3106(9)	3233(117)[6]	C−H stretching modes, combination bands, and overtones
	3170(15)[34]		3230(7)[<1]	
	3145(58)[10]	3080(4)	3189(118)[1]	
3033(39)	3143(117)[22]	3070(5)	3189(66)[4]	
	3106(54)[13]		3118(60)[8]	
2992(19)	3080(74)[13]	3015(2)	3089(81)[9]	
2968(8)		2981(2)		
2922(49)	3027(233)[17]	2942(13)	3032(295)[6]	
2909 sh				
2818(5)				
2737(4)		2735(1)		
2462(5)		2503(1)		
1608(55)	1638(17)[65]	1631(6)	1664(12)[82]	C–C/C–N stretching modes and in-plane ring deformations
		1622(4)		
	1602(5)[14]	1567(2)	1602(12)[82]	
1563(16)	1530(4)[3]	1510(3)	1546(4)[11]	
1505(5)	1491(6)[7]		1491(7)[8]	CH_3 bending modes
	1488(3)[21]		1487(3)[30]	
	1444(2)[9]	1430(2)	1460(3)[10]	
1390(13)	1415(9)[2]	1384(2)	1417(18)[4]	
1345(25)	1365(3)[<0.1]	1373(3)		

		1341(3)	1370(1)[1]	C–C/C–N stretching modes and in-plane ring deformations
1243(19)	1278(2)[<0.1]	1257(2)	1293(1)[2]	
1231(16)	1247(4)[6]	1245(6)	1261(11)[14]	
1224(44)	1239(24)[1]	1221(11)	1240(23)[17]	
1213(12)		1217(11)		
	1117(<0.1)[<0.1]		1149(<1)[<0.1]	
1071(16)	1096(4)[1]	1069(6)	1094(6)[16]	δ_{ip}(CCH)
	1066(<1)[6]		1067(1)[6]	$\omega(CH_3)$
998(90)	1013(27)[6]	1036(9)	1047(9)[21]	NC_5 ring breathing mode
987(12)	1012(<1)[<0.1]		1017(<0.1)[<0.1]	out-of-plane ring deformation
977(9)	1006(<1)[<1]		1013(<0.1)[0]	$\rho(CH_3)$
971(8)	988(<1)[<1]		1002(1)[1]	out-of-plane ring deformations
	892(<1)[<0.1]		881(<1)[<0.1]	
	820(6)[26]		840(7)[30]	
808(100)	809(13)[14]	824(27)	828(26)[12]	δ(C1NC5) – ν(C3C6)
		798(2)		out-of-plane ring deformations
	753(<0.1)[3]		743(<0.1)[9]	
		704(100)	701(49)[68]	$\nu_s(WF_6)$
671(58)	686(4)[<0.1]	675(5)	685(4)[4]	δ_{ip}(NC1C2) + δ_{ip}(C3C4C5)
		667(7)		
		653(1)	660(1)[230]	$\nu_{as}(WF_6)$ [1 − 2 + 3 − 4 + 5 – 6]
		635(2)	645(2)[186]	$\nu_{as}(WF_6)$ [1 + 2 – 3 − 4 – 5 – 6]
		629(2)	642(<1)[174]	$\nu_{as}(WF_4)$ [3 + 4 – 5 – 6] – δ_{ip}(NC1C2) − δ_{ip}(C3C4C5)
		599(3)	589(2)[0]	$\nu_{as}(WF_4)$ [3 – 4 – 5 + 6] + δ_{ip}(NC1C2) + δ_{ip}(C3C4C5)
518(28)	523(5)[5]	550(1)	558(2)[5]	$\nu_{as}(WF_6)$ [1 – 2 – 3 + 4 − 5 + 6]

489(10)	500(<1)[19]		555(1)[4]	ring deformations
		505(1)	517(<1)[16]	
		437(4)	427(2)[1]	δ(F1WF2) + δ(F3WF4) + δ(F5WF6)
	391(<0.1)[<0.1]	400(1)	408(<0.1)[0]	τ(C1NC5) – τ(C2C3C4)
		383(5)	377(2)[<0.1]	ω(F1WF2) – δ(C2C3C6)
		367(2)	361(1)[1]	ω(F1WF2) – δ(C2C3C6)
352(22)	342(<1)[<0.1]			δ(C2C3C6)
		343(2)	340(<1)[21]	ρ(F1WF2) + ω(F3WF5) − ω(F4WF6)
			338(1)[63]	δ(F1WF2) − δ(F3WF4) − δ(F5WF6)
			306(1)[<0.1]	τ(F1WF2) + τ(F3WF4) + τ(F5WF6)
			299(<1)[21]	ω(F1WF2) + δ(F3WF4) − δ(F5WF6)
		298(5)	297(1)[6]	δ_{ip}(F1WN) + δ(F3WF5) − δ(F2WF4)
			294(1)[9]	δ(F3WF4) + δ(F5WF6)
212(15)	208(<1)[<1]		228(<0.1)[<1]	rocking modes
			190(<1)[3]	
		185(13)	157(3)[4]	ν(WN)
		130(16)		rocking, twisting, and lattice modes
			118(<0.1)[<0.1]	
			107(<1)[2]	
		100(22)		
			81(1)[<0.1]	
			63(4)[<0.1]	
			58(2)[<0.1]	
	36(<1)[<1]		24(<1)[<1]	

[a]From Chaudhary, P.; Goettel, J. T.; Mercier, H. P. A.; Sowlati-Hashjin, S.; Hazendonk, P.; Gerken, M. *Chem. Eur. J.* **2015**, *21* (16), 6247–6256. [b]Recorded in a flame-sealed m.p. capillary at ambient temperature. Normalised Raman intensities are given in parentheses. [c]Calculated at the B3LYP/sVTZ level of theory. Absolute Raman intensities (in $Å^4\ u^{-1}$) are given in parentheses and absolute infrared intensities (in km mol^{-1}) are given in square brackets. [d]Symbols and abbreviations denote stretch (ν), bend (δ), rock (ρ), twist (τ), wag (ω), symmetric (s), antisymmetric (as), in-plane (ip), and out-of-plane (op). Numbers in square brackets denote the fluorine atoms involved in the antisymmetric stretching mode. Atom labels are as in Figure 3.1a.

Table A.4. Vibrational Frequencies (cm^{-1}) for 4-$NC_5H_4N(CH_3)_2$ and WF_6{4-$NC_5H_4N(CH_3)_2$}

4-$NC_5H_4N(CH_3)_2$[a]		WF_6{4-$NC_5H_4N(CH_3)_2$}		Assignments[d]
exptl[b]	calcd[c]	exptl[b]	calcd[c]	
3089(11)	3211(13)[14]	3116(1)	3234(182)[6]	C−H stretching modes
3077 sh	3211(156)[3]	3106 sh	3232(4)[1]	
3034(14)	3141(144)[11]	3027(1)	3218(<0.1)[<0.1]	
2999(33)	3138(109)[38]		3218(51)[<1]	
2937 sh	3130(146)[31]		3146(167)[22]	
2910(21)	3118(<1)[2]	2947(1)	3133(1)[2]	
2870(16)	3049(73)[48]	2932(2)	3056(30)[45]	
2855(18)	3048(117)[13]	2873(1)	3055(0)[127]	
2842 sh	2989(324)[65]		3015(365)[36]	
2810(30)	2983(69)[74]	2828(1)	3009(54)[62]	
		1643 sh		C–C/C–N stretching modes and in-plane ring deformations
1614(8)	1637(36)[314]	1633(3)	1670(34)[401]	
1590(61)	1581(1)[45]	1621(3)	1573(2)[23]	
	1547(2)[121]		1570(2)[228]	
1524(5)	1528(8)[10]	1554(2)	1531(7)[21]	CH_3 bending modes
	1514(<1)[4]		1516(1)[4]	
1479(8)	1493(10)[16]	1479(1)	1497(12)[16]	
1465(11)	1488(5)[20]	1456(1)	1490(6)[27]	
1446(20)	1486(6)[2]	1445(3)	1490(<1)[3]	
	1462(<0.1)[<1]		1488(5)[0]	
1417(13)	1448(8)[<1]	1426(3)	1452(9)[<0.1]	

1376(8) 1349(8)	1392(7)[129]	1399(2)	1413(4)[161]	CH_3 bending modes
	1380(<1)[8]		1386(<0.1)[12]	
1277(31)	1316(14)[<1]	1308(2)	1333(8)[1]	in-plane ring deformations
1232(27)	1256(8)[30]	1236(3)	1262(7)[102]	
	1251(<1)[36]		1258(1)[24]	
1184(8)	1201(7)[4]	1192(1)	1206(3)[4]	$\omega_s(CH_3)$
	1144(2)[112]		1158(<0.1)[1]	in-plane ring deformation
	1139(<1)[<1]		1143(<0.1)[<0.1]	$\rho_s(CH_3)$
	1130(<0.1)[4]		1139(<1)[0]	$\rho_{as}(CH_3)$
1064(30)	1093(8)[<0.1]	1068(10)	1095(22)[43]	ν(C3N2)
	1078(<1)[22]		1078(<1)[24]	$\omega_{as}(CH_3)$
	1006(<1)[<0.1]			in-plane deformation and CH_3 rocking mode
985(100)	1006(24)[48]	1018(5)	1039(3)[75]	NC_5 ring breathing mode
	976(<1)[<0.1]		1004(<0.1)[0]	
			988(<1)[<1]	
949(31)	967(18)[16]	950(4)	966(23)[7]	
827(5)	841(1)[<0.1]		837(<1)[55]	ring deformations
810(2)	827(<1)[49]	810(1)	832(<1)[0]	
750(92)	762(18)[7]	769(22)	777(33)[3]	
	757(<1)[1]		755(<0.1)[<1]	
		697(100)	696(77)[83]	$\nu_s(WF_6)$
664(19)	682(3)[1]	680(3)	680(2)[13]	$\nu_{as}(WF_6)$ [1 − 2 + 3 − 4 + 5 – 6] + δ_{ip}(N1C1C2) + δ_{ip}(C3C4C5)
		641(1)	655(3)[203]	$\nu_{as}(WF_6)$ [1 − 2 + 3 − 4 + 5 – 6] − δ_{ip}(N1C1C2) − δ_{ip}(C3C4C5)
			640(<0.1)[200]	$\nu_{as}(WF_4)$ [3 + 4 – 5 – 6]

			639(2)[198]	$\nu_{as}(WF_6)$ [1 + 2 – 3 − 4 – 5 – 6]
		595(1)	588(2)[0]	$\nu_{as}(WF_4)$ [3 – 4 – 5 + 6]
	554(<1)[7]		569(1)[1]	δ(C1N1C5) + δ(C2C3C4) − δ(C6N2C7)
532(5)	544(2)[13]	533(1)	551(1)[4]	$\nu_{as}(WF_6)$ [1 – 2 – 3 + 4 − 5 + 6]
			547(<1)[15]	ring deformations
481(12)	480(3)[3]	498(1)	494(2)[4]	
			428(<0.1)[0]	
	490(<0.1)[<0.1]		427(1)[0]	δ(F1WF2) + δ(F3WF4) + δ(F5WF6) + δ(C6N2C7)
402(16)	389(6)[<1]	420(7)	405(8)[2]	δ(F1WF2) + δ(F3WF4) + δ(F5WF6) − δ(C6N2C7)
			378(<1)[<1]	δ(F1WF3) + δ(F2WF4) − δ(F1WF5) − δ(F2WF6)
			334(1)[20]	ρ(F1WF2) + ω(F3WF5) − ω(F4WF6)
		328(30)	329(1)[86]	δ(F1WF2) − δ(F3WF4) − δ(F5WF6)
			314(1)[16]	ω(F1WF2)
			306(<1)[0]	τ(F1WF2) + τ(F3WF4) + τ(F5WF6)
		300 sh	304(<1)[5]	$\rho(N(CH_3)_2)$
263(5)	268(1)[6]		297(1)[12]	δ(F3WF4) + δ(F5WF6)
	259(<1)[<0.1]		286(<0.1)[10]	ω(F1WF2) + δ(F3WF4) − δ(F5WF6)
		233(1)	222(1)[1]	rocking modes
			220(1)[3]	
153 sh	170(<0.1)[<1]		176(<0.1)[0]	$\tau(CH_3)$
121(18)	140(2)[<0.1]			
		164(3)	140(1)[4]	ν(WN)
			133(<1)[<1]	rocking and twisting modes
			130(<1)[2]	
	83(1)[<0.1]		84(1)[0]	

	76(<0.1)[0]	rocking and twisting modes
66(<1)[3]	74(1)[1]	
	70(<1)[<1]	
	42(2)[<1]	
	39(2)[0]	

[a]From Chaudhary, P.; Goettel, J. T.; Mercier, H. P. A.; Sowlati-Hashjin, S.; Hazendonk, P.; Gerken, M. *Chem. Eur. J.* **2015**, *21* (16), 6247–6256. [b]Recorded in a flame-sealed m.p. capillary at ambient temperature. Normalised Raman intensities are given in parentheses. [c]Calculated at the B3LYP/sVTZ level of theory. Absolute Raman intensities (in $Å^4\ u^{-1}$) are given in parentheses and absolute infrared intensities (in km mol^{-1}) are given in square brackets. [d]Symbols and abbreviations denote stretch (ν), bend (δ), rock (ρ), twist (τ), wag (ω), symmetric (s), antisymmetric (as), in-plane (ip), and out-of-plane (op). Numbers in square brackets denote the fluorine atoms involved in the antisymmetric stretching mode. Atom labels are as in Figure 3.1a.

Table A.5. Vibrational Frequencies (cm^{-1}) for 4,4′-bipy and $F_6W(4,4'\text{-bipy})WF_6$

4,4′-bipy		$F_6W(4,4'\text{-bipy})WF_6$			Assignment[e]
exptl[a]	calcd[b,d]	exptl[a]	calcd[c,d]		
			θ = 0.2°	θ = 89.9°	
3089(2)	3191(300)[0]		3233(240)[0]	3238(243)[0]	C−H stretching modes, combination bands, and overtones
3051(22)	3190(1)[21]		3233(28)[10]	3238(25)[14]	
3026(14)	3185(52)[<1]	3125(1)	3230(4)[1]	3234(4)[3]	
3005(6)	3185(4)[4]	3104(15)	3230(35)[<1]	3234(34)[<1]	
2983(1)	3152(239)[0]	3085(4)	3207(8)[<1]	3207(7)[1]	
2970(3)	3151(17)[21]	3069(4)	3207(73)[0]	3207(84)[0]	
2915(1)	3149(26)[47]		3203(58)[<1]	3203(54)[<1]	
2887(1)	3148(222)[5]		3202(20)[<0.1]	3202(22)[<0.1]	
2807(1)					
2789(1)					
2765(1)					
2442 sh					
2437(2)		2488(1)			
1754(1)					C–C/C–N stretching modes and in-plane ring deformations
1648(2)		1677(2)			
1620(40)	1636(309)[0]	1634(73)	1665(515)[0]	1665(49)[0]	
1606(47)	1631(3)[137]		1661(2)[201]	1661(2)[191]	
	1605(1)[3]		1609(2)[1]	1608(2)[1]	
1595(24)	1575(<1)[43]		1579(<1)[23]	1578(<1)[25]	
1567(1)					
1514 sh					
1510(7)	1538(34)[0]	1524(31)	1557(203)[0]	1557(208)[0]	

	1519(1)[9]		1536(<1)[14]	1535(<1)[19]	C–C/C–N stretching modes and in-plane ring deformations
1423(2)	1450(5)[5]	1438(1)	1469(7)[8]	1468(7)[9]	
	1438(1)[24]	1430(2)	1458(1)[54]	1456(1)[57]	
1343(2)	1368(3)[<0.1]	1340(2)	1378(1)[<0.1]	1377(1)[<0.1]	
	1349(2)[2]	1322(4)	1358(1)[3]	1357(1)[2]	
1298(83)	1311(230)[0]	1308(100)	1319(503)[0]	1319(525)[0]	
	1271(19)[<1]	1243(7)	1286(14)[2]	1287(15)[2]	
	1256(1)[<1]		1269(1)[6]	1271(1)[7]	
1218(21)	1248(29)[0]	1227(28)	1258(85)[0]	1258(76)[0]	
	1245(2)[8]		1257(1)[46]	1256(1)[52]	
	1116(<1)[1]		1149(<0.1)[<1]	1151(<0.1)[<0.1]	
1099(1)	1114(1)[<1]		1147(1)[<0.1]	1149(1)[<0.1]	
1087(4)	1099(5)[0]		1101(<0.1)[47]	1099(<0.1)[46]	
1082 sh					
	1095(<1)[8]	1069(5)	1100(14)[0]	1098(11)[0]	
1042(1)	1062(2)[4]	1050(1)	1070(1)[<1]	1069(1)[<1]	δ_{ip}(CCC)/δ_{ip}(CNC) (as)
1000(100)	1017(42)[0]	1037(32)	1050(49)[0]	1047(45)[0]	NC_5 ring breathing mode (s)
	1015(<0.1)[<1]		1040(2)[21]	1039(2)[21]	NC_5 ring breathing mode (as)
984(4)	1012(54)[0]	989(3)	1015(6)[0]	1017(<0.1)[1]	out-of-plane ring deformations
	1009(1)[9]		1015(<0.1)[1]	1017(6)[0]	
	996(<0.1)[0]		1005(<0.1)[0]	1007(<0.1)[<0.1]	
	993(<0.1)[<1]		1002(<0.1)[<0.1]	1004(<0.1)[0]	
884(1)	894(<1)[1]		887(3)[7]	889(3)[7]	
854(4)	892(10)[0]	870(10)	880(17)[0]	880(<0.1)[<1]	
	874(1)[5]	855(2)	880(<0.1)[<1]	880(17)[0]	
814(1)	825(<1)[64]		844(<1)[71]	846(<1)[73]	

808(1)					ring deformations
756(14)	768(14)[0]	785(36)	795(42)[0]	795(46)[0]	
	771(<0.1)[<1]		780(<1)[<0.1]	779(<1)[<0.1]	
	763(<1)[3]		757(<1)[12]	756(<0.1)[14]	
		708(99)	700(121)[0]	700(122)[0]	$\nu_s(WF_6)$ (s)
			700(<1)[120]	700(<1)[131]	$\nu_s(WF_6)$ (as)
674(1)	690(1)[1]		689(1)[25]	689(1)[13]	in-plane ring deformations
660(23)	677(9)[<1]	667(10)	678(5)[10]	677(8)[6]	
			661(1)[344]	662(<1)[398]	$\nu_{as}(WF_6)$ [1 − 2 + 3 − 4 + 5 – 6] − δ_{ip}(NC1C2) − δ_{ip}(C3C4C5) (s)
		663(20)	660(6)[43]	662(2)[47]	$\nu_{as}(WF_6)$ [1 − 2 + 3 − 4 + 5 – 6] − δ_{ip}(NC1C2) − δ_{ip}(C3C4C5) (as)
			660(<1)[310]	659(<1)[304]	ν(WF1) + ν(WF2) + δ(C1NC5) + δ(C2C3C4) (s)
		654(8)	647(4)[0]	647(4)[0]	$\nu_{as}(WF_6)$ [1 + 2 – 3 − 4 – 5 – 6] (s)
		634(1)	645(<1)[328]	643(<0.1)[193]	$\nu_{as}(WF_4)$ [3 + 4 – 5 – 6] (s)
			645(<0.1)[42]	643(<0.1)[291]	$\nu_{as}(WF_4)$ [3 + 4 – 5 – 6] (as)
608(1)	621(<1)[32]		643(<1)[195]	642(1)[30]	ν(WF1) + ν(WF2) + δ(C1NC5) + δ(C2C3C4) (as)
572(5)	588(2)[5]	602(2)	590(2)[3]	589(2)[3]	out-of-plane ring deformation
		593(3)	589(2)[<0.1]	587(2)[<0.1]	$\nu_{as}(WF_4)$ [3 – 4 – 5 + 6] (as)
		578(4)	589(2)[0]	587(1)[0]	$\nu_{as}(WF_4)$ [3 – 4 – 5 + 6] (s)
			562(1)[6]	562(<1)[9]	$\nu_{as}(WF_6)$ [1 – 2 – 3 + 4 – 5 + 6] (s)
		554(3)	562(3)[1]	562(3)[1]	$\nu_{as}(WF_6)$ [1 – 2 – 3 + 4 – 5 + 6] (as)
500(1)	517(<0.1)[23]		537(<1)[23]	535(<1)[20]	out-of-plane ring deformation
			425(2)[0]	430(3)[0]	δ(F1WF2) + δ(F3WF4) + δ(F5WF6) (s)
		448(3)			out-of-plane ring deformations
			425(<1)[2]	426(1)[3]	
			422(1)[1]	423(<1)[2]	δ(F1WF2) + δ(F3WF4) + δ(F5WF6) (as)
386(5)	395(4)[0]	411(10)	406(12)[0]	410(12)[0]	out-of-plane ring deformations
	389(<0.1)[<1]		402(<1)[<1]	406(<1)[<1]	

	379(<1)[4]	389(2)	383(<1)[<0.1]	369(<1)[0]	δ(F1WF3) + δ(F2WF4) − δ(F1WF5) − δ(F2WF6) (s)
		376(7)	368(<1)[0]	369(<1)[<1]	δ(C1NC5) + δ(C2C3C4)
			356(<1))[5]	366(5)[<1]	δ(F1WF3) + δ(F2WF4) − δ(F1WF5) − δ(F2WF6) (as)
		345(11)	331(3)[0]	357(<1)[2]	δ(F1WF2) − δ(F3WF4) − δ(F5WF6) (s)
			330(<0.1)[163]	337(<0.1)[158]	δ(F1WF2) − δ(F3WF4) − δ(F5WF6) (as)
		336(3)	330(<1)[27]	336(6)[0]	ρ(F1WF2) + ω(F3WF5) − ω(F4WF6) + ω(C2C3C4) (s)
		322(3)	327(1)[4]	333(<1)[43]	ρ(F1WF2) + ω(F3WF5) − ω(F4WF6) + ω(C2C3C4) (as)
		302(3)	324(4)[12]	324(2)[2]	ρ(F1WF2) + ω(F3WF5) − ω(F4WF6) – ω(C2C3C4) (as)
324(10)	309(4)[0]				δ(C1NC5) + δ(C2C3C4)
315(14)					
			303(1)[30]	304(1)[0]	δ(F3WF4) + δ(F5WF6) (as)
			301(<1)[0]	304(1)[<0.1]	τ(F1WF2) + τ(F3WF4) + τ(F5WF6) (s)
			301(1)[<1]	301(<0.1)[39]	τ(F1WF2) + τ(F3WF4) + τ(F5WF6) (as)
		289(2)	295(3)[0]	298(1)[7]	δ(F3WF4) + δ(F5WF6) (s)
			293(<1)[38]	296(1)[28]	ω(F1WF2) + δ(F3WF4) − δ(F5WF6) (s)
			292(<1)[10]	290(2)[0]	ω(F1WF2) + δ(F3WF4) − δ(F5WF6) (as)
			279(1)[2]	276(<1)[3]	ρ(F1WF2) + ω(F3WF5) − ω(F4WF6) – ω(C2C3C4) (s)
262(3)	264(<1)[<0.1]	279(2)	260(1)[<0.1]	263(<0.1)[5]	ring deformations
		219(3)	232(1)[1]	225(<0.1)[2]	
251(2)					
145(10)	129(2)[2]		199(<1)[4]	205(<1)[1]	
			167(<0.1)[2]	163(<0.1)[19]	
			157(<0.1)[17]	144(1)[<0.1]	ν(WN) (as)
		150(40)	148(<1)[1]	139(<1)[4]	rocking and twisting modes
	95(1)[2]	140(33)	103(<1)[<1]	110(<1)[<1]	
			90(<1)[4]	107(<0.1)[1]	
	63(7)[0]		81(3)[0]	87(<1)[1]	

	80(<1)[0]	86(7)[0]	rocking and twisting modes
	73(5)[0]	83(<1)[0]	
	70(<0.1)[<0.1]	81(2)[0]	
	63(2)[0]	65(2)[0]	ν(WN) (s)
	56(<1)[<1]	60(4)[0]	rocking and twisting modes
	45(3)[0]	59(1)[1]	
	30(<0.1)[3]	31(<0.1)[3]	
	17(<0.1)[3]	20(<1)[0]	
	17(<1)[0]	17(<0.1)[3]	

[a]Recorded in a flame-sealed m.p. capillary at ambient temperature. Normalised Raman intensities are given in parentheses. [b]Calculated at the B3LYP/sVTZ level of theory. [c]Calculated at the B3LYP/VTZ level of theory. [d]Absolute Raman intensities (in $Å^4\ u^{-1}$) are given in parentheses and absolute infrared intensities (in km mol^{-1}) are given in square brackets. [e]Symbols and abbreviations denote stretch (ν), bend (δ), rock (ρ), twist (τ), wag (ω), symmetric (s), antisymmetric (as), in-plane (ip), and out-of-plane (op). Symmetric and antisymmetric combinations of the two $WF_6(4\text{-}NC_5H_4)$ moieties are denoted as s or as, respectively, in parentheses. Numbers in square brackets denote the fluorine atoms involved in the antisymmetric stretching mode. Atom labels are as in Figure 3.1a.

Table A.6. Vibrational Frequencies (cm^{-1}) for 2-NC_5H_4F and WF_6(2-NC_5H_4F)

2-NC_5H_4F		WF_6(2-NC_5H_4F)		Assignment[c]
exptl[a]	calcd[b]	exptl[a]	calcd[b]	
3208				C−H stretching modes
3191	3211(175)[<1]	3144	3238(77)[4]	
3152	3201(108)[10]	3133	3220(153)[1]	
3092 sh	3181(71)[6]	3112	3212(103)[1]	
3071	3163(90)[10]	3099	3191(81)[3]	
2936				
3026				
1617	1634(10)[61]		1657(6)[95]	C–C/C–N stretching modes and in-plane ring deformations
1580	1622(9)[74]	1625	1618(12)[38]	
1573 sh				
	1507(1)[75]	1574	1522(2)[89]	
1470	1468(<1)[78]	1490	1480(3)[59]	
	1327(4)[3]	1310	1334(3)[19]	
1303	1307(3)[2]	**1295**	1320(25)[56]	ν(CF)
1247	1276(15)[137]	1244	1290(<1)[9]	C–C/C–N stretching modes and ring deformations
1143	1166(2)[6]	1166	1179(3)[5]	
1097	1119(5)[2]	1117	1134(6)[6]	
1044	1063(17)[6]	**1068**	1080(14)[12]	
	1019(<0.1)[<0.1]		1028(<0.1)[<1]	
994	1012(20)[6]	**1029**	1038(13)[12]	NC_5 ring-breathing mode
	991(<1)[<1]		1000(<1)[1]	ring deformation

840	895(<1)[1]	885	896(<1)[3]	ring deformations
827	852(15)[30]	**843**	860(17)[25]	
786	803(<1)[59]		798(<1)[69]	
736	756(<0.1)[8]		765(<1)[1]	
		712	709(48)[44]	$\nu_s(WF_6)$
		662	669(1)[198]	$\nu_{as}(WF_6)$ [1 − 2 + 3 − 4 + 5 – 6] − δ_{ip}(C1NC5) – δ_{ip}(C2C3C4)
			659(<1)[183]	$\nu_{as}(WF_4)$ [3 + 4 – 5 – 6]
622	636(3)[3]	646	655(2)[129]	$\nu_{as}(WF_6)$ [1 − 2 + 3 − 4 + 5 – 6] + δ_{ip}(C1NC5) + δ_{ip}(C2C3C4)
		633	649(1)[72]	$\nu_{as}(WF_6)$ [1 + 2 – 3 − 4 – 5 – 6] − δ_{ip}(C1NC5) − δ_{ip}(C2C3C4)
		604	593(2)[10]	$\nu_{as}(WF_4)$ [3 – 4 – 5 + 6]
556	561(5)[6]	**565**	568(6)[7]	δ(NC1C2) + δ(C3C4C5)
			565(2)[2]	$\nu_{as}(WF_6)$ [1 – 2 – 3 + 4 – 5 + 6]
518	532(<1)[4]	520	534(<1)[3]	out-of-plane ring deformation
434	435(<1)[<1]	475	467(<1)[<0.1]	δ(NCF)
430	430(<0.1)[4]	468 sh	469(<1)[4]	out-of-plane ring deformation
		434	424(1)[<1]	δ(F1WF2) + δ(F3WF4) + δ(F5WF6)
		372	357(1)[1]	ω(F1WF2) – δ(F3WF4) + δ(F5WF6)
		339	333(<1)[48]	δ(F1WF2) − δ(F3WF4) − δ(F5WF6)
		330	320(<1)[26]	ρ(F1WF2) + ω(F3WF5) − ω(F4WF6)
		320	309(1)[21]	δ(F3WF4) + δ(F5WF6)
		307	303(<1)[22]	ω(F1WF2) + δ(F3WF4) − δ(F5WF6)
		272	294(1)[1]	τ(F1WF2) + τ(F3WF4) + τ(F5WF6)
230	221(2)[<0.1]	233	262(1)[<0.1]	out-of-plane ring deformation
		207	221(1)[4]	rocking modes
		197	184(1)[<1]	

	169(<0.1)[<1]	rocking mode
171	126(1)[6]	ν(WN)
128	97(1)[<0.1]	rocking and twisting modes
112	71(<0.1)[1]	
88	67(3)[<1]	
74	49(1)[<1]	

[a]From Arnaudet, L.; Bougon, R.; Ban, B.; Lance, M.; Nierlich, M.; Vigner, J. *Inorg. Chem.* **1993**, *32* (7), 1142–1146. Intense bands are given in bold. [b]Calculated at the B3LYP/sVTZ level of theory. Absolute Raman intensities (in $Å^4\ u^{-1}$) are given in parentheses and absolute infrared intensities (in km mol^{-1}) are given in square brackets. [c]Symbols and abbreviations denote stretch (ν), bend (δ), rock (ρ), twist (τ), wag (ω), symmetric (s), antisymmetric (as), in-plane (ip), and out-of-plane (op). Numbers in square brackets denote the fluorine atoms involved in the antisymmetric stretching mode. Atom labels are as in Figure 3.1a.

Table A.7. Optimised Gas-Phase Atomic Coordinates (Å) of $WF_6(NC_5H_5)$

W	0.00000000	0.00000000	0.87581200
F	1.33805700	1.21349000	0.36527400
F	0.00000000	-1.15380600	2.34529200
F	1.33805700	-1.21349000	0.36527400
F	-1.33805700	-1.21349000	0.36527400
F	0.00000000	1.15380600	2.34529200
F	-1.33805700	1.21349000	0.36527400
N	0.00000000	0.00000000	-1.46755500
C	0.00000000	-1.15508700	-2.14266000
H	0.00000000	-2.05762000	-1.55237200
C	0.00000000	-1.19441500	-3.52629000
H	0.00000000	-2.14902900	-4.03091700
C	0.00000000	1.15508700	-2.14266000
H	0.00000000	2.05762000	-1.55237200
C	0.00000000	1.19441500	-3.52629000
H	0.00000000	2.14902900	-4.03091700
C	0.00000000	0.00000000	-4.23245200
H	0.00000000	0.00000000	-5.31367400

Table A.8. Optimised Gas-Phase Atomic Coordinates (Å) of $WF_6(4\text{-}NC_5H_4CH_3)$

W	0.00098100	1.14271500	0.00000000
F	1.20807200	0.63797600	1.34780200
F	-1.14918400	2.61493100	0.00000000
F	-1.20882100	0.64447300	1.34771800
F	-1.20882100	0.64447300	-1.34771800
F	1.15910600	2.60868500	0.00000000
F	1.20807200	0.63797600	-1.34780200
N	-0.00437300	-1.19606600	0.00000000
C	-0.00692500	-1.87856200	-1.15142200
H	-0.00849000	-1.29225100	-2.05606900
C	-0.01037400	-3.25977800	-1.18724800
H	-0.01661700	-3.75897400	-2.14597000
C	-0.00692500	-1.87856200	1.15142200
H	-0.00849000	-1.29225100	2.05606900
C	-0.01037400	-3.25977800	1.18724800
H	-0.01661700	-3.75897400	2.14597000
C	-0.00950600	-3.99015500	0.00000000
C	0.01554000	-5.49009900	0.00000000
H	-0.47195600	-5.89607400	0.88498500
H	-0.47195600	-5.89607400	-0.88498500
H	1.04769500	-5.84885100	0.00000000

Table A.9. Optimised Gas-Phase Atomic Coordinates (Å) of $WF_6\{4\text{-}NC_5H_4N(CH_3)_2\}$

W	0.00000000	0.00000000	1.63541400
F	1.34519400	1.21697100	1.14243900
F	0.00000000	-1.15401300	3.11047200
F	1.34519400	-1.21697100	1.14243900
F	-1.34519400	-1.21697100	1.14243900
F	0.00000000	1.15401300	3.11047200
F	-1.34519400	1.21697100	1.14243900
N	0.00000000	0.00000000	-0.66602400
C	0.00000000	-1.14805800	-1.36046900
H	0.00000000	-2.05824500	-0.78177900
C	0.00000000	-1.19693400	-2.73307100
H	0.00000000	-2.16336700	-3.20903900
C	0.00000000	1.14805800	-1.36046900
H	0.00000000	2.05824500	-0.78177900
C	0.00000000	1.19693400	-2.73307100
H	0.00000000	2.16336700	-3.20903900
C	0.00000000	0.00000000	-3.48415200
N	0.00000000	0.00000000	-4.84131900
C	0.00000000	-1.25725500	-5.57540400
H	0.00000000	-1.04650100	-6.63997700
H	0.88620800	-1.85452200	-5.34792500
H	-0.88620800	-1.85452200	-5.34792500
C	0.00000000	1.25725500	-5.57540400
H	-0.88620800	1.85452200	-5.34792500
H	0.88620800	1.85452200	-5.34792500
H	0.00000000	1.04650100	-6.63997700

Table A.10. Optimised Gas-Phase Atomic Coordinates (Å) of $F_6W(4,4'\text{-bipy})WF_6$

W	0.00000000	0.00000000	-5.87531100
F	-0.85724500	1.58825200	-5.35523100
F	-0.38260300	-1.09034500	-7.34171600
F	-1.66323600	-0.70053400	-5.35596300
F	0.85724500	-1.58825200	-5.35523100
F	0.38260300	1.09034500	-7.34171600
F	1.66323600	0.70053400	-5.35596300
N	0.00000000	0.00000000	-3.52403500
C	-0.37839500	-1.08861000	-2.84657500
H	-0.68227500	-1.94177500	-3.43219800
C	-0.38806100	-1.12698800	-1.46495200
H	-0.72230100	-2.02552800	-0.96801400
C	0.37839500	1.08861000	-2.84657500
H	0.68227500	1.94177500	-3.43219800
C	0.38806100	1.12698800	-1.46495200
H	0.72230100	2.02552800	-0.96801400
C	0.00000000	0.00000000	-0.73949600
C	0.00000000	0.00000000	0.73949600
C	-0.38806100	1.12698800	1.46495200
C	0.38806100	-1.12698800	1.46495200
C	-0.37839500	1.08861000	2.84657500
H	-0.72230100	2.02552800	0.96801400
C	0.37839500	-1.08861000	2.84657500
H	0.72230100	-2.02552800	0.96801400
H	-0.68227500	1.94177500	3.43219800
H	0.68227500	-1.94177500	3.43219800
W	0.00000000	0.00000000	5.87531100
F	-0.85724500	-1.58825200	5.35523100
F	-0.38260300	1.09034500	7.34171600
F	-1.66323600	0.70053400	5.35596300
F	0.85724500	1.58825200	5.35523100
F	0.38260300	-1.09034500	7.34171600
F	1.66323600	-0.70053400	5.35596300
N	0.00000000	0.00000000	3.52403500

Table A.11. Optimised Gas-Phase Atomic Coordinates (Å) of $WF_6(2\text{-}NC_5H_4F)$

W	-0.97277400	-0.06875400	0.00000000
F	-0.45553000	1.07733700	1.37746900
F	-2.47246900	-1.17323500	0.00000000
F	-0.45553000	-1.32962100	1.29480600
F	-0.45553000	-1.32962100	-1.29480600
F	-2.40663800	1.12693900	0.00000000
F	-0.45553000	1.07733700	-1.37746900
N	1.44498200	-0.08921800	0.00000000
C	2.06426200	-1.28527900	0.00000000
H	1.41782700	-2.14742200	0.00000000
C	3.43723400	-1.41050200	0.00000000
H	3.88300500	-2.39333000	0.00000000
C	2.20616000	0.99534400	0.00000000
C	3.59262400	0.97536400	0.00000000
H	4.13320900	1.90913900	0.00000000
C	4.21655000	-0.25726600	0.00000000
H	5.29576200	-0.31960800	0.00000000
F	1.59452000	2.16837100	0.00000000

Table A.12. Optimised Gas-Phase Atomic Coordinates (Å) of WF_6 (B3LYP/sVTZ)

W	0.00000000	0.00000000	0.00000000
F	0.00000000	0.00000000	1.84497500
F	0.00000000	1.84497500	0.00000000
F	0.00000000	0.00000000	-1.84497500
F	0.00000000	-1.84497500	0.00000000
F	1.84497500	0.00000000	0.00000000
F	-1.84497500	0.00000000	0.00000000

Table A.13. Optimised Gas-Phase Atomic Coordinates (Å) of 4,4′-bipy

C	-0.36183900	1.07728500	2.85808300
C	-0.37640900	1.12841400	1.47084100
C	0.00000000	0.00000000	0.73991100
C	0.37640900	-1.12841400	1.47084100
C	0.36183900	-1.07728500	2.85808300
H	-0.66009900	1.94446600	3.43602900
H	-0.70072200	2.03019600	0.97065900
H	0.70072200	-2.03019600	0.97065900
N	0.00000000	0.00000000	3.55547000
H	0.66009900	-1.94446600	3.43602900
C	0.00000000	0.00000000	-0.73991100
C	-0.37640900	-1.12841400	-1.47084100
C	0.37640900	1.12841400	-1.47084100
C	-0.36183900	-1.07728500	-2.85808300
H	-0.70072200	-2.03019600	-0.97065900
C	0.36183900	1.07728500	-2.85808300
H	0.70072200	2.03019600	-0.97065900
H	-0.66009900	-1.94446600	-3.43602900
H	0.66009900	1.94446600	-3.43602900
N	0.00000000	0.00000000	-3.55547000

Table A.14. Optimised Gas-Phase Atomic Coordinates (Å) of 2-NC_5H_4F

C	-1.22867700	-0.99978700	0.00000000
C	-0.09392200	-1.79504200	0.00000000
C	1.15087600	-1.17021700	0.00000000
C	1.21316900	0.21306900	0.00000000
C	0.00000000	0.89060800	0.00000000
H	-2.21759400	-1.44113100	0.00000000
H	-0.18110900	-2.87172500	0.00000000
H	2.06102600	-1.75425500	0.00000000
H	2.14617500	0.75600900	0.00000000
N	-1.18373100	0.33823100	0.00000000
F	0.02543800	2.23463300	0.00000000

Appendix B – Supporting Information for Chapter 4

Table B.1. Crystallographic Data Collection and Refinement Parameters for $[C_5H_5NH][W(NC_6F_5)F_5]$, $[N(CH_3)_4][W(NC_6F_5)F_5]$, and $[C_5H_5NH][W_2(NC_6F_5)_2F_9]$

	$[C_5H_5NH][W(NC_6F_5)F_5]$	**$[N(CH_3)_4][W(NC_6F_5)F_5]$**	**$[C_5H_5NH][W_2(NC_6F_5)_2F_9]$**
Identification code	MG16042	MG16014	MG17016
Empirical formula	$C_{11}H_6F_{10}N_2W$	$C_{10}H_{12}N_2F_{10}W$	$C_{17}H_6F_{19}N_3W_2$
Formula weight	540.03	534.07	980.95
T (K)	100.00(10)	100.00(10)	99.9(4)
Crystal system	monoclinic	orthorhombic	monoclinic
Space group	$P2_1/c$	Pnma	P2/n
a (Å)	12.9653(6)	13.1806(6)	6.0442(4)
b (Å)	5.62602(19)	7.6609(3)	8.4463(5)
c (Å)	19.8495(7)	14.9517(8)	22.7740(15)
α (°)	90	90	90
β (°)	104.979(4)	90	91.297(6)
γ (°)	90	90	90
V (Å^3)	1398.68(10)	1509.75(12)	1162.34(13)
Z	4	4	2
ρ_{calc} (g cm^{-3})	2.565	2.35	2.803
μ (mm^{-1})	8.375	7.757	10.055
F(000)	1000	1000	896
Crystal size (mm^3)	0.108 × 0.078 × 0.021	0.134 × 0.076 × 0.042	0.047 × 0.032 × 0.007
GooF	1.055	1.028	1.059
Final *R* indexes [I ≥ 2σ (I)]	R_1 = 0.0168, wR_2 = 0.0347	R_1 = 0.0215, wR_2 = 0.0394	R_1 = 0.0415, wR_2 = 0.0878
Final *R* indexes [all data]	R_1 = 0.0212, wR_2 = 0.0357	R_1 = 0.0291, wR_2 = 0.0411	R_1 = 0.0591, wR_2 = 0.0950
Largest diff. peak/hole (e Å^{-3})	0.85/-0.64	0.77/-0.90	2.28/-2.82

[a] $R_1 = \sum||F_o| - |F_c||/\sum|F_o|$. [b] $wR_2 = [\sum[w(F_o^2 - F_c^2)^2]/\sum w(F_o^4)]^{1/2}$.

Table B.2. Vibrational Frequencies (cm^{-1}) of $[W(NC_6F_5)F_5]^-$

exptl[a]		calcd[d]	Assignment (C_{2v})[e]
$[C_5H_5NH]^+$[b]	$[N(CH_3)_4]^+$[c]		
2545(1)	2545(1)		overtones and combination bands
1712(1)	1706(1)		
1692(1)	1692(1)		
1645(31)	1646(29)	1653(425)[4]	C−C and C−N stretching modes ($2A_1+B_2$)
1534(6)	1529(10)	1623(3)[17]	
1520(30)	1518(23)	1521(1055)[976]	
1482(100)	1481(100)	1505(345)[10]	A_1, $\nu_s(C_6)$
1460(3)	1454(7)	1508(6)[299]	C−C stretching modes (B_2)
1433(1)	1431(2)		
1390(1)	1389(1)		
1362(17)	1353(14)	1358(37)[91]	A_1, $\nu(WN) - \nu(NC) + \nu(C_oF_o) + \nu(C_pF_p)$
1310(1)	1306(1)		C−C stretching modes (B_2)
1285(1)	1281(1)	1287(23)[17]	
1256(12)	1255(12)	1240(38)[117]	A_1, $\nu(WN) - \nu(NC) + \nu(C_mF_m) - (C_pF_p)$
		1138(<0.1)[<1]	B_2, C−F stretching mode
1069(7)	1066(8)	1063(45)[290]	A_1, $\nu(WN) - \nu(C_oF_o) + \nu(C_pF_p)$
		1001(<1)[268]	B_2, C−F stretching mode
810(2)	808(2)	801(13)[<1]	A_1, $\nu(WN) + \nu(NC) - \nu(C_mF_m)$
		799(<0.1)[<1]	ring deformations ($A_2+2B_1+B_2$)
729(1)	728(1)	765(1)[1]	
		676(<0.1)[2]	
		658(<0.1)[0]	
661(6)	650(5)	647(19)[287]	A_1, $\nu_s(WF_5)$

		607(<1)[269]	B_1, $\nu_{as}(WF_4)$ [2 + 3 − 4 – 5]
		606(<1)[247]	B_2, $\nu_{as}(WF_4)$ [2 – 3 − 4 + 5]
585(4)	581(4)	579(19)[10]	A_1, $\nu(WN) + \delta(C_oC_iC_o) + \delta_s(C_oC_mC_p)$
		575(3)[0]	A_2, $\nu_{as}(WF_4)$ [2 – 3 + 4 – 5]
		548(<1)[165]	A_1, $\nu(WF_{ax})$
		502(<1)[3]	B_2, in-plane ring deformation
501(4)	496(6)	497(35)[8]	A_1, $\nu(WN) - \delta(C_oC_iC_o) - \delta(C_mC_pC_m)$
476(3)	479(3)	456(4)[6]	ring deformations ($A_2 + B_1 + B_2$)
434(4)	434(4)	437(5)[<1]	
387(4)	382(4)	372(3)[0]	
356(2)	355(2)	353(7)[9]	A_1, $\nu(WN) + \delta_s(C_iC_oF_o)$
349 sh			ring deformations ($B_1 + B_2$)
		327(<1)[<1]	
		306(<1)[1]	
302 sh			
298(3)	299(3)	294(6)[41]	A_1, $\delta_s(WF_{eq})$
287 sh			
		282(2)[11]	B_2, $\delta(F_{ax}WN) + \delta_{ip}(F2WF5) - \delta_{ip}(F3WF4)$
		280(2)[<0.1]	A_1, $\delta_{ip}(F2WF3) + \delta_{ip}(F4WF5) - \delta_s(C_iC_oF_o) - \delta_s(C_pC_mF_m)$
279(2)	284(4)	279(2)[17]	B_1, $\delta(F_{ax}WN) + \delta_{ip}(F2WF3) - \delta_{ip}(F4WF5)$
		278(<1)[4]	A_1, $\delta_{ip}(F2WF3) + \delta_{ip}(F4WF5) + \delta_s(C_iC_oF_o) + \delta_s(C_pC_mF_m)$
		276(<0.1)[<1]	ring deformations ($B_1 + B_2$)
215(3)	216(2)	208(1)[<0.1]	
		201(<0.1)[0]	A_2, $\delta_{op}(F2WF4) - \delta_{op}(F3WF5)$
		187(<1)[10]	B_2, $\delta(WNC) + \delta_{ip}(F2WF5) - \delta_{ip}(F3WF4)$
		179(<0.1)[4]	B_1, $\delta(WNC) + \delta_{ip}(F2WF3) - \delta_{ip}(F4WF5)$
175(6)	175(6)	170(6)[<1]	A_1, $\nu(WN) + \nu(NC) + \delta_s(WF_{eq}) + \delta(C_oC_iC_o)$

		159(<0.1)[4]	B_1, δ_{ip}(F2WF3) + δ_{ip}(F4WF5)
		135(0)[0]	A_2, out-of-plane ring deformation
133(3)	128(2)	115(1)[<0.1]	B_2, $\delta(F_{ax}WN) - \delta_{ip}$(F2WF5) + δ_{ip}(F3WF4)
		93(<0.1)[<0.1]	B_1, $\delta(F_{ax}WN) - \delta_{ip}$(F2WF3) + δ_{ip}(F4WF5)
		32(<1)[1]	B_1, δ(WNC)
		29(<1)[<1]	B_2, δ(WNC)
		3(<1)[0]	A_2, $\rho(WF_{eq}) - \rho(C_6F_5)$

[a]Recorded in a flame-sealed m.p. capillary at ambient temperature. Normalised Raman intensities are given in parentheses. [b]Cation bands are observed at 3115(4), 3100(4), 3060(2), 1591(1), 1205(5), 1026(6), 1011(13), 639(4), 610(3), 504(4), and 96(11) cm^{-1}. [c]Cation bands are observed at 3044(3), 3033(2), 2999(2), 2970(2), 2934(3), 2831(2), 1176(1), 950(4), 754(5), and 458(2) cm^{-1}. [d]Calculated at the B3LYP/sVTZ level of theory. Absolute Raman intensities (in $Å^4\ u^{-1}$) are given in parentheses and absolute infrared intensities (in km mol^{-1}) are given in square brackets. Symbols and abbreviations denote stretch (ν), bend (δ), rotation (ρ), symmetric (s), antisymmetric (as), in-plane (ip), and out-of-plane (op). Numbers in square brackets denote the fluorine atoms involved in the antisymmetric stretching mode. Atom labels are as in Figure 4.1a.

Table B.3. Vibrational Frequencies (cm^{-1}) of $[W_2(NC_6F_5)_2F_9]^-$

exptl[a]	calcd[b]	Assignment (D_2)[c]
2542(1)		overtones and combination bands
1720(1)		
1691(1)		
1646(25)	1660(1290)[0]	C−C and C−N stretching modes ($2A + 2B_1 + B_2 + B_3$)
1539(12)	1660(3)[<1]	
	1635(2)[5]	
	1635(<1)[17]	
1522(35)	1537(3488)[0]	
	1532(<0.1)[1606]	
	1521(3)[484]	C−C stretching modes ($B_2 + B_3$)
	1520(8)[155]	
1484(100)	1514(1539)[0]	A, $\nu_s(C_6)$ (s)
1455sh		
	1514(<0.1)[28]	B_1, $\nu_s(C_6)$ (as)
1364(18)	1379(167)[0]	A, ν(WN) − ν(NC) + $\nu(C_oF_o)$ + $\nu(C_pF_p)$ (s)
	1376(<0.1)[230]	B_1, ν(WN) − ν(NC) + $\nu(C_oF_o)$ + $\nu(C_pF_p)$ (as)
	1297(46)[2]	C−C stretching modes ($B_2 + B_3$)
	1297(15)[5]	
1259(9)	1266(126)[0]	A, ν(WN) − ν(NC) + $\nu(C_mF_m)$ − (C_pF_p) (s)
	1263(<0.1)[266]	B_1, ν(WN) − ν(NC) + $\nu(C_mF_m)$ − (C_pF_p) (as)
	1157(<0.1)[1]	C−F stretching modes ($B_2 + B_3$)
	1157(<1)[<1]	
1074(6)	1083(104)[0]	A, ν(WN) − $\nu(C_oF_o)$ + $\nu(C_pF_p)$ (s)
	1082(<1)[547]	B_1, ν(WN) − $\nu(C_oF_o)$ + $\nu(C_pF_p)$ (as)
	1010(<1)[370]	C−F stretching modes ($B_2 + B_3$)
	1010(<1)[119]	
821(2)	824(31)[0]	A, ν(WN) + ν(NC) − $\nu(C_mF_m)$ (s)
811sh	823(<1)[6]	B_1, ν(WN) + ν(NC) − $\nu(C_mF_m)$ (as)
	799(<0.1)[<1]	ring deformations ($2B_2 + 2B_3$)
	799(<1)[<1]	
727(2)	736(2)[<1]	
	736(<1)[2]	
	668(<0.1)[551]	B_1, $\nu_s(WF_5)$ (as)
667(7)	665(45)[0]	A, $\nu_s(WF_5)$ (s)
	663(<0.1)]10]	ring deformations ($A + B_1 + B_2 + B_3$)
	663(<1)[3]	
	652(0)[0]	
	652(<0.1)[0]	

	646(0)[420]	B_3, $\nu_{as}(WF_4)$ [2 + 3 − 4 – 5] (s)
	645(0)[397]	B_2, $\nu_{as}(WF_4)$ [2 + 3 − 4 – 5] (as)
	629(<1)[<0.1]	B_2, $\nu_{as}(WF_4)$ [2 – 3 − 4 + 5] (as)
	629(<1)[<1]	B_3, $\nu_{as}(WF_4)$ [2 – 3 − 4 + 5] (s)
	598(3)[0]	A, $\nu_{as}(WF_4)$ [2 – 3 + 4 – 5] (s)
	597(2)[<1]	B_1, $\nu_{as}(WF_4)$ [2 – 3 + 4 – 5] (as)
584(5)	582(34)[0]	A, ν(WN) + $\delta(C_oC_iC_o)$ + $\delta_s(C_oC_mC_p)$ (s)
	582(1)[13]	B_1, ν(WN) + $\delta(C_oC_iC_o)$ + $\delta_s(C_oC_mC_p)$ (as)
	502(4)[1]	B_1, ν(WN) − $\delta(C_oC_iC_o)$ − $\delta(C_mC_pC_m)$ (as)
501(6)	502(67)[0]	A, ν(WN) − $\delta(C_oC_iC_o)$ − $\delta(C_mC_pC_m)$ (s)
	495(<1)[4]	in-plane ring deformations (B_2 + B_3)
	495(<1)[1]	
	464(<0.1)[576]	B_1, $\nu_{as}(F_{ax}W_2)$
	458(2)[8]	ring deformations (2A + 2B_1 + 4B_2 + 4B_3)
470(3)	458(6)[3]	
	437(3)[1]	
434(6)	437(9)[<1]	
383(3)	379(4)[0]	
	379(1)[0]	
357(3)	357(15)[0]	
	353(<0.1)[37]	
	337(1)[3]	
343(1)	337(2)[1]	
	306(<0.1)[1]	
	306(<1)[<1]	
299(6)	296(17)[0]	A, $\delta_s(WF_{eq})$ (s)
	292(<0.1)[13]	B_3, $\delta(F_{ax}WN)$ + δ_{ip}(F2WF5) − δ_{ip}(F3WF4)
	292(2)[1]	B_1, δ_{ip}(F2WF3) + δ_{ip}(F4WF5) (as)
	292(2)[0]	A, δ_{ip}(F2WF3) + δ_{ip}(F4WF5) (s)
	291(<0.1)[10]	B_2, $\delta(F_{ax}WN)$ + δ_{ip}(F2WF5) − δ_{ip}(F3WF4)
	281(<0.1)[29]	ring deformations (A + B_1 + B_2 + B_3)
	277(<1)[0]	
	276(<0.1)[0]	
	276(<0.1)[0]	
	256(0)[318]	B_1, $\delta_s(WF_{eq})$ (as)
223(1)	213(4)[<1]	out-of-plane ring deformations (B_2 + B_3)
	212(1)[1]	
	208(<1)[<0.1]	B_2, δ(WNC) + δ_{ip}(F2WF5) − δ_{ip}(F3WF4) (s)
	208(<1)[<0.1]	B_3, δ(WNC) + δ_{ip}(F2WF5) − δ_{ip}(F3WF4) (as)
	192(<1)[17]	B_2, δ(WNC) + δ_{ip}(F2WF3) − δ_{ip}(F4WF5) (s)

	190(1)[13]	B_3, δ(WNC) + δ_{ip}(F2WF3) − δ_{ip}(F4WF5) (as)
	187(<1)[0]	A, δ_{op}(F2WF4) − δ_{op}(F3WF5) (as)
	186(<0.1)[0]	B_1, δ_{op}(F2WF4) − δ_{op}(F3WF5) (s)
183(5)	181(11)[0]	A, ν(WN) + ν(NC) + δ_s(WF_{eq}) + δ($C_oC_iC_o$) (s)
	179(<1)[2]	B_3, δ(F_{ax}WN) + δ_{ip}(F2WF4) (s)
171sh	177(<1)[<1]	B_2, δ(F_{ax}WN) + δ_{ip}(F2WF4) (as)
	171(<0.1)[2]	B_1, ν(WN) + ν(NC) + δ_s(WF_{eq}) + δ($C_oC_iC_o$) (as)
	164(<1)[4]	B_3, δ(F_{ax}WN) − δ_{ip}(F2WF4) (s)
	154(<1)[1]	B_2, δ(F_{ax}WN) − δ_{ip}(F2WF4) (as)
	134(<0.1)[0]	out-of-plane ring deformations (A + B_1)
	134(<0.1)[0]	
	125(<1)[<0.1]	B_2, δ(F_{ax}WN) (s)
	112(<1)[<1]	B_3, δ(F_{ax}WN) (s)
	86(1)[<0.1]	B_3, δ(F_{ax}WN) (as)
	82(<1)[<0.1]	B_2, δ(F_{ax}WN) (as)
	80(<1)[0]	A, ν_s($F_{ax}W_2$)
	40(<1)[1]	B_3, δ(WNC) (s)
	39(<1)[1]	B_2, δ(WNC) (s)
	21(3)[<0.1]	B_2, δ(WNC) (as)
	20(1)[<0.1]	B_3, δ(WNC) (as)
	11(<0.1)[0]	A, ρ(WF_4) (as)
	7(<1)[0]	B_1, ρ(C_6F_5) − ρ(WF_4) (s)
	4(2)[0]	A, ρ(C_6F_5) (as)
	4(<1)[<1]	B_2, δ($WF_{ax}W$)
	4(<1)[<1]	B_3, δ($WF_{ax}W$)

[a]Recorded in a flame-sealed m.p. capillary at ambient temperature. Normalised Raman intensities are given in parentheses. Cation bands are observed at 3120(2), 1586(1), 1206(2), 1033(2), 1012(10), 638(2), 611(1), and 494(4), and 98(7) cm^{-1}. [b]Calculated at the B3LYP/VTZ level of theory. Absolute Raman intensities (in $Å^4$ u^{-1}) are given in parentheses and absolute infrared intensities (in km mol^{-1}) are given in square brackets. [c]Symbols and abbreviations denote stretch (ν), bend (δ), rotation (ρ), symmetric (s), antisymmetric (as), axial (ax), equatorial (eq), in-plane (ip), and out-of-plane (op). Symmetric and antisymmetric combinations of the two $W(NC_6F_5)F_4$ moieties are denoted as s or as, respectively, in parentheses. Numbers in square brackets denote the fluorine atoms involved in the antisymmetric stretching mode. Atom labels are as in Figure 4.2a.

Table B.4. Calculated Vibrational Frequencies (cm^{-1}) of $[W(NH)F_5]^{-}$[a]

	Assignment (C_{4v})[b]
3647(209)[55]	A_1, ν(NH)
967(69)[172]	A_1, ν(WN)
639(11)[93]	A_1, $\nu_s(WF_5)$
639(<0.1)[476]	E, δ(WNH) − ν(WF2) + ν(WF4)
580(<1)[303]	E, δ(WNH) + ν(WF2) − ν(WF4)
557(3)[0]	B_1, ν(WF2) − ν(WF3) + ν(WF4) − ν(WF5)
518(1)[125]	A_1, $\nu(WF_{ax})$
310(9)[11]	E, $\delta_{ip}(F_{ax}WF4) + \delta_{ip}$(F2WFN)
287(<1)[18]	A_1, $\delta_s(WF_{eq})$
276(2)[0]	B_2, δ_{ip}(F2WF3) + δ_{ip}(F4WF5)
225(1)[20]	E, $\delta(F_{ax}WN) + \delta_{ip}$(F2WF4)
209(<0.1)[0]	B_1, δ_{op}(F2WF4) − δ_{op}(F3WF5)
124(2)[7]	E, $\delta(F_{ax}WN) - \delta_{ip}$(F2WF4)

[a]Calculated at the B3LYP/sVTZ level of theory. Absolute Raman intensities (in $Å^4\ u^{-1}$) are given in parentheses and absolute infrared intensities (in km mol^{-1}) are given in square brackets. [b]Symbols and abbreviations denote stretch (ν), bend (δ), symmetric (s), antisymmetric (as), axial (ax), equatorial (eq), in-plane (ip), and out-of-plane (op). Atom labels are as in Figure 4.1a.

Table B.5. Calculated Vibrational Frequencies (cm^{-1}) of $[W(NF)F_5]^{-}$[a]

	Assignment (C_{4v})[b]
1371(<1)[58]	A_1, ν(WN) − ν(NF)
648(24)[64]	A_1, $\nu_s(WF_5)$
590(<0.1)[482]	E, ν(WF2) − ν(WF4)
559(4)[0]	B_1, ν(WF2) − ν(WF3) + ν(WF4) − ν(WF5)
552(1)[163]	A_1, $\nu(WF_{ax})$
535(18)[86]	A_1, ν(WN) + ν(NF)
484(4)[8]	E, δ(F2WN) − δ(F4WN)
289(3)[19]	E, $\delta(F_{ax}WF2) - \delta(F_{ax}WF4)$
282(<1)[9]	A_1, $\delta_s(WF_{eq})$
275(2)[0]	B_2, δ_{ip}(F2WF3) + δ_{ip}(F4WF5)
213(<0.1)[0]	B_1, δ_{op}(F2WF4) − δ_{op}(F3WF5)
172(<0.1)[24]	E, δ(WNF) + δ_{ip}(F2WF4)
61(<1)[1]	E, δ(WNF) + $\delta(F_{ax}WN)$

[a]Calculated at the B3LYP/sVTZ level of theory. Absolute Raman intensities (in $Å^4\ u^{-1}$) are given in parentheses and absolute infrared intensities (in km mol^{-1}) are given in square brackets. [b]Symbols and abbreviations denote stretch (ν), bend (δ), symmetric (s), antisymmetric (as), axial (ax), equatorial (eq), in-plane (ip), and out-of-plane (op). Atom labels are as in Figure 4.1a.

Table B.6. Calculated Vibrational Frequencies (cm^{-1}) of $[W(NCH_3)F_5]^{-}$[a]

	Assignment (C_s)[b]
2991(195)[48]	C−H stretching modes
2990(194)[48]	
2951(596)[164]	
1474(15)[4]	CH_3 deformations
1473(16)[4]	
1437(4)[<0.1]	
1368(219)[257]	A′, ν(WN) − ν(NC) + $\delta_s(CH_3)$
1119(<0.1)[1]	CH_3 deformations (A′ + A″)
1119(<0.1)[1]	
634(16)[84]	A′, $\nu_s(WF_5)$
600(17)[83]	A′, ν(WN) − ν(NC)
582(<0.1)[286]	A″, ν(WF3) − ν(WF5)
581(<0.1)[286]	A′, ν(WF2) − ν(WF4)
552(3)[<0.1]	A′, ν(WF2) − ν(WF3) + ν(WF4) − ν(WF5)
518(1)[132]	A′, $\nu(WF_{ax})$
432(2)[14]	A′, δ(F3WN) − δ(F5WN)
432(2)[14]	A″, δ(F2WN) − δ(F4WN)
279(<1)[16]	A′, $\delta_s(WF_{eq})$
274(1)[15]	A″, $\delta(F_{ax}WF3) - \delta(F_{ax}WF5)$
274(1)[15]	A′, $\delta(F_{ax}WF2) - \delta(F_{ax}WF4)$
273(2)[<0.1]	A″, $\delta_{ip}(F2WF3) + \delta_{ip}(F4WF5)$
208(<0.1)[<0.1]	A′, $\delta_{op}(F2WF4) - \delta_{op}(F3WF5)$
165(<0.1)[6]	A″, $\delta(WNC) + \delta_{ip}(F2WF4)$
164(<0.1)[[6]	A′, $\delta(WNC) + \delta_{ip}(F3WF5)$
66(2)[<0.1]	A″, $\delta(WNC) + \delta(F_{ax}WN)$
62(2)[<0.1]	A′, $\delta(WNC) + \delta(F_{ax}WN)$
13(<1)[<0.1]	A″, $\rho(WF_{eq}) - \rho(CH_3)$

[a]Calculated at the B3LYP/sVTZ level of theory. Absolute Raman intensities (in $Å^4\ u^{-1}$) are given in parentheses and absolute infrared intensities (in km mol^{-1}) are given in square brackets. [b]Symbols and abbreviations denote stretch (ν), bend (δ), symmetric (s), antisymmetric (as), axial (ax), equatorial (eq), in-plane (ip), and out-of-plane (op). Atom labels are as in Figure 4.1a.

Table B.7. Calculated Vibrational Frequencies (cm^{-1}) of $[W(NCF_3)F_5]^{-}$[a]

	Assignment (C_s)[b]
1410(108)[1503]	A′, ν(WN) − ν(NC)
1063(4)[346]	C−F stretching modes (A′ + A″)
1061(4)[332]	
1059(5)[242]	A′, ν(WN) + ν(NC) − $\delta_s(CF_3)$
711(23)[4]	A′, ν(WN) + ν(NC) + $\delta_s(CF_3)$
653(12)[200]	A′, $\nu_s(WF_5)$
642(<1)[3]	NCF_3 deformations (A′+A″)
641(<1)[3]	
612(<1)[258]	A″, $\nu_{as}(WF_4)$ [2 − 3 − 4 + 5]
612(<1)[258]	A′, $\nu_{as}(WF_4)$ [2 + 3 − 4 – 5]
580(3)[<0.1]	A″, $\nu_{as}(WF_4)$ [2 − 3 + 4 – 5]
548(1)[138]	A′, $\nu(WF_{ax})$
466(1)[1]	CF_3 deformations (A′ + A″)
466(1)[1]	
334(6)[78]	A′, $\delta_s(WF_{eq}) - \delta_s(CF_3)$
292(2)[5]	A′, $\delta_s(WNF_2) + \delta_s(WF_3)$
292(2)[5]	A″,$\delta_s(WNF_2) + \delta_s(WF_3)$
282(2)[<1]	A′, δ_{ip}(F2WF3) + δ_{ip}(F4WF5)
252(<1)[17]	A″, $\delta(F_{ax}WN) + \delta_{ip}$(F2WF5) − δ_{ip}(F3WF4)
252(<1)[17]	A′, $\delta(F_{ax}WN) + \delta_{ip}$(F2WF3) − δ_{ip}(F4WF5)
248(2)[1]	A′, $\delta_s(WF_{eq}) + \delta_s(CF_3)$
202(<0.1)[<0.1]	A″, δ_{op}(F2WF4) − δ_{op}(F3WF5)
154(<1)[3]	A′, $\delta(F_{ax}WN) - \delta_{ip}$(F2WF3) + δ_{ip}(F4WF5)
154(<1)[3]	A″, $\delta(F_{ax}WN) - \delta_{ip}$(F2WF5) + δ_{ip}(F3WF4)
45(0)[<1]	A″, δ(WNC)
45(0)[<1]	A′, δ(WNC)
9(0)[<0.1]	A″, $\rho(WF_{eq}) - \rho(CF_3)$

[a]Calculated at the B3LYP/sVTZ level of theory. Absolute Raman intensities (in $Å^4\ u^{-1}$) are given in parentheses and absolute infrared intensities (in km mol^{-1}) are given in square brackets. [b]Symbols and abbreviations denote stretch (ν), bend (δ), symmetric (s), antisymmetric (as), axial (ax), equatorial (eq), in-plane (ip), and out-of-plane (op). Numbers in square brackets denote the fluorine atoms involved in the antisymmetric stretching mode. Atom labels are as in Figure 4.1a.

Table S16. Calculated Vibrational Frequencies (cm^{-1}) of $[W(NC_6H_5)F_5]^{-}$[a]

	Assignment (C_{2v})[b]
3191(205)[3]	C−H stretching modes ($3A_1 + 2B_2$)
3189(1)[15]	
3174(229)[46]	
3153(153)[28]	
3145(59)[5]	
1624(549)[87]	C−C stretching modes ($2A_1 + 2B_2$)
1594(<1)[4]	
1523(473)[284]	
1476(10)[<0.1]	
1415(1120)[432]	A_1, ν(NC)
1351(7)[<1]	C−C stretching modes and ring deformations ($A_1 + 4B_2$)
1302(3)[<0.1]	
1187(70)[12]	
1171(13)[<1]	
1092(<1)[7]	
1047(32)[25]	A_1, ν(WN) − $\nu_s(C_pC_m)$ + $\nu_s(C_iC_o)$
1025(56)[32]	A_1, ν(WN) + $\delta(C_mC_pC_m)$ − $\delta(C_oC_iC_o)$
1001(80)[2]	A_1, $\nu_s(C_6)$
994(1)[<1]	ring deformations ($2A_2 + 4B_1$)
982(<0.1)[0]	
918(<1)[10]	
847(1)[0]	
779(6)[48]	
706(<1)[39]	
686(30)[6]	A_1, ν(WN) − $\delta(C_mC_pC_m)$ − $\delta(C_oC_iC_o)$
639(3)[<1]	B_2, in-plane ring deformation
636(8)[273]	A_1, $\nu_s(WF_5)$
594(<1)[256]	B_1, $\nu_{as}(WF_4)$ [2 + 3 − 4 – 5]
594(<1)[256]	B_2, $\nu_{as}(WF_4)$ [2 − 3 − 4 + 5]
574(1)[<1]	ring deformations ($B_1 + B_2$)
565(<1)[8]	
563(3)[0]	A_2, $\nu_{as}(WF_4)$ [2 − 3 + 4 – 5]
533(<1)[169]	A_1, $\nu(WF_{ax})$
421(<0.1)[0]	ring deformations ($A_2 + B_1$)
407(1)[9]	
320(19)[44]	A_1, $\delta_s(WF_{eq})$ − $\delta(C_oC_iC_o)$
281(2)[7]	B_2, $\delta(F_{ax}WN)$ + δ_{ip}(F2WF5) − δ_{ip}(F3WF4)
277(1)[13]	B_1, $\delta(F_{ax}WN)$ + δ_{ip}(F2WF3) − δ_{ip}(F4WF5)

275(2)[<1]	A_1, δ_{ip}(F2WF3) + δ_{ip}(F4WF5)
231(5)[1]	A_1, ν(WN) + ν(NC) + δ_s(WF_{eq}) + δ($C_oC_iC_o$)
229(<1)[14]	B_2, δ(F_{ax}WN) − δ_{ip}(F2WF5) + δ_{ip}(F3WF4)
204(<0.1)[0]	A_2, δ_{op}(F2WF4) − δ_{op}(F3WF5)
191(<1)[10]	B_1, δ(WNC) + δ_{ip}(F2WF5) − δ_{ip}(F3WF4)
143(<1)[2]	B_2, δ(F_{ax}WN) − δ_{ip}(F2WF5) + δ_{ip}(F3WF4)
140(<1)[1]	B_1, δ(F_{ax}WN) + δ_{ip}(F2WF5) − δ_{ip}(F3WF4)
39(2)[<1]	B_1, δ(WNC)
32(<0.1)[<1]	B_2, δ(WNC)
4(5)[0]	A_2, ρ(WF_{eq}) − ρ(C_6F_5)

[a]Calculated at the B3LYP/sVTZ level of theory. Absolute Raman intensities (in $Å^4\ u^{-1}$) are given in parentheses and absolute infrared intensities (in km mol^{-1}) are given in square brackets. [b]Symbols and abbreviations denote stretch (ν), bend (δ), symmetric (s), antisymmetric (as), axial (ax), equatorial (eq), in-plane (ip), and out-of-plane (op). Numbers in square brackets denote the fluorine atoms involved in the antisymmetric stretching mode. Atom labels are as in Figure 4.1a.

Table B.8. Optimised Gas-Phase Atomic Coordinates (Å) of $[W(NH)F_5]^-$

W	0.00000000	0.00000000	0.07534600
F	0.00000000	0.00000000	-1.89232700
F	0.00000000	1.89937500	-0.11840300
F	-1.89937500	0.00000000	-0.11840300
F	0.00000000	-1.89937500	-0.11840300
F	1.89937500	0.00000000	-0.11840300
N	0.00000000	0.00000000	1.83900300
H	0.00000000	0.00000000	2.84482300

Table B.9. Optimised Gas-Phase Atomic Coordinates (Å) of $[W(NF)F_5]^-$

W	0.00000000	0.00000000	0.12030900
F	0.00000000	0.00000000	2.05481700
F	0.00000000	1.90203000	0.30550000
F	1.90203000	0.00000000	0.30550000
F	0.00000000	-1.90203000	0.30550000
F	-1.90203000	0.00000000	0.30550000
N	0.00000000	0.00000000	-1.64258300
F	0.00000000	0.00000000	-2.98845700

Table B.10. Optimised Gas-Phase Atomic Coordinates (Å) of $[W(NCH_3)F_5]^-$

W	-0.00194700	0.13182600	0.00000000
F	0.04165400	2.10053300	0.00000000
F	-0.00480200	0.31402900	1.90542600
F	-1.90356300	0.34806600	0.00000000
F	-0.00480200	0.31402900	-1.90542600
F	1.90705300	0.27903900	0.00000000
N	-0.02118200	-1.62967400	0.00000000
C	-0.00480200	-3.03910100	0.00000000
H	-0.51069200	-3.44451700	0.88559700
H	-0.51069200	-3.44451700	-0.88559700
H	1.02272500	-3.42501900	0.00000000

Table B.11. Optimised Gas-Phase Atomic Coordinates (Å) of $[W(NCF_3)F_5]^-$

W	0.30525200	0.60138900	0.00000000
F	1.18954700	2.32855200	0.00000000
F	-0.80363100	1.36366600	1.33269400
F	-0.80363100	1.36366600	-1.33269400
F	1.57091200	0.14975100	-1.33412300
F	1.57091200	0.14975100	1.33412300
N	-0.50865000	-0.99623200	0.00000000
C	-1.11941000	-2.20343800	0.00000000
F	-0.80363100	-2.96899800	1.08797100
F	-0.80363100	-2.96899800	-1.08797100
F	-2.48480400	-2.11833800	0.00000000

Table B.12. Optimised Gas-Phase Atomic Coordinates (Å) of $[W(NC_6H_5)F_5]^-$

W	0.00000000	0.00000000	1.06518400
F	0.00000000	0.00000000	3.02051300
F	-1.34363100	1.34120100	1.23660900
F	1.34363100	1.34120100	1.23660900
F	1.34363100	-1.34120100	1.23660900
F	-1.34363100	-1.34120100	1.23660900
N	0.00000000	0.00000000	-0.71794000
C	0.00000000	0.00000000	-2.07450200
C	0.00000000	-1.20864400	-2.79871800
C	0.00000000	1.20864400	-2.79871800
C	0.00000000	-1.20132200	-4.18493600
H	0.00000000	-2.13757300	-2.24592300
C	0.00000000	1.20132200	-4.18493600
H	0.00000000	2.13757300	-2.24592300
C	0.00000000	0.00000000	-4.89035600
H	0.00000000	-2.14213300	-4.72164100
H	0.00000000	2.14213300	-4.72164100
H	0.00000000	0.00000000	-5.97242900

Table B.13. Optimised Gas-Phase Atomic Coordinates (Å) of $[W(NC_6F_5)F_5]^-$

W	0.00000000	0.00000000	1.86181000
F	0.00000000	0.00000000	3.80300400
F	1.33980100	1.33385800	2.02874400
F	1.33980100	-1.33385800	2.02874400
F	-1.33980100	-1.33385800	2.02874400
F	-1.33980100	1.33385800	2.02874400
N	0.00000000	0.00000000	0.06469500
C	0.00000000	0.00000000	-1.27809500
C	0.00000000	-1.19380100	-2.02919000
C	0.00000000	-1.19661400	-3.41326200
C	0.00000000	0.00000000	-4.11476300
C	0.00000000	1.19661400	-3.41326200
C	0.00000000	1.19380100	-2.02919000
F	0.00000000	-2.36978200	-1.39461400
F	0.00000000	-2.35769200	-4.08861200
F	0.00000000	0.00000000	-5.45822000
F	0.00000000	2.35769200	-4.08861200
F	0.00000000	2.36978200	-1.39461400

Table B.14. Optimised Gas-Phase Atomic Coordinates (Å) of $[W_2(NC_6F_5)_2F_9]^-$

W	0.00000000	0.00000000	-2.11991500
F	0.00000000	0.00000000	0.00000000
F	-1.75280300	0.63780000	-1.86456500
F	-0.64048600	-1.75328400	-1.86977000
F	1.75280300	-0.63780000	-1.86456500
N	0.00000000	0.00000000	-3.87878700
C	0.00000000	0.00000000	-8.04802200
C	-0.59057500	1.04462500	-7.35089200
C	0.58941800	-1.04221300	-5.96627500
C	-0.58941800	1.04221300	-5.96627500
C	0.59057500	-1.04462500	-7.35089200
C	0.00000000	0.00000000	-5.23006600
W	0.00000000	0.00000000	2.11991500
F	-1.75280300	-0.63780000	1.86456500
F	-0.64048600	1.75328400	1.86977000
F	1.75280300	0.63780000	1.86456500
F	0.64048600	-1.75328400	1.86977000
N	0.00000000	0.00000000	3.87878700
C	-0.59057500	-1.04462500	7.35089200
C	0.58941800	1.04221300	5.96627500
C	-0.58941800	-1.04221300	5.96627500
C	0.59057500	1.04462500	7.35089200
C	0.00000000	0.00000000	5.23006600
F	0.64048600	1.75328400	-1.86977000
F	1.16374000	-2.05807500	-5.32393500
F	1.15957800	-2.05118900	-8.02442300
F	0.00000000	0.00000000	-9.38547400
F	-1.15957800	2.05118900	-8.02442300
F	-1.16374000	2.05807500	-5.32393500
F	1.16374000	2.05807500	5.32393500
F	1.15957800	2.05118900	8.02442300
F	0.00000000	0.00000000	9.38547400
F	-1.15957800	-2.05118900	8.02442300
F	-1.16374000	-2.05807500	5.32393500

Appendix C – Supporting Information for Chapter 5

Table C.1. Crystallographic Data Collection and Refinement Parameters for $W(NC_6F_5)F_4(L)$ (L = CH_3CN, C_5H_5N)

	$W(NC_6F_5)F_4(NCCH_3)$	**$W(NC_6F_5)F_4(NC_5H_5)$**
Identification code	MG16045	MG16046
Empirical formula	$C_8H_3N_2F_9W$	$C_{11}H_5N_2F_9W$
Formula weight	481.97	520.02
T (K)	100.00(16)	100.00(16)
Crystal system	triclinic	triclinic
Space group	$P\bar{1}$	$P\bar{1}$
a (Å)	5.0807(3)	8.0731(3)
b (Å)	7.5999(4)	9.1572(4)
c (Å)	16.0822(11)	9.1978(3)
α (°)	92.238(5)	86.670(3)
β (°)	92.833(5)	87.048(3)
γ (°)	90.040(4)	88.811(3)
V (Å^3)	619.74(6)	677.82(5)
Z	2	2
ρ_{calc} (g cm^{-3})	2.583	2.548
μ (mm^{-1})	9.422	8.625
F(000)	440	480
Crystal size (mm^3)	0.2 × 0.2 × 0.1	0.148 × 0.123 × 0.056
GooF	1.063	1.037
Final *R* indexes [I ≥ 2σ (I)]	R_1 = 0.0338, wR_2 = 0.0848	R_1 = 0.0141, wR_2 = 0.0346
Final *R* indexes [all data]	R_1 = 0.0349, wR_2 = 0.0862	R_1 = 0.0148, wR_2 = 0.0348
Largest diff. peak/hole (e Å^{-3})	1.24/-1.54	0.82/-0.84

[a] $R_1 = \sum||F_o| - |F_c||/\sum|F_o|$. [b] $wR_2 = [\sum[w(F_o^2 - F_c^2)^2]/\sum w(F_o^4)]^{1/2}$.

Table C.2. Crystallographic Data Collection and Refinement Parameters for $WOF_4(NC_5H_5)_n$ (n = 1, 2)

	$WOF_4(NC_5H_5)$	**$WOF_4(NC_5H_5)_2$**
Identification code	MG18011b	MG18010
Empirical formula	$C_5H_5NOF_4W$	$C_{10}H_{10}F_4N_2OW$
Formula weight	354.95	434.05
T (K)	109.38(15)	113(4)
Crystal system	orthorhombic	monoclinic
Space group	*Pbcn*	*C*2/*c*
a (Å)	14.0164(6)	8.2014(5)
b (Å)	7.5861(4)	11.1972(5)
c (Å)	14.8604(9)	13.5387(9)
α (°)	90	90
β (°)	90	107.256(7)
γ (°)	90	90
V (Å^3)	1580.10(14)	1187.33(13)
Z	8	4
ρ_{calc} (g cm^{-3})	2.984	2.428
μ (mm^{-1})	14.641	9.769
F(000)	1280	808
Crystal size (mm^3)	0.256 × 0.054 × 0.049	0.309 × 0.164 × 0.077
GooF	1.062	1.078
Final *R* indexes [I ≥ 2σ (I)]	R_1 = 0.0209, wR_2 = 0.0387	R_1 = 0.0208, wR_2 = 0.0511
Final *R* indexes [all data]	R_1 = 0.0326, wR_2 = 0.0418	R_1 = 0.0218, wR_2 = 0.0514
Largest diff. peak/hole (e Å^{-3})	0.62/-0.70	1.44/-1.42

[a] $R_1 = \sum||F_o| - |F_c||/\sum|F_o|$. [b] $wR_2 = [\sum[w(F_o^2 - F_c^2)^2]/\sum w(F_o^4)]^{1/2}$.

Table C.3. Vibrational Frequencies (cm^{-1}) of $[W(NC_6F_5)F_4]_x$

exptl[a]	calcd[b]	Assignment (C_2)[c]
2943(1)		overtones
2550(1)		
1697(2)		C–F/C/N stretching modes and in-plane ring deformations
1643(37)	1659(337)[20]	
	1635(<1)[12]	
1594(2)		
1548(3)		
1519(18)	1535(540)[421]	
	1524(2)[358]	
1475(100)	1509(987)[23]	
1381 sh		
1373(17)	1384(70)[42]	A, $\nu(WN + C_oF_o + C_o'F_o' + C_pF_p)$
1288 sh	1299(19)[<0.1]	in-plane ring deformation
1267(10)	1284(26)[57]	A, $\nu(WN + C_mF_m + C_m'F_m' - C_pF_p)$
1162(1)	1167(1)[1]	in-plane ring deformation
1083(6)	1097(22)[182]	A, $\nu(WN - C_oF_o - C_o'F_o' + C_pF_p)$
	1014(<1)[244]	in-plane ring deformation
825(1)	841(1)[13]	A, $\nu(WN - C_mF_m - C_m'F_m' - C_pF_p)$
	795(<0.1)[<1]	in-plane ring deformation
729(1)	760(<1)[0]	out-of-plane ring deformation
693(6)	698(29)[205]	A, $\nu_s(WF_4)$
	677(2)[184]	A, $\nu_{as}(FWF_t)$
	675(<0.1)[<0.1]	out-of-plane ring deformations
	669(<0.1)[<0.1]	
661(1)	663(2)[219]	B, $\nu_{as}(FWF_t)$
	618(1)[6]	B, $\nu_{as}(WF_4)$
584(4)	585(11)[2]	in-plane ring deformations
501(5)	503(22)[<0.1]	
470 sh	456(4)[2]	in-plane ring deformation
432(5)	425(2)[5]	out-of-plane ring deformations
	409(2)[3]	
381(3)	380(2)[0]	in-plane ring deformations
354(2)	357(2)[1]	
346(2)	323(1)[7]	out-of-plane ring deformation
	323(<0.1)[2]	B, $\delta(FWF_c + F_{c'}WF_t)$
	307(<1)][1]	in-plane ring deformations
282(2)	282(1)[2]	
	277(<0.1)[<0.1]	in-plane ring deformation

252(1)	261(1)[9]	A, $\delta_s(WF_4) + \delta_s(C_iC_oF_o)$
220(1)	236(1)[18]	B, $\omega(FWF_t)$
	220(<1)[18]	A, $\omega(FWF_t)$
	212(1)[2]	out-of-plane ring deformations
	170(<0.1)[0]	
179(3)	168(3)[<1]	A, $\delta_s(WF_4) - \delta_s(C_iC_oF_o)$
	155(2)[<0.1]	rocking and twisting modes
	135(<0.1)[0]	
	114(<1)[<1]	
	110(2)[<1]	
	43(1)[<1]	
	39(<0.1)[<0.1]	
	9(<1)[0]	

[a]Recorded in a flame-sealed m.p. capillary at ambient temperature. Normalised Raman intensities are given in parentheses. Shoulders are denoted as sh. [b]Calculated for monomeric $W(NC_6F_5)F_4$ at the B3LYP/sVTZ level of theory. Absolute Raman intensities ($Å^4\ u^{-1}$) are given in parentheses and absolute IR intensities (km mol^{-1}) are given in square brackets. [c]Symmetry species are assigned for the WNF_4 moiety on the basis of local C_2 symmetry. Abbreviations and symbols denote stretch (ν), bend (δ), wag (ω), symmetric (s), antisymmetric (as), trans to an arbitrary F_{eq} atom (t), and cis to the unlabelled fluorine atom (c, c′).

Table C.4. Vibrational Frequencies (cm^{-1}) of CH_3CN and $W(NC_6F_5)F_4(NCCH_3)$

CH_3CN[a]		$W(NC_6F_5)F_4(NCCH_3)$		Assignment (C_2)[d]
exptl	**calcd**	**exptl**[b]	**calcd**[c]	
3020(1)				overtone
3001(7)	3115(59)[<1]	3011(1)	3126(82)[<1] 3126(82)[<1]	$\nu_{as}(CH_3)$ (CH_3CN)
2943(100)	3048(195)[3]	2948(5)	3052(277)[<1]	$\nu_s(CH_3)$ (CH_3CN)
2888(3)				combination modes and overtones
2847(2)				
2732(2)				
2536(1)				
2293(5)	2363(81)[11]	2328(5)	2421(364)[123]	ν(CN) (CH_3CN)
2253(60)		2300(4)		
2204(1)				combination mode
		1724(1)		C–F/C/N stretching modes and ring deformations
		1682(1)		
		1643(22)	1662(509)[14]	
			1638(<1)[11]	
		1590(1)		
		1533(4)		
		1519(30)	1536(708)[507]	
			1526(3)[345]	
		1479(100)	1510(1568)[4]	
		1457 sh		
		1450 sh		
1443(3)	1475(5)[10]	1434(2)	1466(9)[12]	$\delta_{as}(CH_3)$ (CH_3CN)

1416(2)			1466(9)[12]	$\delta_{as}(CH_3)$ (CH_3CN)
1375(6)	1413(6)[2]	1382(2)	1412(20)[2]	$\delta_{s}(CH_3)$ (CH_3CN)
		1368(10)	1384(96)[67]	A, $\nu(WN(1) + C_oF_o + C_o'F_o' + C_pF_p)$
		1312(1)	1301(25)[<0.1]	in-plane ring deformation
		1261(10)	1280(62)[91]	A, $\nu(WN(1) + C_mF_m + C_m'F_m' - C_pF_p)$
		1157(1)	1168(<1)[1]	in-plane ring deformation
		1077(5)	1094(45)[221]	A, $\nu(WN(1) - C_oF_o - C_o'F_o' + C_pF_p)$
	1063(<1)[2]		1061(<1)[4]	$\rho(CH_3)$ (CH_3CN)
			1061(<1)[4]	
			1016(<1)[238]	in-plane ring deformation
919(18)	928(5)[1]	949(2)	952(18)[20]	ν(CC) (CH_3CN)
		818(1)	834(9)[3]	A, $\nu(WN(1) - C_mF_m - C_m'F_m' - C_pF_p)$
			800(<0.1)[<1]	in-plane ring deformation
		728(1)	736(1)[<1]	out-of-plane ring deformations
			668(<0.1)[4]	
		676(6)	668(29)[173]	A, $\nu_s(WF_4)$
			657(<0.1)[<0.1]	out-of-plane ring deformation
		621(1)	641(<1)[201]	A, $\nu_{as}(FWF_t)$
			639(<1)[211]	B, $\nu_{as}(FWF_t)$
			597(3)[<1]	B, $\nu_{as}(WF_4)$
		582(2)	584(11)[3]	in-plane ring deformations
		562(1)		
		499(4)	503(29)[<1]	
			489(<1)[2]	
		467(2)	460(4)[4]	out-of-plane ring deformations
		431(3)	436(6)[<1]	in-plane ring deformation
380(10)	382(1)[<1]	413(1)	420(2)[1]	δ(NCC) (CH_3CN)

	420(2)[1]	δ(NCC) (CH_3CN)
383(2)	382(3)[0]	out-of-plane ring deformation
358(2)	356(5)[7]	in-plane ring deformation
343(1)	339(<1)[3]	out-of-plane ring deformation
	307(<1)[<1]	in-plane ring deformation
298(2)	297(2)[1]	B, $\delta(FWF_c + F_{c'}WF_t)$
284(6)	285(9)[25]	A, $\delta_s(WF_4) - \delta_s(C_iC_oF_o)$
	276(<0.1)[<0.1]	out-of-plane ring deformation
272(2)	273(3)[23]	A, $\delta_s(WF_4) + \delta_s(C_iC_oF_o)$
233(2)	234(<1)[10]	A, $\omega(FWF_t) + \delta(F_cWN(2))$
	234(<1)[13]	B, $\omega(FWF_t) + \delta(F_cWN(2))$
	212(<1)[<0.1]	A, $\delta(FWF_c - F_{c'}WF_t + N(1)WN(2))$
	194(<1)[6]	A, $\delta(FWF_c - F_{c'}WF_t - N(1)WN(2))$
224(2)	194(10)[11]	A, $\nu(WN(2))$
189(1)	184(<1)[<0.1]	B, $\delta_{as}(WF_4)$
	183(<1)[5]	B, $\delta(FWF_c - F_{c'}WF_t + N(1)WN(2))$
168(2)	166(<1)[1]	B, $\delta(FWF_c - F_{c'}WF_t - N(1)WN(2))$
	159(<0.1)[4]	rocking and twisting modes
147(3)	137(3)[<0.1]	
	134(<0.1)[0]	
116(1)	108(<1)[<1]	
	53(2)[3]	
	52(<1)[2]	
	22(<0.1)[4]	
	21(<1)[4]	
	3(<0.1)[<0.1]	
	2(<1)[0]	

[a]From Nieboer, J.; Hillary, W.; Yu, X.; Mercier, H. P. A.; Gerken, M. *Inorg. Chem.* **2009**, *48* (23), 11251–11258. [b]Recorded in a flame-sealed m.p. capillary at ambient temperature. Normalised Raman intensities are given in parentheses. Shoulders are denoted as sh. [c]Calculated at the B3LYP/VTZ level of theory. Absolute Raman intensities ($Å^4\ u^{-1}$) are given in parentheses and absolute IR intensities (km mol^{-1}) are given in square brackets. [d]Symmetry species are assigned for the WNF_4 moiety on the basis of local C_2 symmetry. Abbreviations and symbols denote stretch (ν), bend (δ), rock (ρ), wag (ω), symmetric (s), antisymmetric (as), trans to the unlabelled fluorine atom (t), and cis to the unlabelled fluorine atom (c, c′). Atom labels are as in Figure 5.5.

Table C.5. Vibrational Frequencies (cm^{-1}) of C_5H_5N and $W(NC_6F_5)F_4(NC_5H_5)$

C_5H_5N[a]		$W(NC_6F_5)F_4(NC_5H_5)$		Assignment (C_2)[d]
exptl	**calcd**	**exptl**[b]	**calcd**[c]	
3173(1)				C–H stretching modes, combination modes, and overtones
3145(3)				
3091(5)				
3056(39)	3194(280)[7]	3095(2)	3219(251)[6]	
3036 sh	3186(36)[24]		3216(2)[1]	
3025 sh	3170(94)[5]	3082(2)	3205(112)[1]	
2988(5)	3148(86)[4]		3201(113)[2]	
2955(5)	3146(95)[27]		3183(90)[3]	
2908(1)				
2871(1)				
2453(1)				
		1681(1)		C–F/C/N stretching modes and ring deformations (C_6F_5 and C_5H_5N)
		1643(26)	1662(622)[17]	
1597(5)	1624(16)[23]	1613(1)	1657(14)[44]	
1581(9)				
			1637(<1)[12]	
1573(7)	1618(9)[10]	1574(1)	1621(11)[2]	
		1519(18)	1534(408)[396]	
			1531(103)[127]	
1482(3)	1516(2)[2]	1497 sh	1525(4)[336]	
		1475(100)	1502(2258)[<0.1]	
		1453 sh		
		1446 sh		

	1474(<1)[26]		1488(<0.1)[41]	in-plane ring deformations (C_5H_5N)
	1389(<1)[<1]	1379(2)	1403(<0.1)[2]	
		1359(19)	1381(152)[76]	A, ν(WN(1) + C_oF_o + $C_o'F_o'$ + C_pF_p)
		1320(1)	1301(29)[<1]	in-plane ring deformations (C_6F_5)
	1282(<1)[0.1]	1284 sh	1292(1)[1]	
		1257(13)	1276(107)[94]	A, ν(WN(1) + C_mF_m + $C_m'F_m'$ – C_pF_p)
1217(8)	1241(8)[4]	1223(2)	1253(5)[56]	in-plane ring deformations (C_6F_5 and C_5H_5N)
1146(2)	1170(2)[3]	1158(1)	1183(2)[4]	
			1167(<1)[1]	
1068(2)	1095(2)[3]		1103(<1)[<1]	
	1078(<1)[<0.1]		1098(<0.1)[1]	
		1074(4)	1091(74)[274]	A, ν(WN(1) – C_oF_o – $C_o'F_o'$ + C_pF_p)
1030(75)	1051(41)[7]	1066(7)	1065(6)[28]	$\delta_{as}(NC_5)$
990(100)	1012(32)[5]	1018(28)	1039(117)[29]	$\nu(NC_5)$ (ring-breathing mode)
980(5)				
			1015(<1)[<0.1]	in-plane ring deformation (C_6F_5)
	1025(<0.1)[<0.1]		1034(0)[<0.1]	out-of-plane ring deformations (C_5H_5N)
	1014(<0.1)[0]		1016(<1)[233]	
	966(<1)[<0.1]		979(<0.1)[<1]	
	902(<1)[0]		894(<0.1)[0]	
		817(2)	829(22)[<1]	A, ν(WN(1) – C_mF_m – $C_m'F_m'$ – C_pF_p)
		807 sh		
			801(<1)[<1]	ring deformations (C_6F_5 and C_5H_5N)
	768(<0.1)[8]		782(<1)[17]	
		726(1)	739(1)[1]	
	722(<0.1)[63]		712(<0.1)[74]	
			670(<0.1)[3]	

652(5)	670(3)[<1]		669(5)[4]	in-plane ring deformations (C_5H_5N)
603(3)	617(2)[4]	666(7)	665(19)[173]	A, $\nu_s(WF_4) - \delta(C_oN(2)C_o' - C_mC_pC_m')$
		653(2)	657(<0.1)[<0.1]	out-of-plane ring deformation (C_6F_5)
		642(4)	649(23)[11]	A, $\nu_s(WF_4) + \delta(C_oN(2)C_o' + C_mC_pC_m')$
			631(<0.1)[161]	A, $\nu_{as}(FWF_t)$
			628(<1)[178]	B, $\nu_{as}(FWF_t)$
		583(3)	590(3)[<1]	B, $\nu_{as}(WF_4)$
			584(10)[3]	ring deformations (C_6F_5 and C_5H_5N)
		503(5)	502(36)[1]	
		495(3)	496(<1)[2]	
		471(4)	469(4)[4]	
406(1)	421(<1)[4]		452(<1)[1]	
		434(5)	437(6)[<1]	
	385(<0.1)[0]		396(<1)[<0.1]	
		381(3)	382(3)[0]	
		358(2)	356(6)[9]	A, $\delta_s(WF_4) - \delta_s(C_iC_oF_o)$
		341(2)	339(<1)[3]	out-of-plane ring deformation (C_6F_5)
			307(<1)[<1]	in-plane ring deformation (C_6F_5)
		299(2)	295(1)[11]	B, $\delta(FWF_c + F_{c'}WF_t)$
		288(7)	287(14)[34]	A, $\delta_s(WF_4) - \delta_s(C_pC_mF_m)$
			276(<0.1)[<1]	in-plane ring deformation (C_6F_5)
			275(2)[16]	A, $\delta_s(WF_4) + \delta_s(C_iC_oF_o) + \delta_s(C_pC_mF_m)$
		246(1)	241(1)[3]	A, $\delta(FWF_c - F_{c'}WF_t + N(1)WN(2))$
		222(2)	224(<0.1)[8]	B, $\delta(FWF_c - F_{c'}WF_t + N(1)WN(2))$
			211(<1)[<0.1]	A, $\delta(FWF_c - F_{c'}WF_t - N(1)WN(2))$
			197(<1)[9]	B, $\delta(FWF_c - F_{c'}WF_t - N(1)WN(2))$
			195(<1)[0]	B, $\delta_{as}(WF_4)$

196(5)	187(9)[4]	A, δ(WN(2))
175(2)	180(<1)[6]	rocking, twisting, and lattice modes
	166(<1)[<1]	
158(3)	160(2)[3]	
	144(<1)[2]	
	134(<0.1)[0]	
123(6)	110(3)[<0.1]	
92(7)		
	83(<1)[<1]	
	66(3)[<1]	
	24(4)[<0.1]	
	21(<0.1)[1]	
	20(<0.1)[1]	
	5(<1)[0]	

[a]From Nieboer, J.; Yu, X.; Chaudhary, P.; Mercier, H. P. A.; Gerken, M. *Z. Anorg. Allg. Chem.* **2012**, *638* (3–4), 520–525. [b]Recorded in a flame-sealed m.p. capillary at ambient temperature. Normalised Raman intensities are given in parentheses. Shoulders are denoted as sh. [c]Calculated at the B3LYP/VTZ level of theory. Absolute Raman intensities ($Å^4\ u^{-1}$) are given in parentheses and absolute IR intensities (km mol^{-1}) are given in square brackets. [d]Symmetry species are assigned for the WNF_4 moiety on the basis of local C_2 symmetry. Abbreviations and symbols denote stretch (ν), bend (δ), symmetric (s), antisymmetric (as), trans to the unlabelled fluorine atom (t), and cis to the unlabelled fluorine atom (c, c′). Atom labels are as in Figure 5.6.

Table C.6. Vibrational Frequencies (cm^{-1}) of C_5H_5N and $W(NC_6F_5)F_4(NC_5H_5)_2$

C_5H_5N[a]		$W(NC_6F_5)F_4(NC_5H_5)_2$		Assignment[d]
exptl	**calcd**	**exptl**[b]	**calcd**[c]	
3173(1)	3194(280)[7]	3106 sh	3240(109)[13]	C–H stretching modes, combination modes, and overtones
3145(3)			3239(73)[9]	
3091(5)	3186(36)[24]		3237(11)[<1]	
3056(39)			3228(45)[2]	
3036 sh	3170(94)[5]	3084(2)	3206(304)[3]	
3025 sh			3206(137)[5]	
2988(5)	3148(86)[4]		3201(103)[4]	
2955(5)			3201(96)[5]	
2908(1)	3146(95)[27]	3064(1)	3181(86)[4]	
2871(1)			3181(90)[4]	
2453(1)				
		1704(1)		C–F/C/N stretching modes and ring deformations (C_6F_5 and C_5H_5N)
		1686(1)		
		1641(24)	1659(542)[11]	
1597(5)	1624(16)[23]	1611(2)	1655(7)[30]	
1581(9)			1654(8)[27]	
			1632(1)[17]	
1573(7)	1618(9)[10]	1575(1)	1622(11)[2]	
			1622(8)[2]	
1482(3)	1516(2)[2]	1523(5)	1530(3)[5]	
			1528(14)[32]	
		1514(10)	1528(161)[475]	
			1517(5)[303]	

		1469(100)	1487(1616)[32]	C–F/C/N stretching modes and ring deformations (C_6F_5 and C_5H_5N)
	1474(<1)[26]	1456(6)	1488(349)[15]	
			1488(56)[24]	
	1389(<1)[<1]		1399(<1)[1]	
			1396(<0.1)[2]	
		1351(11)	1370(117)[39]	ν(WN(1) + C_oF_o + $C_o'F_o'$ + C_pF_p)
			1295(23)[2]	ring deformations (C_6F_5 and C_5H_5N)
	1282(<1)[0.1]		1294(1)[2]	
			1293(<1)[2]	
		1250(8)	1263(82)[62]	ν(WN(1) + C_mF_m + $C_m'F_m'$ – C_pF_p)
1217(8)	1241(8)[4]	1222(2)	1253(17)[33]	ring deformations (C_6F_5 and C_5H_5N)
			1250(7)[46]	
1146(2)	1170(2)[3]		1182(3)[3]	
			1182(2)[4]	
			1159(<1)[3]	
1068(2)	1095(2)[3]		1108(<1)[1]	
			1107(<1)[1]	
	1078(<1)[<0.1]		1098(1)[5]	
			1097(2)[37]	
		1064(5)	1082(64)[233]	ν(WN(1) – C_oF_o – $C_o'F_o'$ + C_pF_p)
1030(75)	1051(41)[7]	1048(2)	1064(12)[13]	$\delta_{as}(NC_5)$
			1064(32)[5]	
990(100)	1012(32)[5]	1022(11)	1040(110)[3]	$\nu(NC_5)$ (ring-breathing mode)
980(5)			1039(22)[14]	
	1025(<0.1)[<0.1]		1030(<0.1)[<0.1]	ring deformations (C_6F_5 and C_5H_5N)
			1030(<0.1)[<0.1]	
	1014(<0.1)[0]		1016(<1)[14]	

			1013(<1)[12]	out-of-plane ring deformations (C_5H_5N)
			1011(1)[195]	
	966(<1)[<0.1]		983(<0.1)[1]	
			980(<0.1)[<1]	
			889(<1)[<0.1]	
	902(<1)[0]		887(<1)[<1]	
		804(1)	813(14)[9]	ν(WN(1) – C_mF_m – $C_m'F_m'$ – C_pF_p)
			801(<1)[<1]	ring deformations (C_6F_5 and C_5H_5N)
	768(<0.1)[8]	771(1)	785(<1)[19]	
			785(<1)[19]	
		729(1)	752(2)[2]	
			711(<1)[55]	
	722(<0.1)[63]		709(<1)[59]	
			674(<0.1)[2]	
652(5)	670(3)[<1]	649(4)	667(5)[2]	
			667(5)[<1]	
			658(<0.1)[<1]	
			656(3)[6]	
603(3)	617(2)[4]		653(2)[22]	
		585(5)	605(25)[172]	ν(WF(1) + WF(3) + WF(4))
		563(1)	583(13)[4]	in-plane ring deformation (C_6F_5)
			569(1)[176]	ν(WF(1) + WF(2))
			544(<1)[121]	ν(WF(3) – WF(4))
			526(4)[32]	ν(WF(1) – WF(2))
			516(1)[11]	ν(N(1)WF(4))
		495(5)	500(30)[1]	ring deformations (C_6F_5 and C_5H_5N)
		487(3)	490(5)[16]	

406(1)	421(<1)[4]		475(1)[5]	ring deformations (C_6F_5 and C_5H_5N)
			469(1)[6]	
		435(3)	439(6)[<1]	
			404(1)[<1]	
	385(<0.1)[0]		402(<1)[<1]	
		383(3)	381(2)[<0.1]	
			379(1)[10]	δ(F(3)WF(4))
		353(2)	355(4)[4]	ring deformations (C_6F_5)
		343(1)	350(3)[37]	
			335(<1)[1]	
			308(<1)[1]	
		298(2)	297(2)[25]	
		287(2)	286(2)[10]	$\delta(F(1)WF(4)) - \delta_s(C_iC_oF_o) - \delta_s(C_pC_mF_m)$
			280(1)[3]	$\delta(F(1)WF(4)) + \delta_s(C_iC_oF_o) + \delta_s(C_pC_mF_m)$
			276(<0.1)[<1]	in-plane ring deformation (C_6F_5)
		274(1)	272(1)[11]	ω(F(3)WF(4))
		249(1)	241(1)[1]	rocking and twisting modes
		222(2)	219(<1)[6]	
		213(2)	213(<1)[2]	
		203(2)	203(1)[2]	
		190(2)	176(3)[9]	ν(WN(2) – WN(3))
		172(5)	171(3)[2]	rocking and twisting modes
			169(3)[1]	
			163(<1)[3]	
			153(1)[2]	ν(WN(2) + WN(3))
			135(<1)[<0.1]	rocking and twisting modes
			131(1)[1]	

125(6)	111(3)[<1]	rocking and twisting modes
	105(<1)[3]	
	74(<1)[<1]	
	60(<1)[2]	
	50(2)[1]	
	49(8)[<1]	
	38(2)[<1]	
	32(3)[2]	
	18(4)[1]	
	9(3)[<1]	

[a]From Nieboer, J.; Yu, X.; Chaudhary, P.; Mercier, H. P. A.; Gerken, M. *Z. Anorg. Allg. Chem.* **2012**, *638* (3–4), 520–525. [b]Recorded in a flame-sealed m.p. capillary at ambient temperature. Normalised Raman intensities are given in parentheses. Shoulders are denoted as sh. [c]Calculated at the B3LYP/VTZ level of theory. Absolute Raman intensities ($Å^4$ u^{-1}) are given in parentheses and absolute IR intensities (km mol^{-1}) are given in square brackets. [d]Symmetry species are assigned for the WNF_4 moiety on the basis of local C_2 symmetry. Abbreviations and symbols denote stretch (ν), bend (δ), wag (ω), symmetric (s), and antisymmetric (as). Atom labels are as in Figure 5.7.

Table C.7. Calculated Vibrational Frequencies (cm^{-1}) of $W(NH)F_4$[a]

	Assignment (C_{4v})[b]
3653(108)[298]	A_1, ν(NH)
1080(43)[86]	A_1, ν(WN)
704(14)[64]	A_1, $\nu_s(WF_4)$
669(1)[435]	E, $\nu_{as}(FWF_t)$
617(3)[0]	B_1, $\nu_{as}(WF_4)$
466(2)[302]	E, δ(WNH)
325(2)[0]	B_2, $\delta(FWF_c + F_{c'}WF_t)$
281(8)[3]	E, δ(NWF)
245(1)[10]	A_1, $\delta_s(WF_4)$
228(1)[24]	E, $\omega(FWF_t)$
114(<1)[0]	B_1, $\delta_{as}(WF_4)$

[a]Calculated at the B3LYP/sVTZ level of theory. [b]Abbreviations and symbols denote stretch (ν), bend (δ), wag (ω), symmetric (s), antisymmetric (as), trans to the unlabelled fluorine atom (t), and cis to the unlabelled fluorine atom (c, c′).

Table C.8. Calculated Vibrational Frequencies (cm^{-1}) of $W(NF)F_4$[a]

	Assignment (C_{4v})[b]
1509(4)[37]	A_1, ν(WN – NF)
704(19)[67]	A_1, $\nu_s(WF_4)$
669(1)[443]	E, $\nu_{as}(FWF_t)$
618(3)[0]	B_1, $\nu_{as}(WF_4)$
607(15)[65]	A_1, ν(WN + NF)
324(2)[0]	B_2, $\delta(FWF_c + F_{c'}WF_t)$
304(2)[34]	E, δ(NWF)
236(1)[6]	A_1, $\delta_s(WF_4)$
225(2)[27]	E, $\omega(FWF_t)$
113(1)[<0.1]	E, δ(WNF)
106(<1)[0]	B_1, $\delta_{as}(WF_4)$

[a]Calculated at the B3LYP/sVTZ level of theory. Absolute Raman intensities ($Å^4\ u^{-1}$) are given in parentheses and absolute IR intensities ($km\ mol^{-1}$) are given in square brackets. [b]Abbreviations and symbols denote stretch (ν), bend (δ), wag (ω), symmetric (s), antisymmetric (as), trans to the unlabelled fluorine atom (t), and cis to the unlabelled fluorine atom (c, c′).

Table C.9. Calculated Vibrational Frequencies (cm^{-1}) of $W(NCH_3)F_4$[a]

	Assignment (C_{4v})[b]
3091(92)[5]	$\nu_{as}(CH_3)$
3090(92)[5]	
3021(353)[18]	$\nu_s(CH_3)$
1475(10)[12]	$\delta_{as}(CH_3)$
1475(10)[12]	
1466(2)[16]	A_1, ν(WN – NC) – $\delta_s(CH_3)$
1382(110)[139]	A_1, ν(WN – NC) + $\delta_s(CH_3)$
1113(<0.1)[1]	δ(NCH)
1113(<0.1)[1]	
692(14)[96]	A_1, $\nu_s(WF_4)$
658(1)[223]	E, $\nu_{as}(FWF_t)$
658(1)[223]	
631(12)[2]	A_1, ν(WN + NC)
608(3)[<0.1]	B_1, $\nu_{as}(WF_4)$
341(1)[15]	E, δ(NWF)
341(1)[15]	
318(2)[<0.1]	B_2, $\delta(FWF_c + F_{c'}WF_t)$
236(1)[8]	A_1, $\delta_s(WF_4)$
223(1)[18]	E, $\omega(FWF_t)$
223(1)[18]	
116(1)[<1]	B_1, $\delta_{as}(WF_4)$
114(2)[2]	E, δ(WNC)
113(2)[1]	
–6(<0.1)[<0.1]	CH_3 twist

[a]Calculated at the B3LYP/sVTZ level of theory. [b]Symmetry species are assigned for the WNF_4 moiety on the basis of local C_{4v} symmetry. Abbreviations and symbols denote stretch (ν), bend (δ), wag (ω), symmetric (s), antisymmetric (as), trans to the unlabelled fluorine atom (t), and cis to the unlabelled fluorine atom (c, c′).

Table C.10. Calculated Vibrational Frequencies (cm^{-1}) of $W(NCF_3)F_4$[a]

	Assignment (C_{4v})[b]
1392(49)[891]	A_1, ν(WN – NC)
1172(2)[331]	$\nu_{as}(CF_3)$
1172(2)[331]	
1106(5)[365]	A_1, ν(WN + NC) – $\nu_s(CF_3)$
754(7)[<0.1]	A_1, ν(WN + NC) – $\delta_s(CF_3)$
709(18)[149]	A_1, $\nu_s(WF_4)$
682(1)[208]	E, $\nu_{as}(FWF_t)$
682(1)[208]	
630(4)[<1]	B_1, $\nu_{as}(WF_4)$
615(<1)[4]	$\delta(CF_2 – NCF)$
615(<0.1)[4]	
451(<1)[<1]	$\delta(CF_2 + NCF)$
451(<1)[<1]	
335(3)[15]	A_1, ν(WN + NC) + $\delta_s(CF_3)$
331(2)[<0.1]	B_2, $\delta(FWF_c + F_{c'}WF_t)$
238(<0.1)[19]	E, $\omega(FWF_t) + \delta(NWF_c)$
238(<0.1)[19]	
223(2)[2]	E, $\omega(FWF_t) – \delta(NWF_c)$
223(2)[1]	
220(2)[2]	A_1, $\delta_s(WF_4)$
106(<1)[0]	B_1, $\delta_{as}(WF_4)$
62(<0.1)[<0.1]	δ(WNC)
61(<0.1)[<0.1]	
3(0)[0]	CF_3 twist

[a]Calculated at the B3LYP/sVTZ level of theory. [b]Symmetry species are assigned for the WNF_4 moiety on the basis of local C_{4v} symmetry. Abbreviations and symbols denote stretch (ν), bend (δ), wag (ω), symmetric (s), antisymmetric (as), trans to the unlabelled fluorine atom (t), and cis to the unlabelled fluorine atom (c, c′).

Table C.11. Calculated Vibrational Frequencies (cm^{-1}) of $W(NC_6H_5)F_4$[a]

	Assignment (C_{4v})[b]
3203(293)[4]	C–H stretching modes
3200(1)[4]	
3192(123)[8]	
3182(120)[5]	
3174(32)[<1]	
1628(311)[<1]	C–C/C–N stretching modes and in-plane ring deformations
1612(2)[4]	
1520(288)[53]	
1483(5)[3]	
1416(1186)[111]	
1356(6)[<1]	
1197(35)[<0.1]	
1184(9)[<0.1]	
1103(<0.1)[7]	
1068(1)[16]	A_1, ν(WN) – $\delta(C_oC_iC_o - C_mC_pC_m)$
1040(9)[<0.1]	ring-breathing mode
1017(<1)[<0.1]	out-of-plane ring deformation
1016(78)[2]	A_1, ν(WN) + $\delta(C_oC_iC_o - C_mC_pC_m)$
993(0)[0]	out-of-plane ring deformations
940(<0.1)[5]	
852(<1)[0]	
779(2)[59]	
703(1)[35]	A_1, ν(WN) − $\delta(C_oC_iC_o + C_mC_pC_m)$
702(<0.1)[33]	out-of-plane ring deformation
684(33)[160]	A_1, $\nu_s(WF_4)$
659(1)[205]	E, $\nu_{as}(WF_4)$
657(2)[206]	
634(5)[<1]	in-plane ring deformation
608(3)[0]	B_1, $\nu_{as}(WF_4)$
527(<0.1)[2]	ring deformations
501(<1)[8]	
414(<0.1)[0]	
358(<1)[7]	
318(2)[<1]	B_2, $\delta(FWF_c + F_{c'}WF_t)$
312(8)[7]	A_1, ν(WN) + $\delta(C_oC_iC_o + C_mC_pC_m)$
230(<0.1)[17]	E, $\delta(FWF_c - F_{c'}WF_t)$
221(1)[19]	
210(3)[1]	in-plane rock

209(2)[2]		A_1, $\delta_s(WF_4)$
183(<1)[<1]		out-of-plane rock
114(<1)[0]		B_1, $\delta_{as}(WF_4)$
58(3)[<0.1]	}	E, δ(WNC)
54(<0.1)[0]		
–7(4)[0]		C_6H_5 twist

[a]Calculated at the B3LYP/sVTZ level of theory. [b]Symmetry species are assigned for the WNF_4 moiety on the basis of local C_{4v} symmetry. Abbreviations and symbols denote stretch (ν), bend (δ), wag (ω), symmetric (s), antisymmetric (as), trans to the unlabelled fluorine atom (t), and cis to the unlabelled fluorine atom (c, c′).

Table C.12. Optimised Gas-Phase Atomic Coordinates (Å) of $W(NC_6F_5)F_4$

W	0.00000000	0.00000000	1.94209300
F	-0.11886600	1.78099800	2.47631100
F	-1.81996200	-0.12208700	2.37125000
F	1.81996200	0.12208700	2.37125000
F	0.11886600	-1.78099800	2.47631100
N	0.00000000	0.00000000	0.21126300
C	0.00000000	0.00000000	-1.15263100
C	0.00000000	1.20137500	-1.87490200
C	0.00023300	1.20484100	-3.25929400
C	0.00000000	0.00000000	-3.95249500
C	-0.00023300	-1.20484100	-3.25929400
C	0.00000000	-1.20137500	-1.87490200
F	0.00006100	2.35885600	-1.21996400
F	0.00057400	2.35485800	-3.92918100
F	0.00000000	0.00000000	-5.28046000
F	-0.00057400	-2.35485800	-3.92918100
F	-0.00006100	-2.35885600	-1.21996400

Table C.13. Optimised Gas-Phase Atomic Coordinates (Å) of $W(NC_6F_5)F_4(NCCH_3)$

W	-1.39759500	0.00060500	-0.00006600
F	-1.72493900	-1.14791400	1.45716600
F	-1.73394400	1.45734000	1.14336200
F	-1.72439900	1.14928000	-1.45723600
F	-1.73440200	-1.45598300	-1.14361900
F	1.77891400	-2.36086300	-0.00156200
F	4.48513000	-2.35591200	-0.00121400
F	5.83902500	-0.00103800	0.00008500
F	4.48623000	2.35446900	0.00134300
F	1.78001400	2.36068100	0.00161000
N	0.34538500	0.00024900	-0.00000200
N	-3.77242500	0.00041700	-0.00006600
C	1.70391400	-0.00007200	0.00002200
C	2.42999100	-1.20073100	-0.00090100
C	3.81435800	-1.20421400	-0.00064100
C	4.50873200	-0.00072700	0.00006300
C	3.81492000	1.20308400	0.00074800
C	2.43055200	1.20024700	0.00096500
C	-4.91517600	-0.00109200	0.00013900
C	-6.36382500	-0.00304400	0.00037200
H	-6.73073100	-0.59764100	-0.83540700
H	-6.73278700	1.01737600	-0.09609300
H	-6.73063000	-0.43039400	0.93285500

Table C.14. Optimised Gas-Phase Atomic Coordinates (Å) of $W(NC_6F_5)F_4(NC_5H_5)$

W	0.97571100	-0.00000100	0.00000200
F	1.30129500	-1.46325100	-1.14516900
F	1.29135700	1.16353600	-1.45400500
F	1.30129500	1.46324600	1.14517800
F	1.29136000	-1.16353400	1.45401200
F	-2.21137900	-2.36001500	-0.07052000
F	-4.91723200	-2.35419300	-0.07004400
F	-6.27056300	0.00000200	-0.00000400
F	-4.91723000	2.35419500	0.07003900
F	-2.21137700	2.36001400	0.07052100
N	-0.77592200	-0.00000100	0.00000200
N	3.34165400	0.00000100	-0.00000200
C	-2.13461600	0.00000000	0.00000000
C	-2.86185100	-1.19966600	-0.03603600
C	-4.24612600	-1.20312800	-0.03585700
C	-4.94029100	0.00000100	-0.00000300
C	-4.24612500	1.20313000	0.03585300
C	-2.86185000	1.19966700	0.03603500
C	4.02150100	-1.14359900	0.15368400
H	3.42978000	-2.03871700	0.27452800
C	5.40534600	-1.18450500	0.15915600
H	5.91205100	-2.12976900	0.28624900
C	6.11105300	0.00000200	-0.00000900
H	7.19255200	0.00000200	-0.00001000
C	5.40534400	1.18450900	-0.15916800
H	5.91204900	2.12977300	-0.28626100
C	4.02150000	1.14360200	-0.15369100
H	3.42977700	2.03872000	-0.27453200

Table C.15. Optimised Gas-Phase Atomic Coordinates (Å) of $W(NC_6F_5)F_4(NC_5H_5)_2$

W	1.23644400	0.10880800	0.48998700
F	1.20072300	1.41835000	1.88426200
F	1.53116600	-0.02087100	-1.42697900
F	1.37789800	-0.96012000	2.07134800
F	3.17835900	0.23908700	0.49686700
N	-0.53000400	-0.02795800	0.30022700
C	-1.87075600	-0.11951500	0.13215600
C	-2.75678800	0.12057100	1.19924500
C	-2.45054900	-0.45332400	-1.10415100
C	-4.12945100	0.02894800	1.04213800
C	-3.82060300	-0.55222800	-1.27000900
C	-4.66504800	-0.30964000	-0.19412600
F	-1.66128200	-0.68736800	-2.15744600
F	-4.33624800	-0.87566900	-2.45821200
F	-5.98482000	-0.39995800	-0.34842200
F	-4.94399100	0.26442300	2.07211500
F	-2.27019000	0.45223200	2.39200900
N	1.29322200	2.25154800	-0.42772900
C	0.44151600	3.19517800	-0.00755700
C	0.46917400	4.48629300	-0.50437400
C	1.43082100	4.82214900	-1.44763900
C	2.32476900	3.84722500	-1.86350000
C	2.21972300	2.56901600	-1.33868900
H	-0.26030700	2.89831400	0.75553700
H	-0.24723500	5.21073900	-0.14586100
H	1.48434600	5.82610400	-1.84631400
H	3.09827300	4.06256900	-2.58591800
H	2.88039200	1.77210000	-1.63869900
N	1.62297500	-2.11654700	-0.10982600
C	2.53723200	-2.82922000	0.55846200
C	0.99276300	-2.67710100	-1.14969800
C	2.85300700	-4.13193000	0.20806200
H	3.01419400	-2.33131600	1.38688600
C	1.23789200	-3.98156800	-1.54267300
H	0.28941000	-2.05244200	-1.67587600
C	2.18768900	-4.72398000	-0.85484600
H	3.60765600	-4.66396100	0.76840300
H	0.69338400	-4.39658600	-2.37813000
H	2.40678700	-5.74278200	-1.14443200

Table C.16. Optimised Gas-Phase Atomic Coordinates (Å) of $W(NH)F_4$

W	0.00000000	0.00000000	0.02611800
F	0.00000000	1.80295000	-0.46822700
F	-1.80295000	0.00000000	-0.46822700
F	0.00000000	-1.80295000	-0.46822700
F	1.80295000	0.00000000	-0.46822700
N	0.00000000	0.00000000	1.73953600
H	0.00000000	0.00000000	2.74672700

Table C.17. Optimised Gas-Phase Atomic Coordinates (Å) of $W(NF)F_4$

W	0.00000000	0.00000000	0.17188900
F	0.00000000	1.80470500	0.66199300
F	1.80470500	0.00000000	0.66199300
F	0.00000000	-1.80470500	0.66199300
F	-1.80470500	0.00000000	0.66199300
N	0.00000000	0.00000000	-1.54703500
F	0.00000000	0.00000000	-2.85803500

Table C.18. Optimised Gas-Phase Atomic Coordinates (Å) of $W(NCH_3)F_4$

W	-0.00028900	0.19204100	0.00000000
F	-1.81434500	0.67417700	0.00000000
F	0.00067500	0.66841600	1.81548800
F	1.81680400	0.66202100	0.00000000
F	0.00067500	0.66841600	-1.81548800
N	-0.00324200	-1.52006700	0.00000000
C	0.00067500	-2.94582100	0.00000000
H	-0.51093900	-3.31924400	-0.88834900
H	-0.51093900	-3.31924400	0.88834900
H	1.02762000	-3.31441700	0.00000000

Table C.19. Optimised Gas-Phase Atomic Coordinates (Å) of $W(NCF_3)F_4$

W	-0.11117500	-0.72753200	0.00000000
F	1.58843900	-1.48498600	0.00000000
F	-0.18583000	-1.21607100	1.79417800
F	-1.95930000	-0.94737500	0.00000000
F	-0.18583000	-1.21607100	-1.79417800
N	0.14936100	0.98005600	0.00000000
C	0.36154200	2.36732000	0.00000000
F	1.67108700	2.64593400	0.00000000
F	-0.18583000	2.93001100	-1.08457100
F	-0.18583000	2.93001100	1.08457100

Table C.20. Optimised Gas-Phase Atomic Coordinates (Å) of $W(NC_6H_5)F_4$

W	0.00000000	0.00000000	1.14982100
F	-1.28107600	1.28616000	1.62245700
F	-1.28107600	-1.28616000	1.62245700
F	1.28107600	1.28616000	1.62245700
F	1.28107600	-1.28616000	1.62245700
N	0.00000000	0.00000000	-0.57269700
C	0.00000000	0.00000000	-1.95364000
C	0.00000000	-1.21386600	-2.64935500
C	0.00000000	-1.20491900	-4.03563100
C	0.00000000	0.00000000	-4.73164900
C	0.00000000	1.20491900	-4.03563100
C	0.00000000	1.21386600	-2.64935500
H	0.00000000	2.14237800	-2.09692800
H	0.00000000	2.14250800	-4.57409200
H	0.00000000	0.00000000	-5.81270500
H	0.00000000	-2.14250800	-4.57409200
H	0.00000000	-2.14237800	-2.09692800

Table C.21. Optimised Gas-Phase Atomic Coordinates (Å) of WOF_4

W	0.00000000	0.00000000	0.03555900
F	0.00000000	1.79265000	-0.45440600
F	-1.79265000	0.00000000	-0.45440600
F	0.00000000	-1.79265000	-0.45440600
F	1.79265000	0.00000000	-0.45440600
O	0.00000000	0.00000000	1.71590500

Table C.22. Optimised Gas-Phase Atomic Coordinates (Å) of WSF_4

W	0.00000000	0.00000000	0.12549500
F	0.00000000	1.79147000	0.62334300
F	1.79147000	0.00000000	0.62334300
F	0.00000000	-1.79147000	0.62334300
F	-1.79147000	0.00000000	0.62334300
S	0.00000000	0.00000000	-1.98293800

Table C.23. Optimised Gas-Phase Atomic Coordinates (Å) of $[WOF_5]^-$

W	0.00000000	0.00000000	0.07853900
F	0.00000000	0.00000000	-1.89767000
F	0.00000000	1.89028100	-0.08669300
F	-1.89028100	0.00000000	-0.08669300
F	0.00000000	-1.89028100	-0.08669300
F	1.89028100	0.00000000	-0.08669300
O	0.00000000	0.00000000	1.79850600

Table C.24. Optimised Gas-Phase Atomic Coordinates (Å) of $[WSF_5]^-$

W	0.00000000	0.00000000	0.07372500
F	0.00000000	1.88275400	0.27709500
F	1.88275400	0.00000000	0.27709500
F	0.00000000	-1.88275400	0.27709500
F	-1.88275400	0.00000000	0.27709500
F	0.00000000	0.00000000	2.03766800
S	0.00000000	0.00000000	-2.11063200

Table C.25. Optimised Gas-Phase Atomic Coordinates (Å) of $[WF_7]^-$

C_{2v}

W	0.00000000	0.00000000	0.02176400
F	1.39686500	1.23128800	-0.34626100
F	0.00000000	-1.14697500	1.54943300
F	1.39686500	-1.23128800	-0.34626100
F	-1.39686500	-1.23128800	-0.34626100
F	0.00000000	1.14697500	1.54943300
F	-1.39686500	1.23128800	-0.34626100
F	0.00000000	0.00000000	-1.89276900

C_{3v}

W	0.00000000	0.00000000	0.02176400
F	1.39686500	1.23128800	-0.34626100
F	0.00000000	-1.14697500	1.54943300
F	1.39686500	-1.23128800	-0.34626100
F	-1.39686500	-1.23128800	-0.34626100
F	0.00000000	1.14697500	1.54943300
F	-1.39686500	1.23128800	-0.34626100
F	0.00000000	0.00000000	-1.89276900

D_{5h}

W	0.00000000	0.00000000	0.00000000
F	0.00000000	1.91964200	0.00000000
F	0.00000000	0.00000000	1.87176000
F	-1.12833700	-1.55302300	0.00000000
F	0.00000000	0.00000000	-1.87176000
F	1.82568800	0.59320200	0.00000000
F	-1.82568800	0.59320200	0.00000000
F	1.12833700	-1.55302300	0.00000000

Appendix D – Supporting Information for Chapter 6

Table D.1. Crystallographic Data Collection and Refinement Parameters for $[WF_5(2,2'\text{-bipy})][Sb_2F_{11}]$, $[WF_5(1,10\text{-phen})][Sb_2F_{11}]$, and $[WF_5(1,10\text{-phen})][SbF_6]\cdot SO_2$

	$[WF_5(2,2'\text{-bipy})][Sb_2F_{11}]$	**$[WF_5(1,10\text{-phen})][Sb_2F_{11}]$**	**$[WF_5(1,10\text{-phen})][SbF_6]\cdot SO_2$**
Identification code	MG18023	MG19003	MG19002
Empirical formula	$C_{10}H_8F_{16}N_2Sb_2W$	$C_{12}H_8F_{16}N_2Sb_2W$	$C_{12}H_8F_{11}N_2O_2SSbW$
Formula weight	887.53	911.55	758.86
T (K)	120.01(10)	100.01(10)	100.01(10)
Crystal system	monoclinic	monoclinic	monoclinic
Space group	$P2_1/c$	$P2/c$	$P2_1/c$
a (Å)	7.9461(3)	12.4250(4)	8.9830(3)
b (Å)	10.5922(4)	10.0286(3)	13.7388(4)
c (Å)	23.7527(9)	16.5730(5)	14.9741(5)
α (°)	90	90	90
β (°)	97.718(4)	104.203(3)	94.133(3)
γ (°)	90	90	90
V (Å^3)	1981.07(13)	2001.96(11)	1843.23(9)
Z	4	4	4
ρ_{calc} (g cm^{-3})	2.976	3.024	2.735
μ (mm^{-1})	8.646	8.561	7.935
F(000)	1608	1656	1400
Crystal size (mm^3)	0.171 × 0.089 × 0.066	0.300 × 0.163 × 0.145	0.137 × 0.063 × 0.039
GooF	1.055	1.052	1.029
Final R indexes [I ≥ 2σ (I)]	R_1 = 0.0282, wR_2 = 0.0576	R_1 = 0.0211, wR_2 = 0.0500	R_1 = 0.0256, wR_2 = 0.0563
Final R indexes [all data]	R_1 = 0.0382, wR_2 = 0.0606	R_1 = 0.0238, wR_2 = 0.0510	R_1 = 0.0319, wR_2 = 0.0583
Largest diff. peak/hole (e Å^{-3})	2.92/-2.44	2.24/-0.91	2.09/-1.43

[a] $R_1 = \sum||F_o| - |F_c||/\sum|F_o|$. [b] $wR_2 = [\sum[w(F_o^2 - F_c^2)^2]/\sum w(F_o^4)]^{1/2}$.

Table D.2. Vibrational Frequencies (cm^{-1}) of 2,2′-bipy and WF_6(2,2′-bipy)

2,2′-bipy		WF_6(2,2′-bipy)			Assignment[e]
exptl[a]	calcd[b]	exptl		calcd[b]	
		IR[c]	Raman[a,d]		
3144(1)					C–H stretching modes, combinations modes, and overtones
3120(2)					
3088 sh	3197(457)[7]			3238(255)[16]	
3076(6)	3195(27)[22]	3150 ms	3146(2)	3237(12)[3]	
3064(10)	3190(182)[6]			3235(78)[1]	
3052(5)	3187(13)[21]			3218(1)[<1]	
3046(5)	3171(36)[9]		3118(2)	3207(365)[<0.1]	
3030(1)	3170(48)[4]		3106 sh	3207(22)[6]	
3008(3)	3145(146)[21]	3100 ms	3092(5)	3187(90)[6]	
2957(1)	3144(96)[26]		3076 sh	3186(133)[4]	
2680(1)		2940 w	2570(1)		
2519(1)					
		1982 w			
		1957 w			
		1872 w			
1759(1)					
1676(1)					C–N/C–C stretching modes and in-plane ring deformations
1633(2)					
1613(5)	1628(3)[79]	1610 s		1645(<0.1)[14]	
1590(83)	1627(383)[5]		1609(100)	1637(354)[18]	
	1617(3)[5]	1575 ms		1626(<1)[12]	
1573(85)	1607(13)[33]		1571(55)	1615(167)[19]	
1548(1)		1537 w	1550(1)		
1531(1)					
1483(29)	1512(87)[6]	1512 ms	1510(49)	1528(134)[12]	

	1503(<0.1)[29]			1515(<1)[36]	C–N and C–C stretching modes and in-plane ring deformations
	1468(2)[54]	1479 s		1478(2)[62]	
1447(49)	1459(26)[5]	1446 s	1434(5) 1429 sh	1469(29)[9]	
1331 sh	1334(4)[4]	1328 s		1347(4)[23]	
1310 sh					
1302(32)	1335(88)[<0.1]		1334(61)	1340(188)[9]	
1294 sh					
1237(36)	1298(155)[<0.1]		1286(5) 1277 sh	1316(149)[<1]	
1217(5)	1279(2)[<1]			1299(6)[2]	
1202 sh					
	1285(1)[3]	1245 ms	1249(4)	1284(16)[22]	
	1180(3)[2]	1226 ms	1181(2)	1206(1)[8]	
1147(10)	1176(7)[6]	1176 m 1157 ms	1161(6)	1187(14)[10]	
	1131(2)[9]	1130 m		1154(<0.1)[<0.1]	
1096(4)	1115(1)[2]	1112 m	1110(2)	1138(<1)[4]	
1092 sh	1101(1)[2]		1089 sh	1104(<1)[2]	
1045(16)	1073(42)[7]	1079 m	1079(5)	1102(63)[8]	
	1059(2)[7]		1048 sh	1069(5)[1]	
995(100)	1010(82)[5]	1037 ms	1033(49)	1033(80)[11]	ring-breathing mode (s)
	1018(2)[<1]			1031(<1)[<0.1]	out-of-plane ring deformations
	1018(<0.1)[<0.1]			1029(<1)[<0.1]	
	1009(2)[2]	1024 m		1025(<1)[4]	ring-breathing mode (as)
	990(<1)[<1]	987 mw		1011(<0.1)[1]	out-of-plane ring deformations
	987(<0.1)[1]	972 mw		1008(<1)[0]	
	917(3)[<1]			911(<0.1)[<0.1]	
	912(<0.1)[<1]	927 mw		903(<1)[<0.1]	

815(4)	837(3)[5]		797(2)	830(1)[<0.1]	out-of-plane ring deformation
764(19)	784(12)[<0.1]		777(7)	786(9)[<1]	δ(N1C1C2 + C3C4C5) (s)
	781(<1)[48]	777 s		782(<1)[77]	out-of-plane ring deformations
	766(<1)[44]	723 ms		759(<0.1)[33]	
744(1)	763(2)[7]			756(<1)[<1]	
	641(2)[5]	647 s	664(31)	692(60)[77]	$\nu_s(WF_6)$ + δ(C1N1C5 + C2C3C4) (s)
	671(2)[10]	637 m	656 sh	669(2)[13]	δ(N1C1C2 + C3C4C5) (as)
			647(32)	661(5)[49]	$\nu_s(WF_6)$ – δ(C1N1C5 + C2C3C4) (s)
614(12)	626(6)[5]			641(2)[26]	δ(C1N1C5 + C2C3C4) (as)
		582 vs		633(<1)[224]	$\nu_{as}(WF_6)$ [1 – 2 – 3 + 4 + 5 – 6]
				627(<1)[168]	$\nu_{as}(WF_6)$ [1 – 2 + 3 – 4 + 5 – 6]
		547 ms		591(3)[27]	$\nu_{as}(WF_4)$ [1 + 2 – 3 – 4]
		527 sh		572(3)[104]	$\nu_{as}(WF_4)$ [3 + 4 – 5 – 6]
550(1)	570(2)[1]			565(<1)[<0.1]	out-of-plane ring deformation
			547(2)	547(2)[1]	$\nu_{as}(WF_4)$ [1 – 2 – 5 + 6]
	508(<0.1)[3]			482(1)[<0.1]	out-of-plane ring deformations
		462 mw		474(<1)[<1]	
439(3)	420(6)[<1]			452(<0.1)[<0.1]	
409(1)	417(<1)[6]	425 m		432(<0.1)[5]	out-of-plane ring deformation
			429(2)	429(2)[1]	δ(F1WF5 + F2WF6)
			380(2)	389(1)[10]	ρ(F3WF4) – ω(F5WF6)
		367 mw	369(2)	371(3)[39]	δ(N1WN2 + F1WF2 – F3WF4 – F5WF6)
	369(<1)[1]	357 mw		363(<1)[21]	δ(F1WF5 – F2WF6)
333(2)	320(3)[<0.1]		348(2)	343(1)[39]	δ(N1WN2 – F1WF2 + F3WF4 – F5WF6)
			311(2)	326(1)[2]	τ(F1WF2 – F3WF4 + F5WF6)
224(10)	253(3)[<1]	296 mw	283(4)	279(2)[14]	τ(N1WN2 – F5WF6)
			252(2)	268(2)[10]	τ(N1WN2 + F5WF6)
				249(<0.1)[1]	ω(F1WF2 + F5WF6)
				249(<0.1)[<0.1]	δ(N1WN2)
			237(3)	246(1)[<1]	ω(N1WN2 + F3WF4)

		203(11)		twisting and lattice modes
			186(<0.1)[3]	
		179(6)	156(2)[10]	
			150(<1)[1]	
			134(2)[<1]	$\nu_{as}(WN_2)$
	125(3)[2]	167 sh		lattice modes
102(44)		123(28)		
		94 sh		
			93(2)[10]	$\nu_s(WN_2)$
	92(1)[4]		92(<1)[1]	twisting modes
	55(8)[<0.1]		57(<1)[<1]	
			29(5)[<1]	
			13(2)[<0.1]	

[a]Recorded in a flame-sealed glass m.p. capillary at ambient temperature. Normalised Raman intensities are given in parentheses. Shoulders are denoted as sh. [b]Calculated at the B3LYP/aVTZ level of theory. Absolute Raman intensities ($Å^4\ u^{-1}$) are given in parentheses and IR intensities (km mol^{-1}) are given in square brackets. [c]From Arnaudet, L.; Bougon, R.; Ban, B.; Lance, M.; Navaza, A.; Nierlich, M.; Vigner, J. *J. Fluorine Chem.* **1994**, *67* (1), 17–25. [d]Bands corresponding to [2,2′-bipy-H][WF_7] were observed at 1016(2), 995(1), and 706(3) cm^{-1}. [e]Abbreviations denote stretch (ν), bend (δ), rock (ρ), twist (τ), and wag (ω). Symmetric and antisymmetric coupling of the two halves of C_2-symmetric 2,2′-bipy are denoted as s and as, respectively. Numbers in square brackets denote the fluorine atoms involved in the antisymmetric stretching mode. Atom labels are as in Figure 6.1b.

Table D.3. Vibrational Frequencies (cm^{-1}) of 1,10-phen and WF_6(1,10-phen)

1,10-phen		WF_6(1,10-phen)		Assignment[d]
exptl[a]	calcd[b]	exptl[a,c]	calcd[b]	
3092 sh		3188(1)		C–H stretching modes
3063(20)	3191(618)[<0.1] 3191(<1)[41]	3159(2)	3228(208)[11 3228(19)[1]	
3052(12)	3176(210)[26] 3165(165)[1] 3164(27)[13]	3126(10)	3205(392)[<0.1] 3205(16)[7] 3189(267)[14]	
	3157(21)[<1]	3094(10)	3179(145)[3]	
3029(6)	3138(185)[27] 3137(123)[21]	3077 sh	3178(64)[5] 3172(25)[<0.1]	
2992(4)		3004(3)		C–N and C–C stretching modes and in-plane ring deformations
2970(2)				
1619(6)	1657(27)[9]	1636(18)	1664(14)[4]	
1609(10)	1646(42)[9]	1612(17)	1648(43)[<1]	
1590(16)	1632(51)[9]	1595(28)	1636(74)[15]	
1560(11)	1589(32)[15]	1581 sh	1613(10)[6]	
1537(2)				
1503(17)	1536(76)[40]	1526(16)	1555(31)[40]	
	1534(5)[8]		1538(3)[7]	
1448(30)	1483(42)[1]	1463(85)	1492(73)[<1]	
1413(35)	1455(5)[47] 1450(8)[1]		1459(3)[59] 1455(8)[1]	
1406 sh 1400(100)	1412(373)[<0.1]	1433(60) 1421 sh	1437(281)[7]	

1343(11)	1379(83)[2]	1404 sh	1379(8)[13]	C–N and C–C stretching modes and in-plane ring deformations
1314 sh	1337(11)[1]	1347 sh	1349(12)[7]	
1293(43)	1321(93)[1]	1317(32)	1337(81)[<1]	
1268(4)	1297(9)[1]	1256(11)	1293(17)[<0.1]	
1259 sh				
1252 sh				
1219(2)	1247(5)[1]	1230(1)	1254(3)[5]	
1204(4)	1229(1)[0]		1244(2)[2]	
1186(4)	1219(35)[<1]	1210(3)	1232(17)[<0.1]	
1137(5)	1167(2)[1] 1162(3)[9]	1156(2)	1175(1)[2] 1172(1)[11]	in-plane ring deformations
1095(7)	1116(18)[11]	1118(18)	1132(20)[16]	
	1095(<0.1)[4]		1120(<1)[<0.1]	
1039 sh 1035(19)	1058(42)[1]	1085 sh 1073(19)	1084(36)[<1]	ring-breathing mode (s)
1001(1)	1054(2)[1]		1063(1)[<0.1]	ring-breathing mode (as)
992(1)	1006(<1)[0] 1002(<0.1)[1]	1022(1)	1024(<0.1)[0] 1022(<0.1)[1]	out-of-plane ring deformations
963(1)	985(<1)[0]		998(<0.1)[0]	
	969(<0.1)[<1]		993(<0.1)[1]	
	968(1)[0]	978(1)	984(1)[0]	
882(2)	898(2)[5]		915(1)[<0.1]	in-plane ring deformations
854(4)	870(3)[5]	871(6)	880(3)[7]	
	864(<1)[0]		869(1)[60]	out-of-plane ring deformations
816(1)	862(1)[54]		865(<0.1)[0]	
	817(<0.1)[0]		818(<0.1)[0]	
	778(<0.1)[20]		788(<0.1)[6]	

768(1)	760(<1)[38]		750(<1)[47]	out-of-plane ring deformation
706(41)	715(36)[3]	743(17)	742(15)[3]	δ(C1C2C3 + C4C5N1) (s)
	742(<1)[4]		741(<1)[8]	δ(N1C1C2 + C3C4C5) (as)
		658(100)	688(72)[122]	$\nu_s(WF_6)$
620(2)	632(1)[7]		653(0)[24]	δ(C1C2C3 + C4C5N1) (s)
		614(1)	632(1)[236]	$\nu_{as}(WF_4)$ [1 – 2 + 5 – 6]
607(1)	620(1)[0]	602(1)	629(1)[0]	out-of-plane ring deformation
			625(<0.1)[149]	ν_{as}(F2WF4)
		579(4)	593(5)[44]	$\nu_{as}(WF_4)$ [1 + 2 – 3 – 4]
			573(6)[80]	$\nu_{as}(WF_4)$ [3 + 4 – 5 – 6]
560 sh	564(1)[0]	561(14)	567(3)[20]	δ(N1C1C2 + C3C4C5) (as)
550(8)	562(6)[<0.1]		566(<1)[0]	out-of-plane ring deformation
			550(1)[<1]	$\nu_{as}(WF_4)$ [1 – 2 – 5 + 6]
511(4)	521(3)[<1]	517(1)	526(1)[1]	δ(F1WF5 + F2WF6 + C5C4C11) (s)
499(1)	507(1)[<1]		525(2)[2]	ring deformations
461(3)	466(2)[<1]	506(3)	499(2)[1]	
429(2)	442(1)[<0.1]		474(1)[<0.1]	
407(21)	414(18)[2]	440 sh	445(1)[0]	
401 sh	412(1)[0]	438(18)	434(10)[2]	δ(F1WF5 + F2WF6 + C5C4C6) (s)
		420(17)	418(10)[<0.1]	δ(F1WF5 + F2WF6 – C5C4C6) (s)
		382(1)	385(1)[10]	ρ(F3WF4) – ω(F5WF6)
		344(12)	364(<1)[17]	δ(F1WF5 – F2WF6)
		332(9)	355(1)[94]	δ(F1WF2 – F3WF4 + N1WN2)
			326(1)[0]	τ(F5WF6 – N1WN2)
			316(4)[<1]	δ(F3WF4 + N1WN2)
253 sh	241(1)[0]	284(3)	286(1)[0]	τ(F5WF6 + N1WN2)
242(10)	240(3)[4]		264(2)[18]	δ(F1WF2 – F5WF6 – N1WN2)

		265(5)	249(1)[13]	ω(F3WF4 + N1WN2)
		240(6)	248(<1)[21]	ω(F1WF2 + F5WF6)
	234(<1)[3]		232(<0.1)[3]	twisting and lattice modes
		194(25)		
			183(<1)[0]	
			174(<1)[1]	ω(F3WF4 – N1WN2)
			162(<0.1)[<1]	twisting and lattice modes
142(15)		159(14)		
			130(2)[2]	$\nu_{as}(WN_2)$
120(24)		123(65)		twisting and lattice modes
100(36)				
	104(<1)[0]		116(1)[0]	
	99(<0.1)[6]		98(<0.1)[2]	
			89(3)[10]	$\nu_s(WN_2)$
			36(5)[1]	twisting modes
			25(3)[0]	

[a]Recorded in a flame-sealed glass m.p. capillary at ambient temperature. Normalised Raman intensities are given in parentheses. Shoulders are denoted as sh. [b]Calculated at the B3LYP/aVTZ level of theory. Absolute Raman intensities ($Å^4$ u^{-1}) are given in parentheses and IR intensities (km mol^{-1}) are given in square brackets. [c]Bands corresponding to [1,10-phen-H][WF_7] were observed at 1043 and 705 cm^{-1}. [d]Abbreviations denote stretch (ν), bend (δ), rock (ρ), twist (τ), and wag (ω). Symmetric and antisymmetric coupling of the two halves of C_{2v}-symmetric 1,10-phen are denoted as s and as, respectively. Numbers in square brackets denote the fluorine atoms involved in the antisymmetric stretching mode. Atom labels are as in Figure 6.1c.

Table D.4. Vibrational Frequencies (cm^{-1}) of 2,2′-bipy and $[WF_5(2,2'\text{-bipy})]^+$

2,2′-bipy		$[WF_5(2,2'\text{-bipy})]^+$		Assignment[d]
exptl[a]	calcd[b]	exptl[c]	calcd[b]	
3144(1)				C–H stretching modes, combination bands, and overtones
3120(2)				
3088 sh	3197(457)[7]		3255(138)[20]	
3076(6)	3195(27)[22]		3255(19)[1]	
3064(10)	3190(182)[6]		3239(140)[2]	
3052(5)	3187(13)[21]		3225(2)[2]	
3046(5)	3171(36)[9]	3100(<1)	3219(354)[1]	
3030(1)	3170(48)[4]		3218(14)[5]	
3008(3)	3145(146)[21]		3202(70)[<0.1]	
2957(1)	3144(96)[26]		3201(121)[<1]	
2680(1)				
2519(1)				
1759(1)				
1676(1)				C–N and C–C stretching modes and in-plane ring deformations
1633(2)				
1613(5)	1628(3)[79]		1650(3)[12]	
1590(83)	1627(383)[5]	1612(6)	1640(316)[51]	
	1617(3)[5]		1617(1)[10]	
1573(85)	1607(13)[33]	1573(4)	1610(234)[7]	
1548(1)				
1531(1)				
1483(29)	1512(87)[6]	1516(2)	1540(176)[20]	
	1503(<0.1)[29]		1518(1)[53]	

	1468(2)[54]		1485(2)[82]	
1447(49)	1459(26)[5]		1476(34)[9]	
1331 sh	1334(4)[4]		1359(3)[29]	
1310 sh				
1302(32)	1335(88)[<0.1]		1351(26)[8]	
1294 sh				
1237(36)	1298(155)[<0.1]		1319(24)[5]	
	1285(1)[3]		1311(30)[<0.1]	
1217(5) 1210 sh	1279(2)[<1]		1279(11)[33]	C–N and C–C stretching modes and in-plane ring deformations
1147(10)	1180(3)[2]		1214(1)[7]	
	1176(7)[6]		1201(9)[13]	
	1131(2)[9]		1162(1)[2]	
1096(4)	1115(1)[2]		1144(3)[8]	
1092 sh	1101(1)[2]	1088(2)	1107(37)[6]	
1045(16)	1073(42)[7]		1106(<0.1)[3]	
	1059(2)[7]		1070(1)[<1]	
	1018(2)[<1]		1049(1)[<1]	
995(100)	1010(82)[5]	1036(5)	1048(101)[25]	ring-breathing mode (s)
	1018(<0.1)[<0.1]		1046(<1)[0]	out-of-plane ring deformation
	1009(2)[2]		1033(1)[16]	ring-breathing mode (as)
	990(<1)[<1]		1015(<1)[1]	
	987(<0.1)[1]		1014(<0.1)[<1]	
	917(3)[<1]		920(<0.1)[<1]	out-of-plane ring deformations
	912(<0.1)[<1]		917(<1)[<0.1]	
815(4)	837(3)[5]		825(1)[<0.1]	
764(19)	784(12)[<0.1]		793(1)[89]	

	781(<1)[48]		786(7)[3]	δ(C1C2C3 + C4C5N1) (s)
	766(<1)[44]		764(<1)[<0.1]	out-of-plane ring deformations
744(1)	763(2)[7]		750(<0.1)[27]	
		716(4)	724(48)[99]	$\nu_s(WF_5)$
			692(1)[177]	$\nu_{as}(WF_5)$ [1 – 2 + 3 – 4 – 5]
			680(<1)[136]	δ(C2C3C4 + C5N1C1) (s)
	671(2)[10]		680(2)[68]	ν_{as}(F2WF4) + δ(C1C2C3 + C4C5N1) (as)
			664(3)[8]	ν_{as}(F2WF4) – δ(C1C2C3 + C4C5N1) (as)
	641(2)[5]		661(4)[16]	$\nu_{as}(WF_3)$ [1 – 3 – 5]
614(12)	626(6)[5]		656(2)[1]	δ(C2C3C4 + C5N1C1) (as)
			602(2)[6]	$\nu_{as}(WF_5)$ [1 – 2 – 3 – 4 + 5]
550(1)	570(2)[1]		557(<1)[<0.1]	ring deformations
			494(2)[<1]	
	508(<0.1)[3]		475(<1)[1]	
439(3)	420(6)[<1]		452(<1)[0]	
409(1)	417(<1)[6]		436(<0.1)[8]	
	369(<1)[1]		421(1)[2]	δ(F1WF2 + F4WF5)
333(2)	320(3)[<0.1]		377(8)[<1]	δ(F3WF5 + N1WN2)
			369(<1)[29]	δ(F1WF5 + F2WF4)
			326(1)[24]	δ(F1WF3)
			319(<1)[10]	ω(F1WF5) – ρ(F2WF4)
			286(1)[15]	δ(F1WF5 – F2WF4)
224(10)	253(3)[<1]		274(2)[2]	ρ(F2WF4) – ω(F2WF5)
			271(2)[2]	δ(F3WF5 – N1WN2)
			248(<1)[9]	ρ(F2WF4) + ω(F2WF5)
			237(1)[4]	ρ(F1WF5) – ω(N1WN2)
			200(2)[4]	$\nu_s(WN_2)$

		199(4)[<1]	$\nu_{as}(WN_2)$
	125(3)[2]	162(2)[2]	
102(44)			
		110(1)[<1]	
	92(1)[4]	98(1)[2]	twisting and lattice modes
	55(8)[<0.1]	85(<1)[1]	
		37(5)[<1]	
		36(2)[<1]	

[a]Recorded in a flame-sealed glass m.p. capillary at ambient temperature. Normalised Raman intensities are given in parentheses. Shoulders are denoted as sh. [b]Calculated at the B3LYP/aVTZ level of theory. Absolute Raman intensities ($Å^4$ u^{-1}) are given in parentheses and IR intensities (km mol^{-1}) are given in square brackets. [c]Recorded in a heat-sealed 4-mm-o.d. FEP sample tube. Normalised Raman intensities are given in parentheses. Bands corresponding to $[Sb_2F_{11}]^-$ are observed at 683(2) and 649(3) cm^{-1}. Bands corresponding to SO_2 are observed at 1338(10), 1145(100), and 521(2) cm^{-1}. Bands corresponding to the FEP sample tube are observed at 1380(1), 1307(1), 733(3), 386(1), and 292(1) cm^{-1}. [d]Abbreviations denote stretch (ν), bend (δ), rock (ρ), twist (τ), and wag (ω). Symmetric and antisymmetric coupling of the two halves of C_s-symmetric 2,2′-bipy are denoted as s and as, respectively. Numbers in square brackets denote the fluorine atoms involved in the antisymmetric stretching mode. Atom labels are as in Figure 6.2a.

Table D.5. Vibrational Frequencies (cm^{-1}) of 1,10-phen and $[WF_5(1,10\text{-phen})]^+$

1,10-phen		$[WF_5(1,10\text{-phen})]^+$			Assignment[e]
exptl[a]	calcd[b]	exptl[a,c]	exptl[a,d]	calcd[b]	
3092 sh		3163(1)			C–H stretching modes
3063(20)	3191(618)[<0.1] 3191(<1)[41]	3124(5)	3123(4)	3244(147)[20] 3244(27)[4]	
3052(12)	3176(210)[26] 3165(165)[1]	3092(6)	3091(6)	3216(381)[1] 3216(9)[3]	
	3164(27)[13]	3080(6)	3068 sh	3203(237)[<0.1]	
3029(6)	3157(21)[<1] 3138(185)[27] 3137(123)[21]	3060 sh	3040 sh	3193(138)[<0.1] 3193(65)[<0.1] 3189(17)[1]	
2992(4)					
2970(2)					
1619(6)	1657(27)[9]	1643(17)	1642(18)	1667(45)[9]	C–N and C–C stretching modes and in-plane ring deformations
1609(10)	1646(42)[9]	1630(6)	1630(8)	1640(40)[3]	
1590(16)	1632(51)[9]	1612(16)	1611(18)	1628(72)[18]	
1560(11)	1589(32)[15]	1590(13)	1590(13)	1616(10)[8]	
1537(2)					
1503(17)	1536(76)[40]	1532(6)	1530(6)	1564(19)[64]	
	1534(5)[8]			1535(1)[9]	
1448(30)	1483(42)[1]	1466(100)	1466(100)	1494(88)[<1]	
1413(35)	1455(5)[47] 1450(8)[1]	1421(8)	1421(11)	1465(3)[70] 1457(6)[18]	
1406 sh 1400(100)	1412(373)[<0.1]	1444(30)	1442(35)	1455(241)[18]	
1343(11)	1379(83)[2]		1358(2)	1382(3)[9]	
1314 sh	1337(11)[1]	1315(22)	1316(20)	1348(5)[6]	
1293(43)	1321(93)[1]	1299(3)		1345(67)[7]	

1268(4) 1259 sh 1252 sh	1297(9)[1]	1258(6) 1255 sh	1259(7) 1255 sh	1287(15)[<0.1]	C–N and C–C stretching modes and in-plane ring deformations
1219(2)	1247(5)[1]			1258(1)[8]	
1204(4)	1229(1)[0]			1254(1)[3]	
1186(4)	1219(35)[<1]	1213(3)	1214(3)	1240(8)[1]	
1137(5)	1167(2)[1]			1186(1)[3]	
	1162(3)[9]			1183(<1)[14]	
1095(7)	1116(18)[11]	1119(3) 1112 sh	1117(7)	1140(10)[17]	
	1095(<0.1)[4]			1131(1)[<1]	
	1054(2)[1]			1063(<0.1)[3]	
1039 sh 1035(19)	1058(42)[1]	1082(10) 1072(7)	1083(11) 1073(13)	1097(40)[1]	ring-breathing mode (s)
1001(1)	1006(<1)[0]	1010(1)	1021(3)	1038(<0.1)[<0.1]	ring-breathing mode (as)
992(1)	1002(<0.1)[1]		1001(3)	1036(<0.1)[1]	out-of-plane ring deformations
963(1)	985(<1)[0]			1013(<1)[<0.1]	
	969(<0.1)[<1]		981(2)	1001(<0.1)[1]	
	968(1)[0]		971(2)	996(<1)[<0.1]	
882(2)	898(2)[5]		920(1)	929(1)[2]	δ(N1C1C2 + C5C4C6) (as)
854(4)	870(3)[5]	878(3)	877(4)	889(3)[13]	δ(N1C1C2 + C5C4C6) (s)
	864(<1)[0]			878(1)[65]	out-of-plane ring deformations
816(1)	862(1)[54]			865(<0.1)[0]	
	817(<0.1)[0]			820(<0.1)[<0.1]	
	778(<0.1)[20]			800(<0.1)[7]	
706(41)	715(36)[3]	756(8)	756(12)	761(12)[4]	δ(C1C2C3 + C4C5N1) (s)
	742(<1)[4]			740(<1)[16]	δ(N1C1C2 + C3C4C5) (as)
768(1)	760(<1)[38]			739(<1)[51]	out-of-plane ring deformation
		717(13)	706(68)	720(59)[143]	$\nu_s(WF_5)$

		707(37)			$\nu_s(WF_5)$
				692(1)[175]	$\nu_{as}(WF_5)$ [1 – 2 + 3 – 4 – 5]
620(2)	632(1)[7]			677(<1)[110]	ν_{as}(F2WF4) + δ(C1C2C3 + C4C5N1) (as)
			665 sh	668(5)[54]	$\nu_{as}(WF_3)$ [1 – 3 – 5]
				664(<1)[15]	ν_{as}(F2WF4) – δ(C1C2C3 + C4C5N1) (as)
607(1)	620(1)[0]			629(1)[<0.1]	out-of-plane ring deformation
		587(1)	589(2)	601(2)[5]	$\nu_{as}(WF_5)$ [1 – 2 – 3 – 4 + 5]
550(8)	562(6)[<0.1]	562(11)	561(12)	571(9)[<1]	δ(C2C3C4 + C5N1C1) (s)
560 sh	564(1)[0]			557(<1)[<0.1]	ring deformations
511(4)	507(1)[<1]			533(1)[1]	
499(1)	521(3)[<1]			526(<1)[1]	
461(3)	466(2)[<1]	506(4)	506(5)	511(3)[1]	
429(2)	442(1)[<0.1]			468(<1)[<0.1]	
				445(1)[<0.1]	
407(21)	414(18)[2]	435(16)	435(15)	435(21)[7]	
401 sh	412(1)[0]	412(1)	407(3)	421(2)[2]	δ(F1WF2 + F4WF5)
				368(<1)[34]	δ(F1WF5 + F2WF4)
			350(3)	342(4)[5]	δ(F3WF5 + N1WN2)
				321(<1)[7]	ω(F1WF5) – ρ(F2WF4)
		328(2)	330(5)	318(2)[14]	δ(F3WF5 – N1WN2)
	241(1)[0]			286(<1)[3]	out-of-plane ring deformation
	240(3)[4]	281(2)		276(1)[17]	δ(F2WF4) – δ(F3WF5)
				241(<0.1)[7]	ρ(F2WF4) – ω(F3WF5)
253 sh		251(3)	250(5)	238(1)[6]	ω(N1WN2)
242(10)	234(<1)[3]			232(<0.1)[6]	out-of-plane ring deformation
				198(3)[5]	$\nu_s(WN_2)$
		214(14)		195(2)[<0.1]	$\nu_{as}(WN_2)$
		191(1)	198(4)	184(1)[1]	twisting and lattice modes
142(15)		139(5)	146(8)		

120(24)		132(8)		twisting and lattice modes
100(36)				
	104(<1)[0]		133(1)[1]	
			111(1)[1]	
			98(1)[2]	
	99(<0.1)[6]		48(3)[<1]	
			44(5)[1]	

[a]Recorded in a flame-sealed glass m.p. capillary at ambient temperature. Normalised Raman intensities are given in parentheses. Shoulders are denoted as sh. [b]Calculated at the B3LYP/aVTZ level of theory. Absolute Raman intensities ($Å^4\ u^{-1}$) are given in parentheses and IR intensities (km mol^{-1}) are given in square brackets. [c]From $[WF_5(1,10\text{-phen})][Sb_2F_{11}]$. Bands corresponding to $[Sb_2F_{11}]^-$ are observed at 681(18), 648(16), 603(2), 346(3), 294(2), and 234(2) cm^{-1}. Bands corresponding to residual SO_2 are observed at 1157 sh and 1150(4) cm^{-1}. [d]From $[WF_5(1,10\text{-phen})][SbF_6]\cdot SO_2$. Bands corresponding to $[SbF_6]^-$ are observed at 646(24), 574(1), and 280(8) cm^{-1}. Bands corresponding to SO_2 are observed at 1157 sh and 1150(7) cm^{-1}. [e]Abbreviations denote stretch (ν), bend (δ), rock (ρ), twist (τ), and wag (ω). Symmetric and antisymmetric coupling of the two halves of C_s-symmetric 1,10-phen are denoted as s and as, respectively. Numbers in square brackets denote the fluorine atoms involved in the antisymmetric stretching mode. Atom labels are as in Figure 6.3a.

Table D.6. Optimised Gas-Phase Atomic Coordinates (Å) of WF_6(2,2′-bipy)

W	-0.00000000	0.00000000	1.21053715
F	1.71648535	0.10069726	0.43729915
F	-1.71648535	-0.10069726	0.43729915
F	-0.19676240	1.82223479	1.57434915
F	0.19676240	-1.82223479	1.57434915
F	1.16106816	0.15171284	2.69003315
F	-1.16106816	-0.15171284	2.69003315
N	-0.03852371	1.34929917	-0.94889185
N	0.03852371	-1.34929917	-0.94889185
C	-0.04134482	2.68160234	-0.90343085
C	-0.00433623	3.47701453	-2.03888585
C	0.04204609	2.85942969	-3.27628685
C	0.04498234	1.47649118	-3.32676085
C	0.00066136	0.73824258	-2.14357985
C	-0.00066136	-0.73824258	-2.14357985
C	-0.04498234	-1.47649118	-3.32676085
C	-0.04204609	-2.85942969	-3.27628685
C	0.00433623	-3.47701453	-2.03888585
C	0.04134482	-2.68160234	-0.90343085
H	-0.07413652	3.12167474	0.07935615
H	-0.00868259	4.55218544	-1.93802485
H	0.07769623	3.43892516	-4.18840985
H	0.08827054	0.97985730	-4.28202085
H	-0.08827054	-0.97985730	-4.28202085
H	-0.07769623	-3.43892516	-4.18840985
H	0.00868259	-4.55218544	-1.93802485
H	0.07413652	-3.12167474	0.07935615

Table D.7. Optimised Gas-Phase Atomic Coordinates (Å) of WF_6(1,10-phen)

W	0.00000000	0.00000000	1.47955100
F	-1.17034500	0.00000000	2.95941100
F	1.17034500	0.00000000	2.95941100
F	0.00000000	1.83437500	1.84094800
F	1.71770800	0.00000000	0.70333800
F	-1.71770800	0.00000000	0.70333800
F	0.00000000	-1.83437500	1.84094800
N	0.00000000	1.35882600	-0.67261400
N	0.00000000	-1.35882600	-0.67261400
C	0.00000000	2.67898300	-0.66260200
C	0.00000000	3.44920900	-1.83388100
C	0.00000000	2.81586200	-3.04945100
C	0.00000000	1.41057400	-3.09184500
C	0.00000000	0.71654300	-1.86030600
C	0.00000000	-0.71654300	-1.86030600
C	0.00000000	-1.41057400	-3.09184500
C	0.00000000	-2.81586200	-3.04945100
C	0.00000000	-3.44920900	-1.83388100
C	0.00000000	-2.67898300	-0.66260200
C	0.00000000	0.67719900	-4.31813700
C	0.00000000	-0.67719900	-4.31813700
H	0.00000000	3.14986700	0.30757900
H	0.00000000	4.52645200	-1.75625200
H	0.00000000	3.37864200	-3.97377100
H	0.00000000	-3.37864200	-3.97377100
H	0.00000000	-4.52645200	-1.75625200
H	0.00000000	-3.14986700	0.30757900
H	0.00000000	1.22918400	-5.24858100
H	0.00000000	-1.22918400	-5.24858100

Table D.8. Optimised Gas-Phase Atomic Coordinates (Å) of $[WF_5(2,2'\text{-bipy})]^+$

W	0.00746302	-1.14852585	0.00000000
F	-0.75031705	-2.82976381	0.00000000
F	0.40323700	-1.75786686	1.69729400
F	-1.75670295	-0.61049277	0.00000000
F	0.40323700	-1.75786686	-1.69729400
F	1.81219304	-0.74407393	0.00000000
N	0.00345511	0.72253615	1.32070200
N	0.00345511	0.72253615	-1.32070200
C	-0.02322190	0.64316216	2.66069600
C	-0.04586385	1.76574116	3.46940600
C	-0.03310979	3.01751616	2.87771700
C	-0.00989779	3.10115015	1.49474700
C	0.00102716	1.93998015	0.73231600
C	0.00102716	1.93998015	-0.73231600
C	-0.00989779	3.10115015	-1.49474700
C	-0.03310979	3.01751616	-2.87771700
C	-0.04586385	1.76574116	-3.46940600
C	-0.02322190	0.64316216	-2.66069600
H	-0.02101994	-0.34231384	3.09276900
H	-0.06966885	1.64233616	4.54165300
H	-0.04327875	3.91613316	3.47816700
H	-0.00236475	4.06653815	1.01574300
H	-0.00236475	4.06653815	-1.01574300
H	-0.04327875	3.91613316	-3.47816700
H	-0.06966885	1.64233616	-4.54165300
H	-0.02101994	-0.34231384	-3.09276900

Table D.9. Optimised Gas-Phase Atomic Coordinates (Å) of $[WF_5(1,10\text{-phen})]^+$

W	-0.00053092	-1.42068801	0.00000000
F	-0.77629280	-3.09319807	0.00000000
F	0.36464513	-2.02622598	1.70772100
F	-1.75280596	-0.84811814	0.00000000
F	0.36464513	-2.02622598	-1.70772100
F	1.81280106	-1.06655788	0.00000000
N	0.03284895	0.44748699	1.33083200
N	0.03284895	0.44748699	-1.33083200
C	0.04004895	0.41412199	2.66035400
C	0.01224087	1.57806899	3.43485500
C	-0.01948422	2.80538799	2.81949600
C	-0.02425523	2.87201699	1.41376400
C	0.00028686	1.65413999	0.70856100
C	0.00028686	1.65413999	-0.70856100
C	-0.02425523	2.87201699	-1.41376400
C	-0.01948422	2.80538799	-2.81949600
C	0.01224087	1.57806899	-3.43485500
C	0.04004895	0.41412199	-2.66035400
C	-0.05039431	4.09767499	0.67843100
C	-0.05039431	4.09767499	-0.67843100
H	0.07182902	-0.55514500	3.12935700
H	0.01760087	1.48549599	4.51050100
H	-0.03968729	3.71705499	3.40138800
H	-0.06916538	5.02864299	1.22781300
H	-0.06916538	5.02864299	-1.22781300
H	-0.03968729	3.71705499	-3.40138800
H	0.01760087	1.48549599	-4.51050100
H	0.07182902	-0.55514500	-3.12935700

Table D.10. Optimised Gas-Phase Atomic Coordinates (Å) of $WF_6(NC_5H_5)_2$

W	0.00000000	0.00000000	0.65558900
F	1.28356900	0.00000000	-0.72517800
F	-1.28356900	0.00000000	-0.72517800
F	1.18442900	1.15441500	1.55843800
F	-1.18442900	1.15441500	1.55843800
F	1.18442900	-1.15441500	1.55843800
F	-1.18442900	-1.15441500	1.55843800
N	0.00000000	2.21114900	-0.46704600
C	0.00000000	3.32897400	0.26127400
C	0.00000000	4.58804900	-0.31966200
C	0.00000000	4.68888000	-1.70315100
C	0.00000000	3.52303600	-2.45612700
C	0.00000000	2.30390800	-1.79747000
H	0.00000000	3.19795200	1.33188200
H	0.00000000	5.46595900	0.30978300
H	0.00000000	5.65679100	-2.18581700
H	0.00000000	3.54872100	-3.53612800
H	0.00000000	1.37237100	-2.34164800
N	0.00000000	-2.21114900	-0.46704600
C	0.00000000	-2.30390800	-1.79747000
C	0.00000000	-3.52303600	-2.45612700
C	0.00000000	-4.68888000	-1.70315100
C	0.00000000	-4.58804900	-0.31966200
C	0.00000000	-3.32897400	0.26127400
H	0.00000000	-1.37237100	-2.34164800
H	0.00000000	-3.54872100	-3.53612800
H	0.00000000	-5.65679100	-2.18581700
H	0.00000000	-5.46595900	0.30978300
H	0.00000000	-3.19795200	1.33188200

Table D.11. Optimised Gas-Phase Atomic Coordinates (Å) of $[WF_5]^+$

D_{3h}

W	0.00000000	0.00000000	0.00000000
F	0.00000000	0.00000000	1.81005900
F	0.00000000	1.78192700	0.00000000
F	0.00000000	0.00000000	-1.81005900
F	1.54319400	-0.89096400	0.00000000
F	-1.54319400	-0.89096400	0.00000000

C_{4v}

W	0.00000000	0.00000000	-0.02011700
F	0.00000000	1.72588700	0.48912000
F	-1.72588700	0.00000000	0.48912000
F	0.00000000	-1.72588700	0.48912000
F	1.72588700	0.00000000	0.48912000
F	0.00000000	0.00000000	-1.79107300

Table D.12. Optimised Gas-Phase Atomic Coordinates (Å) of $[WF_4(2,2'\text{-bipy})_2]^{2+}$

W	-0.00000000	-0.00000000	0.00000000
F	0.00000000	1.75563100	0.58555800
F	1.75563100	-0.00000000	-0.58555800
F	0.00000000	-1.75563100	0.58555800
F	-1.75563100	0.00000000	-0.58555800
N	0.00000000	1.32994900	-1.90226300
N	0.00000000	-1.32994900	-1.90226300
C	0.00000000	2.67123800	-1.83948200
C	0.00000000	3.47141100	-2.96851000
C	0.00000000	2.86972300	-4.21553400
C	0.00000000	1.48625700	-4.28321300
C	0.00000000	0.73178900	-3.11525500
C	0.00000000	-0.73178900	-3.11525500
C	0.00000000	-1.48625700	-4.28321300
C	0.00000000	-2.86972300	-4.21553400
C	0.00000000	-3.47141100	-2.96851000
C	0.00000000	-2.67123800	-1.83948200
H	0.00000000	3.12057100	-0.86251700
H	0.00000000	4.54504700	-2.85328500
H	0.00000000	3.46138000	-5.12015400
H	0.00000000	0.99965600	-5.24463800
H	0.00000000	-0.99965600	-5.24463800
H	0.00000000	-3.46138000	-5.12015400
H	0.00000000	-4.54504700	-2.85328500
H	0.00000000	-3.12057100	-0.86251700
N	1.32994900	-0.00000000	1.90226300
N	-1.32994900	0.00000000	1.90226300
C	2.67123800	-0.00000000	1.83948200
C	3.47141100	-0.00000000	2.96851000
C	2.86972300	-0.00000000	4.21553400
C	1.48625700	0.00000000	4.28321300
C	0.73178900	0.00000000	3.11525500
C	-0.73178900	0.00000000	3.11525500
C	-1.48625700	0.00000000	4.28321300
C	-2.86972300	0.00000000	4.21553400
C	-3.47141100	0.00000000	2.96851000
C	-2.67123800	0.00000000	1.83948200
H	3.12057100	-0.00000000	0.86251700
H	4.54504700	-0.00000000	2.85328500
H	3.46138000	-0.00000000	5.12015400
H	0.99965600	0.00000000	5.24463800
H	-0.99965600	0.00000000	5.24463800
H	-3.46138000	0.00000000	5.12015400
H	-4.54504700	0.00000000	2.85328500
H	-3.12057100	0.00000000	0.86251700

Table D.13. Optimised Gas-Phase Atomic Coordinates (Å) of 2,2′-bipy

N	-0.39768682	1.35644909	-1.12069207
N	0.39768682	-1.35644909	-1.12069207
C	-0.40765343	2.68597307	-1.14340207
C	-0.02331751	3.47944708	-0.06793807
C	0.39321381	2.84640755	1.09378993
C	0.40364417	1.46026099	1.13192093
C	-0.00002589	0.74551932	0.00067193
C	0.00002589	-0.74551932	0.00067193
C	-0.40364417	-1.46026099	1.13192093
C	-0.39321381	-2.84640755	1.09378993
C	0.02331751	-3.47944708	-0.06793807
C	0.40765343	-2.68597307	-1.14340207
H	-0.74179217	3.14264118	-2.06859207
H	-0.04863491	4.55744910	-0.14563307
H	0.71224608	3.42024432	1.95376693
H	0.74352934	0.93799240	2.01504693
H	-0.74352934	-0.93799240	2.01504693
H	-0.71224608	-3.42024432	1.95376693
H	0.04863491	-4.55744910	-0.14563307
H	0.74179217	-3.14264118	-2.06859207

Table D.14. Optimised Gas-Phase Atomic Coordinates (Å) of 1,10-phen

N	0.00000000	1.38322000	-1.55604215
N	0.00000000	-1.38322000	-1.55604215
C	0.00000000	2.70012500	-1.54238315
C	0.00000000	3.47114100	-0.36845415
C	0.00000000	2.81794500	0.83849085
C	0.00000000	1.41131600	0.86503985
C	0.00000000	0.72762500	-0.37906815
C	0.00000000	-0.72762500	-0.37906815
C	0.00000000	-1.41131600	0.86503985
C	0.00000000	-2.81794500	0.83849085
C	0.00000000	-3.47114100	-0.36845415
C	0.00000000	-2.70012500	-1.54238315
C	0.00000000	0.67696400	2.09206085
C	0.00000000	-0.67696400	2.09206085
H	0.00000000	3.19017300	-2.51053415
H	0.00000000	4.55077000	-0.42681615
H	0.00000000	3.36750000	1.77160785
H	0.00000000	1.22836200	3.02392085
H	0.00000000	-1.22836200	3.02392085
H	0.00000000	-3.36750000	1.77160785
H	0.00000000	-4.55077000	-0.42681615
H	0.00000000	-3.19017300	-2.51053415

Appendix E – Supporting Information for Chapter 7

Table E.1. Crystallographic Data Collection and Refinement Parameters for $WF_5(NC_5H_5)_2$

	$WF_5(NC_5H_5)_2$
Identification code	MG18015b
Empirical formula	$C_{10}H_{10}F_5N_2W$
Formula weight	437.05
T (K)	111.5(5)
Crystal system	monoclinic
Space group	*C*2/*c*
a (Å)	8.1621(4)
b (Å)	11.1419(5)
c (Å)	13.6465(7)
α (°)	90
β (°)	107.055(6)
γ (°)	90
V (Å^3)	1186.45(11)
Z	4
ρ_{calc} (g cm^{-3})	2.447
μ (mm^{-1})	9.783
F(000)	812.0
Crystal size (mm^3)	0.129 × 0.079 × 0.051
GooF	1.064
Final *R* indexes [I ≥ 2σ (I)]	R_1 = 0.0099, wR_2 = 0.0234
Final *R* indexes [all data]	R_1 = 0.0100, wR_2 = 0.0235
Largest diff. peak/hole (e Å^{-3})	1.05/-0.42

[a] $R_1 = \sum||F_o| - |F_c||/\sum|F_o|$. [b] $wR_2 = [\sum[w(F_o^2 - F_c^2)^2]/\sum w(F_o^4)]^{1/2}$.

Table E.2. Vibrational Frequencies (cm^{-1}) of NC_5H_5 and $[WF_5(NC_5H_5)_3]^+$

NC_5H_5		$[WF_5(NC_5H_5)_3]^+$		Assignment (C_s)[d]
exptl[a]	calcd[b]	exptl[c]	calcd[b]	
3173(1)				C–H stretching modes, combination modes, and overtones
3145(1)				
3091(5)		3150(6)		
			3245(72)[5]	
3056(39)	3194(277)[8]	3097(33)	3240(97)[2]	
			3239(68)[5]	
			3237(55)[1]	
3036 sh	3186(37)[26]	3077 sh	3232(29)[1]	
			3228(71)[1]	
			3213(294)[<1]	
3025 sh	3171(99)[5]	3038(3)	3213(146)[<1]	
			3212(187)[<1]	
			3208(106)[<1]	
2988(5)	3149(79)[4]	3014(2)	3208(93)[<0.1]	
			3208(92)[<1]	
			3194(74)[1]	
2955(5)	3147(96)[27]	2974(2)	3194(70)[1]	
			3193(81)[1]	
2908(1)		2935(2)		
2871(1)		2904(2)		
2453(1)				
1597(5)	1627(11)[25]	1610(17)	1652(14)[19]	C–N/C–C stretching modes
			1651(14)[20]	

1581(9)			1649(3)[19]	C–N/C–C stretching modes and in-plane ring deformations
			1620(12)[1]	
1573(7)	1621(8)[8]	1575(16)	1617(11)[<1]	
			1617(10)[<1]	
			1531(9)[1]	
1482(3)	1518(2)[2]		1531(<1)[10]	
			1529(<1)[9]	
			1489(<1)[43]	
	1477(<1)[28]	1495(7)	1487(<1)[37]	
			1486(<1)[21]	
			1401(<0.1)[5]	
	1391(<1)[<1]		1399(<0.1)[1]	
			1397(<0.1)[1]	
			1297(<1)[3]	
	1283(2)[<0.1]		1291(<1)[<0.1]	
			1289(<1)[3]	
			1256(12)[6]	in-plane ring deformations
1217(8)	1244(9)[4]	1225[e]	1251(2)[28]	
			1250(7)[37]	
			1190(2)[7]	
1146(2)	1173(2)[2]	1160(4)	1190(2)[1]	
			1189(2)[3]	
			1117(<1)[2]	
1068(2)	1096(2)[4]		1114(1)[1]	
			1114(<1)[<1]	
			1096(3)[2]	
	1080(<1)[<1]	1070(7)	1095(<1)[42]	

			1094(<0.1)[18]	
			1064(106)[1]	
1030(75)	1052(33)[7]	1044(96)	1062(12)[1]	
			1061(24)[0]	in-plane ring deformations
			1045(<1)[<1]	
	1021(<0.1)[<0.1]		1045(<0.1)[<1]	
			1042(<1)[<1]	
			1038(41)[13]	$\nu_s(NC_5)$ [3]
990(100)	1013(26)[5]	1022(73)	1036(39)[23]	$\nu_s(NC_5)$ [1 + 2]
980(5)			1031(5)[19]	$\nu_s(NC_5)$ [1 – 2]
			1020(<0.1)[<1]	
	1010(<0.1)[0]		1019(<0.1)[1]	
			1012(<0.1)[<0.1]	
			987(1)[<1]	
	962(<0.1)[<0.1]		986(<1)[1]	
			977(<0.1)[<0.1]	
			891(<0.1)[<0.1]	
	900(<0.1)[0]		890(<0.1)[<0.1]	out-of-plane ring deformations
			883(<0.1)[<0.1]	
			789(1)[17]	
	768(<1)[7]		786(<0.1)[43]	
			785(<1)[17]	
			714(<1)[37]	
	720(<0.1)[64]		712(<0.1)[108]	
			707(<0.1)[22]	
		667(100)	679(92)[37]	A′, $\nu_s(WF_5)$
652(5)	670(4)[<1]		668(3)[8]	in-plane ring deformation

		649(23)	665(5)[<1]	in-plane ring deformation
			664(5)[1]	
			654(<1)[28]	
603(3)	617(3)[4]		651(1)[51]	
			650(1)[50]	
		629(6)	636(2)[80]	A″, $\nu_{as}(WF_5)$ [1 – 2 – 3 + 4 + 5]
			633(3)[92]	A″, $\nu_{as}(WF_5)$ [1 + 2 + 3 – 4 – 5]
			607(3)[75]	A′, $\nu_{as}(WF_5)$ [1 + 2 – 3 – 4 – 5]
			571(2)[34]	A′, $\nu_{as}(WF_5)$ [1 – 2 + 3 + 4 – 5]
			483(<0.1)[2]	out-of-plane ring deformations
406(1)	421(<1)[4]		477(<1)[2]	
			470(<1)[10]	
		419(2)	414(2)[16]	A′, $\delta(WF_2)$ [1 + 2]
			404(<0.1)[<1]	out-of-plane ring deformations
	385(<0.1)[0]		403(<1)[1]	
			402(<0.1)[<1]	
		371(4)	369(1)[11]	A″, $\delta_{as}(WF_4)$ [2 + 3 – 4 – 5]
			360(2)[56]	A′, $\delta_s(WF_4)$ [2 + 3 + 4 + 5]
			341(1)[4]	A′, $\delta_{as}(WF_4)$ [2 – 3 – 4 + 5]
		297(2)	306(1)[5]	A″, δ(F(1)WF(3) – F(1)WF(5)) + τ(F(2)WF(4))
			286(2)[14]	A′, δ(F(1)WF(2)) + δ(F(4)WN(3))
			285(1)[10]	A′, ρ(F(1)WF(4)) + ω(F(3)WF(5)) + ω(N(1)WN(2))
			265(1)[12]	A″, δ(F(1)WF(3) – F(1)WF(5)) + τ(F(2)WF(4))
			245(1)[1]	A″, τ(F(1)WF(4))
			233(1)[4]	A′, δ(N(1)WN(2))
		203 sh	222(1)[3]	rocking and twisting modes
			196(<1)[3]	

	190 sh	184(1)[<1]	rocking and twisting modes
		175(2)[8]	
		168(2)[13]	A′, $\nu_{as}(WN_3)$ [1 + 2 – 3]
	175(33)	151(8)[2]	A′, $\nu_s(WN_3)$
	158 sh	130(2)[3]	A″, $\nu_{as}(WN_2)$ [1 – 2]
	107(54)	108(3)[1]	twisting modes
		86(1)[1]	
		63(3)[2]	
		55(4)[<1]	
		48(3)[<1]	
		46(8)[1]	
		44(3)[1]	
		35(1)[1]	

[a]From Nieboer, J.; Yu, X.; Chaudhary, P.; Mercier, H. P. A.; Gerken, M. *Z. Anorg. Allg. Chem.* **2012**, *638* (3–4), 520–525. [b]Calculated at the B3LYP/aVTZ level of theory. Absolute Raman intensities ($Å^4\ u^{-1}$) are given in parentheses and IR intensities (km mol^{-1}) are given in square brackets. [c]Recorded in a flame-sealed glass m.p. capillary at ambient temperature. Normalised Raman intensities are given in parentheses. Shoulders are denoted as sh. Bands corresponding to $[O_3SCF_3]^-$ are observed at 1274(3), 1225(13), 1033(46), 755(16), 573(7), 349(16), and 313(13) cm^{-1}. [d]Symmetry assignments are made based on the approximate C_s symmetry of the WF_5N_3 moiety. Abbreviations denote stretch (ν), bend (δ), rock (ρ), and twist (τ). Numbers in square brackets denote the fluorine or nitrogen atoms involved in the stretching mode. Atom labels are as in Figure 7.2a. [e]Expected band overlaps with $[O_3SCF_3]^-$.

Table E.3. Vibrational Frequencies (cm^{-1}) of NC_5H_5 and $WF_5(NC_5H_5)_2$

NC_5H_5		$WF_5(NC_5H_5)_2$		Assignment (C_2)[d]
exptl[a]	calcd[b]	exptl[c]	calcd[b]	
3173(1)				C–H stretching modes, combination modes, and overtones
3145(1)				
3091(5)		3155(1)		
3056(39)	3194(277)[8]	3098(7)	3225(247)[1]	
			3225(67)[13]	
3036 sh	3186(37)[26]		3222(5)[<1]	
			3222(1)[1]	
3025 sh	3171(99)[5]	3085(5)	3205(313)[<1]	
			3205(42)[5]	
2988(5)	3149(79)[4]		3200(150)[3]	
			3200(64)[6]	
2955(5)	3147(96)[27]		3181(103)[1]	
			3181(39)[6]	
2908(1)				
2871(1)				
2453(1)				
1597(5)	1627(11)[25]	1611(11)	1654(23)[35]	C–N/C–C stretching modes and in-plane ring deformations
			1654(104)[4]	
1581(9)				
1573(7)	1621(8)[8]	1577(5)	1620(3)[3]	
			1620(15)[1]	
1482(3)	1518(2)[2]	1490(2)	1529(3)[1]	
			1529(1)[10]	
	1477(<1)[28]		1489(<1)[47]	

	1391(<1)[<1]		1488(<1)[20] 1399(<0.1)[2] 1399(<0.1)[1]	C–N/C–C stretching modes and in-plane ring deformations
	1283(2)[<0.1]		1292(<0.1)[3] 1292(<0.1)[1]	
1217(8)	1244(9)[4]	1219(11)	1251(29)[2] 1249(3)[37]	in-plane ring deformations
1146(2)	1173(2)[2]	1164(6)	1181(2)[5] 1181(4)[2]	
1068(2)	1096(2)[4]		1105(<1)[1] 1104(<1)[<1]	
	1080(<1)[<1]	1069(1)	1097(25)[2] 1096(3)[30]	
1030(75)	1052(33)[7]	1049(8)	1065(8)[2] 1065(<1)[15]	
990(100)	1013(26)[5]	1024(100)	1040(258)[<1]	A, $\nu_s(NC_5)$ (s)
980(5)		1016(5)	1038(20)[7]	B, $\nu_s(NC_5)$ (as)
	1021(<0.1)[<0.1]		1029(<0.1)[<0.1] 1029(<0.1)[<0.1]	out-of-plane ring deformations
	1010(<0.1)[0]	970(1)	1013(<1)[<0.1] 1013(<0.1)[<0.1]	
	962(<0.1)[<0.1]	936(1)	978(<1)[<1] 978(<0.1)[<1]	
	900(<0.1)[0]	872(1)	888(4)[<0.1] 888(<1)[<0.1]	
	768(<1)[7]		785(<0.1)[15] 784(<0.1)[26]	

	720(<0.1)[64]		709(<0.1)[52] 709(<0.1)[72]	out-of-plane ring deformations
652(5)	670(4)[<1]		667(3)[2] 667(6)[1]	
		655(36)	660(18)[1]	A, $\nu_s(WF_5) - \delta(C_oNC_o + C_mC_pC_m)$ (s)
603(3)	617(3)[4]	650(17)	655(5)[12]	B, $\delta(C_oNC_o + C_mC_pC_m)$ (as)
		630(31)	636(5)[43]	A, $\nu_s(WF_5) + \delta(C_oNC_o + C_mC_pC_m)$ (s)
		588(3)	607(9)[125]	A, $\nu_s(WF_{2,\,ax}) + \nu_{as}(WF_{3,\,eq})$
			590(<0.1)[179]	B, $\nu_{as}(WF_{2,\,ax})$
		562(9)	555(11)[19]	A, $\nu_s(WF_{2,\,ax}) + \nu_s(WF_{3,\,eq})$
		505(1)	522(3)[98]	B, $\nu_{as}(WF_{2,\,eq})$
406(1)	421(<1)[4]	469(1)	480(<1)[7] 476(<1)[4]	out-of-plane ring deformations
	385(<0.1)[0]	394(3)	400(2)[<1] 400(<1)[<0.1]	
			397(2)[13]	A, $\delta_{ip}(WF_{2,\,eq})$
		344(1)	340(<1)[40]	B, $\delta_{ip}(F_{eq}WN)$
		291(1)	289(<1)[44]	B, $\rho(WF_{2,\,eq})$
		270(7)	275(1)[7]	B, $\delta_{op}(F_{ax}WF_{eq})$
		249(5)	243(<1)[4]	B, $\delta_s(WF_3N_{2,\,eq})$
			240(1)[4]	A, $\delta(WF_{2,\,ax}) + \delta_{ip}(WN_2)$
		198(3)	204(1)[21]	B, $\omega(WF_{2,\,ax})$
		182(6)	188(1)[9]	A, $\delta(WF_{2,\,ax}) + \tau(WF_{2,\,eq})$
			179(<1)[6]	B, $\delta_{op}(WF_{3,\,eq}) - \delta_{op}(WN_2)$
			177(<1)[2]	A, $\tau(WF_{2,\,eq} + WN_2)$
			163(<0.1)[1]	B, $\nu_{as}(WN_2)$
		167(9)	154(2)[<1]	A, $\nu_s(WN_2)$

	134(36)	140(2)[1]	twisting modes
	102(18)	101(4)[1]	
		65(1)[<0.1]	
		53(<1)[1]	
		48(4)[3]	
		40(10)[<0.1]	
		30(2)[3]	

[a]From Nieboer, J.; Yu, X.; Chaudhary, P.; Mercier, H. P. A.; Gerken, M. *Z. Anorg. Allg. Chem.* **2012**, *638* (3–4), 520–525. [b]Calculated at the B3LYP/aVTZ level of theory. Absolute Raman intensities ($Å^4$ u^{-1}) are given in parentheses and IR intensities (km mol^{-1}) are given in square brackets. [c]Recorded in a flame-sealed glass m.p. capillary at ambient temperature. Normalised Raman intensities are given in parentheses. Shoulders are denoted as sh. Bands corresponding to $WF_6(NC_5H_5)_2$ are observed at 1044 sh and 662 sh cm^{-1}. [d]Abbreviations denote stretch (ν), bend (δ), twist (τ), wag (ω), axial (ax), equatorial (eq), in the WF_3N_2 plane (ip), and out of the WF_3N_2 plane (op). Symmetric and antisymmetric coupling of the two pyridyl ligands are denoted as s and as, respectively.

Table E.4. Optimised Gas-Phase Atomic Coordinates (Å) of $[WF_5(NC_5H_5)_3]^+$

W	-0.32888786	-0.06114297	-0.47836909
F	0.83948815	-0.30862602	-1.91336207
F	-0.31057088	0.22192301	1.37842191
F	-0.83949476	1.71920906	-0.67972009
F	-1.45491385	-0.24530290	-1.96952211
F	-0.84744897	-1.83459994	-0.23101711
N	1.49451805	-1.35615908	0.34018493
C	1.98123604	-1.24451911	1.58357594
C	2.95630398	-2.09644117	2.07337095
C	3.44529094	-3.10488019	1.25596395
C	2.93415496	-3.22375915	-0.02881606
C	1.96094901	-2.33598510	-0.45066707
H	1.57069207	-0.46022109	2.19743794
H	3.31499497	-1.96443720	3.08340096
H	4.20441090	-3.78650423	1.61341896
H	3.27369492	-3.99575917	-0.70329506
H	1.53907802	-2.40780007	-1.44052808
N	1.54369521	1.38599292	-0.09287405
C	1.42633924	2.33549992	0.84896096
C	2.40782229	3.28351987	1.07255398
C	3.55577130	3.26308581	0.29246500
C	3.67436227	2.28571381	-0.68386301
C	2.65180622	1.36638487	-0.84770103
H	0.52050023	2.33209597	1.43234394
H	2.26153032	4.02594287	1.84305598
H	4.33725834	3.99530177	0.44006202
H	4.54276428	2.22813177	-1.32321599
H	2.71100119	0.60240787	-1.60427703
N	-2.56024987	0.03277615	0.27102987
C	-2.96545183	0.99835616	1.10621387
C	-4.27908084	1.10592723	1.52489385
C	-5.20823288	0.18215628	1.06672183
C	-4.78468392	-0.81501773	0.20045883
C	-3.45461991	-0.85641280	-0.17996615
H	-2.21823780	1.69989912	1.43968589
H	-4.55951280	1.90423824	2.19578285
H	-6.24232888	0.24101234	1.37633081
H	-5.46890495	-1.55526469	-0.18659619
H	-3.09032094	-1.60793482	-0.86087915

Table E.5. Optimised Gas-Phase Atomic Coordinates (Å) of $[WF_5(NC_5H_5)_2]^+$

W	-0.51219689	0.02299701	0.00000000
F	-1.99228291	1.12545398	0.00000000
F	0.79103211	0.06542003	1.32473200
F	-1.47820988	-0.80203201	1.34151100
F	-1.47820988	-0.80203201	-1.34151100
F	0.79103211	0.06542003	-1.32473200
N	0.29079507	2.17056202	0.00000000
C	1.63120507	2.33077505	0.00000000
C	2.22150104	3.57683906	0.00000000
C	1.41650502	4.70959905	0.00000000
C	0.04043403	4.54525602	0.00000000
C	-0.49055695	3.26799001	0.00000000
H	2.23192908	1.43689106	0.00000000
H	3.29885404	3.64884008	0.00000000
H	1.85496301	5.69772305	0.00000000
H	-0.63140099	5.39052501	0.00000000
H	-1.55558295	3.11520699	0.00000000
N	0.28712915	-2.10816198	0.00000000
C	0.51776616	-2.74596997	1.16043600
C	0.99085118	-4.04367896	1.19530500
C	1.23206819	-4.70727396	0.00000000
C	0.99085118	-4.04367896	-1.19530500
C	0.51776616	-2.74596997	-1.16043600
H	0.31334515	-2.20019697	2.06736000
H	1.16091919	-4.51834896	2.15003700
H	1.59920921	-5.72406795	0.00000000
H	1.16091919	-4.51834896	-2.15003700
H	0.31334515	-2.20019697	-2.06736000

Table E.6. Optimised Gas-Phase Atomic Coordinates (Å) of $[WF_5(NC_5H_5)(4\text{-H-pypy})]^+$

W	-1.18958899	-0.50090087	-0.30941829
F	-0.50667794	-1.79178646	-1.47113672
F	-0.68393303	1.30288308	-0.11289367
F	-1.74592997	0.15793368	-1.96336108
F	-2.45767196	-1.85426095	-0.14558377
F	-1.33069602	-0.54772350	1.56361069
N	0.83394900	-0.68492102	0.25373168
C	1.31179397	0.11079064	1.28475696
C	2.57886596	0.10416352	1.73214298
C	3.62410099	-0.74844226	1.12660371
C	3.04115803	-1.66032093	0.12096439
C	1.75506803	-1.58285382	-0.26438561
H	0.58840895	0.75106047	1.75918516
H	2.83478993	0.73233724	2.57360720
H	4.23512499	-1.26433049	1.86974255
H	3.66277405	-2.43088977	-0.31234386
H	1.38216906	-2.26865758	-1.00328984
N	4.74292598	0.16900500	0.44329504
C	6.01634898	0.09183888	0.85622904
C	6.99933097	0.86796610	0.27387832
C	6.65062998	1.73664144	-0.75259939
C	5.32449898	1.80240855	-1.16619840
C	4.38743499	1.00172733	-0.54648968
H	6.22137798	-0.60299438	1.65755381
H	8.01736797	0.78678500	0.62410531
H	7.40177897	2.35423061	-1.22460717
H	5.01454798	2.46485182	-1.96041218
H	3.34217499	1.00042840	-0.81580970
N	-3.17110002	0.60544494	0.14844004
C	-3.46675403	1.75659414	-0.47234557
C	-4.64083605	2.44250104	-0.21998136
C	-5.53853306	1.92521671	0.70348645
C	-5.22566304	0.73539449	1.34558805
C	-4.03330803	0.10274062	1.04417786
H	-2.74343102	2.12192940	-1.18311643
H	-4.83959906	3.36450421	-0.74561705
H	-6.46488907	2.43955661	0.91838160
H	-5.89131305	0.29295124	2.07154889
H	-3.75276202	-0.82341254	1.51907255

Table E.7. Optimised Gas-Phase Atomic Coordinates (Å) of $WF_5(NC_5H_5)$(4-pypy)

W	1.50764202	-0.84718612	0.10929479
F	3.26819201	-1.53722713	0.12937167
F	1.44864501	-0.10628683	-1.65870409
F	0.91508600	-2.28478593	-0.99120845
F	0.93205201	-2.11952833	1.40714658
F	1.37242803	0.14887661	1.73886195
N	-0.66140798	-0.26051010	0.03352589
C	-1.32680498	-0.17625490	-1.13475409
C	-2.68126398	0.04618212	-1.21757805
C	-3.44123798	0.19379493	-0.04289203
C	-2.73958298	0.09315373	1.17242595
C	-1.38407398	-0.13758528	1.16415391
H	-0.72845499	-0.28640175	-2.02502711
H	-3.12198799	0.13673029	-2.19682704
H	-3.24136897	0.13888557	2.12514796
H	-0.83734097	-0.24846144	2.08697589
N	-4.81275798	0.42023595	-0.08023599
C	-5.57888498	0.07751514	-1.20242204
C	-6.92236498	0.29941315	-1.23983900
C	-7.60041898	0.88317997	-0.15696990
C	-6.82969097	1.22422678	0.96663015
C	-5.48660597	0.99940577	1.00331411
H	-5.05729999	-0.42181073	-1.99801112
H	-7.45715199	-0.00594470	-2.12815105
H	-8.66376097	1.05916498	-0.18604487
H	-7.28471696	1.69028764	1.82925523
H	-4.87591297	1.30440863	1.83299616
N	2.94313903	1.06953290	-0.03587690
C	3.90667802	1.03132604	-0.96650591
C	4.79534903	2.07483307	-1.16101574
C	4.68240204	3.21043894	-0.37115655
C	3.68338704	3.25182979	0.58954446
C	2.83949803	2.16052377	0.72999728
H	3.95942502	0.13480114	-1.56381806
H	5.55914803	1.98920319	-1.92009076
H	5.36004904	4.04337796	-0.50088441
H	3.55290905	4.11131768	1.23095560
H	2.06221004	2.14006965	1.47701428

Table E.8. Optimised Gas-Phase Atomic Coordinates (Å) of $[WF_5(NC_5H_5)_2]^-$

W	-0.55208424	-0.23693064	0.00000000
F	-0.38901360	1.74679630	0.00000000
F	-1.16515485	-2.10393844	0.00000000
F	1.14103542	-1.26310319	0.00000000
F	-2.00457616	0.02094083	1.26453000
F	-2.00457616	0.02094083	-1.26453000
N	0.45334387	0.11121503	2.00482700
C	1.42080462	-0.65436828	2.55206700
C	1.93629669	-0.42748545	3.81432300
C	1.45794304	0.63948270	4.57158100
C	0.46245330	1.43209303	4.01099500
C	-0.01528480	1.14210618	2.74595800
H	1.76775336	-1.46354740	1.93088300
H	2.70478948	-1.08713670	4.19457200
H	1.84626111	0.84328858	5.56089100
H	0.04939057	2.27663216	4.54607200
H	-0.78747760	1.73035943	2.28119200
N	0.45334387	0.11121503	-2.00482700
C	-0.01528480	1.14210618	-2.74595800
C	0.46245330	1.43209303	-4.01099500
C	1.45794304	0.63948270	-4.57158100
C	1.93629669	-0.42748545	-3.81432300
C	1.42080462	-0.65436828	-2.55206700
H	-0.78747760	1.73035943	-2.28119200
H	0.04939057	2.27663216	-4.54607200
H	1.84626111	0.84328858	-5.56089100
H	2.70478948	-1.08713670	-4.19457200
H	1.76775336	-1.46354740	-1.93088300

Table E.9. Optimised Gas-Phase Atomic Coordinates (Å) of $WF_5(NC_5H_5)_2$

W	0.00000000	0.00000000	0.45344400
F	0.00000000	0.00000000	-1.45022700
F	-1.91486500	0.05365200	0.31716800
F	1.91486500	-0.05365200	0.31716800
F	0.11295500	1.16307800	1.95430400
F	-0.11295500	-1.16307800	1.95430400
N	-0.00279700	2.17230000	-0.28369400
C	-0.94653800	2.60128900	-1.13062300
C	-0.98332500	3.90760600	-1.58832600
C	0.00000000	4.79362300	-1.17135200
C	0.98186600	4.34105500	-0.30094400
C	0.94194000	3.02590800	0.12971600
H	-1.68152400	1.87112900	-1.43246900
H	-1.77180700	4.21506400	-2.25945700
H	0.00049400	5.81838000	-1.51710500
H	1.76967400	4.99214700	0.04837600
H	1.67015300	2.63097300	0.82103700
N	0.00279700	-2.17230000	-0.28369400
C	-0.94194000	-3.02590800	0.12971600
C	-0.98186600	-4.34105500	-0.30094400
C	0.00000000	-4.79362300	-1.17135200
C	0.98332500	-3.90760600	-1.58832600
C	0.94653800	-2.60128900	-1.13062300
H	-1.67015300	-2.63097300	0.82103700
H	-1.76967400	-4.99214700	0.04837600
H	-0.00049400	-5.81838000	-1.51710500
H	1.77180700	-4.21506400	-2.25945700
H	1.68152400	-1.87112900	-1.43246900

Table E.10. Optimised Gas-Phase Atomic Coordinates (Å) of $[4\text{-pypy}]^+$

N	0.00000000	0.00000000	3.49493400
C	-0.53362843	1.01019929	2.81276000
C	-0.56166641	1.06496333	1.42168100
C	0.00000000	0.00000000	0.73652100
C	0.56166641	-1.06496333	1.42168100
C	0.53362843	-1.01019929	2.81276000
H	-0.96739819	1.81348645	3.39507400
H	-1.02816385	1.89490736	0.90997500
H	1.02816385	-1.89490736	0.90997500
H	0.96739819	-1.81348645	3.39507400
N	0.00000000	0.00000000	-0.71908200
C	0.53826344	1.04626902	-1.38719200
C	0.54534117	1.06906544	-2.76431200
C	0.00000000	0.00000000	-3.46676200
C	-0.54534117	-1.06906544	-2.76431200
C	-0.53826344	-1.04626902	-1.38719200
H	0.96454423	1.82926913	-0.78007800
H	0.98480262	1.91361831	-3.27349300
H	0.00000000	0.00000000	-4.54771800
H	-0.98480262	-1.91361831	-3.27349300
H	-0.96454423	-1.82926913	-0.78007800

Table E.11. Optimised Gas-Phase Atomic Coordinates (Å) of $[C_5H_5NH]^+$

N	0.00000000	0.00000000	1.30407798
C	0.00000000	1.18497710	0.66356632
C	0.00000000	1.20662031	-0.71358558
C	0.00000000	0.00000000	-1.40898902
C	0.00000000	-1.20662031	-0.71358558
C	0.00000000	-1.18497710	0.66356632
H	0.00000000	0.00000000	2.31756198
H	0.00000000	2.07117732	1.27977731
H	0.00000000	2.15457064	-1.23004331
H	0.00000000	0.00000000	-2.49027402
H	0.00000000	-2.15457064	-1.23004331
H	0.00000000	-2.07117732	1.27977731

Table E.12. Optimised Gas-Phase Atomic Coordinates (Å) of $[C_5H_5N]^{\bullet+}$

N	0.00000000	0.00000000	1.27153481
C	0.00000000	1.19563500	0.74558481
C	0.00000000	1.21057500	-0.65402919
C	0.00000000	0.00000000	-1.33713119
C	0.00000000	-1.21057500	-0.65402919
C	0.00000000	-1.19563500	0.74558481
H	0.00000000	2.07468200	1.37865281
H	0.00000000	2.16766200	-1.15724719
H	0.00000000	0.00000000	-2.41943519
H	0.00000000	-2.16766200	-1.15724719
H	0.00000000	-2.07468200	1.37865281

Table E.13. Optimised Gas-Phase Atomic Coordinates (Å) of C_5H_5N

N	0.00000000	0.00000000	1.41219002
C	0.00000000	1.13978200	0.71943802
C	0.00000000	1.19342900	-0.66967898
C	0.00000000	0.00000000	-1.37872898
C	0.00000000	-1.19342900	-0.66967898
C	0.00000000	-1.13978200	0.71943802
H	0.00000000	2.05355900	1.30293402
H	0.00000000	2.14805000	-1.17760598
H	0.00000000	0.00000000	-2.46072098
H	0.00000000	-2.14805000	-1.17760598
H	0.00000000	-2.05355900	1.30293402

Table E.14. Optimised Gas-Phase Atomic Coordinates (Å) of $[WF_6]^-$

W	0.00000000	0.00000000	0.00000000
F	0.00000000	1.92622600	0.00000000
F	0.00000000	0.00000000	1.86886500
F	0.00000000	-1.92622600	0.00000000
F	0.00000000	0.00000000	-1.86886500
F	-1.92622600	0.00000000	0.00000000
F	1.92622600	0.00000000	0.00000000

Table E.15. Optimised Gas-Phase Atomic Coordinates (Å) of $[WF_4(NC_5H_5)_4]^+$

W	0.00000000	0.00000000	0.00000000
F	0.67153500	0.99852200	1.49283300
F	-0.67153500	-0.99852200	1.49283300
F	0.67153500	-0.99852200	-1.49283300
F	-0.67153500	0.99852200	-1.49283300
N	1.80702000	-1.27941400	0.78865000
C	1.97513900	-1.39910700	2.11761100
C	3.01198100	-2.12577300	2.67496000
C	3.92112200	-2.75872300	1.83970400
C	3.75232100	-2.63461300	0.46898300
C	2.68996100	-1.89174500	-0.01713500
H	1.25169500	-0.89990700	2.73806400
H	3.09365400	-2.19057300	3.74995600
H	4.73974100	-3.33538900	2.24746500
H	4.42844900	-3.10734000	-0.22801500
H	2.52467400	-1.78485100	-1.07534600
N	1.80702000	1.27941400	-0.78865000
C	2.68996100	1.89174500	0.01713500
C	3.75232100	2.63461300	-0.46898300
C	3.92112200	2.75872300	-1.83970400
C	3.01198100	2.12577300	-2.67496000
C	1.97513900	1.39910700	-2.11761100
H	2.52467400	1.78485100	1.07534600
H	4.42844900	3.10734000	0.22801500
H	4.73974100	3.33538900	-2.24746500
H	3.09365400	2.19057300	-3.74995600
H	1.25169500	0.89990700	-2.73806400
N	-1.80702000	1.27941400	0.78865000
C	-1.97513900	1.39910700	2.11761100
C	-3.01198100	2.12577300	2.67496000
C	-3.92112200	2.75872300	1.83970400
C	-3.75232100	2.63461300	0.46898300
C	-2.68996100	1.89174500	-0.01713500
H	-1.25169500	0.89990700	2.73806400
H	-3.09365400	2.19057300	3.74995600
H	-4.73974100	3.33538900	2.24746500
H	-4.42844900	3.10734000	-0.22801500
H	-2.52467400	1.78485100	-1.07534600
N	-1.80702000	-1.27941400	-0.78865000
C	-2.68996100	-1.89174500	0.01713500
C	-3.75232100	-2.63461300	-0.46898300
C	-3.92112200	-2.75872300	-1.83970400
C	-3.01198100	-2.12577300	-2.67496000
C	-1.97513900	-1.39910700	-2.11761100
H	-2.52467400	-1.78485100	1.07534600
H	-4.42844900	-3.10734000	0.22801500
H	-4.73974100	-3.33538900	-2.24746500
H	-3.09365400	-2.19057300	-3.74995600
H	-1.25169500	-0.89990700	-2.73806400

Table E.16. Optimised Gas-Phase Atomic Coordinates (Å) of $NbF_5(NC_5H_5)_2$

Nb	-0.27953700	-0.62869300	0.00000000
F	0.17558800	0.64231800	1.36144300
F	0.17558800	0.64231800	-1.36144300
F	0.17558800	-1.88095400	1.35515600
F	0.17558800	-1.88095400	-1.35515600
F	-1.96241000	-1.50017600	0.00000000
N	2.11894700	-0.64272600	0.00000000
N	-2.03468100	1.09367900	0.00000000
C	2.79625100	-0.65700300	1.15236100
C	4.18105900	-0.68307200	1.19453100
C	4.88749800	-0.69634800	0.00000000
C	4.18105900	-0.68307200	-1.19453100
C	2.79625100	-0.65700300	-1.15236100
C	-1.63659300	2.37317300	0.00000000
C	-2.53050800	3.42995800	0.00000000
C	-3.89224800	3.15872000	0.00000000
C	-4.30511600	1.83548600	0.00000000
C	-3.34670900	0.83267500	0.00000000
H	2.20004400	-0.65063800	2.05207600
H	4.68707700	-0.69523200	2.14886600
H	5.96896900	-0.71880300	0.00000000
H	4.68707700	-0.69523200	-2.14886600
H	2.20004400	-0.65063800	-2.05207600
H	-0.57105600	2.53891300	0.00000000
H	-2.15788200	4.44393900	0.00000000
H	-4.61524400	3.96322600	0.00000000
H	-5.35246300	1.57082900	0.00000000
H	-3.62056200	-0.21065400	0.00000000

Table E.17. Optimised Gas-Phase Atomic Coordinates (Å) of $[NbF_6]^-$

Nb	0.00000000	0.00000000	0.00000000
F	0.00000000	0.00000000	1.91496200
F	0.00000000	1.91496200	0.00000000
F	0.00000000	0.00000000	-1.91496200
F	0.00000000	-1.91496200	0.00000000
F	1.91496200	0.00000000	0.00000000
F	-1.91496200	0.00000000	0.00000000

Table E.18. Optimised Gas-Phase Atomic Coordinates (Å) of $[NbF_4(NC_5H_5)_4]^+$

Nb	0.00000000	0.00000000	0.00000000
F	-0.58417100	1.30798000	1.24964200
F	0.58417100	1.30798000	-1.24964200
F	-0.58417100	-1.30798000	-1.24964200
F	0.58417100	-1.30798000	1.24964200
N	-1.97059500	0.98391200	-1.04137400
C	-2.24551400	2.27611500	-0.81172800
C	-3.28115300	2.94212200	-1.44457100
C	-4.06829200	2.25120800	-2.35521900
C	-3.78332500	0.91546000	-2.59675400
C	-2.72883100	0.31970200	-1.92373500
H	-1.61578200	2.78183800	-0.09662400
H	-3.45853000	3.98425800	-1.22285100
H	-4.88369000	2.74392800	-2.86643400
H	-4.36229000	0.33370300	-3.29888200
H	-2.47132400	-0.71336300	-2.09412600
N	-1.97059500	-0.98391200	1.04137400
C	-2.72883100	-0.31970200	1.92373500
C	-3.78332500	-0.91546000	2.59675400
C	-4.06829200	-2.25120800	2.35521900
C	-3.28115300	-2.94212200	1.44457100
C	-2.24551400	-2.27611500	0.81172800
H	-2.47132400	0.71336300	2.09412600
H	-4.36229000	-0.33370300	3.29888200
H	-4.88369000	-2.74392800	2.86643400
H	-3.45853000	-3.98425800	1.22285100
H	-1.61578200	-2.78183800	0.09662400
N	1.97059500	0.98391200	1.04137400
C	2.24551400	2.27611500	0.81172800
C	3.28115300	2.94212200	1.44457100
C	4.06829200	2.25120800	2.35521900
C	3.78332500	0.91546000	2.59675400
C	2.72883100	0.31970200	1.92373500
H	1.61578200	2.78183800	0.09662400
H	3.45853000	3.98425800	1.22285100
H	4.88369000	2.74392800	2.86643400
H	4.36229000	0.33370300	3.29888200
H	2.47132400	-0.71336300	2.09412600
N	1.97059500	-0.98391200	-1.04137400
C	2.72883100	-0.31970200	-1.92373500
C	3.78332500	-0.91546000	-2.59675400
C	4.06829200	-2.25120800	-2.35521900
C	3.28115300	-2.94212200	-1.44457100
C	2.24551400	-2.27611500	-0.81172800
H	2.47132400	0.71336300	-2.09412600
H	4.36229000	-0.33370300	-3.29888200
H	4.88369000	-2.74392800	-2.86643400
H	3.45853000	-3.98425800	-1.22285100
H	1.61578200	-2.78183800	-0.09662400

Table E.19. Optimised Gas-Phase Atomic Coordinates (Å) of $MoF_5(NC_5H_5)_2$

Mo	0.00000000	0.00000000	0.54601800
F	0.00000000	0.00000000	-1.35409100
F	-1.90236300	0.05990600	0.39910500
F	1.90236300	-0.05990600	0.39910500
F	0.12246300	1.16185700	2.03702400
F	-0.12246300	-1.16185700	2.03702400
N	-0.00640800	2.17970400	-0.19797000
C	-0.95995300	2.60677300	-1.03143800
C	-0.99590800	3.91191500	-1.49427700
C	0.00000000	4.79265600	-1.09610000
C	0.99257000	4.33839900	-0.23885800
C	0.94982300	3.02500200	0.19897700
H	-1.70222700	1.87769000	-1.31862800
H	-1.79236300	4.22216000	-2.15466900
H	0.00187400	5.81584900	-1.44657100
H	1.78959200	4.98633100	0.09518500
H	1.68413600	2.62706800	0.88253300
N	0.00640800	-2.17970400	-0.19797000
C	-0.94982300	-3.02500200	0.19897700
C	-0.99257000	-4.33839900	-0.23885800
C	0.00000000	-4.79265600	-1.09610000
C	0.99590800	-3.91191500	-1.49427700
C	0.95995300	-2.60677300	-1.03143800
H	-1.68413600	-2.62706800	0.88253300
H	-1.78959200	-4.98633100	0.09518500
H	-0.00187400	-5.81584900	-1.44657100
H	1.79236300	-4.22216000	-2.15466900
H	1.70222700	-1.87769000	-1.31862800

Table E.20. Optimised Gas-Phase Atomic Coordinates (Å) of $[MoF_6]^-$

Mo	0.00000000	0.00000000	0.00000000
F	0.00000000	1.91390000	0.00000000
F	0.00000000	0.00000000	-1.86365900
F	0.00000000	-1.91390000	0.00000000
F	0.00000000	0.00000000	1.86365900
F	1.91390000	0.00000000	0.00000000
F	-1.91390000	0.00000000	0.00000000

Table E.21. Optimised Gas-Phase Atomic Coordinates (Å) of $[MoF_4(NC_5H_5)_4]^+$

Mo	0.00000000	0.00000000	0.00000000
F	0.64377800	1.03189400	1.47273300
F	-0.64377800	-1.03189400	1.47273300
F	0.64377800	-1.03189400	-1.47273300
F	-0.64377800	1.03189400	-1.47273300
N	1.84188500	-1.24365200	0.80077500
C	2.03237000	-1.31032600	2.12779300
C	3.07169700	-2.02881500	2.69236800
C	3.95277500	-2.70790700	1.86285000
C	3.75576800	-2.63855900	0.49201700
C	2.69280400	-1.89941300	-0.00071100
H	1.32761600	-0.77496800	2.74059500
H	3.17692400	-2.05200200	3.76704200
H	4.77236800	-3.27939400	2.27599400
H	4.40934300	-3.15027400	-0.19896200
H	2.50197700	-1.83217100	-1.05853000
N	1.84188500	1.24365200	-0.80077500
C	2.69280400	1.89941300	0.00071100
C	3.75576800	2.63855900	-0.49201700
C	3.95277500	2.70790700	-1.86285000
C	3.07169700	2.02881500	-2.69236800
C	2.03237000	1.31032600	-2.12779300
H	2.50197700	1.83217100	1.05853000
H	4.40934300	3.15027400	0.19896200
H	4.77236800	3.27939400	-2.27599400
H	3.17692400	2.05200200	-3.76704200
H	1.32761600	0.77496800	-2.74059500
N	-1.84188500	1.24365200	0.80077500
C	-2.03237000	1.31032600	2.12779300
C	-3.07169700	2.02881500	2.69236800
C	-3.95277500	2.70790700	1.86285000
C	-3.75576800	2.63855900	0.49201700
C	-2.69280400	1.89941300	-0.00071100
H	-1.32761600	0.77496800	2.74059500
H	-3.17692400	2.05200200	3.76704200
H	-4.77236800	3.27939400	2.27599400
H	-4.40934300	3.15027400	-0.19896200
H	-2.50197700	1.83217100	-1.05853000
N	-1.84188500	-1.24365200	-0.80077500
C	-2.69280400	-1.89941300	0.00071100
C	-3.75576800	-2.63855900	-0.49201700
C	-3.95277500	-2.70790700	-1.86285000
C	-3.07169700	-2.02881500	-2.69236800
C	-2.03237000	-1.31032600	-2.12779300
H	-2.50197700	-1.83217100	1.05853000
H	-4.40934300	-3.15027400	0.19896200
H	-4.77236800	-3.27939400	-2.27599400
H	-3.17692400	-2.05200200	-3.76704200
H	-1.32761600	-0.77496800	-2.74059500

Table E.22. Optimised Gas-Phase Atomic Coordinates (Å) of $TaF_5(NC_5H_5)_2$

Ta	-0.58309600	0.00602000	0.00000000
F	0.75623300	0.09098000	1.37014900
F	0.75623300	0.09098000	-1.37014900
F	-1.56925400	-0.89748200	1.35042600
F	-1.56925400	-0.89748200	-1.35042600
F	-2.02791900	1.23018800	0.00000000
N	0.33951700	-2.19312500	0.00000000
N	0.33184600	2.29355600	0.00000000
C	0.59215500	-2.82378000	1.15254200
C	1.11069400	-4.10769200	1.19434400
C	1.37551000	-4.76298100	0.00000000
C	1.11069400	-4.10769200	-1.19434400
C	0.59215500	-2.82378000	-1.15254200
C	1.66666200	2.42000600	0.00000000
C	2.29880000	3.65115100	0.00000000
C	1.52544700	4.80427900	0.00000000
C	0.14530400	4.67638700	0.00000000
C	-0.41203900	3.40628100	0.00000000
H	0.36459000	-2.27345500	2.05243600
H	1.29758700	-4.57782800	2.14875300
H	1.77879000	-5.76668200	0.00000000
H	1.29758700	-4.57782800	-2.14875300
H	0.36459000	-2.27345500	-2.05243600
H	2.23040500	1.50091300	0.00000000
H	3.37812100	3.69656600	0.00000000
H	1.99028900	5.78094200	0.00000000
H	-0.50177100	5.54141600	0.00000000
H	-1.48038400	3.25923100	0.00000000

Table E.23. Optimised Gas-Phase Atomic Coordinates (Å) of $[TaF_6]^-$

Ta	0.00000000	0.00000000	0.00000000
F	0.00000000	0.00000000	1.91428900
F	0.00000000	1.91428900	0.00000000
F	0.00000000	0.00000000	-1.91428900
F	0.00000000	-1.91428900	0.00000000
F	1.91428900	0.00000000	0.00000000
F	-1.91428900	0.00000000	0.00000000

Table E.24. Optimised Gas-Phase Atomic Coordinates (Å) of $[TaF_4(NC_5H_5)_4]^+$

Ta	0.00000000	0.00000000	0.00000000
F	-0.58512300	1.30798700	1.24831200
F	0.58512300	1.30798700	-1.24831200
F	-0.58512300	-1.30798700	-1.24831200
F	0.58512300	-1.30798700	1.24831200
N	-1.96491400	0.98130600	-1.04077900
C	-2.22793700	2.28038800	-0.83060800
C	-3.26501800	2.94492800	-1.46185800
C	-4.06903300	2.24647100	-2.35176500
C	-3.79820000	0.90453200	-2.57420800
C	-2.74117700	0.31075000	-1.90402500
H	-1.58623300	2.79300800	-0.13151100
H	-3.43064400	3.99204600	-1.25515200
H	-4.88614900	2.73791700	-2.86145400
H	-4.39024600	0.31637800	-3.25987400
H	-2.49535300	-0.72703700	-2.06103300
N	-1.96491400	-0.98130600	1.04077900
C	-2.74117700	-0.31075000	1.90402500
C	-3.79820000	-0.90453200	2.57420800
C	-4.06903300	-2.24647100	2.35176500
C	-3.26501800	-2.94492800	1.46185800
C	-2.22793700	-2.28038800	0.83060800
H	-2.49535300	0.72703700	2.06103300
H	-4.39024600	-0.31637800	3.25987400
H	-4.88614900	-2.73791700	2.86145400
H	-3.43064400	-3.99204600	1.25515200
H	-1.58623300	-2.79300800	0.13151100
N	1.96491400	0.98130600	1.04077900
C	2.22793700	2.28038800	0.83060800
C	3.26501800	2.94492800	1.46185800
C	4.06903300	2.24647100	2.35176500
C	3.79820000	0.90453200	2.57420800
C	2.74117700	0.31075000	1.90402500
H	1.58623300	2.79300800	0.13151100
H	3.43064400	3.99204600	1.25515200
H	4.88614900	2.73791700	2.86145400
H	4.39024600	0.31637800	3.25987400
H	2.49535300	-0.72703700	2.06103300
N	1.96491400	-0.98130600	-1.04077900
C	2.74117700	-0.31075000	-1.90402500
C	3.79820000	-0.90453200	-2.57420800
C	4.06903300	-2.24647100	-2.35176500
C	3.26501800	-2.94492800	-1.46185800
C	2.22793700	-2.28038800	-0.83060800
H	2.49535300	0.72703700	-2.06103300
H	4.39024600	-0.31637800	-3.25987400
H	4.88614900	-2.73791700	-2.86145400
H	3.43064400	-3.99204600	-1.25515200
H	1.58623300	-2.79300800	-0.13151100

Appendix F – Supporting Information for Chapter 8

Table F.1. Crystallographic Data Collection and Refinement Parameters for $[WF_4(NC_5H_5)_4][O_3SCF_3]\cdot 1.5CH_3CN$ and $[WF_4\{P(CH_3)_3\}_4][O_3SCF_3]$

	$[WF_4(NC_5H_5)_4][O_3SCF_3]\cdot 1.5CH_3CN$	**$[WF_4\{P(CH_3)_3\}_4][O_3SCF_3]$**
Identification code	MG19022b	MG19023
Empirical formula	$C_{48}H_{49}F_{14}N_{11}O_6S_2W_2$	$C_{13}H_{36}F_7O_3P_4SW$
Formula weight	1573.8	713.21
T (K)	99.99(10)	100.0(2)
Crystal system	orthorhombic	monoclinic
Space group	*Pbca*	$P2_1/c$
a (Å)	24.4331(9)	14.1007(6)
b (Å)	17.3645(7)	14.4069(4)
c (Å)	27.0448(10)	13.9803(6)
α (°)	90	90
β (°)	90	114.179(5)
γ (°)	90	90
V (Å^3)	11474.3(8)	2590.9(2)
Z	8	4
ρ_{calc} (g cm^{-3})	1.822	1.828
μ (mm^{-1})	4.182	4.848
F(000)	6144	1404
Crystal size (mm^3)	0.47 × 0.091 × 0.06	0.122 × 0.089 × 0.086
GooF	1.001	1.046
Final *R* indexes [I ≥ 2σ (I)]	R_1 = 0.0430, wR_2 = 0.0645	R_1 = 0.0208, wR_2 = 0.0415
Final *R* indexes [all data]	R_1 = 0.0862, wR_2 = 0.0735	R_1 = 0.0275, wR_2 = 0.0429
Largest diff. peak/hole (e Å^{-3})	1.27/-0.98	0.77/-0.54

$^aR_1 = \sum||F_o| - |F_c||/\sum|F_o|$. $^bwR_2 = [\sum[w(F_o^2 - F_c^2)^2]/\sum w(F_o^4)]^{1/2}$.

Table F.2. Vibrational Frequencies (cm^{-1}) of NC_5H_5 and $[WF_4(NC_5H_5)_4]^+$

NC_5H_5		$[WF_4(NC_5H_5)_4]^+$		Assignment (D_2)[d]
exptl[a]	calcd[b]	exptl[c]	calcd[b]	
3173(1)				C–H stretching modes, combination modes, and overtones
3145(1)		3152(5)		
3091(5)				
			3257(174)[0]	
3056(39)	3194(277)[8]	3100(11)	3257(21)[2]	
			3255(12)[7]	
			3255(4)[17]	
			3248(119)[0]	
			3248(<0.1)[13]	
3036 sh	3186(37)[26]	3087(9)	3248(6)[4]	
			3248(<1)[2]	
			3210(754)[0]	
			3210(191)[<1]	
3025 sh	3171(99)[5]	3071(7)	3210(6)[<1]	
			3210(10)[<1]	
			3205(43)[3]	
			3205(145)[0]	
2988(5)	3149(79)[4]	3059(5)	3205(71)[<1]	
			3205(124)[<1]	
			3190(105)[0]	
			3190(54)[1]	
2955(5)	3147(96)[27]		3190(45)[2]	
			3190(89)[1]	

2908(1) 2871(1) 2453(1)				combination modes, and overtones
1597(5)	1627(11)[25]	1612(11)	1652(22)[0] 1652(10)[49] 1651(21)[29]	C–N/C–C stretching modes and in-plane ring deformations
1581(9)			1651(13)[12] 1617(7)[1]	
1573(7)	1621(8)[8]	1574(6)	1615(17)[0] 1615(5)[1] 1615(9)[<1]	
1482(3)	1518(2)[2]	1491(3)	1529(4)[0] 1528(1)[10] 1527(1)[24] 1527(1)[10]	
	1477(<1)[28]		1485(<1)[95] 1485(<1)[0] 1484(<1)[17] 1484(1)[8]	
	1391(<1)[<1]		1399(<0.1)[6] 1396(<1)[0] 1395(<0.1)[1] 1395(<1)[1]	
	1283(2)[<0.1]		1288(<1)[0] 1288(<0.1)[<1] 1287(<0.1)[4] 1287(<1)[<1]	

1217(8)	1244(9)[4]		1258(9)[0]	in-plane ring deformations
			1252(2)[68]	
			1251(0)[17]	
			1251(3)[38]	
1146(2)	1173(2)[2]	1160(4)	1187(1)[14]	
			1187(3)[0]	
			1187(2)[2]	
			1187(4)[1]	
1068(2)	1096(2)[4]		1115(<1)[4]	
			1112(<1)[0]	
			1112(<1)[<0.1]	
			1112(<1)[<0.1]	
	1080(<1)[<1]		1096(1)[0]	
			1095(1)[45]	
			1095(2)[11]	
			1095(1)[24]	
1030(75)	1052(33)[7]	1046(33)	1066(87)[0]	
			1065(26)[1]	
			1064(3)[7]	
			1064(4)[3]	
	1021(<0.1)[<0.1]		1042(<0.1)[<0.1]	
			1042(0)[0]	
			1042(1)[0]	
			1041(<1)[<0.1]	
990(100)	1013(26)[5]	1018(100)	1033(237)[0]	A, $\nu_s(NC_5)$ [1 + 2 + 3 + 4]
980(5)			1032(7)[31]	B_3, $\nu_s(NC_5)$ [1 + 2 – 3 – 4]
			1031(52)[8]	B_2, $\nu_s(NC_5)$ [1 – 2 + 3 – 4]

			1030(11)[21]	B_1, $\nu_s(NC_5)$ [1 – 2 – 3 + 4]
	1010(<0.1)[0]		1022(<0.1)[2]	out-of-plane ring deformations
			1022(<0.1)[<0.1]	
			1022(<0.1)[<1]	
			1021(<1)[0]	
	962(<0.1)[<0.1]		989(<0.1)[<1]	
			989(<1)[1]	
			988(1)[0]	
			987(1)[<0.1]	
	900(<0.1)[0]		893(<0.1)[<0.1]	
			893(<0.1)[<0.1]	
			892(<0.1)[<0.1]	
			891(<1)[0]	
	768(<1)[7]		788(<1)[29]	
			787(1)[0]	
			786(<0.1)[57]	
			785(1)[<0.1]	
	720(<0.1)[64]		713(<0.1)[68]	
			713(<0.1)[135]	
			712(<1)[0]	
			709(<0.1)[<0.1]	
652(5)	670(4)[<1]	652(9)	669(3)[<1]	in-plane ring deformations
			667(6)[0]	
			667(4)[<1]	
			666(2)[<0.1]	
603(3)	617(3)[4]	646(5)	653(2)[0]	
			649(2)[19]	

		638(3)	648(5)[10]	in-plane ring deformations
			648(2)[3]	
			593(1)[113]	B_1, $\nu_{as}(WF_4)$ [1 + 2 – 3 – 4]
		580(14)	587(21)[0]	A, $\nu_s(WF_4)$
			533(1)[74]	B_2, $\nu_{as}(WF_4)$ [1 – 2 + 3 – 4]
			529(<0.1)[100]	B_3, $\nu_{as}(WF_4)$ [1 – 2 – 3 + 4]
406(1)	421(<1)[4]		464(<1)[4]	out-of-plane ring deformations
			461(<0.1)[12]	
			461(1)[0]	
			456(<1)[1]	
			407(<1)[<1]	
	385(<0.1)[0]		407(<1)[1]	
			406(<0.1)[1]	
			406(<1)[0]	
			390(0)[24]	B_1, δ(F(1)WF(2) – F(3)WF(4))
			375(2)[0]	A, δ(F(1)WF(2) + F(3)WF(4))
			344(<0.1)[61]	B_3, δ(F(1)WF(3) – F(2)WF(4))
			316(<1)[2]	rocking and twisting modes
			287(2)[0]	
			284(<1)[<1]	
			273(<1)[<0.1]	
			268(<1)[3]	
			256(<0.1)[26]	B_2, δ(F(1)WF(4) – F(2)WF(3))
			247(1)[0]	rocking and twisting modes
			235(<1)[<0.1]	
			219(<1)[11]	
			178(<0.1)[1]	

	173(<1)[13]	B_3, $\nu_{as}(WN_4)$ [1 + 2 – 3 – 4]
	162(<1)[6]	B_3, δ(N(1)WN(2) – N(3)WN(4))
183(9)	156(2)[0]	A, $\nu_s(WN_4)$
	148(<0.1)[1]	B_1, $\nu_{as}(WN_4)$ [1 – 2 – 3 + 4]
165(6)	129(9)[0]	B_2, δ(N(1)WN(2) + N(3)WN(4))
	128(<1)[6]	B_2, $\nu_{as}(WN_4)$ [1 – 2 + 3 – 4]
130 sh	106(1)[<0.1]	rocking and twisting modes
	87(1)[3]	
100(24)	61(12)[<1]	
	56(6)[1]	
	55(2)[0]	
	44(<1)[<0.1]	
	39(2)[0]	
	39(<1)[1]	
	32(9)[0]	
	26(1)[3]	

[a]From Nieboer, J.; Yu, X.; Chaudhary, P.; Mercier, H. P. A.; Gerken, M. *Z. Anorg. Allg. Chem.* 2012, *638* (3–4), 520–525. [b]Calculated at the B3LYP/aVTZ level of theory. Absolute Raman intensities ($Å^4$ u^{-1}) are given in parentheses and IR intensities (km mol^{-1}) are given in square brackets. [c]Recorded in a flame-sealed glass m.p. capillary at ambient temperature. Normalised Raman intensities are given in parentheses. Shoulders are denoted as sh. Bands corresponding to $[O_3SCF_3]^-$ are observed at 1229(5), 1032(22), 755(6), 575 sh, 348(6), and 313(4) cm^{-1}. [d]Abbreviations denote stretch (ν) and bend (δ). Numbers in square brackets denote the fluorine or nitrogen atoms involved in the stretching mode. Atom labels are as in Figure 8.2a.

Table F.3. Vibrational Frequencies (cm^{-1}) of $P(CH_3)_3$ and $[WF_4\{P(CH_3)_3\}_4]^+$

$P(CH_3)_3$		$[WF_4\{P(CH_3)_3\}_4]^+$		Assignment (D_2)[d]
exptl[a]	calcd[b]	exptl[c]	calcd[b]	
			3152(20)[0]	$\nu_{as}(CH_2)$
			3152(55)[<0.1]	
			3150(24)[<1]	
	3105(220)[30]		3150(7)[1]	
			3146(78)[0]	
			3146(9)[4]	
			3145(47)[<0.1]	
			3145(12)[3]	
			3145(8)[0]	
	3105(0)[0]		3144(21)[<1]	
			3140(3)[7]	
			3139(40)[<0.1]	
			3131(47)[0]	$\nu_{as}(CH_3)$
2968(19)	3091(174)[39]		3131(110)[2]	
			3131(169)[3]	
			3131(88)[2]	
			3128(49)[0]	
		2995(51)	3128(24)[<0.1]	
			3126(92)[2]	
2955(21)	3091(44)[5]		3125(101)[0]	
			3125(318)[7]	
			3125(48)[2]	
			3124(20)[7]	

			3124(77)[<0.1]	$\nu_{as}(CH_3)$
			3051(2017)[0]	$\nu_s(CH_3)$
			3051(32)[23]	
			3051(81)[15]	
	3017(12)[35]		3050(64)[5]	
			3050(63)[0]	
2893(100)		2924(100)	3050(21)[1]	
			3050(16)[<1]	
			3050(37)[<1]	
			3049(71)[<0.1]	
	3016(469)[33]		3049(29)[<0.1]	
			3049(2)[<1]	
			3049(38)[1]	
2869(7)				combination bands and/or overtones
2842(5)		2848(2)		
2823(5)				
2810(12)				
2549(1)		2562(1)		
			1491(<1)[15]	$\delta_{as}(CH_3)$
	1483(2)[10]	1449(5)	1490(6)[0]	
			1488(1)[28]	
			1485(1)[12]	
			1477(1)[3]	
			1476(4)[<1]	
1421(9)	1475(10)[18]	1434 sh	1474(7)[0]	
			1471(3)[0]	
		1423(27)	1470(2)[12]	

	1465(24)[8]	1415 sh	1468(12)[10] 1467(22)[<1] 1467(<1)[14] 1466(<0.1)[7] 1465(4)[3] 1465(4)[<1] 1463(2)[18] 1461(10)[0] 1460(<1)[2] 1460(2)[0] 1459(4)[4] 1453(1)[0] 1451(<1)[<1] 1451(<0.1)[<1] 1448(1)[<1]	$\delta_{as}(CH_3)$
1293(2)	1336(5)[4]	1307(7)	1351(3)[0] 1349(1)[11] 1345(1)[7] 1345(3)[15] 1329(<0.1)[4] 1329(<1)[0] 1328(<0.1)[15] 1328(<1)[30] 1325(1)[0] 1322(<1)[7] 1322(<0.1)[3] 1320(<0.1)[1]	$\delta_s(CH_3)$
	1460(0)[0]	1288(2)		
	1314(<1)[3]	1262(5)		

952(1)	972(3)[25]	985(1)	995(4)[0] 976(<1)[0] 976(3)[311] 976(<1)[<0.1]	$\rho(CH_2) \pm \omega(CH_2)$
938(1)	959(1)[40]	956(10)	973(0)[79] 973(3)[261] 973(12)[49] 972(<0.1)[1] 969(1)[0]	$\rho(CH_2) \pm \omega(CH_2)$
824(1)	842(<1)[<1] 793(0)[0]	854(1)	969(<0.1)[10] 967(<0.1)[22] 967(<0.1)[1] 865(<0.1)[5] 863(<1)[20] 863(<1)[0] 862(<1)[7] 861(1)[0] 860(<1)[4] 857(<1)[3] 855(<0.1)[2] 812(<0.1)[0] 809(<0.1)[<0.1] 809(<0.1)[<0.1] 807(<0.1)[<1]	$\rho(CH_2) \pm \omega(CH_2)$
707(18)	694(20)[26]	741(41)	735(1)[36] 734(16)[7] 733(8)[0]	$\nu_{as}(PC_3)$

			733(1)[1]	$\nu_{as}(PC_3)$
			724(18)[0]	
			724(5)[21]	
			723(2)[10]	
			722(4)[3]	
653(58)	637(21)[1]	678(76)	657(64)[0]	$\nu_s(PC_3)$
			656(1)[3]	
			655(1)[1]	
			654(2)[<0.1]	
		536(4)	550(1)[119]	B_1, $\nu_{as}(WF_4)$ [1 + 2 – 3 – 4]
		519(44)	529(27)[0]	A, $\nu_s(WF_4)$
		479(1)	482(<0.1)[69]	B_2, $\nu_{as}(WF_4)$ [1 – 2 + 3 – 4]
		472(1)	477(<0.1)[38]	B_3, $\nu_{as}(WF_4)$ [1 – 2 – 3 + 4]
302(4)	289(1)[1]	340 sh	329(7)[0]	A, $\delta_s(PC_3)$
			327(1)[13]	B_1, δ(F(1)WF(2) – F(3)WF(4))
			323(<1)[<1]	$\delta_s(PC_3)$
			322(<1)[3]	
			315(1)[3]	
			315(<1)[0]	A, δ(F(1)WF(2) + F(3)WF(4))
		289(20)	287(1)[48]	B_3, δ(F(1)WF(3) – F(2)WF(4))
		274(19)	272(3)[1]	$\delta_{as}(PC_3)$
			271(3)[1]	
			270(1)[0]	
			266(<0.1)[2]	
			259(2)[0]	
262(15)	247(6)[<1]	257 sh	257(1)[<0.1]	
			257(<1)[1]	

		256(<0.1)[0]	$\delta_{as}(PC_3)$
		248(1)[8]	$\tau_s(CH_3)$
	238 sh	242(4)[0]	
		228(<1)[1]	
		225(<0.1)[<1]	
205(3)[<1]		222(2)[0]	
		220(<1)[6]	
		217(<1)[2]	
		212(1)[1]	
		193(<0.1)[<1]	
		193(<0.1)[2]	
185(0)[0]		191(<0.1)[<1]	
		191(<1)[1]	
	195 sh	190(3)[0]	rocking and twisting modes
		187(1)[<0.1]	
		179(3)[0]	
		175(<1)[3]	
		171(<1)[1]	
		163(<0.1)[<0.1]	
		163(<0.1)[<1]	
		162(3)[0]	
		162(<0.1)[1]	
		157(1)[0]	
		155(2)[1]	
		141(1)[<0.1]	
	179(67)	137(20)[0]	A, $\nu_s(WP_4)$
		127(1)[1]	B_2, $\rho(WF_2) + \rho(PC_2)$

	161 sh	126(7)[<1]	B_1, $\nu_{as}(WP_4)$ [1 – 2 – 3 + 4]
		119(1)[2]	B_2, $\nu_{as}(WP_4)$ [1 – 2 + 3 – 4]
	131 sh	109(1)[2]	B_3, $\nu_{as}(WP_4)$ [1 + 2 – 3 – 4]
		97(<1)[1]	rocking and twisting modes
		79(<1)[2]	
	101 (47)	75(2)[0]	
		69(1)[4]	
		64(1)[0]	
		58(1)[0]	
		58(<0.1)[<1]	
		36(<0.1)[1]	
		29(<0.1)[<0.1]	

[a]Recorded in a flame-dried ¼"-o.d. glass tube at ambient temperature. Normalised Raman intensities are given in parentheses. [b]Calculated at the B3LYP/aVTZ level of theory. Absolute Raman intensities ($Å^4\ u^{-1}$) are given in parentheses and IR intensities (km mol^{-1}) are given in square brackets. [c]Recorded in a flame-sealed glass m.p. capillary at ambient temperature. Normalised Raman intensities are given in parentheses. Shoulders are denoted as sh. Bands corresponding to $[O_3SCF_3]^-$ are observed at 1274(3), 1224(5), 1031(59), 753(42), 573(10), 358 sh, 347(17), and 313(20) cm^{-1}. [d]Abbreviations denote stretch (ν), bend (δ), and rock (ρ). Numbers in square brackets denote the fluorine or phosphorus atoms involved in the stretching mode. Atom labels are as in Figure 8.2b.

Table F.4. Optimised Gas-Phase Atomic Coordinates (Å) of $[WF_4\{P(CH_3)_3\}_4]^+$

W	0.00000000	0.00000000	0.00000000
F	-0.69356500	1.01114900	-1.53677600
F	0.69356500	-1.01114900	-1.53677600
F	-0.69356500	-1.01114900	1.53677600
F	0.69356500	1.01114900	1.53677600
P	-1.95032400	1.59770300	0.93731500
P	-1.95032400	-1.59770300	-0.93731500
P	1.95032400	1.59770300	-0.93731500
P	1.95032400	-1.59770300	0.93731500
C	-3.41244900	1.94408600	-0.11719500
H	-3.07290000	2.29837900	-1.08855500
H	-4.03529800	2.70908100	0.34609500
H	-4.01537300	1.05157100	-0.26369400
C	-1.32691500	3.28563200	1.29104300
H	-0.43261100	3.22271700	1.90545500
H	-2.09117900	3.85526900	1.81962600
H	-1.09371700	3.79675900	0.35997800
C	-2.62390100	1.05320000	2.54942300
H	-3.11163900	0.08684200	2.45012100
H	-3.33690500	1.78379100	2.93072400
H	-1.80077000	0.94468500	3.25248200
C	-3.41244900	-1.94408600	0.11719500
H	-3.07290000	-2.29837900	1.08855500
H	-4.03529800	-2.70908100	-0.34609500
H	-4.01537300	-1.05157100	0.26369400
C	-1.32691500	-3.28563200	-1.29104300
H	-0.43261100	-3.22271700	-1.90545500
H	-2.09117900	-3.85526900	-1.81962600
H	-1.09371700	-3.79675900	-0.35997800
C	-2.62390100	-1.05320000	-2.54942300
H	-3.11163900	-0.08684200	-2.45012100
H	-3.33690500	-1.78379100	-2.93072400
H	-1.80077000	-0.94468500	-3.25248200
C	3.41244900	1.94408600	0.11719500
H	3.07290000	2.29837900	1.08855500
H	4.03529800	2.70908100	-0.34609500
H	4.01537300	1.05157100	0.26369400
C	1.32691500	3.28563200	-1.29104300
H	0.43261100	3.22271700	-1.90545500
H	2.09117900	3.85526900	-1.81962600
H	1.09371700	3.79675900	-0.35997800
C	2.62390100	1.05320000	-2.54942300
H	3.11163900	0.08684200	-2.45012100
H	3.33690500	1.78379100	-2.93072400
H	1.80077000	0.94468500	-3.25248200
C	3.41244900	-1.94408600	-0.11719500
H	3.07290000	-2.29837900	-1.08855500
H	4.03529800	-2.70908100	0.34609500
H	4.01537300	-1.05157100	-0.26369400
C	1.32691500	-3.28563200	1.29104300
H	0.43261100	-3.22271700	1.90545500
H	2.09117900	-3.85526900	1.81962600
H	1.09371700	-3.79675900	0.35997800
C	2.62390100	-1.05320000	2.54942300
H	3.11163900	-0.08684200	2.45012100
H	3.33690500	-1.78379100	2.93072400
H	1.80077000	-0.94468500	3.25248200

Table F.5. Optimised Gas-Phase Atomic Coordinates (Å) of $[WF_4(PH_3)_4]^{2+}$

W	0.00000000	0.00000000	0.00000000
F	0.00000000	1.80905900	0.53215500
F	-1.80905900	0.00000000	-0.53215500
F	0.00000000	-1.80905900	0.53215500
F	1.80905900	0.00000000	-0.53215500
P	1.68589400	0.00000000	2.10828100
P	-1.68589400	0.00000000	2.10828100
P	0.00000000	1.68589400	-2.10828100
P	0.00000000	-1.68589400	-2.10828100
H	2.53648100	1.11283200	2.00553900
H	1.29022300	0.00000000	3.45708500
H	2.53648100	-1.11283200	2.00553900
H	-2.53648100	-1.11283200	2.00553900
H	-1.29022300	0.00000000	3.45708500
H	-2.53648100	1.11283200	2.00553900
H	1.11283200	2.53648100	-2.00553900
H	0.00000000	1.29022300	-3.45708500
H	-1.11283200	2.53648100	-2.00553900
H	-1.11283200	-2.53648100	-2.00553900
H	0.00000000	-1.29022300	-3.45708500
H	1.11283200	-2.53648100	-2.00553900

Table F.6. Optimised Gas-Phase Atomic Coordinates (Å) of $[WF_4(PH_3)_4]^+$

D_{2d}

W	0.00000000	0.00000000	0.00000000
F	0.00000000	1.86596100	0.60499500
F	-1.86596100	0.00000000	-0.60499500
F	0.00000000	-1.86596100	0.60499500
F	1.86596100	0.00000000	-0.60499500
P	1.71472500	0.00000000	2.02818700
P	-1.71472500	0.00000000	2.02818700
P	0.00000000	1.71472500	-2.02818700
P	0.00000000	-1.71472500	-2.02818700
H	2.58607900	1.09785200	1.95065900
H	1.38059400	0.00000000	3.39692000
H	2.58607900	-1.09785200	1.95065900
H	-2.58607900	-1.09785200	1.95065900
H	-1.38059400	0.00000000	3.39692000
H	-2.58607900	1.09785200	1.95065900
H	1.09785200	2.58607900	-1.95065900
H	0.00000000	1.38059400	-3.39692000
H	-1.09785200	2.58607900	-1.95065900
H	-1.09785200	-2.58607900	-1.95065900
H	0.00000000	-1.38059400	-3.39692000
H	1.09785200	-2.58607900	-1.95065900

D_2

W	0.00000000	0.00000000	0.00000000
F	0.72152100	0.99615400	1.50021500
F	-0.72152100	-0.99615400	1.50021500
F	0.72152100	-0.99615400	-1.50021500
F	-0.72152100	0.99615400	-1.50021500
P	1.93558000	1.59799800	-0.91616900
P	1.93558000	-1.59799800	0.91616900
P	-1.93558000	1.59799800	0.91616900
P	-1.93558000	-1.59799800	-0.91616900
H	1.64392900	2.96452100	-0.75762900
H	3.22727900	1.54473100	-0.35852600
H	2.21159000	1.51975200	-2.29179700
H	1.64392900	-2.96452100	0.75762900
H	3.22727900	-1.54473100	0.35852600
H	2.21159000	-1.51975200	2.29179700
H	-1.64392900	2.96452100	0.75762900
H	-3.22727900	1.54473100	0.35852600
H	-2.21159000	1.51975200	2.29179700
H	-1.64392900	-2.96452100	-0.75762900
H	-3.22727900	-1.54473100	-0.35852600
H	-2.21159000	-1.51975200	-2.29179700

Table F.7. Optimised Gas-Phase Atomic Coordinates (Å) of $[WF_4(dpe)_2]^{2+}$

S_4

W	0.00000000	0.00000000	0.00000000
F	0.00000000	1.82855100	0.51414200
F	-1.82855100	0.00000000	-0.51414200
F	0.00000000	-1.82855100	0.51414200
F	1.82855100	0.00000000	-0.51414200
P	1.54120400	0.03807600	2.17456900
P	-1.54120400	-0.03807600	2.17456900
P	-0.03807600	1.54120400	-2.17456900
P	0.03807600	-1.54120400	-2.17456900
H	2.57219900	0.98182700	2.03621700
H	2.21489100	-1.19048900	2.29271000
H	-2.21489100	1.19048900	2.29271000
H	-2.57219900	-0.98182700	2.03621700
H	-0.98182700	2.57219900	-2.03621700
H	1.19048900	2.21489100	-2.29271000
H	-1.19048900	-2.21489100	-2.29271000
H	0.98182700	-2.57219900	-2.03621700
C	0.67699600	0.36101800	3.76875900
C	-0.67699600	-0.36101800	3.76875900
H	0.55421300	1.44195500	3.85200800
H	1.30216400	0.03794700	4.60133200
H	-1.30216400	-0.03794700	4.60133200
H	-0.55421300	-1.44195500	3.85200800
C	-0.36101800	0.67699600	-3.76875900
C	0.36101800	-0.67699600	-3.76875900
H	-1.44195500	0.55421300	-3.85200800
H	-0.03794700	1.30216400	-4.60133200
H	0.03794700	-1.30216400	-4.60133200
H	1.44195500	-0.55421300	-3.85200800

D_2

W	0.00000000	0.00000000	0.00000000
F	0.51301500	1.27780300	1.30886100
F	-0.51301500	-1.27780300	1.30886100
F	0.51301500	-1.27780300	-1.30886100
F	-0.51301500	1.27780300	-1.30886100
P	2.17329700	1.12907600	-1.04918700
P	2.17329700	-1.12907600	1.04918700
P	-2.17329700	1.12907600	1.04918700
P	-2.17329700	-1.12907600	-1.04918700
C	3.76844400	0.73651900	-0.21614200
C	3.76844400	-0.73651900	0.21614200
C	-3.76844400	0.73651900	0.21614200
C	-3.76844400	-0.73651900	-0.21614200
H	2.03592700	2.52622500	-1.09562600
H	2.28741500	0.75083400	-2.39858300
H	2.28741500	-0.75083400	2.39858300
H	2.03592700	-2.52622500	1.09562600
H	3.85331600	1.40520200	0.64177000
H	4.60033600	0.95566400	-0.88569700
H	4.60033600	-0.95566400	0.88569700
H	3.85331600	-1.40520200	-0.64177000
H	-2.03592700	2.52622500	1.09562600
H	-2.28741500	0.75083400	2.39858300
H	-2.28741500	-0.75083400	-2.39858300
H	-2.03592700	-2.52622500	-1.09562600
H	-3.85331600	1.40520200	-0.64177000
H	-4.60033600	0.95566400	0.88569700
H	-4.60033600	-0.95566400	-0.88569700
H	-3.85331600	-1.40520200	0.64177000

Table F.8. Optimised Gas-Phase Atomic Coordinates (Å) of $[WF_4(dpe)_2]^+$

S_4

W	0.00000000	0.00000000	0.00000000
F	0.00000000	1.88379300	0.59667500
F	-1.88379300	0.00000000	-0.59667500
F	0.00000000	-1.88379300	0.59667500
F	1.88379300	0.00000000	-0.59667500
P	1.55376500	0.05275200	2.11923000
P	-1.55376500	-0.05275200	2.11923000
P	-0.05275200	1.55376500	-2.11923000
P	0.05275200	-1.55376500	-2.11923000
H	2.57069700	1.01834100	2.04732700
H	2.27549400	-1.13848200	2.31509700
H	-2.27549400	1.13848200	2.31509700
H	-2.57069700	-1.01834100	2.04732700
H	-1.01834100	2.57069700	-2.04732700
H	1.13848200	2.27549400	-2.31509700
H	-1.13848200	-2.27549400	-2.31509700
H	1.01834100	-2.57069700	-2.04732700
C	0.67234800	0.37123800	3.71407300
C	-0.67234800	-0.37123800	3.71407300
H	0.52138900	1.44971700	3.77459700
H	1.28818500	0.07751500	4.56267600
H	-1.28818500	-0.07751500	4.56267600
H	-0.52138900	-1.44971700	3.77459700
C	-0.37123800	0.67234800	-3.71407300
C	0.37123800	-0.67234800	-3.71407300
H	-1.44971700	0.52138900	-3.77459700
H	-0.07751500	1.28818500	-4.56267600
H	0.07751500	-1.28818500	-4.56267600
H	1.44971700	-0.52138900	-3.77459700

D_2

W	0.00000000	0.00000000	0.00000000
F	0.67434600	1.04354600	1.51108100
F	-0.67434600	-1.04354600	1.51108100
F	0.67434600	-1.04354600	-1.51108100
F	-0.67434600	1.04354600	-1.51108100
P	2.08912200	1.37470800	-0.83327400
P	2.08912200	-1.37470800	0.83327400
P	-2.08912200	1.37470800	0.83327400
P	-2.08912200	-1.37470800	-0.83327400
C	3.64718700	0.76693900	-0.04003300
C	3.64718700	-0.76693900	0.04003300
C	-3.64718700	0.76693900	0.04003300
C	-3.64718700	-0.76693900	-0.04003300
H	2.09294800	2.76304500	-0.60832500
H	2.32724900	1.30116200	-2.21758400
H	2.32724900	-1.30116200	2.21758400
H	2.09294800	-2.76304500	0.60832500
H	3.68161900	1.20929000	0.95618300
H	4.51575300	1.12759600	-0.58919800

H	4.51575300	-1.12759600	0.58919800
H	3.68161900	-1.20929000	-0.95618300
H	-2.09294800	2.76304500	0.60832500
H	-2.32724900	1.30116200	2.21758400
H	-2.32724900	-1.30116200	-2.21758400
H	-2.09294800	-2.76304500	-0.60832500
H	-3.68161900	1.20929000	-0.95618300
H	-4.51575300	1.12759600	0.58919800
H	-4.51575300	-1.12759600	-0.58919800
H	-3.68161900	-1.20929000	0.95618300

C_2

W	0.00000000	0.00000000	0.00298900
F	1.70917800	-0.65673300	0.69300700
F	0.00000000	1.83055200	-0.67696400
F	-1.70917800	0.65673300	0.69300700
F	0.00000000	-1.83055200	-0.67696400
P	-0.66822700	-1.46538200	2.08835800
P	0.66822700	1.46538200	2.08835800
P	1.61613500	0.02921900	-2.09791000
P	-1.61613500	-0.02921900	-2.09791000
H	0.16843700	-2.57003400	2.32987700
H	-1.94422500	-2.05688000	2.09246200
H	1.94422500	2.05688000	2.09246200
H	-0.16843700	2.57003400	2.32987700
H	2.28456700	1.23978200	-2.36145500
H	2.67405200	-0.89599700	-2.09088300
H	-2.67405200	0.89599700	-2.09088300
H	-2.28456700	-1.23978200	-2.36145500
C	0.61156000	0.46456100	3.64446300
C	-0.61156000	-0.46456100	3.64446300
C	0.68432100	-0.34677400	-3.65463700
C	-0.68432100	0.34677400	-3.65463700
H	0.60085300	1.12046700	4.51378700
H	1.53769000	-0.11015600	3.67776200
H	-1.53769000	0.11015600	3.67776200
H	-0.60085300	-1.12046700	4.51378700
H	1.26992000	-0.05148100	-4.52399400
H	0.57150500	-1.43099500	-3.68819400
H	-0.57150500	1.43099500	-3.68819400
H	-1.26992000	0.05148100	-4.52399400

Table F.9. Optimised Gas-Phase Atomic Coordinates (Å) of $[WF_4(dpb)_2]^{2+}$

W	0.00000000	0.00000000	0.00000000
F	0.00000000	1.83515800	0.49916100
F	-1.83515800	0.00000000	-0.49916100
F	0.00000000	-1.83515800	0.49916100
F	1.83515800	0.00000000	-0.49916100
P	1.52808500	0.00000000	2.16056000
P	-1.52808500	0.00000000	2.16056000
P	0.00000000	1.52808500	-2.16056000
P	0.00000000	-1.52808500	-2.16056000
H	2.39972700	1.10224100	2.10636800
H	2.39972700	-1.10224100	2.10636800
H	-2.39972700	1.10224100	2.10636800
H	-2.39972700	-1.10224100	2.10636800
H	-1.10224100	2.39972700	-2.10636800
H	1.10224100	2.39972700	-2.10636800
H	-1.10224100	-2.39972700	-2.10636800
H	1.10224100	-2.39972700	-2.10636800
C	0.70154400	0.00000000	3.76791600
C	1.40178500	0.00000000	4.97371100
C	0.69618100	0.00000000	6.17079800
C	-0.69618100	0.00000000	6.17079800
C	-1.40178500	0.00000000	4.97371100
C	-0.70154400	0.00000000	3.76791600
H	2.48344700	0.00000000	4.98814500
H	1.23581200	0.00000000	7.10757800
H	-1.23581200	0.00000000	7.10757800
H	-2.48344700	0.00000000	4.98814500
C	0.00000000	0.70154400	-3.76791600
C	0.00000000	1.40178500	-4.97371100
C	0.00000000	0.69618100	-6.17079800
C	0.00000000	-0.69618100	-6.17079800
C	0.00000000	-1.40178500	-4.97371100
C	0.00000000	-0.70154400	-3.76791600
H	0.00000000	2.48344700	-4.98814500
H	0.00000000	1.23581200	-7.10757800
H	0.00000000	-1.23581200	-7.10757800
H	0.00000000	-2.48344700	-4.98814500

Table F.10. Optimised Gas-Phase Atomic Coordinates (Å) of $[WF_4(dpb)_2]^+$

W	0.00000000	0.00000000	0.00000000
F	0.00000000	1.89053800	0.57259200
F	-1.89053800	0.00000000	-0.57259200
F	0.00000000	-1.89053800	0.57259200
F	1.89053800	0.00000000	-0.57259200
P	1.53929800	0.00000000	2.11492400
P	-1.53929800	0.00000000	2.11492400
P	0.00000000	1.53929800	-2.11492400
P	0.00000000	-1.53929800	-2.11492400
H	2.42398400	1.09257200	2.14422400
H	2.42398400	-1.09257200	2.14422400
H	-2.42398400	1.09257200	2.14422400
H	-2.42398400	-1.09257200	2.14422400
H	-1.09257200	2.42398400	-2.14422400
H	1.09257200	2.42398400	-2.14422400
H	-1.09257200	-2.42398400	-2.14422400
H	1.09257200	-2.42398400	-2.14422400
C	0.70089100	0.00000000	3.73348100
C	1.39549100	0.00000000	4.94370900
C	0.69608800	0.00000000	6.14214300
C	-0.69608800	0.00000000	6.14214300
C	-1.39549100	0.00000000	4.94370900
C	-0.70089100	0.00000000	3.73348100
H	2.47711500	0.00000000	4.95400200
H	1.23667600	0.00000000	7.07827200
H	-1.23667600	0.00000000	7.07827200
H	-2.47711500	0.00000000	4.95400200
C	0.00000000	0.70089100	-3.73348100
C	0.00000000	1.39549100	-4.94370900
C	0.00000000	0.69608800	-6.14214300
C	0.00000000	-0.69608800	-6.14214300
C	0.00000000	-1.39549100	-4.94370900
C	0.00000000	-0.70089100	-3.73348100
H	0.00000000	2.47711500	-4.95400200
H	0.00000000	1.23667600	-7.07827200
H	0.00000000	-1.23667600	-7.07827200
H	0.00000000	-2.47711500	-4.95400200

Table F.11. Optimised Gas-Phase Atomic Coordinates (Å) of $[WCl_4(PH_3)_4]^{2+}$

W	0.00000000	0.00000000	0.00000000
Cl	0.00000000	2.26856000	0.73817300
Cl	-2.26856000	0.00000000	-0.73817300
Cl	0.00000000	-2.26856000	0.73817300
Cl	2.26856000	0.00000000	-0.73817300
P	1.65888600	0.00000000	2.06031900
P	-1.65888600	0.00000000	2.06031900
P	0.00000000	1.65888600	-2.06031900
P	0.00000000	-1.65888600	-2.06031900
H	2.50910500	1.11483500	2.04858400
H	1.13688500	0.00000000	3.36713900
H	2.50910500	-1.11483500	2.04858400
H	-2.50910500	-1.11483500	2.04858400
H	-1.13688500	0.00000000	3.36713900
H	-2.50910500	1.11483500	2.04858400
H	1.11483500	2.50910500	-2.04858400
H	0.00000000	1.13688500	-3.36713900
H	-1.11483500	2.50910500	-2.04858400
H	-1.11483500	-2.50910500	-2.04858400
H	0.00000000	-1.13688500	-3.36713900
H	1.11483500	-2.50910500	-2.04858400

Table F.12. Optimised Gas-Phase Atomic Coordinates (Å) of $[WCl_4(PH_3)_4]^+$

D_{2d}

W	0.00000000	0.00000000	0.00000000
Cl	0.00000000	2.33051600	0.79368000
Cl	-2.33051600	0.00000000	-0.79368000
Cl	0.00000000	-2.33051600	0.79368000
Cl	2.33051600	0.00000000	-0.79368000
P	1.66399100	0.00000000	1.98795900
P	-1.66399100	0.00000000	1.98795900
P	0.00000000	1.66399100	-1.98795900
P	0.00000000	-1.66399100	-1.98795900
H	2.52524400	1.10514900	2.00504500
H	1.16681200	0.00000000	3.30712100
H	2.52524400	-1.10514900	2.00504500
H	-2.52524400	-1.10514900	2.00504500
H	-1.16681200	0.00000000	3.30712100
H	-2.52524400	1.10514900	2.00504500
H	1.10514900	2.52524400	-2.00504500
H	0.00000000	1.16681200	-3.30712100
H	-1.10514900	2.52524400	-2.00504500
H	-1.10514900	-2.52524400	-2.00504500
H	0.00000000	-1.16681200	-3.30712100
H	1.10514900	-2.52524400	-2.00504500

D_2

W	0.00000000	0.00000000	0.00000000
Cl	-0.79205300	1.49759100	-1.78763500
Cl	0.79205300	-1.49759100	-1.78763500
Cl	-0.79205300	-1.49759100	1.78763500
Cl	0.79205300	1.49759100	1.78763500
P	-1.97974200	1.35272400	0.96996400
P	-1.97974200	-1.35272400	-0.96996400
P	1.97974200	1.35272400	-0.96996400
P	1.97974200	-1.35272400	0.96996400
H	-1.80175500	2.73708100	0.85523900
H	-3.26019500	1.18070300	0.40687800
H	-2.22757500	1.15718500	2.33734800
H	-1.80175500	-2.73708100	-0.85523900
H	-3.26019500	-1.18070300	-0.40687800
H	-2.22757500	-1.15718500	-2.33734800
H	1.80175500	2.73708100	-0.85523900
H	3.26019500	1.18070300	-0.40687800
H	2.22757500	1.15718500	-2.33734800
H	1.80175500	-2.73708100	0.85523900
H	3.26019500	-1.18070300	0.40687800
H	2.22757500	-1.15718500	2.33734800

Table F.13. Optimised Gas-Phase Atomic Coordinates (Å) of $[WCl_4(dpe)_2]^{2+}$

S_4

W	0.00000000	0.00000000	0.00000000
Cl	0.00000000	2.29393700	0.68856500
Cl	-2.29393700	0.00000000	-0.68856500
Cl	0.00000000	-2.29393700	0.68856500
Cl	2.29393700	0.00000000	-0.68856500
P	1.54352800	0.08861900	2.12254200
P	-1.54352800	-0.08861900	2.12254200
P	-0.08861900	1.54352800	-2.12254200
P	0.08861900	-1.54352800	-2.12254200
H	2.51735900	1.09070700	2.01363600
H	2.28304600	-1.09844900	2.25308800
H	-2.28304600	1.09844900	2.25308800
H	-2.51735900	-1.09070700	2.01363600
H	-1.09070700	2.51735900	-2.01363600
H	1.09844900	2.28304600	-2.25308800
H	-1.09844900	-2.28304600	-2.25308800
H	1.09070700	-2.51735900	-2.01363600
C	0.66863900	0.37061500	3.72042400
C	-0.66863900	-0.37061500	3.72042400
H	0.53226000	1.44714500	3.82312000
H	1.31178400	0.04114500	4.53732000
H	-1.31178400	-0.04114500	4.53732000
H	-0.53226000	-1.44714500	3.82312000
C	-0.37061500	0.66863900	-3.72042400
C	0.37061500	-0.66863900	-3.72042400
H	-1.44714500	0.53226000	-3.82312000
H	-0.04114500	1.31178400	-4.53732000
H	0.04114500	-1.31178400	-4.53732000
H	1.44714500	-0.53226000	-3.82312000

D_2

W	0.00000000	0.00000000	0.00000000
Cl	0.68593700	1.59241000	1.65152200
Cl	-0.68593700	-1.59241000	1.65152200
Cl	0.68593700	-1.59241000	-1.65152200
Cl	-0.68593700	1.59241000	-1.65152200
P	2.12230400	1.16938600	-1.01111100
P	2.12230400	-1.16938600	1.01111100
P	-2.12230400	1.16938600	1.01111100
P	-2.12230400	-1.16938600	-1.01111100
C	3.71946300	0.73858400	-0.19798500
C	3.71946300	-0.73858400	0.19798500
C	-3.71946300	0.73858400	0.19798500
C	-3.71946300	-0.73858400	-0.19798500
H	2.01433300	2.56646400	-0.97678000
H	2.25193500	0.86668600	-2.37623200
H	2.25193500	-0.86668600	2.37623200
H	2.01433300	-2.56646400	0.97678000
H	3.82106000	1.38820600	0.67151100
H	4.53748000	0.97194500	-0.88065600
H	4.53748000	-0.97194500	0.88065600
H	3.82106000	-1.38820600	-0.67151100
H	-2.01433300	2.56646400	0.97678000
H	-2.25193500	0.86668600	2.37623200
H	-2.25193500	-0.86668600	-2.37623200
H	-2.01433300	-2.56646400	-0.97678000
H	-3.82106000	1.38820600	-0.67151100
H	-4.53748000	0.97194500	0.88065600
H	-4.53748000	-0.97194500	-0.88065600
H	-3.82106000	-1.38820600	0.67151100

Table F.14. Optimised Gas-Phase Atomic Coordinates (Å) of $[WCl_4(dpe)_2]^+$

S_4

W	0.00000000	0.00000000	0.00000000
Cl	0.00000000	2.35857000	0.73740700
Cl	-2.35857000	0.00000000	-0.73740700
Cl	0.00000000	-2.35857000	0.73740700
Cl	2.35857000	0.00000000	-0.73740700
P	1.54598800	0.09039700	2.06149200
P	-1.54598800	-0.09039700	2.06149200
P	-0.09039700	1.54598800	-2.06149200
P	0.09039700	-1.54598800	-2.06149200
H	2.51639000	1.09843600	1.99719200
H	2.30524100	-1.07861400	2.23349800
H	-2.30524100	1.07861400	2.23349800
H	-2.51639000	-1.09843600	1.99719200
H	-1.09843600	2.51639000	-1.99719200
H	1.07861400	2.30524100	-2.23349800
H	-1.07861400	-2.30524100	-2.23349800
H	1.09843600	-2.51639000	-1.99719200
C	0.67129000	0.36715200	3.66833100
C	-0.67129000	-0.36715200	3.66833100
H	0.53032000	1.44341200	3.76171200
H	1.30594600	0.04231800	4.49210000
H	-1.30594600	-0.04231800	4.49210000
H	-0.53032000	-1.44341200	3.76171200
C	-0.36715200	0.67129000	-3.66833100
C	0.36715200	-0.67129000	-3.66833100
H	-1.44341200	0.53032000	-3.76171200
H	-0.04231800	1.30594600	-4.49210000
H	0.04231800	-1.30594600	-4.49210000
H	1.44341200	-0.53032000	-3.76171200
H	1.44714500	-0.53226000	-3.82312000

D_2

W	0.00000000	0.00000000	0.00000000
Cl	0.73451500	1.58258500	1.74903800
Cl	-0.73451500	-1.58258500	1.74903800
Cl	0.73451500	-1.58258500	-1.74903800
Cl	-0.73451500	1.58258500	-1.74903800
P	2.05722700	1.20653300	-0.97224000
P	2.05722700	-1.20653300	0.97224000
P	-2.05722700	1.20653300	0.97224000
P	-2.05722700	-1.20653300	-0.97224000
C	3.66019600	0.74635200	-0.17150700
C	3.66019600	-0.74635200	0.17150700
C	-3.66019600	0.74635200	0.17150700
C	-3.66019600	-0.74635200	-0.17150700
H	1.98963600	2.60427800	-0.89598200
H	2.23704000	0.96678200	-2.34379400
H	2.23704000	-0.96678200	2.34379400
H	1.98963600	-2.60427800	0.89598200
H	3.74839700	1.35639000	0.72693200
H	4.48742200	1.00462500	-0.83189900
H	4.48742200	-1.00462500	0.83189900
H	3.74839700	-1.35639000	-0.72693200
H	-1.98963600	2.60427800	0.89598200
H	-2.23704000	0.96678200	2.34379400
H	-2.23704000	-0.96678200	-2.34379400
H	-1.98963600	-2.60427800	-0.89598200
H	-3.74839700	1.35639000	-0.72693200
H	-4.48742200	1.00462500	0.83189900
H	-4.48742200	-1.00462500	-0.83189900
H	-3.74839700	-1.35639000	0.72693200

Table F.15. Optimised Gas-Phase Atomic Coordinates (Å) of $[WCl_4(dpb)_2]^{2+}$

W	0.00000000	0.00000000	0.00000000
Cl	0.00000000	2.29454800	0.68106700
Cl	-2.29454800	0.00000000	-0.68106700
Cl	0.00000000	-2.29454800	0.68106700
Cl	2.29454800	0.00000000	-0.68106700
P	1.53797500	0.00000000	2.11382900
P	-1.53797500	0.00000000	2.11382900
P	0.00000000	1.53797500	-2.11382900
P	0.00000000	-1.53797500	-2.11382900
H	2.40756700	1.10187900	2.09449600
H	2.40756700	-1.10187900	2.09449600
H	-2.40756700	1.10187900	2.09449600
H	-2.40756700	-1.10187900	2.09449600
H	-1.10187900	2.40756700	-2.09449600
H	1.10187900	2.40756700	-2.09449600
H	-1.10187900	-2.40756700	-2.09449600
H	1.10187900	-2.40756700	-2.09449600
C	0.69886300	0.00000000	3.71592300
C	1.40178500	0.00000000	4.92038900
C	0.69621900	0.00000000	6.11753600
C	-0.69621900	0.00000000	6.11753600
C	-1.40178500	0.00000000	4.92038900
C	-0.69886300	0.00000000	3.71592300
H	2.48353100	0.00000000	4.93489600
H	1.23577500	0.00000000	7.05427200
H	-1.23577500	0.00000000	7.05427200
H	-2.48353100	0.00000000	4.93489600
C	0.00000000	0.69886300	-3.71592300
C	0.00000000	1.40178500	-4.92038900
C	0.00000000	0.69621900	-6.11753600
C	0.00000000	-0.69621900	-6.11753600
C	0.00000000	-1.40178500	-4.92038900
C	0.00000000	-0.69886300	-3.71592300
H	0.00000000	2.48353100	-4.93489600
H	0.00000000	1.23577500	-7.05427200
H	0.00000000	-1.23577500	-7.05427200
H	0.00000000	-2.48353100	-4.93489600

Table F.16. Optimised Gas-Phase Atomic Coordinates (Å) of $[WCl_4(dpb)_2]^+$

W	0.00000000	0.00000000	0.00000000
Cl	0.00000000	2.35868900	0.72351000
Cl	-2.35868900	0.00000000	-0.72351000
Cl	0.00000000	-2.35868900	0.72351000
Cl	2.35868900	0.00000000	-0.72351000
P	1.54103400	0.00000000	2.05587300
P	-1.54103400	0.00000000	2.05587300
P	0.00000000	1.54103400	-2.05587300
P	0.00000000	-1.54103400	-2.05587300
H	2.41564000	1.09682900	2.09155700
H	2.41564000	-1.09682900	2.09155700
H	-2.41564000	1.09682900	2.09155700
H	-2.41564000	-1.09682900	2.09155700
H	-1.09682900	2.41564000	-2.09155700
H	1.09682900	2.41564000	-2.09155700
H	-1.09682900	-2.41564000	-2.09155700
H	1.09682900	-2.41564000	-2.09155700
C	0.69833600	0.00000000	3.67057100
C	1.39656200	0.00000000	4.87808500
C	0.69613700	0.00000000	6.07638400
C	-0.69613700	0.00000000	6.07638400
C	-1.39656200	0.00000000	4.87808500
C	-0.69833600	0.00000000	3.67057100
H	2.47842900	0.00000000	4.88844000
H	1.23633600	0.00000000	7.01275900
H	-1.23633600	0.00000000	7.01275900
H	-2.47842900	0.00000000	4.88844000
C	0.00000000	0.69833600	-3.67057100
C	0.00000000	1.39656200	-4.87808500
C	0.00000000	0.69613700	-6.07638400
C	0.00000000	-0.69613700	-6.07638400
C	0.00000000	-1.39656200	-4.87808500
C	0.00000000	-0.69833600	-3.67057100
H	0.00000000	2.47842900	-4.88844000
H	0.00000000	1.23633600	-7.01275900
H	0.00000000	-1.23633600	-7.01275900
H	0.00000000	-2.47842900	-4.88844000

Table F.17. Optimised Gas-Phase Atomic Coordinates (Å) of $[TaCl_4(dpe)_2]^+$

S_4

Ta	0.00000000	0.00000000	0.00000000
Cl	0.00000000	2.33513400	0.71809000
Cl	-2.33513400	0.00000000	-0.71809000
Cl	0.00000000	-2.33513400	0.71809000
Cl	2.33513400	0.00000000	-0.71809000
P	1.56102600	0.08177300	2.19504100
P	-1.56102600	-0.08177300	2.19504100
P	-0.08177300	1.56102600	-2.19504100
P	0.08177300	-1.56102600	-2.19504100
H	2.55698300	1.07014300	2.16221600
H	2.31610700	-1.08549000	2.41029900
H	-2.31610700	1.08549000	2.41029900
H	-2.55698300	-1.07014300	2.16221600
H	-1.07014300	2.55698300	-2.16221600
H	1.08549000	2.31610700	-2.41029900
H	-1.08549000	-2.31610700	-2.41029900
H	1.07014300	-2.55698300	-2.16221600
C	0.66683200	0.37669200	3.78990600
C	-0.66683200	-0.37669200	3.78990600
H	0.50789700	1.45266500	3.86223500
H	1.29295900	0.07896600	4.62991300
H	-1.29295900	-0.07896600	4.62991300
H	-0.50789700	-1.45266500	3.86223500
C	-0.37669200	0.66683200	-3.78990600
C	0.37669200	-0.66683200	-3.78990600
H	-1.45266500	0.50789700	-3.86223500
H	-0.07896600	1.29295900	-4.62991300
H	0.07896600	-1.29295900	-4.62991300
H	1.45266500	-0.50789700	-3.86223500

D_2

Ta	0.00000000	0.00000000	0.00000000
Cl	0.71611000	1.62340500	1.67923900
Cl	-0.71611000	-1.62340500	1.67923900
Cl	0.71611000	-1.62340500	-1.67923900
Cl	-0.71611000	1.62340500	-1.67923900
P	2.19445100	1.17673700	-1.02861800
P	2.19445100	-1.17673700	1.02861800
P	-2.19445100	1.17673700	1.02861800
P	-2.19445100	-1.17673700	-1.02861800
C	3.78928500	0.74106800	-0.19412400
C	3.78928500	-0.74106800	0.19412400
C	-3.78928500	0.74106800	0.19412400
C	-3.78928500	-0.74106800	-0.19412400
H	2.16280600	2.58001900	-1.01754100
H	2.40755000	0.90073800	-2.39122200
H	2.40755000	-0.90073800	2.39122200
H	2.16280600	-2.58001900	1.01754100
H	3.86195600	1.37622000	0.68885400
H	4.62957100	0.98256600	-0.84371800
H	4.62957100	-0.98256600	0.84371800
H	3.86195600	-1.37622000	-0.68885400
H	-2.16280600	2.58001900	1.01754100
H	-2.40755000	0.90073800	2.39122200
H	-2.40755000	-0.90073800	-2.39122200
H	-2.16280600	-2.58001900	-1.01754100
H	-3.86195600	1.37622000	-0.68885400
H	-4.62957100	0.98256600	0.84371800
H	-4.62957100	-0.98256600	-0.84371800
H	-3.86195600	-1.37622000	0.68885400

Table F.18. Optimised Gas-Phase Atomic Coordinates (Å) of $TaCl_4(dpe)_2$

S_4

Ta	0.00000000	0.00000000	0.00000000
Cl	0.00000000	2.41888000	0.78084600
Cl	-2.41888000	0.00000000	-0.78084600
Cl	0.00000000	-2.41888000	0.78084600
Cl	2.41888000	0.00000000	-0.78084600
P	1.57080500	0.08764200	2.14607600
P	-1.57080500	-0.08764200	2.14607600
P	-0.08764200	1.57080500	-2.14607600
P	0.08764200	-1.57080500	-2.14607600
H	2.55932600	1.08560600	2.15708500
H	2.34566700	-1.05965300	2.40729600
H	-2.34566700	1.05965300	2.40729600
H	-2.55932600	-1.08560600	2.15708500
H	-1.08560600	2.55932600	-2.15708500
H	1.05965300	2.34566700	-2.40729600
H	-1.05965300	-2.34566700	-2.40729600
H	1.08560600	-2.55932600	-2.15708500
C	0.66697200	0.37815600	3.74641100
C	-0.66697200	-0.37815600	3.74641100
H	0.49840400	1.45348700	3.80498200
H	1.28568800	0.09108500	4.59597700
H	-1.28568800	-0.09108500	4.59597700
H	-0.49840400	-1.45348700	3.80498200
C	-0.37815600	0.66697200	-3.74641100
C	0.37815600	-0.66697200	-3.74641100
H	-1.45348700	0.49840400	-3.80498200
H	-0.09108500	1.28568800	-4.59597700
H	0.09108500	-1.28568800	-4.59597700
H	1.45348700	-0.49840400	-3.80498200

D_2

Ta	0.00000000	0.00000000	0.00000000
Cl	0.79907200	1.53695500	1.86202400
Cl	-0.79907200	-1.53695500	1.86202400
Cl	0.79907200	-1.53695500	-1.86202400
Cl	-0.79907200	1.53695500	-1.86202400
P	2.12894700	1.28175600	-0.92599900
P	2.12894700	-1.28175600	0.92599900
P	-2.12894700	1.28175600	0.92599900
P	-2.12894700	-1.28175600	-0.92599900
C	3.72149100	0.75825800	-0.11865400
C	3.72149100	-0.75825800	0.11865400
C	-3.72149100	0.75825800	0.11865400
C	-3.72149100	-0.75825800	-0.11865400
H	2.15529700	2.68324100	-0.80901200
H	2.39859400	1.12714400	-2.29950600
H	2.39859400	-1.12714400	2.29950600
H	2.15529700	-2.68324100	0.80901200
H	-2.15529700	2.68324100	0.80901200
H	-2.39859400	1.12714400	2.29950600
H	-2.39859400	-1.12714400	-2.29950600
H	-2.15529700	-2.68324100	-0.80901200
H	3.77501900	1.29557700	0.82795400
H	4.57484300	1.06177300	-0.72421300
H	4.57484300	-1.06177300	0.72421300
H	3.77501900	-1.29557700	-0.82795400
H	-3.77501900	1.29557700	-0.82795400
H	-4.57484300	1.06177300	0.72421300
H	-4.57484300	-1.06177300	-0.72421300
H	-3.77501900	-1.29557700	0.82795400